BRAIN-be 2.0

Belgian Research Action through Interdisciplinary Networks

2018-2023
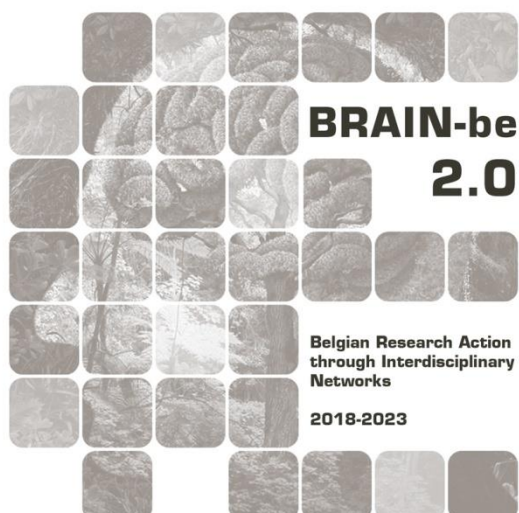
PALc

Pre-screening of anthropogenic lime carbonates for ^{14}C dating

WOJCIESZAK MARINE (KIK-IRPA) – FONTAINE LAURENT (KIK-IRPA) – HAYEN ROALD (KIK-IRPA) – ELSEN JAN (KUL) – GAIA LIGOVICH (KIK-IRPA) – BOUDIN MATHIEU (KIK-IRPA)

Pillar 2: Heritage science

belspo .be

NETWORK PROJECT

PALc

Pre-screening of anthropogenic lime carbonates for ^{14}C dating

Contract - B2/202/P2

FINAL REPORT

PROMOTORS: Boudin Mathieu (RICH-KIK-IRPA, Parc du Cinquantenaire, 1000 Brussels)
Elsen Jan (KU Leuven, Departement of Earth and Environmental Sciences, Celestijnenlaan 200E, 3001 Leuven-Heverlee)

AUTHORS: WOJCIESZAK MARINE (KIK-IRPA)

FONTAINE LAURENT (KIK-IRPA)

HAYEN ROALD (KIK-IRPA)

ELSEN JAN (KUL)

GAIA LIGOVICH (KIK-IRPA)

BOUDIN MATHIEU (KIK-IRPA)

Wojcieszak M., Fontaine L., Hayen R., Elsen J., G. Ligovich, Boudin M. *Pre-screening of anthropogenic lime carbonates for 14C dating*. Final Report. Brussels: Belgian Science Policy Office 2024 – 388 p. (BRAIN-be 2.0 - (Belgian Research Action through Interdisciplinary Networks))

TABLE OF CONTENTS

ABSTRACT

Context

Radiocarbon dating of lime mortars was first developed in the 1960s with very promising first results. However, in addition to the lime binder targeted for radiocarbon dating, different types of carbonates can be present in lime mortars because of their composition, their formation process and possible alteration. These contaminations can false the ^{14}C dating by increasing or decreasing its amount.

Objectives

PALc was developed because we need reference materials such as radiocarbon dated charcoal, a roof structure allowing dendrochronology or contextual information to confirm the radiocarbon dates obtained for a mortar sample. The objective of PALc was to combine the knowledge of mortar characterisation and radiocarbon dating to create a protocol for pre-selecting samples. This protocol will improve the reliability of mortar dating and will be time and cost saving.

Conclusions

The proposed protocol consists of combining complementary analytical techniques that each can give specific clues about the mortar composition and state of preservation. It starts with a macroscopic description of the sample, followed by FTIR analyses, cathodoluminescence and petrographic observations, and thermal analyses. The sample should be rejected for radiocarbon dating using stepwise acid hydrolysis if at any stage of the characterization it is suspected to fail in obtaining a reliable date.

Keywords

Anthropogenic lime mortars ; radiocarbon dating ; stepwise acid hydrolysis ; thin-section petrography ; cathodoluminescence ; FTIR ; TGA/DSC ; SEM-EDS ; XRD

1. INTRODUCTION

Lime mortars have been used to build elements of architecture since the Neolithic period or even to the end of the Palaeolithic (Ronen, Bentur, and Soroka 1991; Kingery, Vandiver, and Prickett 1988; Karkanas 2007; Friesem et al. 2019). They are prepared by the calcination process of geological limestone containing calcium carbonates ($CaCO_3$) at around 900°C; this results to the release of carbon dioxide and the formation of quicklime (CaO); the latter is mixed with water to obtain slaked lime [$Ca(OH)_2$]; and finally the slaked lime is blended with water, aggregates and possible admixtures (such as sand, crushed rocks from sedimentary or pyroclastic deposits, pottery, organic matter, etc.) to form the mortar. During the hardening process, carbonation of the slaked lime will form the lime binder ($CaCO_3$) by the incorporation of atmospheric carbon dioxide. This carbon reflects the moment of mortar formation and allows, in theory, radiocarbon dating. Because of the complexity of these composite and open system materials, several components and phenomena can decrease or increase the ^{14}C content of the samples. These carbonate contaminations are: unburned or underburned limestone used for lime production, fossil carbonates such as shell fragments or limestone grains in calcareous sands, and reused mortar crushed and used as aggregates. Their presence results in a lower ^{14}C/^{12}C ratio which generates an older date, as they are radiocarbon free. A second category of carbonates are secondary carbonate deposits, which can cause a more recent date to be obtained by increasing the ^{14}C/^{12}C ratio but can also incorporate older carbon. A final parameter to be taken into account is the hardening time of the mortars. This varies according to different parameters, in particular according to the distance from the surface (T. S. Daugbjerg et al. 2021). Some mortars may

take several decades or even hundreds of years to fully carbonate. Since the discovery of lime mortars radiocarbon dating in the 1960s by French researchers Jacques Labeyrie and Georgette Delibrias (Labeyrie and Délibrias 1964), the results obtained are mixed.

2. STATE OF THE ART AND OBJECTIVES

Intercomparison between laboratories give consistent results, independently of the technique used, some samples give consistent dates and others a range of dates making them inappropriate for radiocarbon dating using the current common methods available (Hajdas et al. 2017; Hayen et al. 2017). These methods consist of different particle separation techniques, sizes, and reaction processes (Folk and Valastro 1976; Lindroos et al. 2007; Heinemeier et al. 2010; Marzaioli et al. 2011; Luis Angel Ortega et al. 2012; Michalska and Mrozek-Wysocka 2020; Michalska, Czernik, and Goslar 2017; Nonni et al. 2018; Michalska 2019; Sironić et al. 2023); or sequential dissolution based on the fact that the reaction time between carbonates and acid to extract the CO_2 varies depending on the crystal sizes (Lindroos et al. 2007; Thomas Schrøder Daugbjerg et al. 2021; Michalska and Mrozek-Wysocka 2020; M. Van Strydonck et al. 2015); or thermal decomposition (Labeyrie and Délibrias 1964; Toffolo, Regev, et al. 2020; Gerard Thomas Barrett et al. 2021; Gerard T. Barrett et al. 2023; Thomas Schrøder Daugbjerg et al. 2021) because the finer the carbonate crystals are, the faster they will decomposed through heating; there is also the isotope fractionation corrections of bulk mortar dating which determine a sample's content of dead carbon from aggregate and correct the dating result accordingly (M. J. Van Strydonck et al. 1992); and lastly, the extraction of lime inclusion (Lindroos et al. 2018; G. Pesce et al. 2009; G. L. Pesce et al. 2012; Gerard T. Barrett et al. 2023) but this can only be applied when the inclusion are large enough (~20 mg).

Numerous characterisation methods have been implemented to characterise these complex and heterogeneous materials (Bakolas et al. 1998; Bakolas, Aggelakopoulou, and Moropoulou 2008; Casadio, Chiari, and Simon 2005; Degryse, Elsen, and Waelkens 2002; Elsen 2006; Maravelaki-Kalaitzaki, Bakolas, and Moropoulou 2003; Middendorf et al. 2000; Morillas et al. 2019; A. Moropoulou et al. 2002; L. A. Ortega et al. 2008; Paama et al. 1998; Toffolo, Ricci, et al. 2020). Depending on the technique used, different information can be extracted. Petrographic analysis on resin-impregnated thin sections allows to retrieve information about the mortar composition, formation and alteration (Degryse, Elsen, and Waelkens 2002; Lindroos et al. 2007; Pecchioni, Fratini, and Cantisani 2014; Hughes and Cuthbert 2000; Elsen 2006; Nawrocka et al. 2005; Weber, Köberle, and Pintér 2013). Cathodoluminescence is a complementary method to petrographic analyses to detect and confirm the presence of the different types of carbonates (Toffolo, Ricci, et al. 2020; Heinemeier et al. 2010; Lindroos et al. 2007; Luis Angel Ortega et al. 2012; Al-Bashaireh 2013; Addis et al. 2019; Ponce-Antón et al. 2020). Scanning electron microscopy coupled with energy-dispersive X-ray spectroscopy (SEM-EDX) can help confirming the presence and the relative quantity of some elements (Hayen et al. 2016). Raman micro-spectroscopy is also a complementary technique to characterise the mineralogical composition in addition to the detection of amorphous phases and salts (Morillas et al. 2019). Thermogravimetric analysis (TGA) coupled with differential scanning calorimetry (DSC) also gives information about the anthropogenic lime carbonate composition (Hayen et al. 2016). Fourier transform Infrared spectroscopy (FTIR) can be used to determine the global composition of the sample (compounds present in higher concentration) and determine their degree of disorder using the grinding curve method (Regev et al. 2010; Toffolo et al. 2019). Other techniques can also be used but are not developed here since they are not part of the project. The two most common

characterisation methods used in mortar dating studies are thin-section petrography and cathodoluminescence microscopy (T. S. Daugbjerg et al. 2021).

Currently, only a few ^{14}C laboratories are dating lime mortars. All types are processed and the results are compared with the presumed historical dates to see if they could be compatible. This procedure is time and cost consuming since the procedure for CO_2 extraction, the graphitisation and the radiocarbon determination are laborious. The main objective of PALc was to verify the reliability of the radiocarbon dating anthropogenic lime carbonates by developing a pre-screening method. To achieve this goal, a careful characterisation of various types of samples was linked to the way radiocarbon results match the historical dates provided by the archaeologists/historians or historical context and the ^{14}C date obtained on organic materials present inside the mortar. The analytical methods used were complementary for obtaining a wide range of parameters characteristic of each samples. A characterisation protocol was set up to determine if a sample is suitable for dating or not using the stepwise acid hydrolysis. This pre-screening protocol will be implemented to be the most concise and rapid by selecting the more appropriate tools and parameters determinant for a successful dating of the samples. Eventually, this protocol will result in cost and time saving by avoiding to radiocarbon date inappropriate samples.

3. METHODOLOGY

3.1 Materials

In total, 48 mortar samples from 21 sites in Belgium and abroad were fully characterised. Some samples and/or sites initially included in the project were further excluded because of various reasons: the quantity of sample provided was too low to perform all the needed analysis, not enough context information was provided, the sample didn't contain enough carbon, some providers could not respect their commitments or for one site the mortars were not lime-based. The 21 sites are mainly located in Belgium (Saint Martin's church in Rutten (Tongeren), Roman wall in Tongeren, Hertogensite in Leuven, Holy Cross Parish Church in Korbeek-Lo, Residency of the count of Flanders in Brugge, Saint Agatha church in Huldenberg, Ten Bogaerde in Koksijde, Saint Martin's basilica in Halle, Het Steen in Antwerpen, Notre-Dame of Mousty church in Ottignies, Coudenberg Palace in Brussels, Saint Eustache church in Zichem, Archaeological crypt of the Sainte-Gertrude collegiate in Nivelles, Abbatial church Sainte-Marie in Floreffe, Burchtmuur in Antwerp, Castle of Horst in Holsbeek (Figure 1, left) and Park Abbey (Abdij van Park) in Leuven but also in Turkey (Sagalossos), France (Aléria, Figure 1, right) and Italia (Ostia). One to seven samples were analysed per site. The context of each site is described in the Annexes section of this report. The corpus of samples was set to obtain a variety of mortar type, composition, state and temporality.

Figure 1: Examples of sites included in the PALc project: (left) the medieval tower of Castle of Horst in Holsbeek (Belgium) and (right) the Roman site of Aleria in Corsica (France).

Three categories of samples were planned for analysis:

- Samples from the 14C laboratory, some of which had already been radiocarbon dated before the project. Often, charcoal or other organic materials were dated to obtain a reference date. In some cases, what was believed to be charcoal was dated, and the result was much older than expected, suggesting that the material might have been pieces of coal or bottom ash.

- Samples that had been partially characterized by the monuments laboratory but had not been radiocarbon dated.

- New samples that had neither been dated nor characterized before the start of the project.

3.2 Methods

When possible, the **sampling** was carried on by members of the PALc team. It was performed following as much as possible the advice from T. S. Daugbjerg et al. 2021. First, it is important to defining the question (dating the construction, renovations, *etc*.) and have a thorough knowledge of the site. In situ extraction is preferred, the samples should not be scattered on the ground in order to obtain a secure context. It is preferable to sample above ground level on standing and sheltered building units with a clean surface. It should be avoided sampling deep into the mortar (to prevent delayed hardening). The tools used should preferably be a hammer and a chisel (Figure 2). Power tools like drilling should be avoided because they can be source of contamination. Phenolphthalein tests could be performed to ensure the full carbonation of the sample. We sampled around 50 to 100 g to ensure have enough quantity to perform all the analyses. Finally, multiple samples (3) should be collected and the type of mortar should be assessed.

Figure 2: Example of sampling in the Abbatial church Sainte-Marie in Floreffe (Belgium).

A meticulous characterisation of each sample was then carried out in order to understand their compositions. First, the samples were weighted. **Macroscopic descriptions** were made by describing their colours and the different types of inclusions present. We set up a protocol which consisted first of describing the overall colour of the sample with a general colour term and with the help of the Munsell soil colour charts. Then, the inclusions present in the mortar were listed with their sizes and colours. A black friable inclusion is most probably made of charcoal. On the other hand, if it has a high hardness, it may be bottom ash or coal. Grey inclusions are siliceous aggregates if they do not react with hydrochloric acid or limestone grains for the aggregates or even the unburned or underburned limestone pieces from the carbonate rock used to produce the lime binder if ann effervescent reaction occurs so if there is formation of tiny bubbles at the surface due to the release of CO_2. A red inclusion will be attributed to terracotta if it is rather hard and angular; to a sandy-clay agglomerate if it is rather soft or friable and more rounded; or to a siliceous rock if it shows a high hardness. White inclusions are attributed to lime lumps, pieces of limestone or secondary carbonates. The specularity of the samples is also recorded, so whether shinny inclusions can be seen with the naked eye by tilting the sample relative to the light source. These are usually fairly coarse grains of quartz, flakes of mica or well developed crystals of calcite. The samples were also photographed with their characteristic features.

Then **Infrared measurements (FTIR)** were performed on the different macroscopic features observed during the macroscopic descriptions. For this, we used a Bruker vertex 70 which works in transmission with potassium bromide pellets. Each inclusion observed macroscopically was analysed in addition to the homogeneous binder. The spectral range was set from 4000-370 cm^{-1} with a 4 cm^{-1} spectral resolution and 64 scans. A H_2O/CO_2 compensation with OPUS software was applied to the spectra. For some of the samples, FTIR analyses were also performed on the sieved powder obtained after crushing the samples with particles having a size lower than 75 µm. The grinding curve method (Regev et al. 2010; Toffolo et al. 2019; Poduska et al. 2011; Suzuki et al. 2011; Toffolo 2021) was also tested by grinding the same pellet several times until the ratio v_2/v_4 was stabilized. For the data treatment, a linear baseline was drawn between the closest minima on either side of the measured peak. The intensity of the bands v_2 (~874 cm^{-1}), v_3 (~1420 cm^{-1}) & v_4 (~713 cm^{-1}) were collected and the v_2 and v_4 heights are normalized to a v_3 intensity of 1000. Finally, a graph was drawn with v_2 as a function of v_4.

The thin section were prepared at KIK-IRPA with Logitech PM5 Lapper, a width of ± 30 µm, an area ~ 2 x 3 cm^2. They were not covered to allow for cathodoluminescence observations. The observations were performed with a polarizing microscope (ZEISS, Axioplan) equiped with a high resolution digital camera (DeltaPix Invenio 5DII) and the JMicroVision software for image analyses. For the **petrographic observations** of the mortar thin sections, we set up different categories and subcategories (see Table 1). For the binder, we thought about defining the type using UV light and the ability of the resin to be fluorescent. It seems that air hardening lime binders show a higher fluorescence for the significant amount of micropores present, while with increasing hydraulicity, the fluorescence decreases due to the lower amount of porosity (Pecchioni, Fratini, and Cantisani 2014). For the texture, we defined if it is micritic (most common - the individual grains cannot be distinguished from each other, < 4 µm) or micro-sparitic (distinguishable individual grains, 4-10 µm). Also the state of the lumps so if they are completely burned, underburned/incompletely burned (presence of structures coming from the initial limestone in the centre), unburned (initial limestone) or overburned with their average and maximum sizes and frequency. For the aggregates, we identified the grain size (very fine < 125 µm, fine 125-250 µm, medium 250-500 µm, coarse 0.5-1 mm or very coarse 1-2 mm), mineralogy (pure siliceous sand, siliceous sand with few limestone grains/bioclasts, calcareous sand with few quartz grains, crushed ceramics, pozzolanic/volcanic scoria) and general shape (angular, subangular/subrounded, rounded). The next category is the mortar appearance, it comprises the homogeneity (relatively homogeneous, relatively heterogeneous, highly heterogeneous), microporosity (high, medium, low) and the pore appearance (cracks, rounded, irregular/highly, sometimes or not connected/cracks orientation/cracks average length). And we also wrote down if there is some types of admixtures (charcoal, coal, straw, wood, hair, grains, seeds) and alterations (cracks, dissolution, secondary carbonates, gypsum, salts).

Binder	**Texture**	micritic (<4 µm), micro-sparitic (4-10 µm)
	Lump state	completely burned, underburned/incompletely burned, unburned, overburned
	Lump size	average size & maximum size
	Lump frequency	numerous, medium, few
Aggregate	**Granulometry**	very fine < 125 µm, fine 125-250 µm, medium 250-500 µm, coarse 0.5-1 mm or very coarse 1-2 mm
	Mineralogy	pure siliceous sand, siliceous sand with few limestone grains/bioclasts, calcareous sand with few quartz grains, crushed white marble, crushed ceramics, pozzolanic scoria
	Shape	angular, subangular/subrounded, rounded
B/A ratio	**Homogeneity**	relatively homogeneous, relatively heterogeneous, highly heterogeneous (x25)
	Macroporosity	high, medium, low
	Pore appearance	crack, rounded, irregular / highly, sometimes or not connected / cracks orientation / cracks average length
Admixtures	**Type**	charcoal, coal, straw, wood, hair, grains, seeds, *etc.*
Alteration	**Type**	cracks, dissolution, secondary carbonates (recrystallisation, secondary carbonate deposition, dissolution/precipitation), gypsum, salts

Table 1: Main characteristics extracted from the petrographic thin section observations that are valuable to identify for the radiocarbon dating of a lime mortar.

The **cathodoluminescence** observations and photographs were performed both on uncovered thin-sections and on powdered samples with a particle size < 75 µm that are used for radiocarbon dating. The photographs were acquired with an in-house cold-cathode luminescence microscope available at KU Leuven and called Technosyn model 8200, Mark II (Figure 3). The chamber was maintained at ~0.05 Torr vacuum and the beam width measured 5 mm. The current was kept between 600 to 800 µA to obtain around 3 kV electron beam. The images were taken at 40× magnification with a ProgRes® C10plus camera.
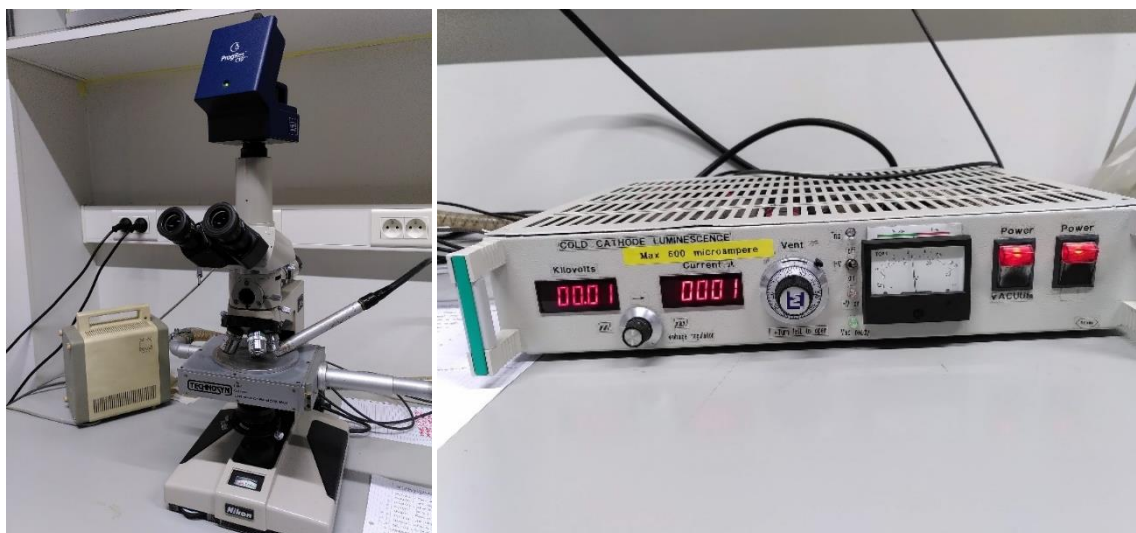
Figure 3: Cathodoluminescence equipment from KU Leuven.

For the determination of the **binder:aggregate ratio**, around 2 g of sample was heated up at 1200 °C to obtained the weight calcined and calculate the percentage of insoluble residue. Then calculation were made using a bulk density of 1.35 kg/dm^3 as a default value for the sand and 0.575 kg/dm^3 as a default value for the lime to obtain the binder:aggregate ratio. If a sample was dissolved or if the aggregate contained a calcareous fraction, the result could be biased.

The **thermal analyses** of the various sources of lime carbonate were performed on a Netzsch STA 449 F3 Jupiter® coupled with TGA-IR (Bruker) for evolved gas analysis, enabling the study of the evolution of weight loss (TG, thermogravimetry) and heat exchange with the environment (DSC, differential scanning calorimetry) upon heating up to a temperature of 1200°C. The thermal analytical equipment is available at KIK-IRPA. The apparent hydraulicity indices (aHI) are determined based on the ratio of the weight loss between 200 and ca. 650°C (usually attributed to water loss from calcium-silicate-hydrate-phases) to the total weight loss between 200 and 800°C (combining both the water loss from calcium-silicate-hydrate-phases and the carbon dioxide loss from calcium carbonate). The temperature limit at ca. 650°C is determined by the onset of the weight loss from the calcium carbonate. For the aHI limits, we considered an air hardening lime mortar when the HI is lower than 10 %, the lime binder is slightly hydraulic between 10.0 and 17,5 %, moderately hydraulic from 17.5 to 25 %, strongly hydraulic when the aHI value reaches 25.0 to 35.0 %, and it is very strongly hydraulic or a cement when the value is over 35.0 %.

Raman measurements were carried on with a Renishaw in Via Raman micro-spectrometer and a wavelength of 785 nm. The power of the laser was kept at 1 % in order to avoid any thermal photodecomposition. A 1200 tt/mm gratting provided a spectral resolution of ~1 cm^{-1} and the spectra were acquired between 80-3200 cm^{-1}. The time of recording depended on the point analysed. Both x5 and x50 LWD objectives were used. The areas analysed were chosen depending on the macro- and microscopic colours observed.

The instrument used to perform the **X-ray powder diffraction measurements (XRD)** was a Bruker D8 advance equipped with a two-circle goniometer with independent stepper motors, optical sensors for the determination of Theta and 2Theta, a copper anticathode and a LYNXEYE silicon strip detector suitable for diffraction experiments using energies between 2 and 30 KeV. For the analyses,

a fragment of mortar was reduced into fine powder with an agate mortar and pestle. The powder was set in the sample holder using a glass slide to obtain a flat surface.

A Carl Zeiss EVO 15 LS was operated to run the **SEM-EDX** observations and measurements. A LaB6 filament was set at 15 kV and 30 Pa with a working distance of 8.5 mm.

The method used at KIK-IRPA to **extract the CO$_2$** from the mortars before radiocarbon dating consists of a stepwise acid hydrolysis which is performed by keeping a powdered sample in suspension using a magnetic stirrer and gradually adding hydrochloric acid to gather different fractions of CO$_2$ (Figure 4).
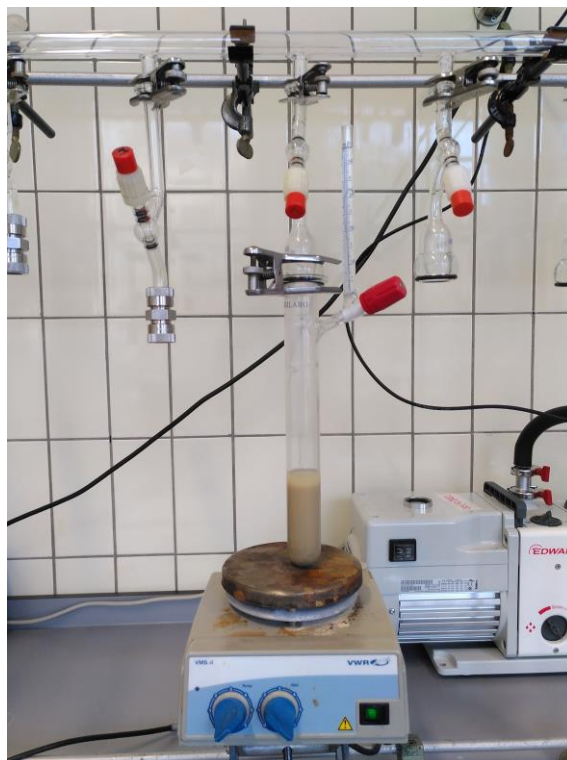
Figure 4: Set up for the CO$_2$ mortar extraction.

The lime binder is believed to react faster than geological limestone because it is finer grained and microporous, and hence presents a larger specific surface area for acid reaction. At KIK-IRPA, 7 to 12 CO$_2$ fractions are gathered and dated; they include the first individual 4 %, the next 6 %, and the following 10, 30 and 50 %. Depending on the shape of the curve obtained for the ^{14}C age as a function of the CO$_2$ percentage, a consensus ^{14}C age value is obtained using the best mathematical fit and the average of the first fractions. For this, the more appropriate pieces of the mortar samples were carefully selected and if necessary, a metallic brush or a scalpel was used to remove any soil particles, paint layer or other residues possibly present on the pieces surface. The mortar pieces were then gently crushed in a ceramic mortar making successive impacts with a metallic pestle. During the process, care was taken to take hard fragments or fragments identified as aggregates out and to apply a relatively soft pression with the pestle. Next, the crushed sample was separated with a series of 500, 250, 125, 100, and 75 µm sieves. The fraction of particles with a size < 75 µm was used for the CO$_2$ extraction because the finer the fraction is, the less sand grains are present (including calcareous ones that could influence the dating results) and it provides sufficient material for extracting 4000 mbar of CO$_2$. Beforehand, to evaluate the quantity of sample needed for CO$_2$ extraction, the carbon percentage

was measured using around 50 mg of the fraction < 75 µm under vacuum with 5 ml of orthophosphoric acid (H_3PO_4) in excess for 30 min. The volume of CO_2 released allowed determining the quantity of carbon present and then the quantity of sample needed to obtain 40 mbar for the first fraction. A statistic analysis on the different CO_2 fractions was performed. Instead of analyzing one single regression curve based the average values of the different CO_2 fractions, a series of regression curves was determined individually based on a random sample from each of the CO_2 fractions according to a Gaussian distribution based on their mean value and standard deviation. For each regression curve the value for the CO_2 fraction equal to zero was determined as the estimated age of the sample. The statistical analysis of the series of regression curves finally determined a mean value and standard deviation for the estimated age, which was defined by both the statistical variation on the measured CO_2 fractions and the selected regression curve. Different regression curves were evaluated including polynomial regression curves of order n (in practice limited to the 4th order), a linear regression curve, a logarithmic regression curve and a regression curve of the form $x / (1 + |x|)$. The logarithmic regression curve has the form $a + b*log(x + c)$, where a and c respectively perform a vertical and horizontal shift on the standard logarithmic function while the value b is a scaling factor. The added parameter c (boundary c > 0), makes a horizontal shift of the logarithmic curve to the left, such that a value at x = 0 is defined and a value for the estimated age can be obtained. The function of the form $x / (1 + |x|)$ is scaled in a comparable fashion, and is defined as $a*x / (1 + |b*x|) + c$. The parameters a and b are responsible for the vertical and horizontal scaling, the parameter c indicates a vertical shift. The original curve intersects the y-axis, so there is no need for a horizontal shift. This curve looks similar to the logarithmic curve, but has the advantage of not going to infinity at x = 0.

The **pure lime inclusion method** is used in combination when possible. For this, the mortar sample needs to contain lime lumps that are large enough to extract the necessary quantity of ^{14}C for dating. It should be around 1 cm and/or 20 mg. The lumps were mechanically extracted from the mortar using metallic tools and reduced into powder with a ceramic mortar and a pestle. The powder was then introduced in one part of a two fingers tube with acid orthophosphoric acid at 14.8 M in the other part. After, putting the tube under vacuum, the acid and the powder were mixed to extract the CO_2. For this method, only one fraction is dated.

When possible, organic matter found inside the mortar (charcoal, wood pieces, straw, *etc.*) was also dated using the protocol followed at the ^{14}C laboratory of KIK-IRPA (Wojcieszak et al. 2020).

The **graphitization** was performed on a manual vacuum line for the mineral samples and on the automated one for the organic samples (Wojcieszak et al. 2020; M. Van Strydonck and Van der Borg 1990; Wacker, Němec, and Bourquin 2010). The **radiocarbon determination** was done with a MIni CArbon DAting System (MICADAS) available at KIK-IRPA (Synal, Stocker, and Suter 2007; Boudin et al. 2015). Finally, the calibrated dates were determined with the OxCal 4.4 program (Bronk Ramsey 2009) using the IntCal20 northern hemisphere radiocarbon age calibration curve (Reimer et al. 2020).

## 4. SCIENTIFIC RESULTS AND RECOMMENDATIONS
4.1 Terminology
When working on the literature survey, we realized that the vocabulary used varied depending on the field of study dominant for an article or a book. The definition of a word or a concept could be ambiguous or confusing when applied to radiocarbon dating of ancient mortars. We decided to try to provide a comprehensive view of lime mortar components (with petrographic and

cathodoluminescence photomicrographs) and their potential influence on radiocarbon dating using stepwise acid hydrolysis (Wojcieszak et al. 2024). For this, we created a diagram summarizing the different components present in lime mortars and the phenomena than can possibly occur with the influence on the radiocarbon content when using an acid reaction to extract the CO_2 (Figure 5). The six primary categories defined are: i) aggregate; ii) binder; iii) binder lime inclusions; iv) organic matter ; v) weathering carbonates; and vi) delayed hardening.

The **inorganic aggregates** were divided into two categories: inert (they are not part of the chemical reaction taking place for the mortar production process) and reactive aggregates. The inert ones won't have any influence on radiocarbon dating if they are made of siliceous aggregates (e.g.: siliceous sands, non-reactive ceramics fragments or slag) but they can decrease the $^{14}C/^{12}C$ ratio if they contain calcareous inclusions (such as calcareous sand, crushed white marble, shell fragments, crushed limestone or crushed reused mortar fragments). Reactive aggregates in opposition to inert that will impart hydraulic properties to the lime binder. The hardening of the mortar happens then both through carbonation of calcium hydroxide and through reaction of calcium hydroxide with hydraulicizing components which forms hydrated calcium silicates and hydrated calcium aluminates. They are called pozzolanic or latent hydraulic materials and are made of pyroclastic rocks (pozzolana, volcanic tuffs), diatomaceous earths, powdered ceramics (the mortars are often called 'cocciopesto' or 'terrazzetto') or calcined clay (metakaolin). When they hardened under water, hydraulic mortars didn't interact with atmospheric CO_2 making them unsuitable for radiocarbon dating. If the hardening of hydraulic mortars happened in the presence of air, radiocarbon dating can also be problematic since the reaction can happen through a long period of time which can increase the $^{14}C/^{12}C$ ratio.

The second important component in historic lime mortars is the **binder**. If its hydraulicity doesn't come from the inorganic reactive aggregate, it can come from the calcined limestone used. Impure limestone such as marly or siliceous limestone naturally contain compounds that will induce hydraulic properties in the lime binder, but this requires high firing temperatures that were rarely reached before the Industrial Revolution. The same issues as listed before can be cited here, and the radiocarbon content can also be higher than expected because the hardening time is slow. The other type of binder is non-hydraulic or air hardening binder. This type of binder is more porous compared to hydraulic binders and also more homogeneous. In general, they give better results for radiocarbon dating unless they contain calcareous aggregate, or unburned limestone inclusions; they can also go through weathering processes or delayed hardening.
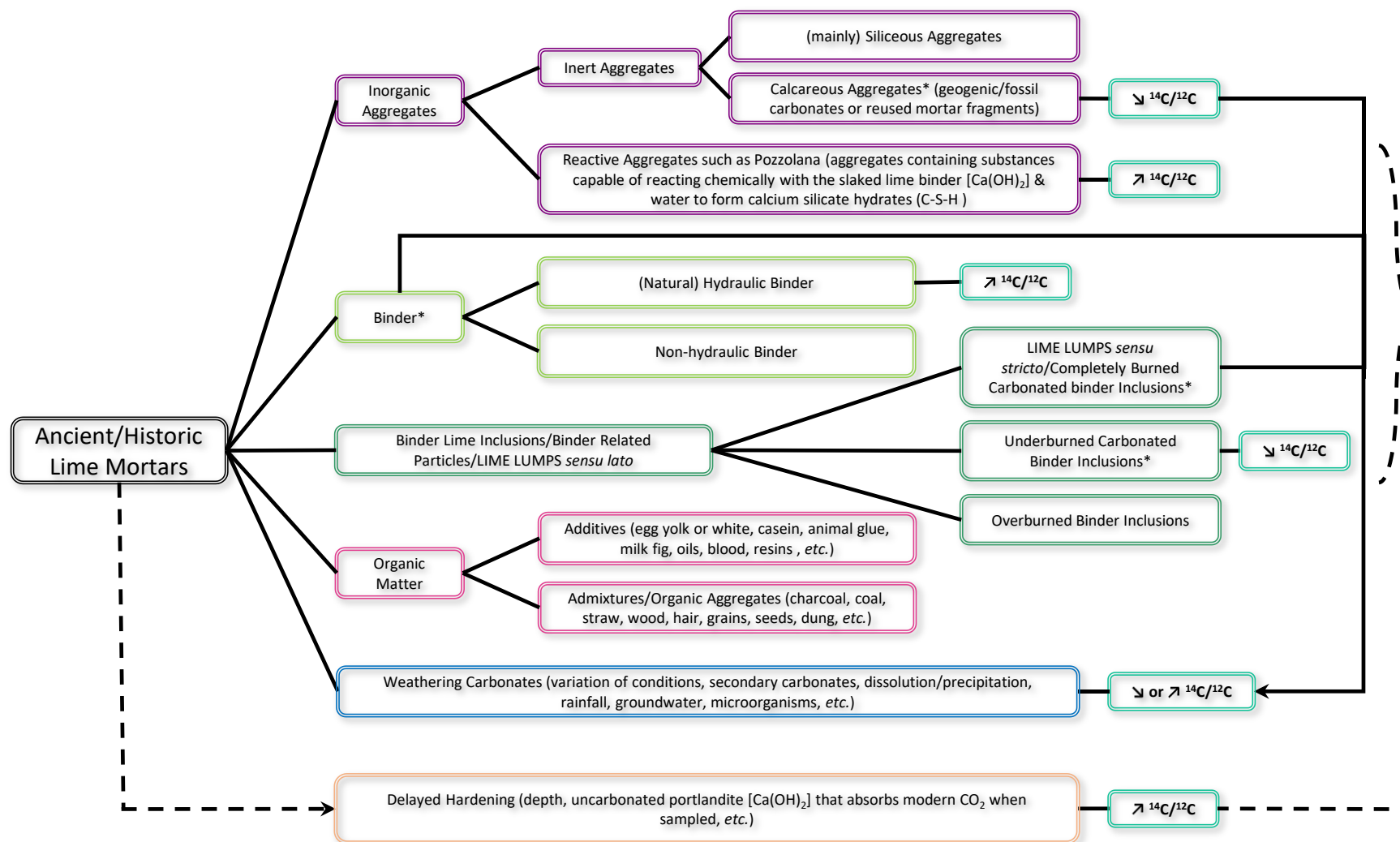
* possible recrystallisation (aragonite/vaterite → calcite) – no influence on ^{14}C/^{12}C

Figure 5: Mortar constituents and potential phenomena occurring with their possible influence on lime binder radiocarbon dating using stepwise acid hydrolysis.

The category '**Binder Lime Inclusions/Binder Related Particles/LIME LUMPS *senso lato*'** is divided in three subcategories. First, there are 'LIME LUMPS *senso stricto*' which are completely burned carbonated binder Inclusions. If they were not subjected to weathering process or delayed hardening, and also big enough, they are good candidates for radiocarbon dating using the pure lime lump technique. Then, there are the underburned carbonated binder inclusions, that can induce a decrease of the $^{14}C/^{12}C$ ratio since they still contain fossil carbon. The last binder related particles are overburned carbonated binder inclusions, these won't contain any carbonates and then won't have an influence for radiocarbon dating.

The next component possibly present in lime mortars is **organic matter**, these won't interfere for dating using acid reaction but can have an impact when thermal decomposition is used to extract the CO_2. It can be added as additive such as egg yolk or white, casein, animal glue, milk fig, oils, blood, resins. A recent study performed by Korean researcher show that the addition of perilla oil increases the resistance to freeze-thaw (Kang and Kang 2022). Organic matter can also be added as admixtures or organic aggregates such as charcoal, coal, straw, wood, hair, grains, seeds, dung, *etc.* Some of these can be precious for radiocarbon dating. For wood and coal, the old wood effect should be considered but they can at least give a terminus post quem.

The next categories includes carbonates resulting from **weathering processes**. In the literature about radiocarbon dating of historic lime mortars, many terms and concepts are used to talk about weathering carbonates. They often include recrystallisation, diagenesis, redeposit, dissolution, rainfall, ambient water, neo-genesis carbonates, ground water, and more (Carmine et al. 2015; Toffolo, Regev, et al. 2020; T. S. Daugbjerg et al. 2021). We consider recrystallisation, metastable polymorphs of carbonates which were already present within the structure of the mortar that spontaneously recrystallise in a more stable form or to the possible transformation of originally micritic binder matrix (calcite crystals < 4 μm) in larger uniform in size and equant calcite crystals up to 10 μm (microsparite). In this sense, recrystallisation should not have any impact on the ^{14}C content since no new source of carbon is incorporated within the matrix. In opposition, secondary carbonates deposits would form because of variations of the initial conditions and can possibly affect the amount of radiocarbon by either incorporating younger or older carbon. This can have an impact on the all the carbonates present within the mortar so the calcareous aggregates, the binder and the binder related particles that contain carbonates. Recrystallisation can happen within the calcareous aggregates, the binder, the completely burned and incompletely burned carbonates binder inclusions, and it won't have an influence on the radiocarbon content.

The last parameter to take into account is the **delayed hardening**. This can happen because of distance from the surface, some samples can take hundreds of years before completely carbonate (Hajdas et al. 2017) or when a mortar didn't fully carbonate when sampled, modern carbon can be incorporated. This phenomena can impact the same components as for the weathering processes and also be related to the reactive aggregates.

4.2 Results per method

In this section of the report, the number of sample analysed with each method are described as well as the general results that were retrieved.

In total, 69 samples were subjected to the **macroscopic descriptions**. As explained in the "3. METHODOLOGY/3.1 Material" section, some samples were removed from the corpus for diverse

reasons. From these 69 samples, most of them appear beige (83%) with few light beige/white (9%), pink (3%) and beige/grey (4%). According to the Munsell soil colour charts, the colours of the samples are pale yellow (52%), very pale brown (30%), white (13%) and pink (4%). All samples contain white inclusions ascribed to lime lumps except the sample from Park Abbey that is very white and for which it is not possible to distinguish them from the binder. Black and soft inclusions assimilated to charcoal were observed for 36 % of the samples and 22% contained black and hard inclusions that could be bottom ashes or coal. Around 58% of the samples exhibited grey inclusions and 52% red ones. From all the samples, one third showed specularity.

For the **FTIR spectroscopy** measurements, 69 samples were analysed with a total of around 322 spectra acquired and treated. As expected, all the samples contained calcite and silicates including quartz. Around 90 % of them included aragonite, for the other ones, it might be present in too low quantity to be detected, or it dissolved, or it recrystallized into calcite. More than 70 % included clay minerals and around one quarter showed the presence of amorphous carbon and organic matter. Nitrates were also often present (36%) and sometimes haematite, gypsum, cellulose and apatite. Few vibrational bands stayed unidentified. For the grinding curve method, from our knowledge, it has been applied on shells, ashes, plasters, natural calcite and these different materials could clearly be distinguished from each other (Regev et al. 2010; Toffolo et al. 2019). Some articles mentioned that it can also be applied on mortars so we tried it on 11 samples and three limestone samples from Belgium (Figure 6). As expected, we can clearly observe a separation between the limestones and the mortars. For the Gobertange stone, the two types of carbonates are present within the stone and have a different order. The results seems reproducible (some samples were processed twice) and samples from each site show a similar order (the plots are often grouped together).
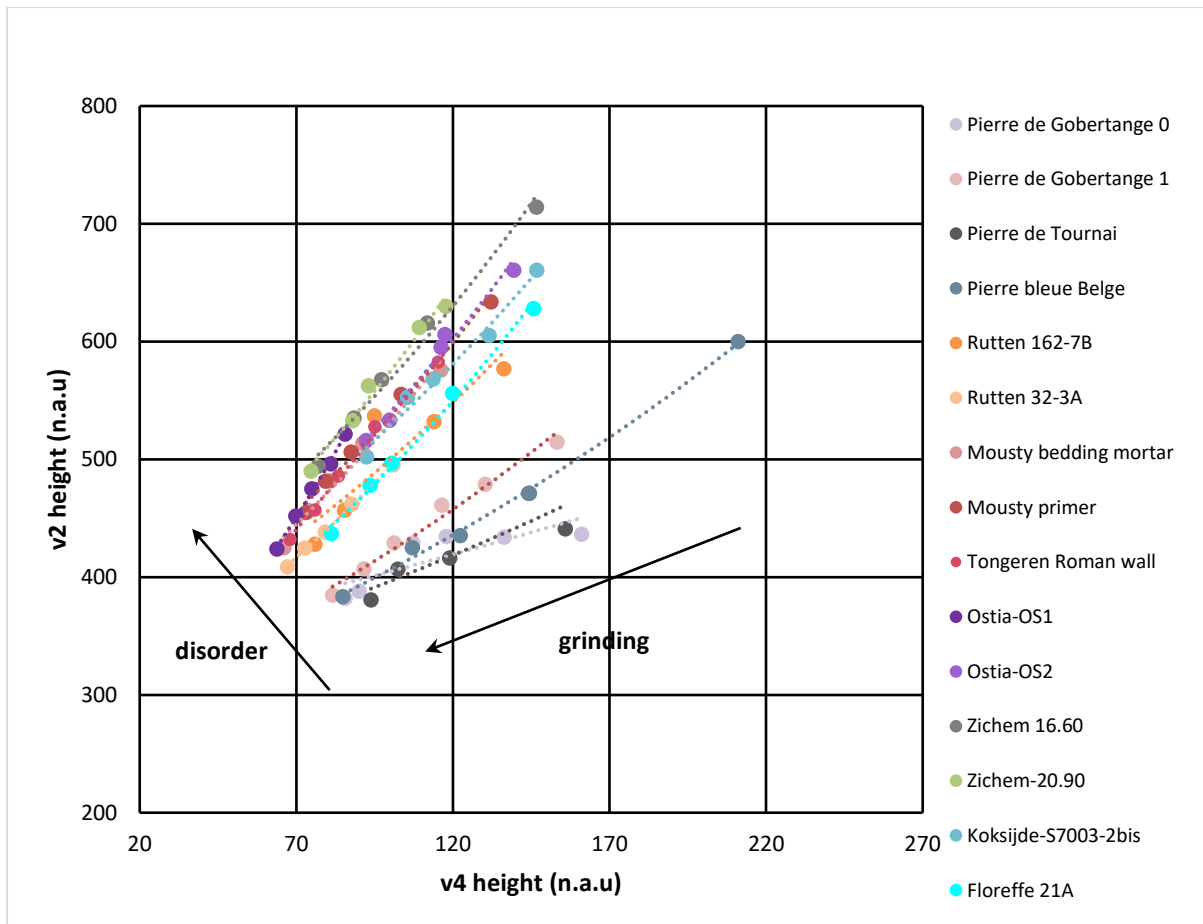
**Figure 6**: Grinding curve method applied on 11 samples and 3 limestones from Belgium.

Another test was performed on the different powdered fraction sizes from Koksijde (Figure 7). It was expected that the finer the fraction is, the more ordered it will be since it would contain less limestone fragments. However, the fraction of sample with a size larger than 500 µm (Figure 7, dark blue) lies in the same area than the one with particles lower than 75 µm (Figure 7, red tile). Only 0.5 mg of sample for each fraction was processed and the amount that was selected might not be representative of the global composition of the fraction having the highest size. These preliminary results did not add much value for the radiocarbon dating pre-screening and were not further explored.
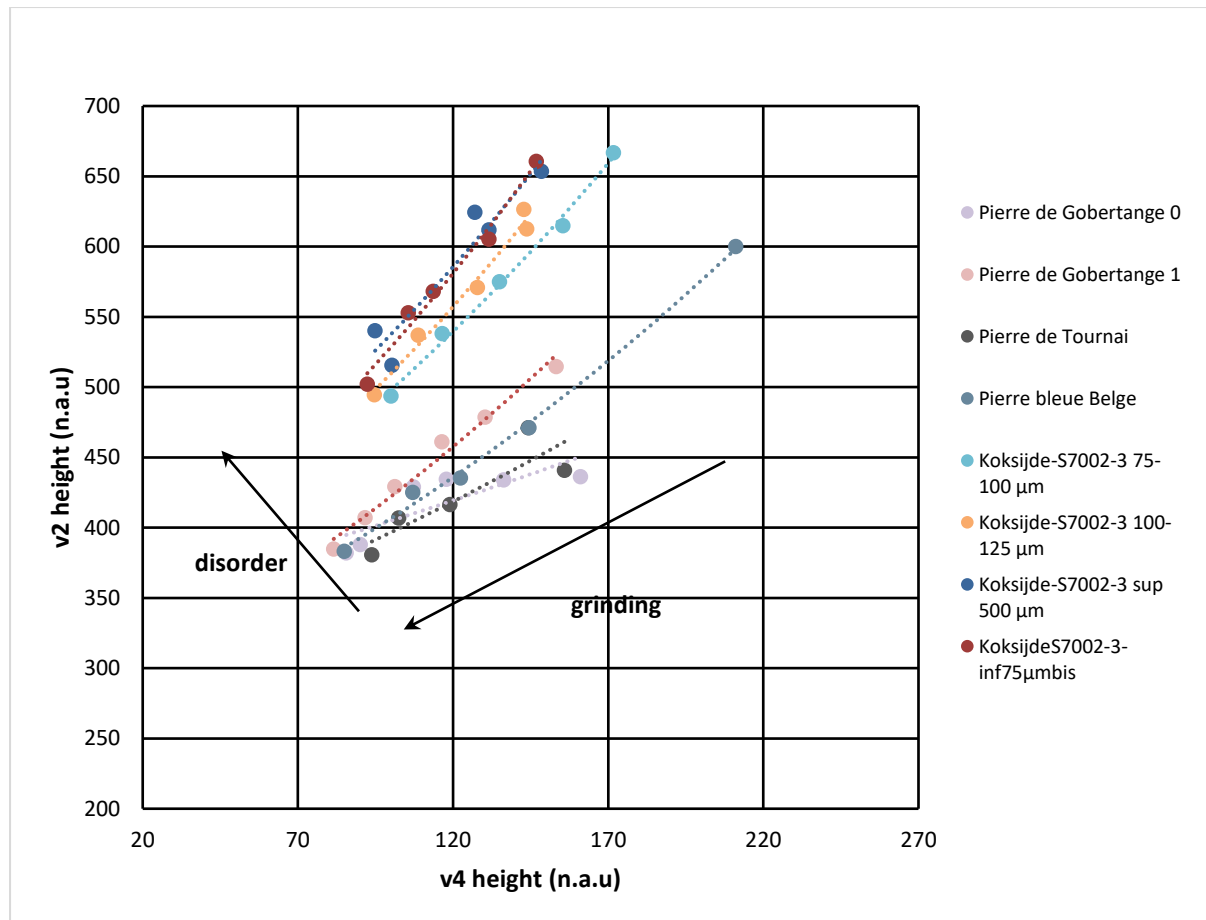
Figure 7: Grinding curve Koksijde samples with different particle sizes.

Petrographic observations were performed on 48 samples. The vast majority exhibited a micritic texture. In rare cases, micro-sparitic grains were observed but they most probably resulted from secondary carbonates formation or recrystallisation (see Figure 8a). Most of the samples contained completely burned lime lumps (Figure 8b) sometimes in combination with incompletely burned (Figure 8b) or unburned fragments. The distinction between the burning state of the lump can been observed thanks to colour variation. For highly dissolved samples, the limp lumps almost disappeared making the assessment impossible (Figure 8f). The size of the lumps (observed on thin-sections) varied between 40 µm and 2 cm. Their frequency varied from a sample to another. For the aggregates of the samples in the corpus, the grain size was often very fine to fine and rarely very coarse. Since the mortars come mainly from Belgium (83%), the majority of the aggregates mineralogy was made of pure siliceous sand (quartz, feldspars, mica, glauconite) sometimes containing a few limestone grains. Glauconite is often found in Belgian mortars, it can come from the limestone making the binder or from the sand used as aggregate, mica flakes (Figure 8j) are less common. Glauconite can be recognized as subrounded particles with a green colour when non oxidized and orange to black when oxidized (Figure 8i). Mortars from the Roman period (from Belgium, Italy, France and Turkey) often contained siliceous volcanic sand, volcanic scoria (Figure 8c) and crushed ceramics (Figure 8d). Almost all aggregates presented a subangular/subrounded shape. In term of appearance, most of the mortar samples were relatively homogeneous and sometimes relatively heterogeneous. The macroporosity was most of the time low to medium, and high when the binder was intensively dissolved (Figure 8f). The porosity was frequently irregular sometimes connected especially when

dissolution was observed, cracks were rarely spotted. Admixtures were rather rare and consisted most of the time of charcoal (Figure 8g) and plant fragments (Figure 8e), sometimes soil, coal and bottom ashes were present within the mortar. In term of alteration, only dissolution and secondary carbonate deposits (Figure 8a & h) were spotted a different degrees. The use of digital image analyses could help gathering quantitative values of the different components and the level of microporosity in future work (Lico et al. 2024).
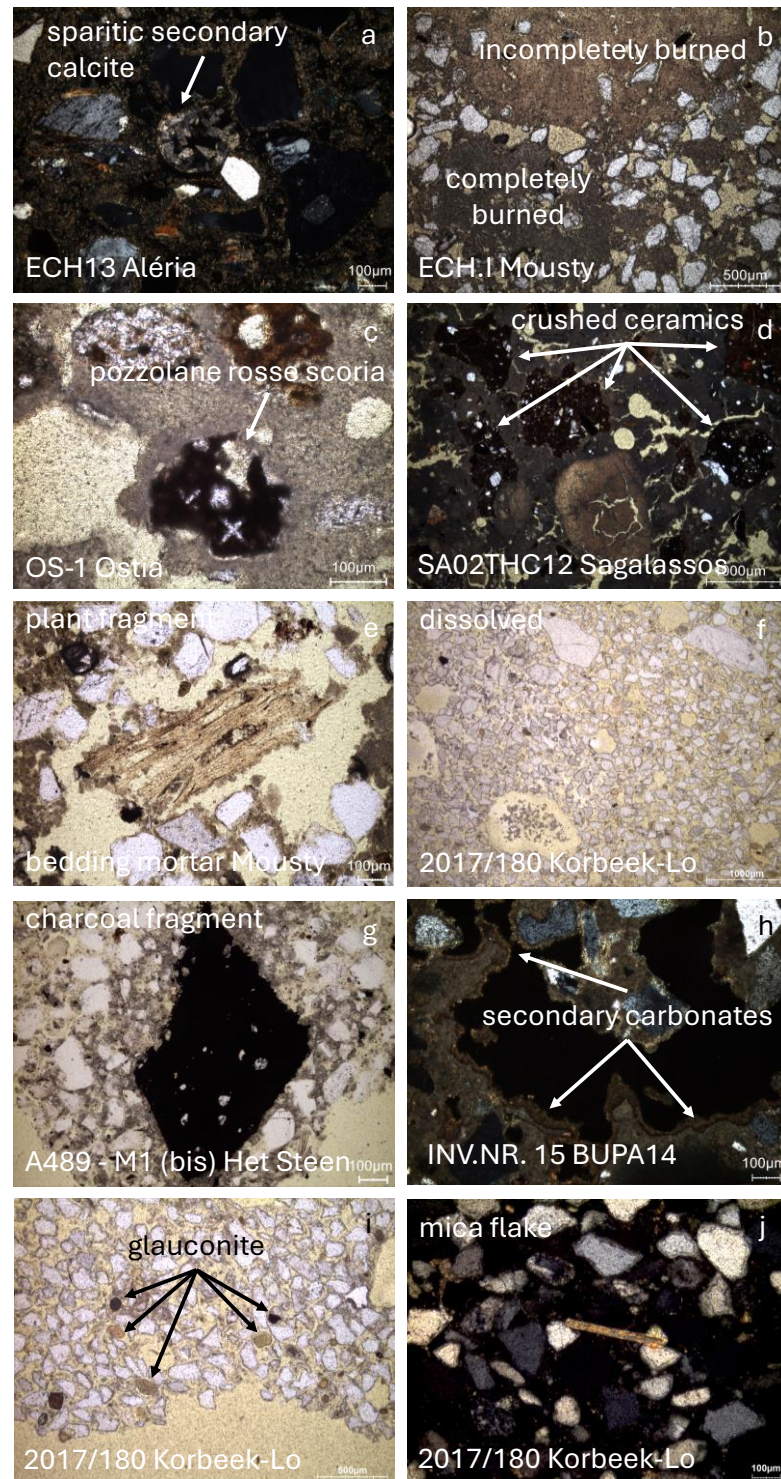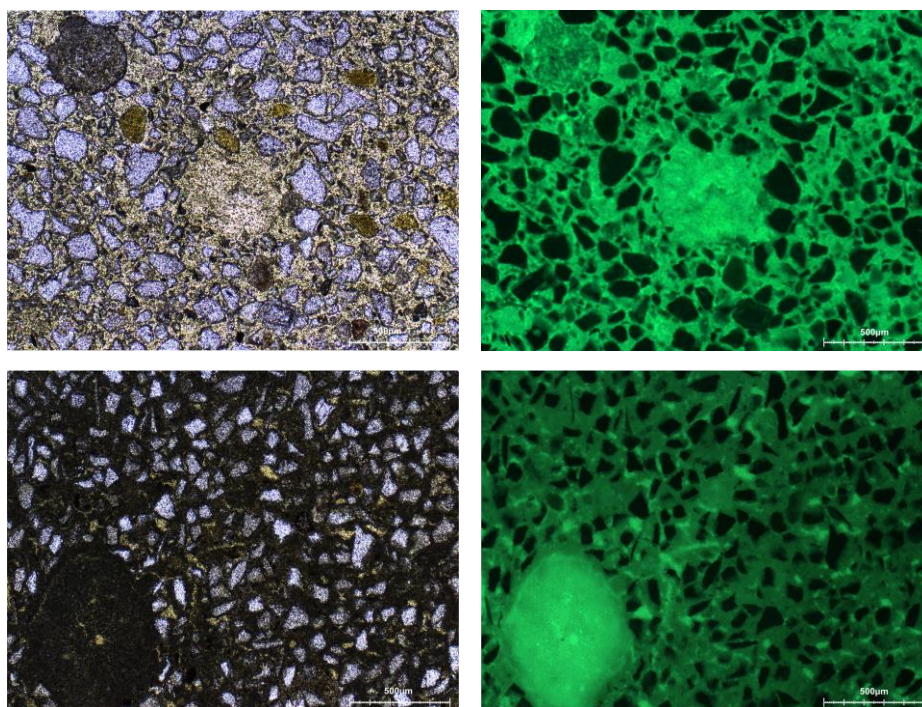

Figure 8: Photomicrographs of thin sections: a) X2264b (ECH13 Aléria) with mirosparitic calcium carbonate crystals in cross polarised light (XPL); b) X2404 (ECHI Mousty) showing lime lumps with different burning

temperatures in plain polarised light (PPL); c) X2272 (OS-1 Ostia) with pozzolane rosse scoria in PPL; d) X2395 (SA02THC12 Sagalassos) displaying multiple ceramic fragments in XPL; e) X2098 (bedding mortar Mousty) exhibiting plant material in PPL; f) X2277 (2017/180 Korbeek-Lo) showing a leached mortar with high porosity in PPL; g) X2079 (A489- M1 (bis) Het Steen) with a large charcoal fragment in PPL; h) X2281 (INV.NR. 15 BUPA14) displaying secondary carbonates at the border of the pore; i) X2277 (2017/180 Korbeek-Lo) showing glauconite oxidised at different degrees in PPL; and j) X2277 (2017/180 Korbeek-Lo) with a mica flake in XPL.

Some **microscopic observation** tests were performed **using UV light** (Figure 8). The goal of these test was to observe the level of fluorescence emitted by the resin impregnating the thin sections to determine if a mortar was hydraulic or not. The higher the fluorescence is, the more microporous the mortar is. Microporous mortars are more susceptible to be non-hydraulic in opposition to hydraulic mortars that possess a lower degree of microporosity. The picture on top of Figure 8 shows a highly deteriorated mortar for which the binder had been dissolved and then, shows a high fluorescence. For the one below, it is probably an air hardening mortar where the pores are highlighted in lighter green. These are interpretations based on observations but will need to be confirmed thanks to thermal analyses. The fact that dissolution can create a biased view and since the thermal analyses already provide an idea for the probable hydraulicity of the binders, these tests were not further explored.


Figure 8: Photomicrographs using plain polarised light (PPL, left) and UV Light (right) of the sample KIK1 from the Burchtmuur (Antwerp, top) and 21A from the Abbatial church Sainte-Marie (Floreffe, bottom).

The **cathodoluminescence** observations and photomicrographs helped in determining the presence of limestone for each samples (Figure 9 & 10). They were performed on 46 thin sections and 47 powders. Most limestones have a strong luminescence, commonly showing a bright red-orange colour, whereas mortars usually show a weak, dull tile-red to brown luminescence (Heinemeier et al. 1997). The top left cathodoluminescence photomicrograph of Figure 9 shows a large limestone fragment present in a sample from the Saint Martin's church in Rutten but smaller fragments present in the sand used as aggregate can also be observed as shown on the bottom cathodoluminescence

microphotographs Figure 9. Incompletely burned lime lumps can be recognized because they exhibit different shades from bright red to red tile (Figure 9, top right). The last observations made from cathodoluminescence is the presence of bright blue K-feldspar grains, bright green plagioclases and dark purple quartz grains (Figure 9, bottom left). Quartz grains can exhibit different shades showing different provenances as it is the case for example for the samples from the Burchtmuur in Antwerp (see Annex Burchtmuur).
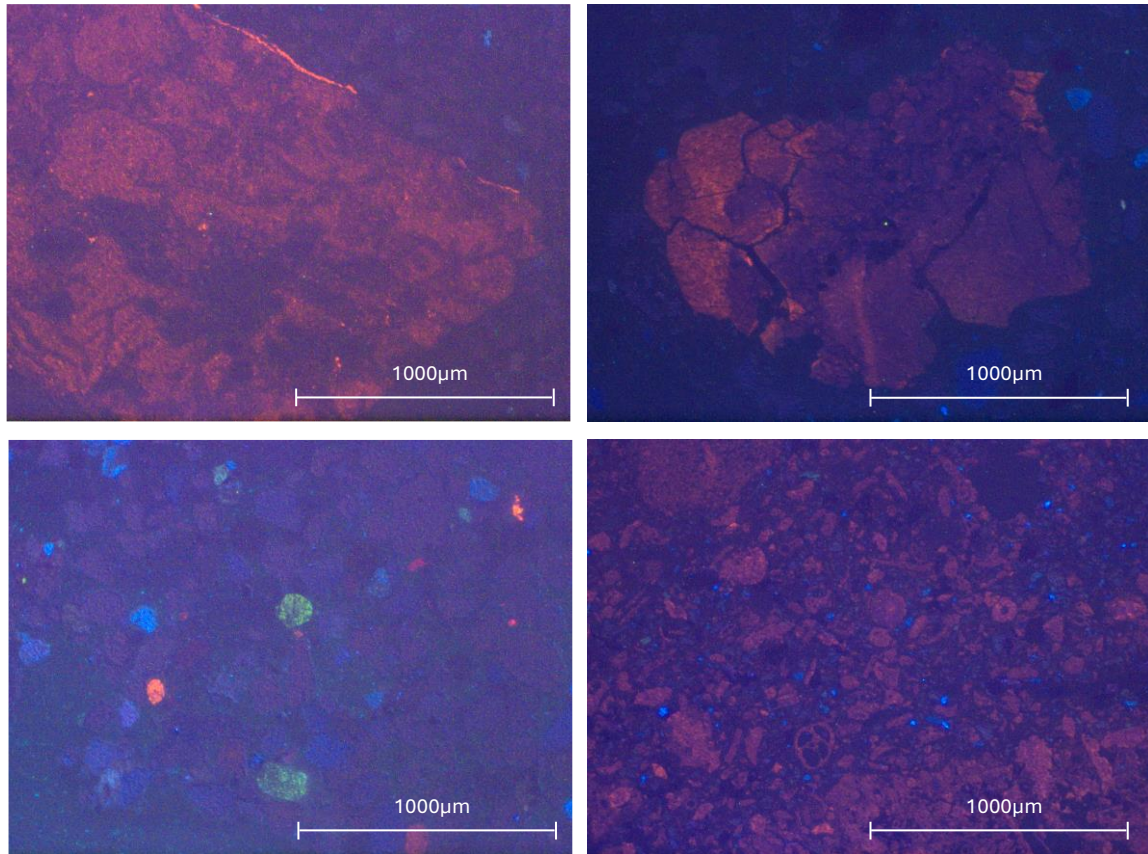
Figure 9: Cathodoluminescence photomicrographs of the thin sections from the mortar samples sp3 8A (top left), sp162 7B (bottom right) both from the Saint Martin's church in Rutten, KIK2 from the Burchtmuur in Antwerp (top right) and BR17BURGST7-1 from the residency of the count of Flanders in Brugge (bottom left).

For the powdered samples with particle size lower than 75 µm used for radiocarbon dating, cathodoluminescence photomicrograph can highlight the quantity of limestone left in the sample by showing more (Figure 10, left) or less (Figure 10, right) bright red particles.
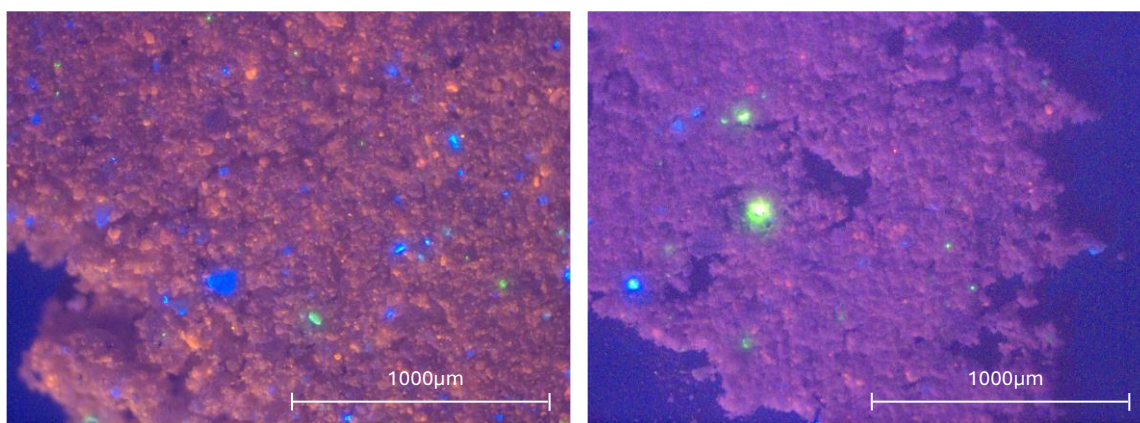
Figure 10: Cathodoluminescence photomicrographs of powders with particle size lower than 75 μm of the mortar samples sp162 7 B (left) and sp33 4 (right) from the Saint Martin's church in Rutten.

The **thermal analyses** were performed on a piece of mortar sample and on the sieved powder obtained from it with particle size lower than 75 μm. In total, 57 whole samples and 46 powders were processed. The curves of the thermal analyses clearly show a large endothermic peak between around 600 and 850°C linked to the decarbonation of the lime binder and other possible carbonates. Sometimes, this peak was split which due to a measurement artifact (the temperature/reaction was too fast and/or the crucible was too full which trapped some CO_2 at the bottom that was released at a later stage). The amount of carbonates present in the mortars can be determined by calculating the weight loss within this temperature range. Often, the quantity of carbonates was higher in the powders compared to the whole samples since a large part of the aggregate was eliminated when sieving. Most of the time, the end temperatures of calcium carbonate decomposition was higher for the powders compared to the whole samples. A possible explanation could be that the powders are more pure compared to the whole mortar samples which increases the decomposition temperature. These analyses also helped defining the degree of hydraulicity of the binder (apparent hydraulic index - aHI). The aHI was determined on the basis of the weight loss between 200 and ca. 650°C (usually attributed to water loss from calcium-silicate-hydrates-phases). We have to bear in mind that the calculation can be biased by the presence of clays in the used aggregates or by the selective dissolution of the air-hardened fraction of the lime binder for example. Loss from structurally bound water of some clays takes place at a similar temperature to structurally bound water in hydraulic components (Middendorf et al. 2005). Also, when crush terracotta was heated at too high temperature, no hydraulic reaction would take place but it presence would increase the aHI. The particle size also has influence of the reaction process. It is necessary to stay critical about the calculation result by taking into account the petrographic observations. Often, it can be overestimated. Moreover, the aHI value is more representative for the whole sample compared to the powder for which elements where discarded when sieving. Sometimes, a peak around 400-70°C was observed which might be due to the release of water from calcium hydroxide (Antonia Moropoulou, Bakolas, and Bisbikou 1995; Klimesch and Ray 1996) and indicate that the mortar did not fully carbonated. This was more often observed for the powdered samples and less for the whole mortar samples. In the latter, it was probably present in too low concentration to be noticeable. The quartz transition phase can be observed around 570°C (Rickard, Riessen, and Walls 2010). It was more often observed for the whole sample and not in the powders since it was removed when sieving. Rarely, the presence of gypsum was spotted thanks to a peak around 120-40°C. Sometimes, some additional peaks around 600-700°C were observed and could be due to the presence of a different form of carbonate possibly coming from the hydraulic

phases. Other additional peaks were more rarely spotted such as a peak at 394°C for some of the samples from Notre Dame of Mousty (see annexes), for which no clear explanation has been found yet.

Raman analyses were performed on only one sample (see Annexes section - Report Monastery of St-Donaas, Brugge). The results revealed the presence of calcite, quartz, amorphous carbon, feldspar, haematite and anatase. The information obtained was redundant with the other techniques used and was not necessary to repeat on all samples. As planned in the project, this technique can be used in a case by case approach to answer specific questions. Another aspect of Raman spectroscopy to be explored in the future is the differentiation between short-range order at the molecular level in order to assess the origin of calcite (Calandra et al. 2024).

XRD measurements were ran for five samples from the archaeological crypt of the Sainte-Gertrude collegiate in Nivelles, the Abbatial church Sainte-Marie in Floreffe, the Burchtmuur in Antwerp and the Castle of Horst in Holsbeek (see corresponding Annexes). These samples were selected because some of the FTIR vibrational band could not be attributed. However, less information could be retrieved from the XRD measurements compared to the FTIR analysis. The diffractograms showed only the presence of calcite, quartz and K-feldspar. The detection limit of the instrument used seems lower compared to the FTIR measurements. Also, the measurement was performed on powder which gives the components present in higher quantity while the FTIR analyses were performed on more local inclusions. This technique was not considered further for the project since it didn't provide essential information for the pre-screening.

Observations and measurements using **SEM-EDX** were only completed for the four mortar samples from the Abbatial church Sainte-Marie in Floreffe (see corresponding Annexe) since the mortar samples and the lime lumps were giving different radiocarbon results. The mortar samples seemed to be highly to moderately hydraulic according to the thermal analyses. Clay minerals were detected by FTIR for all the binders but not in the lime lumps (except for the sample 21D for which the lime lumps contained clay). The goal of the measurements with SEM-EDX was to verify if hydrated calcium silicates and hydrated calcium aluminates were present in higher quantity around the clay particles. This could have confirm the hydraulicity of the mortars and the obtention of a younger date compared to the lime lumps. This phenomena was unfortunately not observed but it revealed the presence of silicon and aluminium, showing the presence of a significant quantity of clay particles deriving from the used sand in the binder. The presence silicon and aluminium was also detected in the lime lump suggesting that the limestone used was not pure, but already contains some clay impurities that may have led to the formation of a slightly hydraulic lime binder, if a sufficiently high firing temperature was reached. The hydraulic properties of the binder might have been amplified by the use of a slightly clayey sand. As for Raman spectroscopy, this method should be used in a case by case approach.

4.3 Pre-screening protocol

Table 2 presents the **radiocarbon results** of the 48 samples completely analyzed with all the techniques and Table 3 provides the keys for Table 2. As explained in the "3. METHODOLOGY/3. Methods" sections, three calculation methods were utilized to determine the radiocarbon content. The first one consist of a simple extrapolation of the curve resulting from the radiocarbon determination as a function of the CO_2 fraction using the best mathematical fit (higher coefficient of

determination, R^2). Using this method (Table 1, column 'Extrapolated date'), approximately half of the samples (44 %) gave a result corresponding to the expected date and/or the ^{14}C date of context. Two samples (6 %) provided a date that did not correspond to the expected date but could be possible (Table 1, column 'Extrapolated date' orange). The other half of the samples did not give an accurate date (Table 1, column 'Extrapolated date' red). The second method for calculating the radiocarbon content is similar but with a statistical calculation more advanced (Table 1, column 'Extrapolated date with stat'). It often allows to reduce the error on the measurement. This can be sometimes beneficial since it can narrow down the calibrated date obtained but it can sometimes make the calibrated date falling out of the expected range of dates. It is slightly the case for the sample from the south façade at 20.90 m L10 in the core brickwork of the Saint Eustache church in Zichem. For the samples ECH.III from Notre-Dame of Mousty church in Ottignies and the OS-1 purple fragment from Ostia, the value obtained with this method is aberrant because too far from the expected date. However, in one case (OS-2 yellow fragment), it increased the error on the radiocarbon determination and allowed to obtain a reliable date while the two other calculation methods were failing. The same percentages of success, failing and possible success than the extrapolated dates without statistic were obtain with the statistic. The samples succeeding or falling matching the expected date are not exactly the same with both calculation methods but most often both dates coincide. The last method for calculating the radiocarbon date is the combination of the first fractions using Oxcal 4.4 program. This method also decreases the error on the radiocarbon determination. Only the fractions that fall into the same range can be combined, often, we used the four first fractions (1, 2, 3 & 4 % of CO_2 extracted). If the values are too scattered, this method cannot be applied. This is why the percentage of dates corresponding to the expected dates is slightly lower (42 %) compared to the first method of calculation. We recommend to use the three methods of calculation and if at least two are within the same range and the results of the characterisation methods shows a mortar in good condition with a low content of contamination, the date can be trusted. A last comment about the radiocarbon results is the slope of the curve obtained. Since the binder is finer grained and microporous, and hence presents a larger specific surface area for acid reaction it is believed to react faster than geological limestone. The slope for the radiocarbon determination as function of the CO_2 fraction is supposed to be positive. This is the case for the majority of samples, the values of the radiocarbon determination increase when the CO_2 increase as well. The last values of the CO_2 fractions often contain a part of CO_2 coming from the limestone reaction with acid. In the case of the samples from Korbeek-Lo, KIK1 and KIK3 from the Burchtmuur in Antwerp (see corresponding Annexes), the slope of the curve is negative. The first fractions are older than the last ones. The latter are closer to the presumed historical dates than the first fractions. These samples have been intensively dissolved. Possible recrystallizations or precipitations could have altered the crystals making them more resistant to the acid reaction compared to the geogenic carbonates present in the mortars. The amount of carbon present in the mortars was also integrated to the summary result table (Table 1) to check it has an impact on the radiocarbon result. Overall, most of the samples that provided an acceptable radiocarbon result contained the higher amounts of carbon. However, a high amount of carbon was not always necessary to obtain reliable results as it is the case for the sample from Residency of the count of Flanders in Brugge or two samples from Sagalassos (see respective Annexes). Indeed, the amount of carbon can sometimes reflect a high dissolution of the binder leading to unreliable radiocarbon measurements but it can also come from a low binder:aggregate ratio. A high amount of carbon does not necessary equal to good radiocarbon result since the aggregates can contain a calcareous fraction or if the mortar is hydraulic, delayed hardening could increase the ^{14}C/^{12}C ratio.

From all the analyses performed, the methods we used that are the most useful for the pre-screening were petrography, FTIR, cathodoluminescence and thermal analyses. Especially a few parameters per technique that were selected in the summary table (Table 1). For the petrographic observations of the thin-sections, they are the aggregate mineralogy, the lump state and the presence of alteration type dissolution and secondary carbonates deposits. These characteristics can influence the ^{14}C amount in the sample by increasing and/or decreasing its content. From the 48 samples for which all analyses were performed, 63% of the aggregates were made of pure siliceous sand, 15% were pure siliceous sand with a few calcareous grains, 6% were mixed siliceous & calcareous sand and the rest was a mix of calcareous sand with few quartz grains, siliceous volcanic sand sometimes calcareous, volcanic scoria, and reused mortar fragments. One sample (Park Abbey in Leuven) did not contain any aggregate. The aggregates containing calcareous particles are susceptible to decrease the ^{14}C/^{12}C ratio while the aggregates with hydraulic properties would increase this ratio. For the lump state, 54% of the samples included completely burned lime lumps, 31% contained completely and incompletely burned lime lumps while 8% showed completely and unburned lime lumps and 6% had dissolved lumps. As explained before, when lime lumps are unburned or incompletely burned, they can decrease the ^{14}C/^{12}C ratio and virtually age the mortar. In term of dissolution, half of the samples did not show any signs whereas a quarter was slightly dissolved and the last quarter showed an intensively dissolved binder. In around more than half of the samples (58%), secondary calcite was spotted observing the thin sections but only 6 % contained a high amount (++). High amount of dissolution and secondary carbonate deposit suggest a highly deteriorated mortar that should not be considered for radiocarbon dating since it could have incorporated younger or older carbon. The presence of secondary calcite in relatively low quantity does not equal to unreliable radiocarbon content since they could form from the carbon incorporated during the hardening of the mortar. Another hypothesis is that their crystallinity differs from the binder and they react within the higher CO_2 fractions. For the FTIR measurements, we included the presence of aragonite, clay, nitrates and gypsum. The absence of aragonite in the sample can be related to an intense leaching process since if it dissolved, aragonite would precipitate in the form of calcite in ambient conditions (Toffolo 2021). Almost all the samples (92%) showed the vibrational band of aragonite in their spectra except the ones that were intensively dissolved and the sample from Sint-Agatha church. For the latter, no dissolution was spotted so either it was present in too low concentration for it to be detected from the FTIR method used or it could have recrystallize into calcite which is a more stable form of calcium carbonate. The presence of clay can be linked to impurities in the sand or in the limestone used to make the binder. As describe earlier, the presence of high quantity of clay (in the Floreffe samples) might be responsible for a delayed hardening of the binder. The detection of nitrates suggests a slight contamination by soluble salts and as the presence of gypsum, they can be linked to weathering processes because of relative humidity and pH variations or the presence of percolating water, rainfall and underground water. These could also impact the mortar by incorporating older or younger carbon to its structure (Thomas Schrøder Daugbjerg et al. 2021). The cathodoluminescence observations allowed to detect the presence of limestone in the samples. Most of the samples (86%) showed a few limestone grains in the photomicrographs. Some were successful for the radiocarbon results and others no. In the fraction of particle with a size lower than 75 µm, limestone grains are often present. This is also observed with the increase in the radiocarbon determination as function of the increase of CO_2 extracted. The two samples showing a high quantity of limestone in the powder used for radiocarbon dating did not provide a trustable ^{14}C measurements. Cathodoluminescence can be an easy tool to detect limestone when someone is not train to identify it using thin sections using

observations with a petrographic microscope. The techniques can be complementary but if someone is well trained, it is not a mandatory technique. It can be useful for observing the powders before radiocarbon dating to detect if the amount of limestone grains is not too high. For the thermal analyses, the percentage of carbonates was selected as an important parameter since it can indicate a dissolution of the binder or the presence of a high quantity of limestone. The last parameter we though determinant in assessing the reliability of a sample for radiocarbon dating is the hydraulicity. As previously mentioned, the apparent hydraulicity index (aHI) determined with the thermal analyses can be compromised by the presence of certain aggregates that create a false hydraulicity or by the dissolution of the binder. The combination of the aHI and petrographic observations provides a critical perspective on the aHI, allowing for an estimation of the mortar's hydraulicity. Often, if some components/phenomena that can influence the results are observed in petrography, the estimation was lowered down. Sometimes, these components/phenomena were too pronounced and the determination was not possible.

Over the 48 samples completely characterized and analyzed, ~33 % provided a reliable date. A pure siliceous sand was mainly used as **aggregate** for these samples but also siliceous sand with few carbonates, siliceous volcanic sand, siliceous volcanic sand slightly calcareous sometimes in combination with crushed ceramics. Mortar samples including mixed siliceous and calcareous sand, calcareous sand with few quartz grains or mainly crushed ceramics did not provide a trustable date and should not be selected for a radiocarbon determination. The presence of **incompletely burned or unburned lime lumps** in combination with completely burned ones did not prevent to obtain reliable dates. The presence of some incompletely burned or unburned lime lump is then not a criteria to rule a sample out for radiocarbon dating. Samples containing only completely burned lime lumps can also provide unreliable dates if combined with other criteria. For the 33 % of sample succeeding the radiocarbon determination, most of them showed little **alteration** or even no alteration at all. Only one sample was highly dissolved. It is the sample ECH.IV from Notre-Dame of Mousty church in Ottignies (see corresponding Annexe). Its percentage of carbon is lower compared to the other samples from the same site but no secondary calcite deposit was observed in the thin section and the aggregate used was pure siliceous sand. Several other samples (the sample from the Holy Cross Parish Church in Korbeek-Lo and the two samples from the archaeological crypt of the Sainte-Gertrude collegiate in Nivelles) that presented the same characteristic did not provide a reliable date. When samples exhibit a high **dissolution** of the binder, they should not be considered for radiocarbon dating. In term of **secondary carbonates deposits**, when observed in low quantity is not crippling for radiocarbon dating but when observed in large quantity in combination with a slight or high leaching process, the mortar sample should not be considered for radiocarbon dating. The **FTIR measurements** are quick and easy to perform is one of the first stages when receiving mortar samples in the protocol. When the relative ratio carbonates-silicates is low, this can be an indication that the binder has been dissolved. This is confirm when no aragonite can be detected in the binder. Most of the samples that did not show the vibrational bands of aragonite did not provide a date matching the expected historical date except the sample from the site BUPA14 in Buizingen. For this latter site, the expected date had a span of 700 years (800-1500 AD) and the correlation of the extrapolated date was too low to be considered so the result is suspicious. When FTIR measurement do not detect aragonite in combination with a low carbonates-silicates relative ratio, it is not worth it to try to date the sample. The presence of clay was often associated with delayed hardening but is not a criteria sufficient to rule a sample out for radiocarbon dating. The same remarque can be done for the presence of gypsum

and nitrates, they are signs to be considered but are determinant for taking the decision to date or not a sample. Cathodoluminescence of samples containing a high amount of limestone in the powder fraction used for radiocarbon dating can also help in eliminating a sample in list for radiocarbon dating. When the percentage of carbonates extracted from the thermal measurements is too low, it can indicate a dissolution of the binder and if it is too high, the presence of a high quantity of limestone. In both cases, samples should not be processed for radiocarbon dating. Samples considered as highly hydraulic are not good candidates for radiocarbon dating since because they are likely to have undergone a delayed hardening. The main reason for the samples to fail the radiocarbon determination were an intensive leaching often in combination with secondary carbonate deposits and delayed hardening. The latter can be caused by a direct application of a plaster on top of the bedding mortar as we suspect it was the case for the castle of Horst. Another example that might be a more common explanation is the composition of the mortar (the binder or aggregate) that provides hydraulic properties leading to a longer carbonation process. Hydraulic mortars should be avoided to be processed for radiocarbon dating. Roman mortars are often hydraulic but depending on the aggregate used some exceptions can be made. It is the case for the samples from Sagalassos and the OS-1 sample from Ostia. They gave reliable radiocarbon results because of the type of aggregate used and the relatively good state of preservation of the samples. In total, 52 % of the samples analyzed did not provide a reliable radiocarbon measurement. A part of the samples (8 %) ended up in the obtention of a reliable date even though their conservation state and/or composition was not auspicious for radiocarbon dating. This could be due to compensation of phenomena (for instance, a delayed hardening with the presence of limestone fragments). Other samples (6%), presented a conservation state and a composition that supposed a certain reliability for radiocarbon dating but provide dates falling out of the presumed historical date. In some cases, the presumed historical date was hypothetic. These can help archeologists/historians in questioning their hypotheses.

Samples	Site/City	Country	Sample id	Sample type	Presume historical date	Extrapolated date	Extrapolated date with stat	Rcombine	%C	Type of aggregate	Lump state	Dissolution	Secondary carbonates	Aragonite	Clay	Nitrates	Gypsum	Limestone	CaCO₃ (w%)	Hydraulicity	Reliability / reasons why it worked or not
14C	Saint-Martins church/Rutten (Tongeren)	Belgium	sp18 9A	fm	Merovingian (480-750 AD, p)	1293 ± 26 BP 665-774 calAD	1038.2 ± 13.5 BP 992-1025 calAD	1089 ± 13 895-995 calAD	2.7	csfq + cc + rmf	cb + ib	+	+	+	+	+	-	+	17.5	+++	☑ Delayed hardening + few alteration + csfq + cc + rmf
			sp33 4		Romanesque (p)	1293 ± 24 BP 670-780 calAD	1236.3 ± 14.1 BP 702-877 calAD	1249 ± 12 BP 700-830 calAD	7.1	ssfc	cb	+	+	+	+	+	-	n/a	32.2	++	☒ Leaching + secondary calcite + ssfc
			sp162 7B		Merovingian (480-750 AD, p)	1471 ± 34BP 552-648 calAD	1349.3 ± 19.2 BP 646-772 calAD	1492 ± 20 BP 565-640 calAD	3.8	csfq	cb	+	-	+	+	-	-	++	58.2	+	☒ Leaching + csfq
			sp32 3A			1244 ± 33 BP 676-880 calAD	1250 ± 16.9 BP 678-864 calAD	1219 ± 20 BP 770-890 calAD	3.4	pss	cb + ib	-	-	+	+	-	-	+	30.6	+	☑ No alteration + pss
	Roman wall/Tongeren		-		Roman (p)	1226 ± 35 BP 700-890 calAD	1100.3 ± 15.6 BP 892-994 calAD	not possible	4.3	cc + ssfc	cb + ib	+	+	+	-	-	-	n/a	21.5	++	☒ Leaching + secondary calcite + delayed hardening (hydraulicity due du cc)
	Hertogensite/Leuven		2017H39	fm	Middle Ages (p)	1765 ± 30 BP 230-380 calAD	1599.5 ± 17 BP 421-538 calAD	1778 ± 16 BP 236-335 cal AD	0.9	pss	cb	+	-	+	-	-	-	+	16.1	++	☒ Leaching
	Holy Cross Parish Church/Korbeek-Lo		2017/180	fm	Middle Ages (1107 or younger, p)	2323 ± 30 BP 410-230 calBC	2310.6 ± 13 BP 420-380 calAD	not possible	0.4	pss	diss	++	-	-	-	-	-	-	8.4	? (strong dissolution)	☒ Leaching
	Residency of the count of Flanders/Brugge		BR17BURGST7-1	n/a	~1050-1100 AD (p)	1121 ± 30 BP 774-995 cal AD	1093 ± 15.7 BP 892-995 calAD	1131 ± 18 BP 883-988 calAD	1.0	ssfc	cb + ib	++	+	+	-	+	-	+	12.2	? (strong dissolution)	☒ Leaching + ssfc
	BUPA14/Buizingen		INV.NR. 15	n/a	800-1500 AD	correlation too low	839.9 ± 10 BP 1176-1260 calAD	850 ± 9 BP 1170-1225 calAD	5.2	ssfc	cb	+	+	-	-	-	-	+	28.6	++	☑ A few alteration + ssfc

	Saint-Agatha church/Huldenberg	north east choir	n/a	Middle Ages (p)	854 ± 25 BP 1150-1270 calAD	848 ± 12.5 BP 1167-1228 calAD	871 ± 11 BP 1165-1220 calAD	5.5	pss	cb	-	+	+	+	-	-	-	n/a	+	☑ A few alteration + pss
	Ten Bogaerde/Koksijde	S7002-3	n/a	1200-1300 AD (p)	610 ± 22 BP 1300-1400 caAD	600.7 ± 13.7 BP 1306-1400 calAD	625 ± 13 BP 1295-1395 calAD	4.8	ssfc	cb	++	+	+	+	-	-	+	16.7	? (strong dissolution)	☒ Leaching + secondary calcite
	Sint-Martin's basilica/Halle	141	n/a	Before 1200 AD (p)	1683 ± 24 BP 259-420 calAD	1677.2 ± 14.2 BP 265-419 calAD	1681 ± 9 BP 265-416 calAD	2.7	pss	cb	++	+	+	-	-	-	+	21.1	+	☒ Leaching + secondary calcite
		1003		Before 1200 AD (p)	1541 ± 24 BP 435-594 calAD	1459.2 ± 17.7 BP 576-645 calAD	not possible	3.6	pss	cb	+	++	+	-	-	-	+	19.7	+	☒ Leaching + secondary calcite
	Het Steen/Antwerpen	A489 - M1 (bis)	n/a	1000-1100 AD (p)	1003 ± 30 BP 991-1154 calAD	1076 ± 22.6 BP 895-1023 calAD	not possible	1.6	ssfc	cb + ib	++	++	-	-	-	+	n/a	n/a	+	☒ Leaching + secondary calcite
		A489 - M2	n/a	1000-1100 AD (p)	1567 ± 30 BP 425-567 calAD	1477.4 ± 17.4 BP 594-640 calAD	not possible	1.5	ssfc	cb + ib	++	++	-	+	-	+	+	n/a		☒ Leaching + secondary calcite + ssfc
Monument	Notre-Dame of Mousty church/Ottignies	bedding mortar	bm	10th-13th century (p) – 1077d post quem & 1205-1206d ante quem (a)	877 ± 25 BP 1047-1226 calAD	833 ± 25 BP 1170-1265 calAD	872 ± 13 BP 1164-1218 calAD	5.2	pss	cb	+	+	+	+	+	-	+	1,73?	? (questionable measurement)	☑ A few alteration + pss
		outdoor render	r		811 ± 25 bP 1180-1275 calAD	788.5 ± 16.6 BP 1224-1273 calAD	850 ± 13 BP 1166-1226 calAD	5.5	pss	cb + ib	-	+	+	-	+	+	+	24.9	++	☑ A few alteration + pss
		wall painting plaster fragment 3/3	p	1500? (p)	842 ± 21 BP 1165-1265 calAD	831.7 ± 11.5 BP 1179-1263 calAD	841 ± 10 BP 1170-1260 calAD	5.6	pss	cb	-	-	+	+	-	-	+	19.0	++	☑ A few alteration + pss
		ECH.I	r	10th-13th century (p) – 1077d post quem & 1205-1206d ante quem (a)	877 ± 25 BP 1047-1226 calAD	877.4 ± 14.1 BP 1160-1219 calAD	888 ± 13 BP 1053-1217 calAD	5.1	pss	cb + ib?	-	+	+	-	+	+	+	20.2	++	☑ A few alteration + pss
		ECH.II	sm (of window frame)		891 ± 27 BP 1045-1222 calAD	897.8 ± 18.2 BP 1047-1218 calAD	891 ± 27 BP 1045-1222 calAD	5.6	pss	cb + ib?	-	+	+	+	+	-	+	22.9	-	☑ A few alteration + pss

Group	Site	Sample	Type	Expected age	Date A	Date B	Date C		pss	cb/ib										Assessment
		ECH.III	bm		781 ± 27 BP 1222-1278 calAD	497 ± 29.9 BP 1400-1451 calAD	871 ± 15 BP 1162-1219 calAD	5.9	pss	cb + ib	-	+	+	+	+	+	+	32.9	++	☑ A few alteration + pss
		ECH.IV	bm		797 ± 22 BP 1220-1273 calAD	870.4 ± 14.8 BP 1162-1219 calAD	859 ± 10 BP 1170-1220 calAD	3.3	pss	cb + ib	++	-	+	+	+	-	+	9.0	? (strong dissolution)	☑ Leaching
	Coudenberg Palace/Brussels	M4	bm	15th century (1452-60, a)	456 ± 20 BP 1430-1460 calAD	451,6 ± 8,9 BP 1435-1463 calAD	469 ± 7 BP 1430-1450 calAD	7.3	pss	cb	-	+	+	+	-	-	+	n/a	+	☑ A few alteration + pss
		M16	i		24 ± 25BP 1690-1820 calAD	20.2 ± 60.8 BP 1680-1940 calAD	47 ± 10 1700-1910 calAD	5.2	pss	diss	++	+	+	-	+	-	+	9.2	? (strong dissolution)	☒ Leaching + secondary calcite
	Saint-Eustache church/Zichem	south façade at 20.90 m L10 in the core brickwork	bm		520 ± 21 BP 1395-1440 calAD	519.2 ± 12 BP 1406-1432 calAD	553 ± 12 BP 1325-1425 calAD	6.7	pss	cb + ib	-	-	+	+	-	-	+	17.5	+++	☑ A few alteration + pss + slight delayed hardening
		north façade at 11.25 m behind a facing stone approximately at 26 cm depth	bm	~1300AD (p)	551 ± 22 BP 1320-1430 calAD	571 ± 12.6 BP 1323-1410 calAD	588 ± 9 BP 1320-1405 calAD	4.8	pss	cb	-	-	+	-	-	-	+	14.4	+++	☑ A few alteration + pss + slight delayed hardening
		north façade at 16.60 m L8	bm		411 ± 22 BP 1430-1620 calAD	411 ± 11.6 BP 1446-1478 calAD	406 ± 13 BP 1440-1490 calAD	6.0	pss	cb + ib	-	-	+	+	+	-	+	22.3	+	☒ Later repair
New	Archaeological crypt of the Sainte-Gertrude collegiate/Nivelles	NIV21STG Z02	n/a	700-900 (p)	158 ± 25 BP 1670-1950 calAD	159.2 ± 12.7 BP 1668-1950 calAD	184 ± 10 BP 1660-now calAD	3.8	pss	cb	++	-	+	+	+	-	+	14.7	? (strong dissolution)	☒ Leaching
		NIV21STG Z01	n/a	10th century (p)	114 ± 25 BP 1683-1936 calAD	94.6 ± 16.3 BP 1694-1917 calAD	167 ± 23 BP 1663-now calAD	3.1	pss	cb + ib	++	-	+	+	+	-	+	10.7	? (strong dissolution)	☒ Leaching
	Abbatial church Sainte-Marie/Floreffe	buttress 21A	bm	10-11th centuries (p)	660 ± 25 BP 1281-1392 calAD	659.4 ± 12.9 BP 1286-1389 calAD	678 ± 11 BP 1281-1381 calAD	5.4	pss	cb + ib	-	-	+	+	+	+	+	14.7	++	☒ Delayed hardening
		angle 21B	bm		654 ± 25 BP 1282-	655.8 ± 22.6 BP	602 ± 11 BP	5.5	pss	cb	-	-	+	+	+	-	+	17.1	+++	☒ Delayed hardening

Project B2/202/P2/PALc - Pre-screening of anthropogenic lime carbonates for ^{14}C dating

Site	Country	Sample	Type	Period	Date 1	Date 2	Date 3		Petro	cb										Result
					1394 calAD	1285-1391 calAD	1308-1399 calAD													
		wall north-south 21D	bm		801 ± 25 BP 1216-1276 calAD	737.5 ± 28.1 BP 1226-1299 calAD	791 ± 12 BP 1225-1270 calAD	4.1	pss	cb	-	-	+	+	+	-	+	20.5	++	☒ Delayed hardening
		wall Est-West 21E	bm	13th or 17th (p)	325 ± 25 BP 1490-1641 calAD	325.8 ± 11.8 BP 1500-1639 calAD	352 ± 25 BP 1476-1631 calAD	7.4	pss	cb + ub	-	+	+	+	+	-	+	46.6	+	☑ A few alteration + pss
Sagalassos	Turkey	SA02THC03		late 4th - early 5th AD (a)	1619 ± 24 BP 410-540 calAD	1629.5 ± 15.4 BP 407-535 calAD	1637 ± 12 BP 410-540 calAD	0.8	svsfc + cc	cb	-	+	+	+	-	-	+	8.1	+++	☑ A few alteration + svsfc + cc
		SA02THC04	bm	late 4th - early 5th AD (a)	1630 ± 32 BP 376-544 calAD	1628.8 ± 18.4 BP 407-536 calAD	1642 ± 15 BP 401-534 calAD	2.5	svs + cc	cb	+	+	+	+	-	+	+	14.5	+++	☑ A few alteration + svs + cc
		SA02THC12		4th-6th AD ? (not sure because of renovations, p)	1781 ± 31 BP 212-362 calAD	1780.6 ± 14.2 BP 236-330 calAD	1811 ± 14 BP 211-319 calAD	6.9	ssfc	cb	-	+	+	-	-	-	+	64.4	-	☑ A few alteration + ssfc
Aleria/Corsica	France	ECH 10	i	Ancient Rome (50-25 BC, a)	1035 ± 29 BP 897-1119 calAD	911.7 ± 16.3 BP 1044-1207 calAD	not possible	5.0	mscs	cb	-	+	+	+	-	-	+	19.8	+++	☒ Secondary calcite + delayed hardening
		ECH 13	i		1997 ± 29 BP 48 calBC - 113 calAD	1965.7 ± 16.9 BP 26 calBC - 120 calAD	1956 ± 19 BP 13-124 calAD	4.0	mscs	cb	+	+	+	+	-	+	+	8.6	+++	☒ Leaching + secondary calcite + delayed hardening
		ECH14	i		1566 ± 23 BP 423-571 calAD	1178.6 ± 45.7 BP 166-406 calAD	not possible	3.6	mscs	cb	+	+	+	+	-	-	+	11.8	+++	☒ Leaching + secondary calcite + delayed hardening
Burchtmuur/Antwerp	Belgium	A539 - SL2 (A) - 23 - kik1	i	1000-1200 AD (p)	1120 ± 26 BP 881-994 calAD	1129.8 ± 15.5 BP 885-980 calAD	970 ± 11 BP 1028-1151 calAD	8.5	pss	cb + ub	++	+	+	-	-	-	+	7.5	? (strong dissolution)	☒ Leaching + secondary calcite
		A539 - SL2 (A) - 23 - kik2	bm		1326 ± 20 BP 650-780 calAD	1326 ± 12.8 BP 656-774 calAD	not possible	2.4	pss	cb + ub	++	+	+	+	-	-	+	21.5	? (strong dissolution)	☒ Leaching + secondary calcite
		A539 - SL4 (A) - S88 - kik3	i		1192 ± 20 BP 770-890 calAD	1183 ± 11 BP 772-890 calAD	1064 ± 12 BP 904-1023 calAD	7.6	pss	cb + ub +	++	+	+	-	+	-	+	6.9	? (strong dissolution)	☒ Leaching + secondary calcite

Site	Country	Sample		Period																	Reliability
										diss											
Ostia	Italy	OS-1 - purple fragment	p	First half of 1rst century BC (a)	2145 ± 27 BP 350-50 calBC	1837.9 ± 13.3 BP 132-244 calAD	2105 ± 19 BP 180-40 calBC	7.1	svsfc	cb	-	-	+	+	-	-	+	40.6	+		☑ No alteration + svsfc
		OS-2 - yellow fragment	p	Second half of 4rst century AD (a)	1856 ± 22 BP 120-240 calAD	1665.6 ± 39.6 BP 256-537 calAD	not possible	7.6	svsfc + vs	cb	-	-	+	+	-	-	++	36.4	++		☒ Limestone (svsfc) + delayed hardening
Castle of Horst/Holsbeek	Belgium	KVH1	p	15th century (a)	582 ± 22 BP 1320-1410 calAD	582.2 ± 15.9 BP 1319-1408 calAD	582 ± 22 BP 1320-1410 calAD	5.8	pss	cb	-	-	+	+	+	-	+	16.9	? (presence of clay)		☑ No alteration + pss
		KVH2	p	15th century (a)	634 ± 22 BP 1300-1400 calAD	633.7 ± 10.7 BP 1299-1393 calAD	634 ± 22 BP 1300-1400 calAD	6.8	pss	cb	-	-	+	+	+	-	+	13.4	? (presence of clay)		☑ No alteration + pss
		KVH3	bm	15th century (a)	447 ± 23 BP 1430-1470 calAD	431.6 ± 15.4 BP 1436-1471 calAD	447 ± 23 BP 1430-1470 calAD	6.3	pss	cb	-	-	+	-	+	-	+	16.7	? (presence of clay)		☒ Delayed hardening
Park abbey (ABDIJ VAN PARK)/Heverlee/Leuven		OO.0.8 Trapzall	bm	13th century (ca. 1225-1228, a)	833 ± 21 BP 1174-1265 calAD	832.8 ± 13.1 BP 1179-1263 calBC	848 ± 13 BP 1166-1253 calAD	8.3	none	cb + ub	-	-	+	+	+	+	+	89.0	-		☑ No alteration + no aggregate

Table 2: Summary result table of the radiocarbon outcome (with the three methods used to determine the date), the most important parameters retrieved from the analytical methods, and the reliability of dating with the reason why.

Sample type	Presume historical date	^{14}C / Reliability	Agregate type	Lump state	Dissolution	Secondary carbonates	FTIR	Limestone	Hydraulicity
bm = bedding mortar	a = attested & precise	= expected date &/or ^{14}C date of context	pss = pure siliceous sand	cb = completely burned	- = none	- = none	+ = present	- = none	- = none
p = indoor plaster	p = probable	≠ expected date but could be possible	ssfc = siliceous sand with few carbonates	ib = incompletely burned	+ = slight	+ = few	- = absent	+ = few	+ = slight
r = outdoor render		≠ expected date &/or ^{14}C date of context	csfq = calcareous sand with few quartz grains	ub = unburned	++ = intensively	++ = many		++ = many	++ = moderate
i = infill mortar		= expected date but characterisation suggest that the ^{14}C dating should be unreliable	svs = siliceous volcanic sand	diss = dissolved					+++ = highly
sm = sealing mortar			svsfc = siliceous volcanic sand slightly calcareous						
fm = foundation mortar			cc = crushed ceramics						
			vs = volcanic scoria						
			rmf = reused mortar fragments						
			mscs = mixed siliceous & calcareous sand						
			none = no aggregate						
n/a = not avaliable									

Table 3: Key abbreviation from Table 1.

5. DISSEMINATION AND VALORISATION

The project and the results were disseminated at numerous national and international conferences:

2024   Journée d'études Dater les peintures murales médiévales approches interdisciplinaires, Paris, France

Oral presentation: Datation ^{14}C & caractérisation interdisciplinaire des enduits & mortiers de chaux du donjon du château médiéval de Horst (Holsbeek, Brabant flamand, Belgique) – Résultats, interprétations & limites (Marine Wojcieszak, Laurent Fontaine, Marjolein Deceuninck, Roald Hayen, Jan Elsen, Mathieu Boudin)

2023   GMPCA, Nice, France

Oral presentation: Caractérisation Interdisciplinaire & Datation Radiocarbone des Mortiers de Chaux de l'Abbatiale Sainte-Marie de Floreffe (Belgique) (M. Wojcieszak, F. Chantinne, L. Fontaine, G. Ligovich, R. Hayen, J. Elsen, M. Boudin)

2022   Journées d'Archéologie en Wallonie (JAW), Beez, Belgique

Oral presentation: La Datation au Radiocarbone des Mortiers de Chaux de Bâtiments Wallons : Défis & Perspectives (M. Wojcieszak, L. Fontaine, R. Hayen, J. Elsen, M. Boudin)

Historic Mortars Conference (HMC), Ljubljana, Slovenia

Oral presentation (online): Pre-screening of Lime Mortars for ^{14}C Dating – Preliminary Results (M. Wojcieszak, L. Fontaine, R. Hayen, J. Elsen, T., Van den Brande, G. Ligovich, M. Boudin)

24th Radiocarbon Conference + 10th 14C & Archaeology Conference Zurich, Suisse

Poster 1 : Preliminary study to reduce the amount of sampling for 14C dating of non-buried ivory (M. Wojcieszak, G. Ligovich, T. Van den Brande, M. Boudin)

Poster 2 : Pre-screening of lime mortars for ^{14}C dating – Preliminary results (M. Wojcieszak, L., Fontaine, R. Hayen, J. Elsen, T. Van den Brande, A. Oostvogels, G. Ligovich, M. Rich, M. Boudin)

GMPCA, Chambéry, France

Oral presentation: Développement d'un protocole de présélection des mortiers de chaux pouvant procurer des datations 14C fiables (M. Wojcieszak, L. Fontaine, R. Hayen, T. Van den Brande, A. Oostvogels, J. Elsen, G. Ligovich, M. Boudin)

2021   900e anniversaire de la (re)fondation de l'abbaye de Floreffe, Floreffe, Belgique

Oral presentation: La datation au carbone 14 des mortiers peut-elle aider à reconstituer l'histoire de l'abbaye de Floreffe ? - méthode et résultats préliminaires (M. Wojcieszak, L. Fontaine, R. Hayen, J. Elsen, M. Boudin)

They were also presented during workshops for Master students:

2024   Seminar Science in Cultural Heritage (Interdisciplinary thinking) - TUM School of Engineering and Design, Munich, Germany (online)

Oral presentation: ^{14}C Dating of Historic Lime Mortars (Marine Wojcieszak, Laurent Fontaine, Roald Hayen, Jan Elsen, Mathieu Boudin)

2022   PlaCe, Beyond the eye-ball and below the slip: chemical and mineralogical study of archaeological ceramics and plasters, Leuven, Belgique

Oral presentation: 14C Dating of mortars: new developments (M. Wojcieszak & J. Elsen)

6. PUBLICATIONS

7. ACKNOWLEDGEMENTS

BIBLIOGRAPHY

Addis, Anna, Michele Secco, Fabio Marzaioli, Gilberto Artioli, Alexandra Chavarría Arnau, Isabella Passariello, Filippo Terrasi, and Gian Pietro Brogiolo. 2019. "Selecting the Most Reliable 14 C Dating Material inside Mortars: The Origin of the Padua Cathedral." *Radiocarbon* 61 (2): 375–93.

Al-Bashaireh, K. 2013. "Plaster and Mortar Radiocarbon Dating of Nabatean and Islamic Structures, South Jordan." *Archaeometry* 55 (2): 329–54.

Bakolas, A., E. Aggelakopoulou, and A. Moropoulou. 2008. "Evaluation of Pozzolanic Activity and Physico-Mechanical Characteristics in Ceramic Powder-Lime Pastes." *Journal of Thermal Analysis and Calorimetry* 92 (1): 345–51.

Bakolas, A., G. Biscontin, A. Moropoulou, and E. Zendri. 1998. "Characterization of Structural Byzantine Mortars by Thermogravimetric Analysis." *Thermochimica Acta* 321 (1–2): 151–60.

Barrett, Gerard T., Kerry Allen, Paula J. Reimer, Åsa Ringbom, Jesper Olsen, and Alf Lindroos. 2023. "Ramped Pyrolysis Radiocarbon Dating of Lime Lumps: Establishing the Earliest Mortar-Based Construction Phase of Turku Cathedral, Finland." *Journal of Cultural Heritage* 61 (May):201–10. https://doi.org/10.1016/j.culher.2023.04.004.

Barrett, Gerard Thomas, Evelyn Keaveney, Alf Lindroos, Colm Donnelly, Thomas Schrøder Daugbjerg, Åsa Ringbom, Jesper Olsen, and Paula J. Reimer. 2021. "Ramped Pyroxidation: A New Approach for Radiocarbon Dating of Lime Mortars." *Journal of Archaeological Science* 129:105366.

Boudin, Mathieu, Mark Van Strydonck, Tess van den Brande, Hans-Arno Synal, and Luckas Wacker. 2015. "RICH–a New AMS Facility at the Royal Institute for Cultural Heritage, Brussels, Belgium." *Nuclear Instruments and Methods in Physics Research Section B: Beam Interactions with Materials and Atoms* 361:120–23.

Bronk Ramsey, Christopher. 2009. "Bayesian Analysis of Radiocarbon Dates." *Radiocarbon* 51 (1): 337–60.

Brunello, Vallentina. 2020. "Mortars: A Complex Material in Cultural Heritage. A Multi-Analytical Procedure to Characterize Historical Mortars." Università degli studi dell'insubria. https://core.ac.uk/reader/322778010.

Calandra, Sara, Emma Cantisani, Claudia Conti, Barbara Salvadori, Serena Barone, Lucia Liccioli, Mariaelena Fedi, et al. 2024. "A New Multi-Analytical Procedure for Radiocarbon Dating of Historical Mortars." *Scientific Reports* 14 (1): 19979. https://doi.org/10.1038/s41598-024-70763-2.

Carmine, Lubritto, Marta Caroselli, Stefano Lugli, Fabio Marzaioli, Sara Nonni, S. Marchetti Dori, and Filippo Terrasi. 2015. "AMS Radiocarbon Dating of Mortar: The Case Study of the Medieval UNESCO Site of Modena." *Nuclear Instruments and Methods in Physics Research Section B: Beam Interactions with Materials and Atoms* 361:614–19.

Casadio, F., G. Chiari, and S. Simon. 2005. "Evaluation of Binder/Aggregate Ratios in Archaeological Lime Mortars with Carbonate Aggregate: A Comparative Assessment of Chemical, Mechanical and Microscopic Approaches." *Archaeometry* 47 (4): 671–89.

Daugbjerg, T. S., A. Lindroos, J. Heinemeier, Å. Ringbom, G. Barrett, D. Michalska, I. Hajdas, R. Raja, and J. Olsen. 2021. "A Field Guide to Mortar Sampling for Radiocarbon Dating." *Archaeometry* 63 (5): 1121–40. https://doi.org/10.1111/arcm.12648.

Daugbjerg, Thomas Schrøder, Alf Lindroos, Irka Hajdas, Åsa Ringbom, and Jesper Olsen. 2021. "Comparison of Thermal Decomposition and Sequential Dissolution—Two Sample Preparation Methods for Radiocarbon Dating of Lime Mortars." *Radiocarbon* 63 (2): 405–27.

De Mulder, Guy, Roald Hayen, Mathieu Boudin, Tess Van den Brande, Louise Decq, Magdalena Salas Burguera, Damià Ramis, Herlinde Borms, and Mark Van Strydonck. 2014. "14C Dating and Material Analysis of the Lime Burial of Cova de Na Dent (Mallorca, Spain)." *Radiocarbon* 56 (2): 387–98.

Degryse, Patrick, Jan Elsen, and Marc Waelkens. 2002. "Study of Ancient Mortars from Sagalassos (Turkey) in View of Their Conservation." *Cement and Concrete Research* 32 (9): 1457–63.

Elsen, Jan. 2006. "Microscopy of Historic Mortars—a Review." *Cement and Concrete Research* 36 (8): 1416–24.

Folk, Robert L., and Salvatore Valastro. 1976. "Successful Technique for Dating of Lime Mortar by Carbon-14." *Journal of Field Archaeology* 3 (2): 195–201.

Friesem, David E., Itay Abadi, Dana Shaham, and Leore Grosman. 2019. "Lime Plaster Cover of the Dead 12,000 Years Ago–New Evidence for the Origins of Lime Plaster Technology." *Evolutionary Human Sciences* 1.

Hajdas, Irka, Alf Lindroos, Jan Heinemeier, Åsa Ringbom, Fabio Marzaioli, Filippo Terrasi, Isabella Passariello, Manuela Capano, Gilberto Artioli, and Anna Addis. 2017. "Preparation and Dating of Mortar Samples—Mortar Dating Inter-Comparison Study (MODIS)." *Radiocarbon* 59 (6): 1845–58.

Hayen, Roald, Mark Van Strydonck, Elisabetta Boaretto, Alf Lindroos, Jan Heinemeier, Åsa Ringbom, Sophie Hueglin, Danuta Michalska, Irka Hajdas, and F. Marzaoili. 2016. "Absolute Dating of Mortars–Integrating Chemical and Physical Techniques to Characterize and Select the Mortar Samples." In *Proceedings of the 4th Historic Mortars Conference-HMC2016*, 656–67.

Hayen, Roald, Mark Van Strydonck, Laurent Fontaine, Mathieu Boudin, Alf Lindroos, Jan Heinemeier, Åsa Ringbom, et al. 2017. "Mortar Dating Methodology: Assessing Recurrent Issues and Needs for Further Research." *Radiocarbon* 59 (6): 1859–71.

Heinemeier, Jan, Högne Jungner, Alf Lindroos, Åsa Ringbom, Thorborg von Konow, and Niels Rud. 1997. "AMS 14C Dating of Lime Mortar." *Nuclear Instruments and Methods in Physics Research Section B: Beam Interactions with Materials and Atoms*, Accelerator Mass Spectrometry, 123 (1): 487–95. https://doi.org/10.1016/S0168-583X(96)00705-7.

Heinemeier, Jan, Ålsa Ringbom, Alf Lindroos, and Árnỳ E. Sveinbjörnsdóttir. 2010. "Successful AMS 14 C Dating of Non-Hydraulic Lime Mortars from the Medieval Churches of the Åland Islands, Finland." *Radiocarbon* 52 (1): 171–204.

Hughes, John J., and Simon J. Cuthbert. 2000. "The Petrography and Microstructure of Medieval Lime Mortars from the West of Scotland: Implications for the Formulation of Repair and Replacement Mortars." *Materials and Structures* 33 (9): 594–600.

Kang, Sanha, and Soyeong Kang. 2022. "Characteristics of the Traditional Korean Lime Plaster after and Addition of Perilla Oil." *Materials and Technology* 56 (5): 479–89. https://doi.org/10.17222/mit.2022.528.

Karkanas, Panagiotis. 2007. "Identification of Lime Plaster in Prehistory Using Petrographic Methods: A Review and Reconsideration of the Data on the Basis of Experimental and Case Studies." *Geoarchaeology: An International Journal* 22 (7): 775–96.

Kingery, David W., Pamela B. Vandiver, and Martha Prickett. 1988. "The Beginnings of Pyrotechnology, Part II: Production and Use of Lime and Gypsum Plaster in the Pre-Pottery Neolithic Near East." *Journal of Field Archaeology* 15 (2): 219–43.

Klimesch, Danielle S., and Abhi Ray. 1996. "The Use of DTA/TGA to Study the Effects of Ground Quartz with Different Surface Areas in Autoclaved Cement: Quartz Pastes. Part 1: A Method for Evaluating DTA/TGA Results." *Thermochimica Acta* 289 (1): 41–54. https://doi.org/10.1016/S0040-6031(96)03033-X.

Labeyrie, J., and G. Délibrias. 1964. "Dating of Old Mortars by the Carbon-14 Method." *Nature* 201 (4920): 742–742.

Lico, Alessia, Maya Akouche, Matteo Maria Niccolò Franceschini, Giulia Misseri, Silvia Rescic, and Luisa Rovero. 2024. "Florence City Centre Historical Mortars: Digital Image Analysis of Thin Sections in View of Conservation Actions." *MATEC Web of Conferences* 403:07012. https://doi.org/10.1051/matecconf/202440307012.

Lindroos, Alf, Jan Heinemeier, Å Ringbom, Mats Braskén, and Ámy Sveinbjörnsdóttir. 2007. "Mortar Dating Using AMS 14 C and Sequential Dissolution: Examples from Medieval, Non-Hydraulic Lime Mortars from the Åland Islands, SW Finland." *Radiocarbon* 49 (1): 47–67.

Lindroos, Alf, Åsa Ringbom, Jan Heinemeier, Greg Hodgins, Pia Sonck-Koota, Pia Sjöberg, Lynne Lancaster, Riikka Kaisti, Fiona Brock, and Heikki Ranta. 2018. "Radiocarbon Dating Historical Mortars: Lime Lumps and/or Binder Carbonate?" *Radiocarbon* 60 (3): 875–99.

Maravelaki-Kalaitzaki, P., A. Bakolas, and A. Moropoulou. 2003. "Physico-Chemical Study of Cretan Ancient Mortars." *Cement and Concrete Research* 33 (5): 651–61.

Marzaioli, Fabio, Carmine Lubritto, Sara Nonni, Isabella Passariello, Manuela Capano, and Filippo Terrasi. 2011. "Mortar Radiocarbon Dating: Preliminary Accuracy Evaluation of a Novel Methodology." *Analytical Chemistry* 83 (6): 2038–45.

Michalska, Danuta. 2019. "Influence of Different Pretreatments on Mortar Dating Results." *Nuclear Instruments and Methods in Physics Research Section B: Beam Interactions with Materials and Atoms* 456:236–46.

Michalska, Danuta, Justyna Czernik, and Tomasz Goslar. 2017. "Methodological Aspect of Mortars Dating (Poznań, Poland, MODIS)." *Radiocarbon* 59 (6): 1891–1906.

Michalska, Danuta, and Ma\lgorzata Mrozek-Wysocka. 2020. "Radiocarbon Dating of Mortars and Charcoals from Novae Bath Complex: Sequential Dissolution of Historical and Experimental Mortar Samples with Pozzolanic Admixture." *Radiocarbon* 62 (3): 579–90.

Middendorf, B., G. Baronio, K. Callebaut, and J. J. Hughes. 2000. "Chemical-Mineralogical and Physical-Mechanical Investigations of Old Mortars." In *Proceedings of the International RILEM-Workshop "Historic Mortars: Characteristics and Tests", Paisley*, 53–61.

Middendorf, B., J. J. Hughes, K. Callebaut, G. Baronio, and I. Papayianni. 2005. "Investigative Methods for the Characterisation of Historic Mortars—Part 1: Mineralogical Characterisation." *Materials and Structures* 38 (8): 761–69. https://doi.org/10.1007/BF02479289.

Morillas, Héctor, Gladys Huallparimachi, Maite Maguregui, Iker Marcaida, Euler Gallego-Cartagena, Fernando Astete, and Juan Manuel Madariaga. 2019. "Characterization of Restoration Lime Mortars and Decay By-Products in the Meditation Area of Machu Picchu Archaeological Site." *Science of The Total Environment* 692:23–31.

Moropoulou, A., A. S. Cakmak, G. Biscontin, A. Bakolas, and E. Zendri. 2002. "Advanced Byzantine Cement Based Composites Resisting Earthquake Stresses: The Crushed Brick/Lime Mortars of Justinian's Hagia Sophia." *Construction and Building Materials* 16 (8): 543–52.

Moropoulou, Antonia, Asterios Bakolas, and Katerina Bisbikou. 1995. "Characterization of Ancient, Byzantine and Later Historic Mortars by Thermal and X-Ray Diffraction Techniques." *Thermochimica Acta* 269:779–95.

Nawrocka, Danuta, Jacek Michniewicz, Jacek Pawlyta, and Anna Pazdur. 2005. "APPLICATION OF RADIOCARBON METHOD FOR DATING OF LIME MORTARS." *Geochronometria: Journal on Methods & Applications of Absolute Chronology* 24.

Nonni, Sara, Fabio Marzaioli, Silvano Mignardi, Isabella Passariello, Manuela Capano, and Filippo Terrasi. 2018. "Radiocarbon Dating of Mortars with a Pozzolana Aggregate Using the Cryo2SoniC Protocol to Isolate the Binder." *Radiocarbon* 60 (2): 617–37.

Ortega, L. A., M. C. Zuluaga, A. Alonso-Olazabal, M. Insausti, and A. Ibañez. 2008. "Geochemical Characterization of Archaeological Lime Mortars: Provenance Inputs." *Archaeometry* 50 (3): 387–408.

Ortega, Luis Angel, M. Cruz Zuluaga, Ainhoa Alonso-Olazabal, Maite Insausti, Xabier Murelaga, and Alex Ibañez. 2012. "Improved Sample Preparation Methodology on Lime Mortar for Reliable 14C Dating." *Radiometric Dating*, 3–20.

Paama, Lilli, Ilkka Pitkänen, Hannu Rönkkömäki, and Paavo Perämäki. 1998. "Thermal and Infrared Spectroscopic Characterization of Historical Mortars." *Thermochimica Acta* 320 (1–2): 127–33.

Pecchioni, E., F. Fratini, and E. Cantisani. 2014. "Atlas of the Ancient Mortars in Thin Section under Optical Microscope." *Nardini Editore, Firenze* 78.

Pesce, Giovanni LA, Richard J. Ball, Gianluca Quarta, and Lucio Calcagnile. 2012. "Identification, Extraction, and Preparation of Reliable Lime Samples for 14 C Dating of Plasters and Mortars with the 'Pure Lime Lumps' Technique." *Radiocarbon* 54 (3–4): 933–42.

Pesce, Giovanni, Gianluca Quarta, Lucio Calcagnile, M. D'Elia, Paola Cavaciocchi, Carolina Lastrico, and Rosita Guastella. 2009. "Radiocarbon Dating of Lumps from Aerial Lime Mortars and Plasters: Methodological Issues and Results from San Nicolò of Capodimonte Church (Camogli, Genoa, Italy)." *Radiocarbon* 51 (2): 867–72.

Poduska, Kristin M., Lior Regev, Elisabetta Boaretto, Lia Addadi, Steve Weiner, Leeor Kronik, and Stefano Curtarolo. 2011. "Decoupling Local Disorder and Optical Effects in Infrared Spectra: Differentiating between Calcites with Different Origins." *Advanced Materials* 23 (4): 550–54.

Ponce-Antón, Graciela, Alf Lindroos, Åsa Ringbom, Luis Angel Ortega, Maria Cruz Zuluaga, Irka Hajdas, Jesper Olsen, and Juantxo Agirre Mauleon. 2020. "Comparison of Sample Preparation Procedures for Mortar Radiocarbon Dating. Case Study of Irulegi Castle (Navarre, Spain)." *Quaternary Geochronology* 60:101110.

Regev, Lior, Kristin M. Poduska, Lia Addadi, Steve Weiner, and Elisabetta Boaretto. 2010. "Distinguishing between Calcites Formed by Different Mechanisms Using Infrared

Spectrometry: Archaeological Applications." *Journal of Archaeological Science* 37 (12): 3022–29.

Reimer, Paula J., William EN Austin, Edouard Bard, Alex Bayliss, Paul G. Blackwell, Christopher Bronk Ramsey, Martin Butzin, Hai Cheng, R. Lawrence Edwards, and Michael Friedrich. 2020. "The IntCal20 Northern Hemisphere Radiocarbon Age Calibration Curve (0–55 Cal kBP)." *Radiocarbon* 62 (4): 725–57.

Ronen, Avraham, Arnon Bentur, and Itzhak Soroka. 1991. "A Plastered Floor from the Neolithic Village, Yiftahel (Israel)." *Paléorient*, 149–55.

Sironić, Andreja, Alexander Cherkinsky, Damir Borković, Suzana Damiani, Jadranka Barešić, Eduard Visković, and Ines Krajcar Bronić. 2023. "A New Approach on Data Extrapolation for Mortar Dating in the Zagreb Radiocarbon Laboratory." *Nuclear Instruments and Methods in Physics Research Section B: Beam Interactions with Materials and Atoms* 537:119–24.

Suzuki, Michio, Yannicke Dauphin, Lia Addadi, and Steve Weiner. 2011. "Atomic Order of Aragonite Crystals Formed by Mollusks." *CrystEngComm* 13 (22): 6780–86.

Synal, Hans-Arno, Martin Stocker, and Martin Suter. 2007. "MICADAS: A New Compact Radiocarbon AMS System." *Nuclear Instruments and Methods in Physics Research Section B: Beam Interactions with Materials and Atoms*, Accelerator Mass Spectrometry, 259 (1): 7–13. https://doi.org/10.1016/j.nimb.2007.01.138.

Toffolo, Michael B. 2021. "The Significance of Aragonite in the Interpretation of the Microscopic Archaeological Record." *Geoarchaeology* 36 (1): 149–69. https://doi.org/10.1002/gea.21816.

Toffolo, Michael B., Lior Regev, Stéphan Dubernet, Yannick Lefrais, and Elisabetta Boaretto. 2019. "FTIR-Based Crystallinity Assessment of Aragonite–Calcite Mixtures in Archaeological Lime Binders Altered by Diagenesis." *Minerals* 9 (2): 121.

Toffolo, Michael B., Lior Regev, Eugenia Mintz, Ifat Kaplan-Ashiri, Francesco Berna, Stéphan Dubernet, Y. Xin, Johanna Regev, and Elisabetta Boaretto. 2020. "Structural Characterization and Thermal Decomposition of Lime Binders Allow Accurate Radiocarbon Age Determinations of Aerial Lime Plaster." *Radiocarbon* 62 (3): 633–55.

Toffolo, Michael B., Giulia Ricci, Rémy Chapoulie, Luisa Caneve, and Ifat Kaplan-Ashiri. 2020. "Cathodoluminescence and Laser-Induced Fluorescence of Calcium Carbonate: A Review of Screening Methods for Radiocarbon Dating of Ancient Lime Mortars." *Radiocarbon*, 1–20.

Van Strydonck, Mark, Roald Hayen, Mathieu Boudin, Tess van den Brande, Magdalena Salas Burguera, Damià Ramis, Herlinde Borms, and Guy De Mulder. 2015. "14 C Dating of the Lime Burial of Cova de Na Dent (Mallorca, Spain): Optimization of the Sample Preparation and Limitations of the Method." *Radiocarbon* 57 (1): 161–71.

Van Strydonck, Mark JY, Klaas Van Der Borg, Arie FM De Jong, and Eduard Keppens. 1992. "Radiocarbon Dating of Lime Fractions and Organic Material from Buildings." *Radiocarbon* 34 (3): 873–79.

Van Strydonck, Mark, and K Van der Borg. 1990. "The Construction of a Preparation Line for AMS-Targets at the Royal Institute for Cultural Heritage, Brussels." *Bulletin Koninklijk Instituut Voor Kunstpatrimonium* 23:228–34.

Wacker, L., M. Němec, and J. Bourquin. 2010. "A Revolutionary Graphitisation System: Fully Automated, Compact and Simple." *Nuclear Instruments and Methods in Physics Research Section B: Beam Interactions with Materials and Atoms*, Proceedings of the Eleventh International Conference on Accelerator Mass Spectrometry, 268 (7): 931–34. https://doi.org/10.1016/j.nimb.2009.10.067.

Weber, J., T. Köberle, and F. Pintér. 2013. "Methods of Microscopy to Identify and Characterise Hydraulic Binders in Historic Mortars—A Methodological Approach." In *Historic Mortars*, 21–31. Springer.

Wojcieszak, Marine, Tess Van den Brande, Gaia Ligovich, and Mathieu Boudin. 2020. "Pretreatment Protocols Performed at the Royal Institute for Cultural Heritage (RICH) Prior to AMS 14C Measurements." *Radiocarbon*, 1–11. https://doi.org/10.1017/RDC.2020.64.

Wojcieszak, Marine, Laurent Fontaine, Jan Elsen, Roald Hayen, Alexander Lehouck, and Mathieu Boudin. 2024. "HISTORIC LIME MORTARS COMPOSITION AND TERMINOLOGY FOR RADIOCARBON DATING—CASE STUDIES BASED ON THIN-SECTION PETROGRAPHY AND CATHODOLUMINESCENCE." *Radiocarbon*, 1–21.

ANNEXES

Study of mortars from Saint Martin's church (Rutten - Tongeren) for the BRAIN 2.0 PalC project

Context of the site

The present St Martin's church is a neo-classical church. It was built in 1844 against the preserved 13th-century Romanesque tower. The church is centrally located in a walled cemetery (Ginst and Smeets 2014). As part of the installation of an underfloor heating system at St. Martin's Church in Rutten, the Flanders Heritage Agency mandated a surface excavation (Figure 1) to carry out a planar excavation (2014/055). The survey was entrusted to Studiebureau Archeologie bvba. The site work was carried out in phases from 27 February 2014 to 28 March 2014.
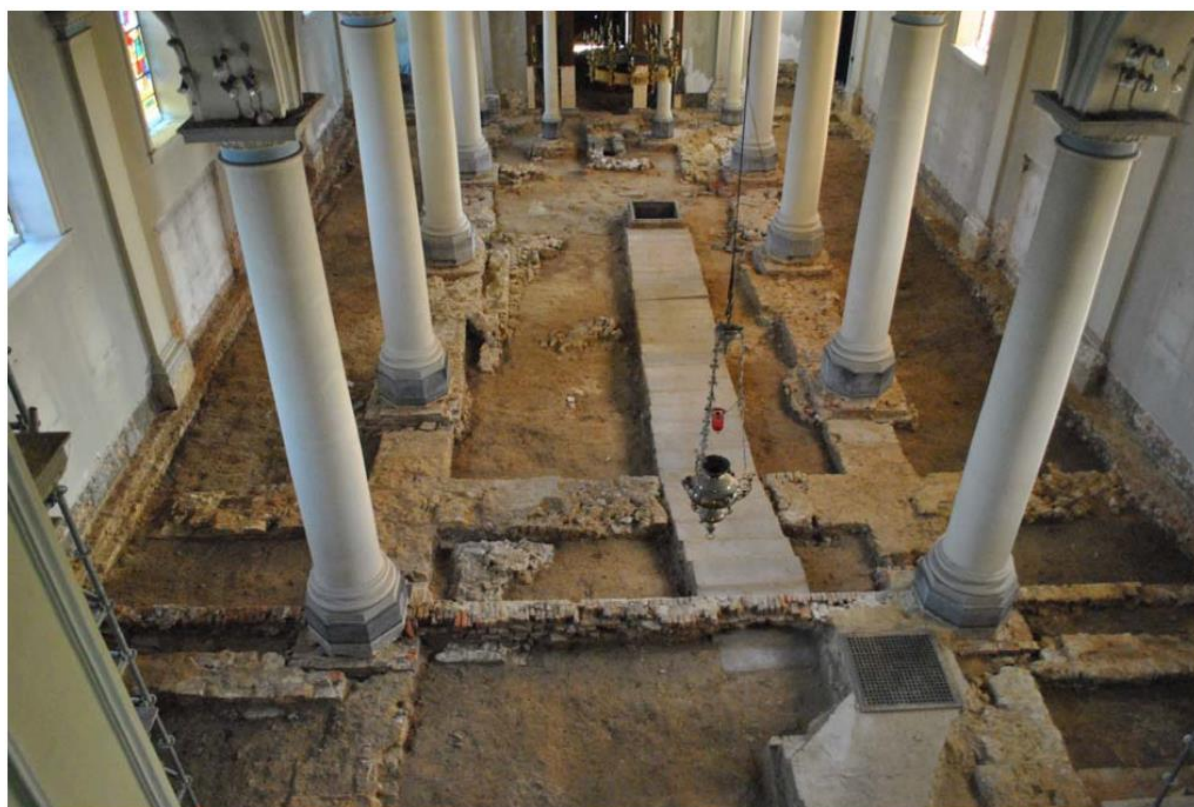
Figure 1: Upper view of the planar excavation of the St. Martin's Church in Rutten.

Material

From these excavations, numerous mortar samples were collected for radiocarbon dating. For the PALc project, four of them were included because enough matter was still available to perform the necessary analyses. Two of them were dated several years ago (sp162 7B and sp32 3A) and two were dated during the PALc project (sp18 9A and sp33 4). The presumed historical date is the Merovingian period (480-880 AD) for all of them except for sp33 4 which was suspected to come from the Romanesque period (1000-1150 AD).

Results & Discussion

Macroscopic descriptions

The main colour of all the samples (Figure 2) is beige tending to very pale brown (10YR 8/3 to 10YR 8/2) according to the Munsell soil colour charts. They are all specular, probably due to the presence of coarse grains of quartz, mica or well crystallised calcite. The lime lumps appear as white inclusions with a main size of ~1 mm and the biggest ones measure ~2 to 6 mm. All samples contain grey inclusions that do not react with dilute hydrochloric acid which indicates that they are probably siliceous aggregates. Samples sp33 4 and sp162 7B exhibit black soft inclusions that are most probably charcoal fragments. Red soft and angular inclusions can be observed for all samples and are most likely terracotta fragments.
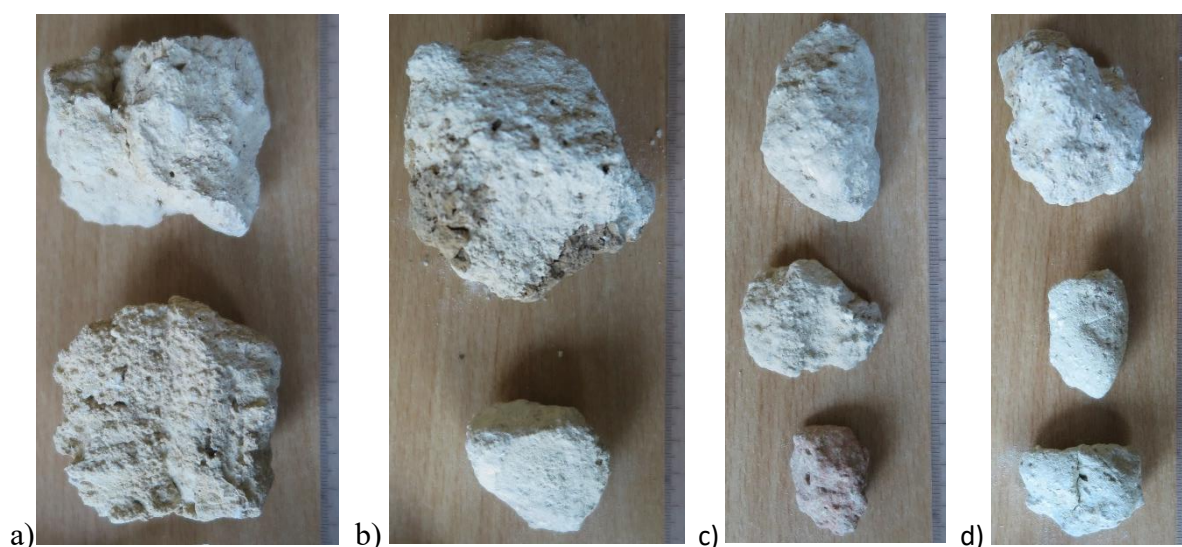
Figure 2: Mortar samples: a) sp18 9A , b) sp33 4, c) sp162 7B and d) sp32 3A.

Fourier transform Infrared (FTIR) spectroscopy on inclusions & binder

The binders (beige, Figure 3) contain calcite and silicates including quartz and clay. The binders of sp18 9A and sp32 3A also contain nitrates and aragonite, respectively. The lime lumps (white, Figure 3) are mainly made of calcium carbonates (calcite and aragonite) sometimes with a bit of silicates (that probably come from the binder). Contrary to what was expected from the macroscopic descriptions, the grey inclusions (grey, Figure 3) are not made of silicates but carbonates (calcite & aragonite) except for sample sp18 9A for which silicates including quartz and clay with nitrates are present. The spectra of the red inclusions (red, Figure 3) exhibit the features of silicates including quartz and maybe sometimes haematite. Amorphous carbon was detected for the black inclusions (black, Figure 3). The brown spread on the surface of sample sp33 4 comprises silicates including quartz and clay with some nitrates.
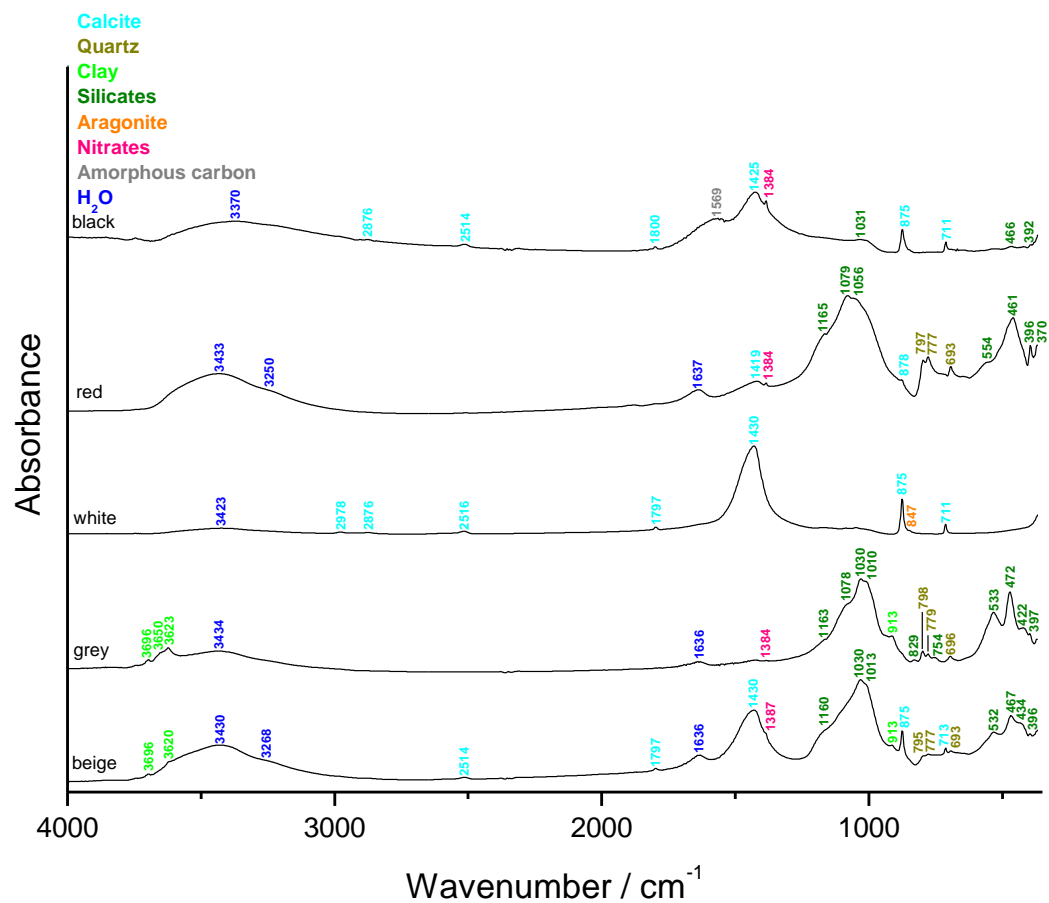
a)
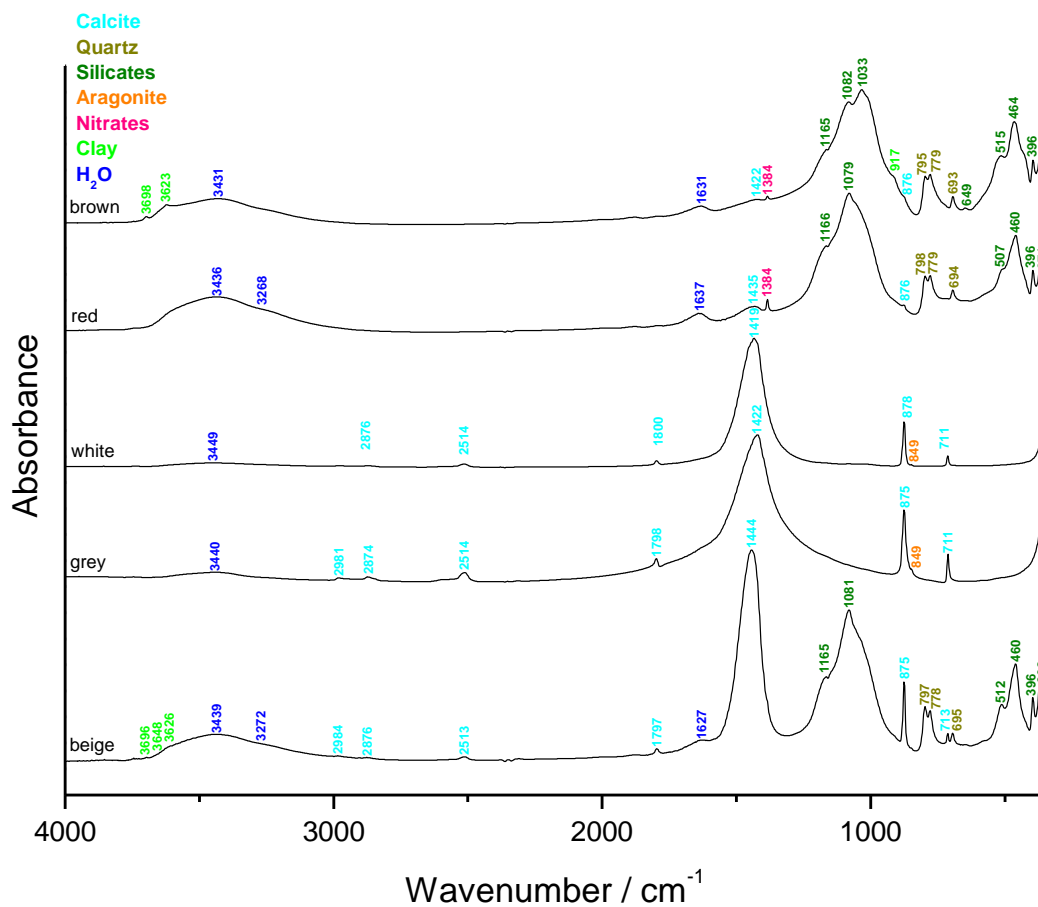
b)
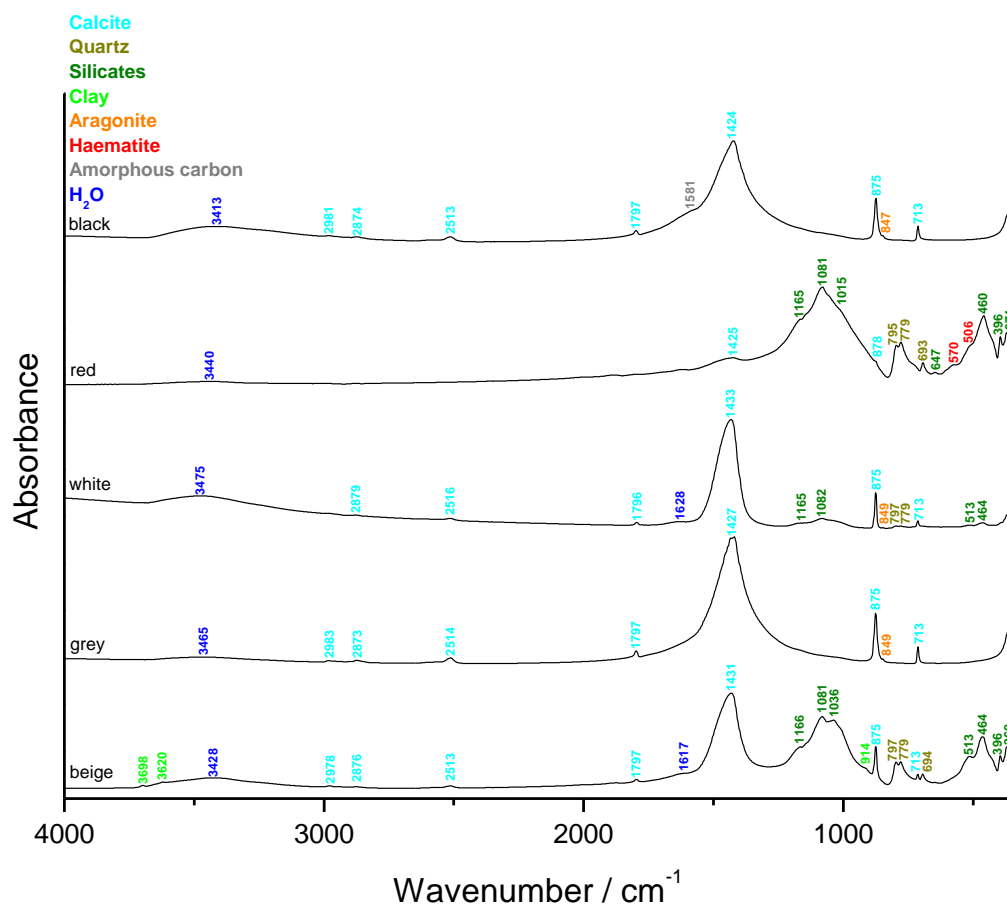
c)
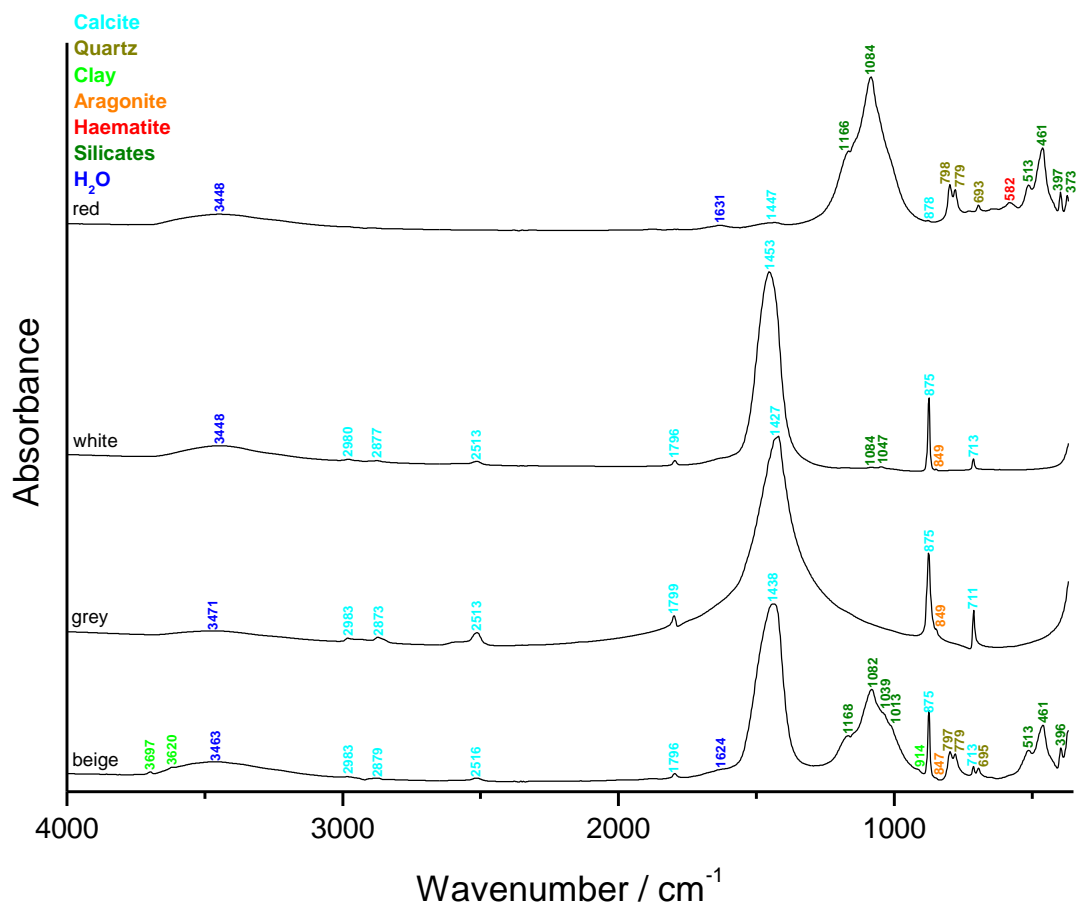
d)

Figure 3: FTIR spectra obtained on the inclusions and binder (beige) of the mortar samples: a) sp18 9A, b) sp33 4, c) sp162 7B and d) sp32 3A.

Binder:sand ratio

The calculated binder:sand ratio (in volume unit) using a bulk density of 1.35 kg/dm^3 for the sand and 0.575 kg/dm^3 for the lime is close to 3:2 for the sample sp18 9A, close to 5:2 for the sample sp33 4, close to 5:3 for the sample sp162 7B, and close to 2:1 for the sample sp32

	sp18 9A	sp33 4	sp162 7B	sp32 3A
Sample weight (g)	2,4	1,8	2,4	2,8
Crucible weight (g)	14,6	16,8	19,5	19,2
Weight calcined (g)	16,1	17,7	20,6	20,7
%ins	**61,5**	**50,0**	**58,2**	**54,2**

Table 1: Percentage of insoluble residue

Cathodoluminescence

Cathodoluminescence observations of the thin-sections and powders of the samples sp33 4, sp162 7B and sp32 3A are presented Figure 4. All the thin-sections (Figure a, c & e) exhibit the presence of quartz grains with a dark purple hue, K-feldspars in bright blue and the binder is dull. For sp33 4 (Figure 4a) and sp32 3A (Figure 4e), only a few bright red limestone grains are observed and some of the lime lumps exhibit are reddish colour because they are incompletely burnt. The sample sp162 7B (Figure 4c) contains a large quantity of bright red limestone fragments that ended up in the powdered sample with particles size lower than 75 µm (Figure 4d). The powdered samples of sp33 4 (Figure 4b) and sp32 3A (Figure 4f) display mainly a red tile or dull colour (binder) with a few bright blue K-feldspars, also some plagioclase green grains and a few bright red limestone grains.
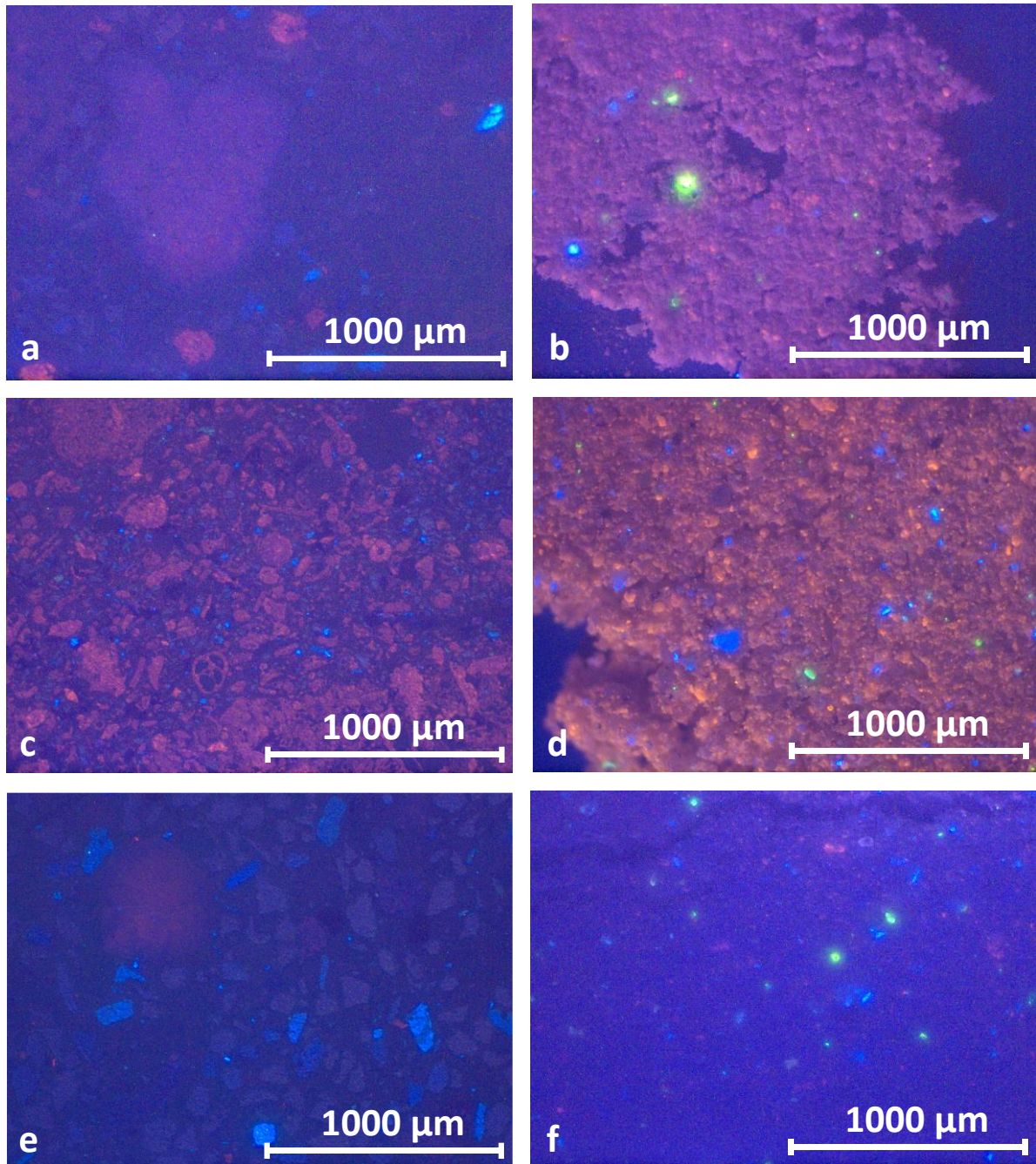
Figure 4: Characteristic cathodoluminescence images of: a) the thin section X2127 of sp33 4, b) the powdered sp33 4 mortar with particle size lower than 75 µm, c) the thin-section X2277 of sp162 7B, d) the powdered sp162 7B mortar with particle size lower than 75 µm, e) the thin-section X2278 of sp32 3A, and f) the powdered sp32 3A mortar with particle size lower than 75 µm.

Thin-section petrography

The mortar sp18 9A (Figure 5 & Table 2) is rather in poor condition, it has been partially dissolved. Secondary carbonates are present in pores (Figure 5b). The lime inclusions are completely burned and underburned (Figure 5f). Crushed ceramic fragments are present (Figure 5c) as well as limestone (Figure 5d) and reused mortar fragments. The fragments of reused mortar are not dissolved in opposition to the intergranular binder.
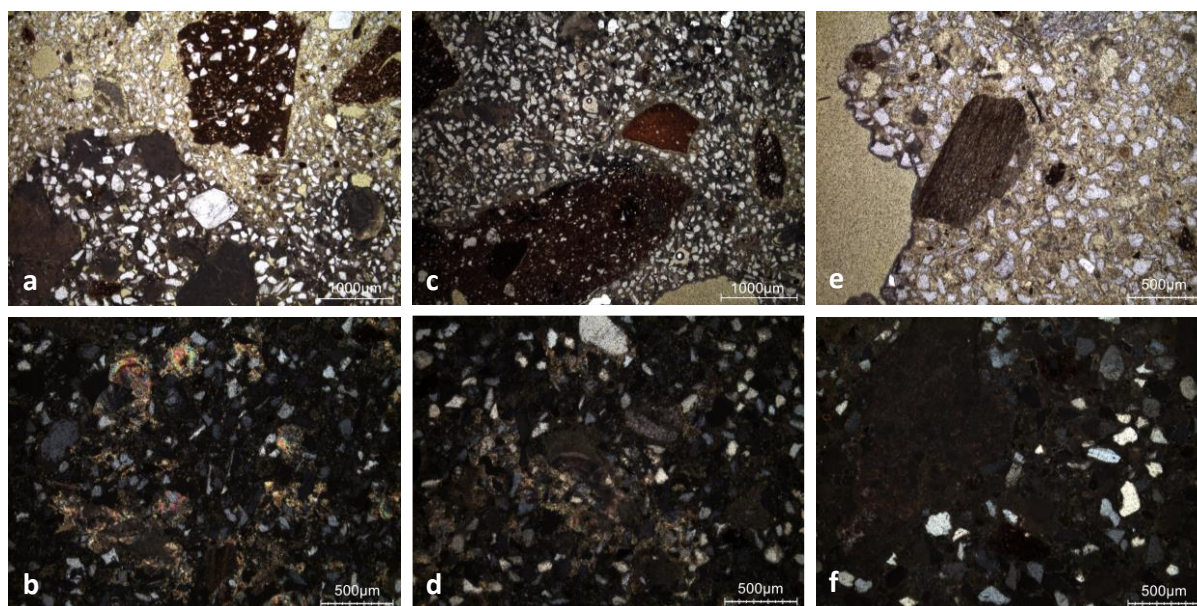
Figure 5: Representative photomicrographs of the sp18 9A thin-section X2124: a) overview image in plain polarised light (PPL); b) secondary carbonates in cross polarised light (XPL); c) PPL image showing terracotta; d) possible limestone fragments in XPL; e) PPL image with a schist fragment; f) partially burned lime lump in XPL.

Binder	**Texture**	micritic
	Lump state	completely burned, underburned
	Lump size	916 µm ; 1.45 mm ; 480 µm ; 1.45 mm ; 845 µm
	Lump frequency	medium
Aggregate	**Grain size**	very fine to medium (some very coarse terracotta & reused mortar fragments)
	Mineralogy	siliceous sand (quartz, K-feldspars, schist, sandstone, glauconite, mica) with terracotta, limestone and reused mortar fragments
	Shape	subangular / subrounded
Appearance	**Homogeneity**	relatively heterogeneous
	Macroporosity	high
	Pore structure	irregular / sometimes connected
Admixtures	**Type**	-
Alteration	**Type**	dissolution secondary carbonates

Table 2: Main characteristics of the mortar sp18 9A retrieved from the observations of the thin-section X2124.

The mortar sp33 4 is rather in poor condition (Figure 6 & Table 3), it has been partially dissolved. Some parts are unaltered, and some others dissolved. Secondary carbonates are present in pores (Figure 6d). The lime inclusions are completely burned. Crushed ceramic fragments are also present (Figure 6c).
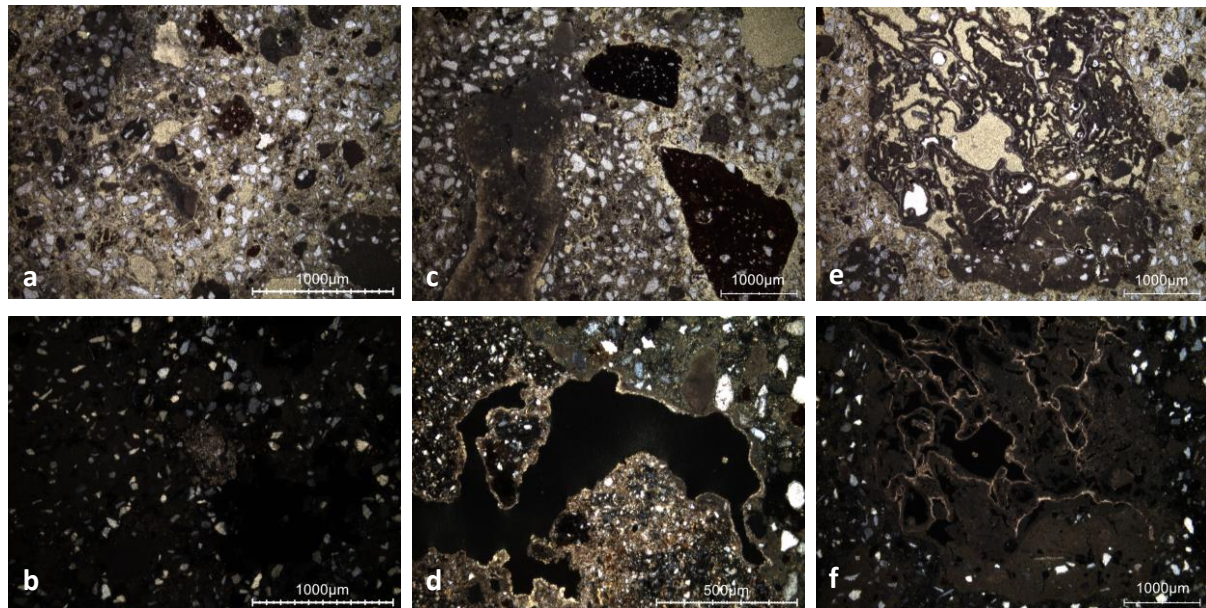
Figure 6: Representative photomicrographs of the sp33 4 thin-section X2127: a) overview image in PPL; b) limestone grains from aggregate in XPL; c) PPL image showing crushed ceramic fragments; d) secondary carbonates and silty-clay agglomerate in XPL; e) PPL image with spongiform lump with secondary carbonates; f) partially burned lime lump in XPL.

Binder	**Texture**	micritic
	Lump state	completely burned
	Lump size	80 µm, 2.6 mm, 5 mm
	Lump frequency	numerous
Aggregate	**Grain size**	very fine to fine
	Mineralogy	siliceous sand (quartz, K-feldspars, glauconite) with a few limestone grains and crushed ceramics
	Shape	subangular / subrounded
Appearance	**Homogeneity**	relatively homogeneous
	Macroporosity	high
	Pore structure	irregular / sometimes connected
Admixtures	**Type**	-

Alteration	**Type**	dissolution secondary carbonates

Table 3: Main characteristics of the mortar sp33 4 retrieved from the observations of the thin-section X2127.

The thin-section examination of the sample sp162 7B (Figure 7 & Table 4) highlighted a high quantity of limestone in the aggregate used. It was recognised because of the presence of sandy biopelmicrite (Figure 7e) and fossil inclusions (Figure 7d & f). Secondary carbonates were observed in cracks (Figure 7b).
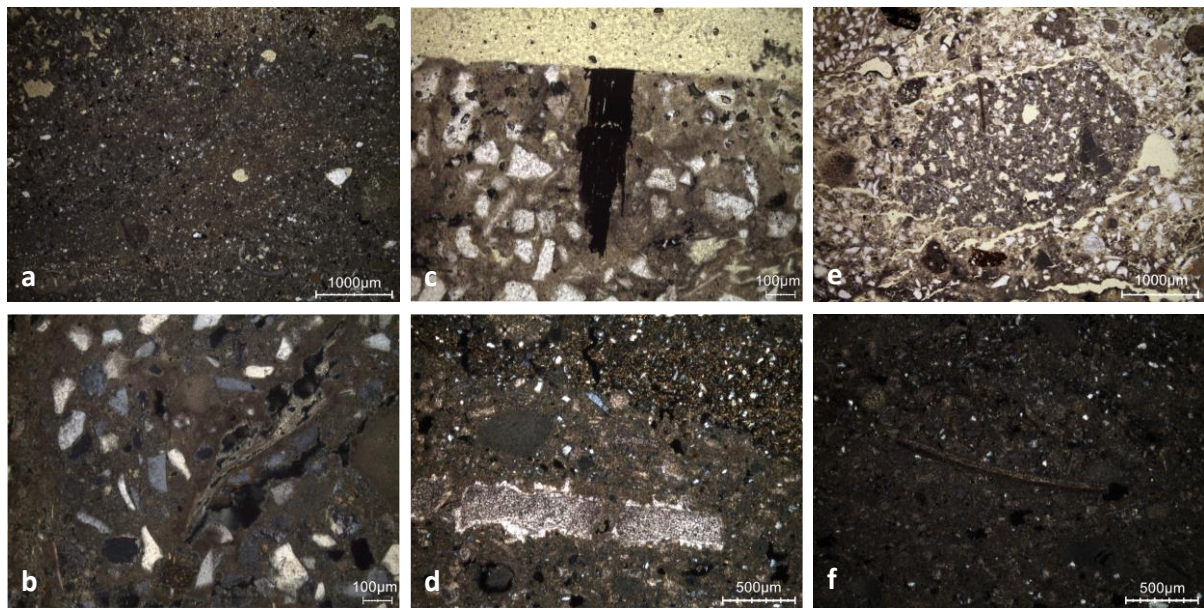
Figure 7: Representative photomicrographs of the sp162 7B 4 thin-section X2128 & X1438: a) overview image in PPL; b) secondary carbonates in crack in XPL; c) PPL image showing a charcoal fragment; d) large limestone fragment in XPL; e) PPL image with sandy biopelmicrite; f) thin shell fragment in XPL.

Binder	**Texture**	micritic
	Lump state	completely burned
	Lump size	150 μm to 2.5 mm
	Lump frequency	numerous
Aggregate	**Grain size**	very fine to coarse
	Mineralogy	mixed siliceous & calcareous sand (biopelmicrite, quartz, K-feldspar, glauconite) (sand with bioclasts/calcareous grains)
	Shape	subangular / subrounded
Appearance	**Homogeneity**	relatively homogeneous
	Macroporosity	low
	Pore structure	irregular / sometimes connected

Admixtures	**Type**	soil
Alteration	**Type**	cracks? dissolution?

Table 4: Main characteristics of the mortar sp162 7B retrieved from the observations of the thin-section X2128 & X1438.

The mortar sp32 3A is rather is good condition (Figure 8 & Table 5). A pure siliceous sand was used as aggregate (slightly glauconitic and micaceous quartz sand). No secondary carbonates were found. Most of the lime lumps are completely burned but some of them are underburned (Figure 8c, d & e).
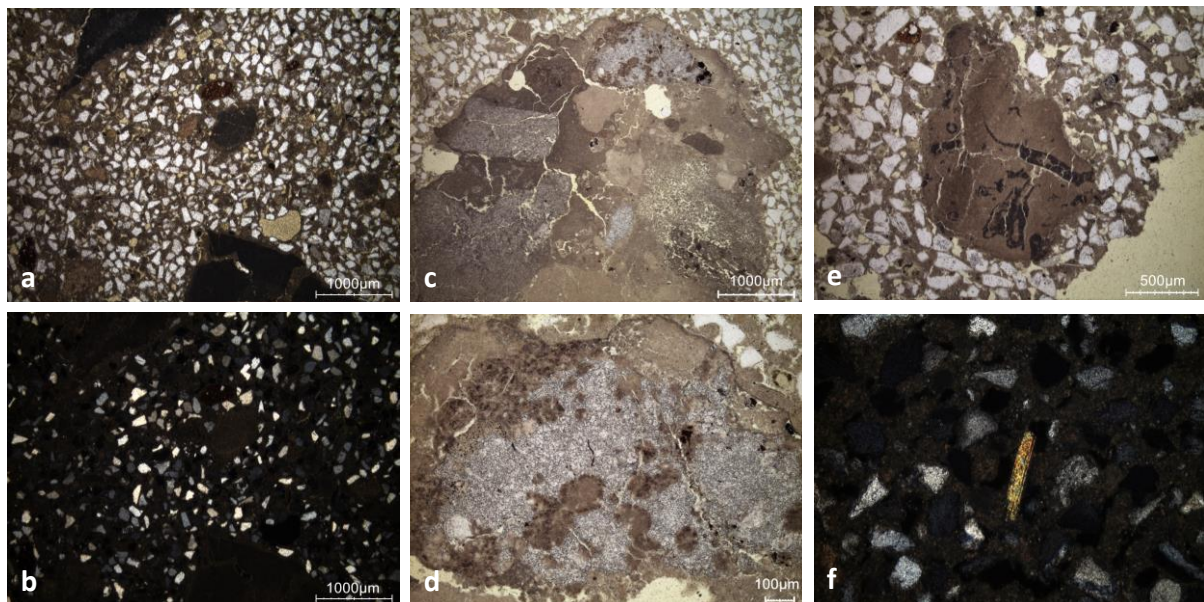
Figure 8: Representative photographs of the sp32 3A 4 thin-section X2129 & X1433: a) overview image in PPL; b) same image in XPL in XPL; c) PPL image showing a big lime lump with incompletely burned limestone; d) big lime lump detail incompletely burned fragment in PPL; e) PPL image with a lime lump underburned (remnants of fossils in dark); f) mica flake in XPL.

Binder	**Texture**	micritic
	Lump state	underburned & completely burned
	Lump size	275 µm to 5 mm
	Lump frequency	numerous
Aggregate	**Grain size**	very fine to medium (or to coarse considering sandy-clay agglomerates)
	Mineralogy	siliceous sand (quartz, K-feldspar, mica, glauconite) + sandy-clay agglomerates
	Shape	subangular / subrounded
Appe	**Homogeneity**	relatively homogeneous

	Macroporosity	medium / high
	Pore structure	cracks, irregular, sometimes connected
Admixtures	**Type**	-
Alteration	**Type**	cracks

Table 5: Main characteristics of the mortar sp32 3A retrieved from the observations of the thin-section X2129 & X1433.

Thermogravimetric analysis (TGA) on whole samples

The apparent hydraulicity index (aHI) calculated from Figures 9-12 is around 43, 22, 13 and 15% for samples sp18 9A, sp33 4, sp162 7B and sp32 3A, respectively. This values might indicate a strong hydraulicity forsp18 9, a moderate hydraulicity for sp33 4 and a slight hydraulicity for sp162 7B and sp32 3A. However, the values obtained from the thermal analyses might not reflect the reality when the mortars have been dissolved or contain clayish aggregate that can compromise the calculation. The amount of carbonates is ~18, 32, 58 and 31 wt% for samples sp18 9A, sp33 4, sp162 7B and sp32 3A, respectively. The temperature of quartz transition phase is observed around 571-9°C (Rickard, Riessen, and Walls 2010) for both samples (Figure 6 & 7). The main weight loss of ancient mortars is expected between 600 and 900 °C and is indicative of the decomposition of calcium carbonate ($CaCO_3$) into calcium oxide (CaO) and carbon dioxide (CO_2) (Ahmmed et al. 2024). The end temperature of calcium carbonate decomposition is ~798, 818, 841 and 810°C for samples sp18 9A, sp33 4, sp162 7B and sp32 3A, respectively. No gypsum was detected. The percentage of carbonates and the end temperature are higher for the sample sp162 7B because it contains a high amount of fossil carbonates.
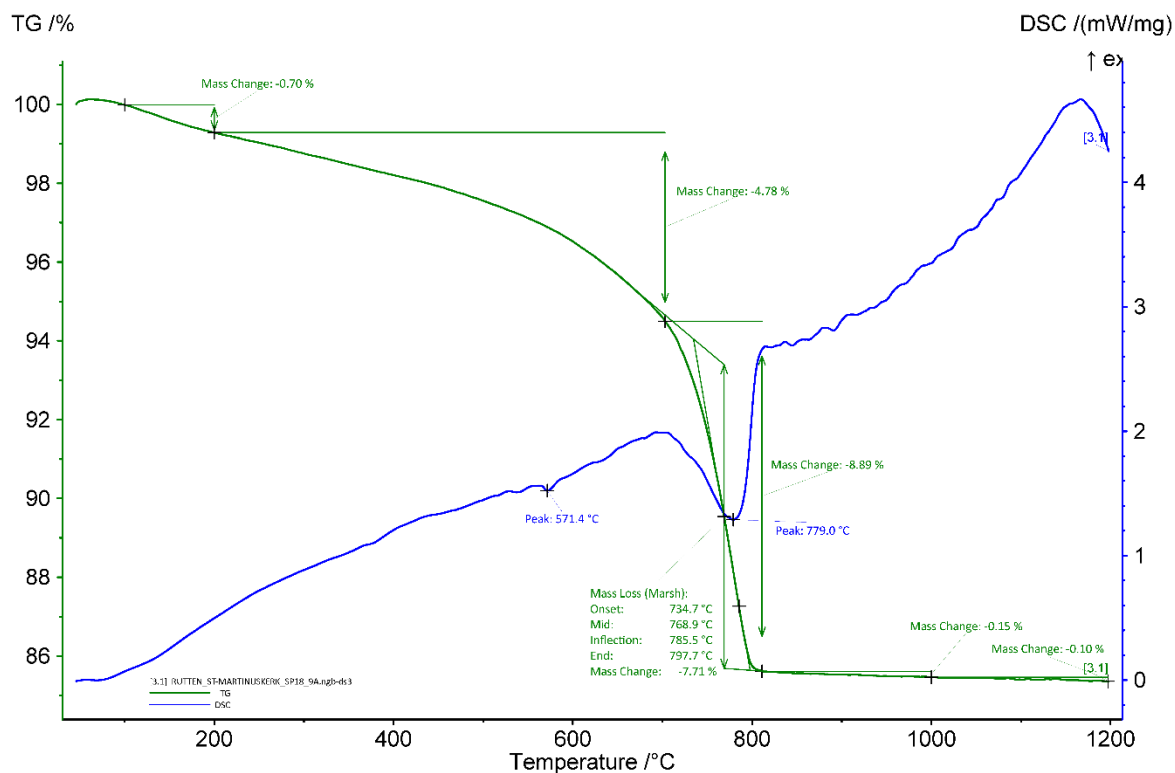
Figure 9: Coupled TG-DSC analysis of the plaster sp18 9A upon heating to a temperature of 1200° C at a heating rate of 20 °C/min under an inert atmosphere (He flushed at 50 ml/min). The weight loss determined by thermogravimetric analysis (TG, wt%, green curve) and the result of the differential scanning calorimetric analysis (DSC, mW/mg, blue curve) are both presented.
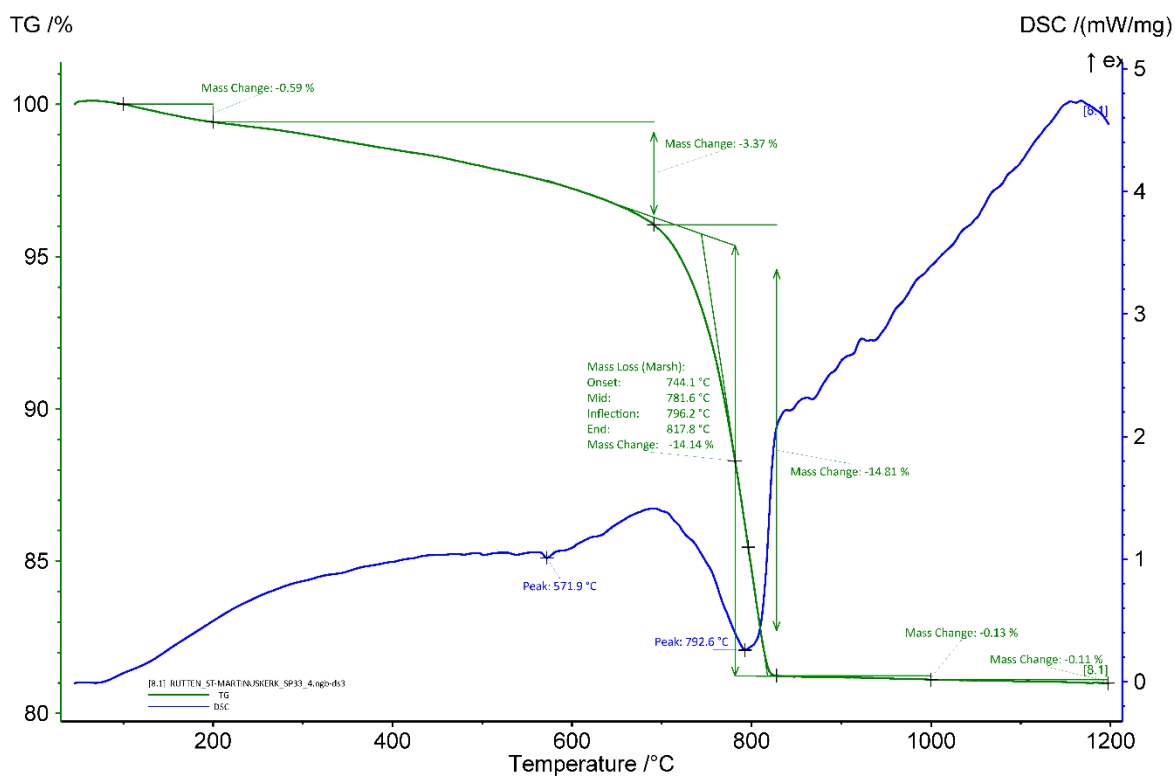
Figure 10: Coupled TG-DSC analysis of the plaster sp33 4 upon heating to a temperature of 1200° C at a heating rate of 20 °C/min under an inert atmosphere (He flushed at 50 ml/min). The weight loss determined by thermogravimetric analysis (TG, wt%, green curve) and the result of the differential scanning calorimetric analysis (DSC, mW/mg, blue curve) are both presented.
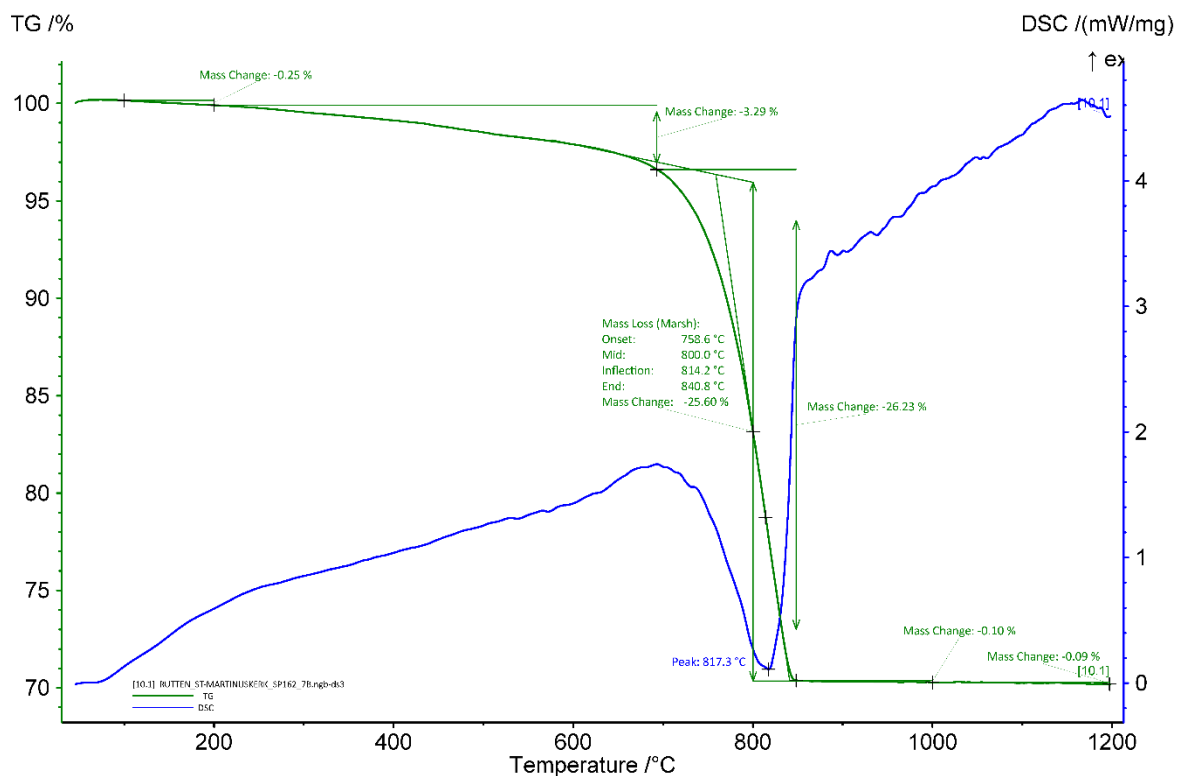
Figure 11: Coupled TG-DSC analysis of the plaster sp162 7B upon heating to a temperature of 1200° C at a heating rate of 20 °C/min under an inert atmosphere (He flushed at 50 ml/min). The weight loss determined by thermogravimetric analysis (TG, wt%, green curve) and the result of the differential scanning calorimetric analysis (DSC, mW/mg, blue curve) are both presented.
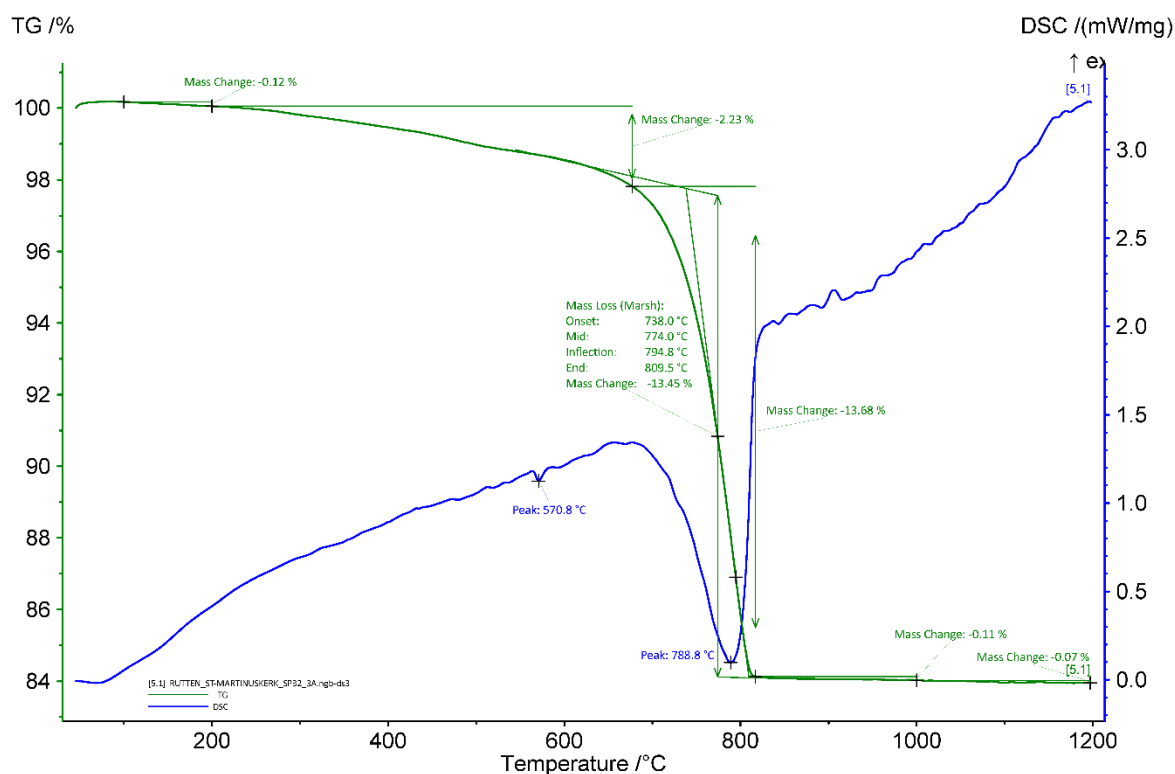
Figure 12: Coupled TG-DSC analysis of the plaster sp32 3A upon heating to a temperature of 1200° C at a heating rate of 20 °C/min under an inert atmosphere (He flushed at 50 ml/min). The weight loss determined by thermogravimetric analysis (TG, wt%, green curve) and the result of the differential scanning calorimetric analysis (DSC, mW/mg, blue curve) are both presented.

Grinding/particle separation

While grinding sample sp18 9A, red (terracotta) and grey (possible limestone) were removed. Sample sp33 4 was rather hard to grind, the mud (brown) on the surface was scratched away and the grey/white angular pieces were removed while grinding. For sample sp162 7B, a large limestone fragment was removed (3-4 cm, very hard & grey, 5.4 g); also a lot of red, grey, white and beige pieces were present in the fraction with particules > 500 μm. The later observation is also valid for the sample sp32 3A that was very hard to grind; while gently grinding the sample, red, and brown pieces were removed.

FTIR on powders with particle size <75 μm

Only the powdered samples with particle size lower than 75 μm from the mortars sp162 7B and sp32 3A were analysed by FTIR (Figure 13). They show a similar spectrum with calcite, silicates, quartz and clay. Aragonite was only detected for the sample sp162 7B.
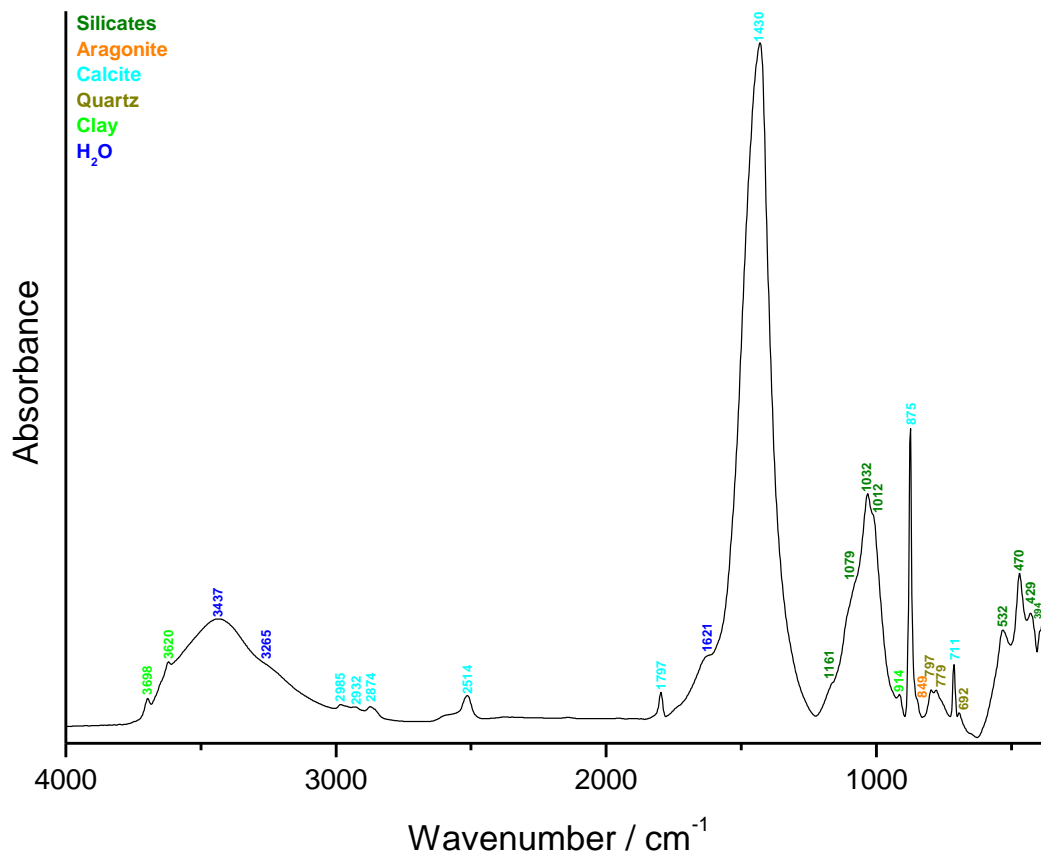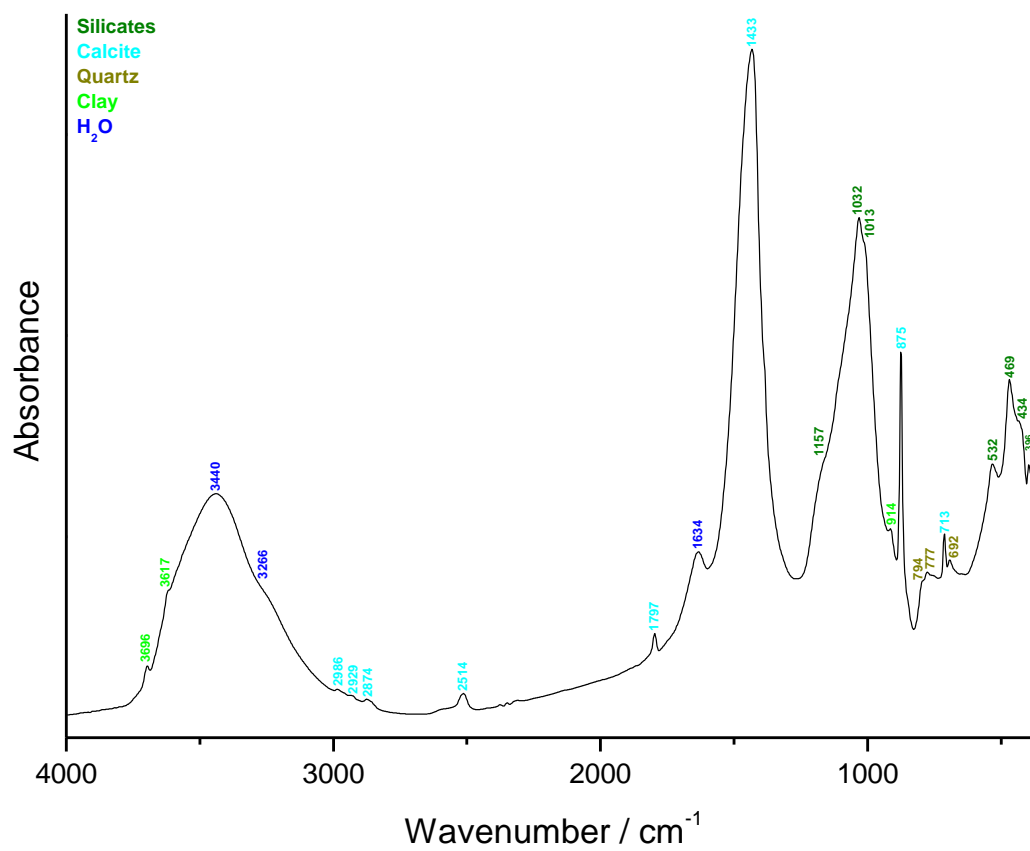
Figure 13: FTIR spectra of the powdered samples with particle size < 75 μm: a) sp162 7B and b) sp32 3A.

TGA on powders with particle size <75 μm

For the samples sp162 7B and sp32 3A, the aHI is higher for the powders with particle size <75 μm (~19 and 39%, respectively) compared to the whole mortar sample (13 and 15%, respectively). It is around 14% for the powder sample sp33 4 which is lower compared to the whole sample (~22%). These differences could be explained by the presence of clayish particles that end up in more or less important quantity in the powdered sieved samples. The powder from the sample sp18 9A was not processed. The quantity of carbonates is lower in the powder (~39 w%) compared to the whole sample (~58 wt%) for sample sp162 7B, a part of the larger limestone fragments was removed. The same is observed for the powdered sample sp32 3A (~24 w%) compared to the whole sample (~31 w%). For the sample sp33 4, it is higher in the powder (~63 w%) compared to the whole sample (~32 w%) because a large part of the sand was eliminated when sieved. Indeed, no quartz was detected in the powder (Figure 14). The end temperature of calcium carbonate decomposition is ~848, 831 and 809°C for the powdered samples sp33 4, sp162 7B and sp32 3A, respectively. It is higher compared to the whole sample sp33 4 (818°C) maybe because the powder is more pure compared to the whole mortar sample which increases the decomposition temperature. It is lower compared to the whole sample sp162 7B (841°C) because, as for the carbonates quantity, the larger limestone fragments were isolated when sieving. It is the same for the whole sample sp32 3A (810°C).

Figure 14: Coupled TG-DSC analysis of the powdered mortar sp33 4 with particle size < 75 μm upon heating to a temperature of 1200° C at a heating rate of 20 °C/min under an inert atmosphere (He flushed at 50 ml/min). The weight loss determined by thermogravimetric analysis (TG, wt%, green curve) and the result of the differential scanning calorimetric analysis (DSC, mW/mg, blue curve) are both presented.

Figure 15: Coupled TG-DSC analysis of the powdered mortar sp162 7B with particle size < 75 µm upon heating to a temperature of 1200° C at a heating rate of 20 °C/min under an inert atmosphere (He flushed at 50 ml/min). The weight loss determined by thermogravimetric analysis (TG, wt%, green curve) and the result of the differential scanning calorimetric analysis (DSC, mW/mg, blue curve) are both presented.

Figure 16: Coupled TG-DSC analysis of the powdered mortar sp32 3A with particle size < 75 µm upon heating to a temperature of 1200° C at a heating rate of 20 °C/min under an inert atmosphere (He flushed at 50 ml/min). The weight loss determined by thermogravimetric analysis (TG, wt%, green curve) and the result of the differential scanning calorimetric analysis (DSC, mW/mg, blue curve) are both presented.

Radiocarbon results

The tests prior to the CO_2 extraction revealed a good amount of carbon (Table 6) for the sample sp33 4 (7 %) and medium to low for the other samples (2.6 to 3.7 %).

RICH	Sample type	Method	C (%)	σ (%)	m (g)	Age BP	Calibrated date (oxcal - 95.4%)	Age BP extrapolated	Calibrated date (oxcal - 95.4%)	Age BP extrapolated with stat	Calibrated date (oxcal - 95.4%)	Age BP average first dates	Calibrated date (oxcal - 95.4%)	Reliability of dating
35457 (sp189A)	mortar < 75 µm	HCl (10 fractions)	2.64	0.15	3.83	-	-	1293 ± 26	665-774 calAD	1038.2 ± 13.5	992-1025 calAD	(first 4 fractions) 1089 ± 13	895-995 calAD	☒
32648 (sp33 4)	mortar < 75 µm	HCl (10 fractions)	7.08	0.13	1.36	-	-	1293 ± 24	670-780 calAD	1236.3 ± 14.1	702-877 calAD	(F1. F2. F3 & F5) 1249 ± 12	700-830 calAD	☒
21058 (sp162 7B)	charcoal	AAA (60/30/60)	-	-	-	1297 ± 32	657-776 calAD	-	-	-	-	-	-	☑
21428.4 (sp162 7B)	mortar < 38 µm	HCl (8 fractions)	3.79	-	-	-	-	1471 ± 34	552-648 calAD	1349.3 ± 19.2	646-772 calAD	(first 3 fractions) 1492 ± 20	565-640 calAD	☒
21064 (sp32 3A)	charcoal	HCl	-	-	-	1293 ± 32	657-797 calAD	-	-	-	-	-	-	☑
21517.2 (sp32 3A)	mortar <38 µm	HCl (8 fractions)	3.43	-	-	-	-	1244 ± 33	676-880 calAD	1250 ± 16.9	678-864 calAD	(first 3 fractions) 1219 ± 20	770-890 calAD	☑

Table 6: Radiocarbon results

The radiocarbon dating of the sample sp18 9A give mixed results (Table 6 & Figure 17). The extrapolation of the curve provides a plausible date (1293 ± 26 BP - 665-774 calAD) but the average of the first four dates (1089 ± 13 BP - 895-995 calAD) and the extrapolated date with statistic (1038.2 ± 13.5 BP - 992-1025 calAD) are older compared to the expected date (Merovingian – 480-880 AD).
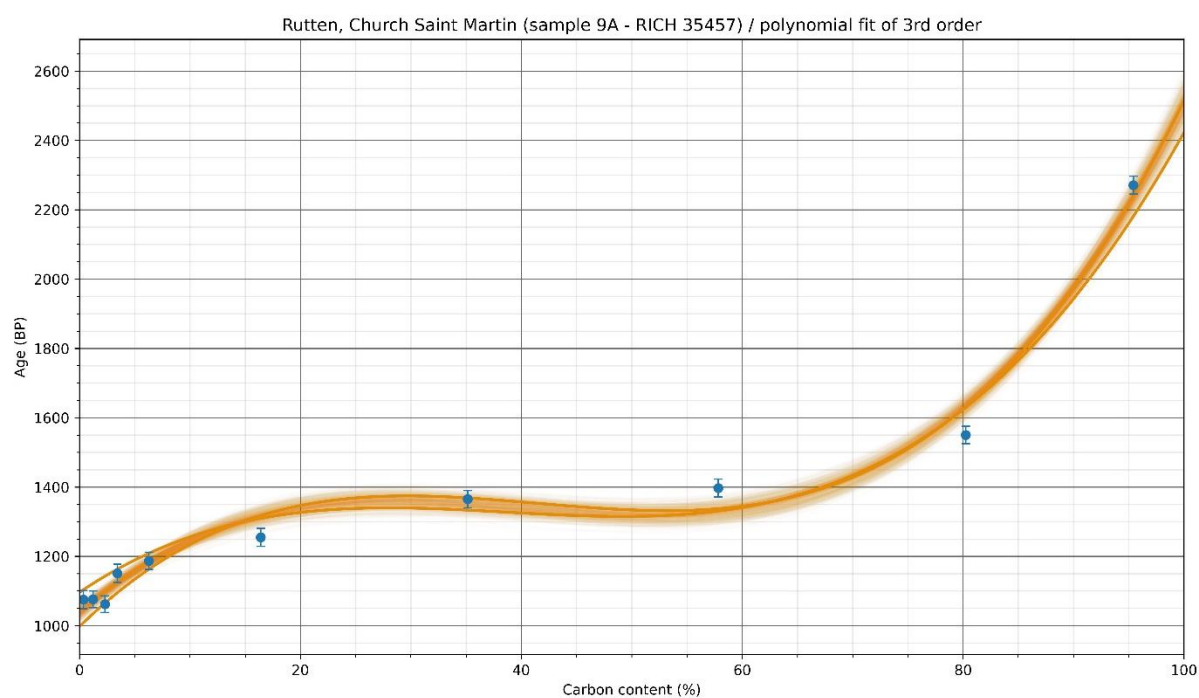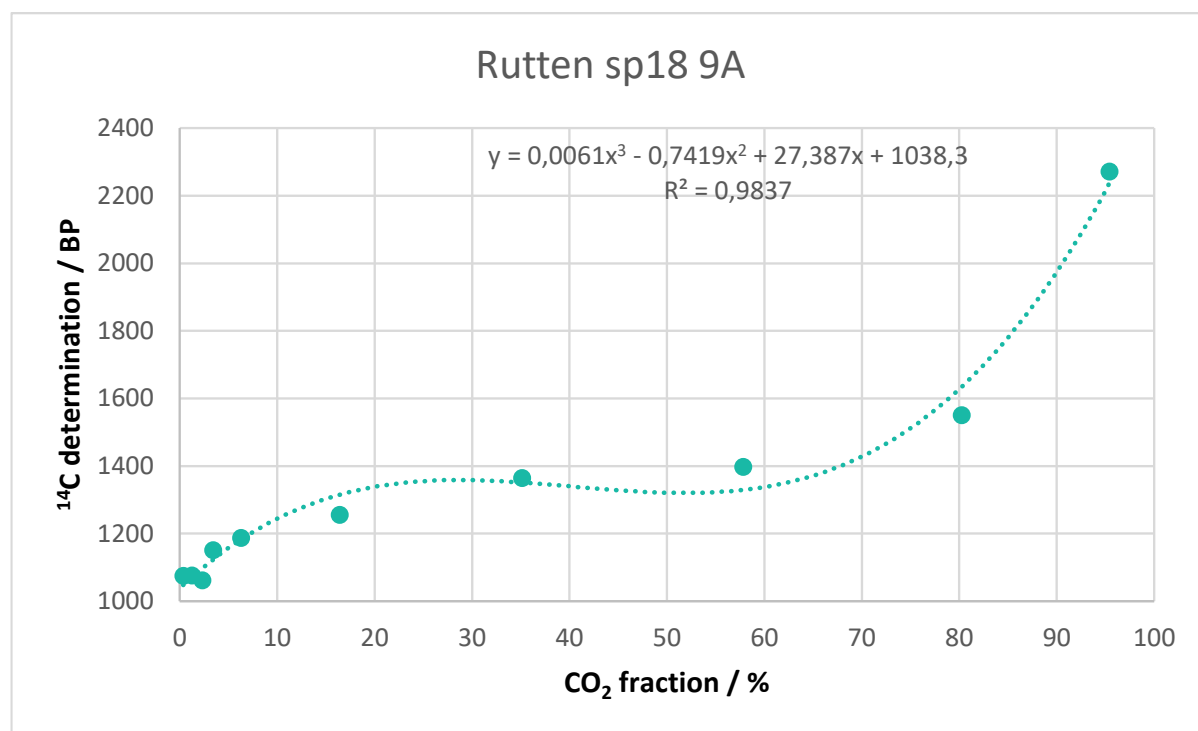
Figure 17: Radiocarbon results for the powdered mortar sp18 9A with particles < 75 µm as a function of the CO_2 fraction.

For the sample sp33 4, the result of the extrapolation (Table 4 & Figure 18), the statistic on the extrapolation and the average all fall within the Merovingian period. However, this sample was expected to date from the Romanesque period (1000-1150). The first fractions are spread and the second fraction is younger than the first one which is rather uncommon. The results are not in favour of a reliable dating.
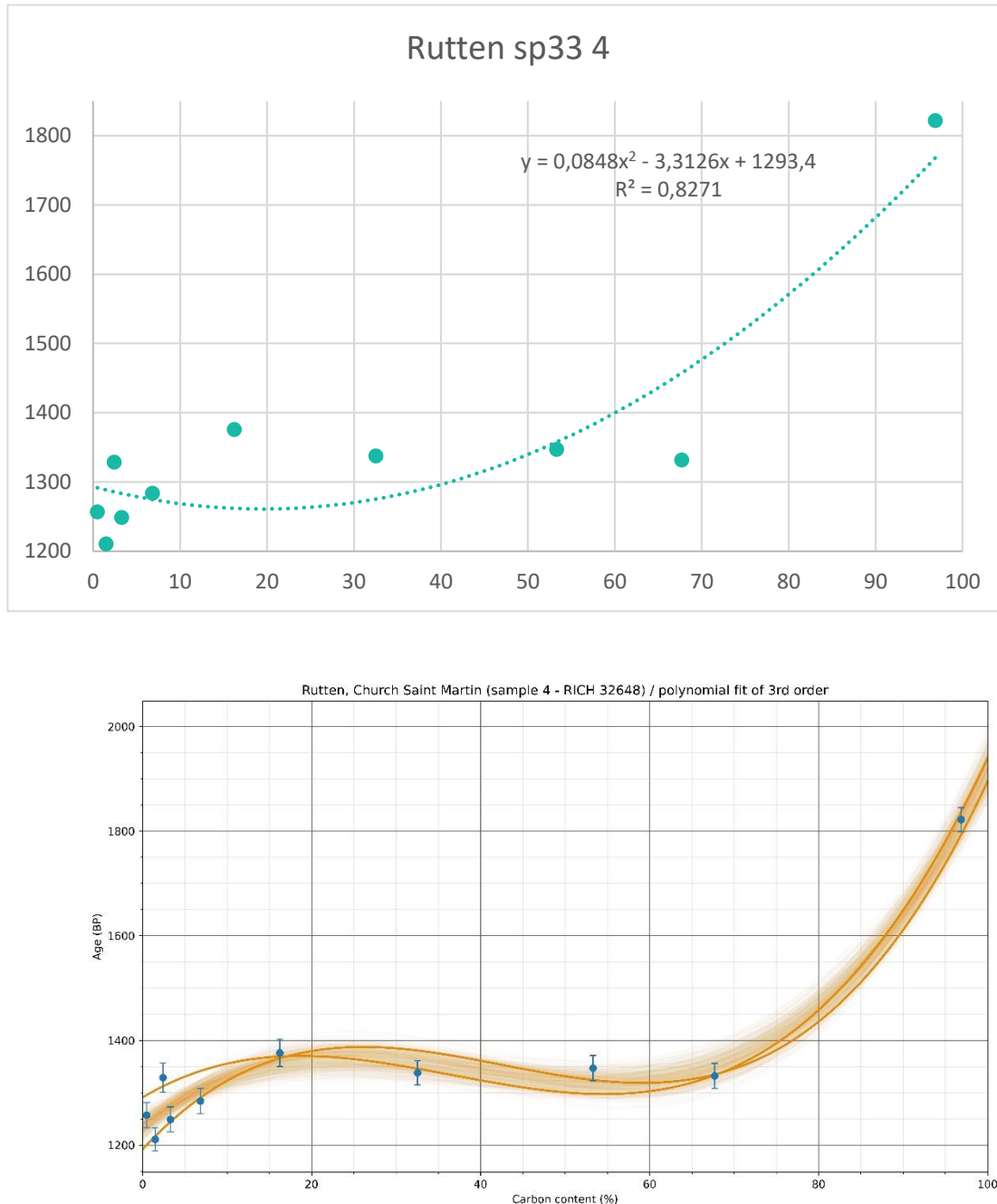
Figure 18: Radiocarbon results for the powdered mortar sp33 4 with particles < 75 μm as a function of the CO_2 fraction (the graph at the bottom shows the statistic on the results).

In the case of sample sp162 7B, both the extrapolation and the average dates (Table 4 & Figure 19) provide a similar result falling in the Merovingian period. However, the date obtained for the charcoal (1297 ± 32 BP) - 657-776 calAD) is younger than the mortar (1471 ± 34 BP - 552-648 calAD) which is impossible. The charcoal date should be the same or older than the mortar.

This sample is thus not appropriate for radiocarbon dating. The extrapolated date with statistic falls (1349.3 ± 19.2 BP - 646-772 calAD) however in the same time period as the charcoal.

Rutten sp162 7B

$$y = -0,0007x^3 + 0,0309x^2 + 32,43x + 1471,1$$
$$R^2 = 0,995$$
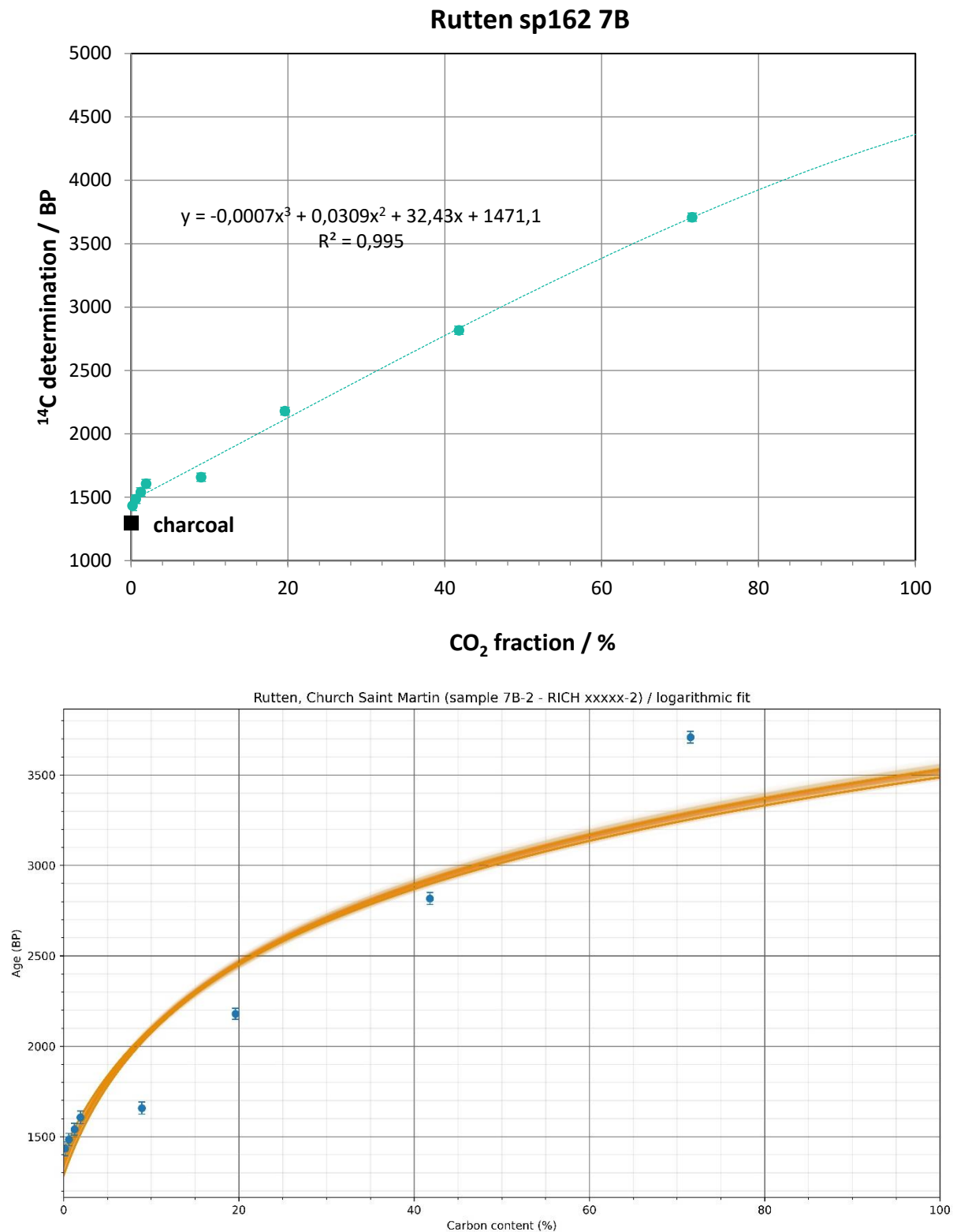
Figure 19: Radiocarbon results for the powdered mortar sp162 7B with particles < 75 μm as a function of the CO_2 fraction (the graph at the bottom shows the statistic on the results).

For sample sp32 3A, the result of the extrapolation (Table 4 & Figure 20), the statistic on the extrapolation and the average all fall within the same range corresponding to the late Merovingian period. The charcoal is slightly older than the mortar (1293 ± 32 BP - 657-797 calAD). The results of the mortar dating are therefore most probably reliable.
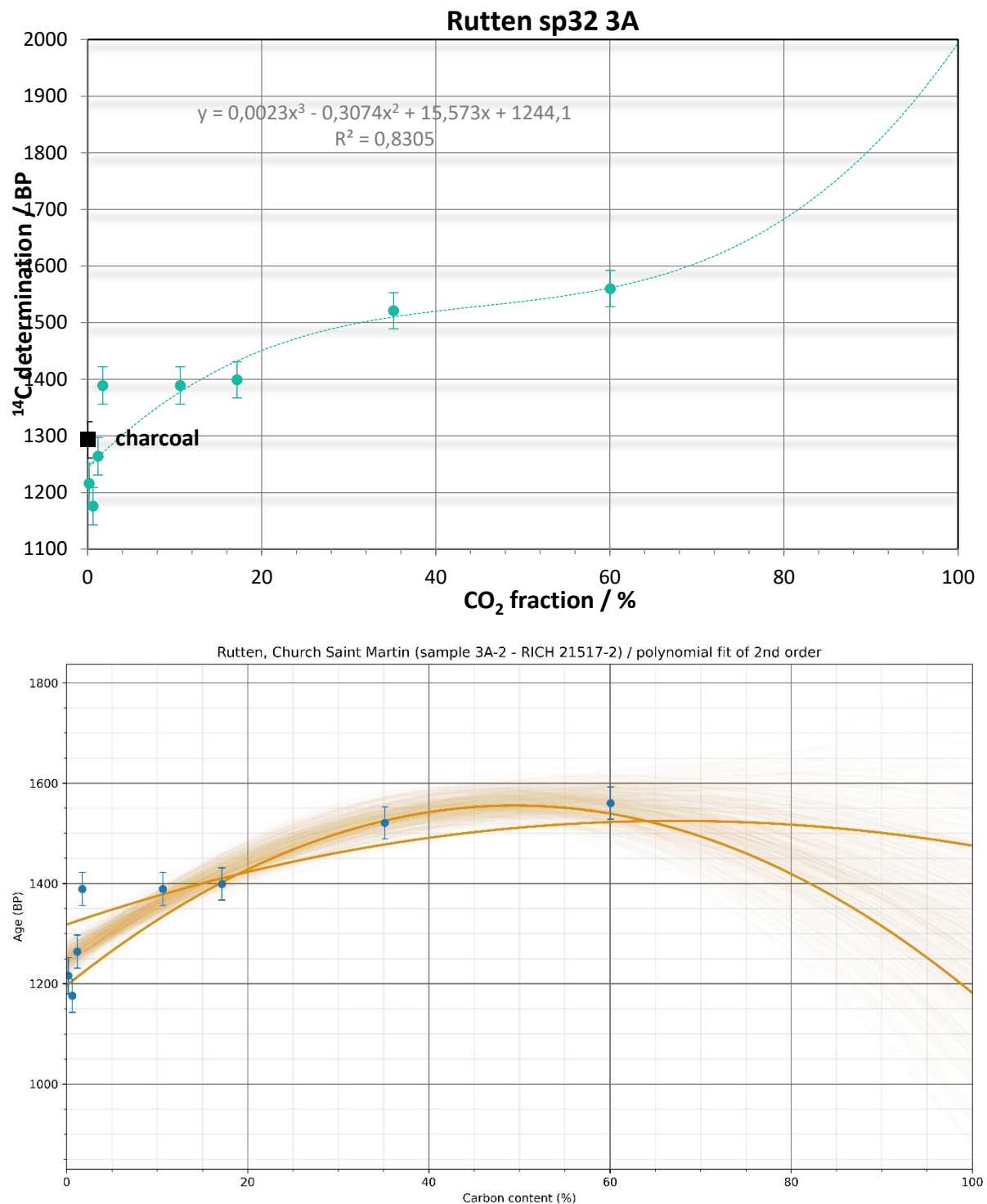
Figure 20: Radiocarbon results for the powdered mortar sp32 3A with particles < 75 μm as a function of the CO_2 fraction (the graph at the bottom shows the statistic on the results).

Conclusions

From the four samples selected for the project, only the sample sp32 3A provides a reliable carbon date because of its good preservation state and the use of a pure siliceous sand. Sample sp162 7B is not considered as a reliable mortar for radiocarbon dating because of the use of a calcareous sand that make the radiocarbon result older than the reality. For the sample sp18 9A, the poor state of preservation with the presence of dissolution and precipitation are also not suitable for radiocarbon dating, the date obtained is older than expected. The sample sp33 4 supposed to be from the Romanesque period by the archaeologists is rather is a good state of preservation which question the presumed historical date. It could maybe have been set during the Merovingian period.

Bibliography

Ginst. Vanessa Vander. and Maarten Smeets. 2014. "Het Archeologisch Onderzoek in de Sint-Martinuskerk Te Rutten." *Rapportage Onroerend Erfgoed Vlaanderen* 786. https://oar.onroerenderfgoed.be/publicaties/ROEV/786/ROEV0786-001.pdf.

Study of mortars from a Roman wall in Tongeren for the BRAIN 2.0 PalC project

Context of the site

In 2014, the radiocarbon laboratory was contracted to sample a Roman city wall in Tongeren (Limburg Province) that was estimated to date from the 4th century AD. The wall was being destroyed to build an underground parking lot. The external façade of the Roman wall had very wide mortar joints so that the bedding mortar would continue through to the mortar used for the central infill of the wall (Hayen et al. 2017). It is a cocciopesto mortar obtained from the city wall of the roman city *Atuatuca Tungrorum*. It consisted of the bedding mortar and rendering of the external facade of the wall (Hayen et al. 2016).

Figure 1: Photograph showing the excavation of the Roman wall in Tongeren.

Material

The Roman mortar came from a wall partially preserved in curb and in foundation. Only the curb was sampled. The red colour is almost certainly from the use of terracotta as filler. Charcoal fragments from a brown layer that was present very fragmentarily perhaps as a finishing layer were also sampled and dated. The sample was taken a few centimetres below the surface of wall remains that originally came from the rising part of the structure (Hayen et al. 2017).

Results & Discussion

Macroscopic descriptions

The main colour of the mortar is pink (Figure 2, 2.5Y 8/3) according to the Munsell soil colour charts. It is very heterogeneous. The lime lumps appear as white inclusions with a main size of ~ 2 mm and the biggest ones measure ~6 mm. White and hard inclusions not reacting with HCl might be some earthenware or siliceous aggregate. Grey inclusions could be siliceous aggregates but the large one (several centimetres) might be a limestone fragment. The red inclusions are probably made of terracotta and the black and soft ones of charcoal.

Figure 2: Representative pieces of the mortar from the Roman wall.

Fourier transform Infrared (FTIR) spectroscopy on inclusions & binder

The binder (pink, Figure 3) mainly contains calcium carbonates (calcite and aragonite) and silicates including quartz. The lime lumps (hard white, Figure 3) are also mainly made of calcium carbonates (calcite and aragonite) with a few silicates. The white pebble is exclusively made of silicates including quartz. The beige fraction of the mortar only contains calcium carbonates (calcite and aragonite). The large grey fragment is probably made of limestone since it also only contain calcium carbonates (calcite and aragonite). Silicates including quartz and possibly haematite were detected for the red inclusions. Finaly, the spectrum of the black inclusions comprises amorphous carbon with calcium carbonates (calcite and aragonite) and silicates including quartz.
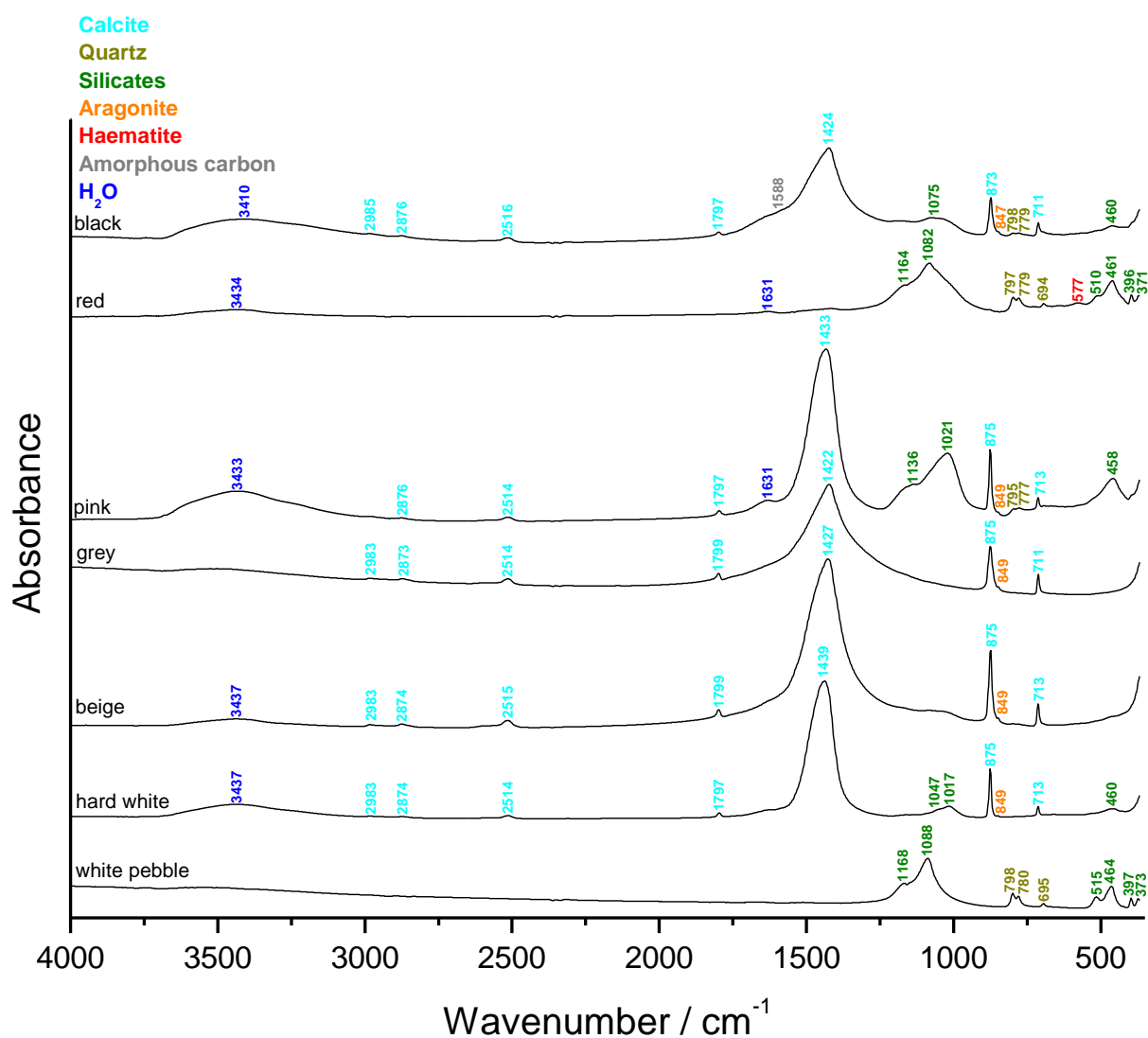
Figure 3: FTIR spectra obtained on the inclusions and binder (pink) of the mortar sample from the Roman wall.

Thin-section petrography

Rounded spots (ghosts of hydromagnesite, now almost completely replaced by secondary carbonates) are recognised both inside lime lumps (Figure 4c & d) and in the intergranular binder, indicating the use of a dolomitic limestone to produce the lime mortar. Small limestone fragments, presumably from the limestone used for lime production, are also observed. The aggregate consists mainly of pulverised terracotta (Figure 4e & f). Quartz grains are also found, where one can consider that a part (or the whole) comes from the grinding of terracotta. The original binder was most likely subjected to several dissolution-precipitation processes.
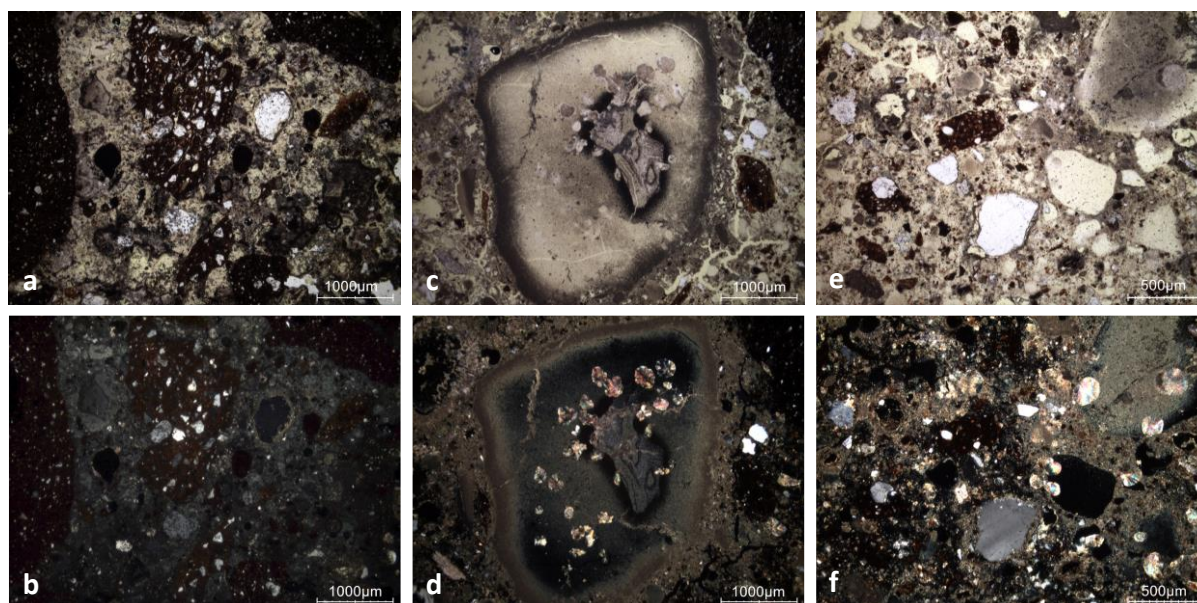
Figure 4: Representative photographs of the thin-section X1469: a) overview image in plain polarised light (PPL); b) overview image in cross polarised light (XPL); c) PPL image a lime lump with rounded spots; d) same image in XPL; e) PPL image of the binder; f) same image in XPL.

Binder	**Texture**	micritic, presence of rounded spots (ghosts of hydromagnesite)
	Lump state	completely burned & unburned, presence of rounded spots (ghosts of hydromagnesite)
	Lump size	0.4 mm
	Lump frequency	numerous
Aggregate	**Grain size**	very coarse (max 2 cm)
	Mineralogy	crushed ceramic / terracotta + small amount of siliceous sand with few limestone grains
	Shape	subangular
Appearance	**Homogeneity**	relatively heterogenous
	Macroporosity	high (due to dissolution)
	Pore structure	irregular highly connected / microcracks
Admixtures	**Type**	-
Alteration	**Type**	dissolution & secondary carbonates (dissolution / precipitation)

Table 1: : Main characteristics of the mortar retrieved from the observations of the thin-section X1469.

Thermogravimetric analysis (TGA) on whole sample

The apparent hydraulicity index (aHI) calculated from Figure 5 is around 34% indicating that the mortar is hydraulic. However, the values obtained from the thermal analyses might not entirely reflect the reality since the mortar was slightly dissolved. The amount of carbonates present in the mortar is around 23 wt%. The quartz transition phase cannot be observed around 570°C, it should be due to the fact that it is present at low concentration. The main weight loss of ancient mortars is expected between 600 and 900 °C and is indicative of the decomposition of calcium carbonate ($CaCO_3$) into calcium oxide (CaO) and carbon dioxide (CO_2) (Ahmmed et al. 2024). The end temperature of the calcium carbonate decomposition for the mortar sample is around 805°C. A peak at 605°C is observed, it could be due to the presence of a different form of carbonate possibly coming from the hydraulic phases. No gypsum was detected.
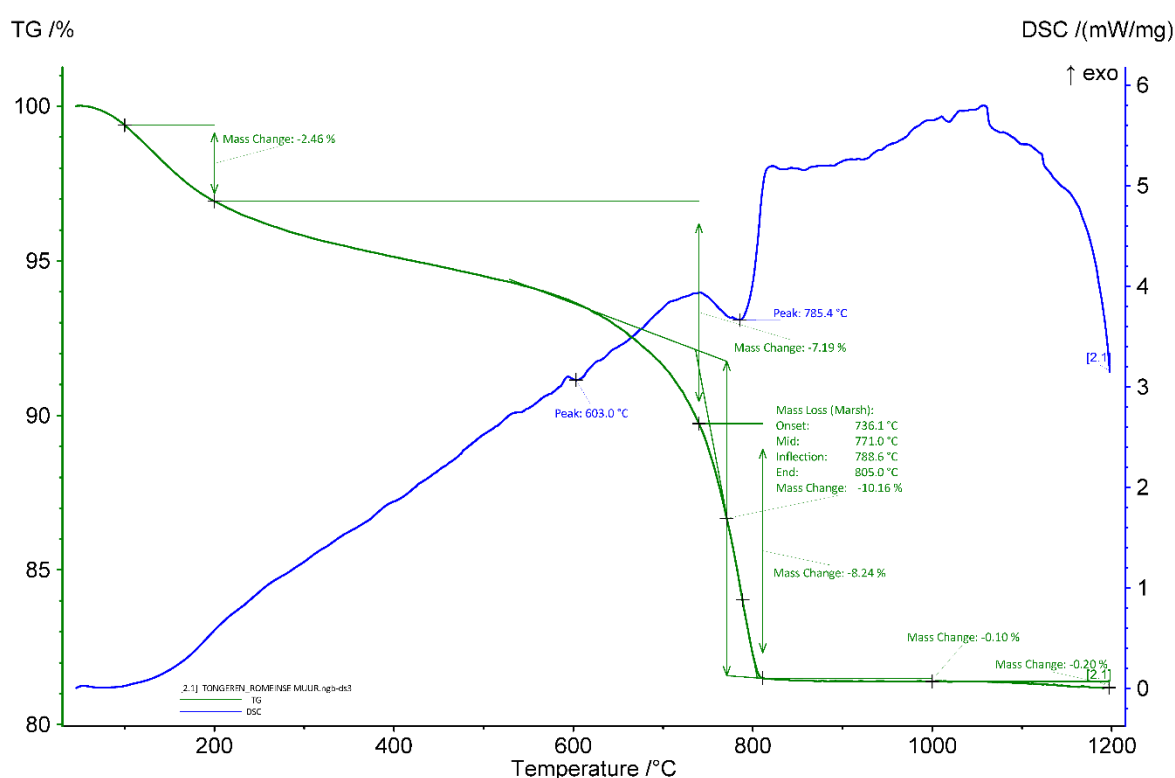
Figure 5: Coupled TG-DSC analysis of the Roman mortar upon heating to a temperature of 1200°C at a heating rate of 20°C/min under an inert atmosphere (He flushed at 50 ml/min). The weight loss determined by thermogravimetric analysis (TG, wt%, green curve) and the result of the differential scanning calorimetric analysis (DSC, mW/mg, blue curve) are both presented.

FTIR on powders with particle size <75 μm

The FTIR spectrum of the powdered sample with particle size lower than 75 μm (Figure 6) shows the presence of calcium carbonates (calcite and aragonite), silicates including quartz as well as organic matter.
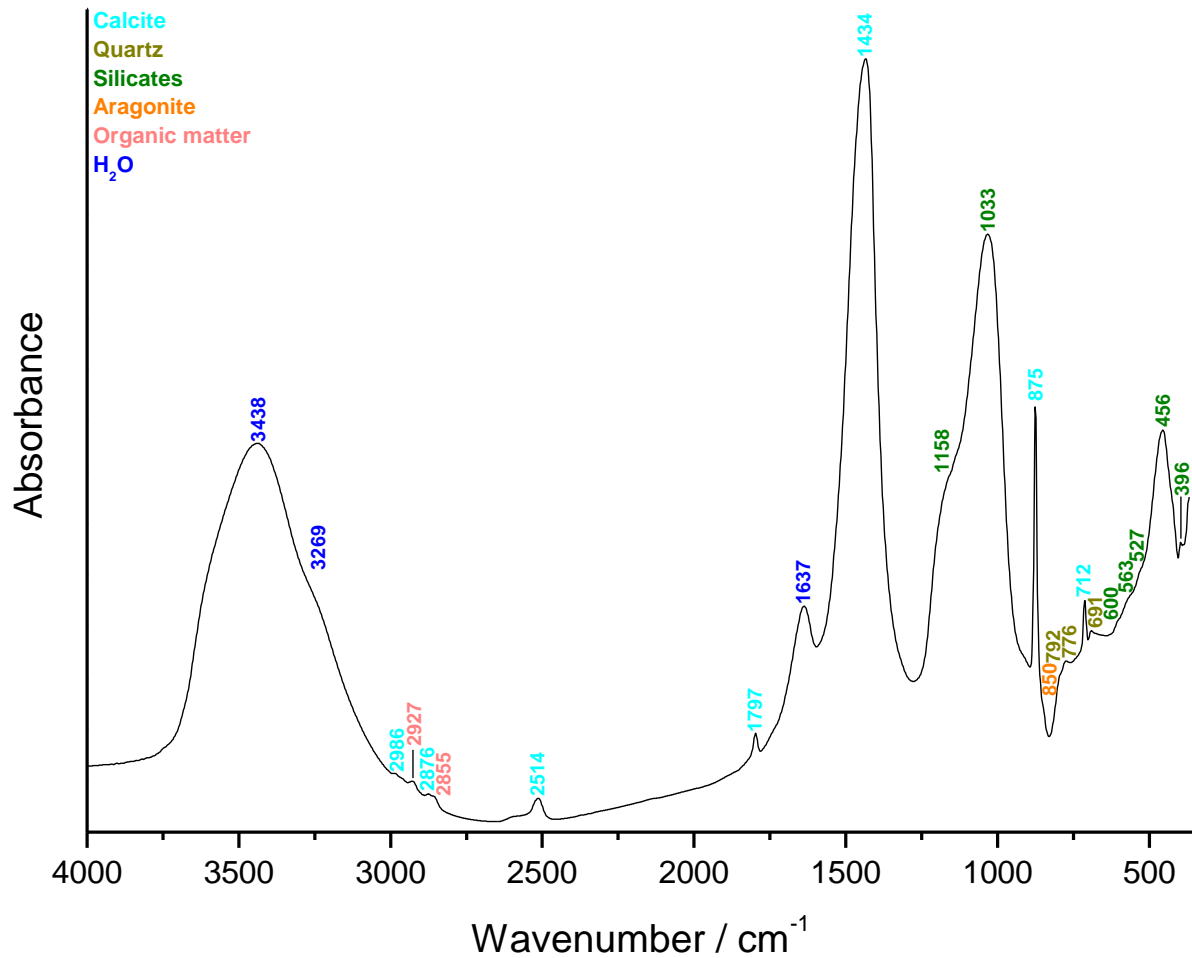
Figure 6: FTIR spectra obtained on the powdered sample with particle size lower than 75 µm.

TGA on powders with particle size <75 µm

The aHI is higher (~51 wt%) for the powder compared to the whole mortar sample (~34%). An explanation could be a concentration of the hydraulic components (clay) in the powder. The quantity of carbonates is slightly lower in the powder (~21 wt%) compared to the whole sample (23 w%). The end temperature of calcium carbonate decomposition is 816°C for the powdered sample. It is lower compared to the whole sample (805°C). A possible explanation could be that the powder is more pure compared to the whole mortar sample which increases the decomposition temperature.

Figure 7: Coupled TG-DSC analysis of the powdered mortar with particle size < 75 µm upon heating to a temperature of 1200°C at a heating rate of 20°C/min under an inert atmosphere (He flushed at 50 ml/min). The weight loss determined by thermogravimetric analysis (TG, wt%, green curve) and the result of the differential scanning calorimetric analysis (DSC, mW/mg, blue curve) are both presented.

Radiocarbon results

The test prior to the CO_2 extraction revealed a rather medium to low amount of carbon (Table 2) in the samples (~6 or 7 %). A relatively hight amount of powder < 38 µm was necessary for the carbon extraction (~5 g).

RICH	Sample type	Method	C (%)	m (g)	Age BP extrapolated	Calibrated date (oxcal - 95.4%)	Age BP extrapolated with stat	Calibrated date (oxcal - 95.4%)	Age BP average first dates	Calibrated date (oxcal - 95.4%)	Reliability of dating
21531.1	red mortar < 38 μm	HCl (7 fractions)	4.29	5.16	913 ± 34	1039-1212 calAD	1100.5 ± 16	892-994 calAD	(first 3 fractions) 974 ± 20	1020-1160 calAD	☒
21531.2		HCl (8 fractions)			1226 ± 35	700-890 calAD	1100.3 ± 15.6	892-994 calAD	not possible	-	☒
21354	charcoal	-	-	-	1739 ± 32	246-402 calAD	-	-	-	-	☑

Table 2: Radiocarbon results.

Both dates obtained for the lime mortar with particle size lower than 38 µm (Table 2 & Figure 8) are too young (8th to 13th centuries) compared to the archaeological context and the dating of the charcoal from the same context (3rd to 5th centuries AD).
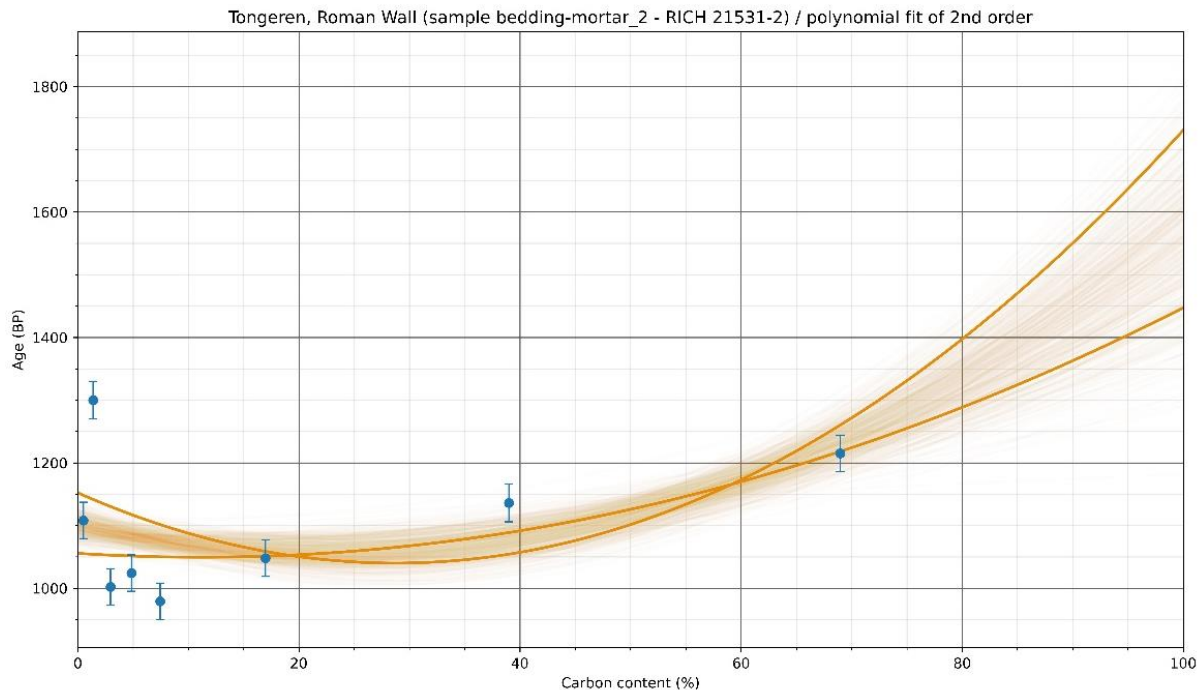
Figure 8: Radiocarbon results for the powdered mortar with particles < 38 µm as a function of the CO_2 fraction on the sample 21531.2.

Conclusions

The leaching of the lime binder in combination with delayed hardening due to the use of terracotta as aggregate making the mortar strongly hydraulic, and possible secondary carbonate deposits lead to the obtention of a younger age. This type of mortar is not suitable for radiocarbon dating.

Bibliography

Hayen, Roald, Mark Van Strydonck, Elisabetta Boaretto, Alf Lindroos, Jan Heinemeier, Åsa Ringbom, Sophie Hueglin, Danuta Michalska, Irka Hajdas, and F. Marzaoili. 2016. "Absolute Dating of Mortars–Integrating Chemical and Physical Techniques to Characterize and Select the Mortar Samples." In *Proceedings of the 4th Historic Mortars Conference-HMC2016*, 656–67.

Hayen, Roald, Mark Van Strydonck, Laurent Fontaine, Mathieu Boudin, Alf Lindroos, Jan Heinemeier, Åsa Ringbom, et al. 2017. "Mortar Dating Methodology: Assessing Recurrent Issues and Needs for Further Research." *Radiocarbon* 59 (6): 1859–71.

Study of mortars from Hertogensite, Leuven for the BRAIN 2.0 PalC project

Context of the site

It used to be assumed that Leuven's first stone city wall (with the towers) was built between 1156 and 1165, but actually this should move up to the first quarter of the 13th century. A second, larger wall was made in the 14th century.

Material

The mortar sample 2017H39 comes from the foundations, about a metre below present ground level.

Results & Discussion

Macroscopic descriptions

The main colour of the mortar is beige (Figure 1) tending towards pale yellow (2.5Y 8/3) according to the Munsell soil colour charts. It is slightly specular, probably due to the presence of coarse grains of quartz, mica or well crystallised calcite. The lime lumps appear as white inclusions with a main size of ~1 mm and the biggest one measure ~4 cm. Large piece of brown inclusions probably made of soil are noticed as well as large white fragments with a size higher than 1 cm.

Figure 1: Mortar sample 2017H39.

Fourier transform Infrared (FTIR) spectroscopy on inclusions & binder

The binder (beige – Figure 2) mainly contains silicates including quartz and a bit of calcite and aragonite. This might reflect a partial dissolution of the binder. The lime lumps (white – Figure 3) also comprise some silicates including quartz but are mainly made of calcite. The large brown inclusions mainly contain silicates including quartz, calcite, clay and organic matter.
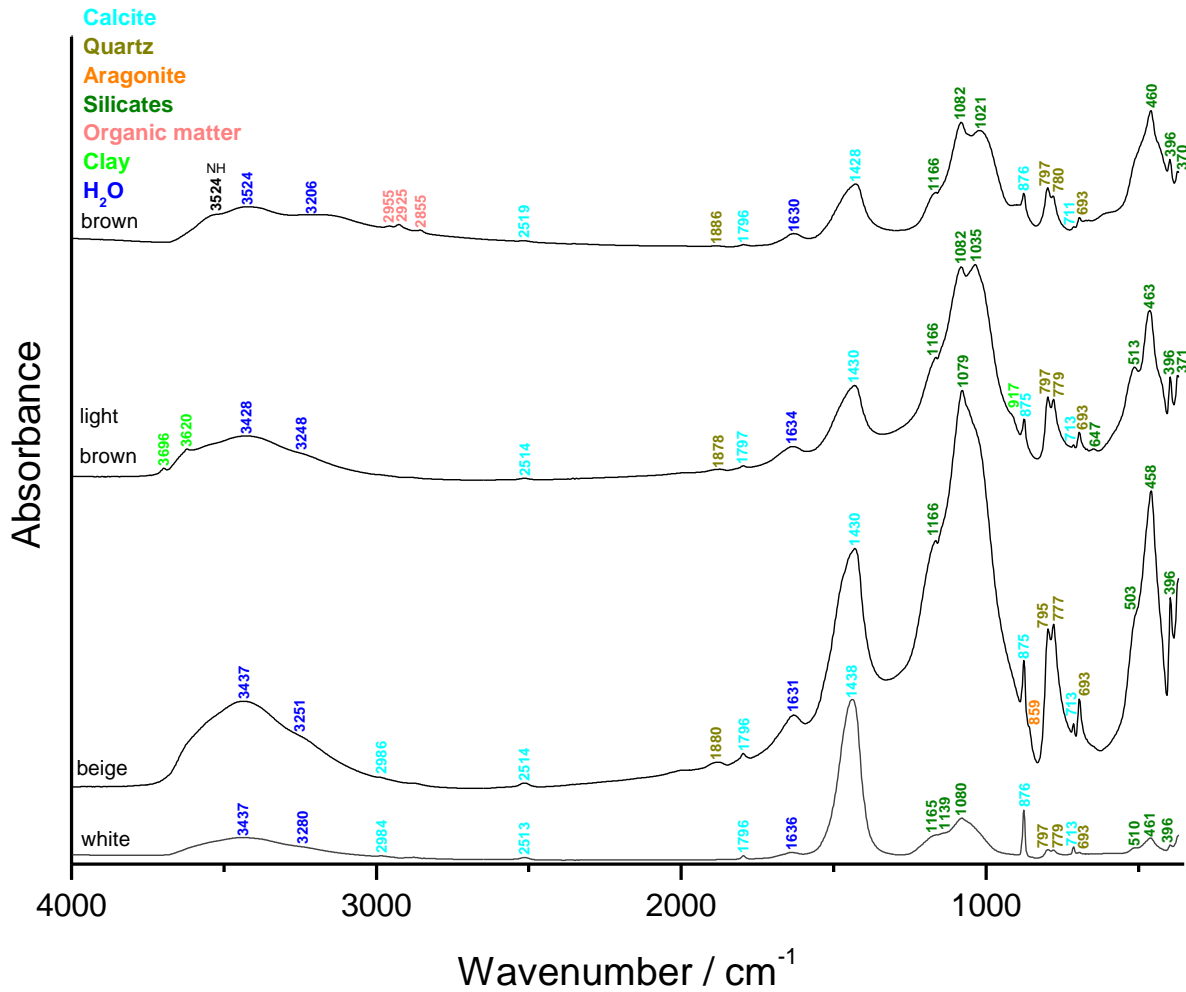
Figure 2: FTIR spectra obtained on the inclusions and binder (beige) of the mortar sample 2017H39.

Binder:sand ratio

The calculated binder:sand ratio using a bulk density of 1.35 kg/dm^3 for the sand and 0.575 kg/dm^3 for the lime is 1:1 in volume unit.

	2017H39
Sample weight (g)	2.8
Crucible weight (g)	15.3
Weight calcined (g)	17.25
%ins	**69.6**

Table 1: Percentage of insoluble residue

Cathodoluminescence

Cathodoluminescence images of thin-section X2120 shows the presence of two types of quartz grains (two shades of purple hue, Figure 3a). A few K-feldspars can also be observed in bright blue as well as a few little bright red limestone fragments. Plagioclases can also be observed as small green grains. The binder is dull. For the powder with particle size lower than 75 μm, it is mainly dull with a few bright red limestone grains and a few green plagioclase grains.
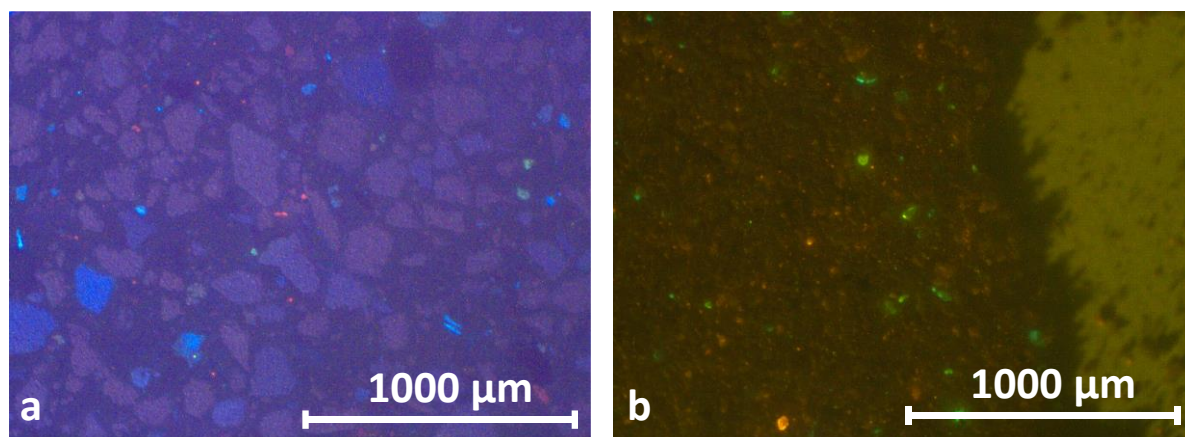
Figure 3: Characteristic cathodoluminescence images of a) the thin section X2120, and b) the powdered mortar with particle size lower than 75 µm.

Thin-section petrography

The mortar is in poor condition, both the binder & the lime lumps have been partially dissolved (Figure 4a to d and Table 2). The binder exhibits a micritic texture and numerous lumps are present with a size varying from ~660 µm to ~7 mm. The aggregate is made of a siliceous sand containing quartz, K-feldspars, glauconite more or less oxidised and mica. One limestone grain was observed (Figure 4e & f). Quartz grains and (fired) glauconite grains are present within the lime lump indicating the use of a Brusselian sandy limestone for lime production.
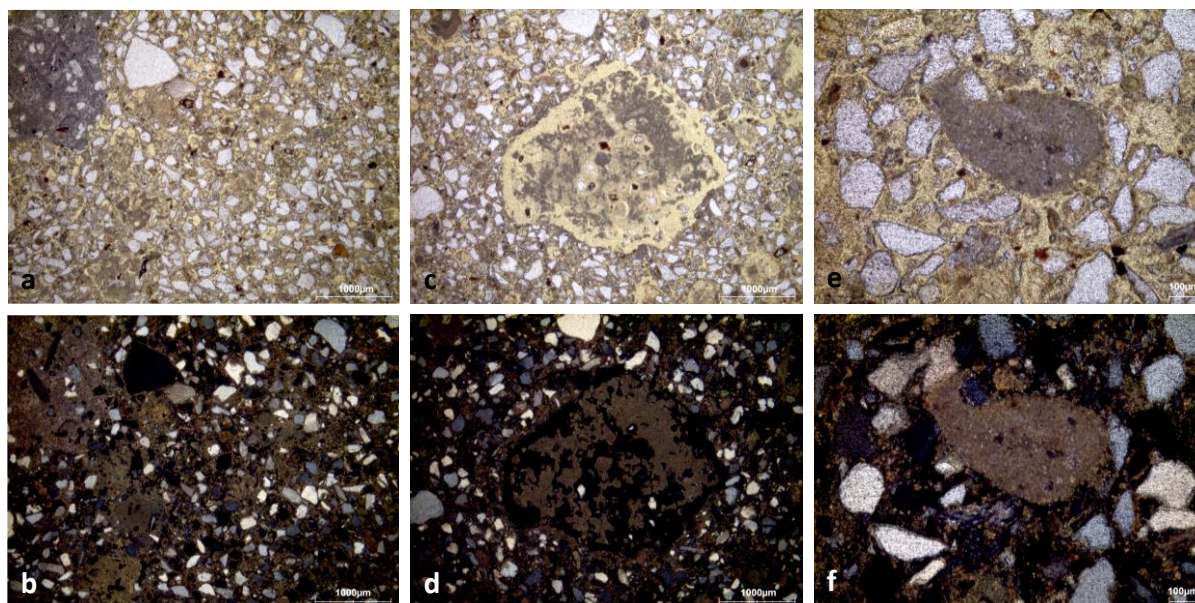
Figure 4: Representative photomicrographs of the thin-section X2120: a) overview image in plain polarised light (PPL); b) overview image in cross polarised light (XPL); c) PPL image showing a partially dissolved lime lump ; d) same image in XPL; e) PPL image with a limestone grain; f) same image in XPL.

Binder	**Texture**	micritic
	Lump state	completely burned
	Lump size	7 mm, 3 mm, 660 µm

	Lump frequency	numerous
Aggregate	**Grain size**	very fine to coarse
	Mineralogy	pure siliceous sand (quartz, K-feldspar, glauconite more or less oxidised)
	Shape	subangular / subrounded
Appearance	**Homogeneity**	relatively heterogeneous
	Macroporosity	high
	Pore structure	irregular/sometimes connected
Admixtures	**Type**	-
Alteration	**Type**	dissolved

Table 2: Main characteristics of the mortar 2017H39 retrieved from the observations of the thin-section X2120.

Thermogravimetric analysis (TGA) on whole sample

The apparent hydraulicity index (aHI) calculated from Figure 5 is around 27% indicating that the mortar is strongly hydraulic. However, the values obtained from the thermal analyses might not reflect the reality since the mortar was dissolved. The amount of carbonates still present in the mortar is around 16 wt%. At 572.9°C, the quartz transition phase can be observed (Rickard et al., 2010). The main weight loss of ancient mortars is expected between 600 and 900 °C and is indicative of the decomposition of calcium carbonate ($CaCO_3$) into calcium oxide (CaO) and carbon dioxide (CO_2) (Ahmmed et al. 2024). The end temperature of the calcium carbonate decomposition for the mortar sample is around 798°C. No gypsum was detected.
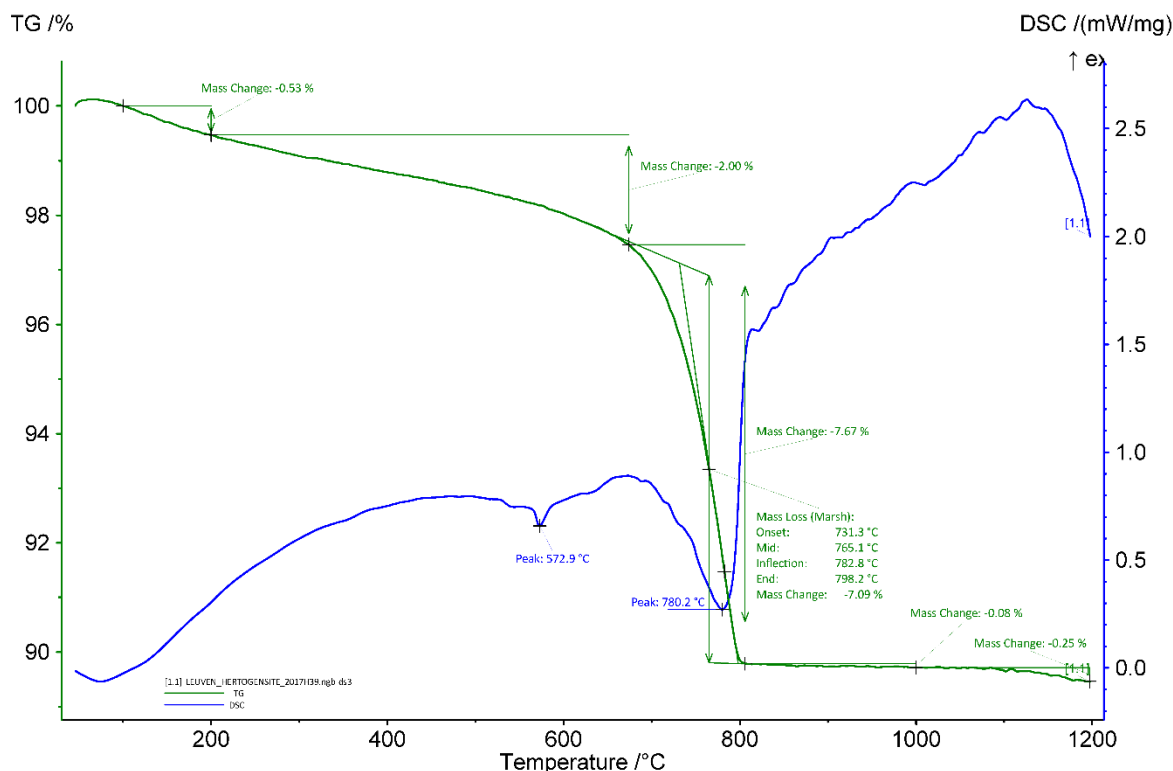
Figure 5: Coupled TG-DSC analysis of the mortar 2017H39 upon heating to a temperature of 1200°C at a heating rate of 20 °C/min under an inert atmosphere (He flushed at 50 ml/min). The weight loss determined by thermogravimetric analysis (TG, wt%, green curve) and the result of the differential scanning calorimetric analysis (DSC, mW/mg, blue curve) are both presented.

Grinding/particle separation

The mortar was rather soft and easy to crush 'gently'.

TGA on powder with particle size 125-250 μm

The aHI is slightly higher (~30 wt%) for the powder compared to the whole mortar sample (~27%). An explanation could be a concentration of the hydraulic components (clay) in the powder. The quantity of carbonates is lower in the powder (~9 wt%) compared to the whole sample (16 w%). This might be due to the fact that the powder analysed was with particle size between 125-250 μm, the majority of the carbonates might have been in the fraction with particle size lower that 75 μm. The choice to use this fraction was made before the project, and the reason why was lost. The end temperature of calcium carbonate decomposition is 782°C for the powdered sample. It is lower compared to the whole sample (798°C). A possible explanation is that the powdered contained less limestone compared to the whole sample. A peak at 605°C is observed, it could be due to the presence of a different form of carbonate possibly coming from the hydraulic phases.

Figure 6: Coupled TG-DSC analysis of the powdered mortar with particle size 125-250 μm upon heating to a temperature of 1200° C at a heating rate of 20°C/min under an inert atmosphere (He flushed at 50 ml/min). The weight loss determined by thermogravimetric analysis (TG, wt%, green curve) and the result of the differential scanning calorimetric analysis (DSC, mW/mg, blue curve) are both presented.

Radiocarbon results

The test prior to the CO_2 extraction revealed a low amount of carbon (Table 4) in the sample (~0.9 %), again reflecting the dissolution of the mortar. In 2017, prior to the PalC project, the choice was made to use the fraction of particle between 125 and 250 μm to gather enough carbon for dating.

RICH	Sample type	Method	C (%)	σ (%)	m (g)	Age BP extrapolated	Calibrated date (oxcal - 95.4%)	Age BP extrapolated with stat	Calibrated date (oxcal - 95.4%)	Age BP average first 4 dates	Calibrated date (oxcal - 95.4%)	Reliability of dating
25471	mortar 125-250 µm	8 fractions	0.87	0.09	12.1	1765 ± 30	230-380 calAD	1599.5 ± 17	421-538 calAD	1778 ± 16	236-335 cal AD	☒

Table 4: Radiocarbon results

The radiocarbon results don't match the expected date, they are older than expected.

Foundation tower field side - 2017H39

$$y = -0.122x^2 + 30.093x + 1765.2$$
$$R^2 = 0.9795$$

Leuven, Hertogensite (sample 2017H39 - RICH 25471) / polynomial fit of 3rd order
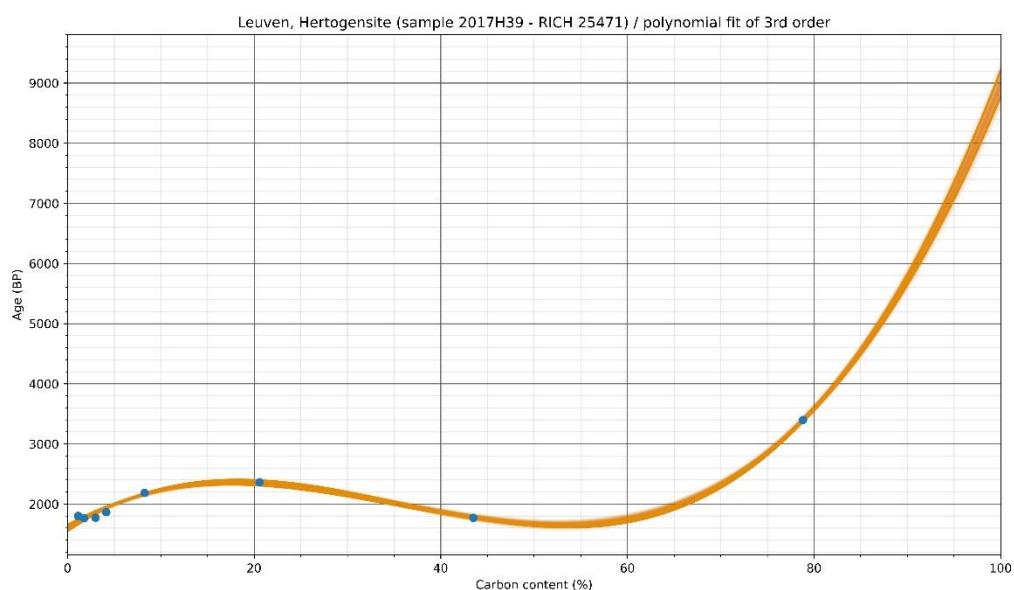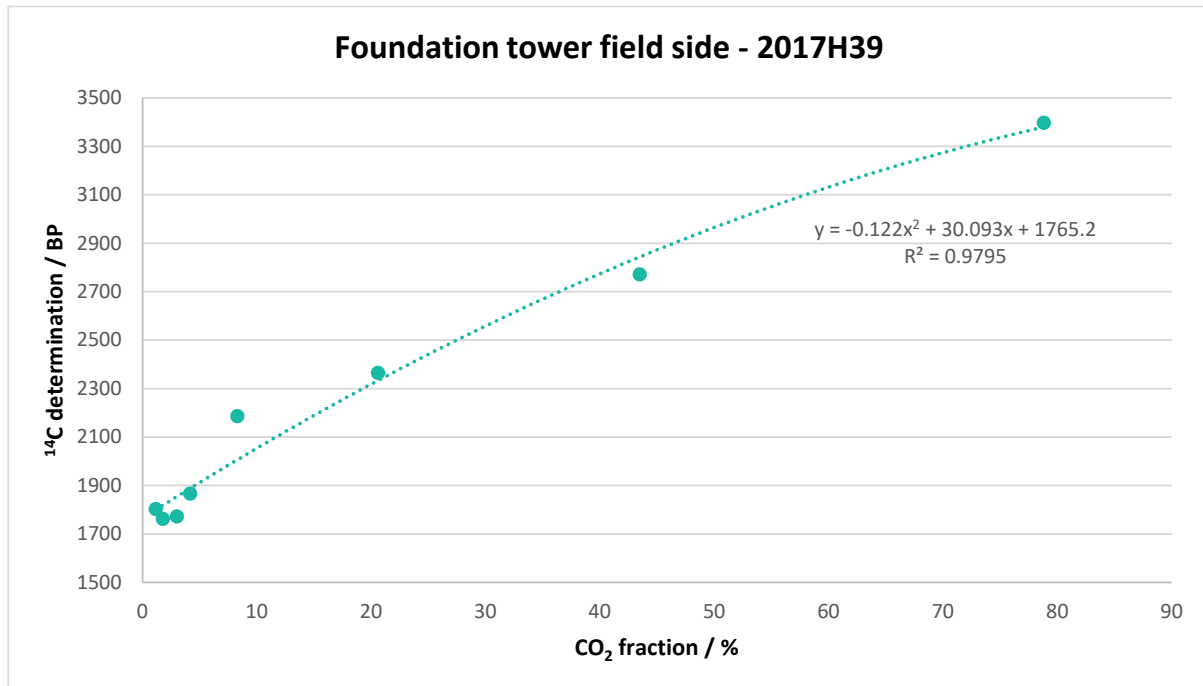
Figure 6: Radiocarbon results for the powdered mortar with particles of 125-250 μm as a function of the CO_2 fraction (the graph at the bottom shows the statistic on the results).

Conclusions

The mortar is highly deteriorated, it has been dissolved and the carbon/carbonate content is low. The thermal analyses showed that the mortar is highly hydraulic but it might be overestimated because of the leaching. The date obtained is older than expected. This mortar is not suitable for radiocarbon dating.

Study of Mortars from the Holy Cross Parish Church in Korbeek-Lo (Bierbeek, Flemish Brabant) for the BRAIN 2.0 PalC Project

Context of the site

The Holy Cross Parish Church is located in the borough of Korbeek-Lo (Figure 1) which is part of the municipality of Bierbeek in the Flemish Brabant province (Belgium). A few information is known about the origin of the parish. The oldest mention goes back to a papal bull of 1107 (*Parochiekerk Heilig Kruis*, 2021). The current structure of the church (bricks and limestone) dates mainly from the 17th and 18th centuries (*Parochiekerk Heilig Kruis*, 2021).

Figure 1: Holy Cross Parish Church with cemetery wall in 2006 (photo credit Vandevorst Kris).

Material

A mortar sample from the old foundation under the choir was submitted by Annelies De Raymaeker and Maarten Smeets (from Studiebureau Archeologie) to the radiocarbon laboratory prior to the PalC project (in 2019). Black inclusions were extracted, pretreated and dated (KIK-014436). The sampling was possibly performed outdoor. The sample identification number is 2017/180. When selected for the project, a weigh of ~50 g was left in the bag.

Results & Discussion

Macroscopic descriptions

The main colour of the mortar is beige (Figure 2) tending towards pale yellow (2.5Y 8/2) according to the Munsell soil colour charts. It is slightly specular, probably due to the presence of coarse grains of quartz, mica or well crystallised calcite. The lime lumps appear as white inclusions with a main size of ~2 mm and the biggest one measure ~1 cm. Black inclusions are present within the mortar. They are rather hard but brittle, they are probably bottom ashes. Translucent inclusions of around 1 mm are also present, it might be some types of quartz or quartzite.

Figure 2: Mortar sample 2017/180 from the old foundation under the choir of the Holy Cross Parish Church in Korbeek-Lo.

Fourier transform Infrared (FTIR) spectroscopy on inclusions & binder

The binder (beige – Figure 3) mainly contains silicates including quartz and a bit of calcite. This might reflect a partial dissolution of the binder. The lime lumps also include a large part of silicates in comparison to calcite and might also have partially been dissolved. The translucent inclusions are made of a well crystallised silicates including quartz. As expected the black inclusions consist of organic matter.
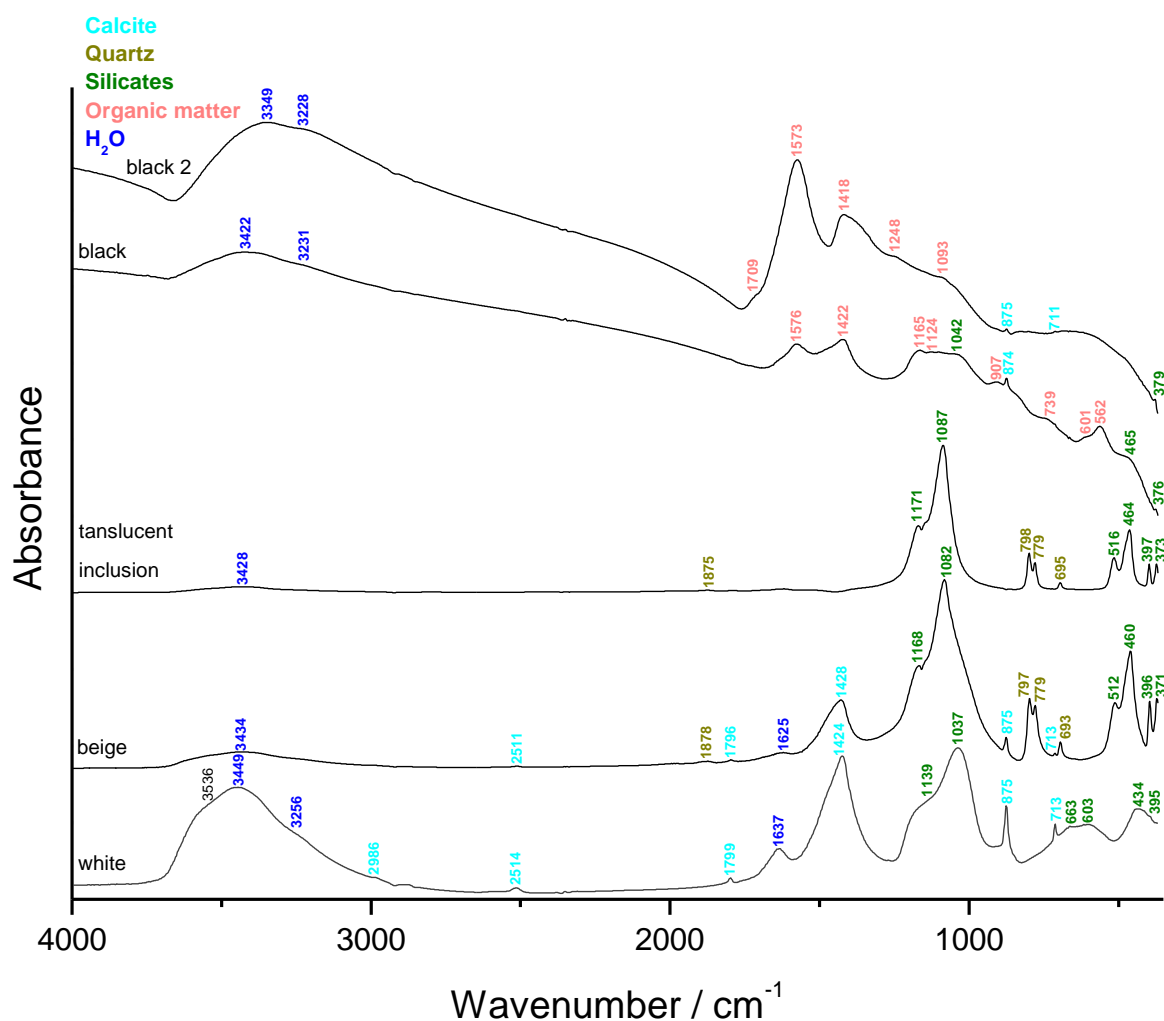
Figure 3: FTIR spectra obtained on the inclusions and binder (beige) of the mortar sample 2017/180 from the old foundation under the choir of the Holy Cross Parish Church in Korbeek-Lo

Binder:aggregate ratio

The calculated binder:aggregate ratio using a bulk density of 1.35 kg/dm^3 for the sand and 0.575 kg/dm^3 for the lime is 2:3 in volume unit. This ratio should be distorted because of the binder dissolution and might have initially been close to 1:1.

	S7020
Sample weight (g)	2.79
Crucible weight (g)	16.85
Weight calcined (g)	19.03
%ins	**78.1**

Table 1: Percentage of insoluble residue

Cathodoluminescence

Cathodoluminescence performed on thin-section X2277 shows the presence of quartz grains exhibiting a purple hue (Figure 4a). A few K-feldspars can also be observed in bright blue as well as two little bright red limestone fragments. The binder is dull. Observations performed on the powder with particle size lower than 75 μm used for radiocarbon dating (Figure 4b)

shows also a low amount of limestone grains (in bright red), a few K-feldspars (in bright blue) and the binder in dull.
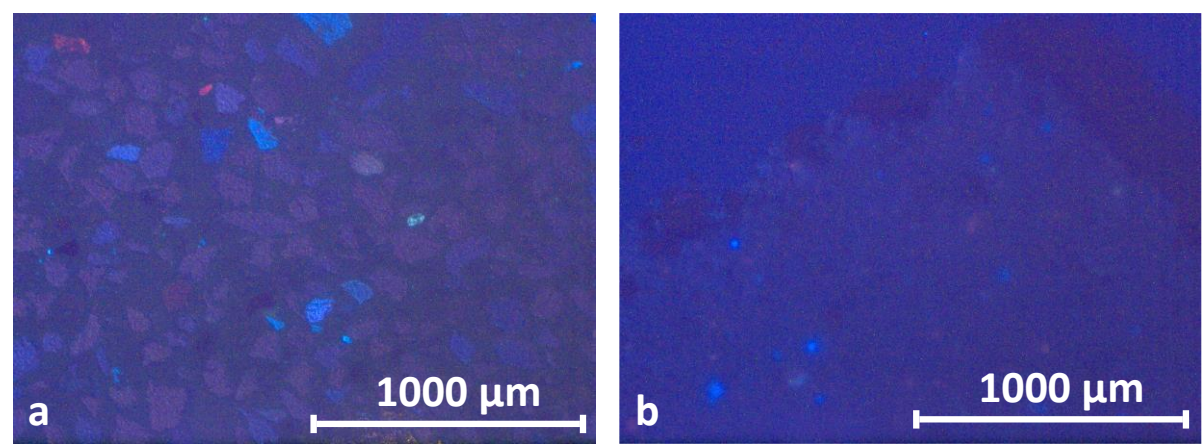
Figure 4: Characteristic cathodoluminescence images of a) the thin section X2277, and b) the powdered mortar with particle size lower than 75 µm.

Thin-section petrography

The mortar is in poor condition, both the binder & the lime lumps have been dissolved (Figure 5 and Table 2). The binder exhibits a micritic texture and numerous lumps were present with a size varying from ~200 µm to ~5 mm. The aggregate is made of a siliceous sand containing quartz, K-feldspars, glauconite more or less oxidised and mica.
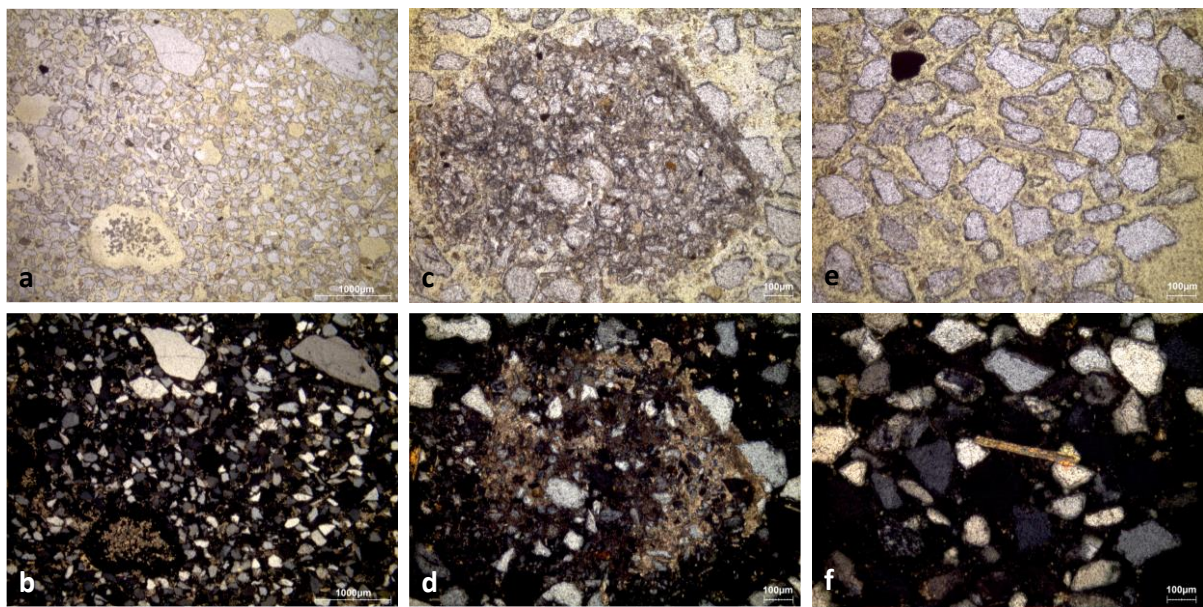
Figure 5: Representative photomicrographs of the thin-section X2277: a) overview image in plain polarised light (PPL); b) overview image in cross polarised light (XPL); c) PPL image showing possible remnant of the limestone used to make the mortar or secondary carbonate deposit; d) same image in XPL; e) PPL image with a mica flake in the centre; f) same image in XPL.

Binder	Texture	micritic
	Lump state	dissolved

	Lump size	235 µm, 314 µm, 738 µm, 870 µm, > 5 mm
	Lump frequency	numerous but dissolved
Aggregate	**Grain size**	very fine to coarse
	Mineralogy	pure siliceous sand (quartz, K-feldspars, glauconite more or less oxidised, mica)
	Shape	subangular/subrounded
Appearance	**Homogeneity**	relatively homogeneous
	Macroporosity	high because of dissolution
	Pore structure	irregular/highly connected
Admixtures	**Type**	-
Alteration	**Type**	dissolution

Table 2: Main characteristics of the mortar 2017/180 from the old foundation under the choir of the Holy Cross Parish Church in Korbeek-Lo retrieved from the observations of the thin-section X2277.

Thermogravimetric analysis (TGA) on whole samples

The apparent hydraulicity index (aHI) calculated from Figure 6 is around 26% indicating that the mortar is strongly hydraulic. However, the values obtained from the thermal analyses might not reflect the reality since the mortar was dissolved. The amount of carbonates still present in the mortar is around 8.4 wt%. At 572.4°C, the quartz transition phase can be observed (Rickard et al., 2010). The main weight loss of ancient mortars is expected between 600 and 900 °C and is indicative of the decomposition of calcium carbonate ($CaCO_3$) into calcium oxide (CaO) and carbon dioxide (CO_2) (Ahmmed et al. 2024). The end temperature of the calcium carbonate decomposition for the mortar sample is around 768°C. No gypsum was detected.
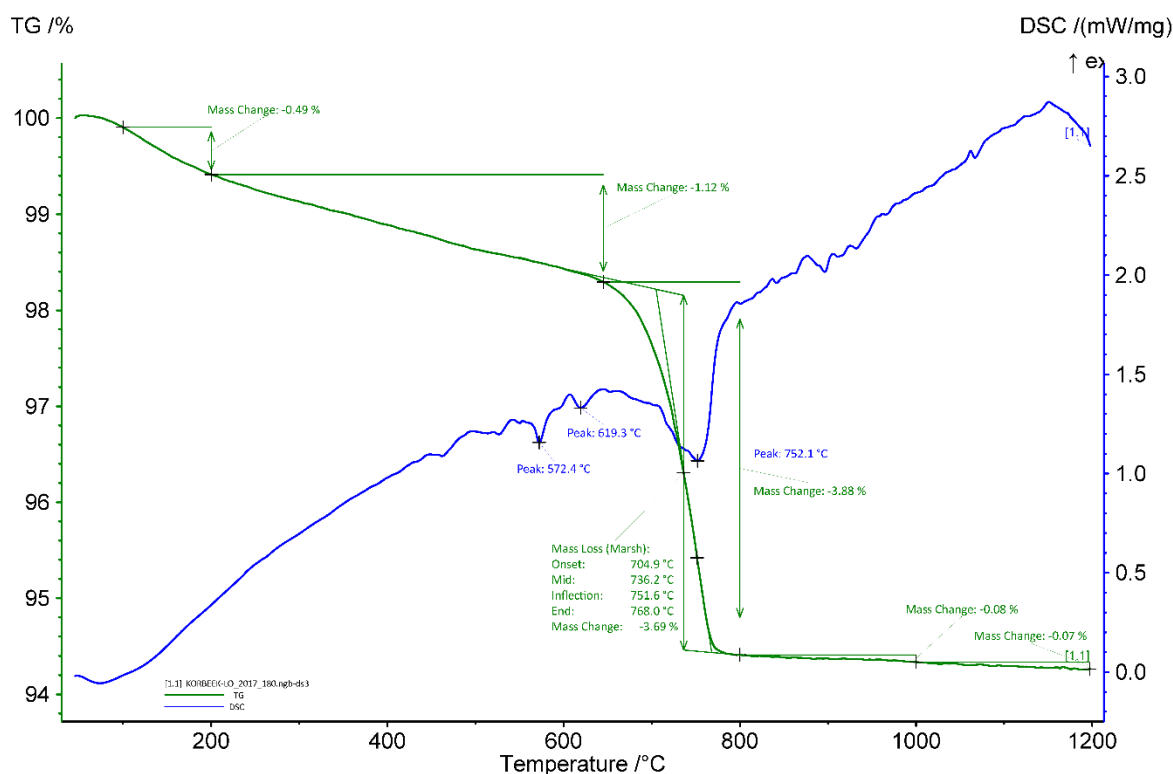
Figure 13: Coupled TG-DSC analysis of the mortar 2017/180 from the old foundation under the choir of the Holy Cross Parish Church in Korbeek-Lo upon heating to a temperature of 1200°C at a heating rate of 20 °C/min under an inert atmosphere (He flushed at 50 ml/min). The weight loss determined by thermogravimetric analysis (TG, wt%, green curve) and the result of the differential scanning calorimetric analysis (DSC, mW/mg, blue curve) are both presented.

TGA on powders with particle size <75 μm

The aHI is higher (32 wt%) for the powder compared to the whole mortar sample (~20%). An explanation could be a concentration of the hydraulic components (clay) in the powder. The quantity of carbonates is higher in the powder (~26 wt%) compared to the whole sample (8.4 w%) since a large part of the sand was removed. Indeed, no quartz was detected in the powders. The end temperature of calcium carbonate decomposition is 806°C for the powdered sample. It is higher compared to the whole sample (768°C). A possible explanation could be that the powder is more pure compared to the whole mortar sample which increases the decomposition temperature.
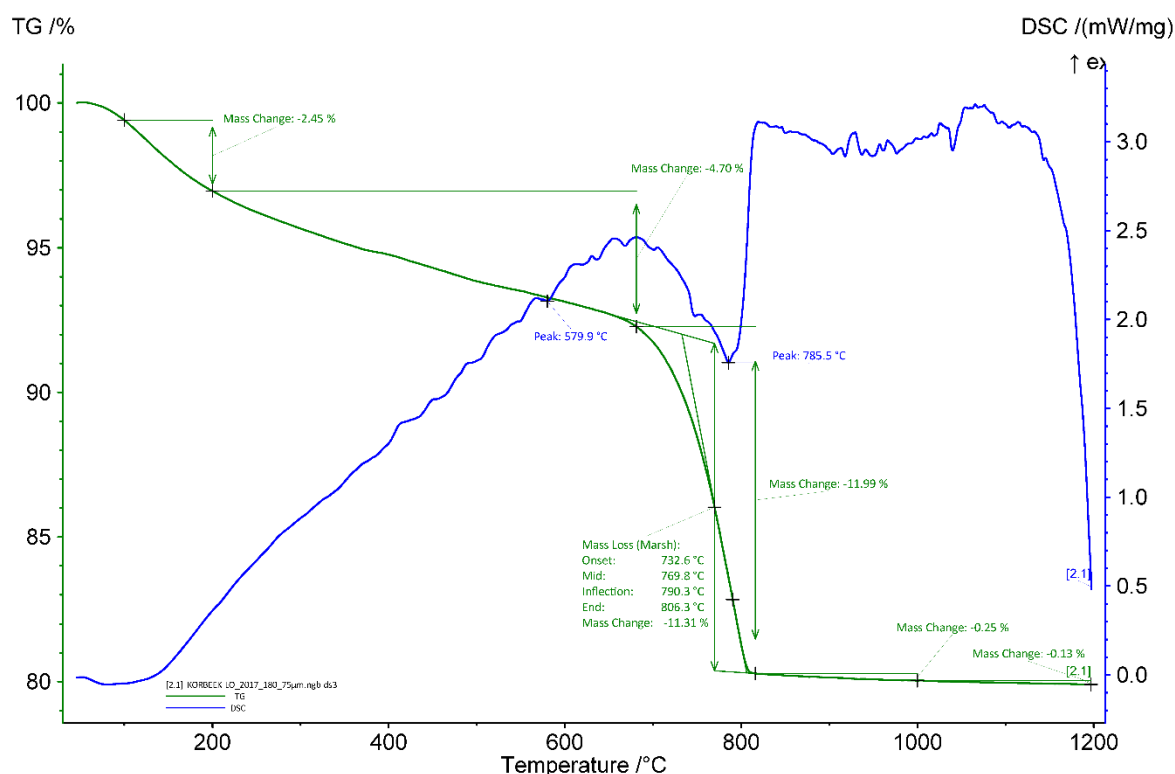
Figure 16: Coupled TG-DSC analysis of the powdered mortar 2017/180 from the old foundation under the choir of the Holy Cross Parish Church in Korbeek-Lo with particle size < 75 μm upon heating to a temperature of 1200° C at a heating rate of 20°C/min under an inert atmosphere (He flushed at 50 ml/min). The weight loss determined by thermogravimetric analysis (TG, wt%, green curve) and the result of the differential scanning calorimetric analysis (DSC, mW/mg, blue curve) are both presented.

Radiocarbon results

The test prior to the CO_2 extraction revealed a very low amount of carbon (Table 4) in the sample (~0.3 %), again reflecting the dissolution of the mortar. In 2019, prior to the PalC project, the choice was made to use the fraction of particle < 125 μm to gather enough carbon for dating.

RICH	Sample type	Method	C (%)	σ (%)	m (g)	Age BP extrapolated	Calibrated date (oxcal - 95.4%)	Age BP extrapolated with stat	Calibrated date (oxcal - 95.4%)	Age BP average first 4 dates	Calibrated date (oxcal - 95.4%)	Reliability of dating
26712	mortar <125 μm	8 fractions	0.361	0.052	15	2323 ± 30	410-230 calBC	2310.6 ± 13	420-380 calAD	-	-	☒

Table 4: Radiocarbon results.

The radiocarbon results are unusual (Figure 6). The first fractions give older dates compared to the last fractions of the CO_2 extracted from the powder with particle size < 125 µm. The extrapolation of the curve gives a range of dates (2323 ± 30 BP) which cannot be related to the context of the church. The older date obtained on the powder with particle size < 125 µm (1427 ± 24 BP; reaction of around the second half of the powder with particle size < 125 µm) give rise to 596 (95.4 %) 656 calAD which is more probable but the poor state of the mortar is not compatible with a reliable ^{14}C dating.
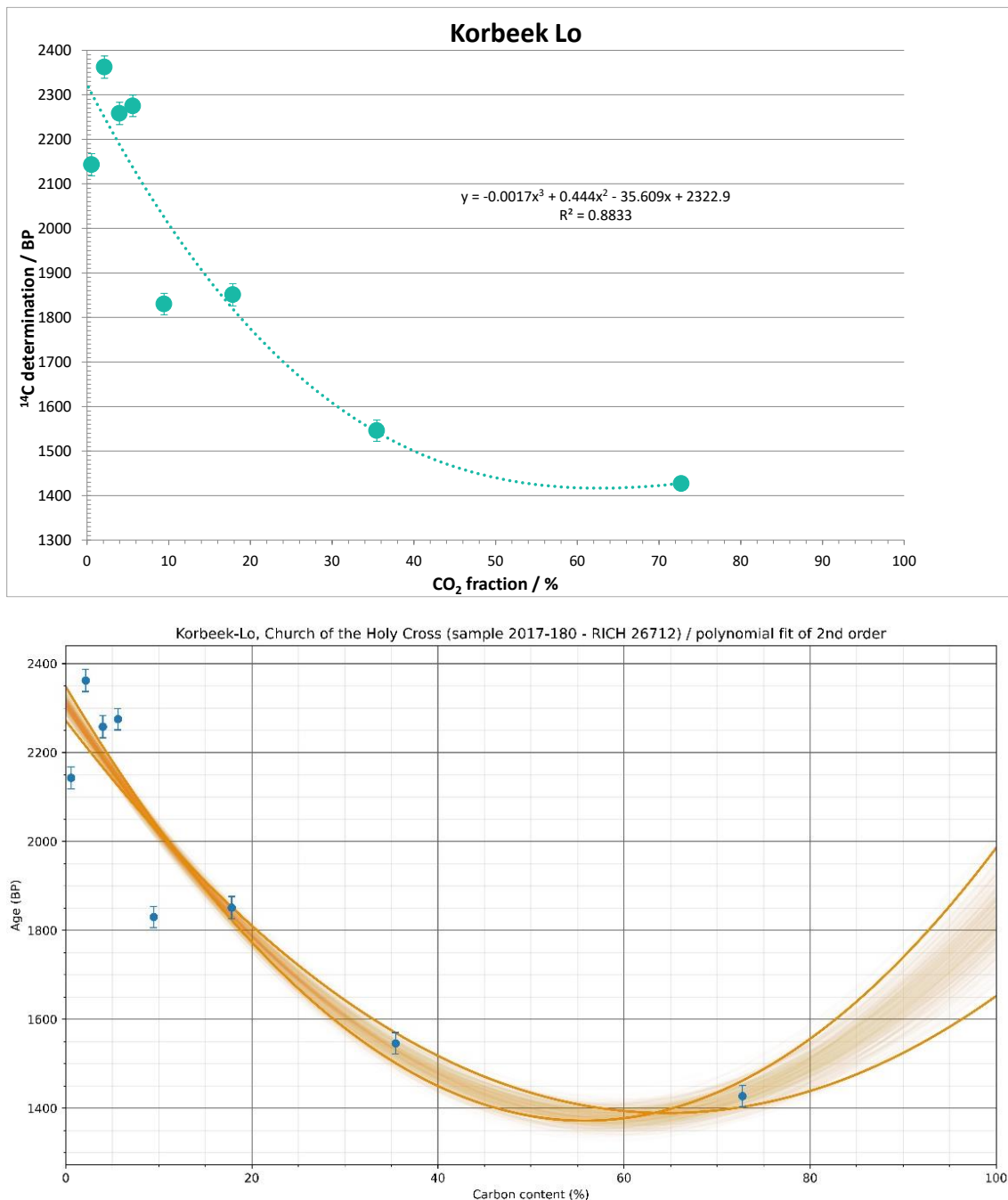
Figure 6: Radiocarbon results for the powdered mortar with particles < 125 µm as a function of the CO_2 fraction (the graph at the bottom shows the statistic on the results).

Conclusions

The characterisation of the mortar shows a poor preservation. The mortar is highly dissolved confirming it was sampled in an area exposed to weathering conditions. The radiocarbon results are in accordance with the state of the sample and cannot be trusted.

Bibliography

Parochiekerk Heilig Kruis. (2021, October 8).

https://inventaris.onroerenderfgoed.be/erfgoedobjecten/41565

Study of mortar from the residence of the Count of Flanders in Bruges for the BRAIN 2.0 PalC project

Context of the site

The building was constructed around 1050 as the residence of the Count of Flanders, but was used until the 17th century and regularly rebuilt (for example as a prison).

Material

Several samples were provided by Frederik Roelens to the radiocarbon laboratory in 2017. One sample was selected for the PALc project because sufficient material was left to perform all the necessary analyses. It is BR17BURGST7-1. It is supposed come from the first construction of the building (1050-1100 AD).

Results & Discussion

Macroscopic descriptions

The main colour of the mortar is light beige/white (Figure 2). The lime lumps appear as white inclusions with a main size of ~1 mm and the biggest one measures ~5 mm. A large light brown inclusion (~1 cm) probably made of silicates can be noticed on one fragment.

Figure 2: Photographs of mortar BR17BURGST7-1.

Fourier transform Infrared (FTIR) spectroscopy on inclusions & binder

The binder (beige, Figure 3) mainly contain calcium carbonates (calcite and aragonite) with silicates including quartz. The lime lumps (white, Figure 3) are also mainly made of calcium carbonates (calcite and aragonite) and very few silicates. The grey inclusions are made of carbonates and silicates too, which indicate that they might be limestone fragments. The brown inclusion visible Figure 2 is made of silicates including quartz. All inclusions and binders contain nitrates that shows a certain alteration of the mortar.
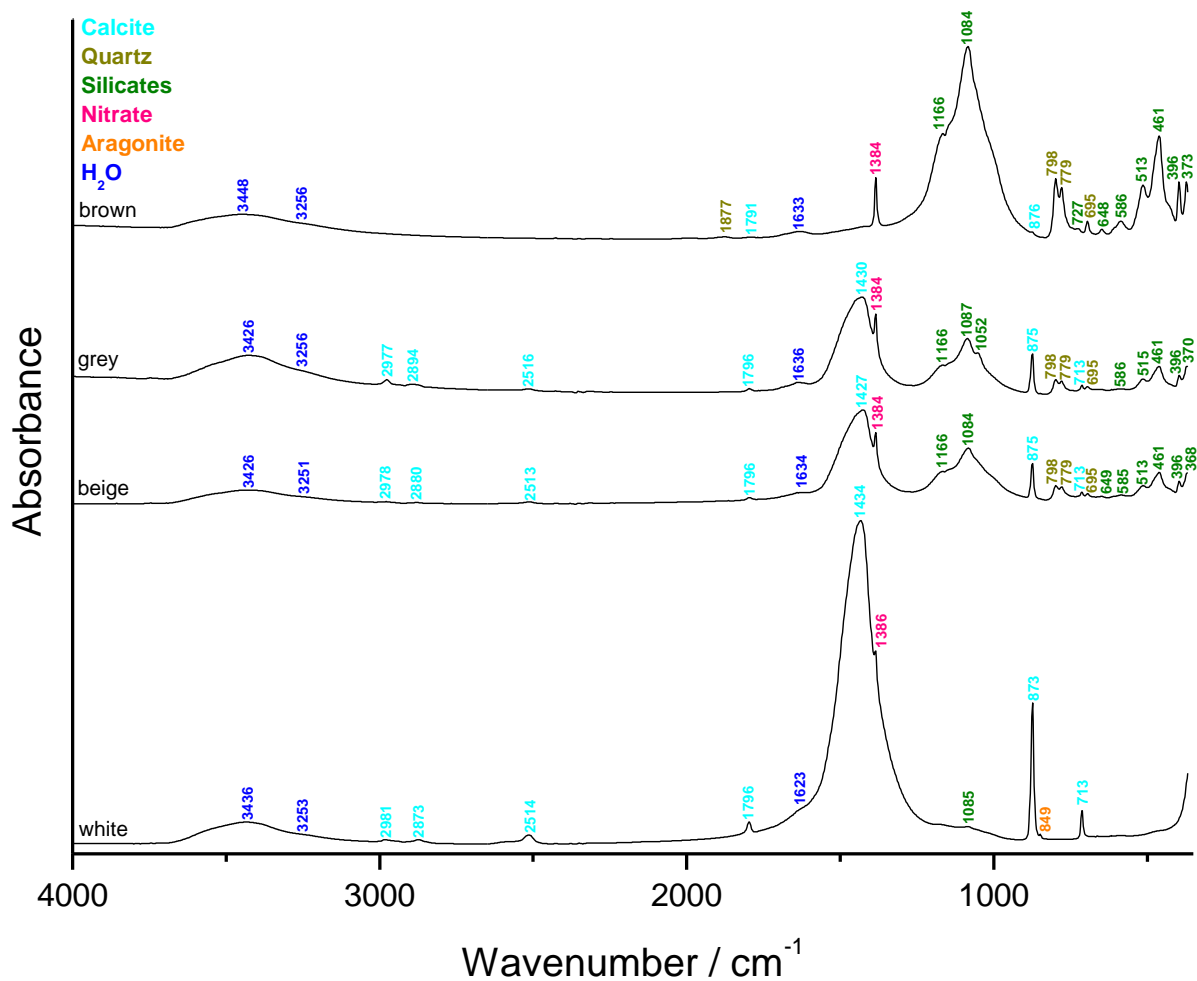
Figure 3: FTIR spectra obtained on the inclusions and binder (beige) of the mortar sample BR17BURGST7-1.

Binder:sand ratio

The calculated binder:sand ratio using a bulk density of 1.35 kg/dm^3 for the sand and 0.575 kg/dm^3 for the lime is close to 5:3 in volume unit.

	BR17
Sample weight (g)	2.7
Crucible weight (g)	19.2
Weight calcined (g)	20.8
%ins	**59.3**

Table 1: Percentage of insoluble residue

Cathodoluminescence

Cathodoluminescence observations of the thin-section and powder show similar results (Figure 4). The thin-section exhibits the presence of quartz grains with a dark purple hue, K-feldspars in bright blue, bright green plagioclases and the binder is dull (Figure 4a). The powdered sample displays mainly a red tile colour (binder) with a few bright blue K-feldspars, also some green plagioclase grains and a few bright red limestone fragments (Figures 4b).
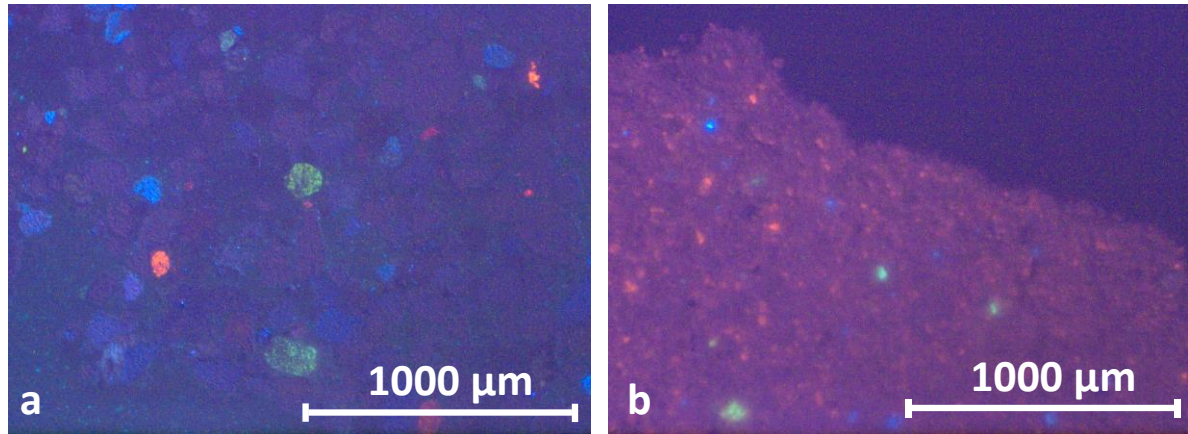
Figure 4: Characteristic cathodoluminescence images of a) the thin section X2278 and b) the powdered mortar with particle size lower than 75 µm.

Thin-section petrography

The mortar is relatively in good condition (Figure 5 & Table 2). The microporosity is high and the binder has been strongly dissolved. Secondary carbonates are observed at the border of the pores but are limited (Figure 5b). Very few limestone grains are observed (Figure 5 c & d). A few lime lumps are underburned (Figure 5e & f).
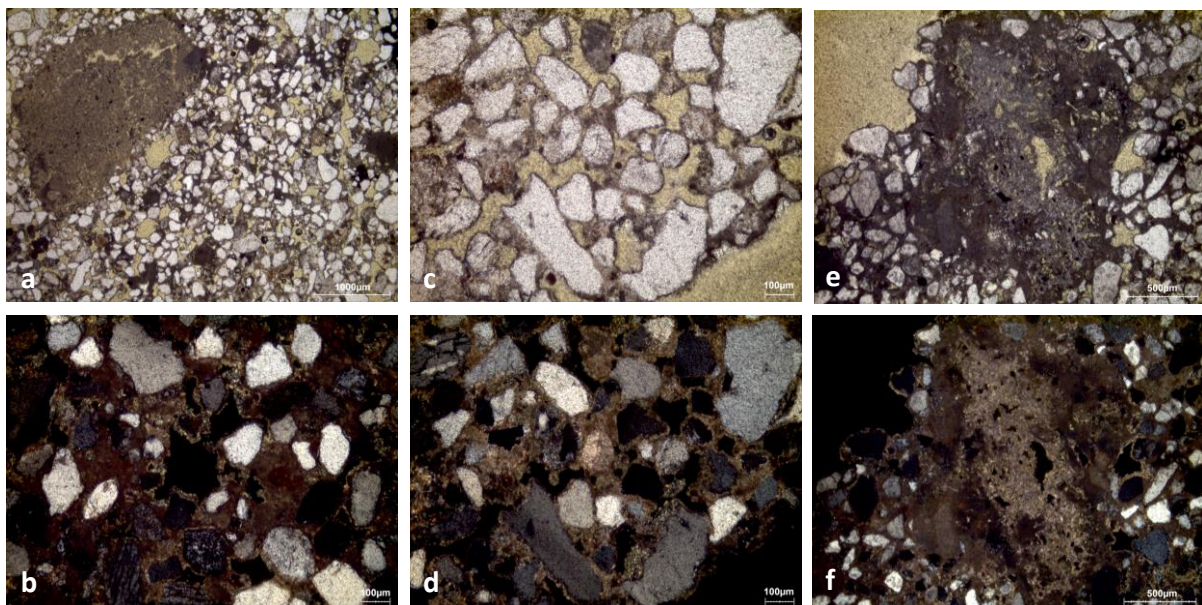
Figure 5: Representative photographs of the thin-section X2278: a) overview image in plain polarised light (PPL); b) secondary carbonates around pores in cross polarised light (XPL); c) PPL image showing a limestone grain; d) same image in XPL; e) PPL image with an underburned lime lump; f) same image in XPL.

Binder	Texture	micritic
	Lump state	completely burned, underburned
	Lump size	2.9 mm, 3 mm, 522 µm
	Lump frequency	numerous

Aggregate	**Grain size**	very fine to medium
	Mineralogy	siliceous sand (quartz, feldspar, plagioclase, glauconite) with few limestone grains
	Shape	subangular/subrounded
Appearance	**Homogeneity**	relatively homogeneous
	Macroporosity	high
	Pore structure	irregular/highly connected
Admixtures	**Type**	-
Alteration	**Type**	dissolution, secondary carbonates around pores

Table 2: Main characteristics of the mortar retrieved from the observations of the thin-section X2278.

Thermal analysis on whole samples

The apparent hydraulicity index (aHI) calculated from Figure 6 is around 60% indicating that the mortar is very strongly hydraulic. However, the values obtained from the thermal analyses might not reflect the reality since the mortar was strongly dissolved. The amount of carbonates still present in the mortar is around 12 wt%. At 573.9°C, the quartz transition phase can be observed (Rickard et al., 2010). The main weight loss of ancient mortars is expected between 600 and 900 °C and is indicative of the decomposition of calcium carbonate ($CaCO_3$) into calcium oxide (CaO) and carbon dioxide (CO_2) (Ahmmed et al. 2024). The end temperature of the calcium carbonate decomposition for the mortar sample is around 765°C. Two peaks at 625 and 657°C are observed, it could be due to the presence of a different form of carbonate possibly coming from the hydraulic phases. Another peak at 470°C is also observed and might be due to the release of water from calcium hydroxide (Moropoulou, Bakolas, and Bisbikou 1995; Klimesch and Ray 1996) indicated that the mortar did not fully carbonated. No gypsum was detected.
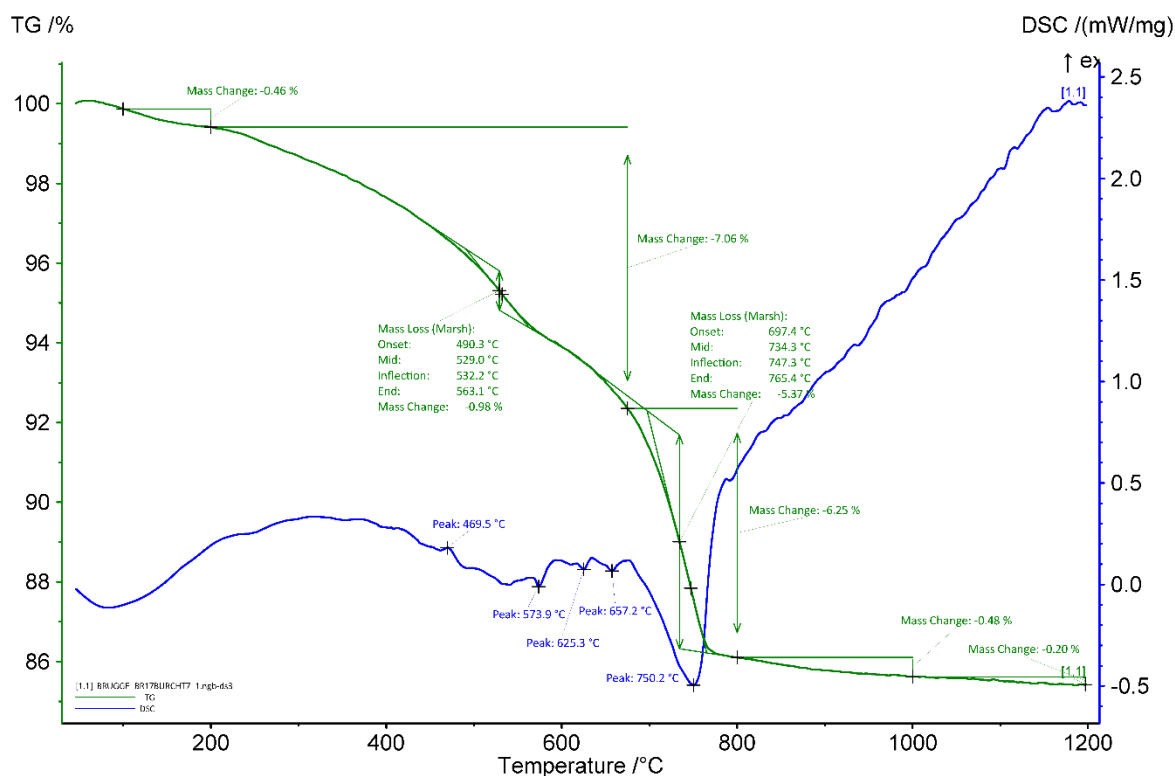
Figure 6: Coupled TG-DSC analysis of the whole mortar sample upon heating to a temperature of 1200°C at a heating rate of 20°C/min under an inert atmosphere (He flushed at 50 ml/min). The weight loss determined by thermogravimetric analysis (TG, wt%, green curve) and the result of the differential scanning calorimetric analysis (DSC, mW/mg, blue curve) are both presented.

Raman spectroscopy

The Raman analyses (Figure 7) revealed the presence of calcite, nitrates, quartz and feldspar on a white inclusion; haematite, quartz, amorphous carbon, and anatase on the beige binder as well as amorphous carbon on a grey inclusion and quartz on a brown one (data not shown).
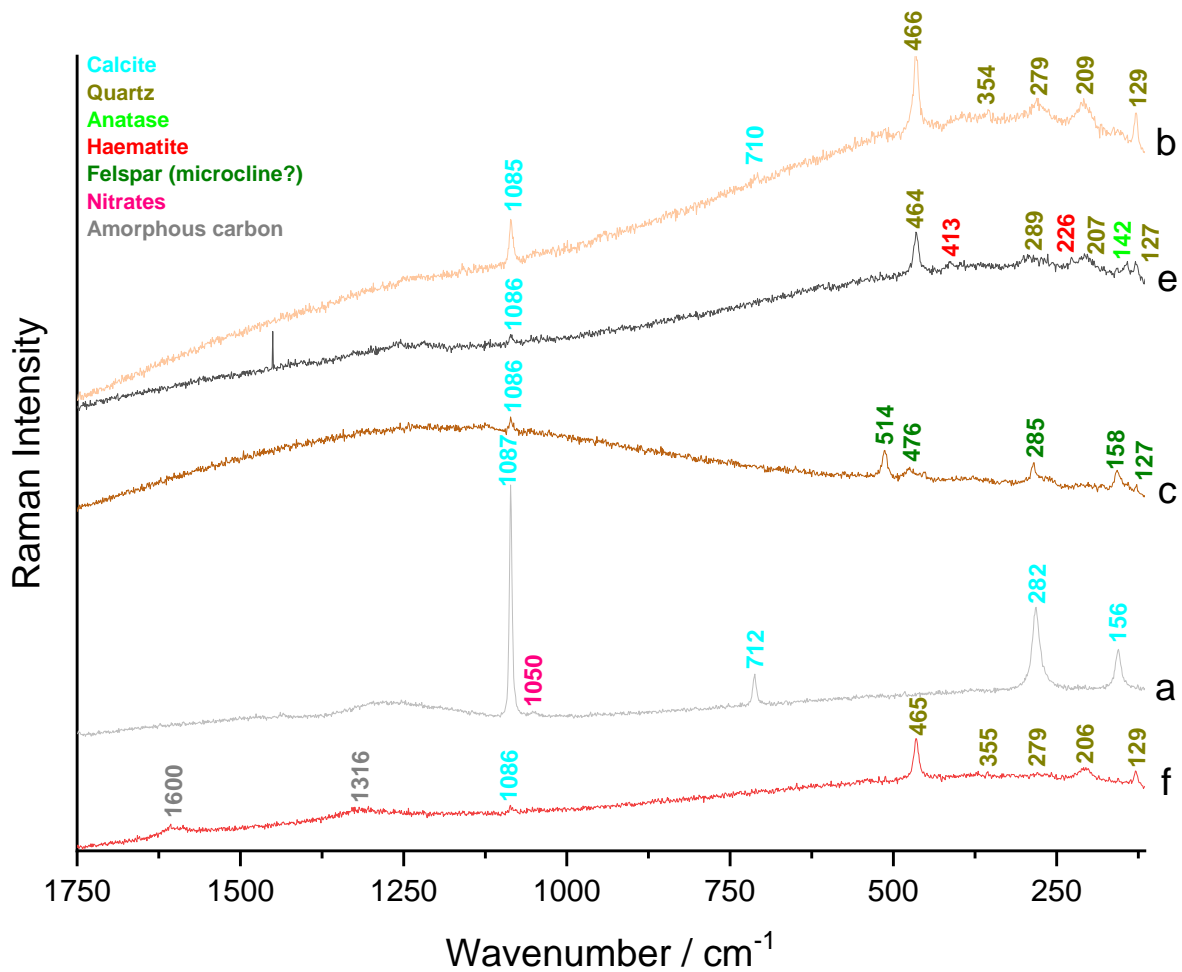
Figure 7: Characteristic Raman spectra obtained on the a white macroscopic inclusions (a, b & c) and on the beige binder (e & f); the colour of the spectra correspond to the colour of the microscopic area analysed.

Thermal analysis on powders with particle size <75 μm

The aHI is lower (~46 wt%) for the powder compared to the whole mortar sample (~60%). An explanation could be a lower concentration of the hydraulic components (clay) in the powder. The quantity of carbonates is higher in the powder (~40 wt%) compared to the whole sample (12 w%) since a large part of the sand was removed. Indeed, no quartz was detected in the powders. The end temperature of calcium carbonate decomposition is 806°C for the powdered sample. It is higher compared to the whole sample (765°C). A possible explanation could be that the powder is more pure compared to the whole mortar sample which increases the decomposition temperature. The peaks possibly coming from the hydraulic phases don't appear anymore for the powder.
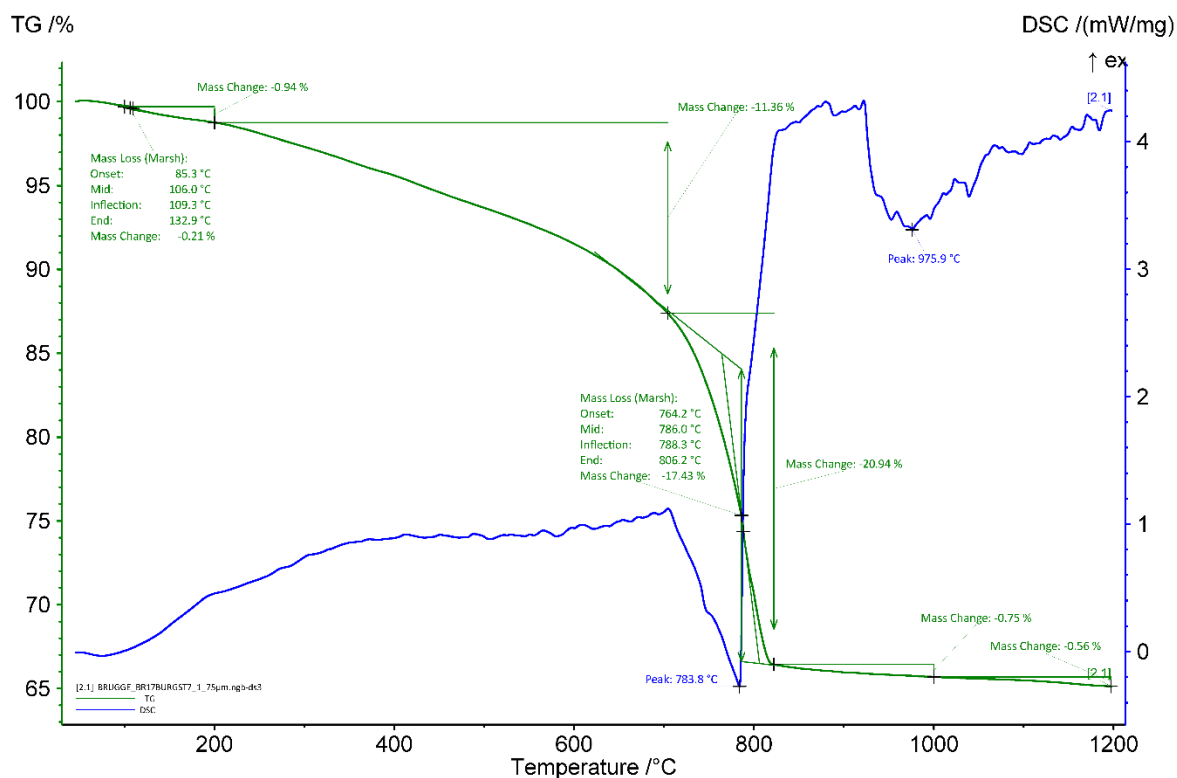
Figure 8: Coupled TG-DSC analysis of the powdered mortar with particle size < 75 µm upon heating to a temperature of 1200°C at a heating rate of 20°C/min under an inert atmosphere (He flushed at 50 ml/min). The weight loss determined by thermogravimetric analysis (TG, wt%, green curve) and the result of the differential scanning calorimetric analysis (DSC, mW/mg, blue curve) are both presented.

Radiocarbon results

The test prior to the CO_2 extraction revealed a low amount of carbon (Table 3) in the samples (~1 %). A relatively high amount of powder <75 µm was necessary for the carbon extraction (~8.5 g). This is reason why the fraction with higher particle size (125-250 µm) was used for the analyses.

RICH	Sample type	Method	C (%)	σ (%)	m (g)	Age BP extrapolated	Calibrated date (oxcal - 95.4%)	Age BP extrapolated with stat	Calibrated date (oxcal - 95.4%)	Age BP average first 4 dates	Calibrated date (oxcal - 95.4%)	Reliability of dating
25530	mortar 125-250 µm	8 fractions	1,03	0,151	8,55	1121 ± 30	774-995 cal AD	1093 ± 15.7	892-995 calAD	1131 ± 18	883-988 calAD	☒

Table 3: Radiocarbon results.

The first CO_2 fractions are within the same range (Figure 9). The dates obtained by each method (extrapolation, extrapolation with statistic, and the combination of the first four fractions) are within the same timeframe. They are slightly older (774-995 cal AD) compared to the presumed historical date (~1050-1100 AD).
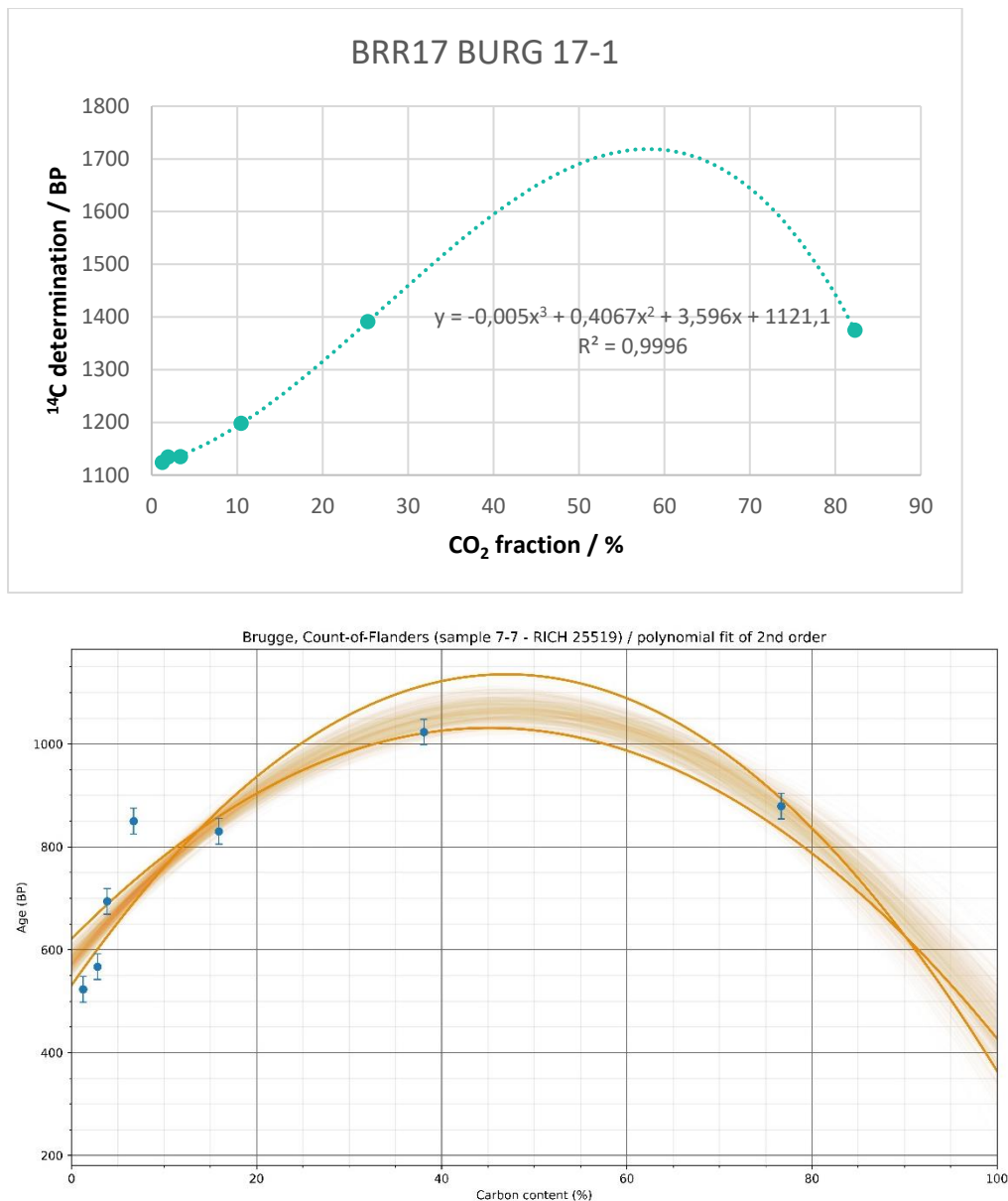
Figure 9: Radiocarbon results for the powdered mortar with particles 125-250 µm as a function of the CO_2 fraction (the graph at the bottom shows the statistic on the results).

Conclusions

The mortar sample is in poor condition. It has been strongly dissolved. The radiocarbon results are older compared to the expected historical date. It is not a good candidate for radiocarbon dating.

Study of mortars from BUPA14, Buizingen for the BRAIN 2.0 PalC project

Context of the site

In its current form, the castle of Gemeenteplein in the Belgian village of Buizingen (Halle) in the Flemish Brabant consists of a two-storey L-shaped wing and a square corner tower built of local rubble. The castle probably has a medieval core, but was fairly completely renovated several times in the 18th century. Annual anchors on the south façade indicate the year '1752'. During the 19th and 20th centuries, the castle was modified several times. Remains of the castle's pools have been preserved in the surrounding parkland. In 1948, the castle was bought by the municipality of Buizingen, which used it as the town hall. The castle is not protected (Vlaanderen, 2012).

Figure 1: Castle and church at Buizingen (photo credit: Ferdinand Leys).

Material

In 2017, Bert Heyvaert (archaeologist at Group Monument) and Bart Bartholomieux (archaeologist at Monument Vandekerckhove) submitted numerous samples coming from the castle, the church, and the graveyard. The presumed historical date ranges between 800 and 1500 AD. From the samples sent in 2017, eight had a sufficient weight to be included in the PalC project but only one was finally selected. It is the inventory number 15 that was sampled from the wall S809 which certainly seemed to be the oldest track in the north of the site. There is small possibility that this construction served as a graveyard wall. To the north of this wall, the ground no longer seemed to contain any bone material, while it did to the south.

Results & Discussion

Macroscopic descriptions

The main colour of the sample INV.NR. 15 (Figure 2) is beige tending to pinkish white (7.5 8/2) according to the Munsell soil colour charts. The main size of the lime lumps are around 1 mm and the maximum size around 3 mm. Grey inclusions were observed in all the fragments of the sample, they showed no reaction with dilute hydrochloric acid and are thus probably silicates. Black and hard inclusions identified as bottom ashes are present in the sample.

Figure 2: Photograph of the mortar fragments of INV.NR. 15 from Buizingen.

Fourier transform Infrared (FTIR) spectroscopy on inclusions & binder

The binder (beige – Figure 3) is made of calcite and silicates including quartz. The lime lumps are also made of calcite and silicates. The hard black inclusions show the features of organic matter. The composition of the grey inclusions is as expected silicates including quartz. The ratio carbonates/silicates is rather low, most probably due to dissolution process. The absence of aragonite might also be due to a leaching of the binder.
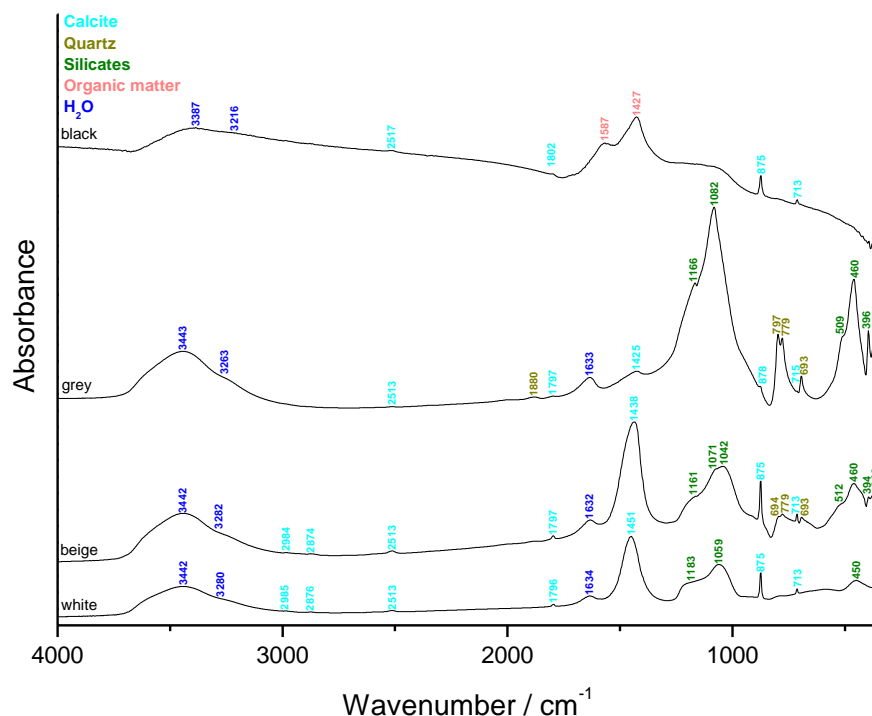
Figure 3: FTIR spectra obtained on the inclusions and binder (beige) of the mortar sample INV.NR. 15 from Buizingen.

Binder:sand ratio

The calculated binder:sand ratio using a bulk density of 1.35 kg/dm^3 for the sand and 0.575 kg/dm^3 for the lime is rather close to 1:1 in volume unit for sample 15.

	15
Sample weight (g)	3.0
Crucible weight (g)	14.6
Weight calcined (g)	16.8
%ins	**73.8**

Table 1: Percentage of insoluble residue of the mortar sample from Buizingen.

Cathodoluminescence

Cathodoluminescence observations of the thin-section and powder show similar results (Figure 4). The thin-section (Figure 4a) exhibits the presence of quartz grains with a light brown hue, small plagioclase grains in bright green, one bright red limestone fragment. The binder and lime lumps are dull. The powdered sample (Figure 4b) displays mainly a red tile colour (binder) with a few green plagioclase grains and a few bright red limestone grains.
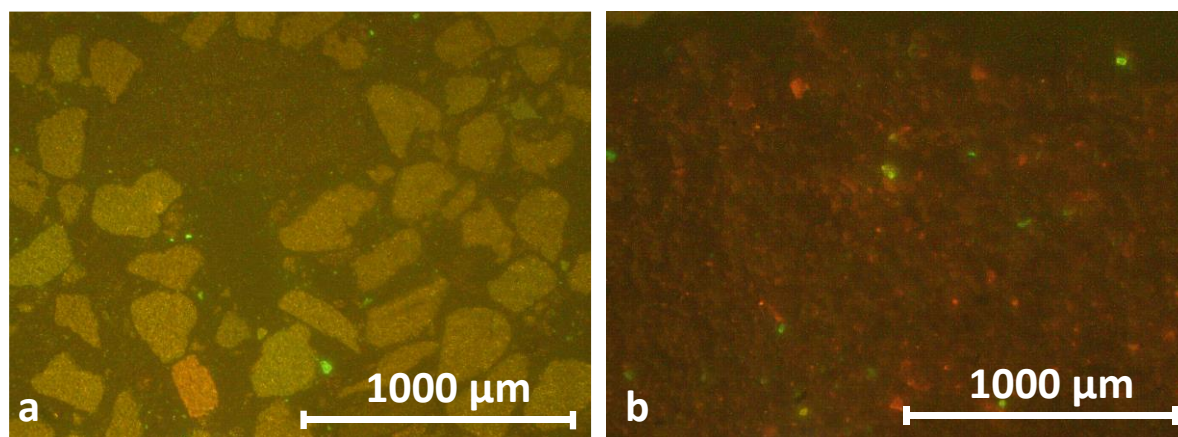
Figure 4: Characteristic cathodoluminescence images of a) the thin section X2281 and b) the powdered mortar with particle size lower than 75 μm.

Thin-section petrography

The mortar is rather in good condition (Figure 5 & Table 2). A slight dissolution of the binder in some areas can be deduced from the spongy-like structure of the macropores (Figure 5e & f). Secondary carbonates are observed at the border of these macropores (Figure 5e & f). The aggregate contains very few limestone grains (Figure 5c & d).
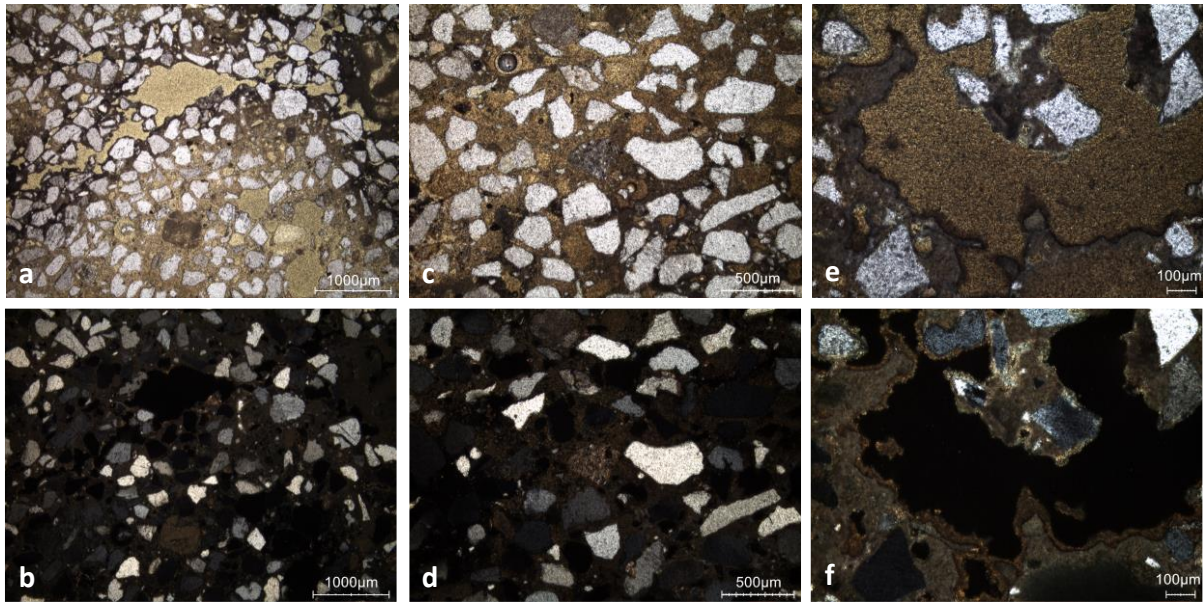
Figure 5: Representative photomicrographs of the thin-section X2281: a) overview image in plain polarised light (PPL); b) overview image in cross polarised light (XPL); c) PPL image showing a limestone grain; d) same image in XPL; e) PPL image showing the spongy-like structure of the pores with secondary carbonates at the border; f) same image in XPL.

Binder	**Texture**	micritic
	Lump state	completely burned
	Lump size	540 µm ; 971 µm ; 2 mm ; 1.96 mm
	Lump frequency	few (but large)
Aggregate	**Grain size**	very fine to medium
	Mineralogy	siliceous sand (quartz, feldspar) with a few limestone grains
	Shape	subangular / subrounded
Appearance	**Homogeneity**	relatively homogeneous
	Macroporosity	medium
	Pore structure	irregular / sometimes connected
Admixtures	**Type**	-
Alteration	**Type**	dissolution, secondary carbonates

Table 2: Main characteristics of the mortar retrieved from the observations of the thin-section X2281.

Thermogravimetric analysis (TGA) on whole samples

The apparent hydraulicity index (aHI) calculated from Figure 6 is around 20% indicating that the mortar is moderately hydraulic. The amount of carbonates present in the mortar around 29 wt%. At 572.5°C, the quartz transition phase can be observed (Rickard et al., 2010). The main weight loss of ancient mortars is expected between 600 and 900 °C and is indicative of the decomposition of calcium carbonate ($CaCO_3$) into calcium oxide (CaO) and carbon dioxide (CO_2) (Ahmmed et al. 2024). The end temperature of the calcium carbonate decomposition for the mortar sample INV.NR. 15 is around 817°C. No gypsum was detected.
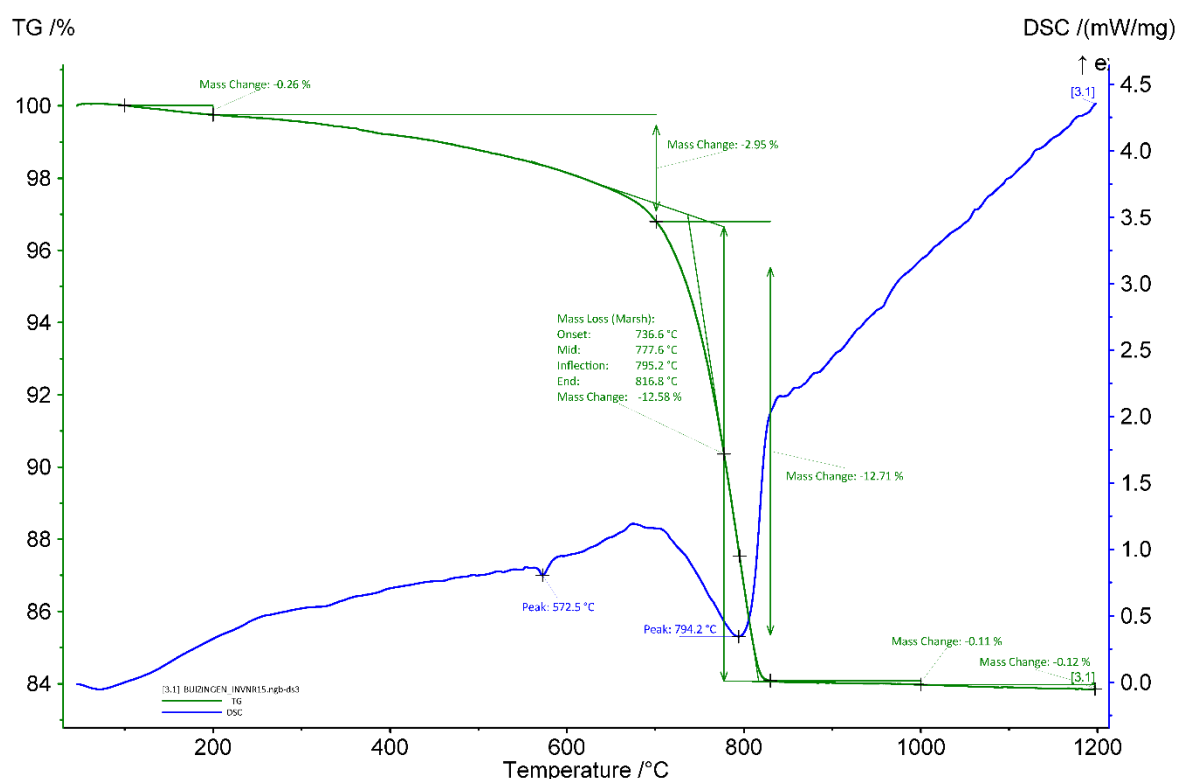
Figure 6: Coupled TG-DSC analysis of the mortar sample INV.NR. 15 upon heating to a temperature of 1200° C at a heating rate of 20°C/min under an inert atmosphere (He flushed at 50 ml/min). The weight loss determined by thermogravimetric analysis (TG, wt%, green curve) and the result of the differential scanning calorimetric analysis (DSC, mW/mg, blue curve) are both presented.

Grinding/particle separation

Black and grey inclusions were carefully removed when grinding sample 15.

TGA on powders with particle size <75 μm

The aHI is the same for the powder as for the whole mortar sample (~20%). The quantity of carbonates is higher in the powder compared to the whole sample since a large part of the sand was removed (~45 wt%). Indeed, no quartz was detected in the powders. The end temperature of calcium carbonate decomposition is 826 °C for the powdered sample. It is slightly higher compared to the whole sample. A possible explanation could be that the powder is more pure

compared to the whole mortar sample which increases the decomposition temperature.
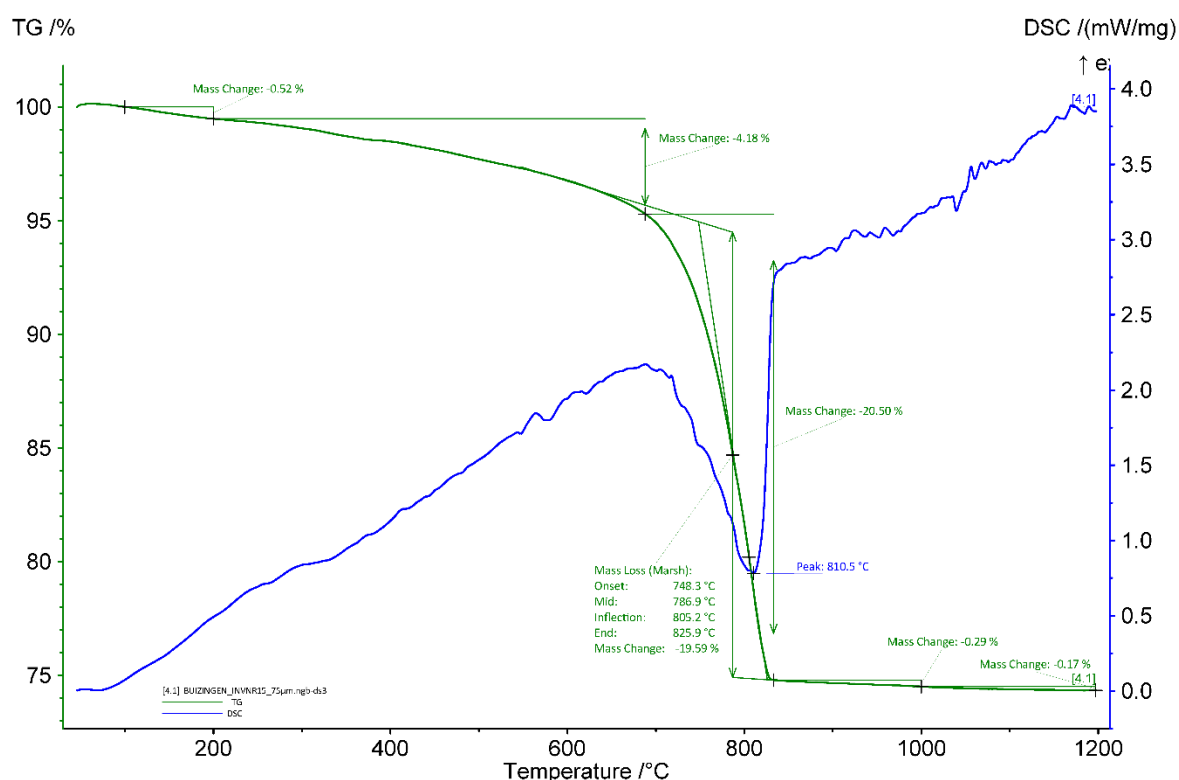
Figure 16: Coupled TG-DSC analysis of the powdered mortar sample INV.NR. 15 with particle size < 75 µm upon heating to a temperature of 1200° C at a heating rate of 20 °C/min under an inert atmosphere (He flushed at 50 ml/min). The weight loss determined by thermogravimetric analysis (TG, wt%, green curve) and the result of the differential scanning calorimetric analysis (DSC, mW/mg, blue curve) are both presented.

Radiocarbon results

The test prior to the CO_2 extraction revealed an average amount of carbon (Table 3) in the sample (~5 %). A relatively low amount of powder <75 µm was necessary for the carbon extraction (~2 g).

RICH	Sample type	Method	C (%)	σ (%)	m (g)	Age BP extrapolated	Calibrated date (oxcal - 95.4%)	Age BP extrapolated with stat	Calibrated date (oxcal - 95.4%)	Age BP average first 4 dates	Calibrated date (oxcal - 95.4%)	Reliability of dating
32267	mortar < 75 µm	8 fractions	5,23	0,067	1,83	correlation too low	-	839.9 ± 10	1176-1260 calAD	(6 first dates) 850 ± 9	1170-1225 calAD	☑

Table 3: Radiocarbon results.

The radiocarbon determination is within the same range for the first four fractions (Figure 6). The correlation of the extrapolation was too low so the date was not considered. However, the statistical analyses and the average date of the four first fractions (1170-1260 calAD) fall within the range of the expected date (800-1500 AD).
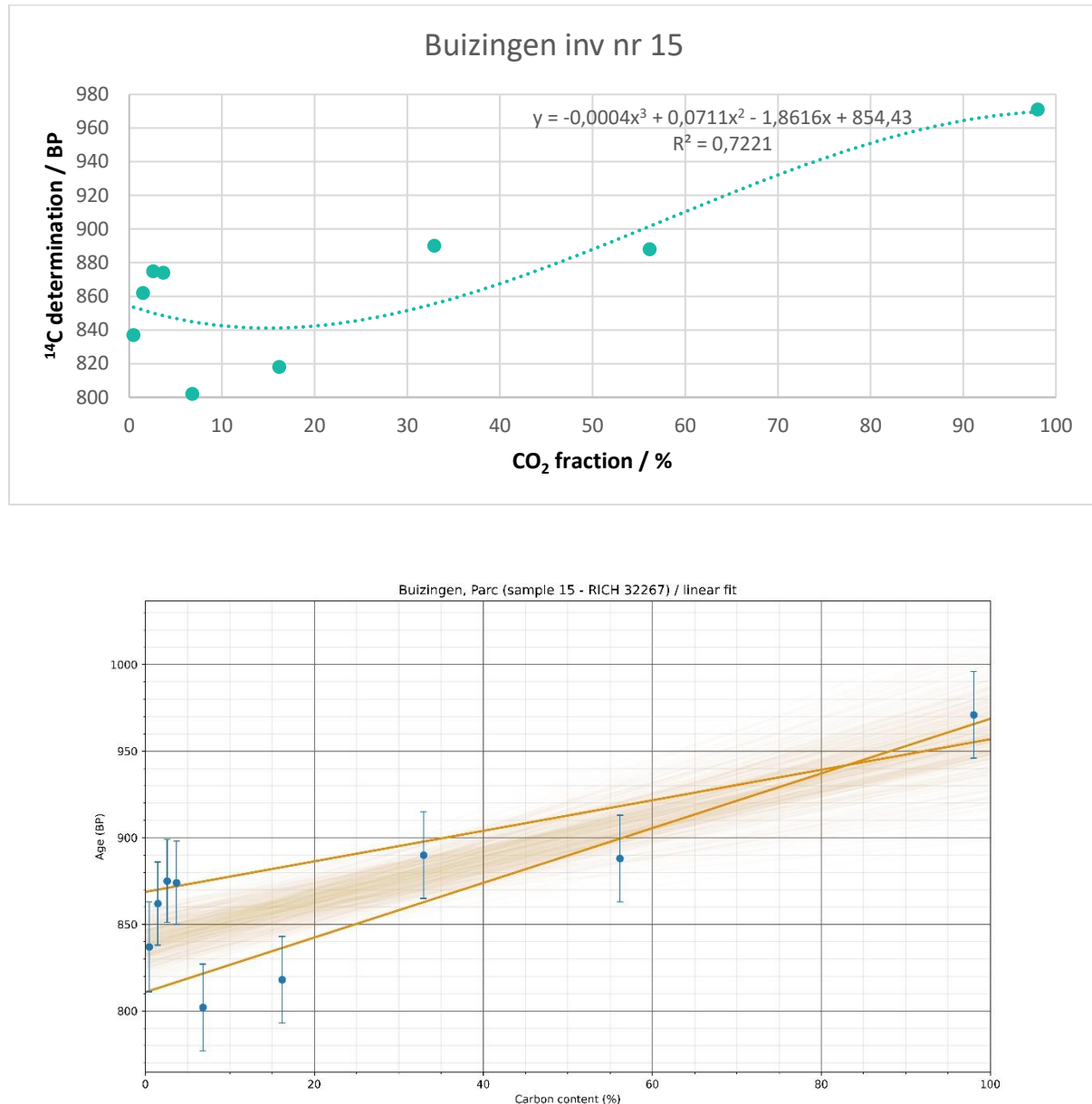
Figure 6: Radiocarbon results for the powdered mortar with particles < 75 μm as a function of the CO_2 fraction (the graph at the bottom shows the statistic on the results).

Conclusions

The mortar is in relatively good condition. Only a slight dissolution and a few secondary carbonates were observed in the thin sections. The aggregate is made up of siliceous sand with few carbonates. The moderate hydraulicity of the binder could involve a slight delayed hardening for the binder. Two of the radiocarbon dates obtained fall within the same range and shall indicate a reliable dating for the sample 15 since they are within the range of the estimated

historical date. However, the range for the estimated historical date is rather large (800-1500), hence the need for more information, clues and research to confirm the radiocarbon dating.

Bibliography

Rickard, W. D. A., Riessen, A. V., & Walls, P. (2010). Thermal Character of Geopolymers

Synthesized from Class F Fly Ash Containing High Concentrations of Iron and α-

Quartz. *International Journal of Applied Ceramic Technology*, *7*(1), 81–88.

https://doi.org/10.1111/j.1744-7402.2008.02328.x

Vlaanderen, A. (2012). *Kasteel, Buizingen* [Photo].

https://www.flickr.com/photos/erfgoed/6883359771/

Study of mortars from Saint-Agatha church (Huldenberg) for the BRAIN 2.0 PalC project

Context of the site

The origins of Sint-Agatha-Rode probably date back to the 11th century. The Count of Leuven, Godfried I, probably built a church here at that time. In 1140, Godfried II transferred the tithe rights to the chapter of the collegiate church of St Peter in Leuven. It is highly likely that a church of Romanesque origin was built at this site and that it was rebuilt around 1400 in its current appearance. ("Parochiekerk Sint-Agatha met kerkhof" 2021).

Figure 1: Saint-Agatha church in 1945 (CC by KIK-IRPA, Brussels (Belgium), A004007).

Material

Following the restoration with installation of a new heating system in the Saint-Agatha church in Huldenberg, the Flanders Heritage Agency (Agentschap Onroerend Erfgoed) imposed an archaeological excavation (permit number 2016/196). The fieldwork was carried out by Studiebureau Archeologie bvba in phases between 16-06-2016 and 04-09-2017. In this context, several mortar samples were collected and dated mainly with the extraction of charcoal. Four samples were selected for the PALc project but only one matched the required quantities and carbon percentage necessary to perform all the required analyses. It is a mortar from the north east choir that was estimated to date between 1040 and 1300 AD.

Results & Discussion

Macroscopic descriptions

The main colour of the mortar is beige (Figure 2) tending towards pale yellow (2.5Y 8/4) according to the Munsell soil colour charts. The lime lumps appear as white inclusions with a main size of ~ 2 mm and the biggest ones measure ~ 5 mm. A large grey inclusion (~5 mm) was observed but since it does not seem to react with HCl, it is probably a siliceous aggregate.

Figure 2: Mortar sample from the north east choir.

Fourier transform Infrared (FTIR) spectroscopy on inclusions & binder

The binder (beige, Figure 3) mainly contains calcium carbonates (calcite and aragonite) and silicates including quartz. The lime lumps (white, Figure 3) are also mainly made of calcium carbonates (calcite and aragonite) with a few silicates. The grey inclusion contains calcium carbonates (calcite and aragonite) with a few silicates, it is then a limestone inclusion and not a siliceous aggregate. A black inclusion was also analysed and mainly comprises amorphous carbon with silicates including quartz and clay. It is probably a piece of charcoal but it was too little to be radiocarbon dated.
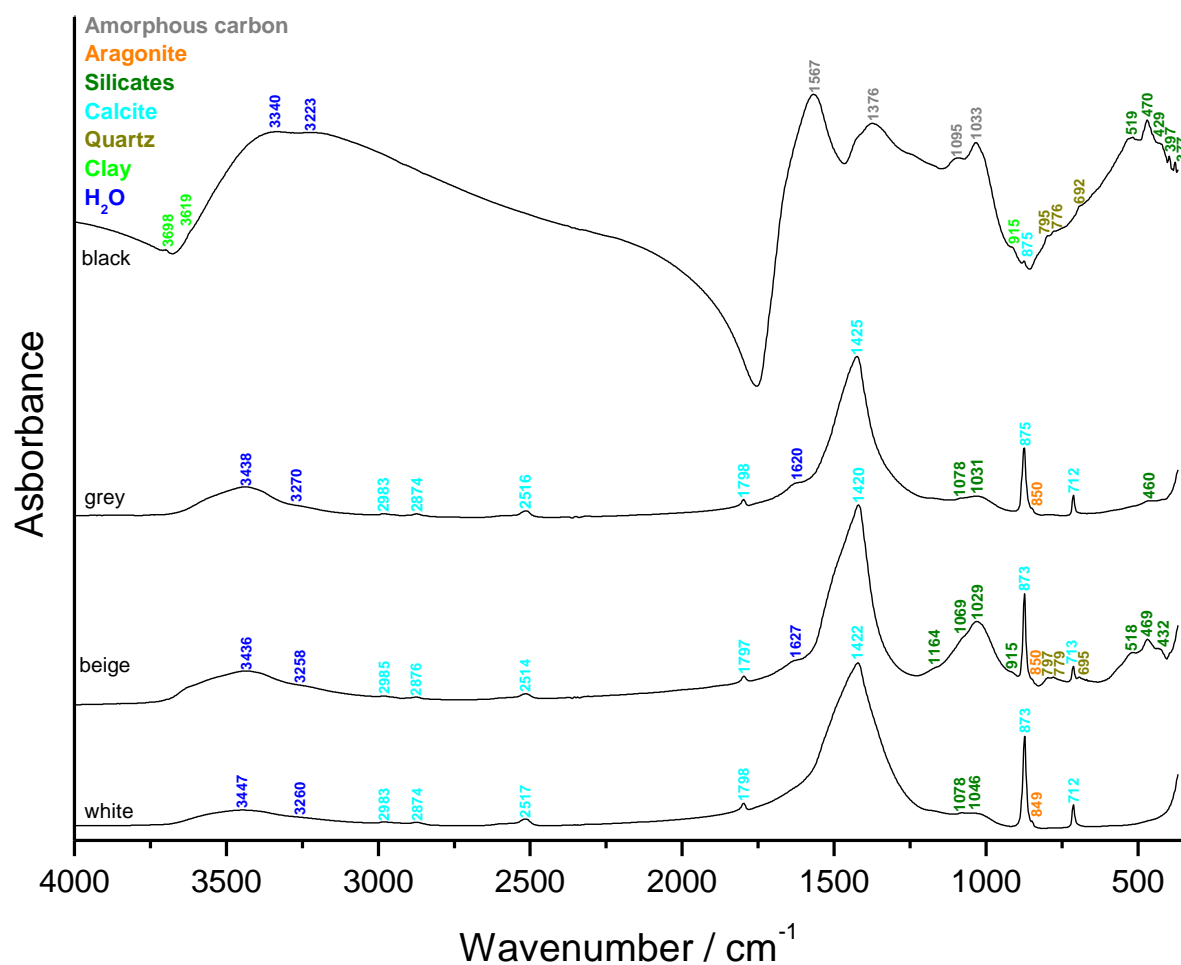
Figure 3: FTIR spectra obtained on the inclusions and binder (beige) of the mortar sample.

Binder:sand ratio

The calculated binder:sand ratio using a bulk density of 1.35 kg/dm^3 for the sand and 0.575 kg/dm^3 for the lime is close to 2:1 in volume unit.

	north east choir
Sample weight (g)	2.5
Crucible weight (g)	14.6
Weight calcined (g)	16.1
%ins	**57.2**

Table 1: Percentage of insoluble residue.

Cathodoluminescence

Cathodoluminescence observations of the three thin-sections and powders show similar results (Figure 4). The thin-sections exhibit the presence of quartz grains with a light brown hue, and the binder is dull. The powdered sample shows a red tile colour.
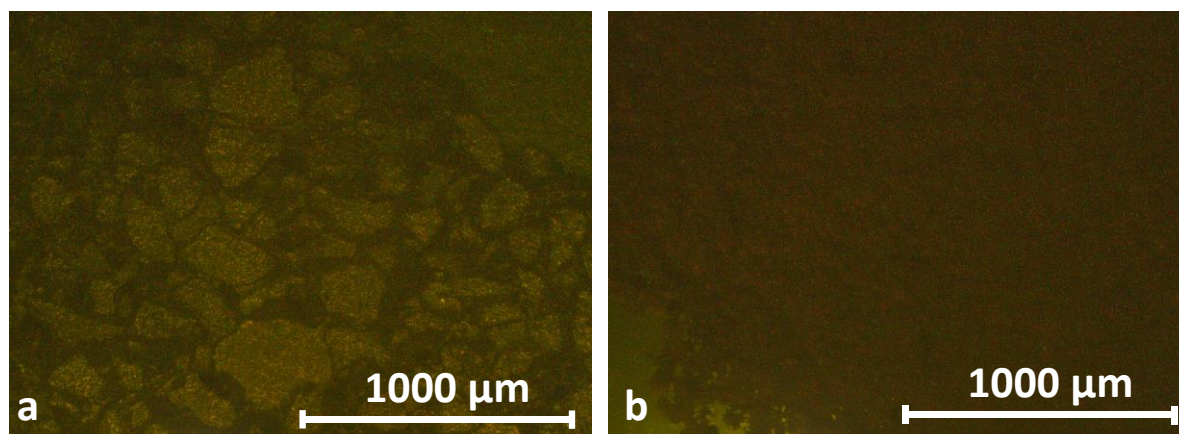
Figure 4: Characteristic cathodoluminescence images of a) the thin section X2289 and b) the powdered mortar with particle size lower than 75 µm.

Thin-section petrography

The mortar is in relatively good condition (Figure 5 & Table 2). The aggregate is made of pure siliceous sand. A large quantity of clay cutans is observed (Figure c & d).
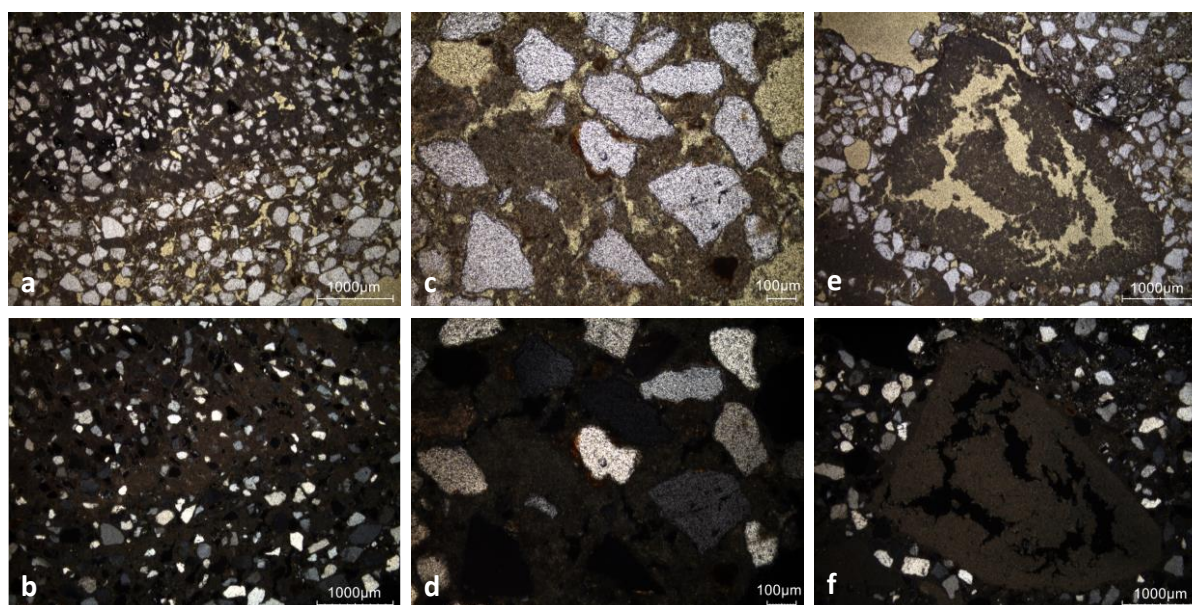
Figure 5: Representative photomicrographs of the thin-section X2289: a) overview image in plain polarised light (PPL); b) overview image in cross polarised light (XPL); c) PPL image showing a clay cutan; d) same image in XPL; e) PPL image with a large lime lump; f) same image in XPL.

Binder	**Texture**	micritic
	Lump state	completely burned
	Lump size	1.6 cm? ; 3.8 mm
	Lump frequency	few but large
Aggregate	**Grain size**	very fine to medium
	Mineralogy	pure siliceous sand (quartz, feldspar, lots of glauconite)

	Shape	subangular / subrounded
Appearance	**Homogeneity**	relatively homogeneous
	Macroporosity	medium
	Pore structure	irregular / sometimes connected
Admixtures	**Type**	-
Alteration	**Type**	secondary carbonates

Table 2: Main characteristics of the mortar retrieved from the observations of the thin-section X2289.

TGA on powders with particle size <75 µm

The apparent hydraulicity index (aHI) calculated from Figure 6 is around 39% indicating that the mortar is strongly hydraulic. However, the values obtained from the thermal analyses might not reflect the reality since only the powder was analysed. Other samples from the church were analysed and showed a moderate hydraulicity. We assume that it is the case for this sample. The amount of carbonates present in the powdered mortar is around 38 wt%. At 579°C, the quartz transition phase can be observed (Rickard et al., 2010). The main weight loss of ancient mortars is expected between 600 and 900 °C and is indicative of the decomposition of calcium carbonate ($CaCO_3$) into calcium oxide (CaO) and carbon dioxide (CO_2) (Ahmmed et al. 2024). The end temperature of the calcium carbonate decomposition for the mortar sample is around 827°C. No gypsum was detected.
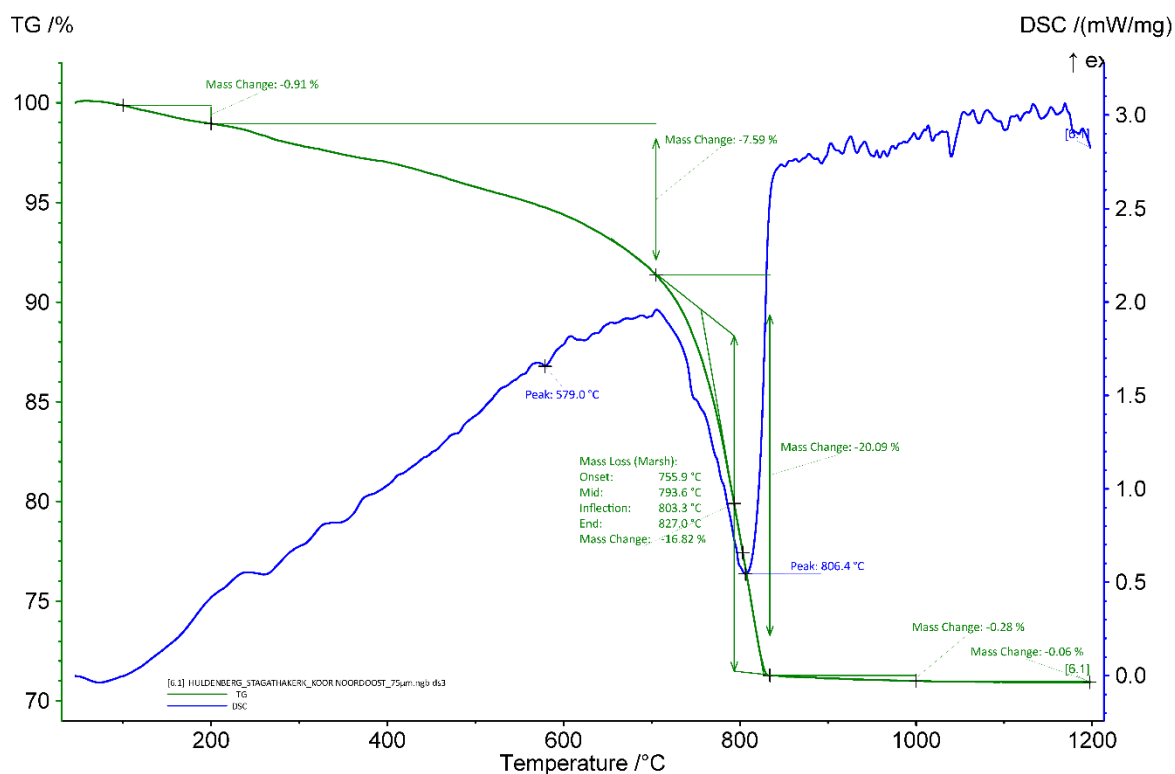
Figure 6: Coupled TG-DSC analysis of the powdered mortar of the north east choir with particle size < 75 μm upon heating to a temperature of 1200°C at a heating rate of 20°C/min under an inert atmosphere (He flushed at 50 ml/min). The weight loss determined by thermogravimetric analysis (TG, wt%, green curve) and the result of the differential scanning calorimetric analysis (DSC, mW/mg, blue curve) are both presented.

Radiocarbon results

The test prior to the CO_2 extraction revealed an correct amount of carbon (Table 3) in the sample (~5 or 6 %). A relatively low amount of powder <75 μm was necessary for the carbon extraction (~2 g).

RICH	Sample type	Method	C (%)	σ (%)	m (g)	Age BP extrapolated	Calibrated date (oxcal - 95.4%)	Age BP extrapolated with stat	Calibrated date (oxcal - 95.4%)	Age BP average first 4 dates	Calibrated date (oxcal - 95.4%)	Reliability of dating
32378	mortar < 75 µm	8 fractions	5,45	0,306	1,86	854 ± 25	1150-1270 calAD	848 ± 12.5	1167-1228 calAD	871 ± 11	1165-1220 calAD	☑

Table 4: Radiocarbon results

All the radiocarbon results (extrapolated, extrapolated with statistics and average – Table 3 & Figure 6) are in accordance with the presumed historical date (between 1040 and 1300 AD). The radiocarbon determination of the first CO_2 fractions are within the same range. The radiocarbon dating of the mortar seems to be reliable.
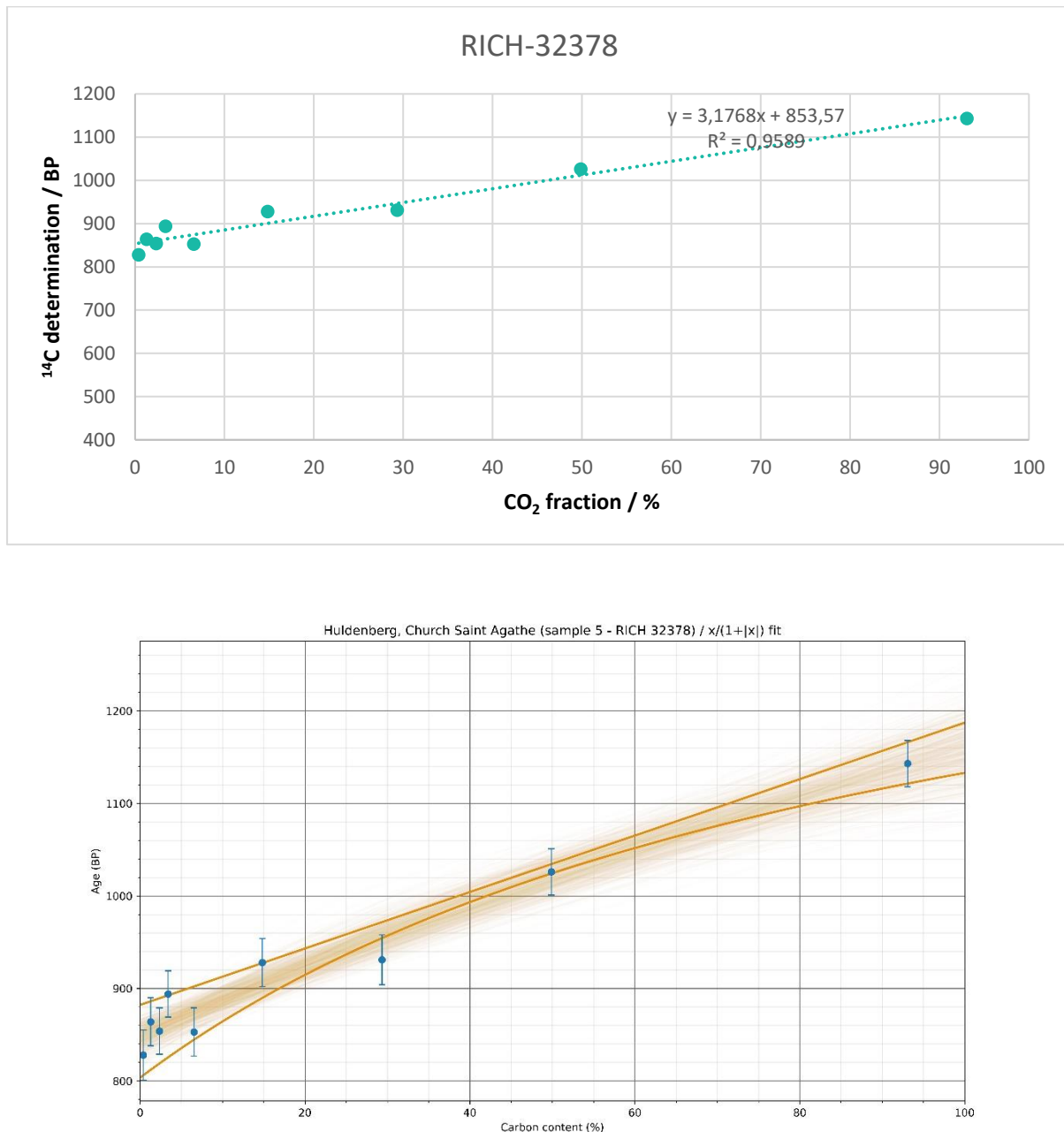
Figure 6: Radiocarbon results for the powdered mortar with particles < 75 μm as a function of the CO_2 fraction (the graph at the bottom shows the statistic on the results).

Conclusions

The mortar is in relatively good condition. Only a few secondary carbonates were observed in the thin sections. The aggregate is made up of pure siliceous sand. The presence of clay cutans overestimate the hydraulicity of the binder which we can consider to be low. The radiocarbon

date obtained fall within the range of the estimated historical date and shall indicate a reliable dating for the sample.

Bibliography

"Parochiekerk Sint-Agatha met kerkhof." 2021. October 8, 2021. https://inventaris.onroerenderfgoed.be/erfgoedobjecten/43320.

Study of mortars from Ten Bogaerde (Koksijde) for the BRAIN 2.0 PalC project

Context of the site

The Ten Bogaerde site at Koksijde is a monastic grange of the Cistercian abbey of the Dunes, dating back from before 1183. The 13th century medieval barn, built in brick architecture by abbot Nicholas of Baillieul (1232/3-1253), is one of the most imposing buildings preserved, but the building has lost its impressive postroof in a fire in 1593. The inner floor of the barn has been excavated in 2014. The lost piers of the medieval postroof has been discovered during the excavations. Two pier types of the original 13th century postroof could be distinguished: brick piers and piers of reused stone material. Besides that, two brick piers can be related to a renovation (undated between 1250 and 1600) of the original construction (Lehouck and Termote 2016).

Figure 1: The gate of Ten Bogaerde farmstead, ca. 1900. The old 18th-century gate wings are clearly visible here (CC-BY KIK-IRPA, Bruxelles).

Material

An investigation of the archaeological structures was possible after cleaning up by use of clear water. Afterwards, several mortar samples have been taken from the outer part of the structures for radiocarbon dating. To exclude contamination by groundwater, sheltered places were selected for sampling which resulted in dry mortar samples. Mortar with cracks and fractures were discarded. The bulk samples were kept in open grip seal bags, thus not airtight, to allow ventilation and to prevent fungi.

Nine samples were selected for dating in 2017 and one was selected for the PALc project (because it has enough quantity to perform all the analyses). Radiocarbon dating on charcoal (RICH 24018; RICH 24019), found in the mortar, resulted into an old wood effect. Three other samples were characterised as inconsistent lime mortars (RICH 25773; RICH 25776; RICH 24841) because of a high percentage of sand or contained a high level of fossil carbonates. As a consequence, this was dated much older than might be.

The sample selected is 7002-3.

Results & Discussion

Macroscopic descriptions

The main colour of the sample is beige (Figure 2) tending towards very pale brown (10YR 8/2) according to the Munsell soil colour charts. Some grey and milky aggregates were observed and are probably siliceous aggregates. The lime lumps appear as white inclusions with a main size of 1 mm and the biggest ones measure 5 mm.

Figure 2: Mortar 7002-3 from Ten Bogaerde site at Koksijde.

Fourier transform Infrared (FTIR) spectroscopy on inclusions & binder

The binder (beige, Figure 3) mainly contains calcium carbonates (calcite and aragonite) and silicates including quartz. The grey and milky inclusions are mainly made of calcium carbonates (calcite and aragonite) with some silicates that include quartz but also clay for the grey ones. The white inclusions are made of silicates with a low amount of carbonates that should come from the mortar when sampled for the analyses.
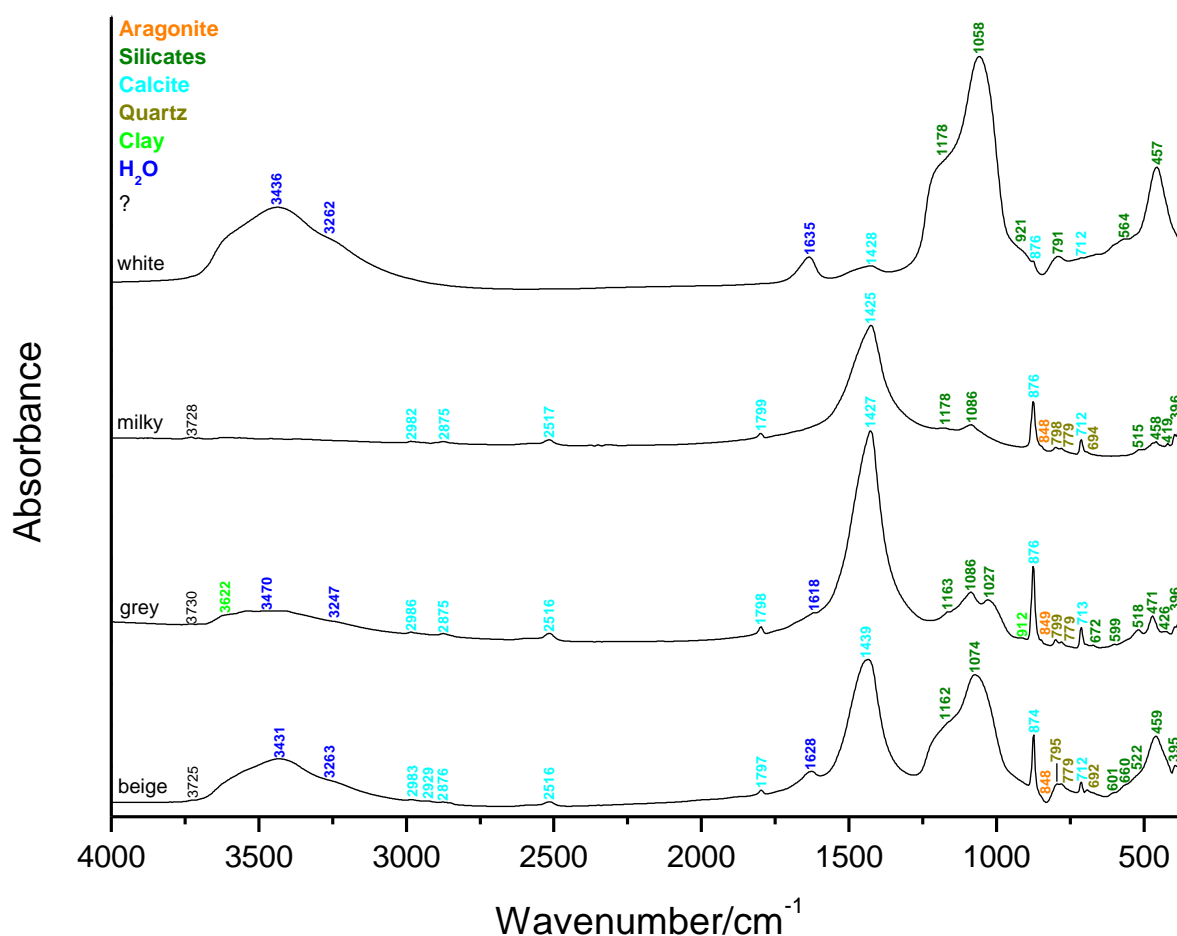
Figure 3: FTIR spectra obtained on the inclusions and binder (beige) of the mortar sample.

Binder:sand ratio

The calculated binder:sand ratio using a bulk density of 1.35 kg/dm^3 for the sand and 0.575 kg/dm^3 for the lime is close to 2:3 in volume unit.

	S7002-3
Sample weight (g)	2.8
Crucible weight (g)	16.8
Weight calcined (g)	19.0
%ins	**78.1**

Table 1: Percentage of insoluble residue

Cathodoluminescence

Cathodoluminescence observations of the thin-section and powder show similar results (Figure 4). The thin-sections exhibit the presence of quartz grains with a dark purple hue, K-feldspars in bright blue, bright green plagioclases and the binder is dull. The powder is mainly dull with a few bright red limestone grains and bright blue K-felspars.
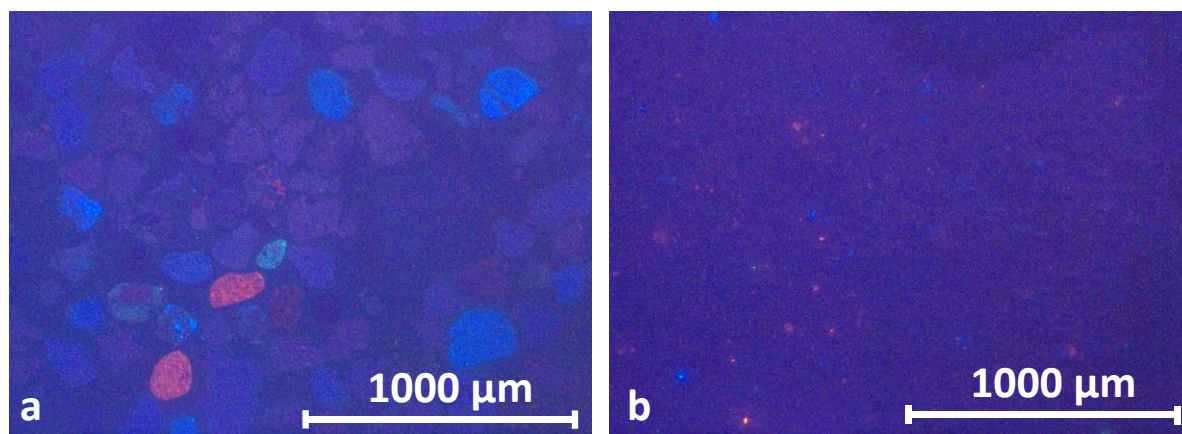
Figure 4: Characteristic cathodoluminescence images of a) the thin section X2291 and b) the powdered mortar with particle size lower than 75 μm.

Thin-section petrography

The mortar is deteriorated (Figure 5 & Table 2), it has been dissolved. Secondary carbonation is observed at the border of the pores (Figure 5e & f). Moreover, the aggregate contains some limestone grains (Figure 5c & d) that are partially micritic and tend to be visually similar to incompletely burned lime lumps.
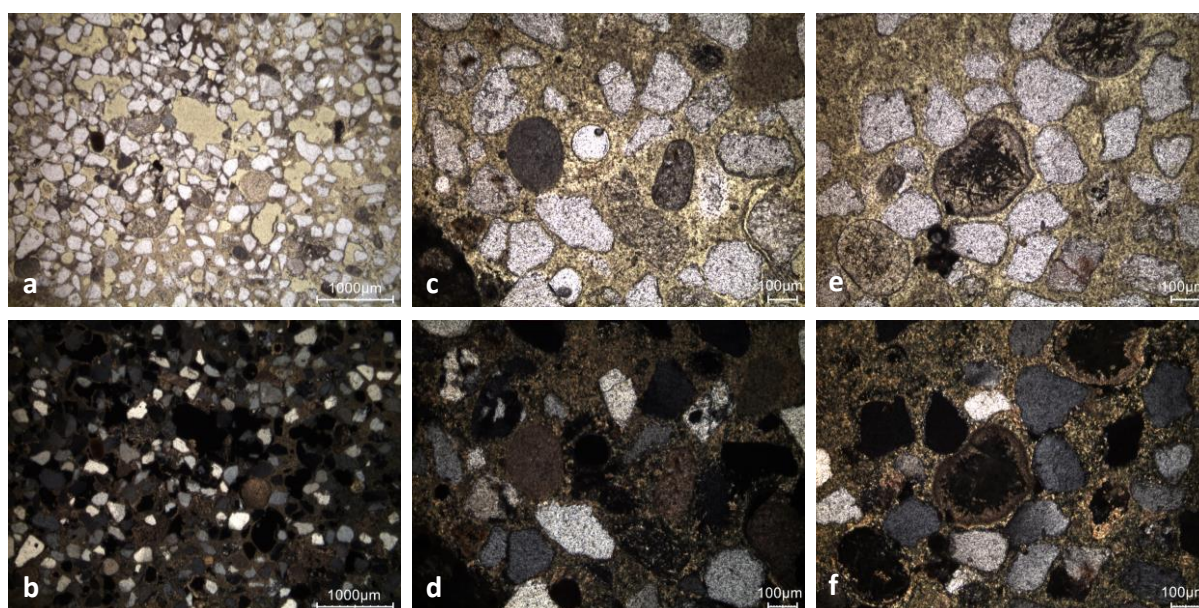
Figure 5: Representative photographs of the thin-section X2291: a) overview image in plain polarised light (PPL); b) overview image in cross polarised light (XPL); c) PPL image some limestone grains; d) same image in XPL; e) PPL image with secondary carbonates in pores; f) same image in XPL.

Binder	**Texture**	micritic
	Lump state	completely burned but dissolved
	Lump size	max 3.4 mm
	Lump frequency	few (might be because of dissolution)
Ag gr	**Grain size**	very fine to medium

Aggregate	**Mineralogy**	siliceous sand with few limestone grains (quartz, K-feldspar, plagioclase, glauconite more or less oxidised)
	Shape	subangular / subrounded
Appearance	**Homogeneity**	relatively homogenous
	Macroporosity	high
	Pore structure	irregular / sometimes connected
Admixtures	**Type**	none
Alteration	**Type**	secondary carbonates, dissolution

Table 2: Main characteristics of the mortar retrieved from the observations of the thin-section X2291.

Thermogravimetric analysis (TGA) on whole sample

The apparent hydraulicity index (aHI) calculated from Figure 6 is around 28% indicating that the mortar is strongly hydraulic. However, the values obtained from the thermal analyses might not reflect the reality since the mortar was dissolved. The amount of carbonates still present in the mortar is around 17 wt%. At 570.9°C, the quartz transition phase can be observed (Rickard et al., 2010). The main weight loss of ancient mortars is expected between 600 and 900 °C and is indicative of the decomposition of calcium carbonate ($CaCO_3$) into calcium oxide (CaO) and carbon dioxide (CO_2) (Ahmmed et al. 2024). The end temperature of the calcium carbonate decomposition for the mortar sample is around 796°C. No gypsum was detected.
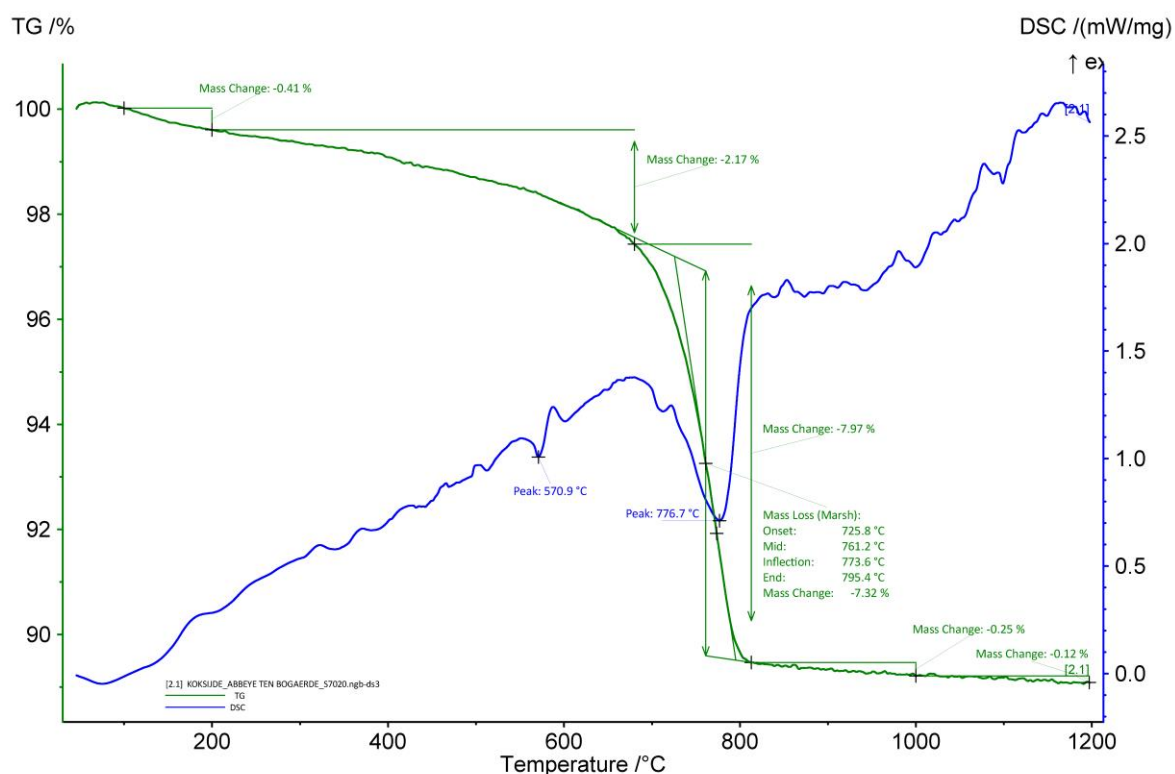
Figure 6: Coupled TG-DSC analysis of the mortar upon heating to a temperature of 1200°C at a heating rate of 20°C/min under an inert atmosphere (He flushed at 50 ml/min). The weight loss determined by thermogravimetric analysis (TG, wt%, green curve) and the result of the differential scanning calorimetric analysis (DSC, mW/mg, blue curve) are both presented.

TGA on powder with particle size <75 μm

The aHI is approximately the same (~30 wt%) for the powder compared to the whole mortar sample (~28%). The quantity of carbonates is higher in the powder (~39 wt%) compared to the whole sample (17 w%) since a large part of the sand was removed when sieving. Indeed, no quartz was detected in the powder. The end temperature of calcium carbonate decomposition is ~819°C for the powdered sample. It is higher compared to the whole sample (7986°C). A possible explanation could be that the powder is more pure compared to the whole mortar sample which increases the decomposition temperature.
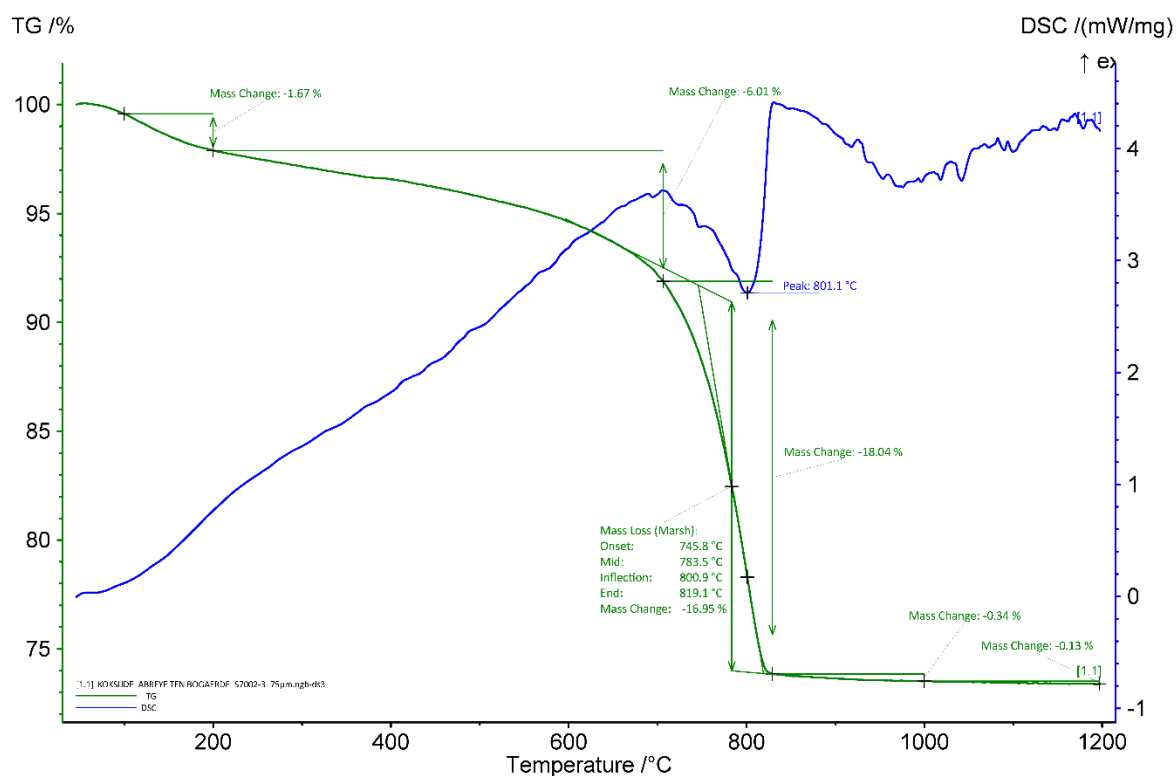
Figure 7: Coupled TG-DSC analysis of the mortar with particle size < 75 μm upon heating to a temperature of 1200°C at a heating rate of 20°C/min under an inert atmosphere (He flushed at 50 ml/min). The weight loss determined by thermogravimetric analysis (TG, wt%, green curve) and the result of the differential scanning calorimetric analysis (DSC, mW/mg, blue curve) are both presented.

Radiocarbon results

The tests prior to the CO_2 extraction revealed a higher amount of carbon (Table 3) in the fraction <75 μm (~5 %) compared to the fraction < 125 μm (~2 %). More sand is present in the later so more powder is needed to extract CO_2.

RICH	Sample type	Method	C (%)	σ (%)	m (g)	Age BP extrapolated	Calibrated date (oxcal - 95.4%)	Age BP extrapolated with stat	Calibrated date (oxcal - 95.4%)	Age BP average first dates	Calibrated date (oxcal - 95.4%)	Reliability of dating
25990	mortar powder < 125 μm	7 fractions	2,00	0,09	4,7	602 ± 24	1302-1405 calAD	600.7 ± 20.9	1304-1403 calAD	not possible	-	☒
32226	mortar powder < 75 μm	9 fractions	4,75	0,10	2,86	610 ± 22	1300-1400 caAD	600.7 ± 13.7	1306-1400 calAD	(3 first fractions) 625 ± 13	1295-1395 calAD	☒

Table 3: Radiocarbon results

The extrapolated radiocarbon age obtained for both fractions of powders (Figure 8, 9 & Table 3) are within the same range (~600 BP – 1300-1400 calAD). Differences can however be noticed between the two curves (Figures 8 & 9). The first CO_2 fractions are more scattered in the case of the powder with particle size < 125 μm, an average date could not be obtained. Also, the last fraction dated (~80 %) is much older for the powder with particle size < 125 μm (~4500 BP) compared to the powder with particle size < 75 μm (~95 %, ~1800 BP). The lower the size of the particles is, the less limestones grains are present. In both cases, the radiocarbon dates obtained do not match with the context (1232/3–1253 AD).
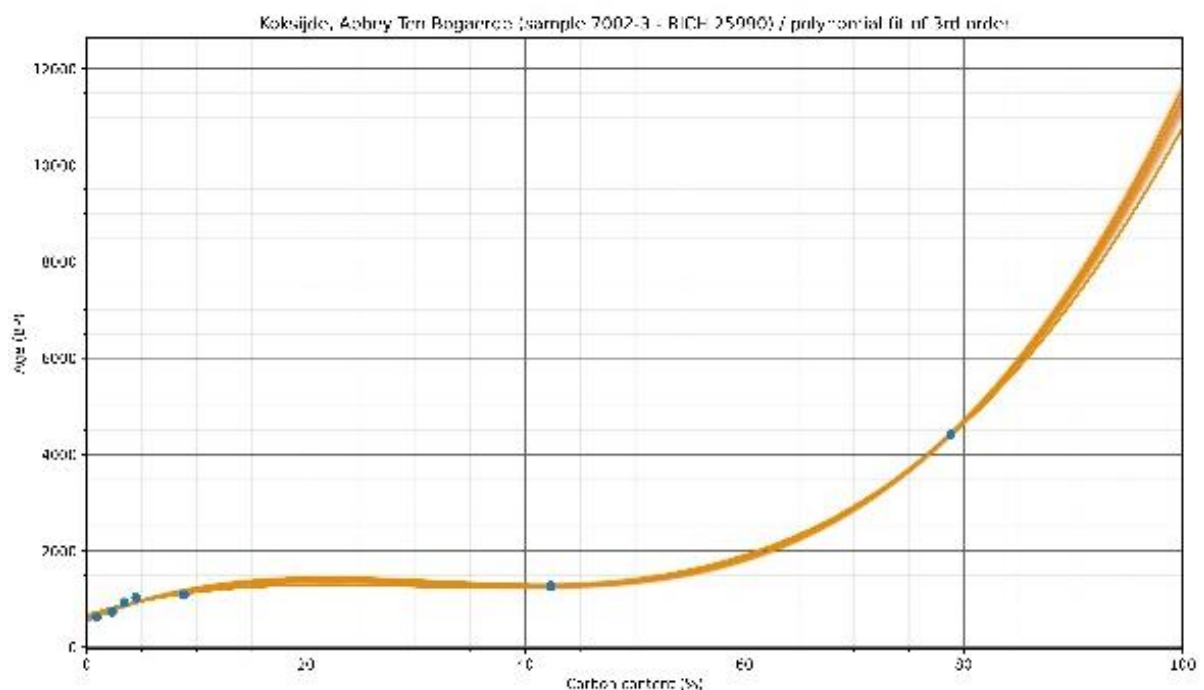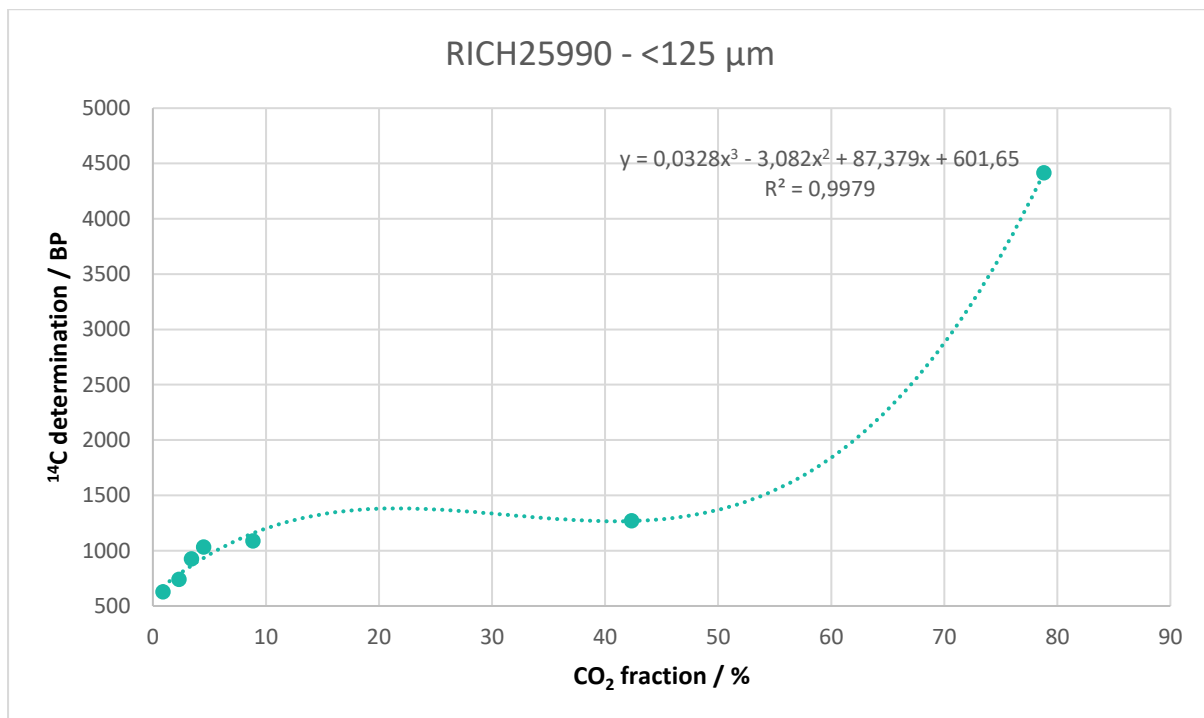
RICH25990 - <125 μm

$y = 0{,}0328x^3 - 3{,}082x^2 + 87{,}379x + 601{,}65$
$R^2 = 0{,}9979$

Koksijde, Aobey Ten Bogaerco (sample 7002-3 - RICH 25990) / polynomial fit of 3rd order

Figure 8: Radiocarbon results for the powdered mortar with particles < 125 µm as a function of the CO_2 fraction (the graph at the bottom shows the statistic on the results).
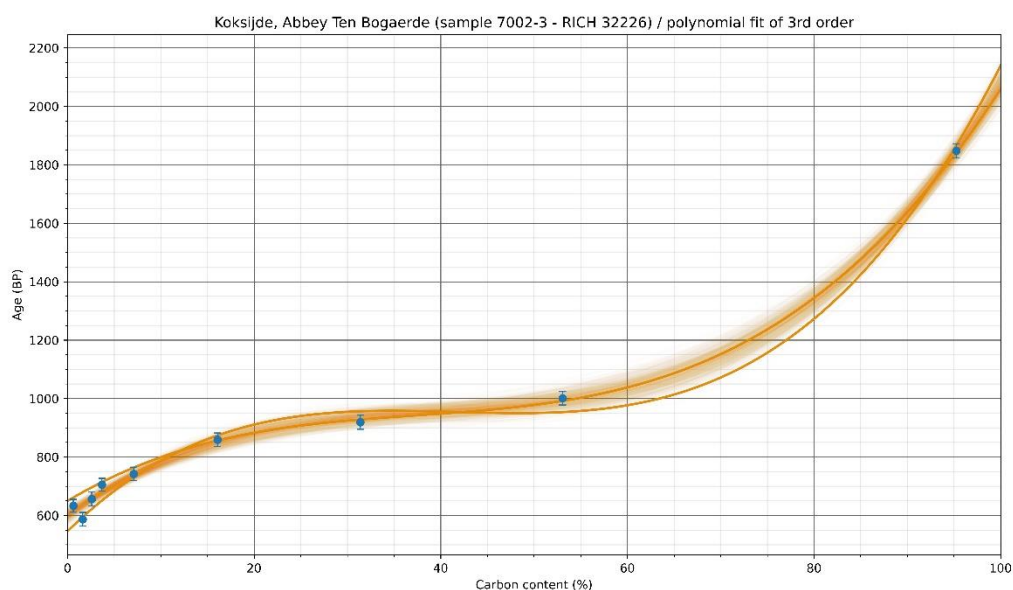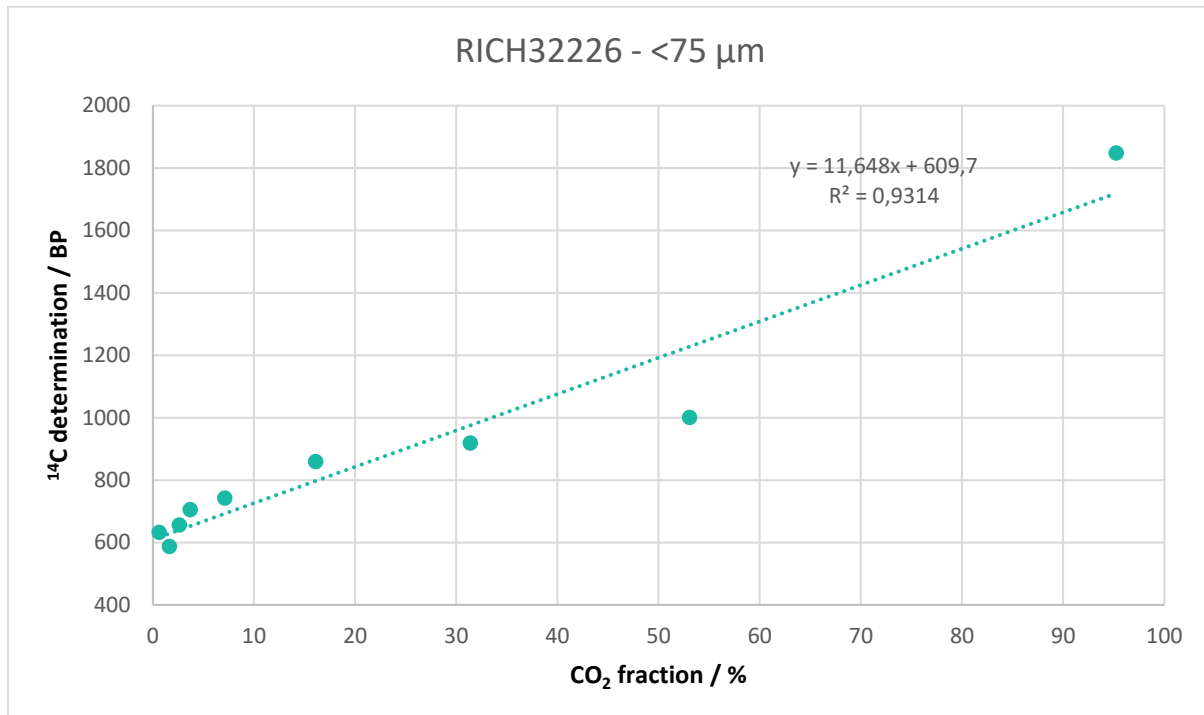
Figure 9: Radiocarbon results for the powdered mortar with particles < 75 µm as a function of the CO_2 fraction (the graph at the bottom shows the statistic on the results).

Conclusions

The weathering of the mortar inducing dissolution and precipitation of carbonates introduced younger carbon resulting in an inaccurate radiocarbon dating of the mortar sample.

Bibliography

Lehouck, Alexander, and Johan Termote. 2016. "Het Poortgebouw van de Abdijhoeve Ten Bogaerde (Koksijde, W.-Vl.)." In *Archaeologia Mediaevalis*, 39:86–89. vzw Archaeologia Mediaevalis asbl.

Study of mortars from Saint-Martin's basilica (Halle) for the BRAIN 2.0 PalC project

Context of the site

St. Martin's Basilica is a Gothic church (Figure 0a) in the Flemish Brabant town of Halle, dedicated to St Martin of Tours. Numerous works of art from the period of its construction are still present in situ. Halle is known to many as an important pilgrimage site that is still visited by many pilgrims to this day. When the domain of Halle was donated in 661 by the high noble Saint Waltrudis to the abbey of Mons, it is suspected that a church building in Halle was already present in this early period. The donation of the devotional statue of Our Lady to Halle, via countess Aleidis (count's daughter of Holland and wife of John I of Avesnes) took place in 1267. At that time, therefore, there must therefore already have been a church of some standing at Halle (Bradt 2015).

In connection with the interior restoration of the Basilica of Saint Martin in Halle, a new heating system was installed in the building: an underfloor heating system accompanied by a destructive intervention in the soil, as a result of which the Flanders Heritage Agency (Agentschap Onroerend Ergoed) decided that an archaeological excavation had to be carried out prior to the works. A team from Monument Vandekerckhove nv carried out an archaeological survey in several phases from 30 April to 5 December 2013 on the archaeologically threatened areas within the basilica. The client for the research was the fabric committee of the St. Martin's church (Bradt 2015).
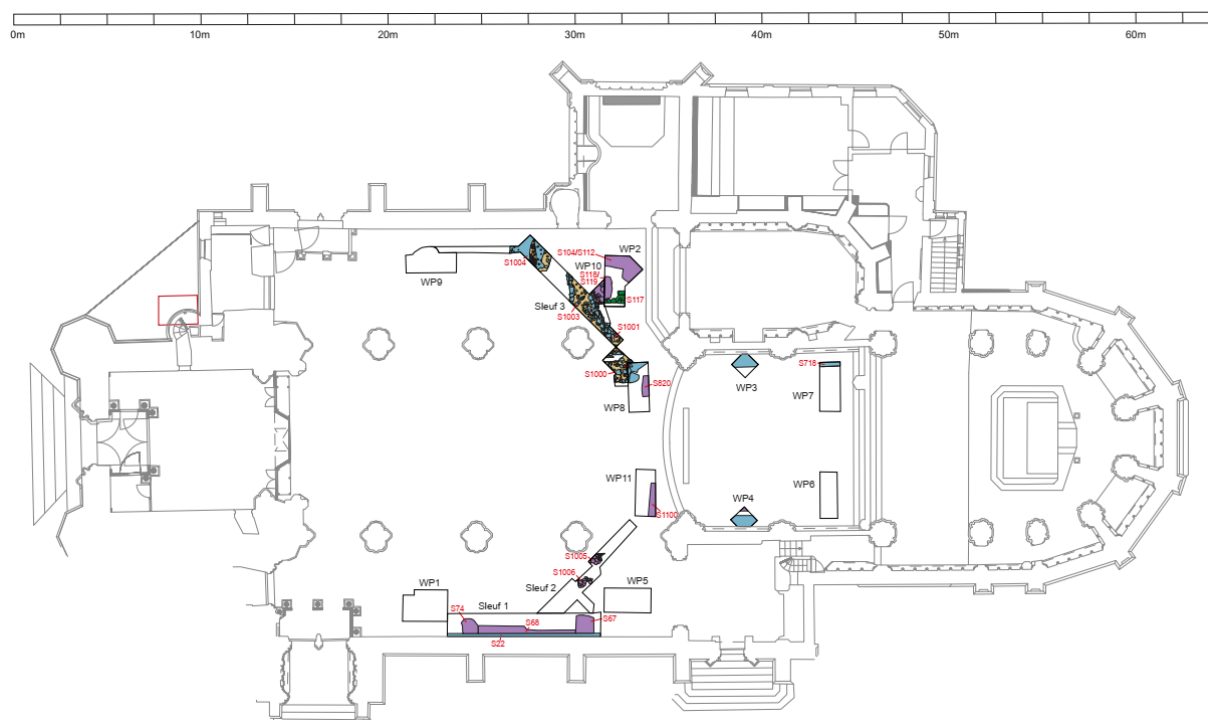
Figure 0a: Site plan walls (from Bradt 2015).

Material

Two samples from the Saint-Martin's basilica in Halle were selected:

- HABA14, 2013/144, A3048, S117, invnr. 141
- HABA14, 2013/144, A3048, S117, invnr. 1003

Both are supposed to date from before 1200, it should be pre-Roman (late 9th - early 11th century). At the very bottom of WP10 (Figure 0b), at the maximum depth of -1m, a 75 cm-wide natural stone east-west oriented structure was found (S117). To be able to see and interpret this structure better, local deepening was carried out at this spot. The trench in which this structure was found was unfortunately too small to determine an axis difference with the present church. North-west of this structure there was also a remarkable round natural stone structure (S118/119) along which additional excavation was carried out. In this way, it could be established that S117 had been partly broken out to build the round structure, which means that S117 is older than S118/119. Both structures are probably foundation walls. This presumably oldest structure (S117), which was held together by soft yellow-green sand mortar was built of a mix of Brusselian and Ledian sandy limestones (or calcareous sandstones).

Figure 0b: View from the south of the natural stone structures in WP10 (left) and top view from the west of S118/S119 and S117 in WP10, S117 appears to be intersected by S118/S119 (right) (from Bradt 2015).

Results & Discussion

Macroscopic descriptions

The main colour of both samples is beige (Figure 1) tending towards pale yellow (2.5Y 7/3) according to the Munsell soil colour charts. The lime lumps appears as white inclusions with a main size of ~ 1 mm and the biggest one measure ~7 mm. Sample 1003 contains a large white inclusions (> 1.5 cm) which is possibly a limestone fragment.

Figure 1: Mortar sample 141 (left) and 1003 (right).

Fourier transform Infrared (FTIR) spectroscopy on inclusions & binder

The binders (beige, Figure 2) are made of calcium carbonates (calcite and aragonite) and silicates including quartz. The lime lumps (white, Figure 2) are mainly made of calcium carbonates (calcite and aragonite) in addition to silicates. The later include quartz for the sample 1003.
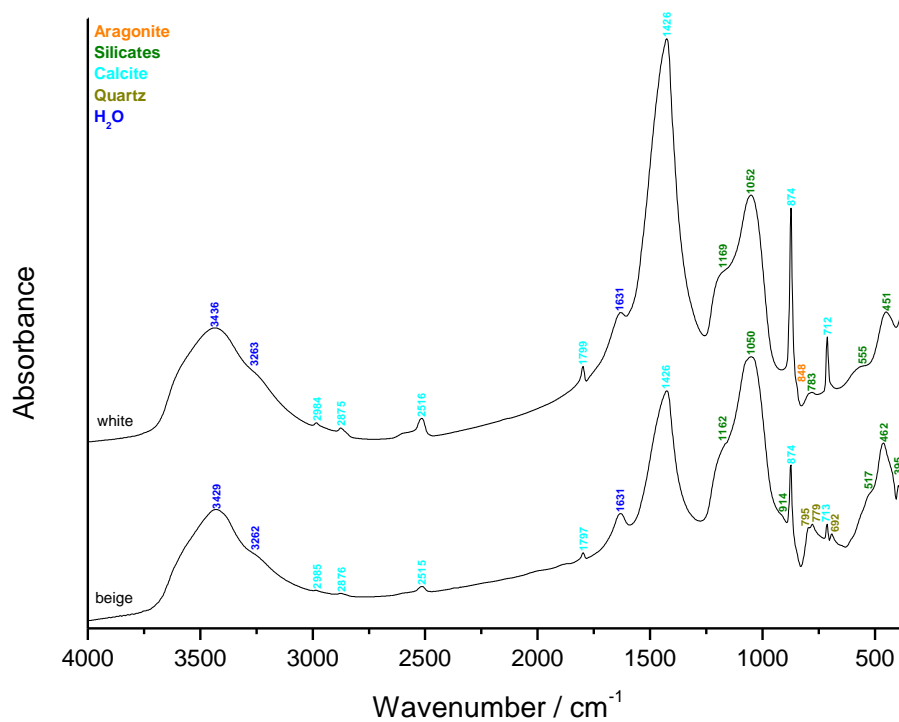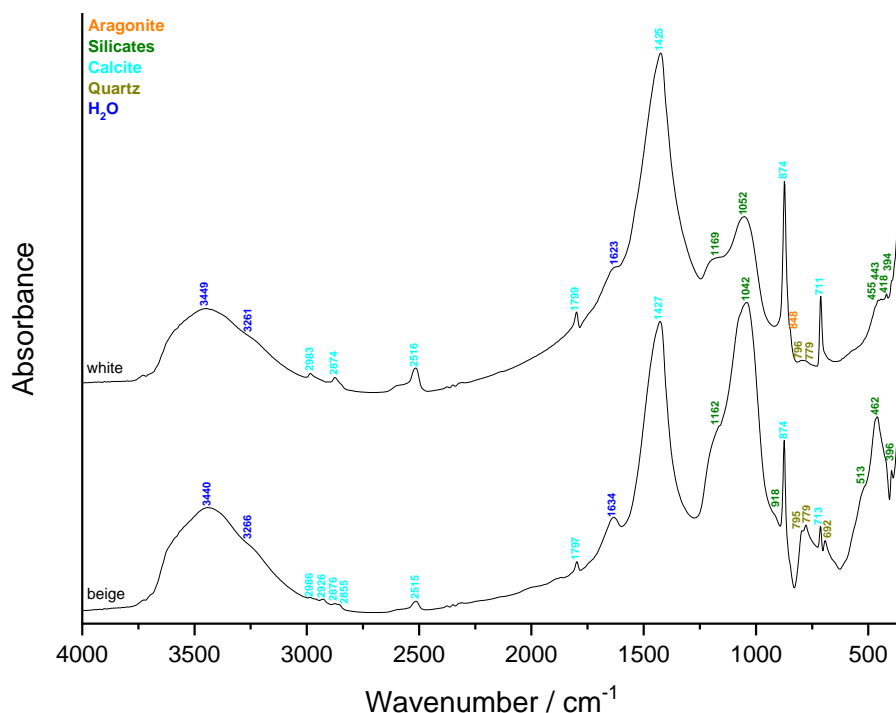
Figure 2: FTIR spectra obtained on the white inclusions and binder (beige) of the mortar samples 141 (top) and 1003 (bottom).

Binder:sand ratio

The calculated binder:sand ratio (in volume unit) using a bulk density of 1.35 kg/dm^3 for the sand and 0.575 kg/dm^3 for the lime is close to 3:4 for the sample 141 and close to 2:3 for the sample 1003.

	inv 141	inv 1003
Sample weight (g)	2.6	2.9
Crucible weight (g)	15.1	16.9
Weight calcined (g)	17.2	19.2
%ins	**75.9**	**77.1**

Table 1: Percentage of insoluble residue

Cathodoluminescence

Cathodoluminescence observations of the two thin-sections and powders show similar results (Figure 8). The thin-sections exhibit the presence of quartz grains with a dark purple hue, K-feldspars in bright blue and the binder is dull. The powdered samples display the same components in addition to some bright red grains from limestone and a few bright green particles from plagioclases.
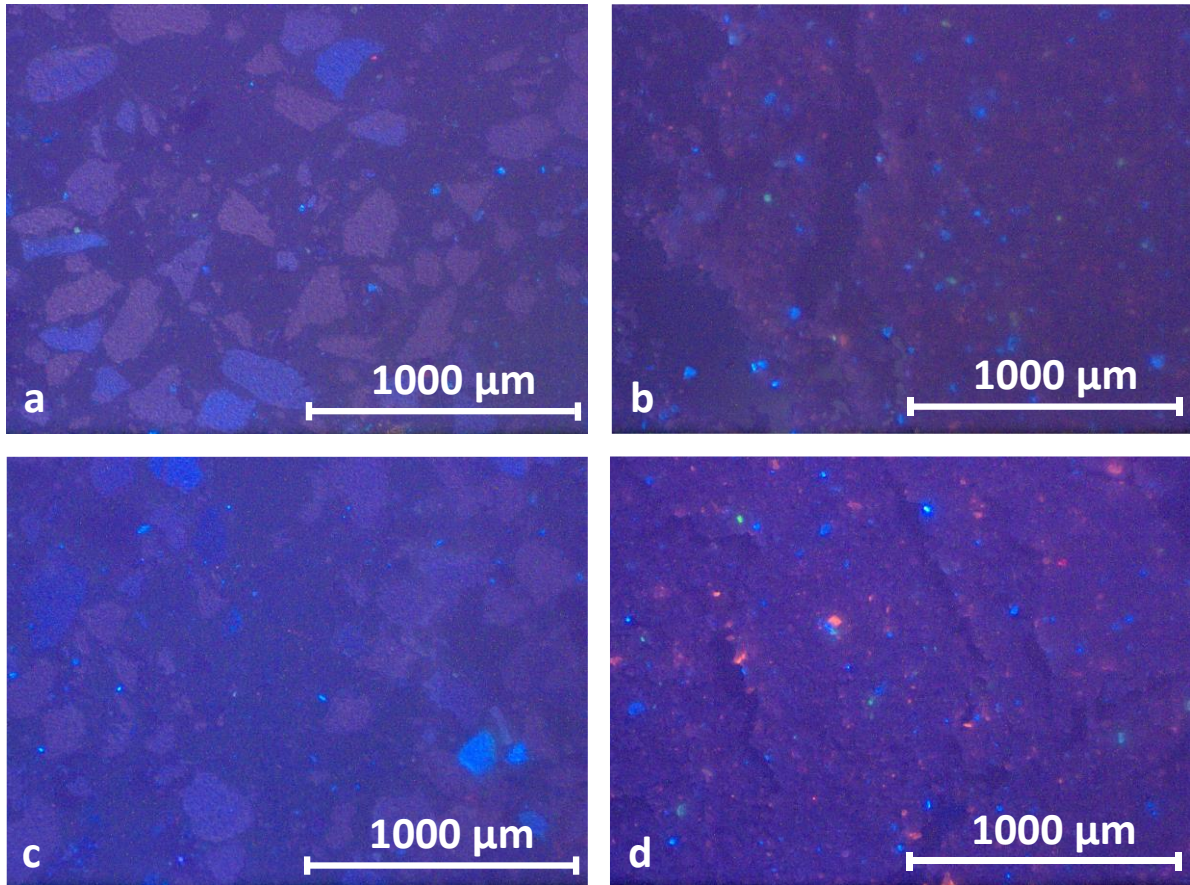
Figure 3: Characteristic cathodoluminescence images of a) the thin section X2292 of the sample 141, b) the powdered sample 141 with particle size lower than 75 µm, c) the thin-section X2293 of sample 1003, d) the powdered sample 1003 with particle size lower than 75 µm

Thin-section petrography

The mortar 141 is in poor condition (Figure 4 & Table 2), it shows an extensive dissolution of the binder in addition to the presence of secondary carbonates. The lime inclusions are completely burned and some of them contain silicates (Figure 4c & d).
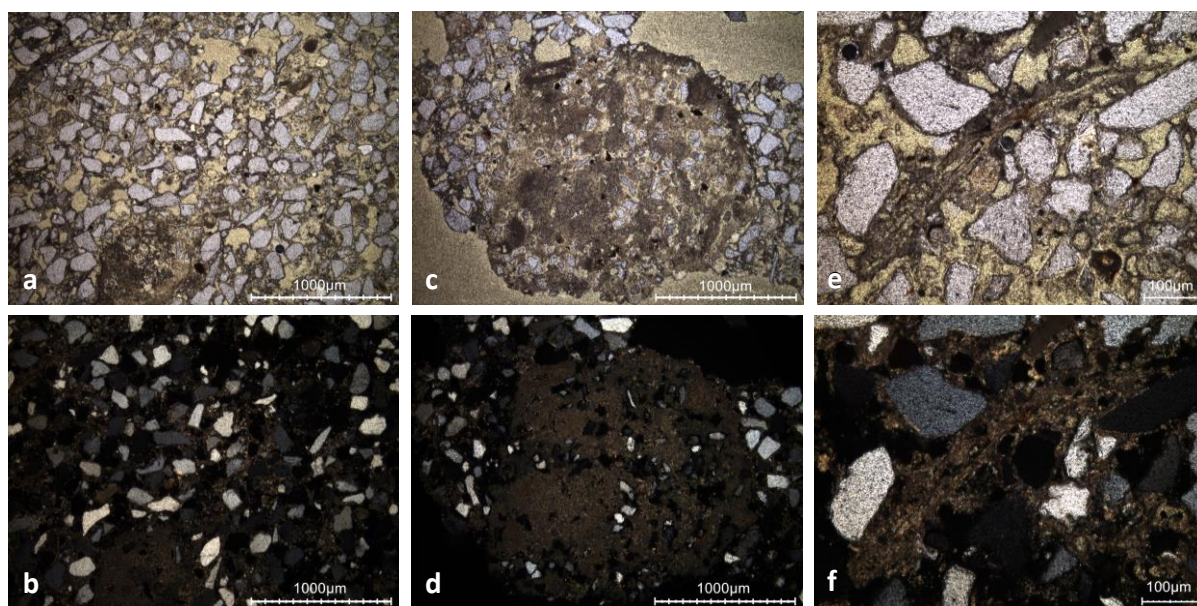
Figure 4: Representative photomicrographs of the thin-section X2292 made from sample 141: a) overview image in plain polarised light (PPL); b) overview image in cross polarised light (XPL); c) PPL image showing a large lump containing quartz and fired glauconite grains; d) same image in XPL; e) PPL image with a possible plant fibre; f) same image in XPL.

Binder	Texture	micritic
	Lump state	completely burned
	Lump size	62 µm to 2 mm (contains quartz & fired glauconite grains)
	Lump frequency	medium
Aggregate	Grain size	very fine to medium
	Mineralogy	pure siliceous sand (quartz, K-feldspars, sandy-clay agglomerates, oxidised or partially oxidised glauconite)
	Shape	subangular / subrounded
Appearance	Homogeneity	relatively homogeneous
	Macroporosity	high
	Pore structure	Irregular / highly connected
Admixtures	Type	possible plant fibre
Alteration	Type	dissolution & secondary carbonates

Table 2: Main characteristics of the sample 141 retrieved from the observations of the thin-section X2292.

The mortar 1003 is also in poor condition (Figure 5 & Table 3), it has been dissolved and secondary carbonates are often observed lining the pores. The lime inclusions are completely burned and sometimes partially dissolved.
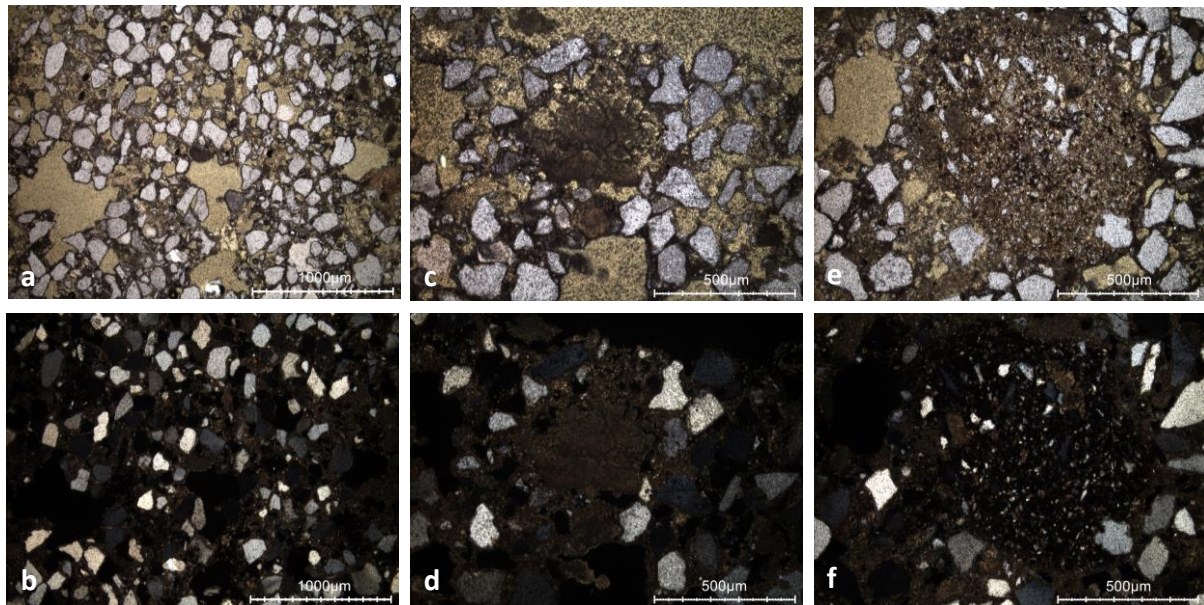
Figure 5: Representative photomicrographs of the sample 1003 thin-section X2293: a) overview image in PPL; b) overview image in XPL; c) PPL image showing a partially dissolved lump and secondary carbonates in pores; d) same image in XPL; e) PPL image with a sandy-clay agglomerate; f) same image in XPL.

Binder	**Texture**	micritic
	Lump state	completely burned
	Lump size	137-530 μm
	Lump frequency	medium
Aggregate	**Grain size**	very fine to medium
	Mineralogy	pure siliceous sand (quartz, K-feldspars, sandy-clay agglomerate, oxidised / partially oxidised glauconite)
	Shape	subangular / subrounded
Appearance	**Homogeneity**	relatively homogeneous
	Macroporosity	medium to high
	Pore structure	irregular / sometimes connected
Admixtures	**Type**	-

Alteration	**Type**	dissolution & secondary carbonates

Table 3: Main characteristics of the sample 1003 retrieved from the observations of the thin-section X2293.

Thermogravimetric analysis (TGA) on whole samples

Both mortars are moderately hydraulic with apparent hydraulicity indices (aHI) of ~23%. The amount of carbonates is ~21 wt% for the sample 141 and 20 wt% for the sample 1003. The temperature of quartz transition phase is observed around 573°C (Rickard, Riessen, and Walls 2010) for both samples (Figure 6 & 7). The main weight loss of ancient mortars is expected between 600 and 900 °C and is indicative of the decomposition of calcium carbonate ($CaCO_3$) into calcium oxide (CaO) and carbon dioxide (CO_2) (Ahmmed et al. 2024). The end temperature of calcium carbonate decomposition is ~806°C for the sample 141, it was not possible to calculate it for the sample 1003. No gypsum was detected.
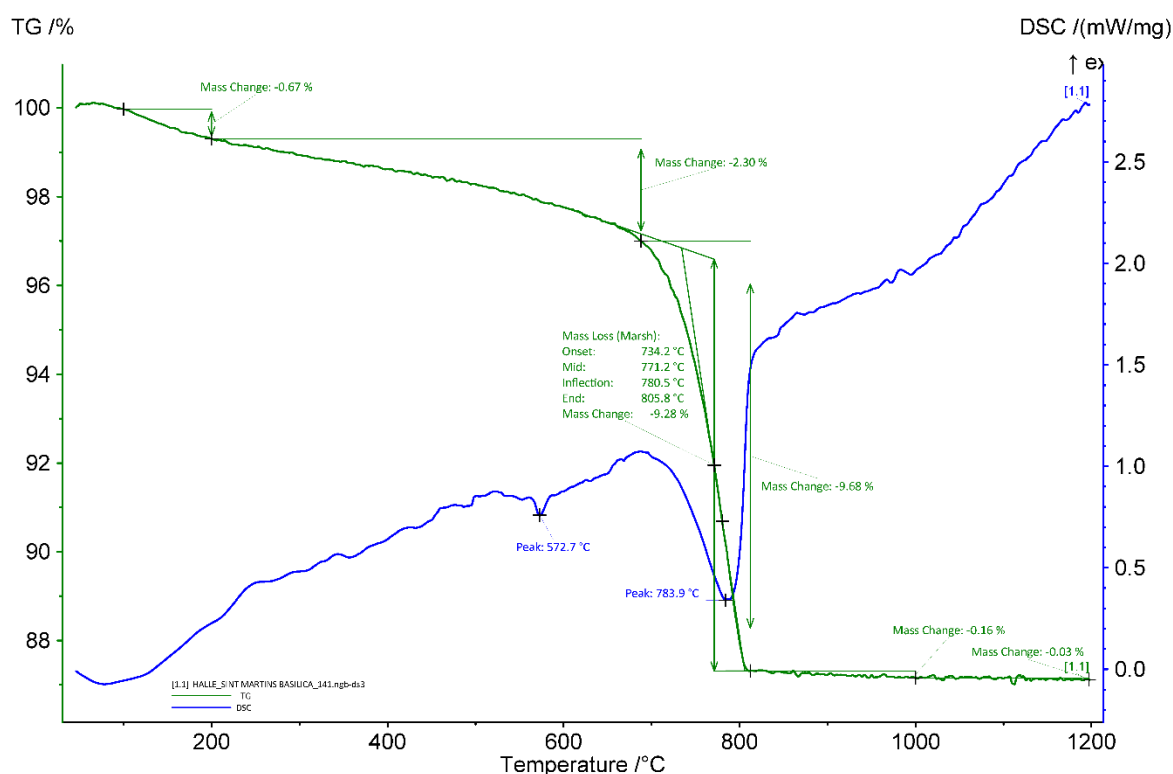
Figure 6: Coupled TG-DSC analysis of the sample 141 upon heating to a temperature of 1200°C at a heating rate of 20°C/min under an inert atmosphere (He flushed at 50 ml/min). The weight loss determined by thermogravimetric analysis (TG, wt%, green curve) and the result of the differential scanning calorimetric analysis (DSC, mW/mg, blue curve) are both presented.
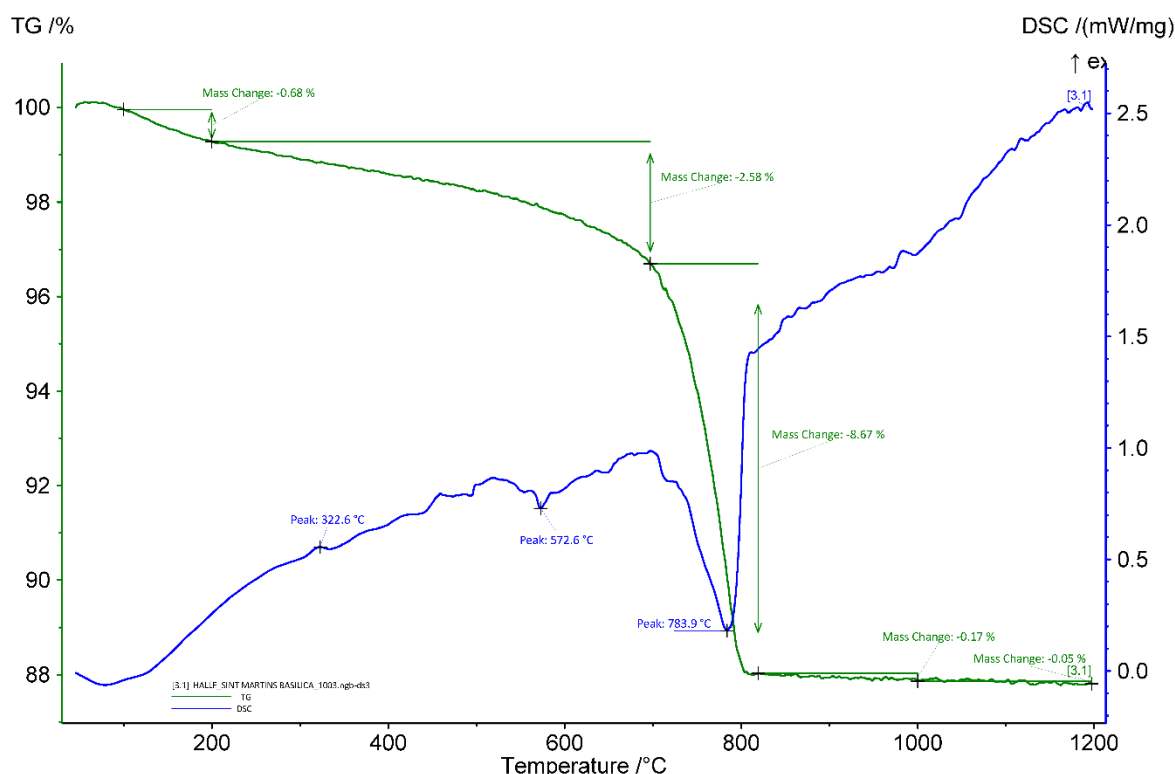
Figure 7: Coupled TG-DSC analysis of the sample 1003 upon heating to a temperature of 1200°C at a heating rate of 20°C/min under an inert atmosphere (He flushed at 50 ml/min). The weight loss determined by thermogravimetric analysis (TG, wt%, green curve) and the result of the differential scanning calorimetric analysis (DSC, mW/mg, blue curve) are both presented.

Grinding/particle separation

The mortar samples were gently crushed with a ceramic mortar and a metallic pestle. For sample 141, soil on the surface was removed with a soft brush before grinding.

TGA on powders with particle size <75 μm

For both mortars, the aHI is higher for the powder with particle size <75 μm compared ~28% for sample 141 and ~32% for sample 1003 to the whole mortar sample (23 %). These differences could be explained by the presence of clay that end up in more important quantity in the powdered sieved samples. The quantity of carbonates is higher in the powder compared to the whole samples since a large part of the sand is removed (~24 wt% for the sample 141 and ~29 wt% for the sample 1003). Indeed, no quartz was detected in the powders. For sample 141 (Figure 8), a peak around 417°C is observed and might be due to the release of water from calcium hydroxide (Moropoulou, Bakolas, and Bisbikou 1995; Klimesch and Ray 1996) indicating that the mortar did not fully carbonated. This was not observed for the whole mortar sample. It was probably present in too low concentration to be noticeable. The end temperature of calcium carbonate decomposition is 806 and 812°C for the powdered samples 141 and 1003, respectively. It is the same than the whole samples.
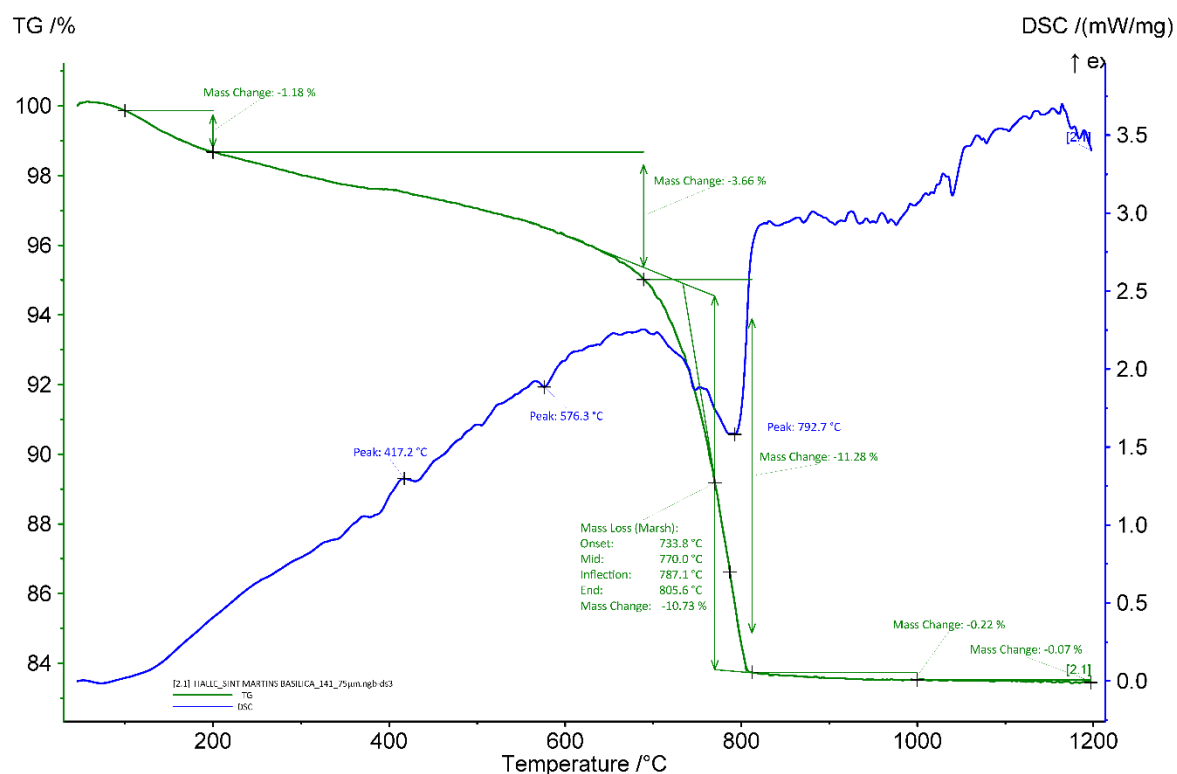
Figure 8: Coupled TG-DSC analysis of the powdered sample 141 with particle size < 75 μm upon heating to a temperature of 1200°C at a heating rate of 20°C/min under an inert atmosphere (He flushed at 50 ml/min). The weight loss determined by thermogravimetric analysis (TG, wt%, green curve) and the result of the differential scanning calorimetric analysis (DSC, mW/mg, blue curve) are both presented.

Figure 9: Coupled TG-DSC analysis of the powdered sample 1003 with particle size < 75 μm upon heating to a temperature of 1200°C at a heating rate of 20°C/min under an inert atmosphere (He flushed at 50 ml/min). The weight loss determined by thermogravimetric analysis (TG, wt%, green curve) and the result of the differential scanning calorimetric analysis (DSC, mW/mg, blue curve) are both presented.

Radiocarbon results

The test prior to the CO_2 extraction revealed an amount of carbon (Table 4) around 2.7 % for the sample 141 and 3.6 % for the sample 1003 which is rather low compared to other mortars.

RICH	Sample type	Method	C (%)	σ (%)	m (g)	Age BP	Calibrated date (oxcal - 95.4%)	Age BP extrapolated	Calibrated date (oxcal - 95.4%)	Age BP extrapolated with stat	Calibrated date (oxcal - 95.4%)	Age BP average	Calibrated date (oxcal - 95.4%)	Reliability of dating
34107 (141)	mortar <75 μm	10 fractions	2,73	0,099	3,64	-	-	1683 ± 24	259-420 calAD	1677.2 ± 14.2	265-419 calAD	(7 1rst fractions) 1681 ± 9	265-416 calAD	☒
20977 (141 + 1003)	charcoal	HCl	-	-	-	1091 ± 31	890-1020 calAD	-	-	-	-	-	-	☑
32649 (1003)	mortar <75 μm	9 fractions	3,58	0,335	2,85	-	-	1541 ± 24	435-594 calAD	1459.2 ± 17.7	576-645 calAD	(1rst fraction) 1312 ± 24	660-780 calAD	☒

Table 4: Radiocarbon results

The radiocarbon result obtained for the charcoal fragments gathered from the samples revealed an age ranging between the 9th and the 11th centuries compatible with the expected date (before 1200). For both mortar samples, the first fractions (1 to 5 %) are spread which often is not a good sign to obtain a reliable dating. Indeed, the results of the extrapolation, the extrapolation with statistic and the average of the first fractions are much older compared to the charcoal fragment.

Halle Basiliek S117 INV141

$y = 1E\text{-}05x^4 - 0{,}0024x^3 + 0{,}1352x^2 - 1{,}7562x + 1682{,}5$
$R^2 = 0{,}8298$

x-axis: CO_2 fraction / %
y-axis: ^{14}C determination / BP

Halle, Basilica Saint Martin (sample S117 - RICH 34107) / polynomial fit of 3rd order

x-axis: Carbon content (%)
y-axis: Age (BP)
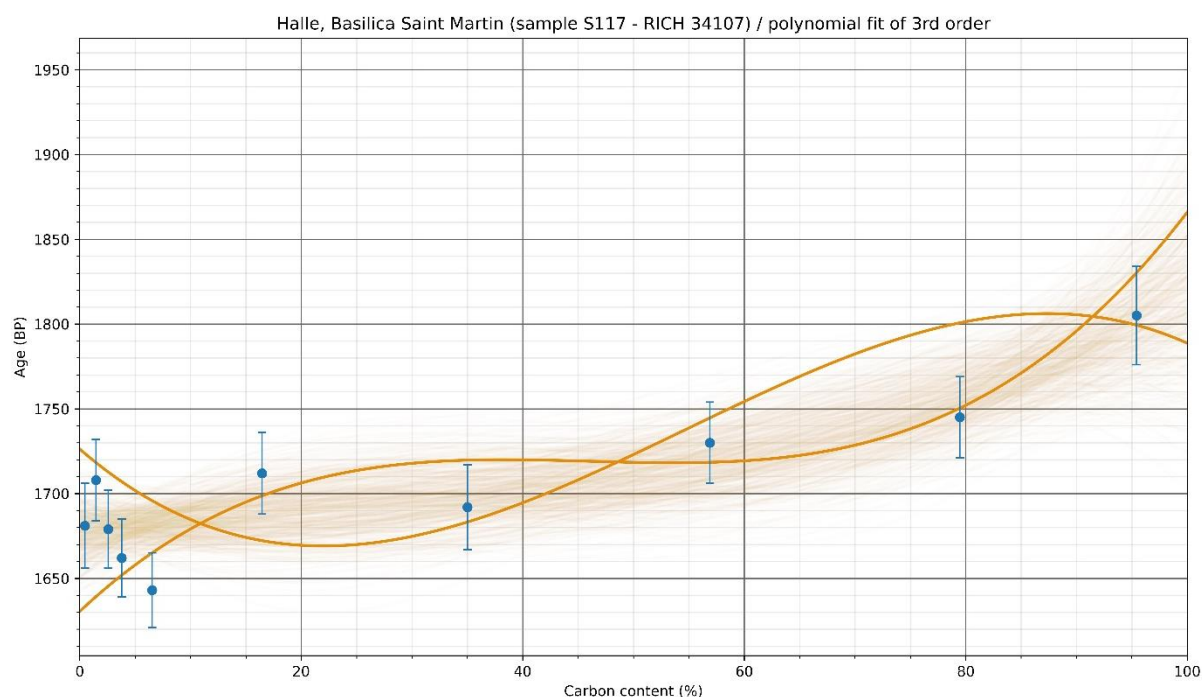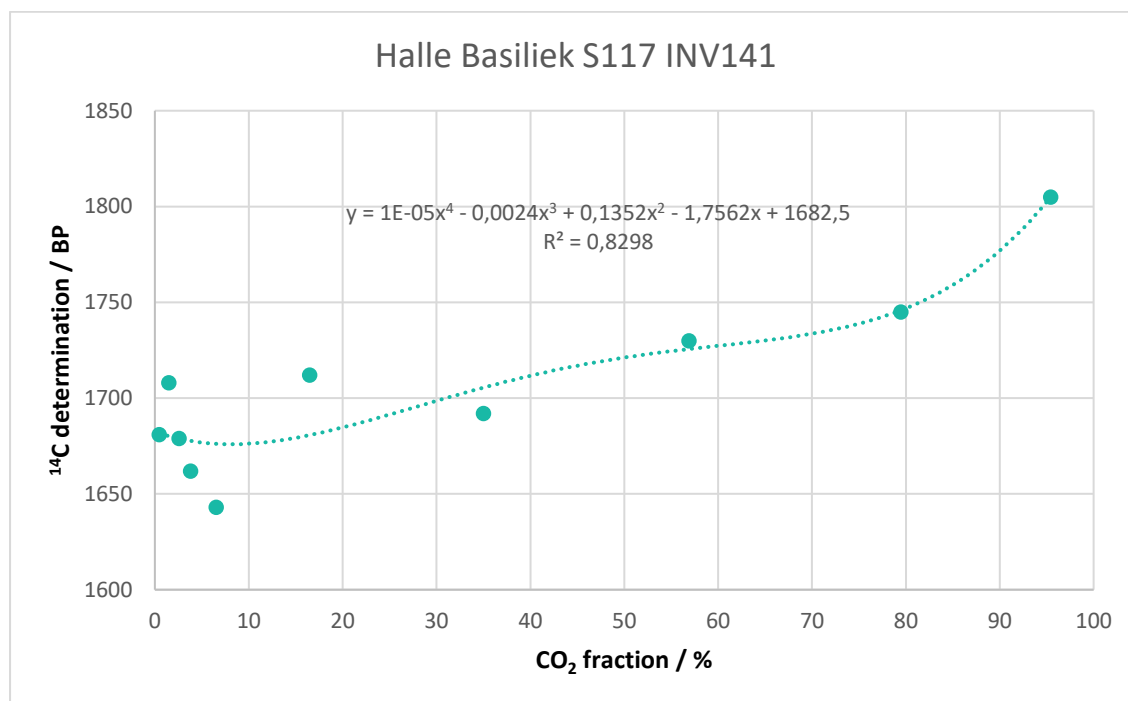
Figure 10: Radiocarbon results for the powdered mortar 141 with particles < 75 μm as a function of the CO_2 fraction (the graph at the bottom show the statistic on the results).
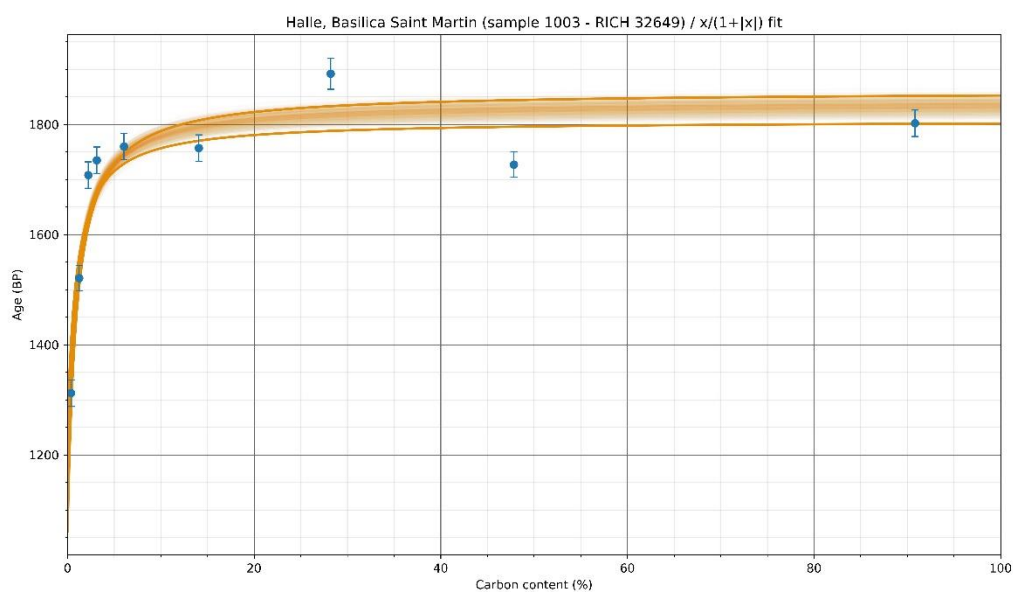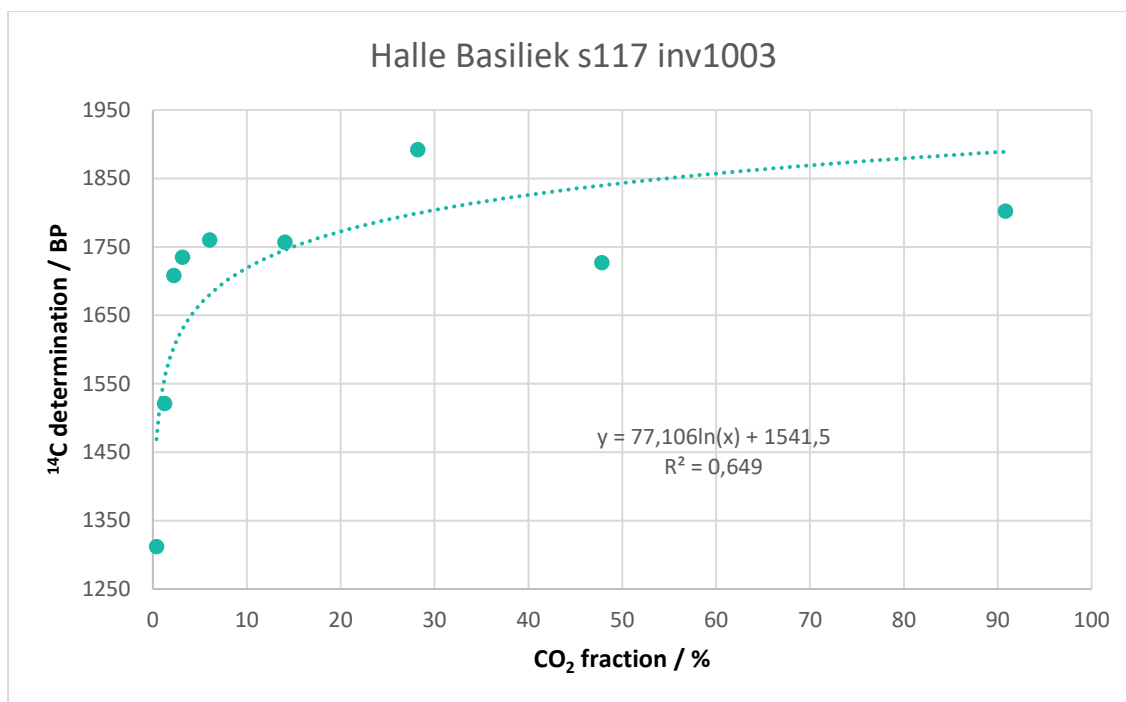
Figure 11: Radiocarbon results for the powdered mortar 1003 with particles < 75 μm as a function of the CO_2 fraction (the graph at the bottom show the statistic on the results).

Conclusions

The mortars are in poor condition, they have been extensively dissolved and secondary carbonates are present. They are made of with pure sand containing a clay fraction that might overestimate the hydraulicity. We considered them slightly hydraulic. The radiocarbon results are too old compared to the estimated historical date and the radiocarbon dating of the charcoal. They are not reliable samples for ^{14}C dating.

Study of mortars from Het Steen, Antwerp for the BRAIN 2.0 PalC project

Context of the site

Het Steen is a medieval building constructed against the fortification wall (Burcht) and adjacent to the south city gate of Antwerp. The surviving structure was presumably built between 1200 and 1225 as a gateway to a larger castle of the Dukes of Brabant which was demolished in the 19th century. "Het Steen" translates from Dutch "the rock", it used to be employed for "fortress" or "palace".

Figure 1: Het Steen te Antwerpen in 1875 (CC-BY KIK-IRPA, Bruxelles).

Material

In 2020, three samples were sent to KIK-IRPA for analysis: A489-M1 (RICH-28515), A489-M2 (RICH-28892) and A489-M1bis (RICH-28910). They come from the fortress wall.

Results & Discussion

Macroscopic descriptions

Only the mortar M1bis was photographed before the project. It is beige in colour and regularly shows white lime lumps measuring 1 to 2 mm in diameter. A 1 mm charcoal fragment was also observed.

Figure 2: Mortar sample A489-M1.

Fourier transform Infrared (FTIR) spectroscopy

Only the powders from M1 and M2 with a particle size higher than 100 µm were left in the bag after the ^{14}C dating performed in 2020 and were analysed by FTIR. The overall composition of the particles having a size higher than 100 µm for M1 shows the presence of calcite, silicates, quartz and gypsum (Figure 3a), and for sample M2, calcite, silicates, quartz, clay, gypsum and possibly organic matter (Figure 3b).

a)
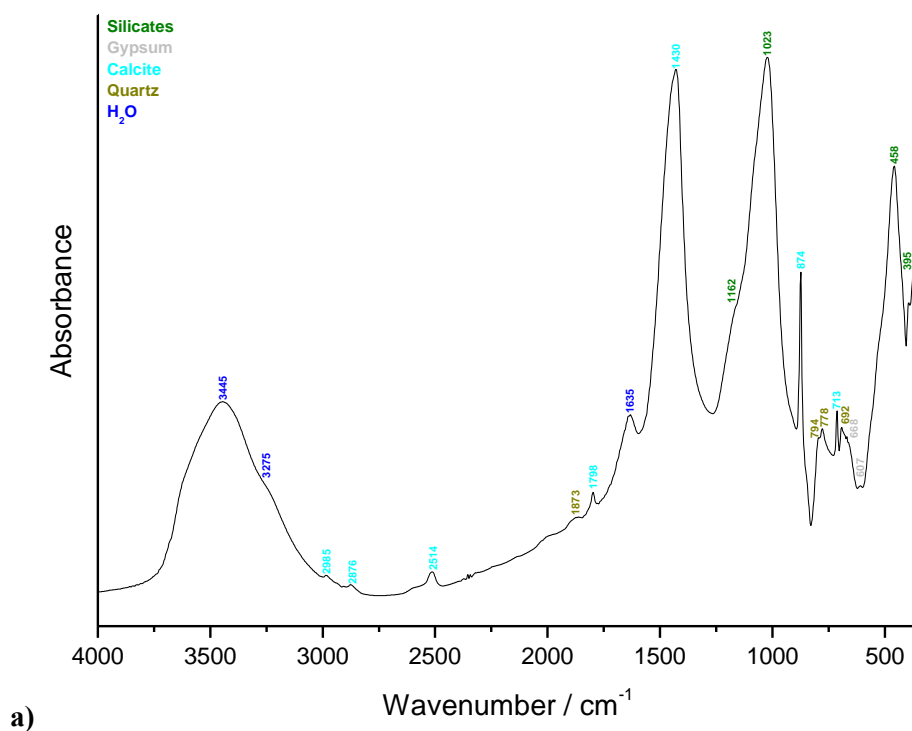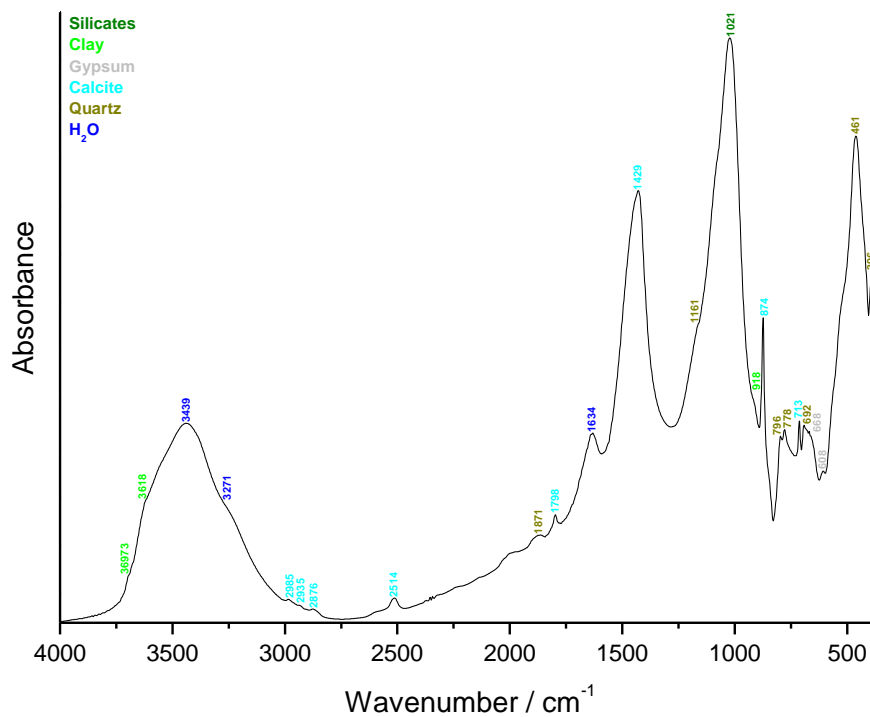
b)

Figure 3: FTIR spectra obtained on the powders > 100 μm: a) A489-M1 and b) A489-M2.

Cathodoluminescence

The observations by cathodoluminescence on the powder from sample A489-M2 (Figure 4) shows the presence of quartz grains in dark purple, K-feldspars in bright blue, one plagioclase grain (Figure 4a) in green and a few limestone grains in bright red.
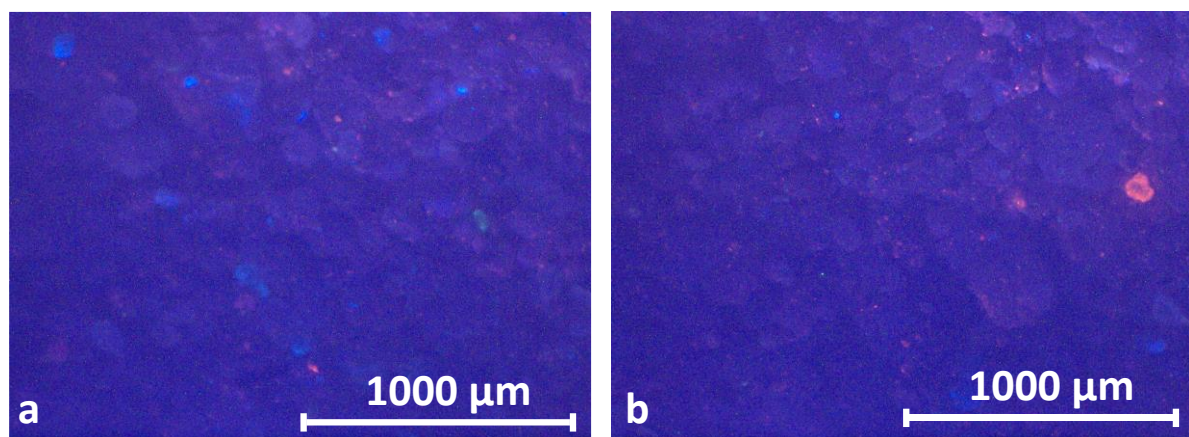
Figure 4: Characteristic cathodoluminescence images of the powder left in the A489-M2 bag after the 2020 analyses.

Thin-section petrography

The mortar is deteriorated, it has been leached with a consequent pronounced dissolution of the binder (only a very small proportion of the original lime binder is still present within the structure of the mortar sample). Secondary carbonates are observed at the border of cracks and throughout the sample (Figure 5c & d). The original extremely fine carbonate crystals of the

lime binder (micritic texture, crystals < 4 µm) was replaced by larger calcite crystals that now exhibit a microsparitic texture (crystals of about 10 µm size).

The aggregate used is a quartz sand that can be classified as medium-coarse according to the NBN B 11-011 standard. The quartz grains are mainly monocrystalline, but micro- and polycrystalline grains can also be observed. The sand contains some feldspar and glauconite grains. Fossil debris (Figure 5e) is very rare. Small charcoal fragments, with dimensions of max. 100 µm, are finely distributed in the lime binder. The largest charcoal fragment found is 1 mm long.
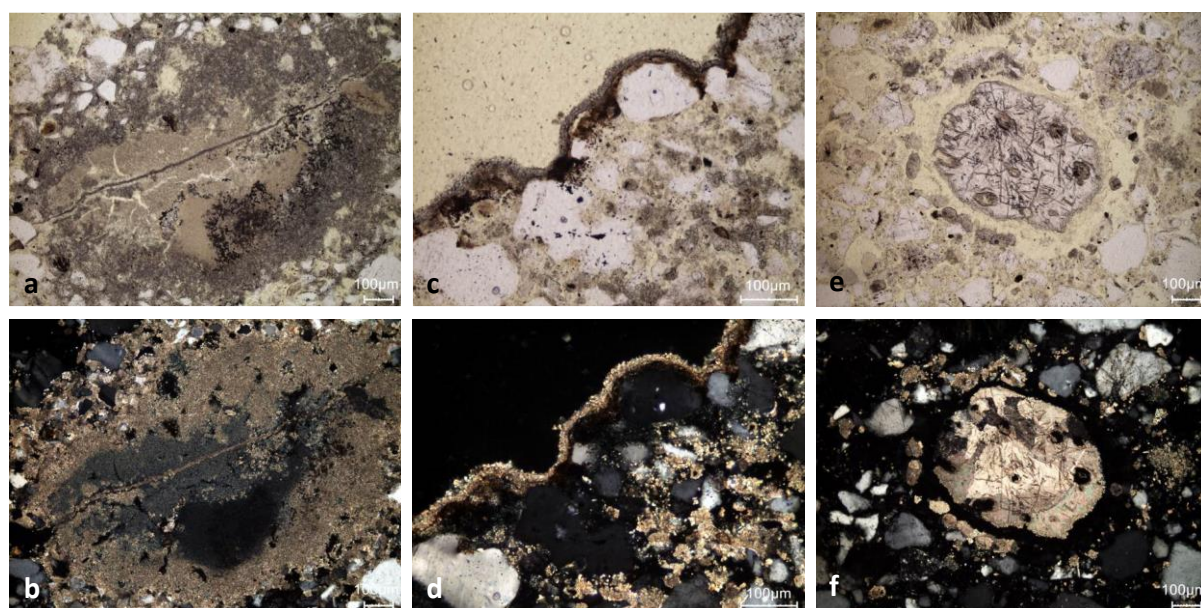
Figure 5: Representative photomicrographs of the thin-section X2079 of the mortar M1bis: a) lime lump showing secondary carbonates surrounding the original micritic texture in the centre in plain polarised light (PPL); b) same image in cross polarised light (XPL); c) PPL image showing secondary carbonates with a thickness of 20 µm on the border of a pore ; d) same image in XPL; e) PPL image of an unidentified calcareous grain (bioclast?); f) same image in XPL.

Binder	**Texture**	micritic
	Lump state	completely burned, partially dissolved
	Lump size	2.1 mm ; 1.4 mm ; 225 µm ; 736 µm
	Lump frequency	medium
Aggregate	**Grain size**	very fine to coarse
	Mineralogy	siliceous sand (quartz, K-feldspar, glauconite) with few bioclasts
	Shape	subangular / subrounded
Appearance	**Homogeneity**	relatively heterogeneous
	Macroporosity	high
	Pore structure	irregular sometimes connected

Admixtures	**Type**	charcoal
Alteration	**Type**	dissolution & secondary carbonates (dissolution / precipitation)

Table 1: Main characteristics of the mortar M1bis retrieved from the observations of the thin-section X2079.

Thermogravimetric analysis (TGA) on whole samples

The apparent hydraulicity index (aHI) of the M1bis lime binder calculated from the thermal analysis (Figure 6) is 24.4%, indicating at first glance the use of moderately hydraulic lime. Nevertheless, the aHI obtained must be largely put into perspective since the pronounced dissolution of the binder artificially increases this index. Taking this into account, the lime used is best described as a (very) slightly hydraulic lime. The peak between about 650 and 800°C is caused by the release of carbon dioxide from the calcium carbonate in the binder. The weight loss between 200 and around 650°C, on the other hand, is generally attributed to the release of water from the hydrated components of the hydraulic phases. The peak at 574.2°C in the calorimetric curve is due to the use of quartz sand.
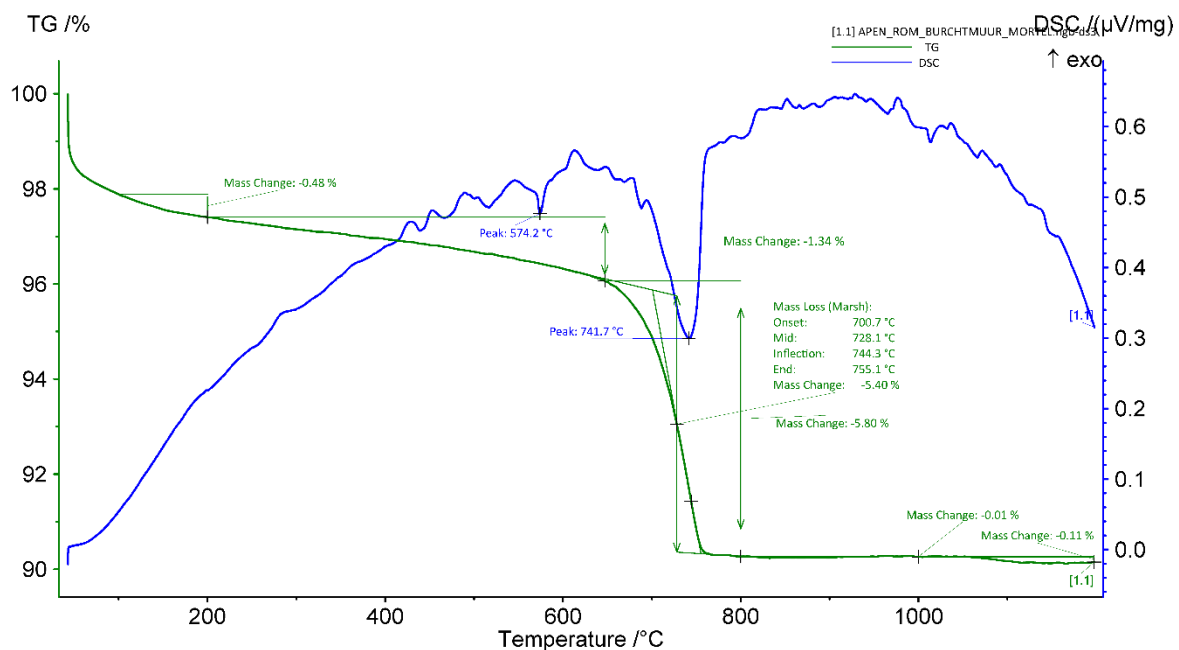
Figure 6: Results of thermogravimetric analysis (TG, green line) and differential calorimetric analysis (DSC, blue line) of the mortar M1bis when heated to 1200°C. The peak between about 650 and 800°C is caused by the release of carbon dioxide from the calcium carbonate of the binder. In contrast, the weight loss between 200 and about 650°C is generally attributed to the release of water from hydrated components of hydraulic phases. Here, the accumulated weight loss in this temperature range is 24.4%. The peak at 574.2°C in the calorimetric curve is due to the use of quartz sand.

Radiocarbon results

The test prior to the CO_2 extraction revealed a low amount of carbon (Table 4) in the sample (~1.5 %), again reflecting the dissolution of the mortar.

RICH	Sample type	Method	C (%)	σ (%)	m (g)	Age BP extrapolated	Calibrated date (oxcal - 95.4%)	Age BP extrapolated with stat	Calibrated date (oxcal - 95.4%)	Age BP average first dates	Calibrated date (oxcal - 95.4%)	Reliability of dating
28515 (M1)	mortar < 75 μm	8 fractions	1.69	0.007	5.75	1746 ± 30	241-401 calAD	1746.3 ± 16.7	245-375 calAD	(first fraction) 1668 ± 24	260-433 calAD	☒
28910 (M1bis)	mortar < 75 μm	8 fractions	1.62	-	2.19	1003 ± 30	991-1154 calAD	1076 ± 22.6	895-1023 calAD	(first fraction) 1031 ± 23	987-1037 calAD	☑☒
28892 (M2)	mortar < 75 μm	8 fractions	1.46	0.033	4.8	1567 ± 30	425-567 calAD	1477.4 ± 17.4	594-640 calAD	(first fraction) 1484 ± 30	549-643 calAD	☒

Table 4: Radiocarbon results

The radiocarbon results don't match the expected date for M1 (28515) and M2 (28892), they are older than expected (Table 4 & Figure 7). For M1bis (28910), the results fall within the expectation but since the sample state is very poor, the result cannot be trusted.
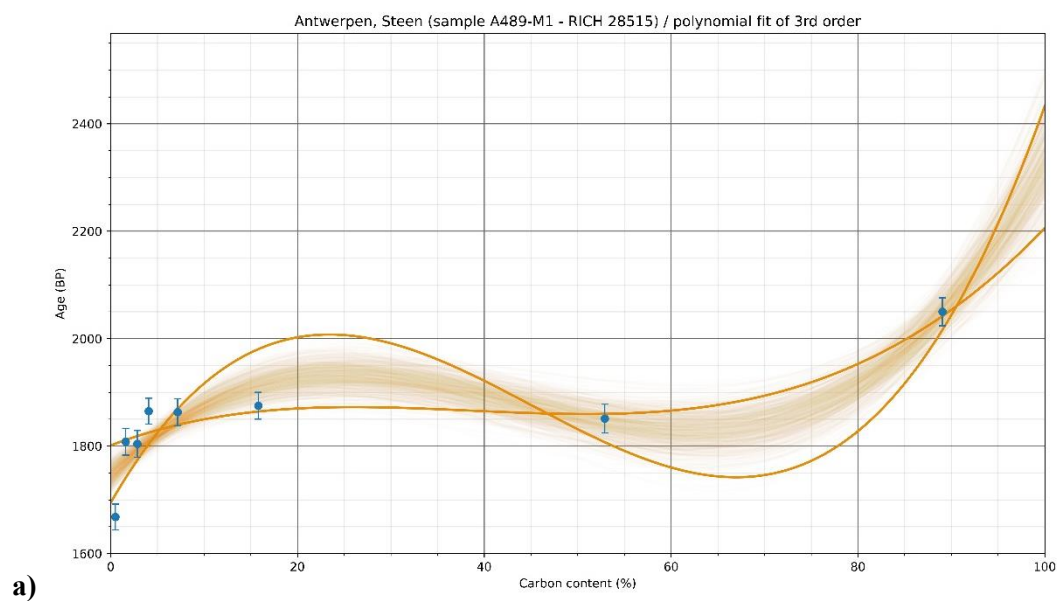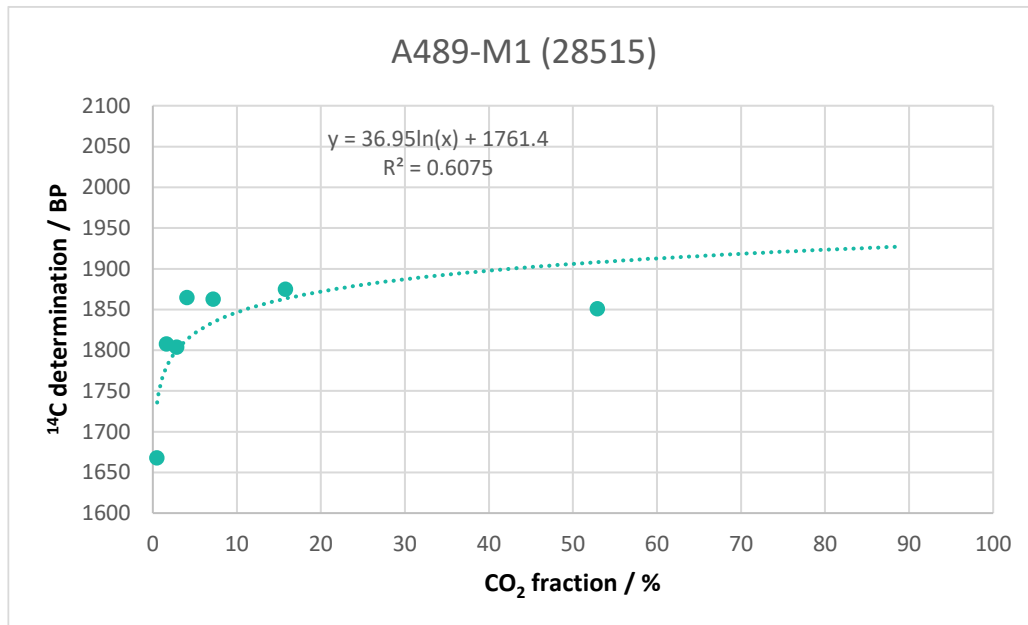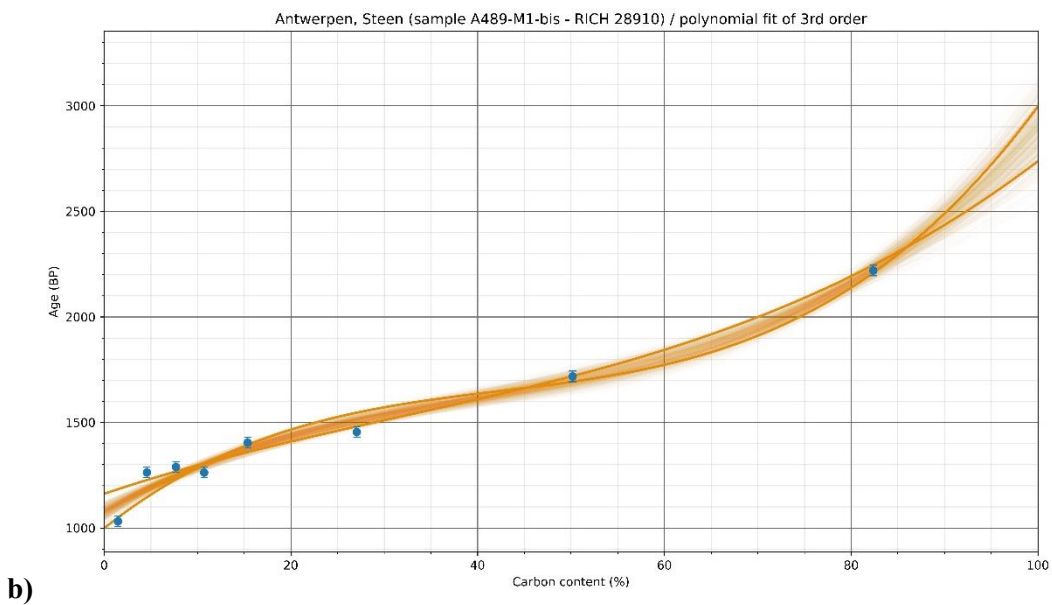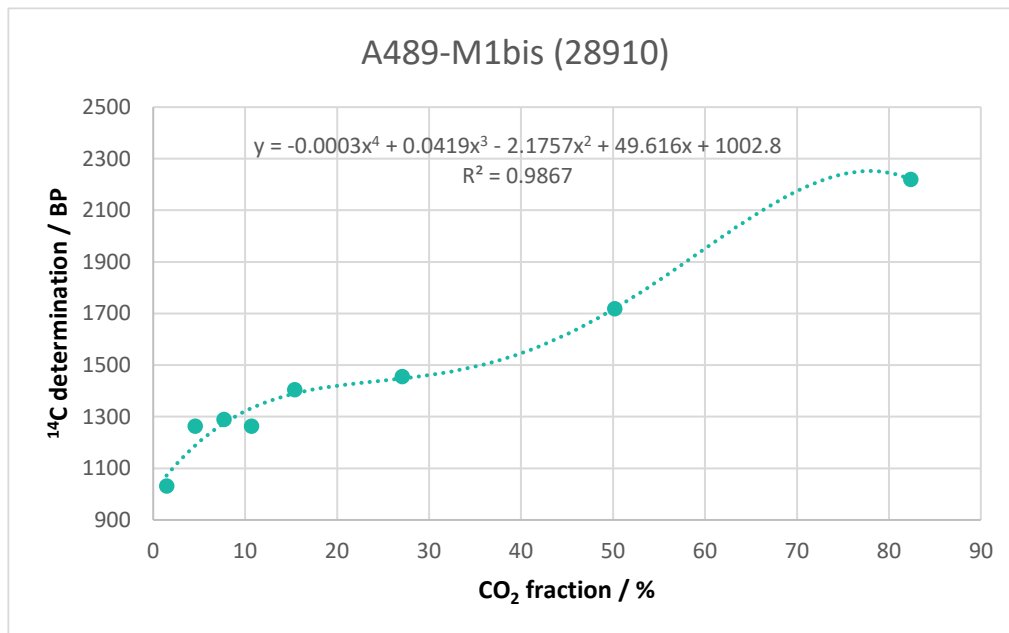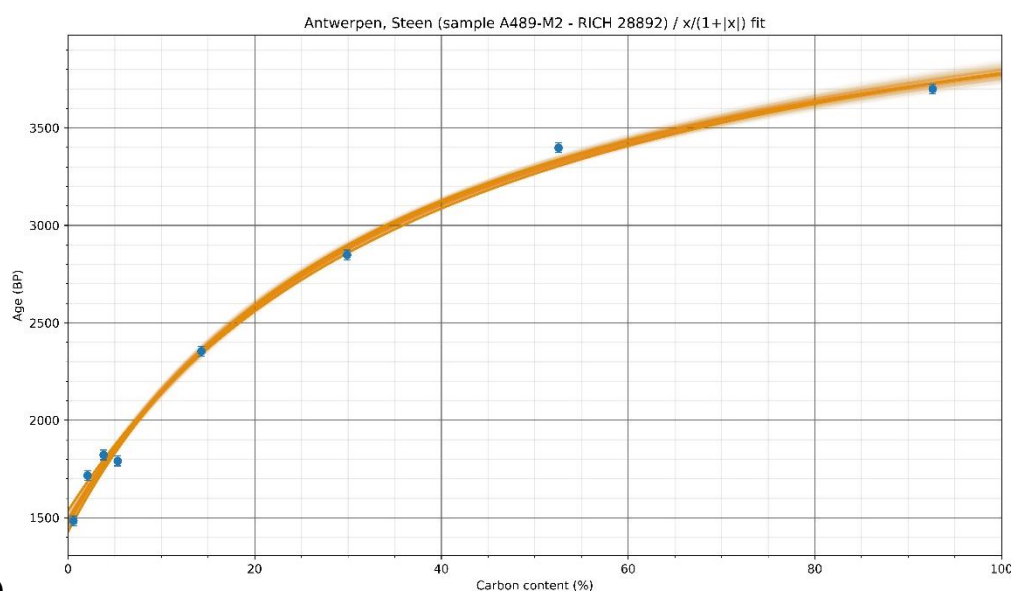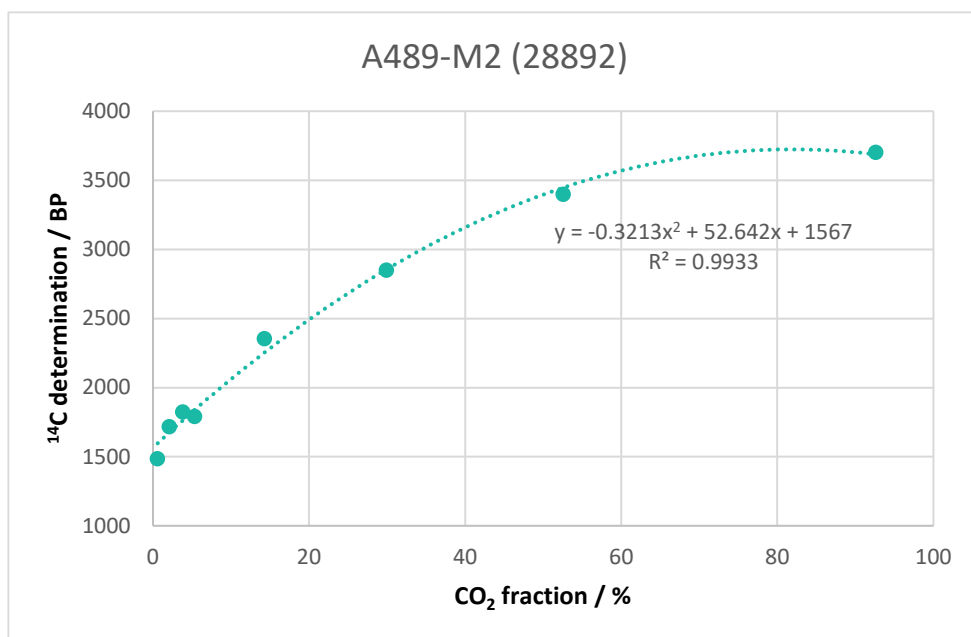
a)

A489-M1bis (28910)

$y = -0.0003x^4 + 0.0419x^3 - 2.1757x^2 + 49.616x + 1002.8$

$R^2 = 0.9867$

Antwerpen, Steen (sample A489-M1-bis - RICH 28910) / polynomial fit of 3rd order

b)

Figure 6: Radiocarbon results for the powdered mortar with particles < 75 μm as a function of the CO_2 fraction: a) A489-M1, b) A489-M1bis and c) A489-M2 (the graphs at the bottom show the statistic on the results).

Conclusions

The radiocarbon dating results are scattered. Even though the results obtained for sample M1bis could correspond to the context, the sample should nevertheless be discarded by intellectual honesty because its poor state of preservation makes it unsuitable for dating. The Steen is located on the river bank, the mortar from the foundations has probably undergone numerous immersion and drying cycles causing dissolution and secondary carbonates formed with carbon of fossil origin.

Study of mortars from Notre-Dame of Mousty church (Ottignies) for the BRAIN 2.0 PalC project

Context of the site

The church (Figure 1, left) of *Notre-Dame* (Our Lady) in Mousty (Céroux-Mousty - Walloon Brabant) is a former collegiate church and now a parish church (Gautier et al. 2021). It is traditionally dated to the 11th century (Genicot 1975) and it is incorporated into a later 18th-century structure. It has, as some others dioceses in the Liège, a Romanesque roof structure (Figure 1, right) initially dendro-dated to the years 1200-1210d (Hoffsummer 1995). More recently, dendrochronological studies dated a window frame (Figure 1, middle) to 1077d (terminus post quem), while the existing Romanesque roof frame can be dated to around 1206 (Gautier et al. 2021).

Figure 1: Photographs of the *Notre-Dame* church of Mousty (left), the window frame dated to 1077d (middle) and the existing Romanesque roof frame dated to around 1206 (Gautier et al. 2021).

Material

Before the start of the PALc project, three samples were taken from the church of Mousty (Table 1 & Figure 2). The study of the building was performed in collaboration with Patrice Gautier and Louise Hardenne, both archaeologists at the Royal Museums of Art and History (RMAH). Two of the samples were dated before the project: the bedding mortar and the outdoor render of the old north gutter wall that supported the original roof structure. The later was quickly replaced by the current Romanesque roof structure. This wall, that was originally external, has therefore been protected from the elements since the addition of the Romanesque roof frame. A fragment of wall painting was also sampled in the past but only dated during the PALc project (wall painting plaster fragment 3/3). It comes from the other side of the north gutter wall, where remains of wall paintings can be seen above the vaults added in the 18th century.

During the project, it was decided to sample again to get more insight about the chronology of the building. Four more mortars were sampled (Figure 2): ECH.I is an outdoor render of a window (north gutter wall, second bay from the west i.e. where the dendro-dated window frame comes from); ECH.II is a mortar used for sealing the inside of the frame (same location); ECH. III is a bedding mortar of the masonry in the nave in contact with the choir (east end of the

north gutter wall); and ECH.IV is a mortar used for laying the eaves purlin on the masonry (south gutter wall, first bay).

Sample id	Presumed historical date	¹⁴C before project
Bedding mortar	10th-13th century – 1077d post quem & 1205-1206d ante quem	x
Outdoor render		x
Wall painting plaster fragment 3/3	1500?	-
ECH I (outdoor render window)	10th-13th century – 1077d post quem & 1205-1206d ante quem	-
ECH.II (sealing mortar window)		-
ECH.III (bedding mortar)		-
ECH.IV (bedding mortar eaves purlin)		-

Table 1: List of samples studied with their presumed historical date and whether they were dated or not before the start of the PALc project.
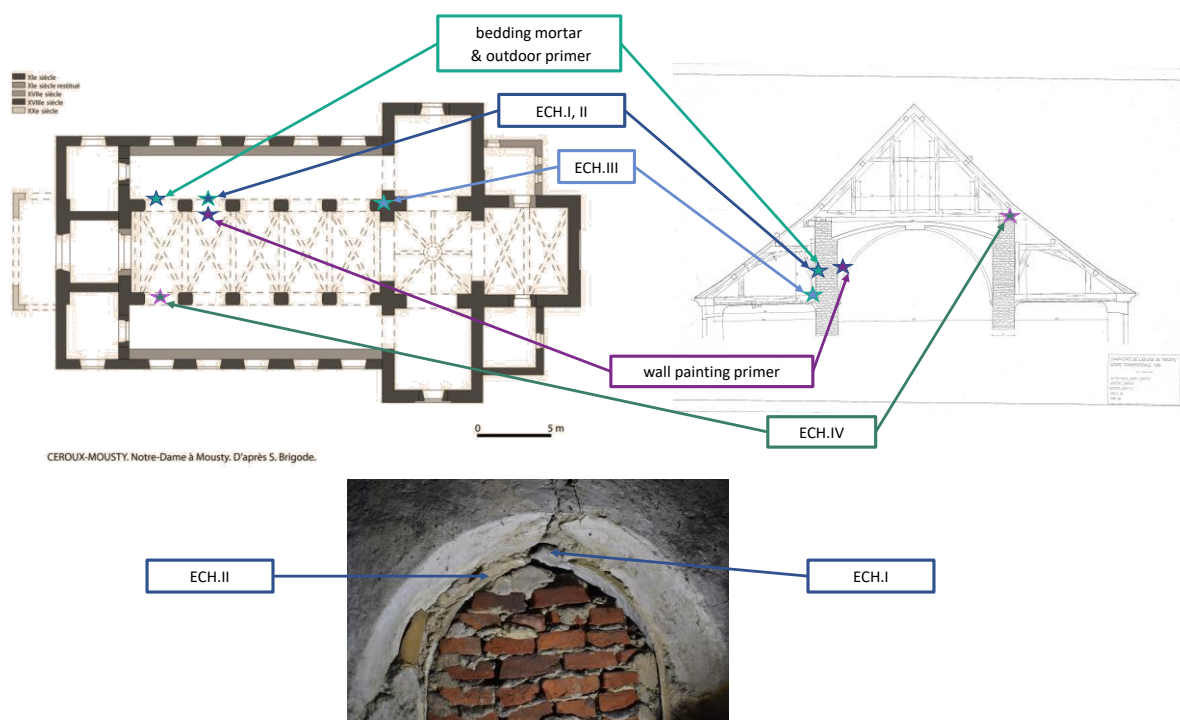
Figure 2: Location of the sampled mortars.

Results & Discussion

Macroscopic descriptions

The main colour of all the samples is beige (Figure 3) tending to pale yellow with different colour names according to the Munsel soil colour charts: 2.5Y 8/3 for the bedding mortar, the outdoor render and ECH.I; 2.5Y 8/2 for the wall painting plaster and ECH.II; and 2.5Y 7/3 for ECH.III and ECH.IV. Lime lumps are noticeable in all samples. Their main size is lower than 1 mm for the bedding mortar, the outdoor render, the wall painting plaster and ECH.IV; around 3 mm for ECH.I and ECH.II and around 5 mm for ECH.III. Red inclusions possibly due to the presence of terracotta are present in all samples. The outdoor render, ECH.I, and ECH.IV exhibit some grey inclusions that don't seem to react with HCl and are therefore most probably

silicate inclusions. The outdoor render (Figure 3b), the wall painting plaster, ECH.I (Figure 3d) and ECH.II (Figure 3e) display a thin white layer on their surface that is also covered by different shadows of red pigment in the case of the wall painting plaster (figure 3c). The outdoor render showed translucent rounded inclusions. A 1 cm long plant fibre was observed on the back of the wall painting plaster (data not shown). The bottom surfaces of ECH.I and ECH.III were covered by a brown/black dust (data not shown). Finally, a 1 cm large piece of charcoal was noticed for ECH.II (Figure 3e).
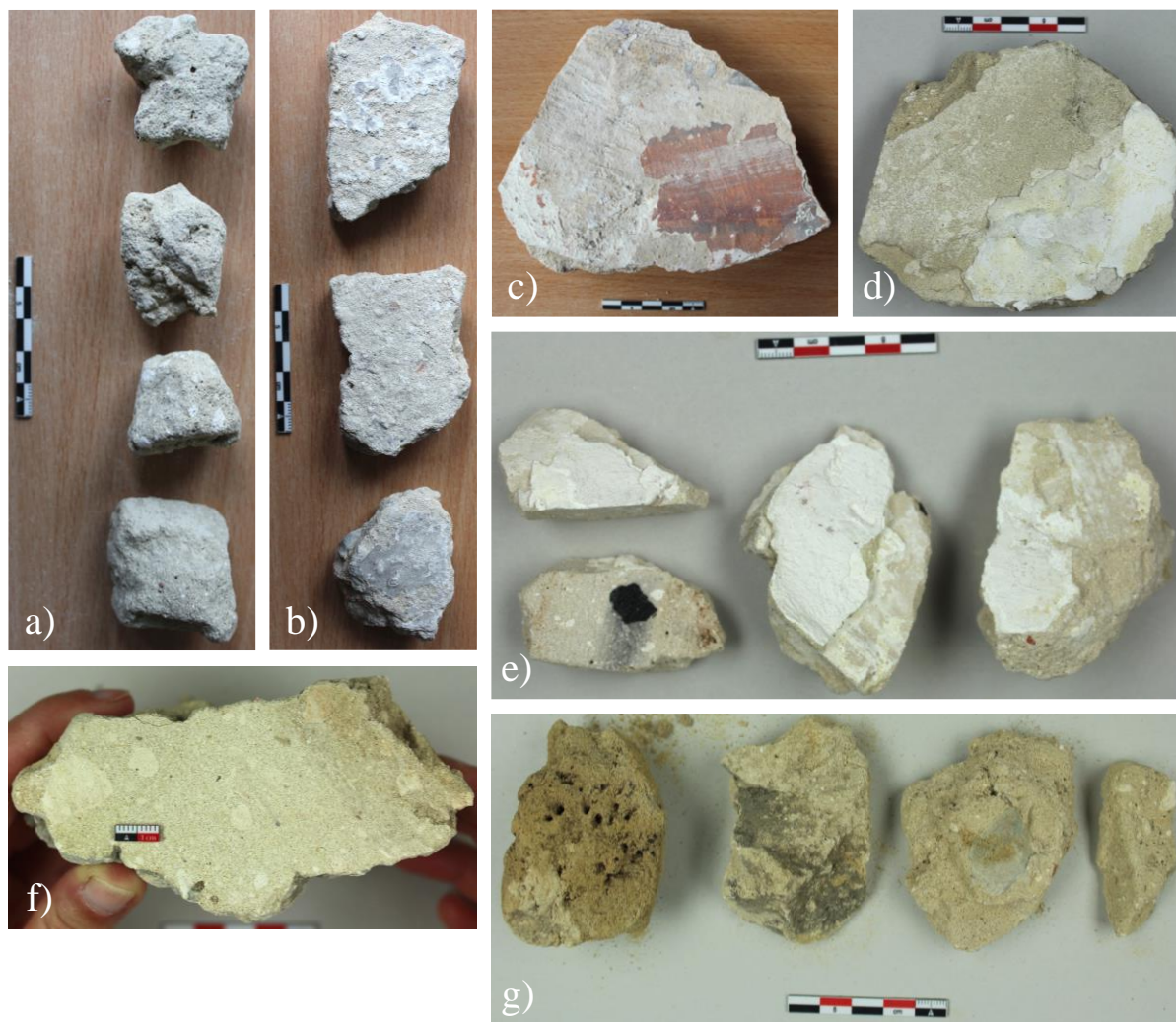
Figure 3: Photographs of the different samples: a) bedding mortar; b) outdoor render; c) wall painting plaster fragment 3/3; d) ECH.I (outdoor render window); e) ECH.II (sealing mortar window); f) ECH.III (bedding mortar); and g) ECH.IV (bedding mortar eaves purlin).

Fourier transform Infrared (FTIR) spectroscopy on inclusions & binder

All the binders (beige, Figure 4) exhibit a similar spectrum with the features of calcium carbonates (calcite and aragonite) and silicates including quartz. For the wall painting plaster fragment 3/3, ECH.II and ECH.III clay was also detected. The lime lumps (white/white inclusion, Figure 4) are made of carbonates (mainly calcite with a low proportion of aragonite) with some silicates, and for ECH.III nitrates were also identified as well as gypsum for the outdoor render. The grey inclusions are made of clay for the bedding mortar, carbonates and silicates for ECH.I, and silicates for ECH.IV. The brown inclusion of the bedding mortar

contains calcite, silicates including quartz and nitrates and the brown dust on the bottom of ECH.I is made of calcite, silicates including quartz, gypsum and organic matter. The spectra of white layers on top of the mortars all show the features of calcite and aragonite, as well as silicates for the white layer of the wall painting plaster fragment 3/3 and ECH.I, and also gypsum for the outdoor render and ECH.I. The pink and red inclusions mainly contains silicates including quartz and some calcite. In addition, The red inclusions of ECH.II and ECH.III possibly include haematite; nitrates and aragonite were also detected for the red inclusions of ECH.I in addition to nitrate and gypsum for the ones in the outdoor render and ECH.III. The spectrum of black inclusion analysed from the outdoor render only shows a mineral signal made of nitrates, silicates including quartz and gypsum. The large black fragment inside ECH.II contains amorphous carbon, calcite, nitrates, organic matter and silicates.
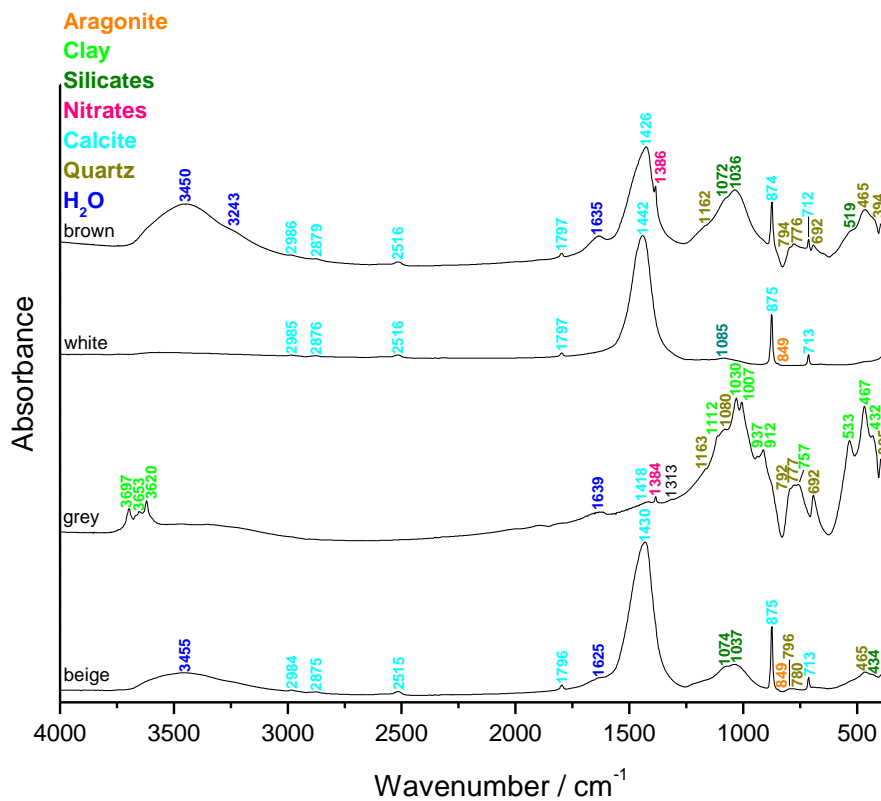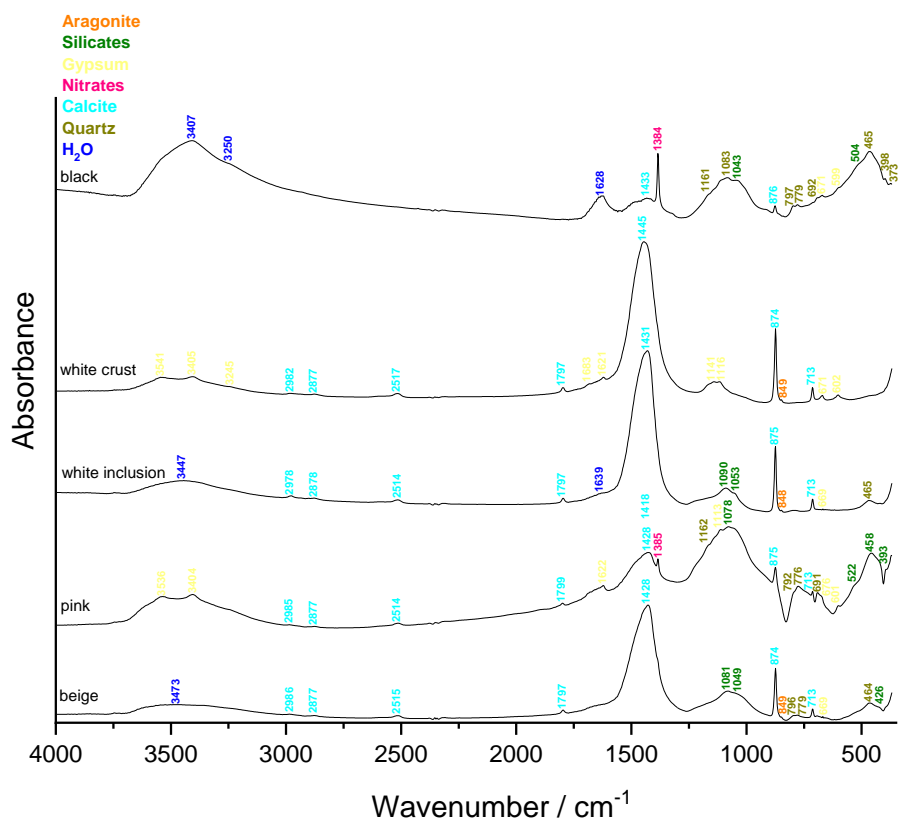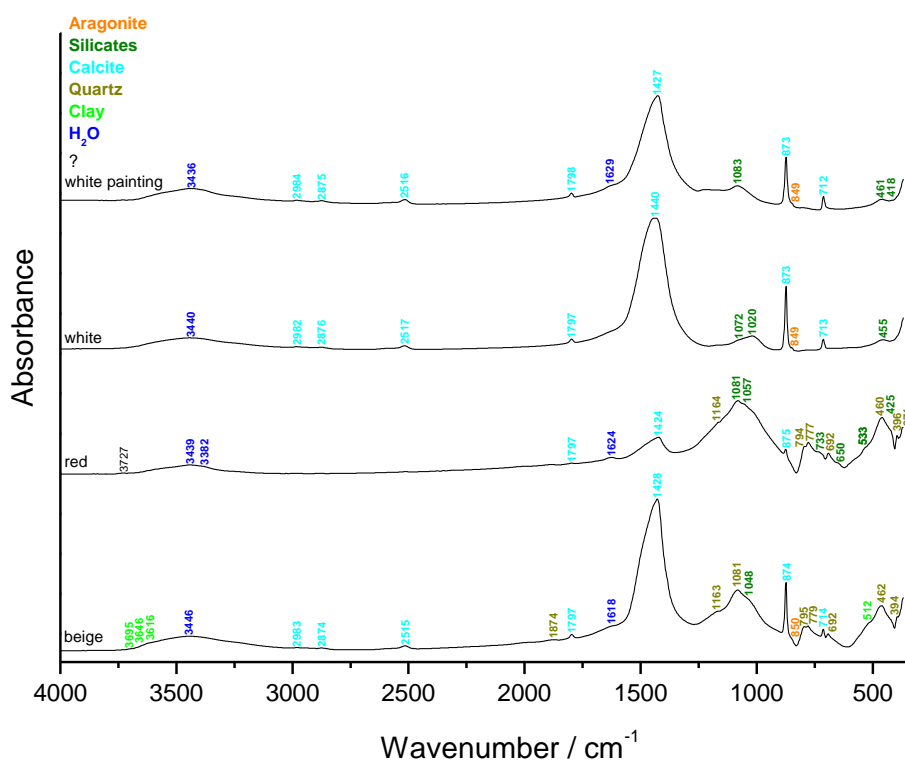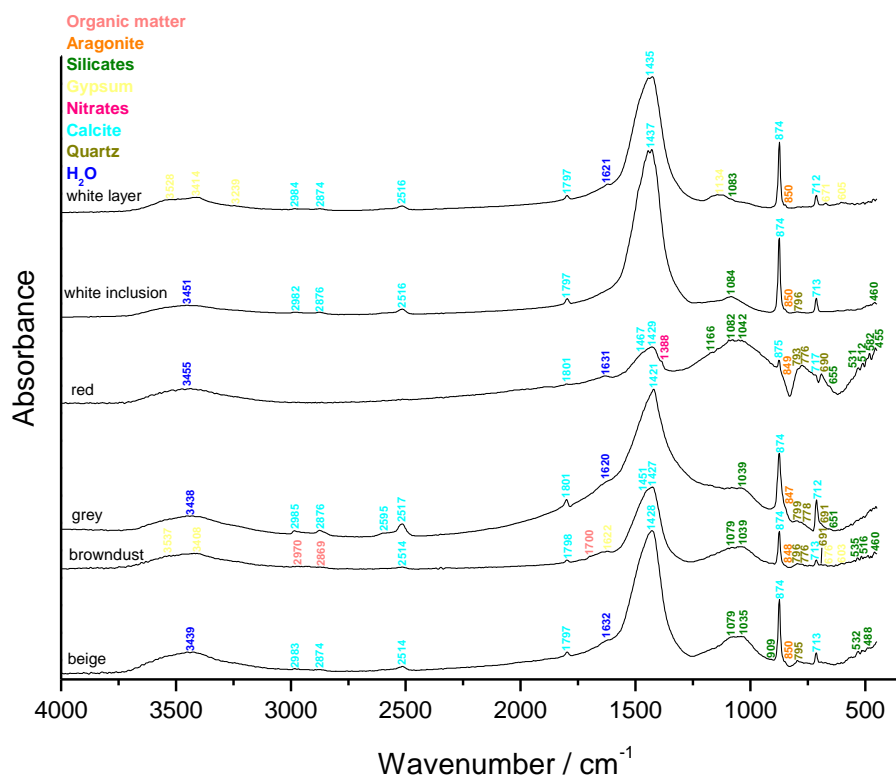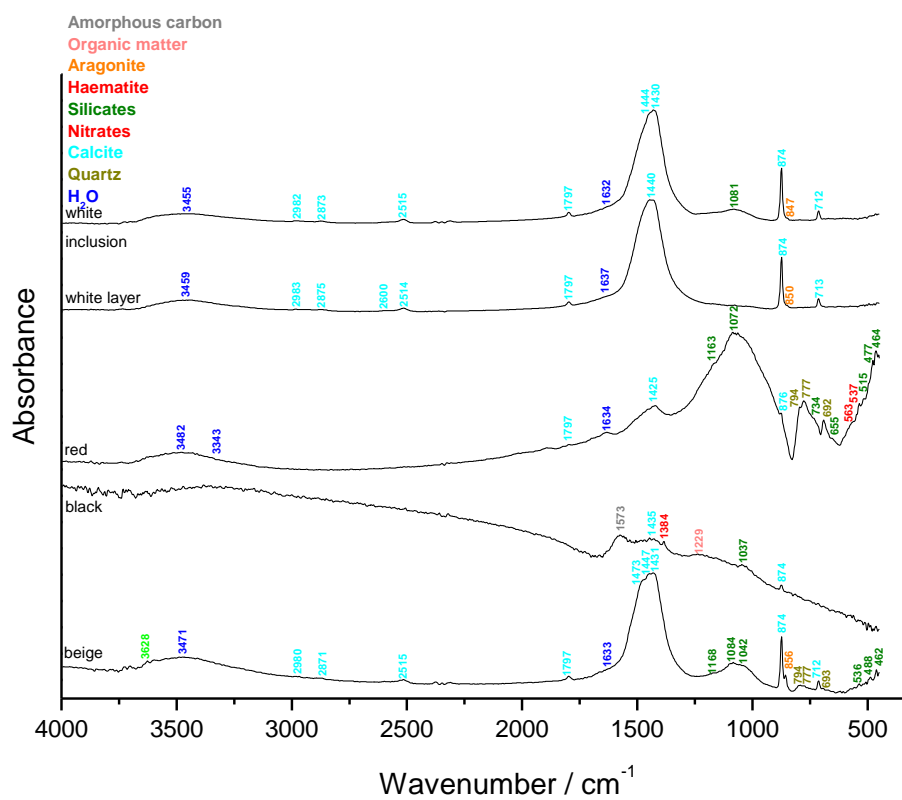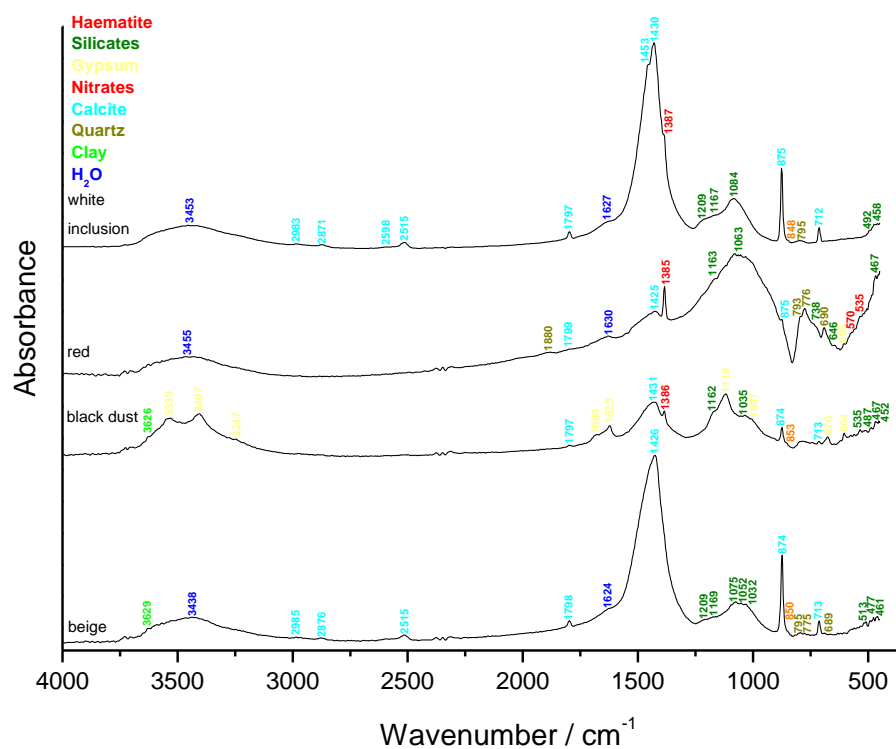
b)

c)

d)

e)
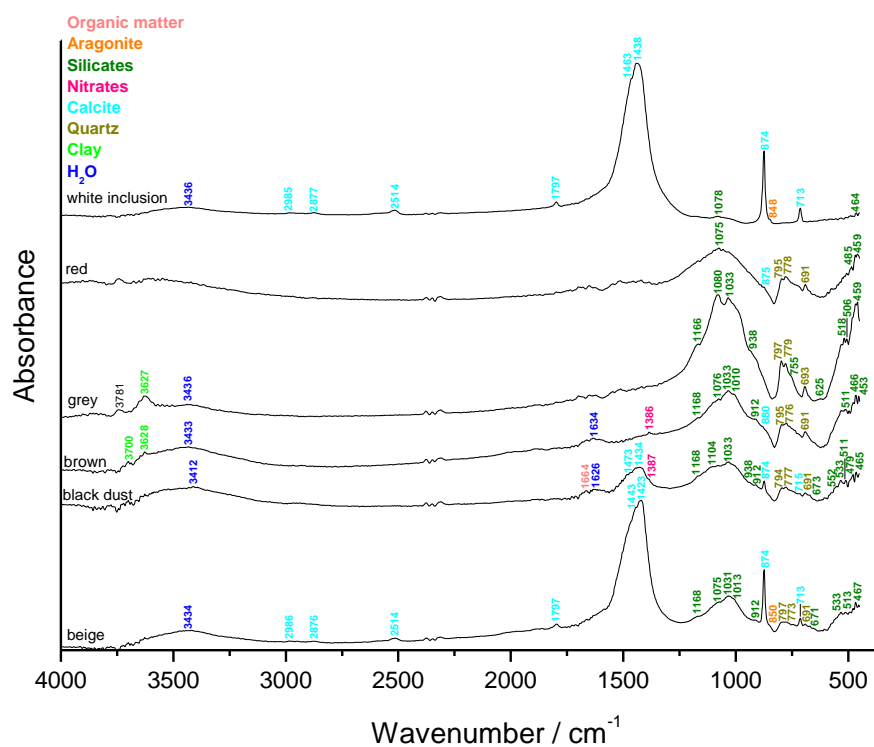
Figure 3: FTIR spectra obtained on the inclusions and binder (beige) of the mortar samples: a) bedding mortar; b) outdoor render; c) wall painting plaster fragment 3/3; d) ECH.I (bedding mortar); e) ECH.II (sealing mortar); f) ECH.III; and g) ECH.IV (bedding mortar of the eaves purnil).

Binder:aggregate ratio

The calculated binder:aggregate ratio using a bulk density of 1.35 kg/dm^3 for the sand and 0.575 kg/dm^3 for the lime is close to 1:1 in volume unit for the bedding mortar, the wall painting

plaster and ECH.II (sealing mortar window); close to 3:2 for ECH.I (outdoor render window); and close to 2:1 for ECH.III (bedding mortar). The binder:aggregate ratio of ECH. IV (bedding mortar of the eaves purlin) is close to 1:2, which is rather low compared to the other bedding mortars of Mousty but can be explained by the bad state of conservation of the mortar (granular disintegration). The binder:aggregate ratio of 6:1 obtained for the outdoor render is not in line with the petrographic observations. A possible explanation for this is that the analysed subsample contained a large lime lump.

	bedding mortar	outdoor render	wall painting plaster fragment 3/3	ECH.I	ECH.II	ECH.III	ECH.IV
Sample weight (g)	2.7	2.83	2.8	2.5	2.3	2.6	1.9
Crucible weight (g)	15.3	16.9	19.3	18.1	17.5	18.2	17.6
Weight calcined (g)	17.3	17.7	21.3	19.7	19.1	19.6	19.1
%ins	**73.2**	**29.0**	**73.1**	**62.6**	**68.5**	**57.4**	**83.0**

Table 2: Percentage of insoluble residue

Cathodoluminescence

For the outdoor render and the bedding mortar, only the powdered samples with particle size lower than 75 μm were observed (Figure 4a & b), because the thin sections were covered by a glass slide before the start of the project (making impossible their use for cathodoluminescence). Most of the powdered samples (Figure 4a, b, d, f, h, j & l) show a predominance of tile red (binder) with a few bright red grains (limestone), a few blue grains (K-feldspars) and rare green grains (plagioclases). The thin section of the wall painting plaster fragment 3/3 (X2160 – Figure 4c) shows a bright red border of limestone representative of the paint layer. It was removed before grinding the sample and should then not be an issue for radiocarbon dating. This paint layer probably contains finely crushed chalk because this layer exhibits a tile red tint typical of unburned limestone. The rest of the thin section X2160 (Figure 4c) displays completely burned lime lumps and binder in dull, a few K-felsdpars in bright blue and numerous quartz grains in dark purple. The same description can be done for the X2405 (Figure 4g) of ECH.II. For all other thin sections (Figure 4e, I & k), it can be observed that some of the lime lumps are partially burned, the lumps appear red with some part of the lumps brighter compared to other parts.
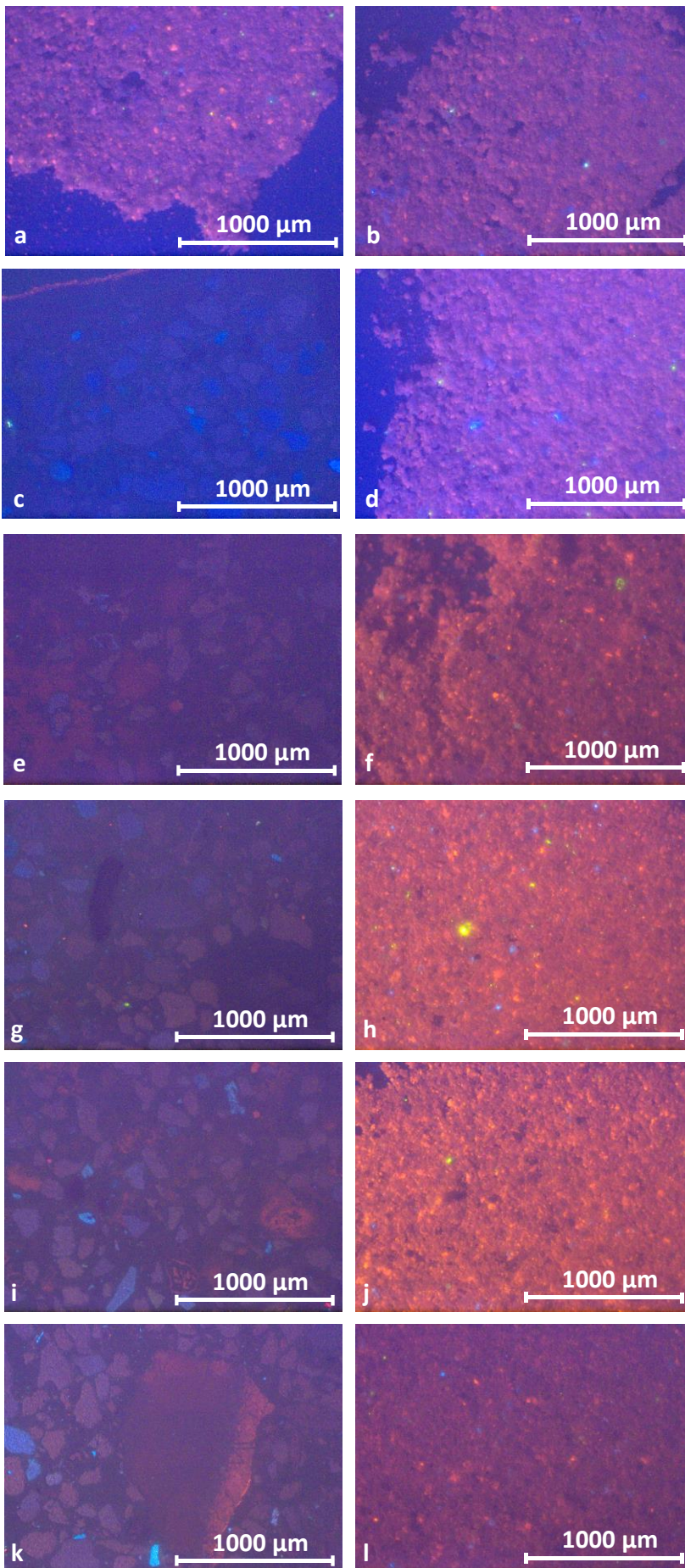
Figure 4: Characteristic cathodoluminescence images of a) the powdered bedding mortar with particle size lower than 75 µm, b) the powdered outdoor primer with particle size lower than 75 µm, c) the thin section X2160 of wall painting plaster fragment 3/3, d) the powdered wall painting plaster fragment 3/3 with particle size lower than 75 µm, e) the thin section X2404 of ECH.I, and f) the powdered ECH.I with particle size lower than 75 µm, g) the thin section X2405 of ECH.II, and h) the powdered ECH.II with particle size lower than 75 µm, i) the thin section X2406 of ECH.III, and j) the powdered ECH.III with particle size lower than 75 µm, k) the thin section X2407 of ECH.IV, and l) the powdered ECH.IV with particle size lower than 75 µm,.

Thin-section petrography

The bedding mortar (Figure 5 & Table 3) presents lime lumps containing quartz grains which is an intrinsic feature of the limestone used. Both limestone and sand aggregate come from the Brussels Formation. The glauconite present in the lumps is totally oxidised (black) because of the calcination process. The glauconite from the aggregate is not oxidised (green) or only partially oxidised (brown – Figure 5f). No bioclast is observed (it is rather common in the Brussels Formation, with the exception of decalcified upper levels). The mortar is very porous which might have been due to a dissolution process. Secondary carbonates are observed in lime lumps (around quartz grains – Figure 5e).
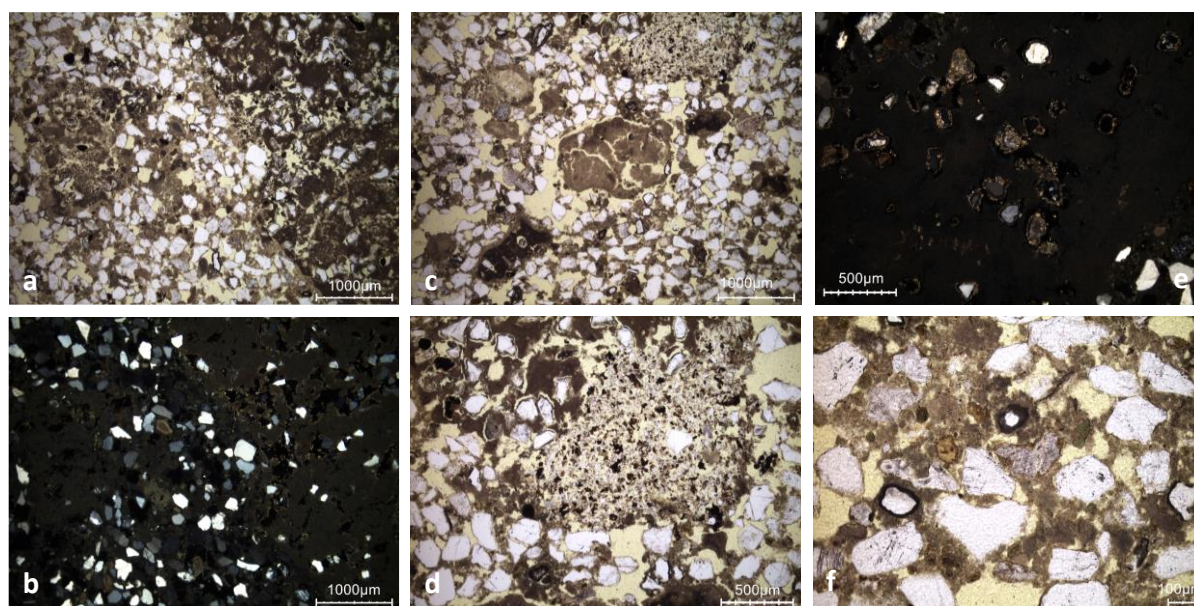
Figure 5: Representative photomicrographs of the bedding mortar thin-section X2098: a) overview image in plain polarised light (PPL); b) overview image in cross polarised light (XPL); c) PPL image showing a shrinked lime lump; d) clay-silt agglomerate in PPL; e) XPL image with secondary carbonates inside lump; f) brown & green glauconite in PPL.

	Texture	micritic
Binder	**Lump state**	completely burned
	Lump size	from 40 µm to 1.7 cm
	Lump frequency	numerous
Aggr	**Grain size**	very fine to medium

	Mineralogy	siliceous sand (quartz, feldspar, silty clay agglomerates, glauconite more or less oxidised)
	Shape	subangular / subrounded
Appearance	**Homogeneity**	relatively heterogeneous
Appearance	**Macroporosity**	high
Appearance	**Pore structure**	irregular / sometimes connected
Admixtures	**Type**	plant fragment (not shown)
Alteration	**Type**	dissolution, secondary carbonates in the pores of the lime lumps

Table 3: Main characteristics of the bedding mortar retrieved from the observations of the thin-section X2098.

The lime lumps of the outdoor render (Figure 6 & Table 4) contain silicates, the limestone used naturally contains them and probably originates from the Brussels Formation. One unburned lime fragment was observed (Figure 6d). Secondary carbonates are present in the pores of the lime lumps (Figure 6f).
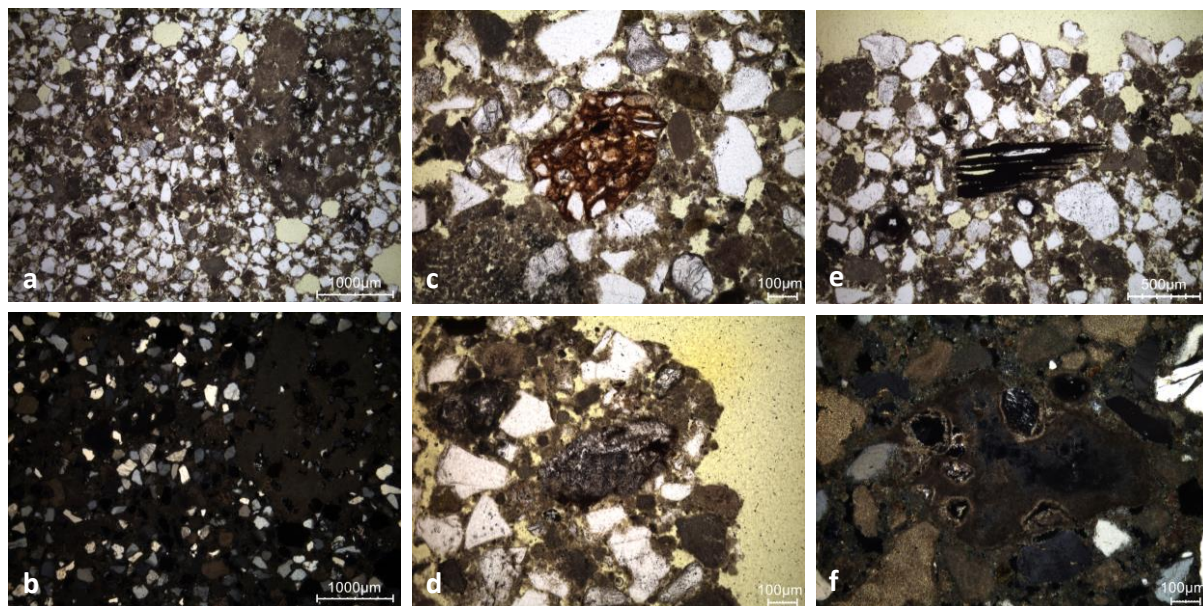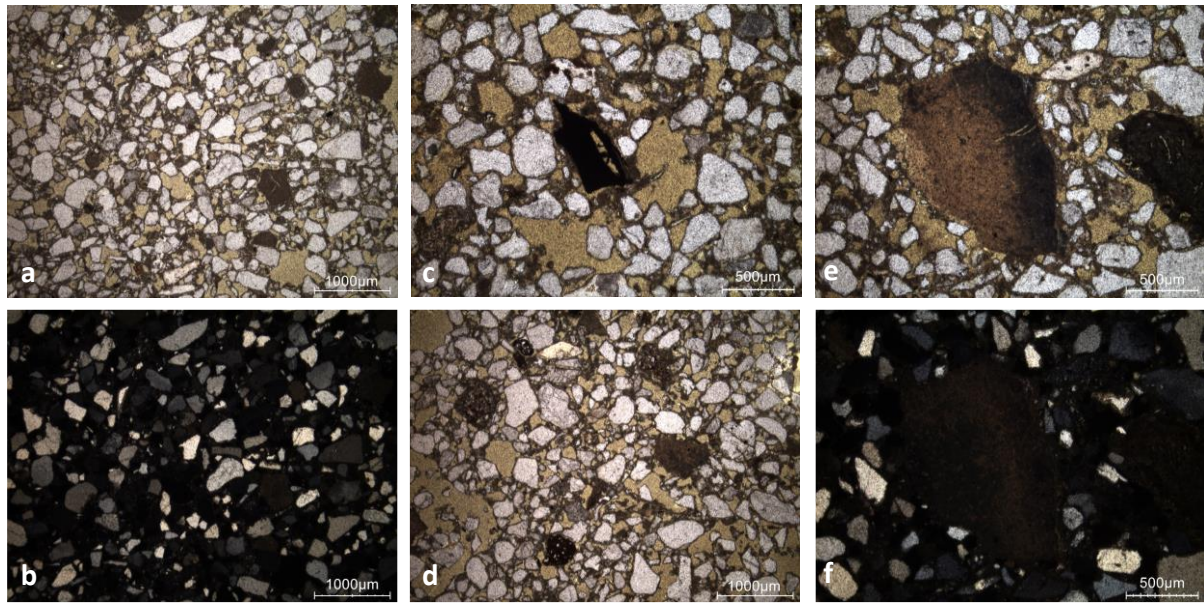

Figure 6: Representative photomicrographs of the outdoor primer thin-section X2099: a) overview image in PPL; b) overview image in XPL; c) PPL image showing a silty clay agglomerate; d) limestone fragment from lime production in PPL; e) PPL image with charcoal; f) secondary carbonates in XPL.

Binder	**Texture**	micritic
Binder	**Lump state**	completely burned, unburned
Binder	**Lump size**	max 7.3 cm

	Lump frequency	numerous
Aggregate	**Grain size**	very fine to medium
	Mineralogy	siliceous sand (quartz, feldspar, glauconite, silty clay agglomerate)
	Shape	subangular / subrounded
Appearance	**Homogeneity**	relatively homogeneous
	Macroporosity	high
	Pore structure	irregular / not connected
Admixtures	**Type**	charcoal
Alteration	**Type**	secondary carbonates in the pores of the lime lumps

Table 4: Main characteristics of the outdoor primer retrieved from the observations of the thin-section X2099.

The wall painting plaster fragment 3/3 is in good condition (Figure 7 & Table 5). The lime lumps are completely burned, and the binder is well conserved. No alterations are observed, and the aggregate is made of siliceous sand.
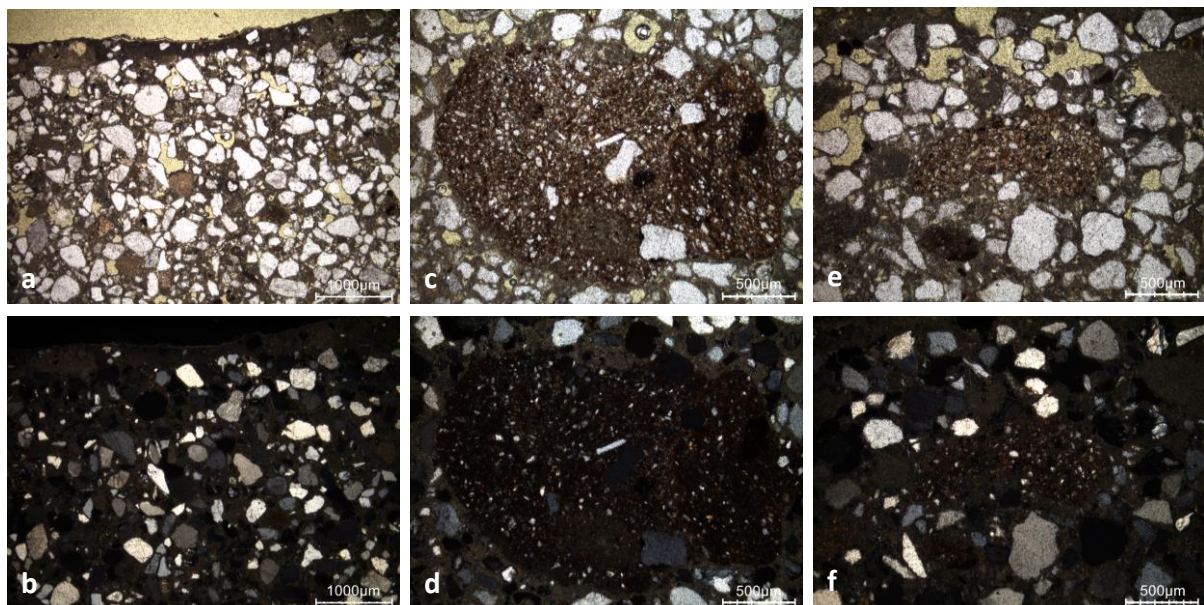
Figure 7: Representative photomicrographs of the wall painting plaster fragment 3/3 thin-section X2160: a) overview image in PPL; b) overview image in XPL; c) PPL image showing a sandy/silty clay agglomerate; d) same image in XPL; e) PPL image with a silty clay agglomerate; f) same image in XPL.

Binder	**Texture**	micritic
	Lump state	completely burned

	Lump size	max 1.4 mm
	Lump frequency	medium
Aggregate	**Grain size**	very fine to coarse (some very coarse sandy-clay agglomerates)
	Mineralogy	siliceous sand (quartz, feldspar, silty clay agglomerates, glauconite more or less oxidised, sandy-clayey agglomerate)
	Shape	subangular / subrounded
Appearance	**Homogeneity**	relatively homogeneous
	Macroporosity	medium
	Pore structure	irregular / not connected
Admixtures	**Type**	-
Alteration	**Type**	-

Table 5: Main characteristics of the wall painting plaster fragment 3/3 retrieved from the observations of the thin-section X2160.

The ECH.I mortar is rather in good condition (Figure 8 & Table 6). Secondary carbonates are present in the micropores of the lime lumps (Figure 8d). The colour of the lime lumps varies between light brown and dark brown, the lighter colour in PPL might indicate that some lumps are incompletely burned (Figure 8e & f). The lime lumps contain silicates, the limestone used naturally contains them and probably originates from the Brussels Formation.
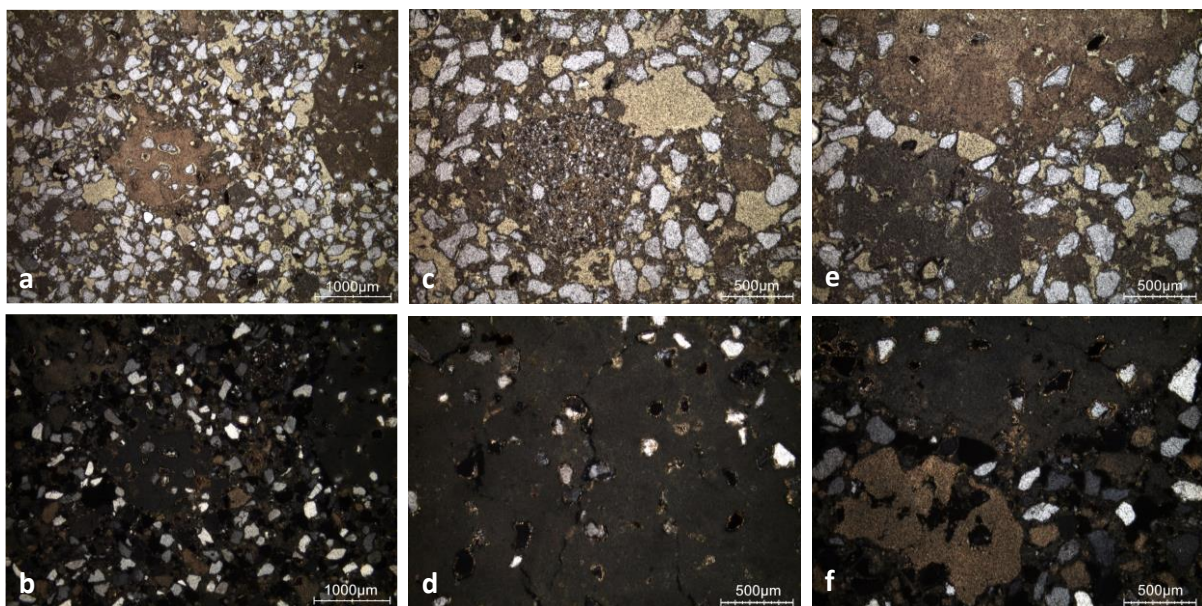
Figure 8: Representative photomicrographs of ECH.I thin-section X2404: a) overview image in PPL; b) overview image in XPL; c) PPL image showing a sandy clay agglomerate; d) secondary carbonates

in pores in XPL; e) PPL image with underburned & completely burned lime lumps; f) same image in XPL.

Binder	**Texture**	micritic
	Lump state	completely burned, possibly underburned
	Lump size	215 µm ; 511 µm ; 1.3 mm ; 3.1 mm ; 5 mm
	Lump frequency	numerous
Aggregate	**Grain size**	very fine to fine (some coarse sandy clay agglomerates)
	Mineralogy	siliceous sand (quartz, feldspar, glauconite more or less oxidised, sandy clay agglomerate)
	Shape	subangular / subrounded
Appearance	**Homogeneity**	relatively homogeneous
	Macroporosity	medium
	Pore structure	irregular / sometimes connected
Admixtures	**Type**	-
Alteration	**Type**	secondary carbonates in the pores of lime lumps

Table 6: Main characteristics of ECH.I retrieved from the observations of the thin-section X2404.

The lime lumps of ECH.II (Figure 9 & Table 7) contain silicates, the limestone used naturally contains them and probably originates from the Brussels Formation. The lime lumps are completely burned, and some are possibly underburned (because lighter in colour). The mortar is in good condition except the presence of secondary carbonates.
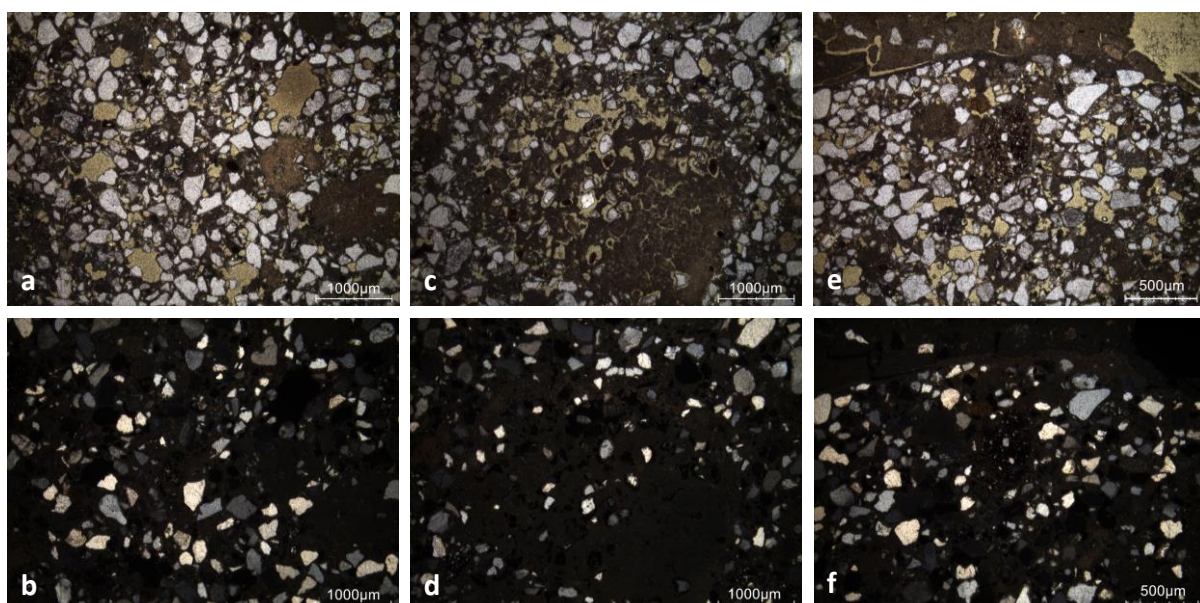
Figure 9: Representative photomicrographs of ECH.II thin-section X2405: a) overview image in PPL; b) overview image in XPL; c) PPL image showing lime lump with secondary carbonates; d) same image in XPL; e) PPL image with a sandy clay agglomerate; f) same image in XPL.

Binder	**Texture**	micritic
	Lump state	completely burned, possibly underburned
	Lump size	682 µm ; 872 µm ; 1.8 mm ; 4.1 mm
	Lump frequency	numerous
Aggregate	**Grain size**	very fine to medium (coarse / very coarse for sandy clay agglomerates)
	Mineralogy	siliceous sand (quartz, feldspar, glauconite, sandy clay agglomerates)
	Shape	subangular / subrounded
Appearance	**Homogeneity**	relatively homogeneous
	Macroporosity	medium
	Pore structure	irregular / sometimes connected
Admixtures	**Type**	-
Alteration	**Type**	secondary carbonates

Table 7: Main characteristics of ECH.II retrieved from the observations of the thin-section X2405.

ECH.III (Figure 10 & Table 8) is very similar to ECH.II, the description is the same except one occurrence of pyroxene (Figure 10e), but it is not significant.
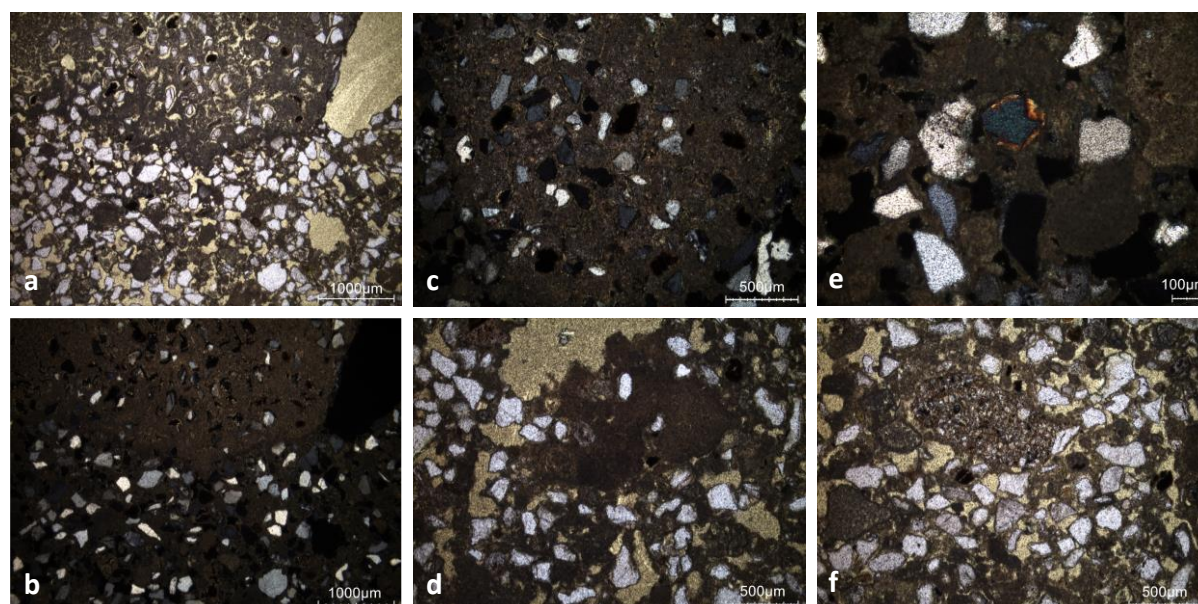
Figure 10: Representative photomicrographs of ECH.III thin-section X2406: a) overview image in PPL; b) overview image in XPL; c) PPL image showing a lime lump incompletely burned with secondary calcite in cracks; d) lime lump incompletely burned in PPL; e) XPL image of a pyroxene; f) PPL image of a sandy clay agglomerate with glauconite.

Binder	**Texture**	micritic
	Lump state	completely burned, underburned
	Lump size	1 mm, 2 mm, 4.8 mm
	Lump frequency	numerous
Aggregate	**Grain size**	very fine to fine (medium-sized sandy-clay agglomerate)
	Mineralogy	siliceous sand (quartz, feldspar, glauconite more or less oxidised, silty clay agglomerate, olivine?)
	Shape	subangular / subrounded
Appearance	**Homogeneity**	relatively homogeneous
	Macroporosity	medium
	Pore structure	irregular / cracks / sometimes connected
Admixtures	**Type**	-
Alteration	**Type**	secondary carbonates

Table 8: Main characteristics of ECH.III retrieved from the observations of the thin-section X2406.

ECH.IV is in poor condition (Figure 11 & Table 9). The binder has strongly been dissolved. The lime lumps are completely burned and incompletely burned. The limestone used comes from the Brusselian because silicates are observed inside the lime lumps.

Figure 11: Representative photomicrographs of ECH.IV thin-section X2407: a) overview image in PPL; b) overview image in XPL; c) PPL image showing charcoal; d) sandy clay agglomerate in PPL; e) PPL image of a partially burned lime lump; f) same image in XPL.

Binder	**Texture**	micritic
	Lump state	most completely burned, some partially burned
	Lump size	488 µm; 1.5 mm
	Lump frequency	numerous
Aggregate	**Grain size**	very fine to coarse
	Mineralogy	siliceous sand (quartz, K-feldspar, glauconite, plagioclase, sandy clay agglomerates)
	Shape	subangular / subrounded
Appearance	**Homogeneity**	relatively homogeneous
	Macroporosity	high
	Pore structure	irregular / sometimes connected
Admixtures	**Type**	charcoal
Alteration	**Type**	dissolved

Table 9: Main characteristics of ECH.IV retrieved from the observations of the thin-section X2407.

Thermogravimetric analysis (TGA) on whole samples

The graphs of the thermal analyses of the whole samples are presented in Figures 12 to 18. The apparent hydraulicity indexes (aHI), determined on the basis of the weight loss between 200 and ca. 650°C (usually attributed to water loss from calcium-silicate-hydrates-phases (C-S-H)), shows that the bedding mortar is very strongly hydraulic (65%); the outdoor render (33%), ECH.I (31), III (34) and IV(28%) are strongly hydraulic; the wall painting plaster is moderately hydraulic (21%); and ECH.II is slightly hydraulic (16%). For the bedding mortar and ECH.IV, the hydraulicity index cannot be considered reliable, due to dissolution of the binder, which strongly influences the obtained value upwards. Also, for all the samples, the presence of clay might also artificially increase the hydraulicity since it also releases water in the same range as the C-S-H. The amount of carbonates is ~1,7 wt% for the bedding mortar, 25 w% for the outdoor render, 21 w% for the wall painting fragment, 20 w% for ECH.I, 23 % for ECH.II, 33 w% for ECH.III, and 9 wt% for ECH.IV. A peak at 394°C is observed for the bedding mortar and the wall painting fragment (Figures 12 and 14), it might be due to organic impurities, or to the conversion of soluble to insoluble form of anhydrite, or to the rearrangement in anhydrous $CaSO_4$ from hemihydrate to anhydrate structure (Brunello 2020). For most mortars (Figures 12-18), a peak around ~421-6°C is observed and might be due to the release of water from calcium hydroxide (Moropoulou, Bakolas, and Bisbikou 1995; Klimesch and Ray 1996) indicating that the mortar did not fully carbonated. The outdoor primer also gave a peak at 492°C that could be due to dicalcium silicate hydrate I $[Ca_2(HSiO_4)(OH)]$ (Brunello 2020). The temperature of quartz transition phase is observed around 564-9°C (Rickard, Riessen, and Walls 2010) for all samples. The main weight loss of ancient mortars is expected between 600 and 900 °C and is indicative of the decomposition of calcium carbonate ($CaCO_3$) into calcium oxide (CaO) and carbon dioxide (CO_2) (Ahmmed et al. 2024). The end temperature of calcium carbonate decomposition is ~756°C for the outdoor render, 796°C for the wall painting fragment, 801°c for ECH.I, 804°C for ECH.II, 817°C for ECH.III, and 775°C for ECH.IV. The value for the bedding mortar was impossible to calculate, the graph obtained as well as the values for the aHI and the carbonate quantity are rather uncommon. The piece of mortar selected for the measurement was probably not representative. Gypsum was detected only for ECH.I (1.1 w%).
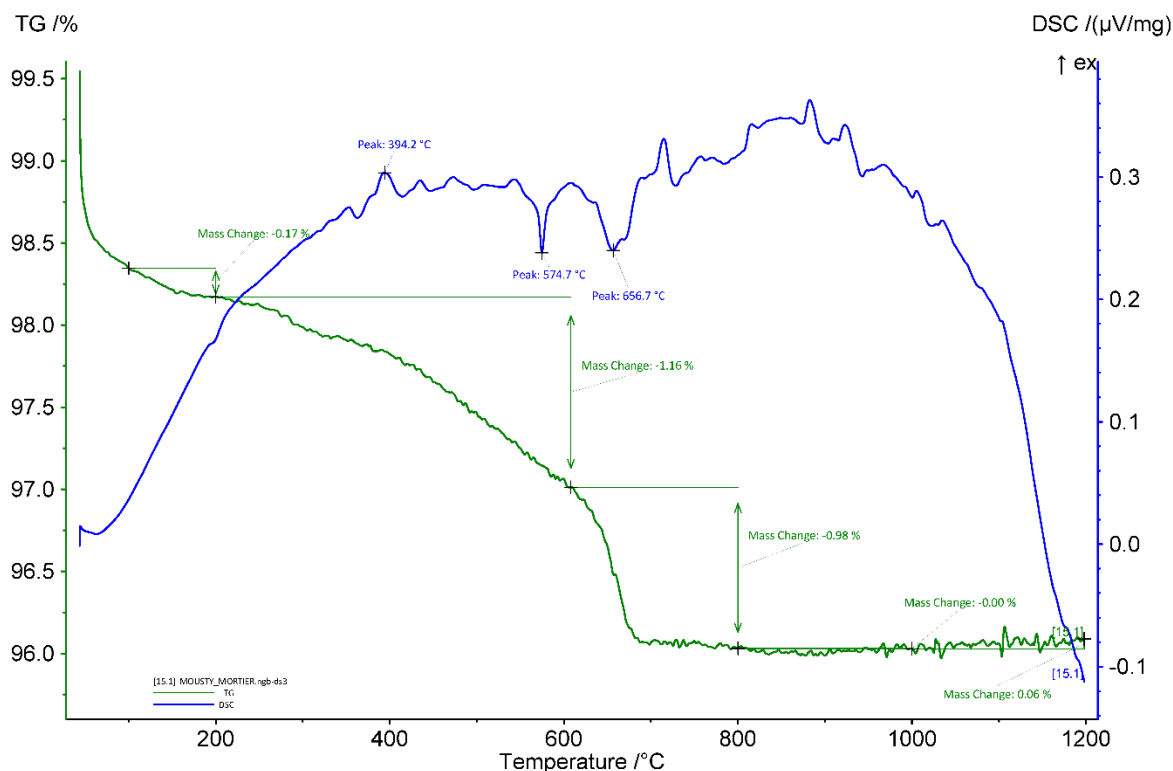
Figure 12: Coupled TG-DSC analysis of the bedding mortar upon heating to a temperature of 1200°C at a heating rate of 20°C/min under an inert atmosphere (He flushed at 50 ml/min). The weight loss determined by thermogravimetric analysis (TG, wt%, green curve) and the result of the differential scanning calorimetric analysis (DSC, mW/mg, blue curve) are both presented.
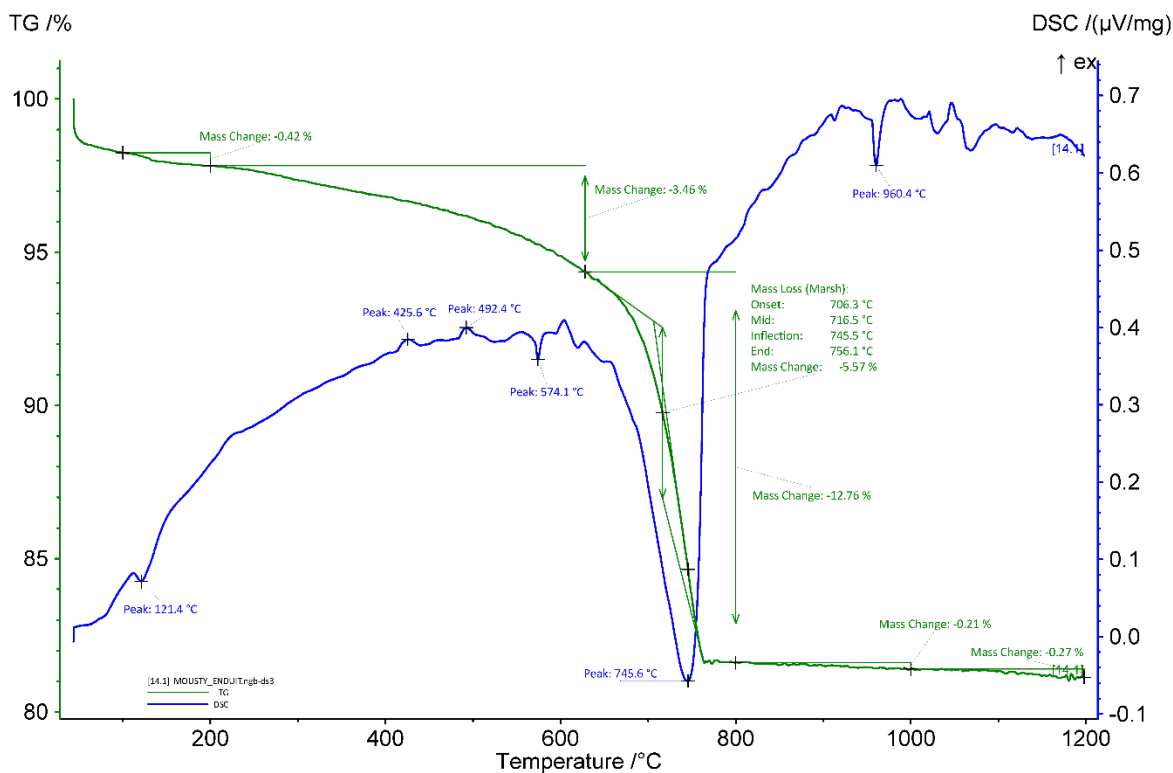
Figure 13: Coupled TG-DSC analysis of the outdoor render upon heating to a temperature of 1200°C at a heating rate of 20°C/min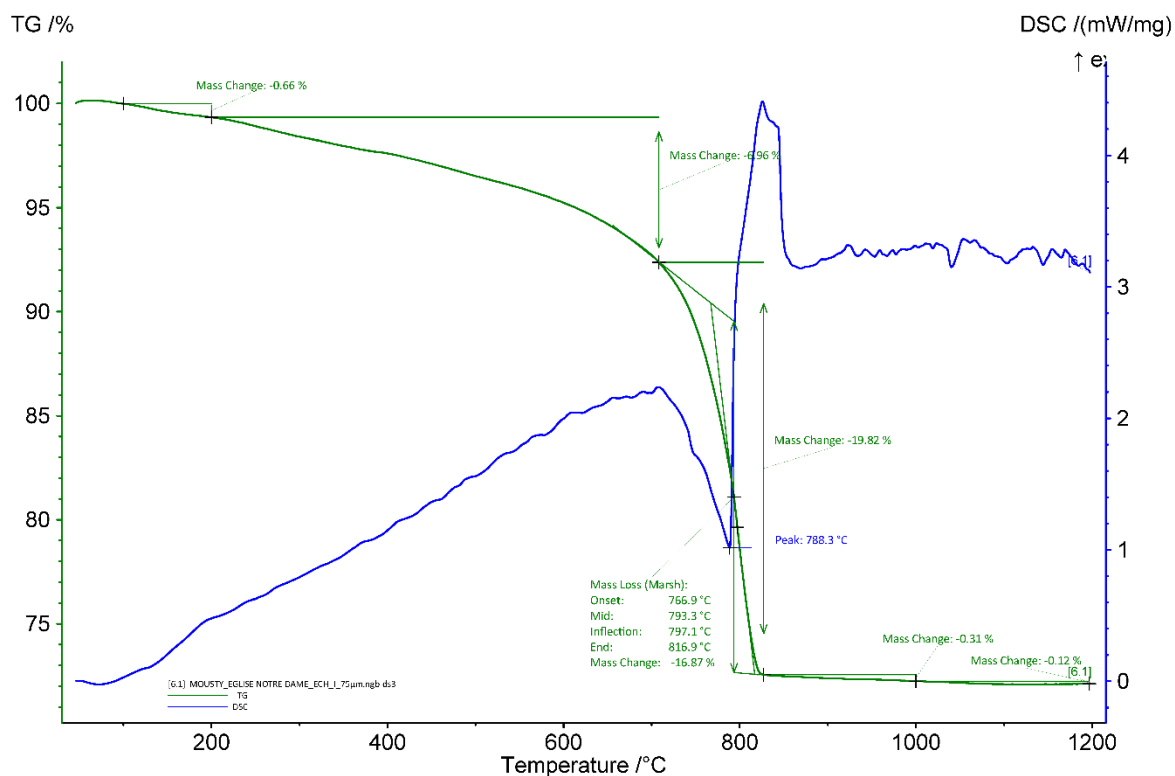 under an inert atmosphere (He flushed at 50 ml/min). The weight loss determined by thermogravimetric analysis (TG, wt%, green curve) and the result of the differential scanning calorimetric analysis (DSC, mW/mg, blue curve) are both presented.
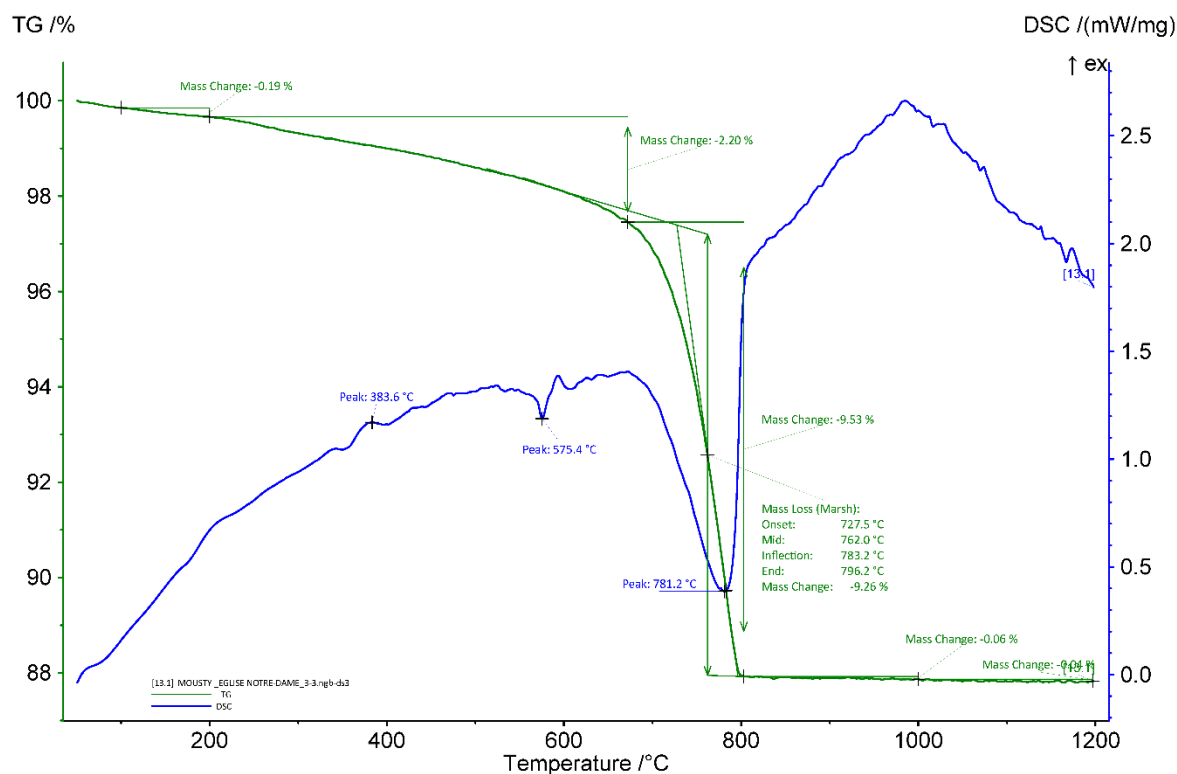
Figure 14: Coupled TG-DSC analysis of the wall painting plaster fragment 3/3 upon heating to a temperature of 1200°C at a heating rate of 20°C/min under an inert atmosphere (He flushed at 50 ml/min). The weight loss determined by thermogravimetric analysis (TG, wt%, green curve) and the result of the differential scanning calorimetric analysis (DSC, mW/mg, blue curve) are both presented.
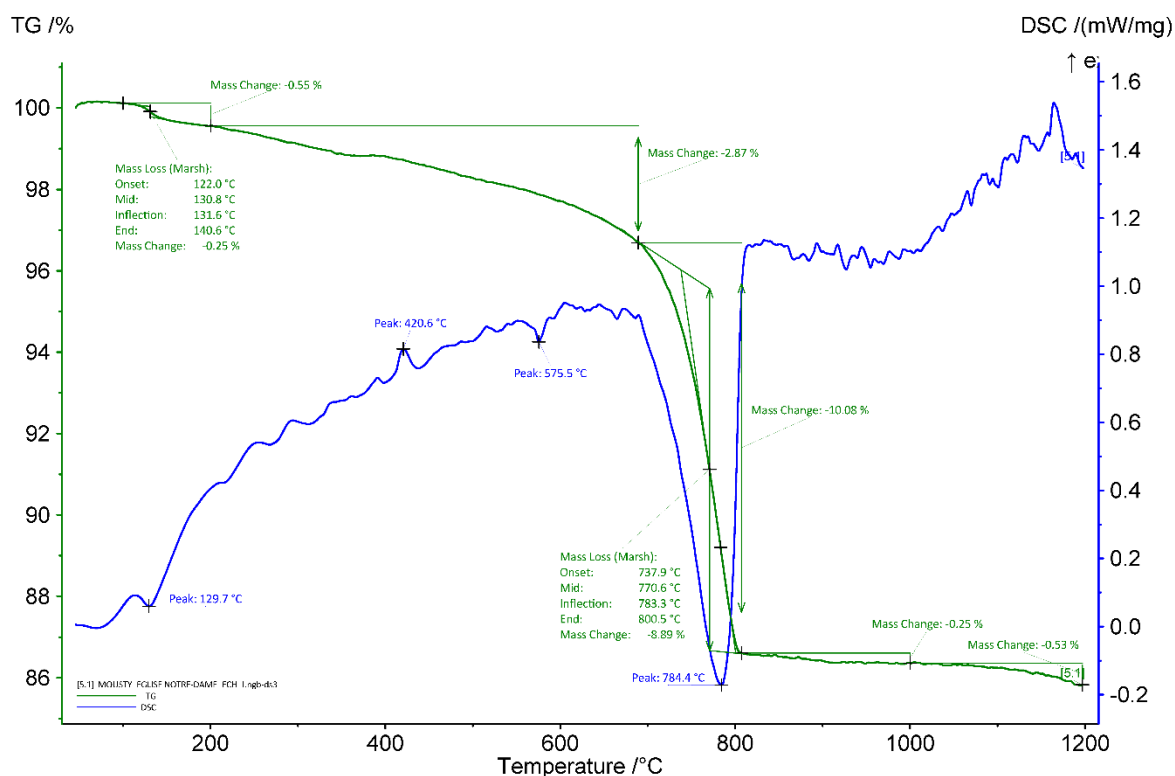
Figure 15: Coupled TG-DSC analysis of ECH.I upon heating to a temperature of 1200°C at a heating rate of 20°C/min under an inert atmosphere (He flushed at 50 ml/min). The weight loss determined by thermogravimetric analysis (TG, wt%, green curve) and the result of the differential scanning calorimetric analysis (DSC, mW/mg, blue curve) are both presented.
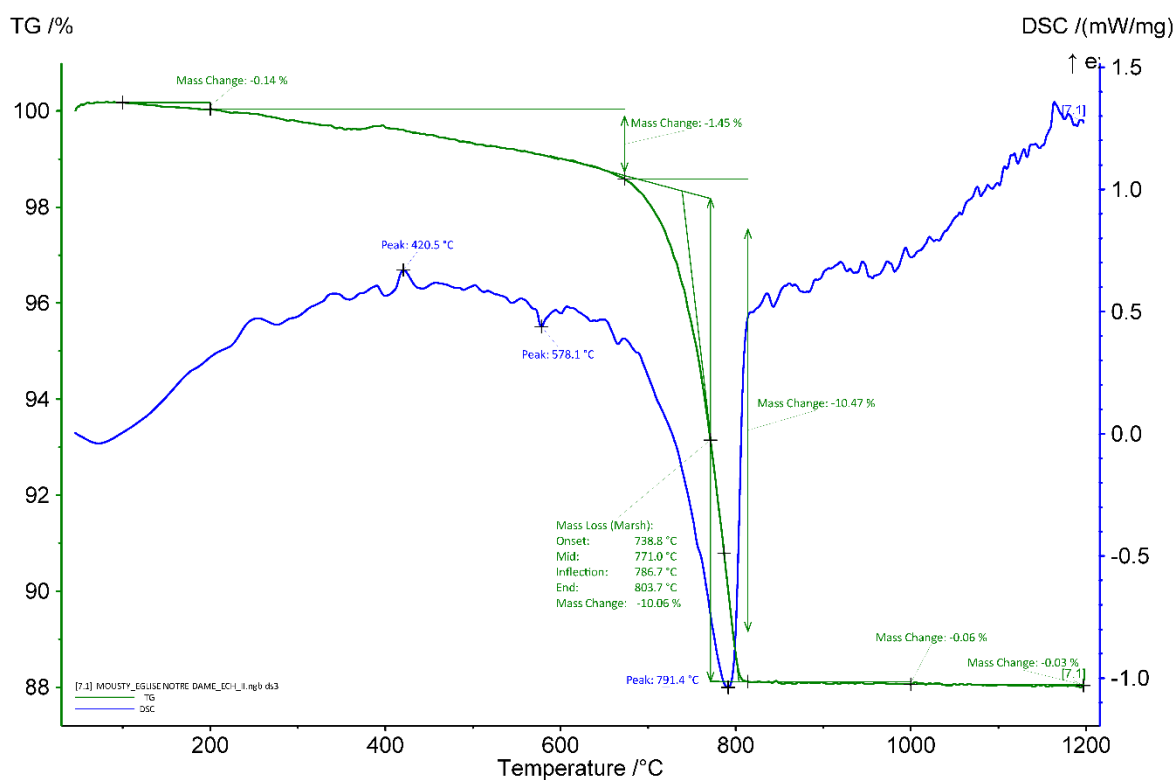
Figure 16: Coupled TG-DSC analysis of ECH.II upon heating to a temperature of 1200°C at a heating rate of 20°C/min under an inert atmosphere (He flushed at 50 ml/min). The weight loss determined by thermogravimetric analysis (TG, wt%, green curve) and the result of the differential scanning calorimetric analysis (DSC, mW/mg, blue curve) are both presented.
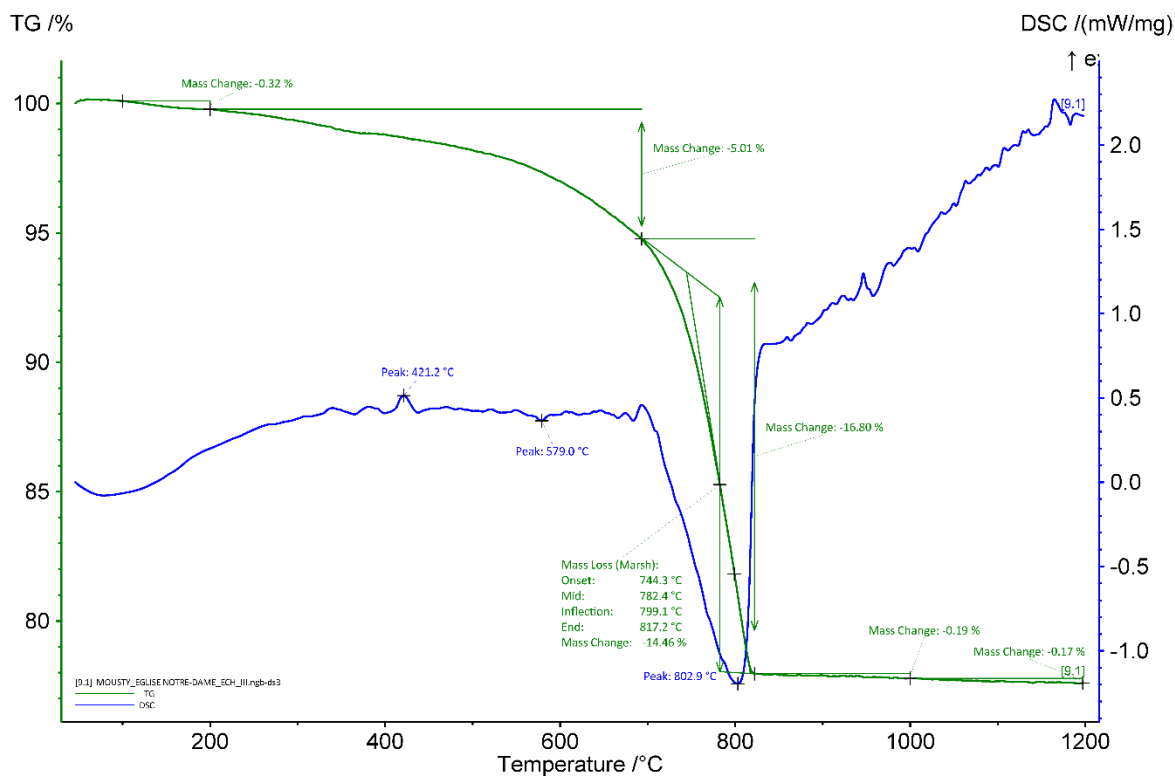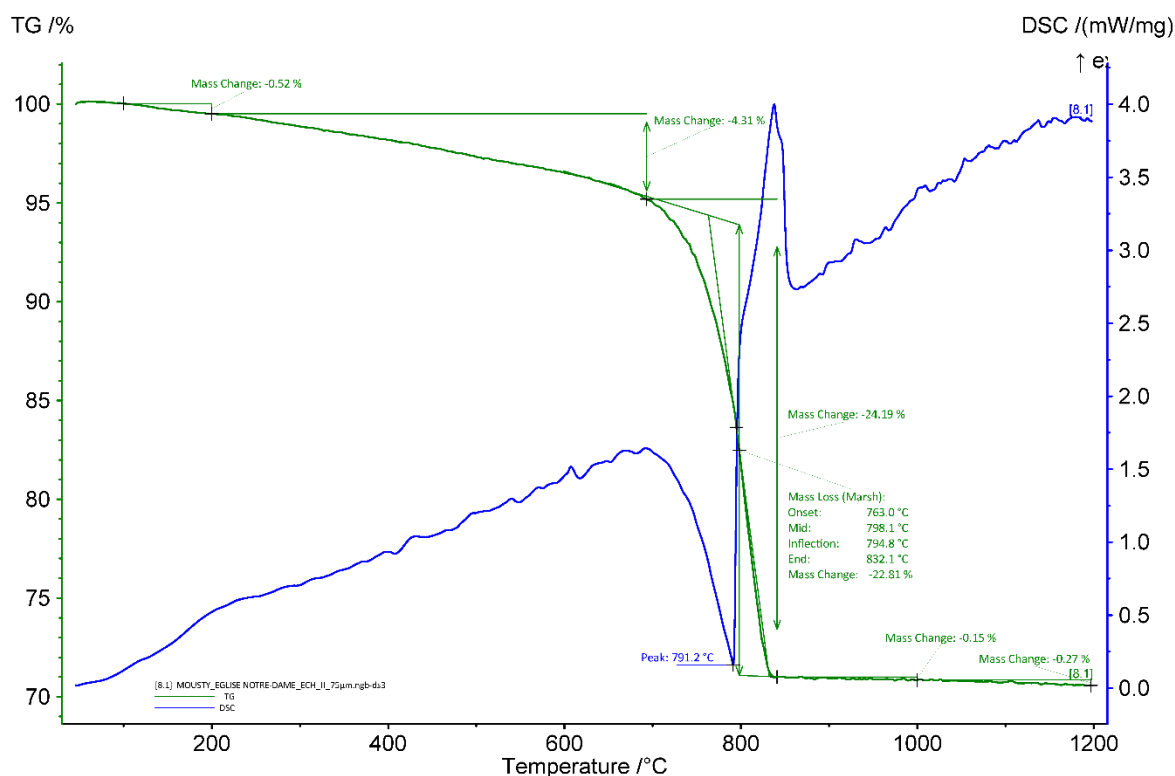

Figure 17: Coupled TG-DSC analysis of ECH.III upon heating to a temperature of 1200°C at a heating rate of 20°C/min under an inert atmosphere (He flushed at 50 ml/min). The weight loss determined by thermogravimetric analysis (TG, wt%, green curve) and the result of the differential scanning calorimetric analysis (DSC, mW/mg, blue curve) are both presented.
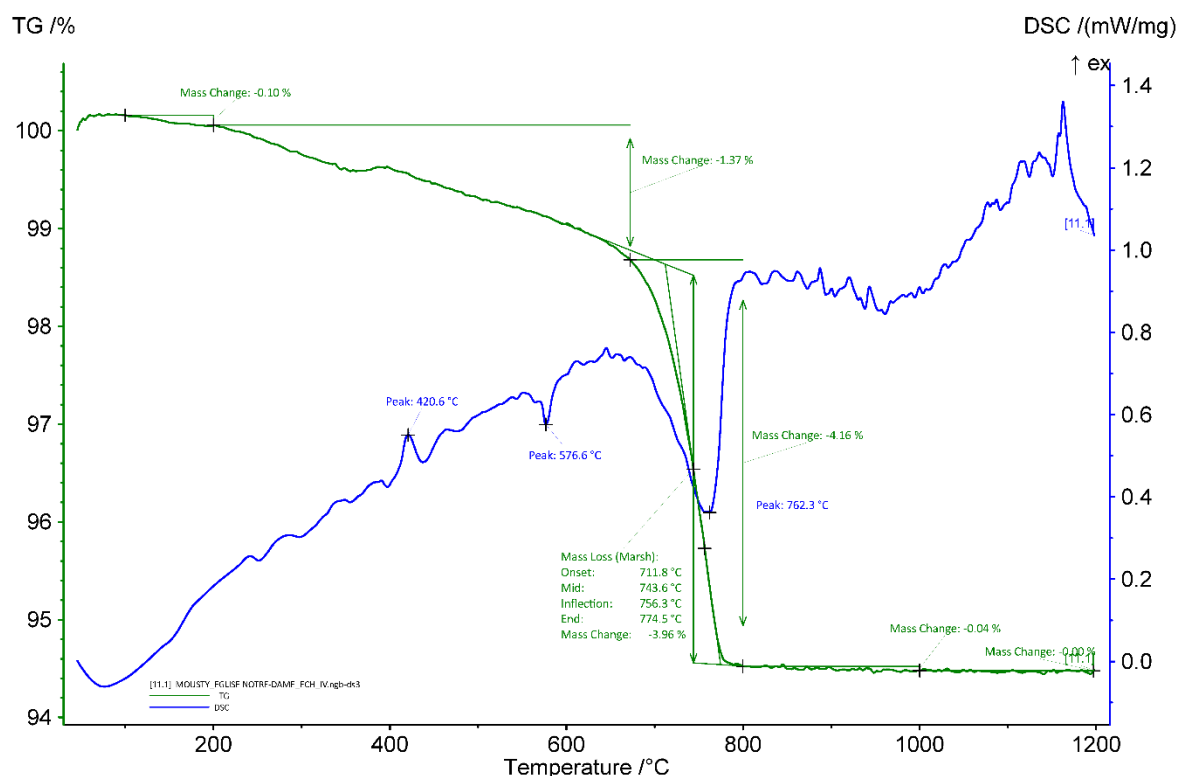
Figure 18: Coupled TG-DSC analysis of ECH.IV upon heating to a temperature of 1200°C at a heating rate of 20°C/min under an inert atmosphere (He flushed at 50 ml/min). The weight loss determined by thermogravimetric analysis (TG, wt%, green curve) and the result of the differential scanning calorimetric analysis (DSC, mW/mg, blue curve) are both presented.

Grinding/particle separation

The bedding mortar and the outdoor render were ground before the start of the project. For the wall painting plaster fragment 3/3, the paint layer was scratched away before grinding. The white layer present on ECH.I was removed thanks to a sharp tool before the gentle grind. For ECH.II, a piece of charcoal was extracted from the mortar, the white layer was removed thanks to a sharp tool & the surface was cleaned with a metallic brush. ECH.III was scratched with a metallic brush to remove the black/grey dust, a large piece of charcoal (1-2 cm) was found when grinding and dated, and a lump was extracted to be dated.

FTIR on powders with particle size <75 μm

The FTIR spectra of the powdered bedding mortar, outdoor render and wall painting fragment used for radiocarbon dating are presented in Figure 19. For the bedding mortar (Figure 19, top), the spectrum is similar to the spectrum of the binder (Figure 3a), no clay nor nitrates are present as it was the case for the inclusions present in the mortar. The spectrum obtained for the outdoor render (Figure 19, middle) contains the same components as the bedding mortar in addition to gypsum that was present in the other inclusions of the outdoor render as well as organic matter. The spectrum of the powder obtained from the wall painting plaster fragment 3/3 (Figure 19, bottom) is the same as the spectrum of the binder (Figure 3c) but also contains some organic matter.
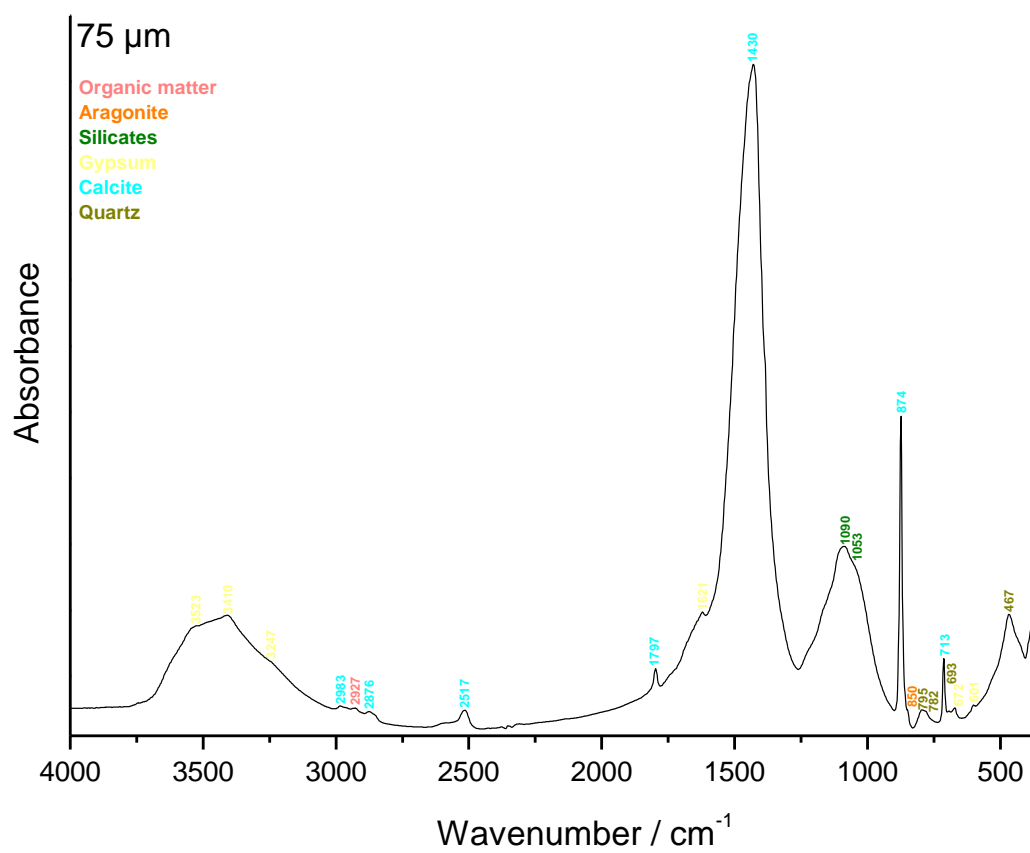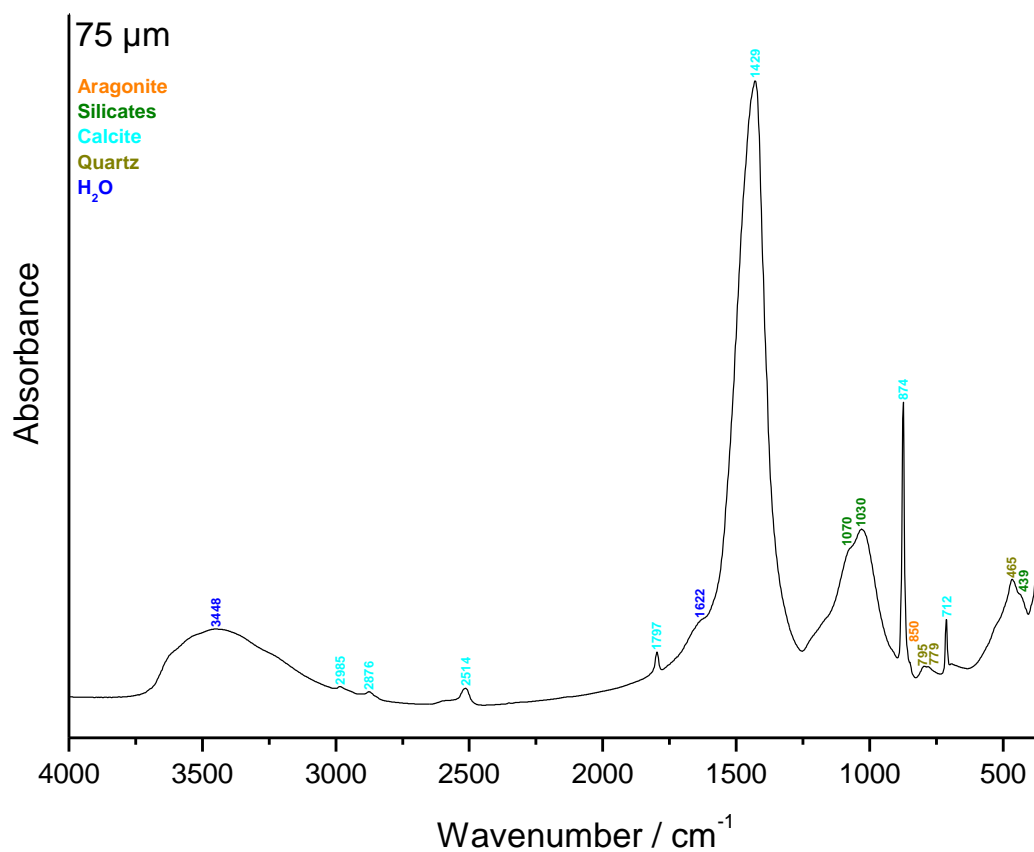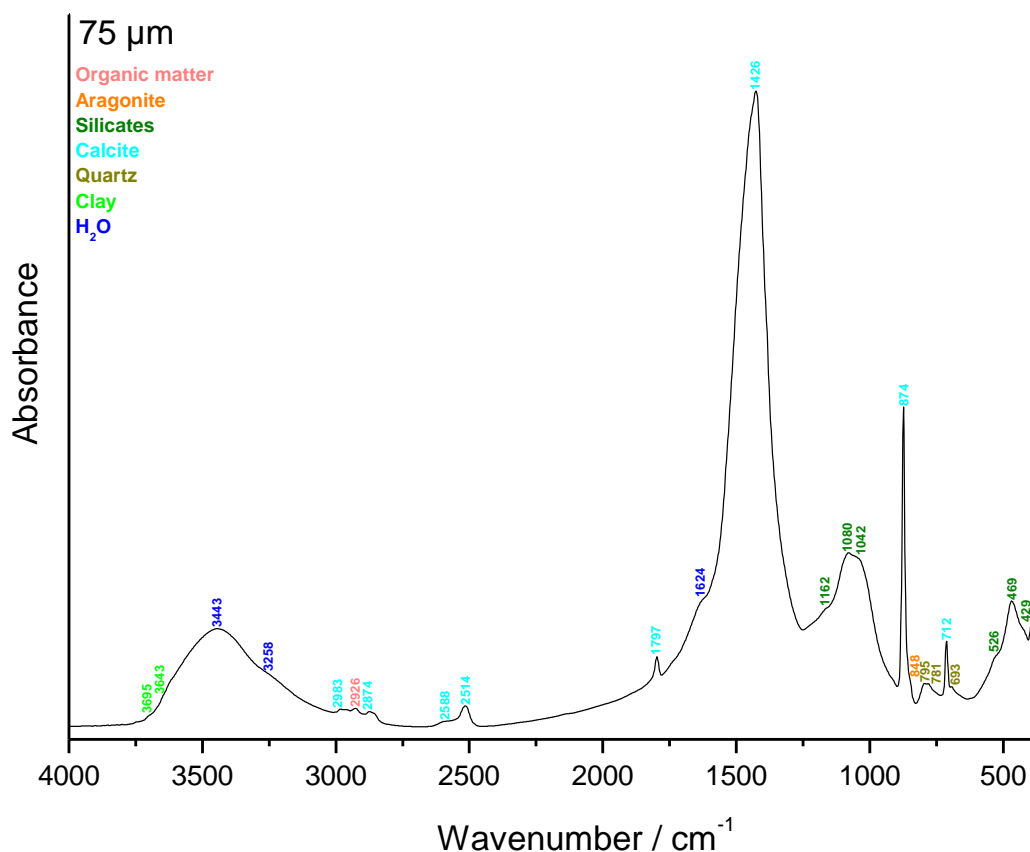
Figure 19: FTIR spectra obtained on the powders with particle size < 75 μm of the mortar samples from the bedding mortar (top), the outdoor render (middle) and from the wall painting plaster fragment 3/3 (bottom).

TGA on powders with particle size <75 μm

For ECH.III and IV, the aHI is the same for the powder with particle size <75 μm and the whole mortar sample (34 and 30 %, respectively). The other samples show a difference between the two values: for the bedding mortar, it decreased (from 68% for the whole sample to 38% for the powder) and for the other samples, it increased. These differences could be explained by the presence of clay that end up in more or less important quantities in the powdered sieved samples. The quantity of carbonates is higher in the powders compared to the whole samples since a large part of the sand is removed (~37 wt% for the bedding mortar, 35 w% for the outdoor render, 46 w% for the wall painting fragment, 38 w% for ECH.I, 52 w% for ECH.II, 46 w% for ECH.III, and 30 wt% for ECH.IV). Indeed, no quartz was detected in the powders. Gypsum was detected in the powdered outdoor render and ECH.III at 2.5 and 1.2 wt%, respectively (peak around 139°C – Figure 21 and 141°C – Figure 25) (Moropoulou, Bakolas, and Bisbikou 2000). At 244°C a peak is observed for the powdered ECH.III (Figure 25) but was not attributed. For the bedding mortar (Figure 21), a peak around ~417°C is observed and might again be due to the release of water from calcium hydroxide (Moropoulou, Bakolas, and Bisbikou 1995; Klimesch and Ray 1996) and might indicate that the mortar did not fully carbonated. This was not observed for the whole mortar sample. It was probably present in too low concentration to be noticeable. The end temperatures of calcium carbonate decomposition are 813, 808, 835, 817, 832, 802 and 804°C for the powdered bedding mortar, outdoor render, wall painting fragment, for ECH.I, ECH.II, ECH.III, and ECH.IV, respectively. For most of

them, it is higher compared to the whole samples. A possible explanation could be that the powder is more pure compared to the whole mortar sample which increases the decomposition temperature. Only for ECH.III, it is lower compared to the whole sample maybe because the underburned lime lumps did not end up in the powder.
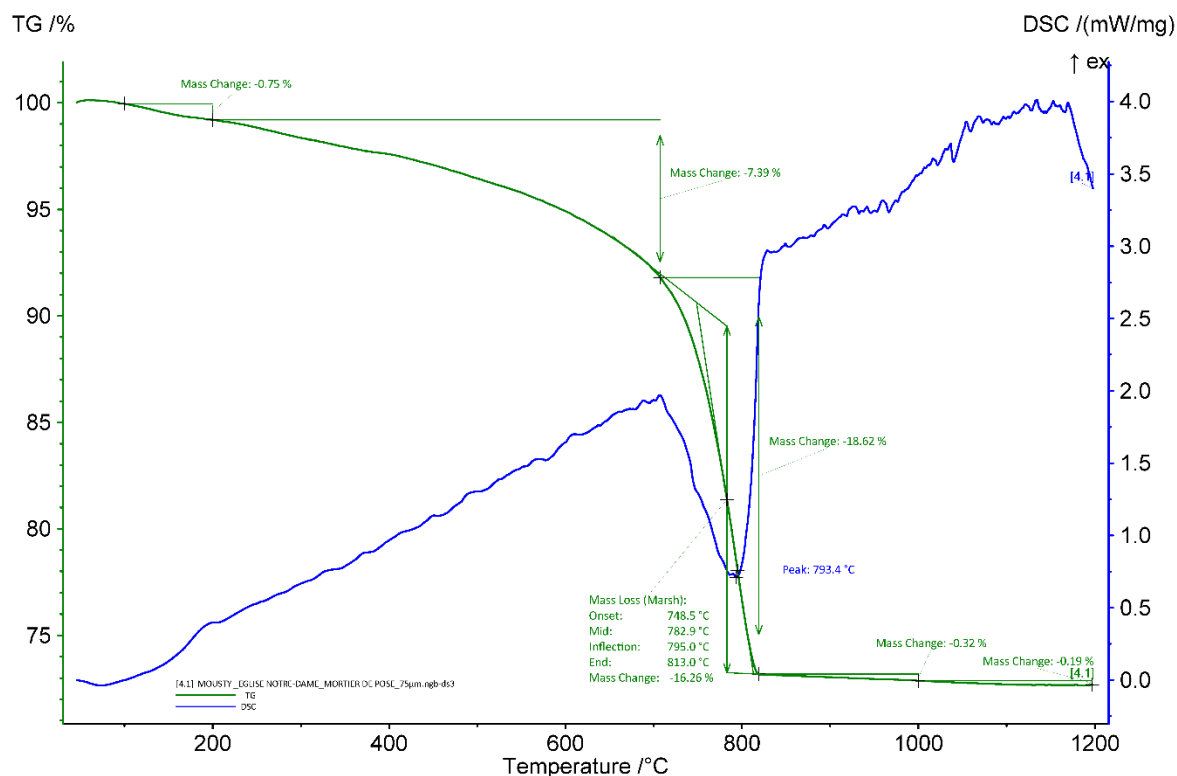
Figure 20: Coupled TG-DSC analysis of the powdered bedding mortar with particle size < 75 µm upon heating to a temperature of 1200°C at a heating rate of 20°C/min under an inert atmosphere (He flushed at 50 ml/min). The weight loss determined by thermogravimetric analysis (TG, wt%, green curve) and the result of the differential scanning calorimetric analysis (DSC, mW/mg, blue curve) are both presented.
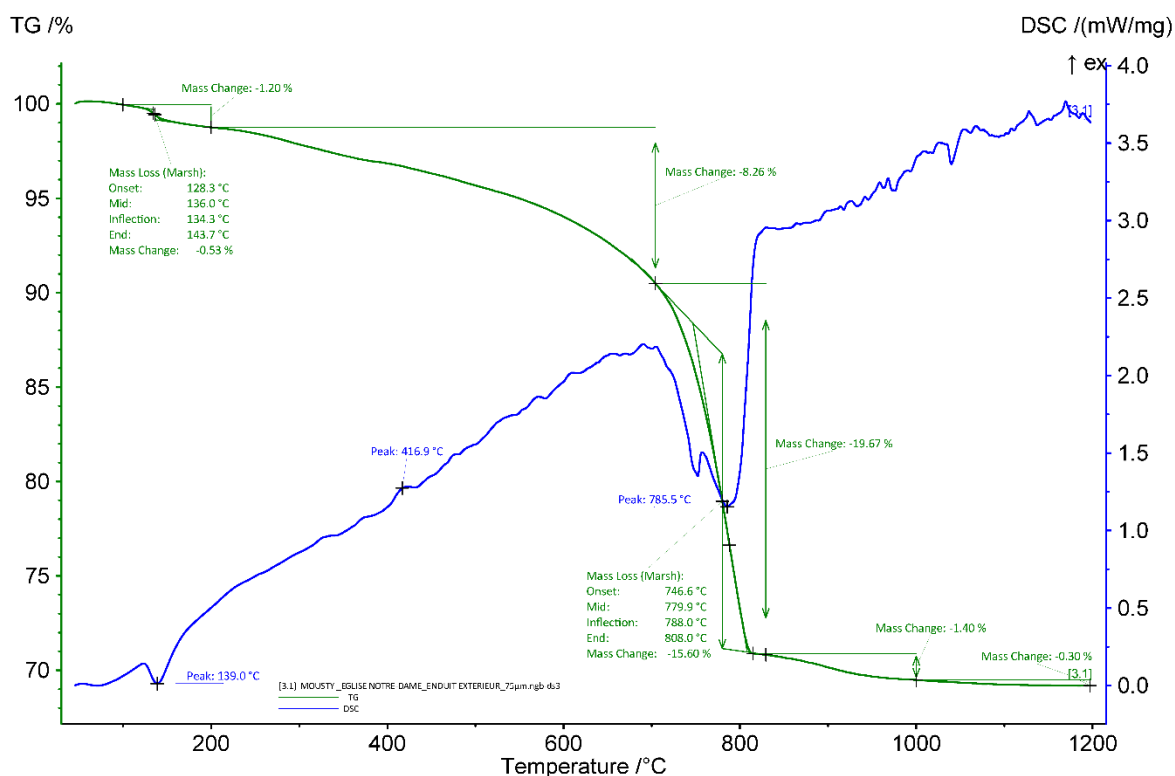
Figure 21: Coupled TG-DSC analysis of the powdered outdoor render with particle size < 75 µm upon heating to a temperature of 1200°C at a heating rate of 20°C/min under an inert atmosphere (He flushed at 50 ml/min). The weight loss determined by thermogravimetric analysis (TG, wt%, green curve) and the result of the differential scanning calorimetric analysis (DSC, mW/mg, blue curve) are both presented.

Figure 22: Coupled TG-DSC analysis of the powdered wall painting plaster fragment 3/3 with particle size < 75 µm upon heating to a temperature of 1200°C at a heating rate of 20°C/min under an inert atmosphere (He flushed at 50 ml/min). The weight loss determined by thermogravimetric analysis (TG, wt%, green curve) and the result of the differential scanning calorimetric analysis (DSC, mW/mg, blue curve) are both presented.

Figure 23: Coupled TG-DSC analysis of the powdered ECH.I with particle size < 75 µm upon heating to a temperature of 1200°C at a heating rate of 20°C/min under an inert atmosphere (He flushed at 50 ml/min). The weight loss determined by thermogravimetric analysis (TG, wt%, green curve) and the result of the differential scanning calorimetric analysis (DSC, mW/mg, blue curve) are both presented.

Figure 24: Coupled TG-DSC analysis of the powdered primer ECH.II with particle size < 75 µm upon heating to a temperature of 1200°C at a heating rate of 20°C/min under an inert atmosphere (He flushed at 50 ml/min). The weight loss determined by thermogravimetric analysis (TG, wt%, green curve) and the result of the differential scanning calorimetric analysis (DSC, mW/mg, blue curve) are both presented.
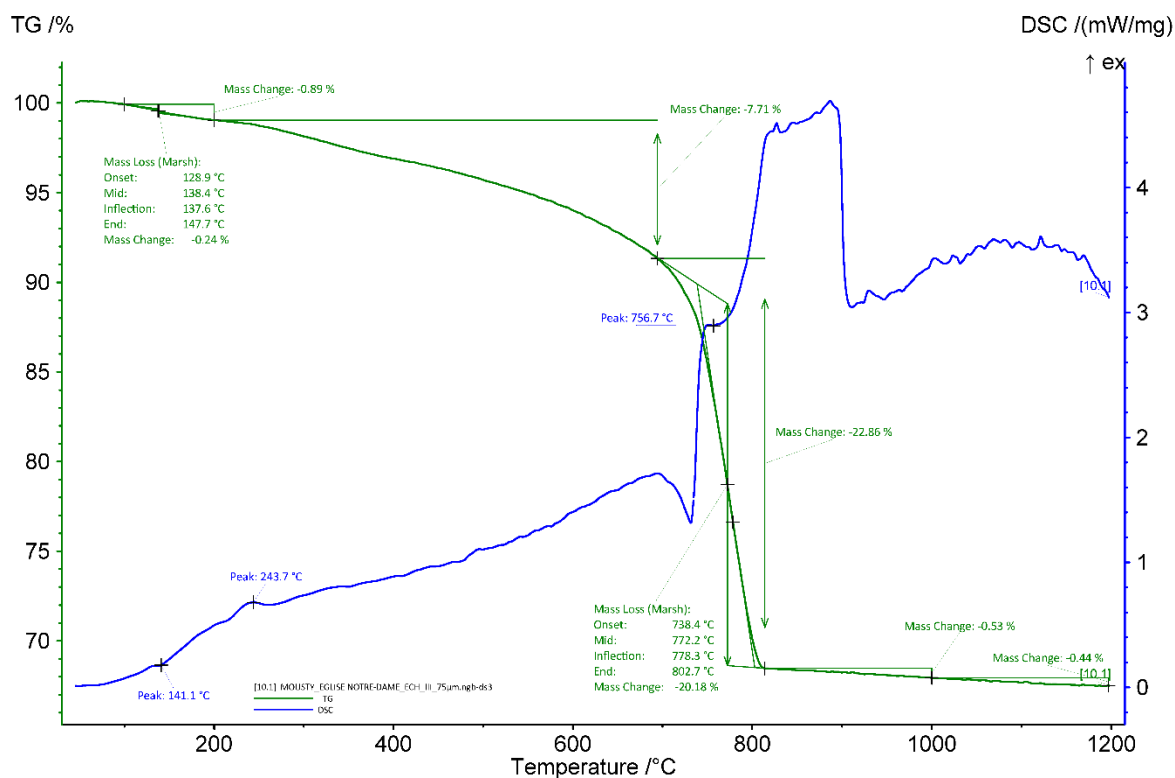
Figure 25: Coupled TG-DSC analysis of the powdered ECH.III with particle size < 75 μm upon heating to a temperature of 1200°C at a heating rate of 20°C/min under an inert atmosphere (He flushed at 50 ml/min). The weight loss determined by thermogravimetric analysis (TG, wt%, green curve) and the result of the differential scanning calorimetric analysis (DSC, mW/mg, blue curve) are both presented.
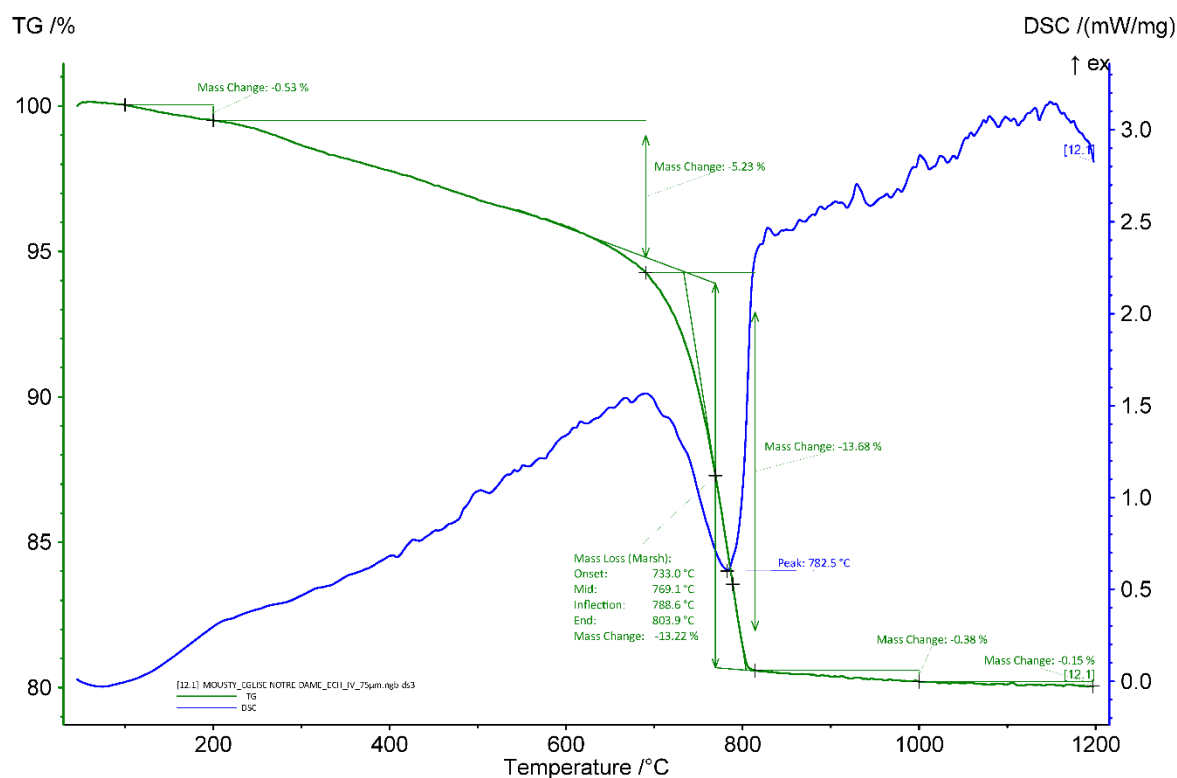
Figure 26: Coupled TG-DSC analysis of the powdered ECH.IV with particle size < 75 μm upon heating to a temperature of 1200°C at a heating rate of 20°C/min under an inert atmosphere (He flushed at 50 ml/min). The weight loss determined by thermogravimetric analysis (TG, wt%, green curve) and the result of the differential scanning calorimetric analysis (DSC, mW/mg, blue curve) are both presented.

Radiocarbon results

The test prior to the CO_2 extraction revealed an amount of carbon (Table 4) of around 5-6 % for the samples located around the window frame. ECH.III coming from the masonry in the nave in contact with the choir contains a higher carbon content (~7%) and ECH.IV used for laying the eaves purlin on the masonry shows a lower percentage (~3%). The later was very friable when sampled and shows a higher microporosity due to a partial dissolution of the binder.

RICH	Sample type	Method	C (%)	σ (%)	m (g)	Age BP	Calibrated date (95.4%)	Age BP extrapolated	Calibrated date (95.4%)	Age BP extrapolated with stat	Calibrated date (oxcal - 95.4%)	Age BP average first dates	Calibrated date (95.4%)	Reliability of dating
29229 (bedding mortar)	mortar <75 μm	8 fractions	5.22	0.27	2.03	-	-	877 ± 25	1047-1226 calAD	833 ± 25	1170-1265 calAD	(3 first fractions) 872 ± 13	1164-1218 calAD	☑
29233 (outdoor render)	mortar <75 μm	8 fractions	5.47	0.06	1.82	-	-	811 ± 25	1180-1275 calAD	788.5 ± 16.6	1224-1273 calAD	(F1. F4 & F5) 850 ± 13	1166-1226 calAD	☑
31814 (wall painting plaster)	mortar <75 μm	8 fractions	5.55	0.14	1.76	-	-	842 ± 21	1165-1265 calAD	831.7 ± 11.5	1179-1263 calAD	(4 first fractions) 841 ± 10	1170-1260 calAD	☑
34103 (ECH.I)	mortar <75 μm	8 fractions	5.12	0.03	1.9	-	-	877 ± 25	1047-1226 calAD	877 ± 14.1	1160-1219 calAD	(4 first fractions) 888 ± 13	1053-1217 calAD	☑
34110 (ECH.II)	mortar <75 μm	8 fractions	5.61	0.05	1.74	-	-	891 ± 27	1045-1222 calAD	897.8 ± 18.2	1047-1218 calAD	(3 first fractions) 891 ± 27	1045-1222 calAD	☑
34102 (ECH.II)	charcoal	HCl 8%	-	-	-	1186 ± 32	709-971 calAD	-	-	-	-	-	-	☑
34111 (ECH.II)	white layer on top of mortar	H_3PO_4	9.7	-	0.0341	494 ± 24	1407-1446 calAD	-	-	-	-	-	-	☑
34112 (ECH.III)	mortar <75 μm	8 fractions	5.86	0.03	1.66	-	-	781 ± 27	1222-1278 calAD	497 ± 29.9	1400-1451 calAD	(F2 & F4) 871 ± 15	1162-1219 calAD	☑
33878 (ECH.III)	charcoal	HCl 8%	40.01	-	0.00609	1028 ± 24	978-1040 calAD	-	-	-	-	-	-	☑
34113 (ECH.III)	lime lump	H_3PO_4	7.086	-	0.0605	979 ± 32	995-1159 calAD	-	-	-	-	-	-	☑
34114 (ECH.IV)	mortar <75 μm	10 fractions	3.26	0.18	2.84	-	-	797 ± 22	1220-1273 calAD	870.4 ± 14.8	1162-1219 calAD	(5 first fractions) 859 ± 10	1170-1220 calAD	☑

Table 4: Radiocarbon results

The dating of all binders with all the calculation methods (Table 4 and Figures 27-33) resulted in a calibrated date ranging from 1045 to 1278 calAD (781 to 898 BP) except for the extrapolation with statistic of ECH.III that provides a younger date (1400-1451 calAD). Some of them (bedding mortar, ECH.I & ECH.II) fall within the time framework obtained for the window frame of the church old structure by dendrochronology (1077d), and all fit into the one of the younger roof structure (1205-1206d). The charcoal pieces extracted from ECH.II (709-971 calAD) and ECH.III (978-1040 calAD) are older compared to window frame which could be caused by an old wood effect. These give a terminus post quem that include the window frame. The lime lump extracted from ECH.III provides a date (995-1159 calAD) fitting in between the result for the charcoal and the binder which encompass only the date of the old window frame (and not the newer roof structure).

Bedding mortar

$y = 41{,}023\ln(x) + 877{,}05$
$R^2 = 0{,}9154$

x-axis: CO_2 fraction / %
y-axis: ^{14}C determination / BP
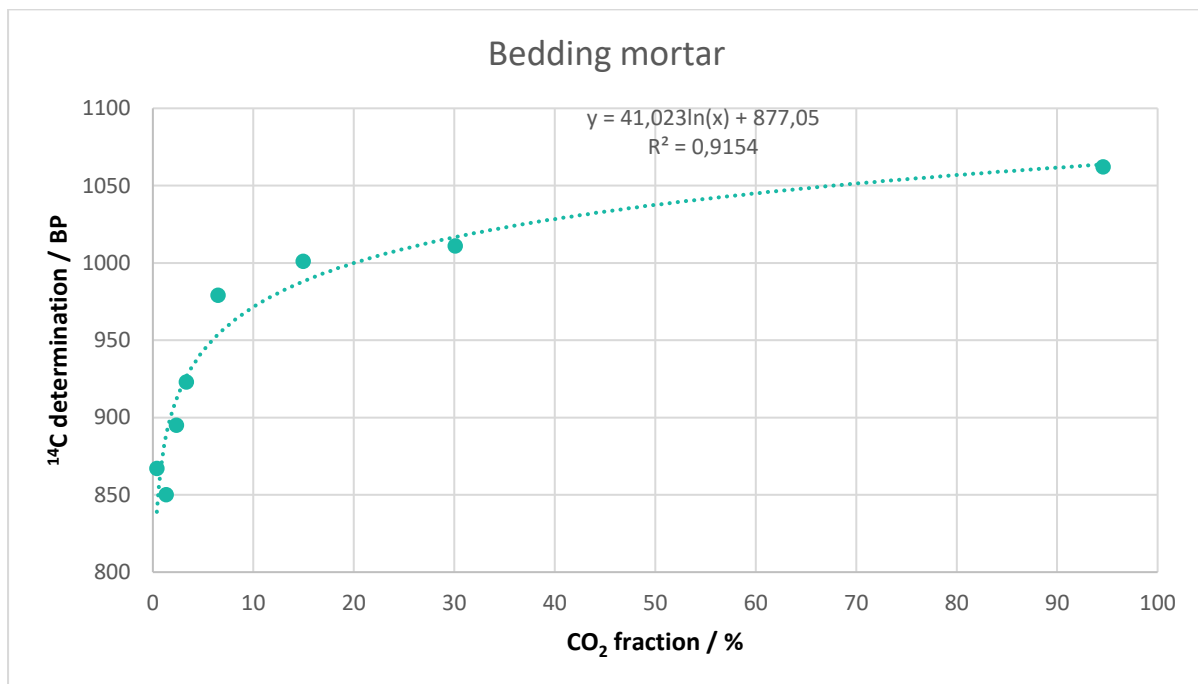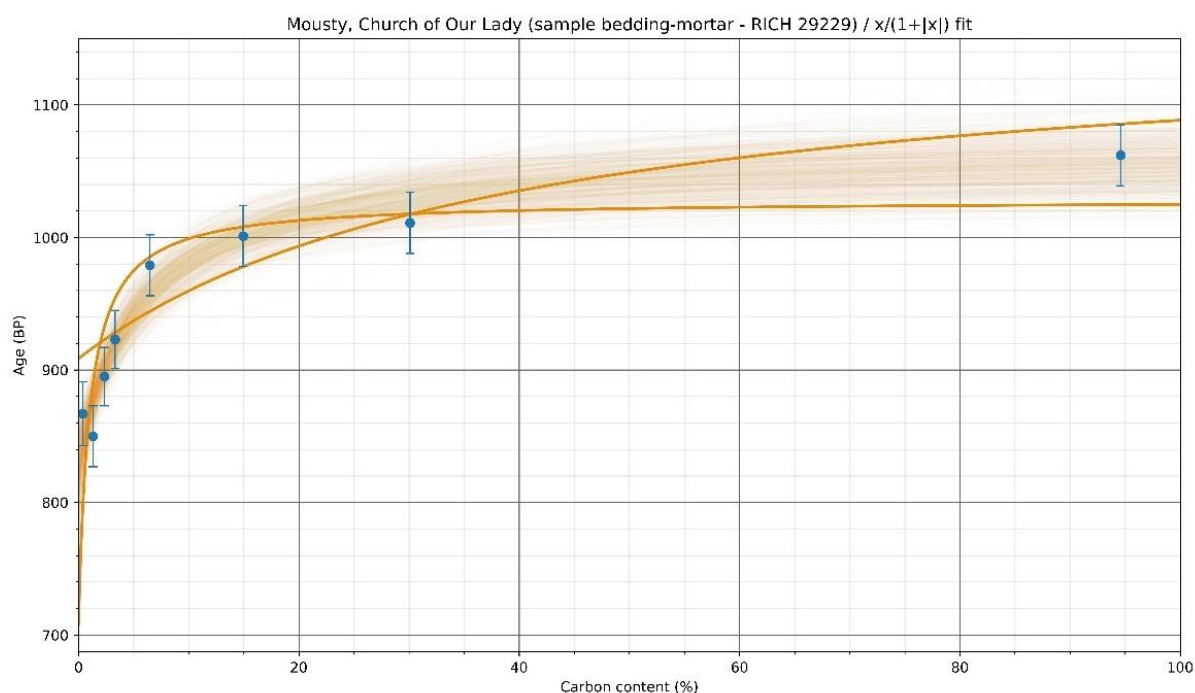
Figure 27: Radiocarbon results for the powdered bedding mortar (RICH-29229) with particles < 75 µm as a function of the CO_2 fraction (the graph at the bottom show the statistic on the results).
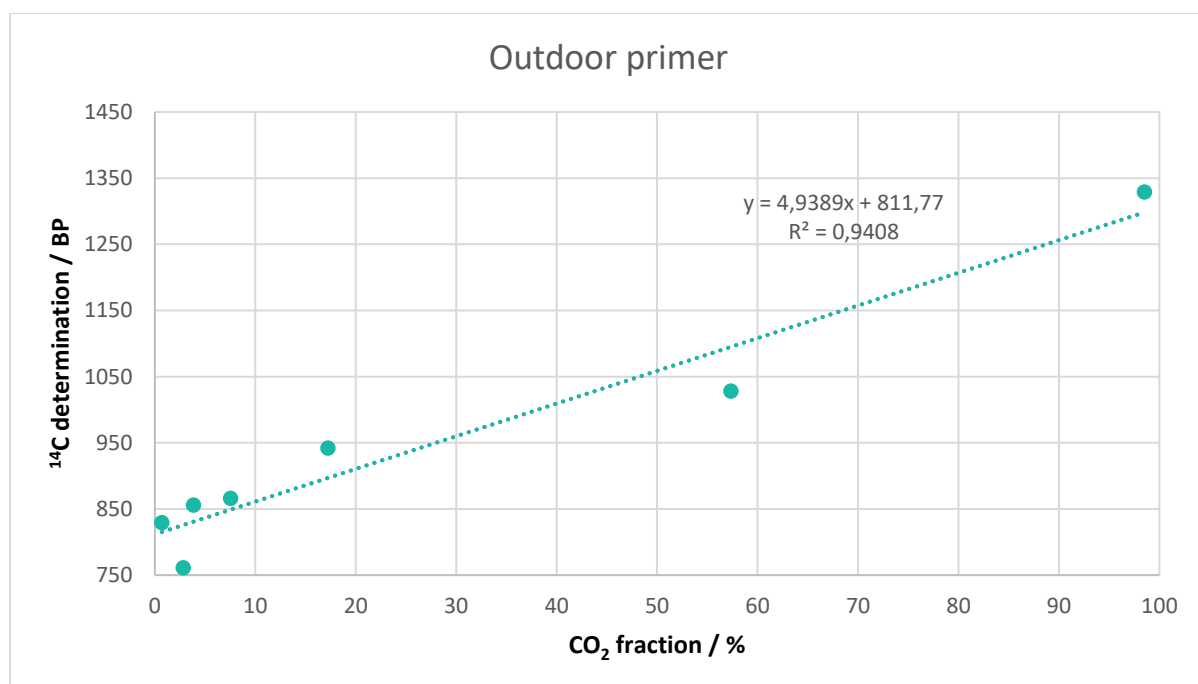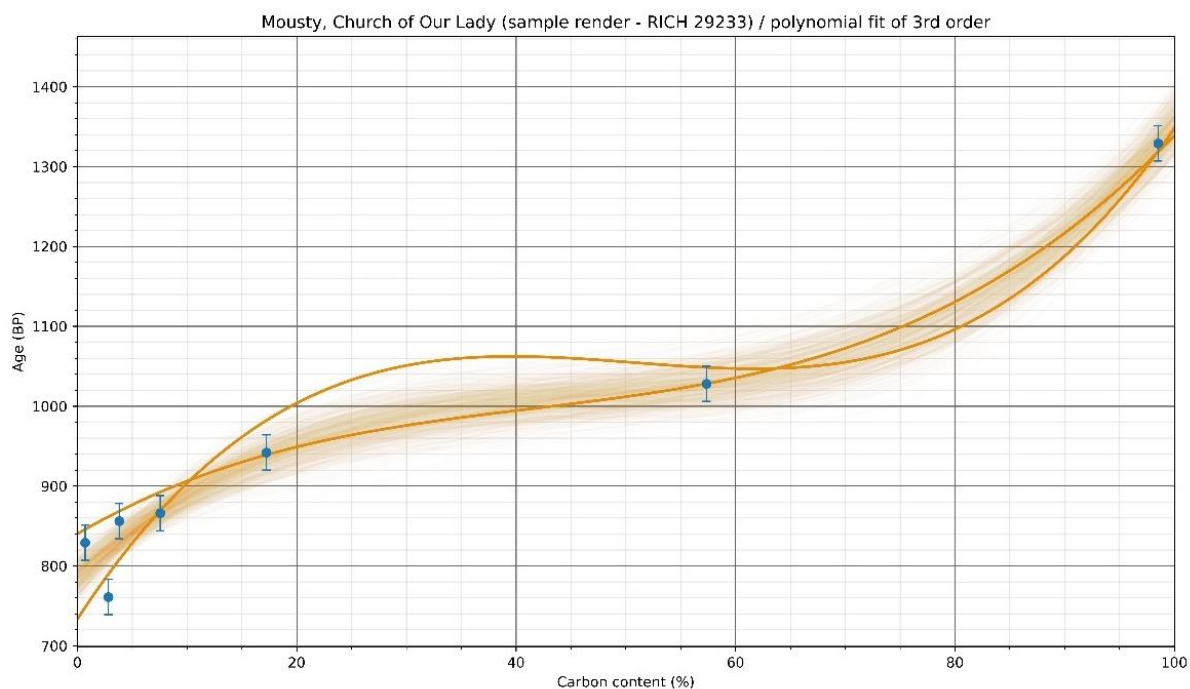
Figure 28: Radiocarbon results for the powdered outdoor render (RICH-29223) with particles < 75 µm as a function of the CO_2 fraction (the graph at the bottom show the statistic on the results).
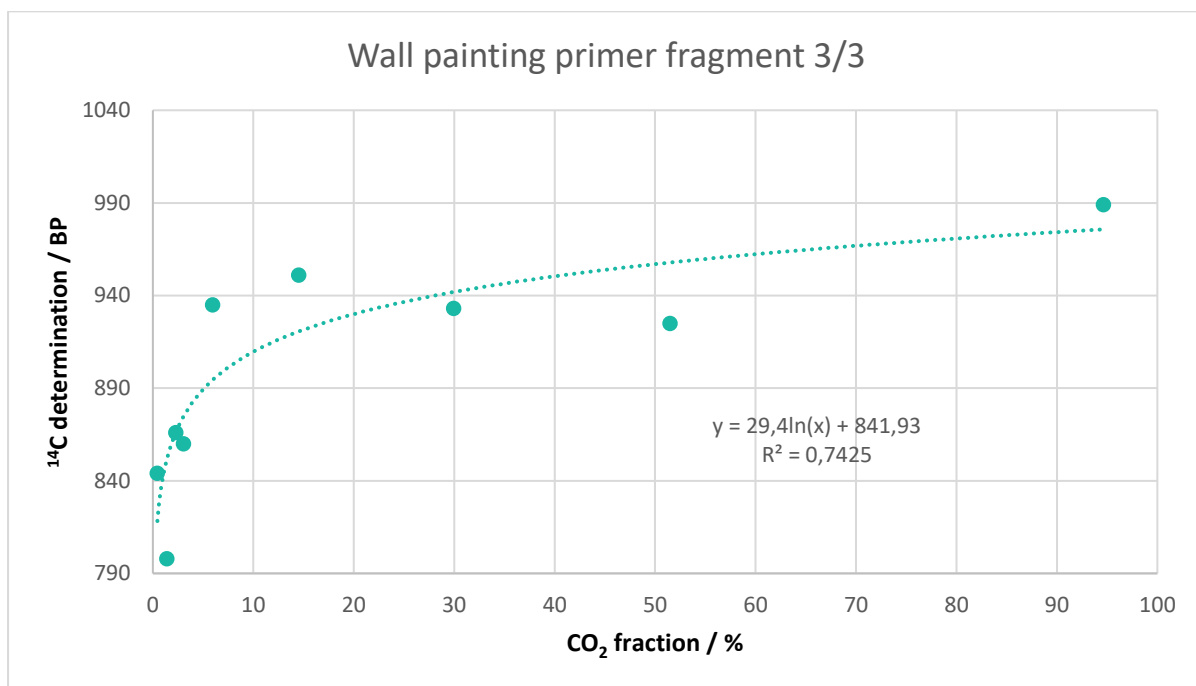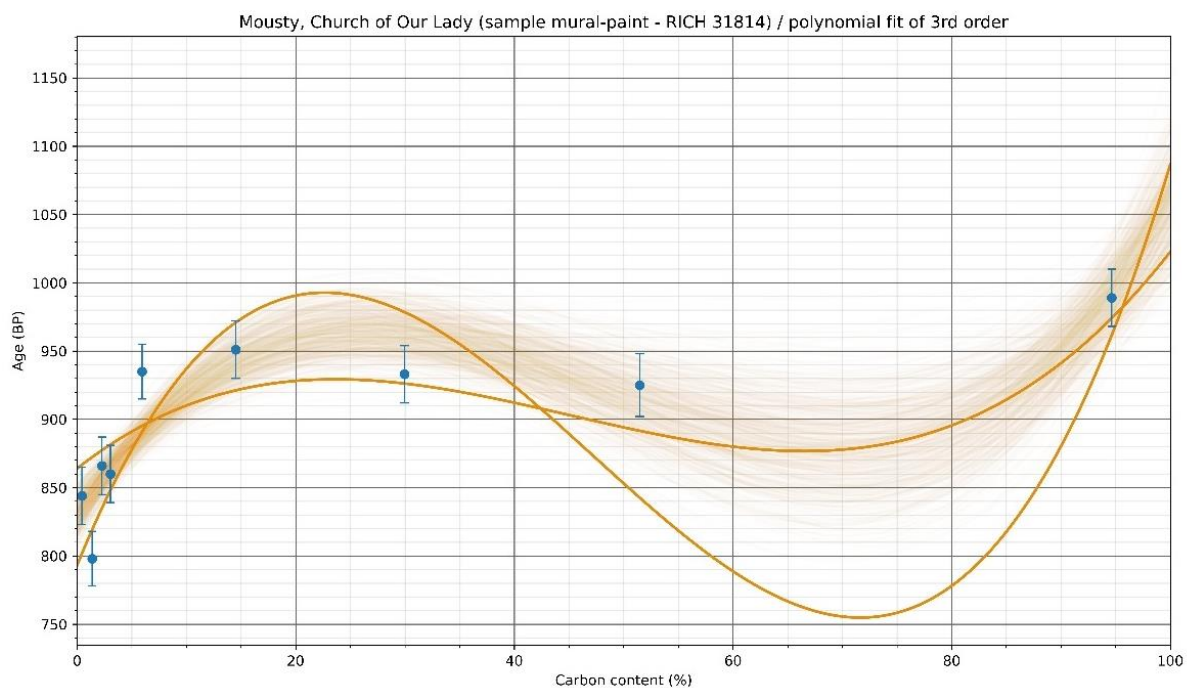
Figure 29: Radiocarbon results for the powdered wall painting plaster fragment 3/3 (RICH-31814) with particles < 75 μm as a function of the CO_2 fraction (the graph at the bottom show the statistic on the results).
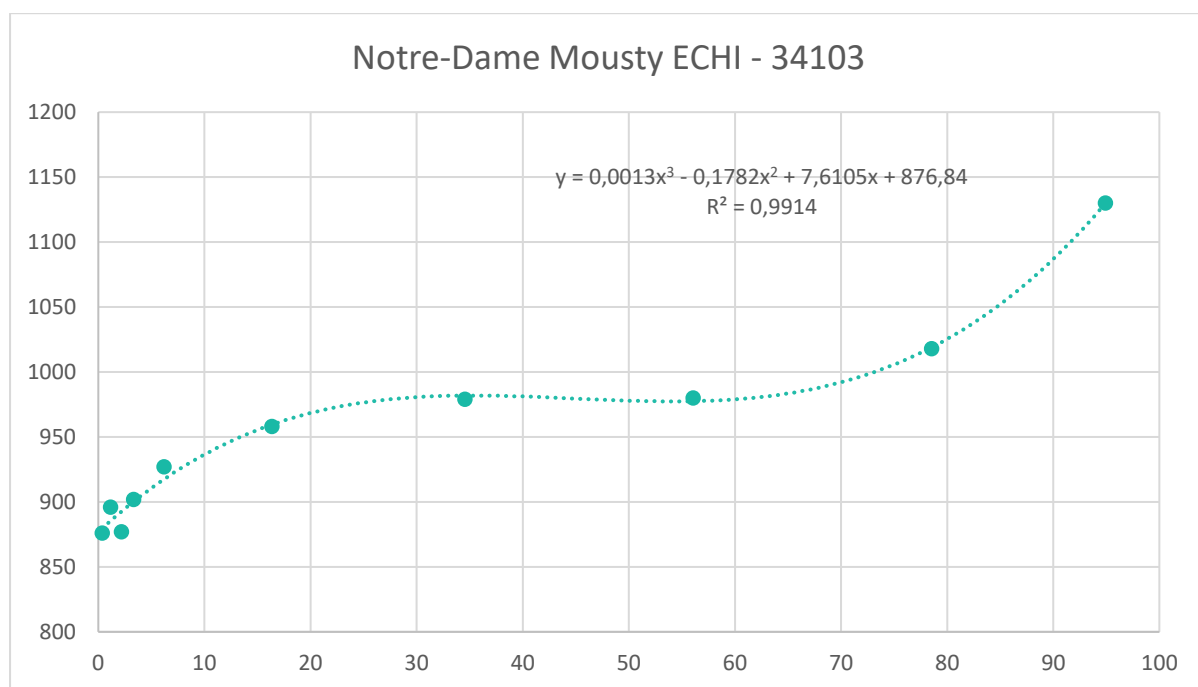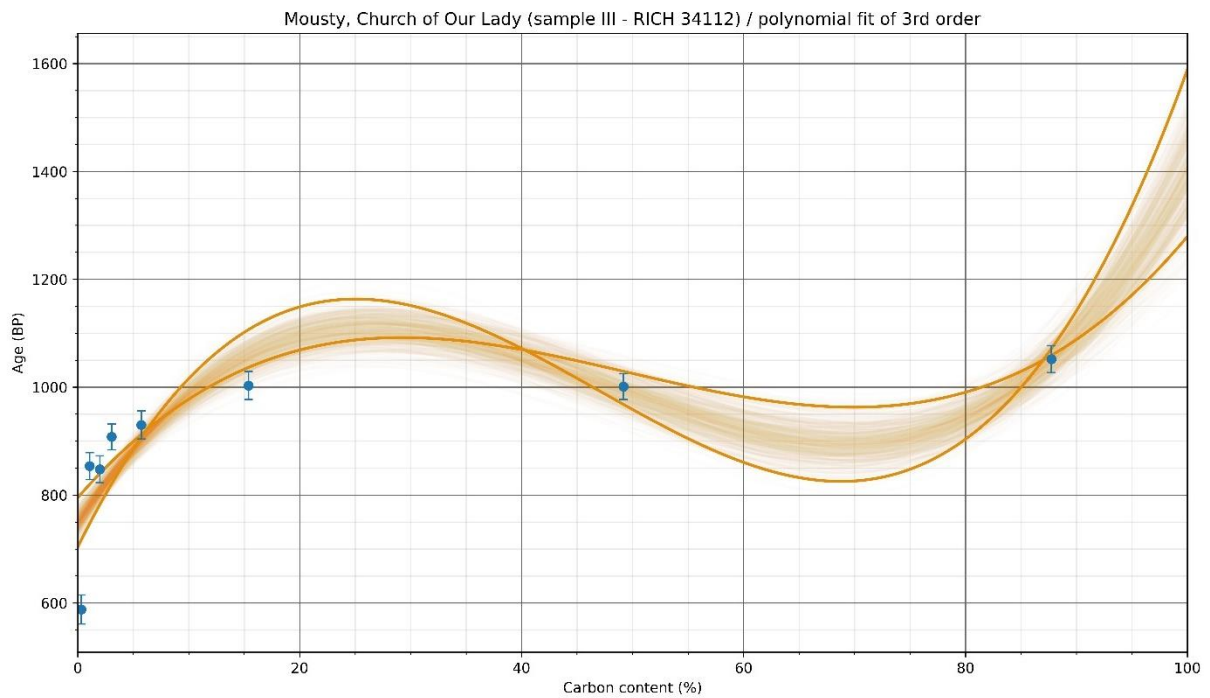
Figure 30: Radiocarbon results for the powdered ECH.I (RICH-34103) with particles < 75 μm as a function of the CO_2 fraction (the graph at the bottom show the statistic on the results).
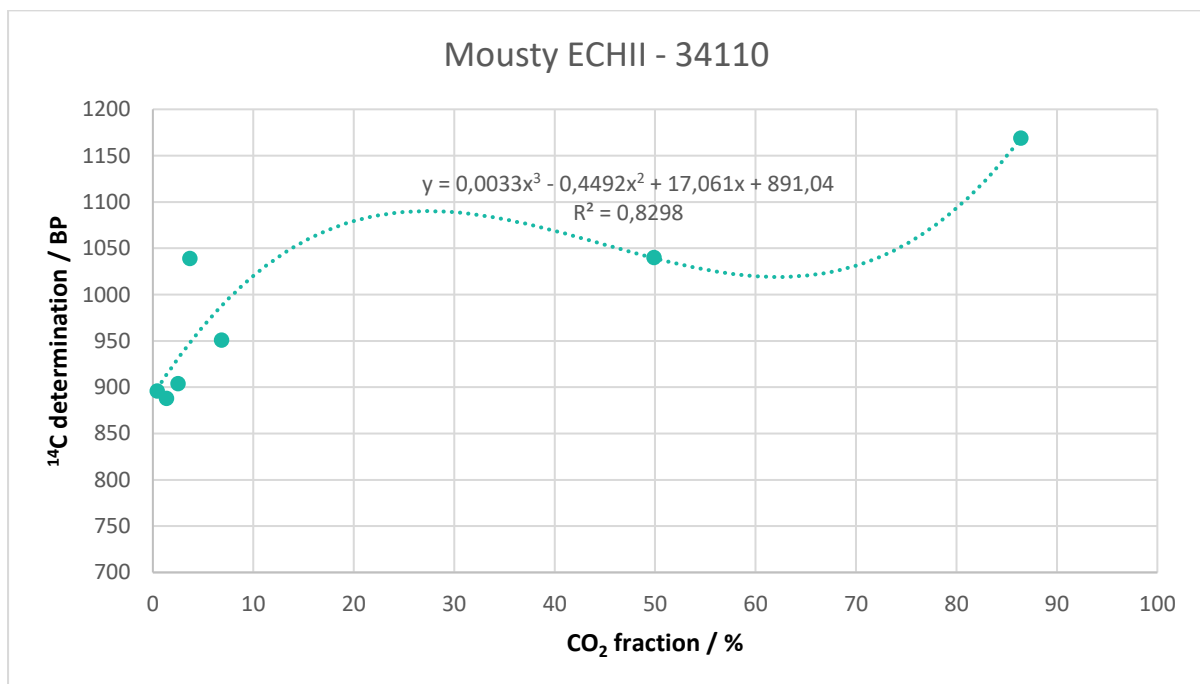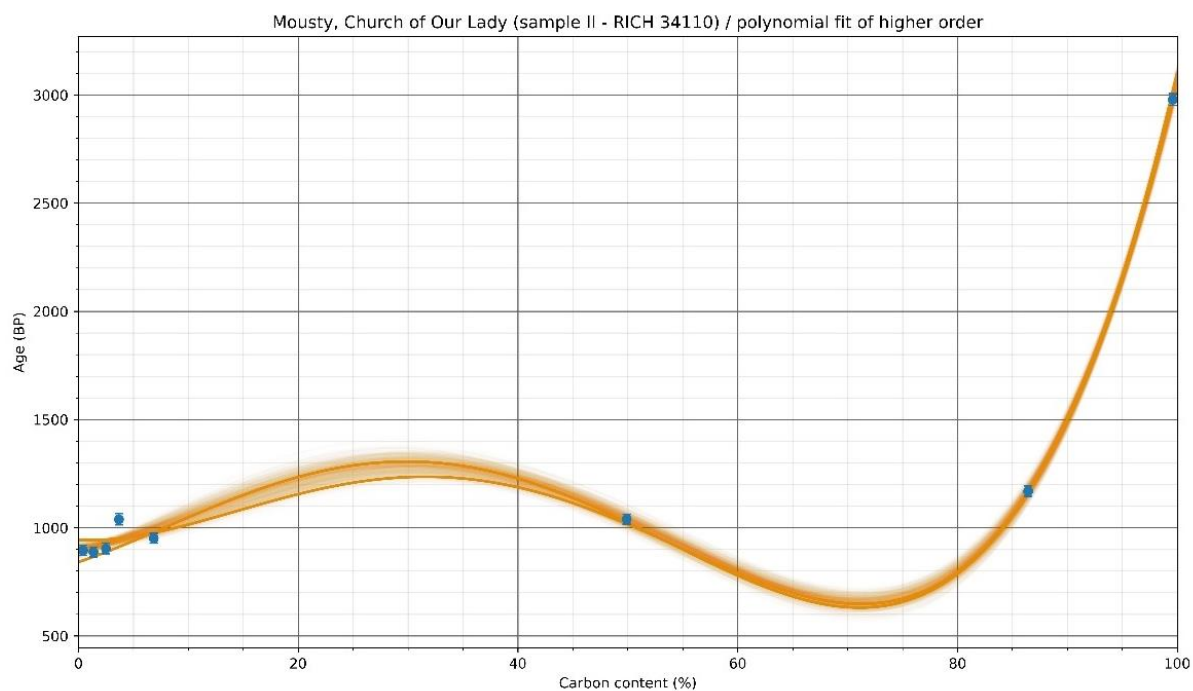
Figure 31: Radiocarbon results for the powdered ECH.II (RICH-34110) with particles < 75 µm as a function of the CO_2 fraction (the graph at the bottom show the statistic on the results).
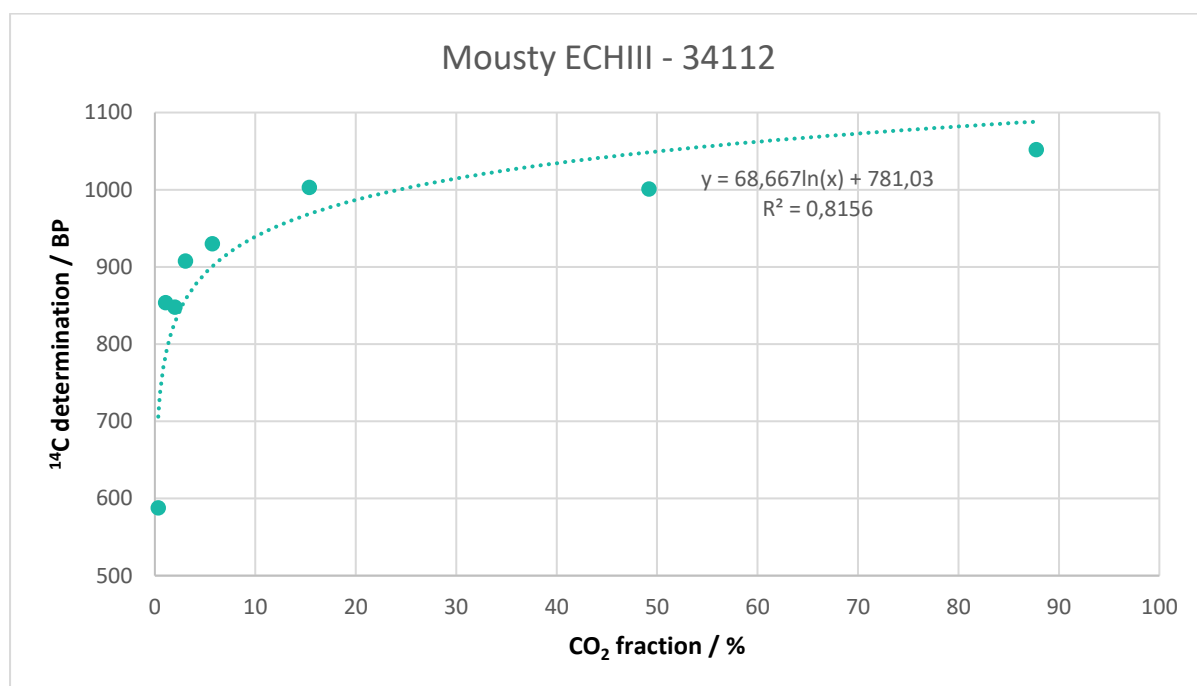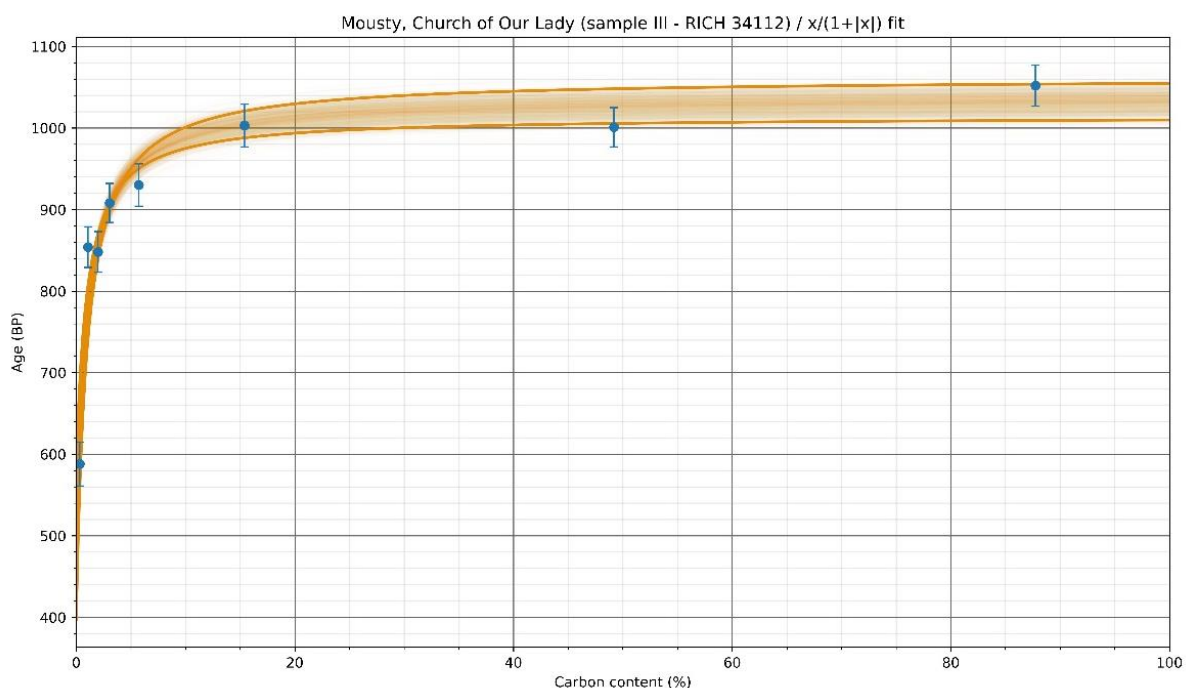
Figure 32: Radiocarbon results for the powdered ECH.III (RICH-34112) with particles < 75 μm as a function of the CO_2 fraction (the graph at the bottom show the statistic on the results).
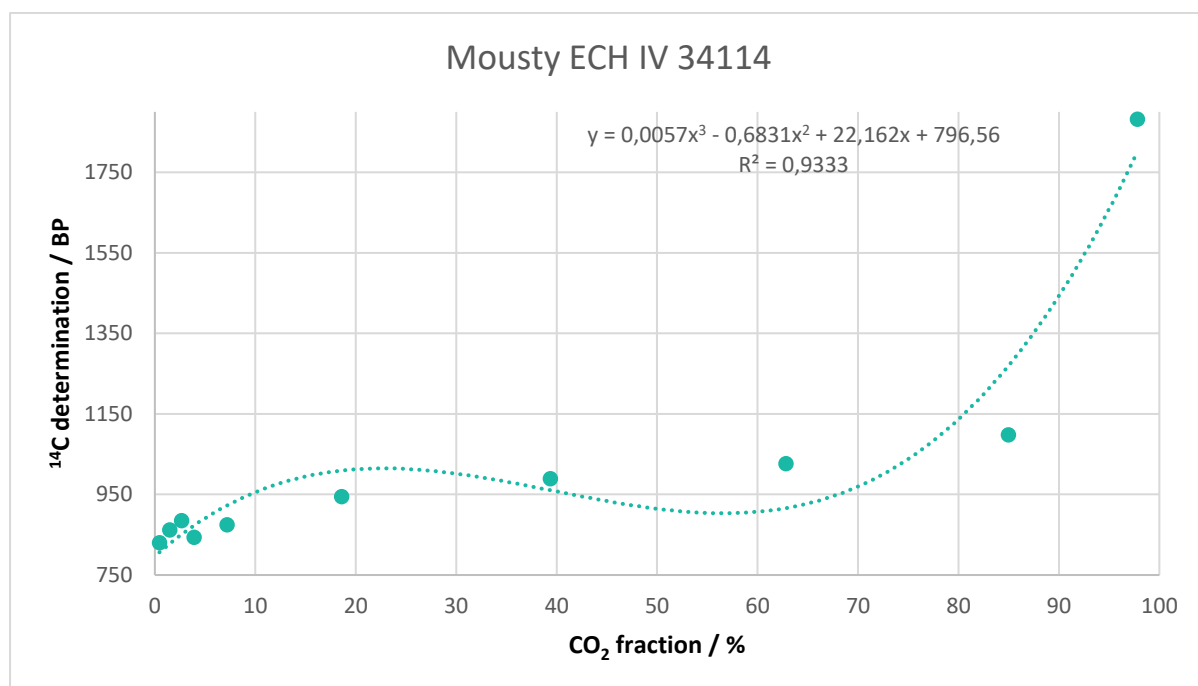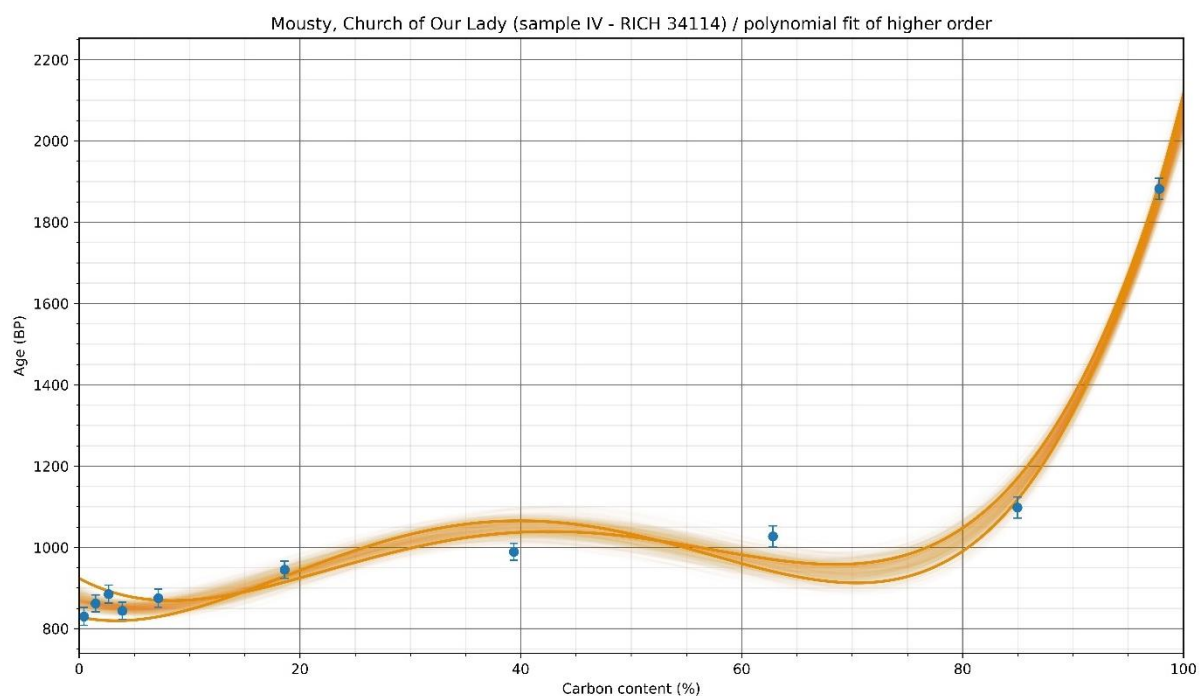
Figure 33: Radiocarbon results for the powdered ECH.IV (RICH-34114) with particles < 75 μm as a function of the CO_2 fraction (the graph at the bottom show the statistic on the results).

Conclusions

The radiocarbon dating measurements show that the bedding mortar of the old north gutter wall is slightly older than the outdoor render, which seems consistent. The dating range for the wall painting plaster is fairly similar to the bedding mortar and the outdoor render (between 1170 and 1265). At first glance. it is disappointing to find that the dating ranges for the bedding mortar and the outdoor plaster do not lie around the terminus post quem provided by the primitive window frame (1077), at least for the bedding mortar, since it originally supported the primitive frame which has now disappeared. However. It is important to bear in mind that we are not actually dating the mortar's application but rather its carbonation, a process that can take several years or even decades depending on environmental conditions and on the mortar composition. While the ranges obtained for the bedding mortar and the outdoor plaster do not fit in as hoped with the time constraints provided by dendrochronology, they should not be considered at odds due to the uncertainty surrounding the speed of the carbonation process. On the other hand, it is interesting to note that the range of 1175-1190 obtained for the wall painting plaster is comparable to the bedding mortar of the masonry on which it has been applied. It is therefore possible that the murals were painted before the painted ceiling dated around 1500, if the painting layers were applied immediately after the application of the plaster analysed. Petrographic observations show the presence of secondary carbonate deposits at the edges of some macropores. which may also explain the more recent radiocarbon dates compared to what was expected. These secondary carbonate deposits are only observed for the outdoor render and can be linked to dissolution/precipitation processes due to variations in humidity and pH, since the wall was once located outside the building where environmental conditions are more likely to vary.

The radiocarbon dating of mortars ECH.I and ECH.II are within the same range compared to the first samples analysed around the window frame. The piece of charcoal found inside ECH.II

is much older (709-971 calAD) but this could be due to the old wood effect. The white layer on top of ECH.II was clearly applied in a later stage (15th century). The date obtained for ECH.III and ECH.IV are slightly younger compared to ECH.I and ECH.II but the date for the lime lump of ECH.III is in accordance with the dendrochronological estimation of the window frame. The charcoal extracted from ECH.III is slightly older but again, it is probably due to the old wood effect. The lime lump extracted from ECH.III correspond to the date of the window frame. Most of the samples fall within the post quem date of the window frame and the ante quem date of the roof structure. In addition, they are well preserved (except ECH.IV) with a composition that can be trusted. They are considered as reliable samples for radiocarbon dating.

Bibliography

Ahmmed, Tanjil, Ana Raquel Silva, José Carlos Quaresma, Patrícia Moita, and Cristina Galacho. 2024. "Analytical Characterization of Historical Mortars from the Roman Villa of Frielas (Loures, Portugal)." *Acta IMEKO* 13 (3): 1–11.

Brunello, Vallentina. 2020. "Mortars: A Complex Material in Cultural Heritage. A Multi-Analytical Procedure to Characterize Historical Mortars." Università degli studi dell'insubria. https://core.ac.uk/reader/322778010.

Gautier, Patrice, Louise Hardenne, Christophe Maggi, and Eric Bousmar. 2021. "L'église Notre-Dame de Mousty. Étude Archéologique et Dendrochronologique de Ses Structures Médiévales En Bois (11e–16e Siècles)." https://dial.uclouvain.be/pr/boreal/object/boreal:251855.

Genicot, Luc Fr. 1975. "Apres La Restauration de Notre Dame a Mousty." *Wavriensia Bulletin Du Cercle Historique et Archeologique de Wavre et de La Region* 24 (5): 85–107.

Hoffsummer, Patrick. 1995. *Les charpentes de toitures en Wallonie. Typologie et dendrochronologie (XIe-XIXe siècle)*. Études et documents, Monuments et sites. Namur: Ministère de la Région wallonne, Division du Patrimoine.

Klimesch, Danielle S., and Abhi Ray. 1996. "The Use of DTA/TGA to Study the Effects of Ground Quartz with Different Surface Areas in Autoclaved Cement: Quartz Pastes. Part 1: A Method for Evaluating DTA/TGA Results." *Thermochimica Acta* 289 (1): 41–54. https://doi.org/10.1016/S0040-6031(96)03033-X.

Moropoulou, Antonia, Asterios Bakolas, and Katerina Bisbikou. 1995. "Characterization of Ancient, Byzantine and Later Historic Mortars by Thermal and X-Ray Diffraction Techniques." *Thermochimica Acta* 269:779–95.

———. 2000. "Investigation of the Technology of Historic Mortars." *Journal of Cultural Heritage* 1 (1): 45–58.

Rickard, William D. A., Arie Van Riessen, and Philip Walls. 2010. "Thermal Character of Geopolymers Synthesized from Class F Fly Ash Containing High Concentrations of Iron and α-Quartz." *International Journal of Applied Ceramic Technology* 7 (1): 81–88. https://doi.org/10.1111/j.1744-7402.2008.02328.x.

Study of mortars from Coudenberg Palace (Brussels) for the BRAIN 2.0 PalC project

Context of the site

The Coudenberg archaeological site is considered as a former palace of Brussels and is located underground in the area of the current one, more precisely under the *place Royale* (Cnockaert et al. 2014). Its construction started as a small twelfth-century castle that was transformed to become the largest and most beautiful of Europe's princely residences up to the beginning of the eighteenth century (Cnockaert et al. 2014). In 2010, studies about the deterioration process of the site were undertaken by the monument laboratory of KIK-IRPA. Seventeen mortars were sampled from the different building phases (Figure 1) that are ranging from the 12th to the 18th centuries (Cnockaert et al. 2014).
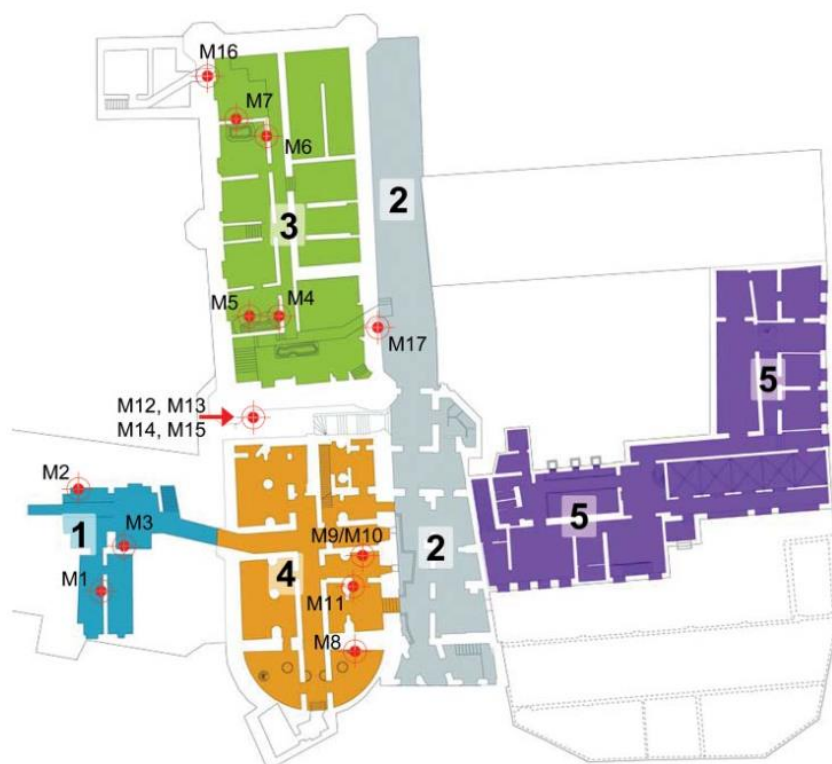
Figure 1: Plan overlaying the Coudenberg archaeological site and museum on the Royal Square (1. Main building; 2. Rue Isabelle (Isabella Street); 3. Aula Magna; 4. Chapel; and 5. Hôtel d'Hoogstraeten (Hoogstraeten House)). The 17 mortars sampled in 2011 are marked on the plan. (from Fontaine et al. 2014).

Material

From the mortars sampled in 2011, two were selected for the PALc project. The selection depended on the quantity of sample still available and on the estimated date (avoiding the period 1650-1850 that is not ideal for radiocarbon dating). The two samples matching these criteria were M4 and M16. They both come from the Aula Magna. M4 is a bedding mortar sampled in the interior wall (Figure 2), and M16 is an infill mortar from the exterior wall. Both

of them date to 1452-60 according to archive documents and an in-depth historic building investigation led by archaeologists of the Royal archaeological society of Brussels (Fontaine et al. 2014).
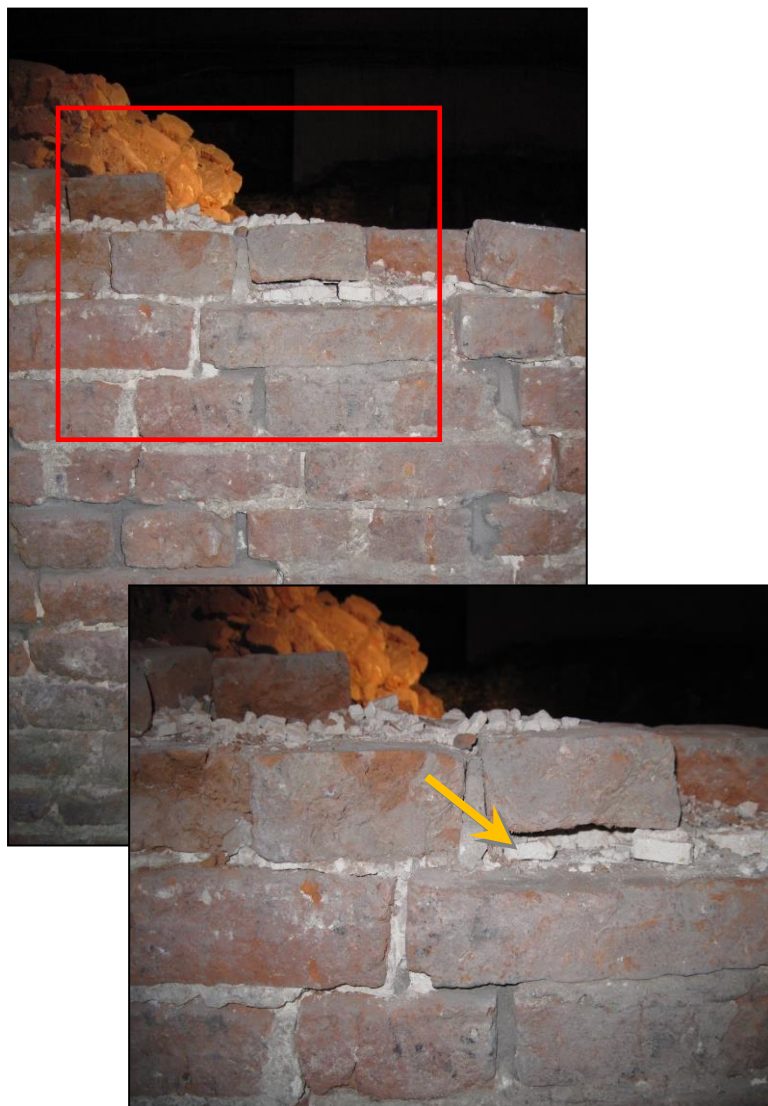
Figure 2: Sampling location mortar M4.

Results & Discussion

Macroscopic descriptions

Both samples exhibit a beige colour tending toward very pale brown (10YR 8/2) according to the Munsell soil colour charts (Figure 3). They are rather homogeneous white lime lumps showing mainly a size < 1 mm and a maximum size of 4 to 5 mm. They both contain soft and round red inclusions probably due to the presence of red bricks fragments (Figure 3 top left). The red residues spread on one side of the M4 fragments are bricks residues. Some yellow residues are also present but their origin is unknown (Figure 3 top left). M16 contains a large black inclusion that is most likely made of charcoal (Figure 3 bottom right). It also shows some grey spread on the surface, some white particles looking like salts and a purple inclusion (Figure 3 bottom middle).

Figure 3: Mortar samples M4 (top) and M16 (bottom).

Fourier transform Infrared (FTIR) spectroscopy on inclusions & binder

The binders (beige, Figure 4) mainly contain calcium carbonates (calcite and aragonite) and silicates including quartz. The binder of M16 also comprises nitrates which shows a certain alteration, certainly because it was located on the outside part of the wall. The lime lumps (white, Figure 4) are also mainly made of calcium carbonates (calcite and aragonite) in addition to silicates, including clay for M4. The red spread on the surface of M4 (Figure 4, top) is made of silicates including quartz, and the yellow (Figure 4, top) was not identified with certainty. It is possibly humboldtine ($FeC_2O_4 \cdot 2H_2O$), a ferrous oxalate that is the product of lichen growth (Frost 2004) (e.g., *Acarospora smargdula*) on Fe-rich limestones (Burford, Kierans, and Gadd 2003). The grey spread on the surface of M16 (Figure 4, bottom) is mainly made of calcite and aragonite with silicates including quartz. The white on M16 (Figure 4, bottom) looking like salt shows vibrational features of calcite, silicates and nitrates. Silicates including quartz, calcite, nitrates and two unidentified features are present in the red inclusion of M16 (Figure 4, bottom).
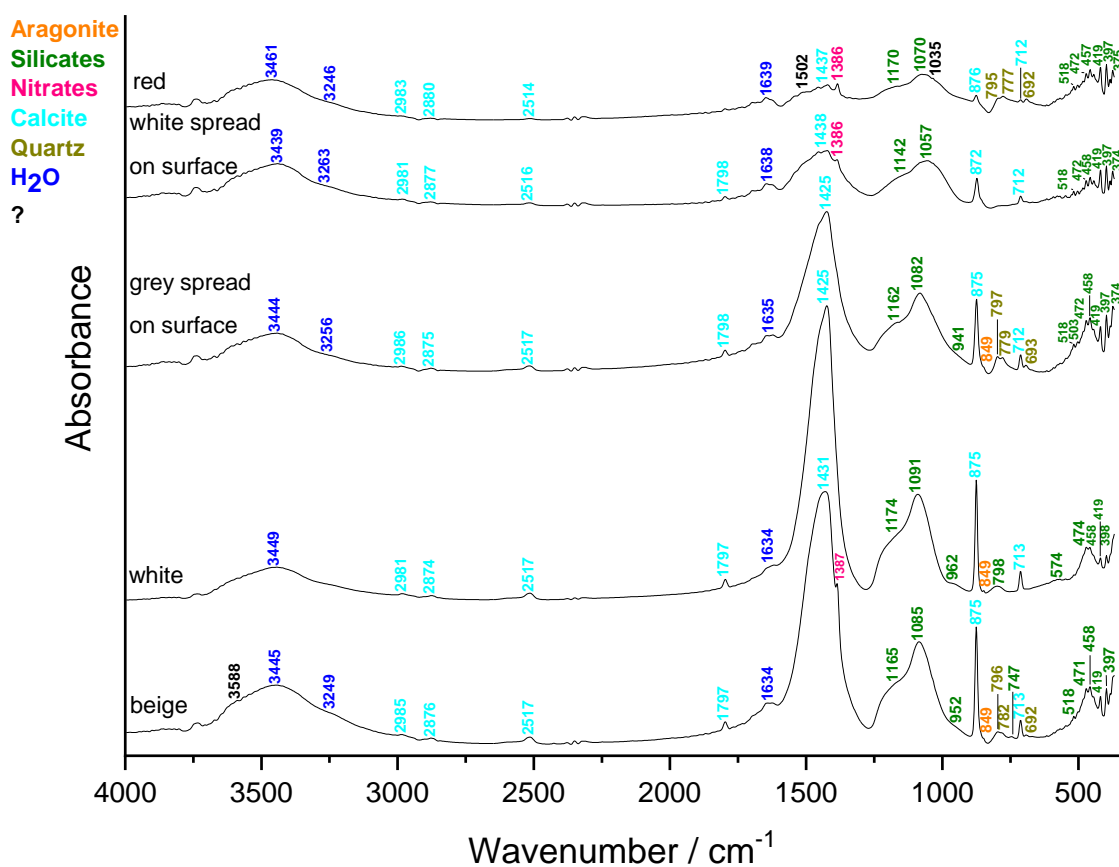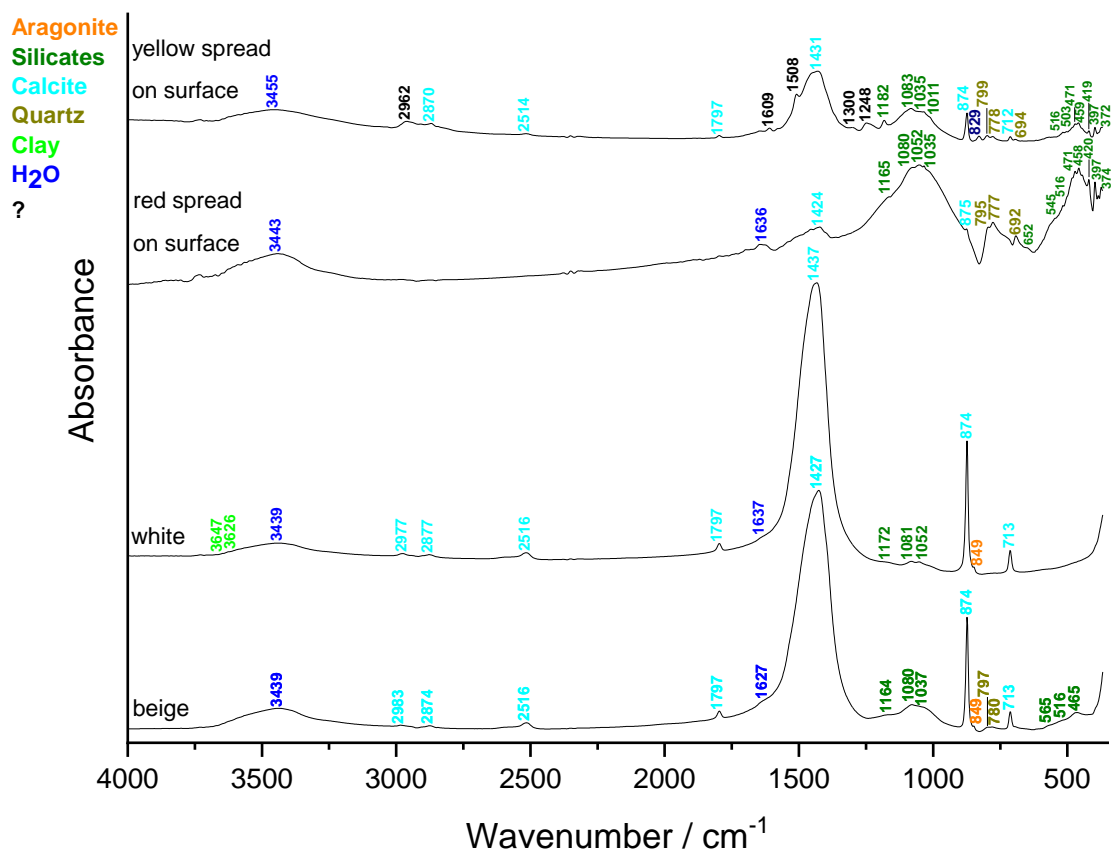
Figure 4: FTIR spectra obtained on the inclusions and binder (beige) of the mortar sample M4 (top) and M16 (bottom).

Binder:aggregate ratio

The calculated binder:aggregate ratio using a bulk density of 1.35 kg/dm³ for the sand and 0.575 kg/dm³ for the lime is close to 3:5 in volume unit for sample M4, and close to 6:5 for sample M16.

	M4	**M16**
Sample weight (g)	1.3	2.7
Crucible weight (g)	17.5	18.0
Weight calcined (g)	18.5	19.7
%ins	**79.9**	**66.4**

Table 1: Percentage of insoluble residue.

Cathodoluminescence

Cathodoluminescence observations of both thin-sections revealed two shades of purple for the quartz crystals (Figure 4a, b, d & e). The previous study of the mortar samples shows that most of the mortars contain a Brusselian sand of the Neerijse or the Diegem-type (Fontaine et al. 2014). The limestone used to prepare the mortars is the sandy limestone of the Brussels Formation (or Brusselian stone) (Fontaine et al. 2014). The binder of both thin sections is dull and numerous blue K-felspars from the sand aggregate are observed (Figure 4a, b, d & e). In M4, some rare small bright red limestone fragments are present (Figure 4a). Figure 4b shows a partially burned lime lump in M4 with some red area appearing among the dull lump. The powdered samples display mainly a red tile colour (binder), a few bright red limestone grains (Figure 4c & f) and with a few bright blue K-feldspars for M16 (Figure 4f).
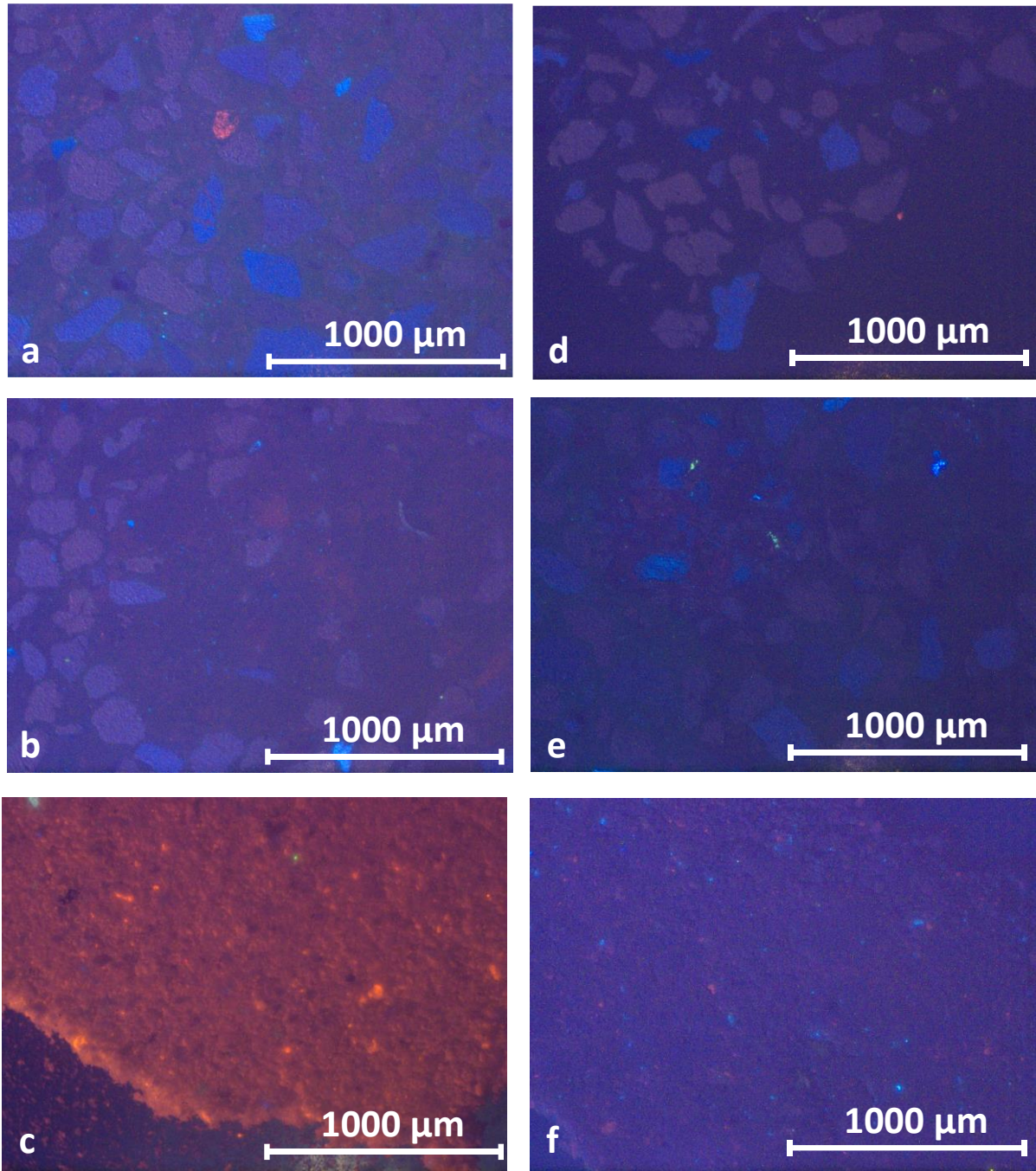
Figure 4: Characteristic cathodoluminescence images of a) & b) the thin section X2348 of the M4 mortar, c) the powdered M4 mortar with particle size lower than 75 µm, d) & e) the thin section X2349 of the M16 mortar and f) the powdered M16 mortar with particle size lower than 75 µm.

Thin-section petrography

The petrographic observations indicate that the mortar M4 is in good condition (Figure 5 & Table 2) and little secondary carbonates are observed around pores and in the cracks of the lime lumps (Figure 5 c & d). As said previously, the limestone used contained silicates because the lime lumps include sand grains. Some of the quartz grains appear light brown in PPL, and in XPL it can be observed that they are made of numerous tiny crystals i.e. microcrystalline quartz (Figure 5e & f) that has a sedimentary origin (flint fragments). Glauconite grains from sand are green/yellow and the ones from the burned limestone are red/black because oxidised during

the lime-making process. A sandstone fragment (agglomerate made of siliceous sand cemented by microcrystalline silica) is observed which confirms the use of sand from the Brussels Formation.
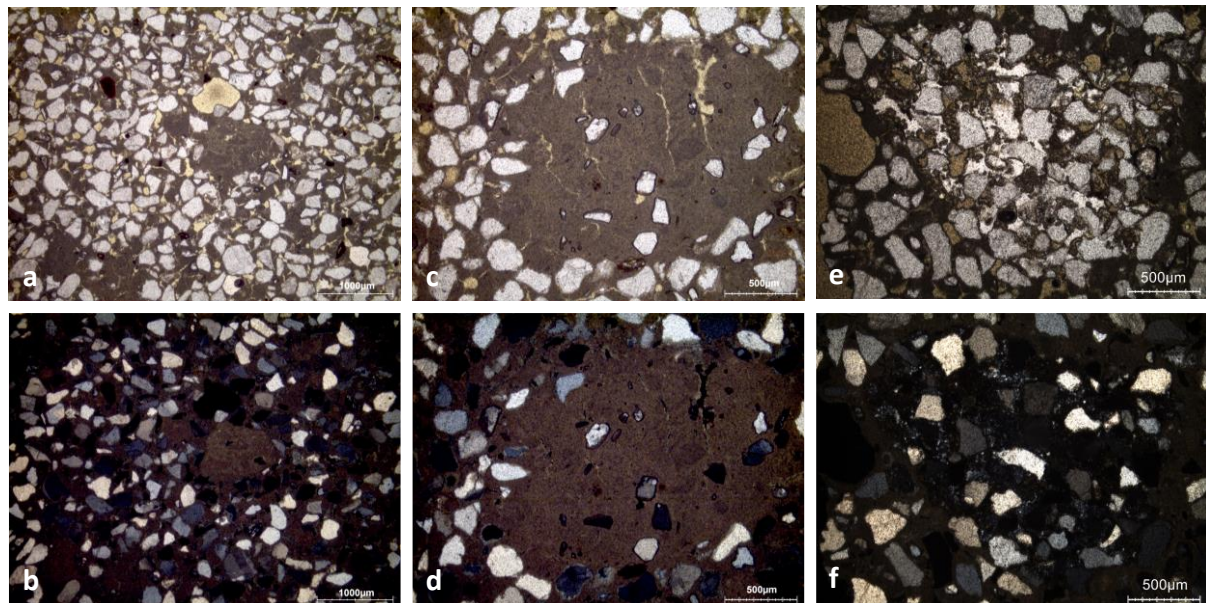
Figure 5: Representative photomicrographs of the thin-section X2348 of the M4 mortar: a) overview image in plain polarised light (PPL); b) overview image in cross polarised light (XPL); c) PPL image showing a completely burned lime lump with secondary calcite in cracks; d) same image in XPL; e) PPL image showing quartz grains cemented by microcrystalline silica; f) same image in XPL.

Binder	Texture	micritic
	Lump state	completely burned
	Lump size	400 µm to 2.5 mm
	Lump frequency	numerous
Aggregate	Grain size	very fine to coarse
	Mineralogy	pure siliceous sand (quartz, feldspars, more or less oxidised glauconite, sandy-clay agglomerates & sandstone fragment)
	Shape	subangular / subrounded
Appearance	Homogeneity	relatively homogeneous
	Macroporosity	medium
	Pore structure	Irregular / cracks / sometimes connected
Admixtures	Type	-
Alteration	Type	secondary carbonates around pores a& in lime lump cracks

Table 2: Main characteristics of the M4 mortar retrieved from the observations of the thin-section X2348.

The mortar M16 is in poor condition (Figure 6 & Table 3). The binder and the lime lumps have mainly been dissolved (Figure 6c & d). Secondary carbonates are observed in cracks and around pores (Figure 6 e & f).
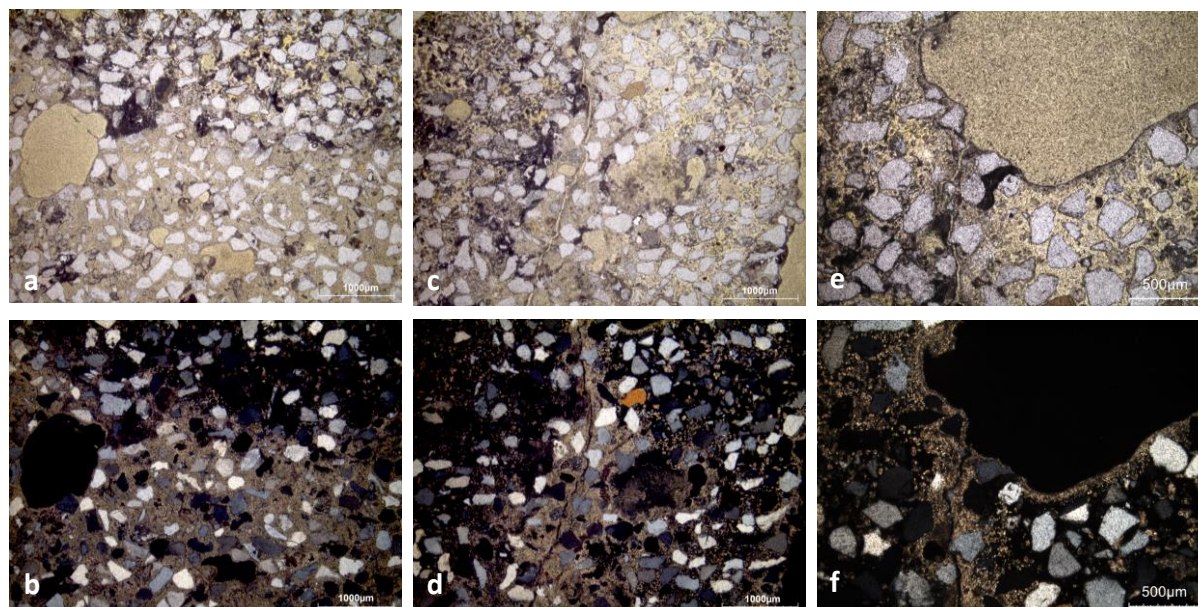
Figure 6: Representative photomicrographs of the thin-section X2349 of the M16 mortar: a) overview image in plain polarised light (PPL); b) overview image in cross polarised light (XPL); c) PPL image showing a dissolved lump; d) same image in XPL; e) PPL image with secondary carbonates around cracks and pores; f) same image in XPL.

Binder	**Texture**	micritic
	Lump state	dissolved
	Lump size	1 mm (complicated to measure because of dissolution)
	Lump frequency	few (because of dissolution?)
Aggregate	**Grain size**	very fine to coarse
	Mineralogy	siliceous sand (quartz, K-feldspars, more or less oxidised glauconite)
	Shape	subangular / subrounded
Appearance	**Homogeneity**	relatively homogeneous
	Macroporosity	high
	Pore structure	irregular / sometimes connected
Admixtures	**Type**	-

Alteration	**Type**	dissolution, secondary carbonates in cracks & pores

Table 3: Main characteristics of the M16 mortar retrieved from the observations of the thin-section X2349.

Thermogravimetric analysis (TGA) on whole samples

The graphs of the thermal analyses are presented in Figures 7 and 8. The apparent hydraulicity indexes (aHI) determined on the basis of the weight loss between 200 and ca. 650°C (usually attributed to water loss from calcium-silicate-hydrates-phases) show that the mortar binder is slightly hydraulic for sample M4 (14.3 %) and very strongly hydraulic for sample M16 (57.5 %). For the latter, the hydraulicity index cannot be considered reliable, due to the high degree of dissolution of the binder in sample M16, which strongly influences the obtained value upwards. The amount of carbonates is ~22 wt% for the mortar M4 and 9.2 wt% for M16. The temperature of quartz transition phase is observed around 567°C (Rickard, Riessen, and Walls 2010) for both samples. The main weight loss of ancient mortars is expected between 600 and 900 °C and is indicative of the decomposition of calcium carbonate ($CaCO_3$) into calcium oxide (CaO) and carbon dioxide (CO_2) (Ahmmed et al. 2024). The end temperature of calcium carbonate decomposition is ~770°C for M16 (It could not be determined for M4). No gypsum was detected.
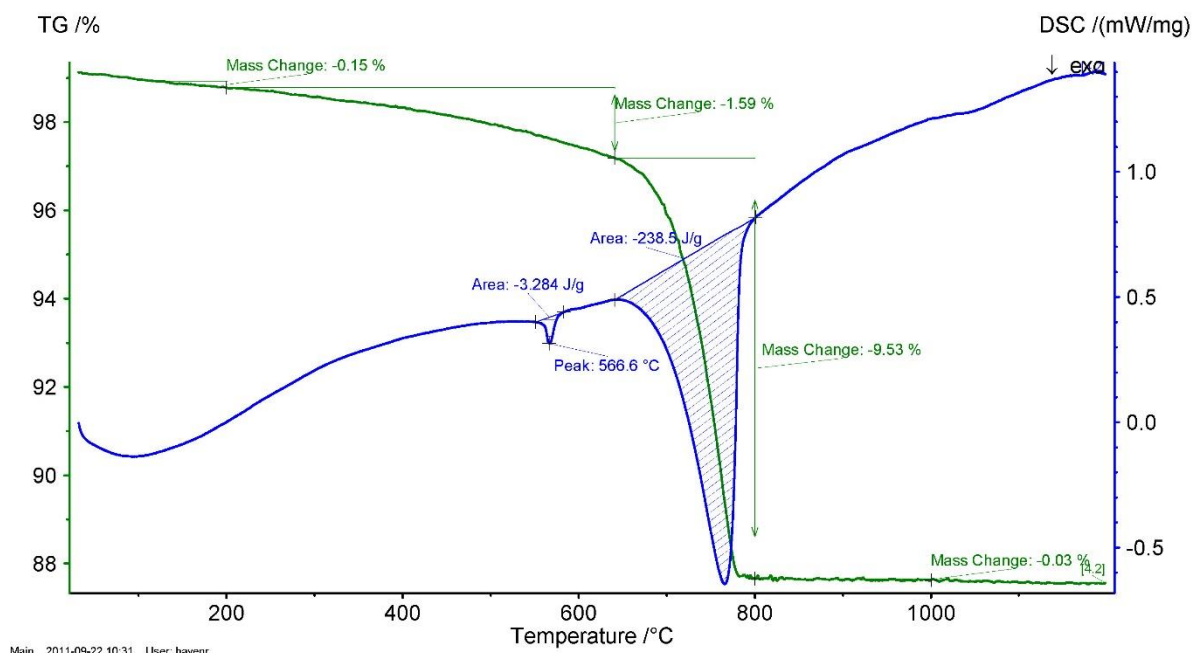
Figure 7: Coupled TG-DSC analysis of the mortar M4 upon heating to a temperature of 1200°C at a heating rate of 20°C/min under an inert atmosphere (He flushed at 50 ml/min). The weight loss determined by thermogravimetric analysis (TG, wt%, green curve) and the result of the differential scanning calorimetric analysis (DSC, mW/mg, blue curve) are both presented.
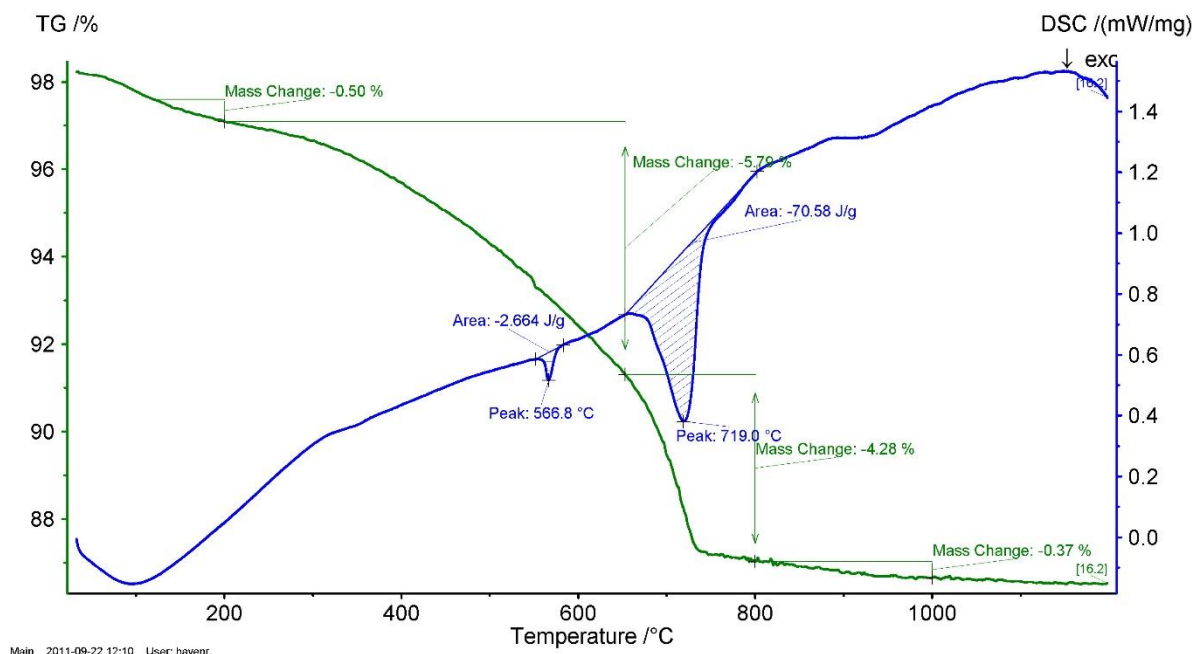
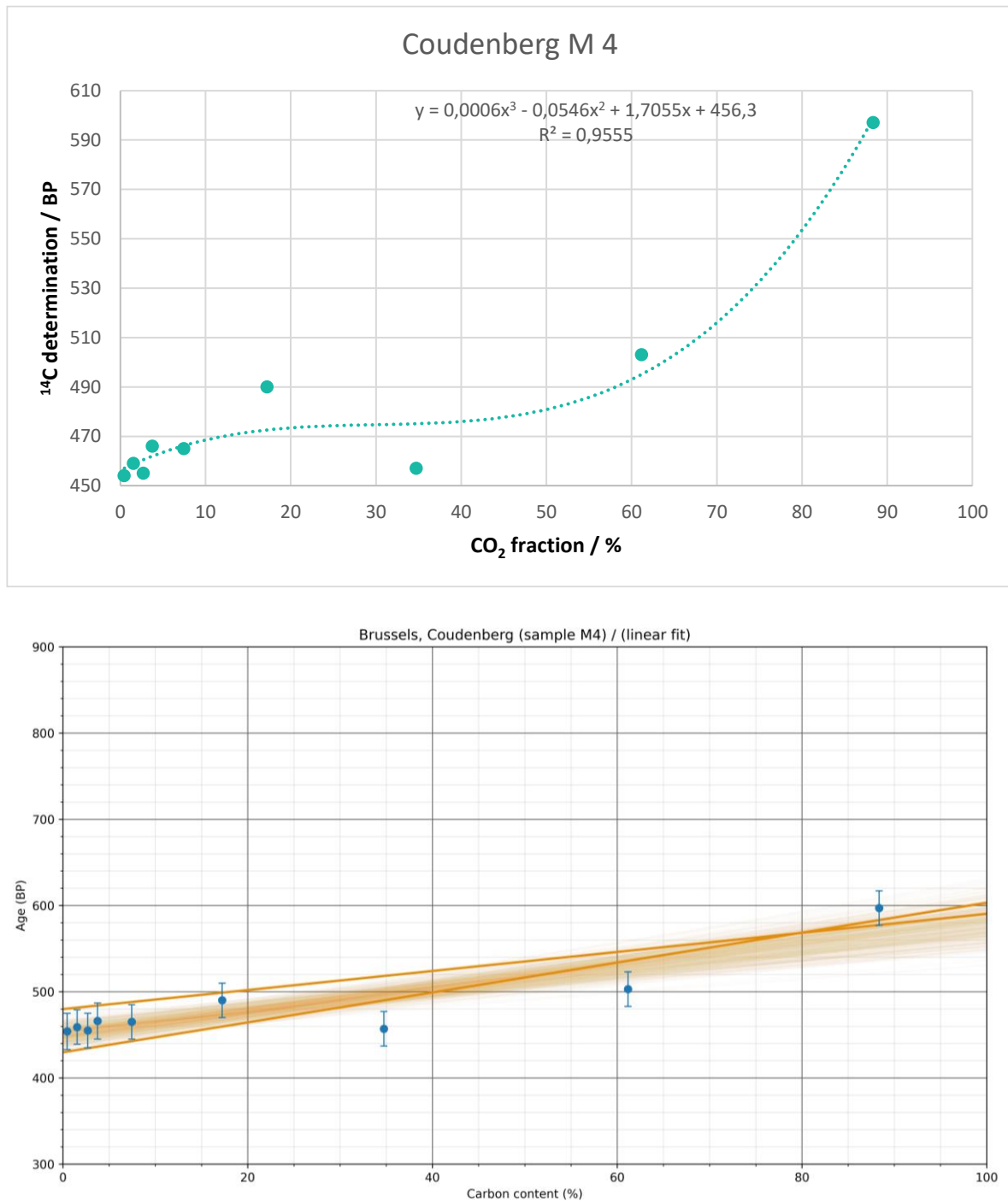**Figure 8:** Coupled TG-DSC analysis of the mortar M16 upon heating to a temperature of 1200°C at a heating rate of 20°C/min under an inert atmosphere (He flushed at 50 ml/min). The weight loss determined by thermogravimetric analysis (TG, wt%, green curve) and the result of the differential scanning calorimetric analysis (DSC, mW/mg, blue curve) are both presented.

Grinding/particle separation

For the mortar M4, the brown spread on the surface was scratched away and the lime lump was extracted before grinding.

For the mortar M16, the grey and white spread on the surface were scratched away and the charcoal was extracted before grinding.

TGA on powders with particle size <75 μm

The aHI of the powders with particles < 75 μm, determined on the basis of the weight loss between 200 and ca. 650°C, are 22.5 % for mortar M4 and 73.9 % for mortar M16 (Figures 9 and 10). The obtained values on powders are thus higher than those on whole samples. These differences could be explained by the presence of clay that end up in more quantities in the powdered sieved samples. The small amount of gypsum (2,7 %) detected in the powder of sample M16 confirms that this mortar is weathered. The quantity of carbonates is higher in the powders compared to the whole samples since a large part of the sand is removed (63 and 16 wt% for M4 and M16, respectively). Indeed, no quartz was detected in the powders. For M16 (Figure 10), a peak around 406°C is observed and might be due to the release of water from calcium hydroxide (Moropoulou, Bakolas, and Bisbikou 1995; Klimesch and Ray 1996) indicating that the mortar did not fully carbonated. This was not observed for the whole mortar samples. It was probably present in too low concentration to be noticeable. The end temperatures of calcium carbonate decomposition are ~831 and 781°C for the powdered samples M4 and M16, respectively. It is higher compared to the whole samples. A possible explanation could be that the powder is more pure compared to the whole mortar sample which increases the decomposition temperature.
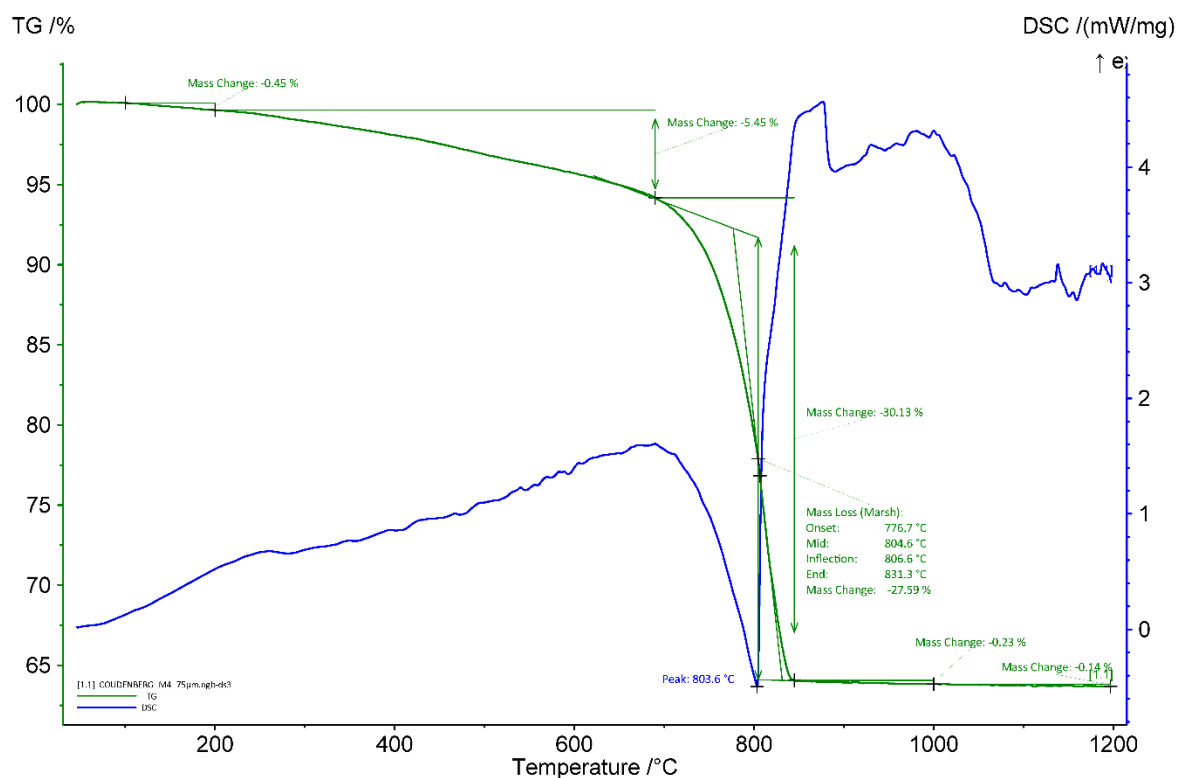
Figure 9: Coupled TGA-DSC analysis of the powdered mortar M4 with particle size < 75 µm upon heating to a temperature of 1200°C at a heating rate of 20°/min under an inert atmosphere (He flushed at 50 ml/min). The weight loss determined by thermogravimetric analysis (TG, wt%, green curve) and the result of the differential scanning calorimetric analysis (DSC, mW/mg, blue curve) are both presented.
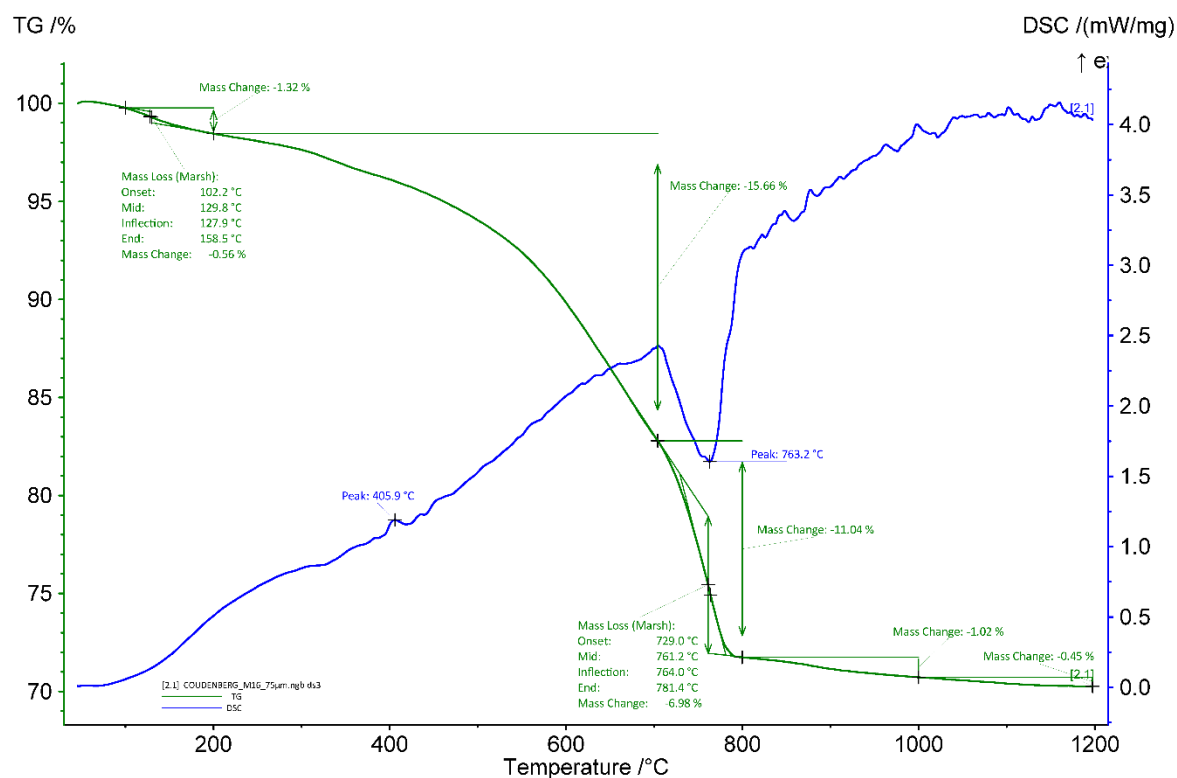
Figure 10: Coupled TGA-DSC analysis of the powdered mortar M16 with particle size < 75 μm upon heating to a temperature of 1200°C at a heating rate of 20°/min under an inert atmosphere (He flushed at 50 ml/min). The weight loss determined by thermogravimetric analysis (TG, wt%, green curve) and the result of the differential scanning calorimetric analysis (DSC, mW/mg, blue curve) are both presented.

Radiocarbon results

The test prior to the CO_2 extraction revealed a good amount of carbon for M4 (Table 4) (~7 %), a relatively low amount of powder <75 μm was necessary for the carbon extraction (~1 g). This confirm the good state of preservation of the mortar. M16 exhibits a lower carbon percentage compared to M4 (~5%), twice more powder was therefore needed for the CO_2 extraction (~2g).

RICH	Sample type	Method	C (%)	σ (%)	m (g)	Age BP	Calibrated date	Age BP extrapolated	Calibrated date	Age BP extrapolated with stat	Calibrated date (oxcal - 95.4%)	Age BP average	Calibrated date	Reliability of dating
33067 (M4)	mortar <75 μm	8 fractions	7.29	0.42	1.11	-	-	456 ± 20 BP	1430-1460 calAD	451.6 ± 8.9 BP	1435-1463 calAD	469 ± 7 BP	1430-1450 calAD	☑
34108 (M4)	lump	H_3PO_4	9.73	-	0.0341	398 ± 32 BP	1437-1630 calAD	-	-	-	-	-	-	☑
33043 (M16)	mortar <75 μm	8 fractions	5.17	0.48	2.07	-	-	24 ± 25BP	1690-1820 calAD	20.2 ± 60.8 BP	1680-1940 calAD	(6 first fractions) 47 ± 10	1700-1910 calAD	☒
32802 (M16)	charcoal	HCl 8 %	14.00	-	3.55 mg	1286 ± 25BP	660-780 calAD	-	-	-	-	-	-	☒

Table 4: Radiocarbon results

Both the extrapolated date (Figure 11) and the average date (Table 4) obtained for the < 75 μm of M4 are in accordance with the well-defined historical date of construction of the Aula Magna (1452-60). The date obtained for the lime lump (Table 4) is slightly younger but still falls within the range of the expected date. For M16, as expected from the poor state of preservation, the date obtained does not match the expectations and is way much younger than expected (Figure 8 & Table 4). The charcoal fragment extracted from M16 is older compared to the supposed date (Table 4). This can be explained by the old wood effect or by the fact that the sample was also degraded. It contains only 14 % of carbon (Table 4).

Figure at top:
Coudenberg M 4

$y = 0{,}0006x^3 - 0{,}0546x^2 + 1{,}7055x + 456{,}3$
$R^2 = 0{,}9555$

y-axis: ^{14}C determination / BP
x-axis: CO_2 fraction / %

Figure at bottom:
Brussels, Coudenberg (sample M4) / (linear fit)
y-axis: Age (BP)
x-axis: Carbon content (%)

Figure 11: Radiocarbon results for the powdered mortar M4 with particles < 75 μm as a function of the CO_2 fraction (the graph at the bottom shows the statistic on the results).
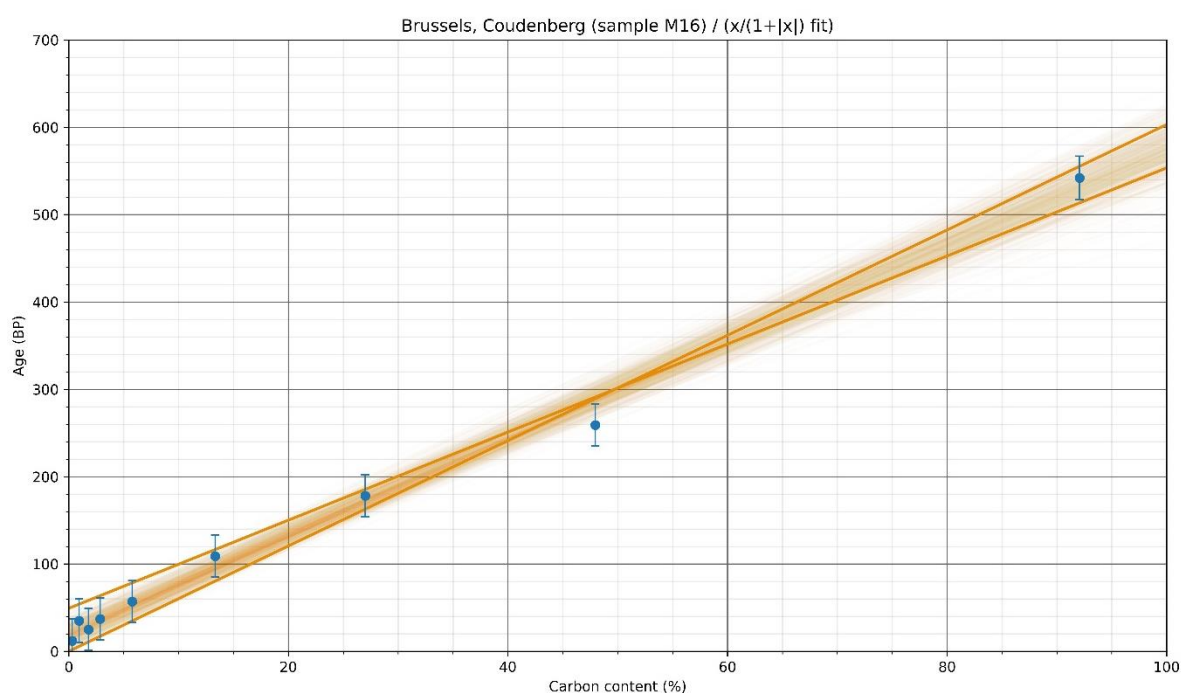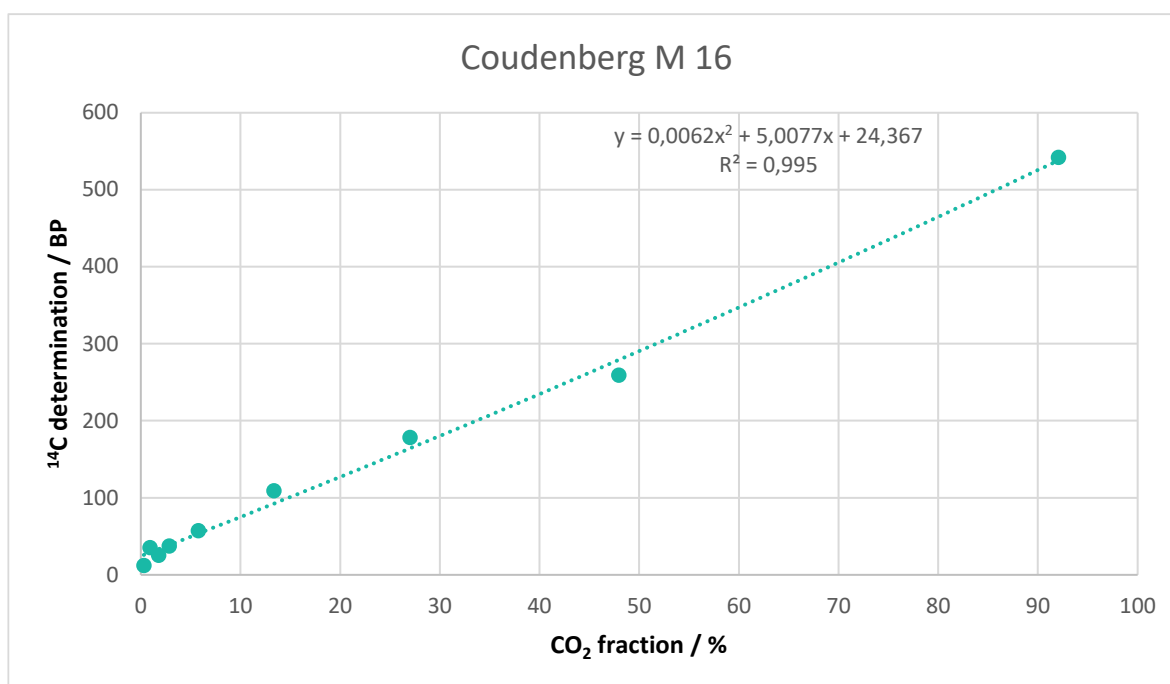
Figure 12: Radiocarbon results for the powdered mortar M16 with particles < 75 µm as a function of the CO_2 fraction (the graph at the bottom shows the statistic on the results).

Conclusions

The mortar M4 gives a reliable radiocarbon date because of its good state of preservation and a favourable composition (pure siliceous sand used as aggregate). On the other hand, the mortar M16 is not suitable for radiocarbon dating, it has been weathered with intensive leaching and the presence of secondary carbonates. This is most probably because the sample comes from

the exterior wall. This shows that two samples from similar locations can give totally different results. Hence the need to sample several mortar when radiocarbon dating a site.

Bibliography

Burford, Euan P., Martin Kierans, and Geoffrey M. Gadd. 2003. "Geomycology: Fungi in Mineral Substrata." *Mycologist* 17 (3): 98–107.

Cnockaert, Laetitia, Stéphane Demeter, Aude Henriques de Granada, and Frédérique Honoré. 2014. "Paper 1: The Coudenberg Archaeological Site in Brussels: The Stakeholders Involved in the Renovation Process." *Conservation and Management of Archaeological Sites* 16 (1): 5–15. https://doi.org/10.1179/1350503314Z.00000000067.

Fontaine, Laurent, Roald Hayen, Sebastiaan Godts, and Hilde De Clercq. 2014. "Paper 5: Historic Mortars from the Coudenberg Archaeological Site: Characterization and Source of Raw Materials." *Conservation and Management of Archaeological Sites* 16 (1): 71–84. https://doi.org/10.1179/1350503314Z.00000000071.

Frost, Ray L. 2004. "Raman Spectroscopy of Natural Oxalates." *Analytica Chimica Acta* 517 (1–2): 207–14.

Study of mortars from Saint-Eustache church (Zichem, Belgium) for the BRAIN 2.0 PalC project

Context of the site

The Saint-Eustache church (Sint-Eustachiuskerk) is located in the centre of Zichem, a village of the town of Scherpenheuvel-Zichem in the Belgian province of Flemish Brabant. The oldest parts of the church date back to the 13th century, but it was only completed in the middle of the 16th century. The north and east facades of the tower in all likelihood still include the original gable parapet in ferruginous stone from the 13th century. Although the core of the tower probably dates from the 13th century, the gable parapet on the west and south facades was completely replaced at a later stage - possibly in the late 19th, early 20th century. The side of the church located along the Demer river is the most decorated to show Zichem's wealth to ships passing. It exhibits a rust-brown façade made of ferruginous sandstone, typical for most churches in the Demer valley. The showpiece of the church is the stained-glass window donated by the lord of Zichem in 1387. This makes it the oldest preserved stained-glass window in our country ("Parochiekerk Sint-Eustachius" 2021).

Figure 1: St Eustachius church (top picture from (De munten van Reinhard, n.d.) and bottom image from KIK-IRPA, Brussels (Belgium), photograph A004519, 1893).

Material

Samples from the Saint Eustache church were stored at KIK-IRPA from a previous study by the monuments laboratory in 2018. They were sampled by Roald Hayen. Three mortar samples coming from different parts of the tower presented a quantity suitable for the PALc protocol: one from the south façade at 20.90 m height taken from the core work right behind the facing stone, and two from the north façade, one of them at 11.25 m height, also taken from behind a facing stone at approximately 26 cm depth, and the other one at 16.60 m height lifted from the bedding mortar close to the exterior surface. Historical documents situate the construction of the tower around 1300. The northern and eastern façades of the tower retained their original facing stone in ferruginous sandstone, except for some local brick masonry repairs, while the facing stone on the southern and western façades were completely renewed around 1895. However, all samples were taken from either the historic core or the historic facing stonework and can therefore be situated around 1300. Both mortar samples from the core masonry (at about 20 to 30 cm depth) might have been subjected to delayed hardening.

Figure 2: Sampling area of the mortar samples from the south façade at 20.90 m height from the core work (left), the north façade at 11.25 m height, again from the core work at approximately 26 cm depth, (middle) and from the bedding mortar from the north façade at 16.60 m height (right).

Results & Discussion

Macroscopic descriptions

The three mortar samples exhibit a beige colour tending toward pale yellow (2.5Y 8/2 for the sample from the south façade and 2.5Y 8/3 for the two samples from the north façade) according to the Munsell soil colour charts (Figure 3). The lime lumps mainly display a size < 2 mm and can reach up to 2 cm, especially for the mortar from the north façade at 11.25 m from which a lump was extracted from the mortar (Figure 2 middle). They all show some brown inclusions resulting from soil particle and/or siliceous aggregates. For the mortar from the north façade at 16.60 m, soft and angular inclusion attributed to terracotta or brick fragments were observed as well as more or less large grey inclusions that are most probably limestone.

Figure 3: Mortar samples from the south façade at 20.90 m height from the core work (left), the north façade at 11.25 m height, again from the core work at approximately 26 cm depth, (middle) and from the bedding mortar from the north façade at 16.60 m height (right).

Fourier transform Infrared (FTIR) spectroscopy on inclusions & binder

The binders (beige, Figure 4) mainly contain calcium carbonates (calcite and aragonite) and silicates including quartz. The lime lumps (white, Figure 4) and the white large inclusion from the mortar of the north façade at 16.60 m are also mainly made of calcium carbonates (calcite and aragonite) in addition to some silicates. A grey/dark brown inclusion extracted from the mortar sample from the south façade at 20.90 m is made of silicates, possibly montmorillonite (Figure 4 top). The grey inclusion from the mortar of the north façade at 16.60 m is made of calcite, aragonite and silicates and then should be a limestone fragment (Figure 4 bottom). The brown inclusions of the three samples mainly contain silicates including quartz (and clay for the south façade mortar at 20.90 m and the north façade mortar at 16.60 m), calcite and organic matter.
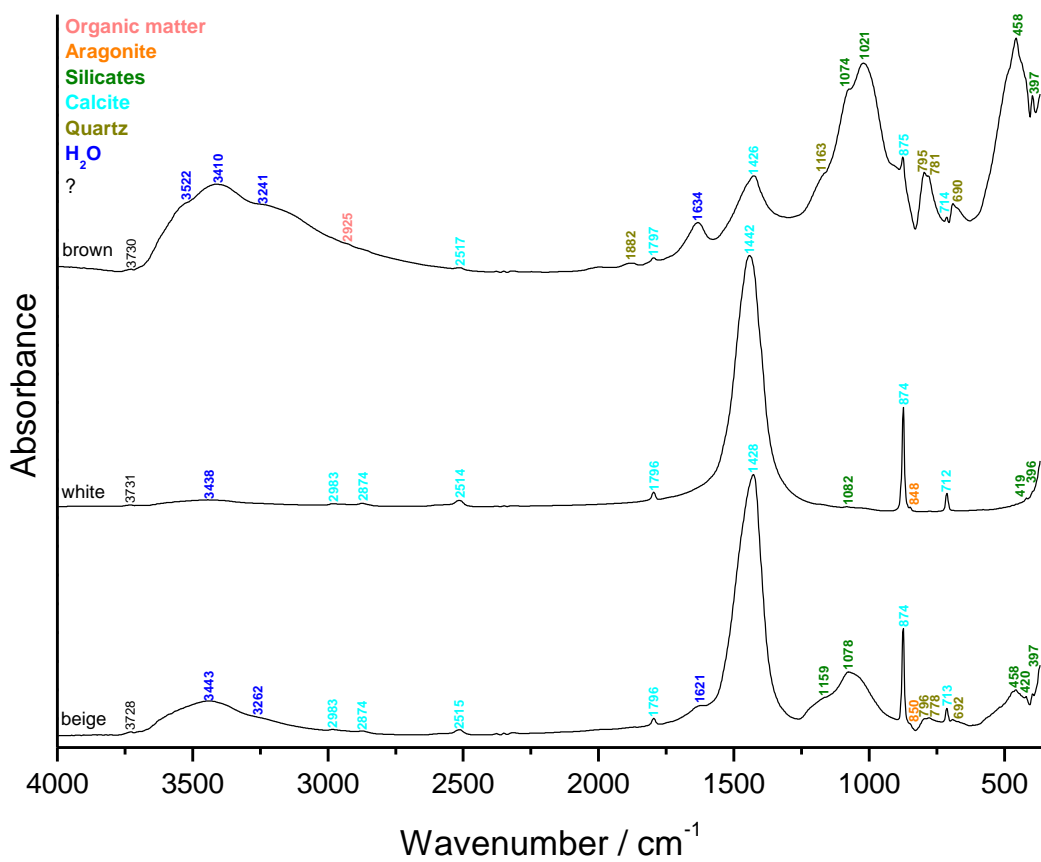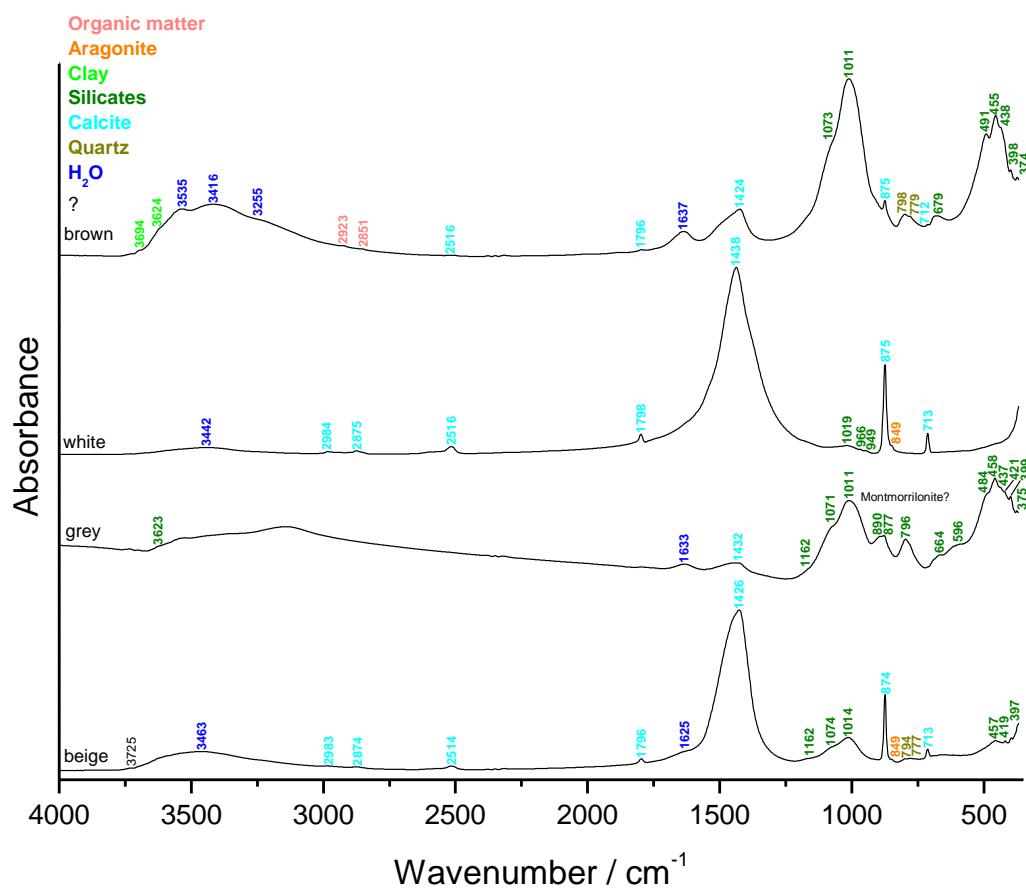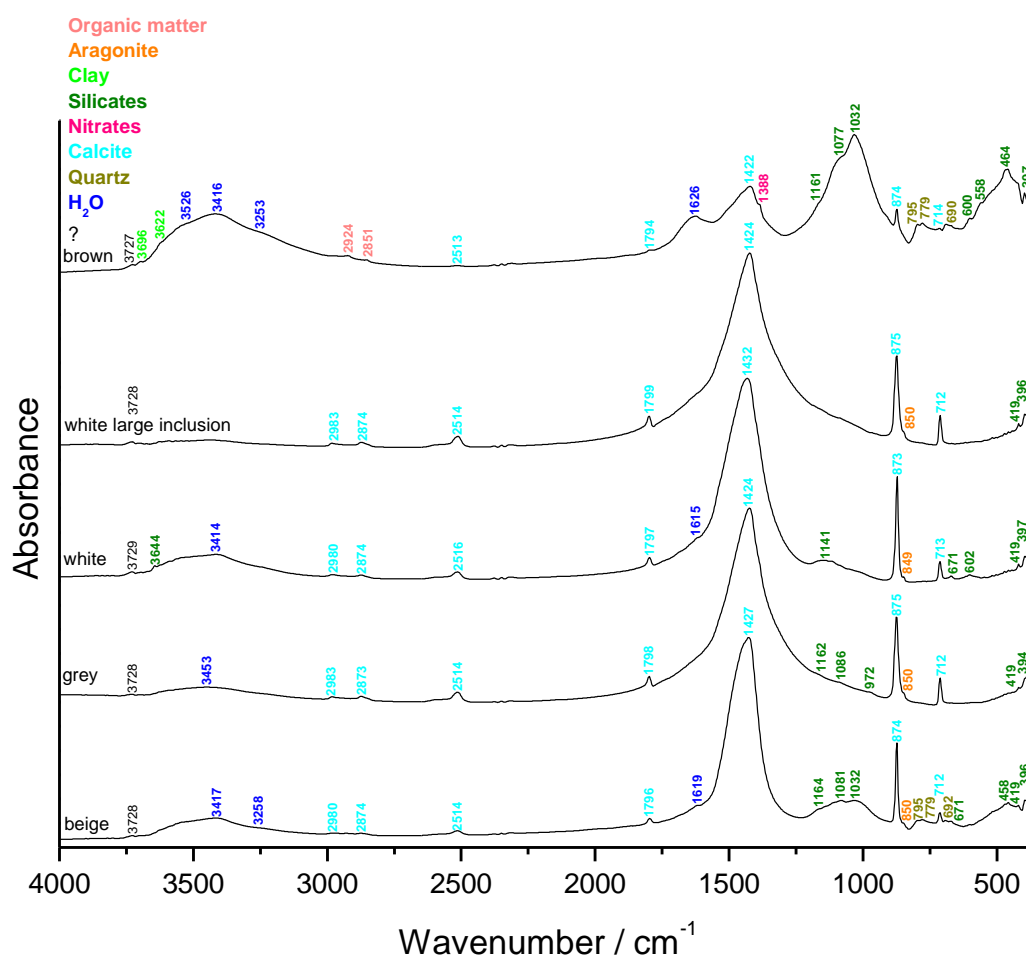
Figure 4: FTIR spectra obtained on the inclusions and binder (beige) of the mortar sample from the south façade at 20.90 m (top), from the north façade at 11.25 m (middle), and from the north façade at 16.60 m (bottom).

Binder:aggregate ratio

The calculated binder:aggregate ratio using a bulk density of 1.35 kg/dm^3 for the sand and 0.575 kg/dm^3 for the lime is close to 1:1 in volume unit for the 3 samples.

	S 20.90 m	N 11.25 m	N 16.60 m
Sample weight (g)	2.4	1.95	2.45
Crucible weight (g)	15.1	16.85	14.69
Weight calcined (g)	16.9	18.28	16.38
%ins	**72.7**	**73.3**	**69.0**

Table 1: Percentage of insoluble residue

Cathodoluminescence

The three thin sections (Figure 5a, c & e) show the presence of quartz with a dark purple hue, potassic feldspar with a bright blue colour and glauconite in black. The majority of the lime lumps are dull as the binder but some of the lime lumps of the mortar sample from the south façade at 20.90 m and the mortar sample from the north façade at 16.60 m also show patches of red because they are underburned (Figure 5a & e). The powdered samples with particle size lower than 75 μm (Figure 5b, d & f) exhibit mostly a red tile colour due to the binder, and a

few bright blue potassic feldspars as well as some bright red particles due to the presence of limestone.
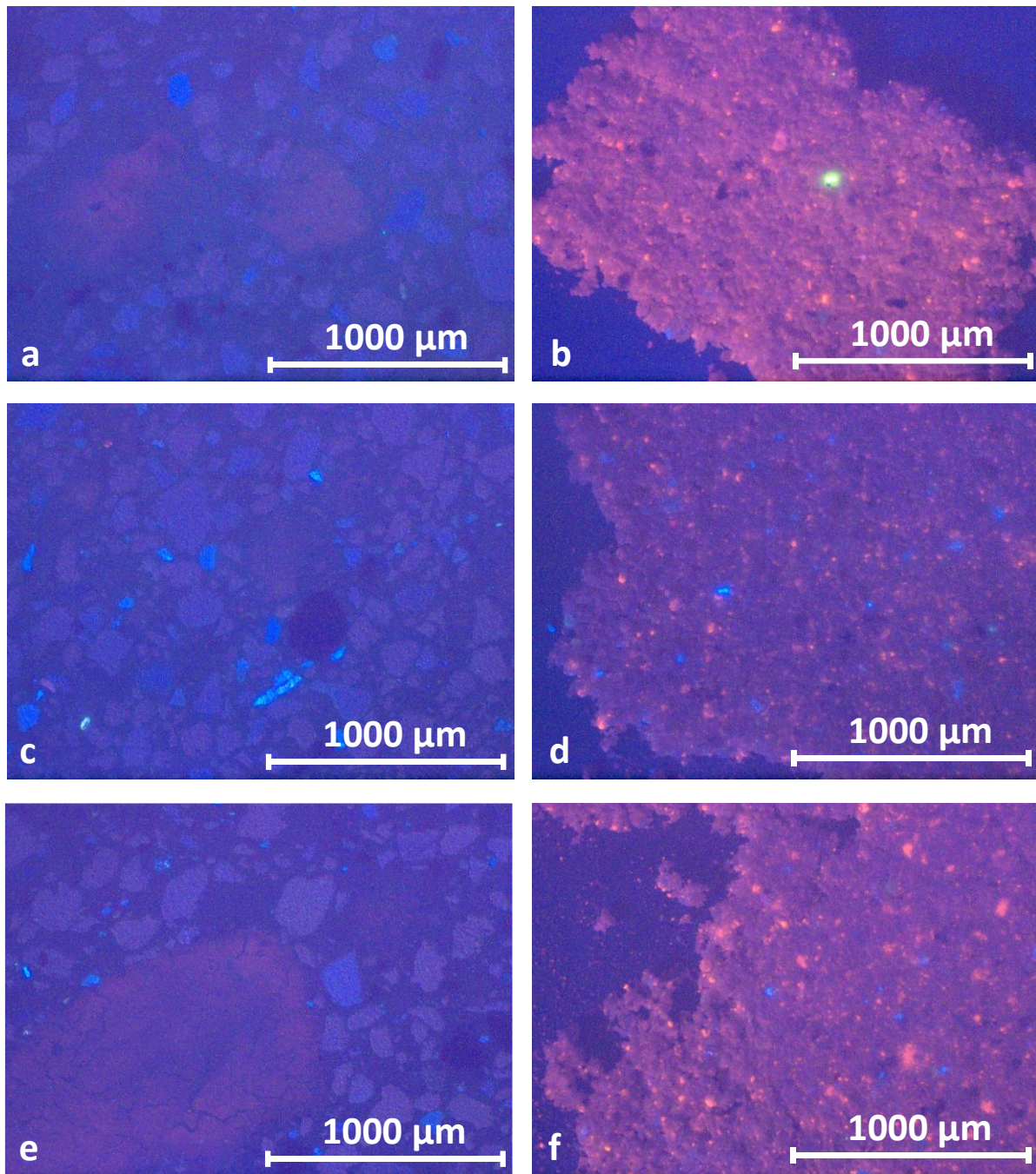
Figure 5: Characteristic cathodoluminescence images of a) the thin section X2294 of the mortar sample from the south façade at 20.90 m, b) the powdered mortar sample from the south façade at 20.90 m with particle size lower than 75 µm, c) the thin section X2295 of the mortar sample from the north façade at 11.25 m, d) the powdered mortar sample from the north façade at 11.25 m with particle size lower than 75 µm, e) the thin section X2296 of the mortar sample from the north façade at 16.60 m and f) the powdered mortar sample from the north façade at 16.60 m with particle size lower than 75 µm.

Thin-section petrography

The petrographic observations indicate that the mortar sample from the south façade at 20.90 m from the core work is in good condition (Figure 6 & Table 2). The lime lumps are completely burnt (one is not fully carbonated – Figure 6e & f)), the binder does not show signs of dissolution/secondary carbonates and the siliceous aggregate does not seem to contain any limestone inclusions. Some fragments of the ferruginous sandstone of Diest (local natural stone made of quartz and glauconite grains in similar proportion agglomerated together by a ferruginous cement) are observed in the aggregate (Figure 6c & d).
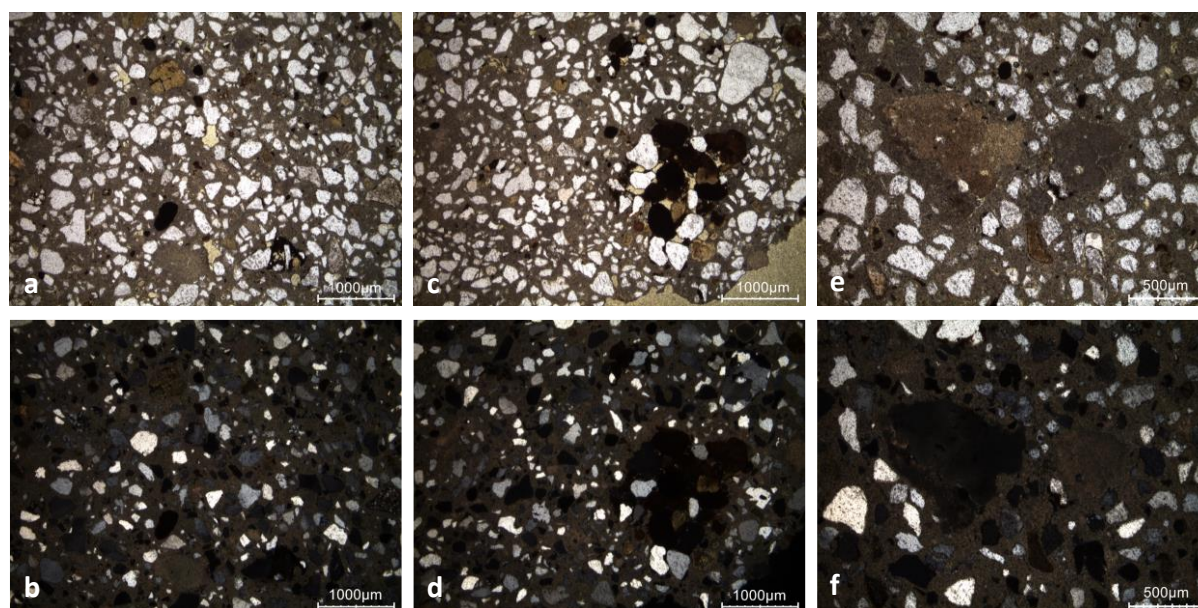
Figure 6: Representative photomicrographs of the thin-section X2294 of the mortar sample from the south façade at 20.90 m, a) overview image in plain polarised light (PPL); b) overview image in cross polarised light (XPL); c) PPL image showing a fragment of ferruginous sandstone; d) same image in XPL; e) PPL image with incompletely carbonated lime inclusion; f) same image in XPL.

Binder	**Texture**	micritic
	Lump state	completely burned (one incompletely carbonated)
	Lump size	max 2 cm
	Lump frequency	medium
Aggregate	**Grain size**	very fine to coarse
	Mineralogy	siliceous sand (quartz, K-feldspars, glauconite)
	Shape	subangular / subrounded
Appearance	**Homogeneity**	relatively homogenous
	Macroporosity	low / medium
	Pore structure	irregular / not connected

Admixtures	**Type**	-
Alteration	**Type**	-

Table 2: Main characteristics of the mortar sample from the south façade at 20.90 m from the core work based on the observations of the thin-section X2294.

The petrographic observations revealed a good state of preservation for the mortar sample from the north façade at 11.25 m from the core work (Figure 7 & Table 3). The lime inclusions are completely burned. The aggregate does not seem to contain any limestone fragments. Some fragments of the ferruginous sandstone of Diest (local natural stone – top left of the picture Figure 7a & b) are observed in the aggregate.
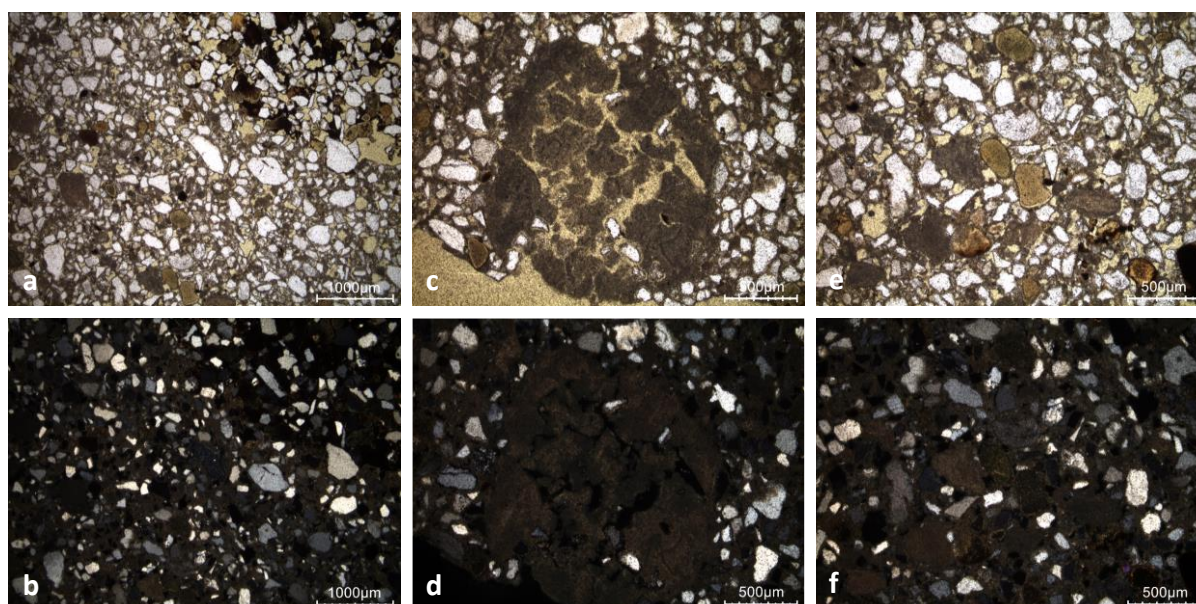
Figure 7: Representative photographs of the thin-section X2295 of the mortar sample from the north façade at 11.25 m, a) overview image in plain polarised light (PPL); b) overview image in cross polarised light (XPL); c) PPL image showing a completely burned lime inclusion; d) same image in XPL; e) PPL image glauconite; f) same image in XPL.

Binder	**Texture**	micritic
	Lump state	completely burned
	Lump size	max 1.9 mm
	Lump frequency	numerous
Aggregate	**Grain size**	very fine to coarse
	Mineralogy	siliceous sand (quartz, K-feldspars, glauconite more or less oxidised, mica?)
	Shape	subangular / subrounded

Appearance	**Homogeneity**	relatively homogenous
	Macroporosity	medium
	Pore structure	irregular / sometimes connected
Admixtures	**Type**	-
Alteration	**Type**	-

Table 3: Main characteristics of the mortar sample from the north façade at 11.25 m from the core work based on the observations of the thin-section X2295.

The petrographic observations suggest that the bedding mortar sample from the north façade at 16.60 m is in good condition (Figure 8 & Table 4). The lime inclusions are burned at different levels. Some are completely burned (Figure 8a & b), some are partially burned (Figure 8c & d) and some are unburned (Figure 8e & f). Cracks are observed with no particular direction, it is more porous compared to the two other samples. Some fragments of the ferruginous sandstone of Diest (local natural stone) are observed in the aggregate.
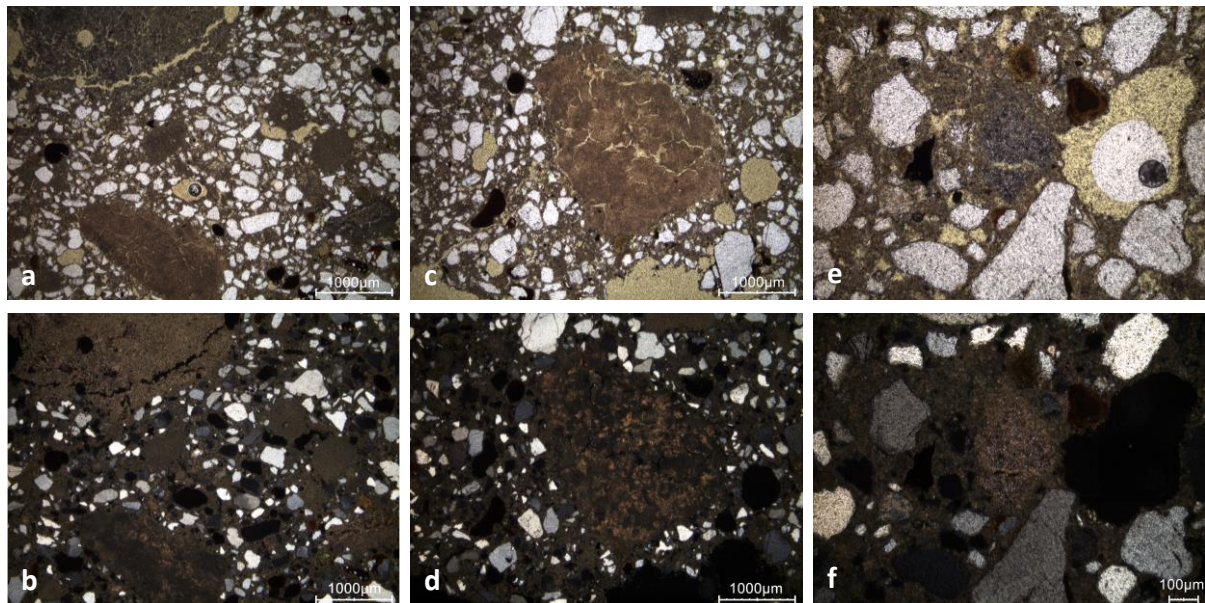
Figure 8: Representative photographs of the thin-section X2296 of the mortar sample from the north façade at 16.60 m L8, bedding mortar surface with stone, a) overview image in plain polarised light (PPL); b) overview image in cross polarised light (XPL); c) PPL image showing a completely burned lime inclusion; d) same image in XPL; e) PPL image glauconite; f) same image in XPL.

Binder	**Texture**	micritic
	Lump state	incompletely & completely burned
	Lump size	max 6.4 mm

	Lump frequency	numerous
Aggregate	**Grain size**	very fine to coarse
	Mineralogy	siliceous sand (quartz, K-feldspars, glauconite)
	Shape	subangular / subrounded
Appearance	**Homogeneity**	relatively heterogenous
	Macroporosity	medium
	Pore structure	irregular/sometimes connected/cracks in different direction
Admixtures	**Type**	-
Alteration	**Type**	-

Table 4: Main characteristics of the bedding mortar sample from the north façade at 16.60 m based on the observations of the thin-section X2296.

Thermogravimetric analysis (TGA) on whole samples

Both mortars from the core work (at 20.90 & 11.25) are very strongly hydraulic with apparent hydraulicity indices (aHI) between 35 and 42%. The bedding mortar retrieved from the surface of the north façade (at 16.60 m), however, is characterized by a moderate apparent hydraulicity (only 20 %). The amount of carbonates is 14.35 wt% for the mortar at 11.25 m, 22.26 wt% for the sample at 16.60 m and 17.53 wt% for the one at 20.90 m. The temperature of quartz transition phase is observed around 576-7°C (Rickard, Riessen, and Walls 2010). For the mortar sample at 16.60 m (Figure 11), the presence of gypsum was estimated at 1.2 wt% (peak around 130°C) (Moropoulou, Bakolas, and Bisbikou 2000). The main weight loss of ancient mortars is expected between 600 and 900 °C and is indicative of the decomposition of calcium carbonate ($CaCO_3$) into calcium oxide (CaO) and carbon dioxide (CO_2) (Ahmmed et al. 2024). The end temperature of calcium carbonate decomposition is 792, 784 and 775°C for the samples at 11.25 m, 16.60 m and 20.90 m, respectively.

Figure 9: Coupled TG-DSC analysis of the mortar sample from the south façade at 20.90 m upon heating to a temperature of 1200 ° C at a heating rate of 20 °C/min under an inert atmosphere (He flushed at 50 ml/min). The weight loss determined by thermogravimetric analysis (TG, wt%, green curve) and the result of the differential scanning calorimetric analysis (DSC, mW/mg, blue curve) are both presented.
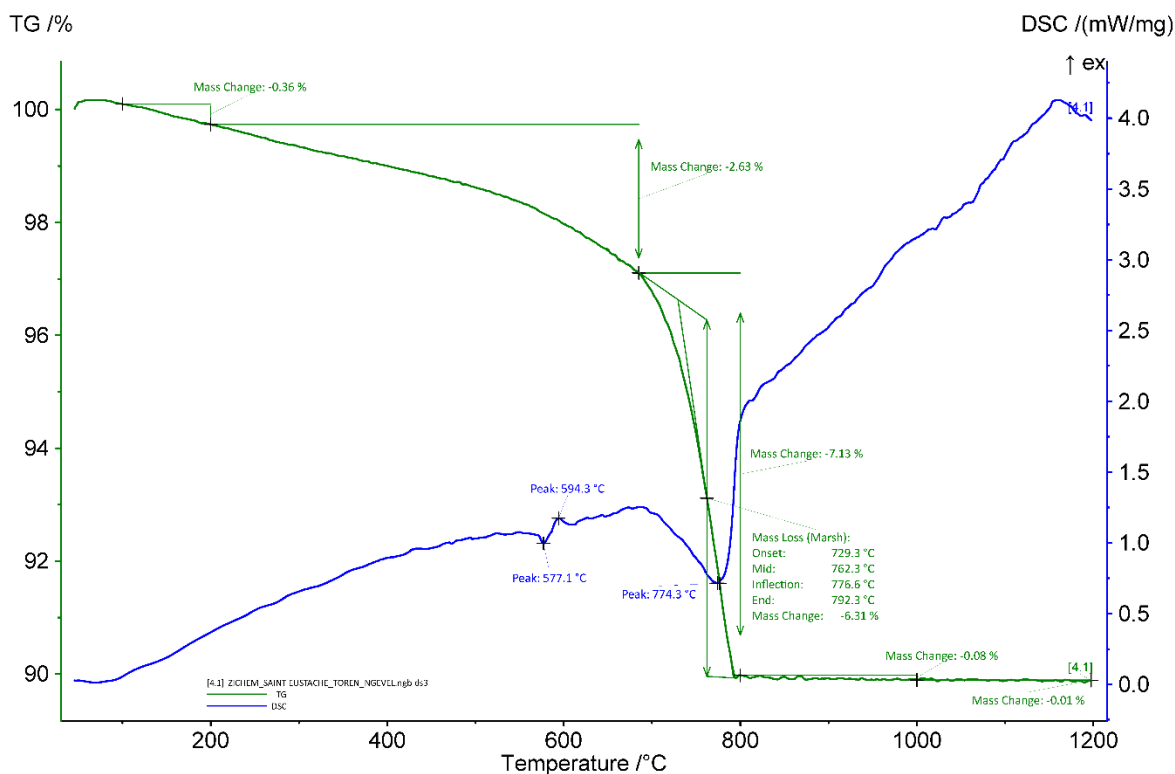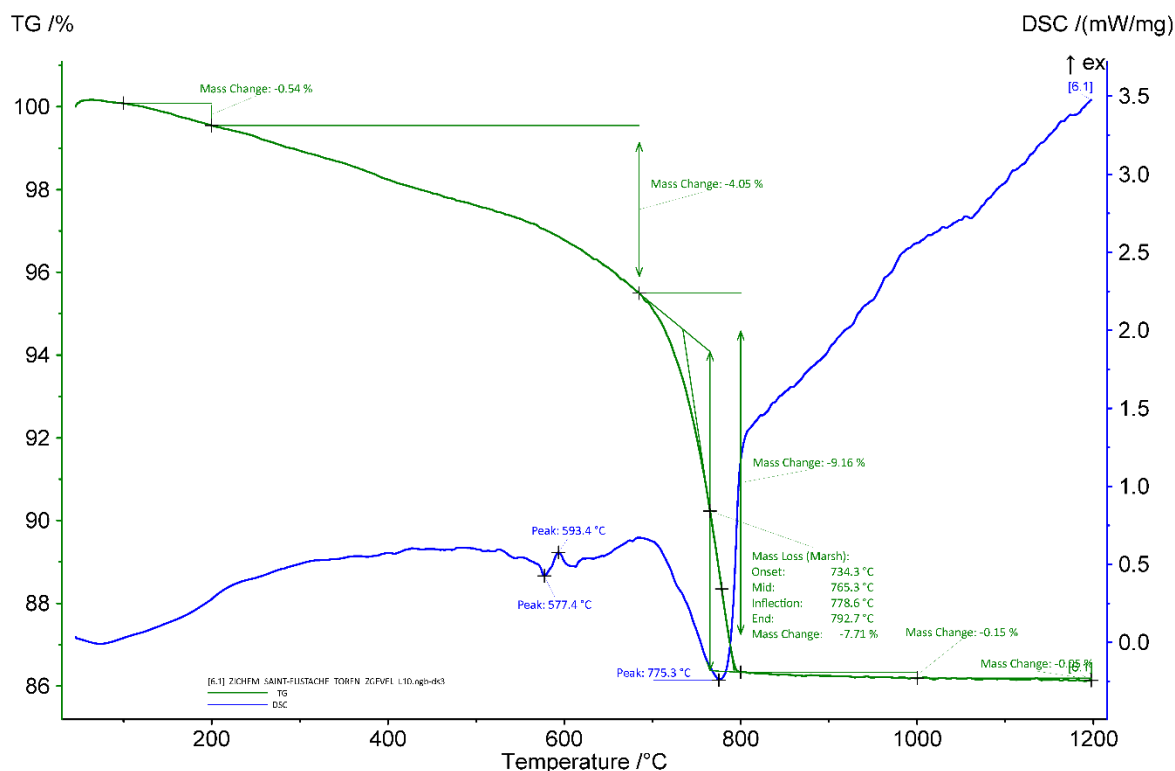
Figure 10: Coupled TG-DSC analysis of the mortar sample from the north façade at 11.25 m upon heating to a temperature of 1200°C at a heating rate of 20°C/min under an inert atmosphere (He flushed at 50 ml/min). The weight loss determined by thermogravimetric analysis (TG, wt%, green curve) and the result of the differential scanning calorimetric analysis (DSC, mW/mg, blue curve) are both presented.
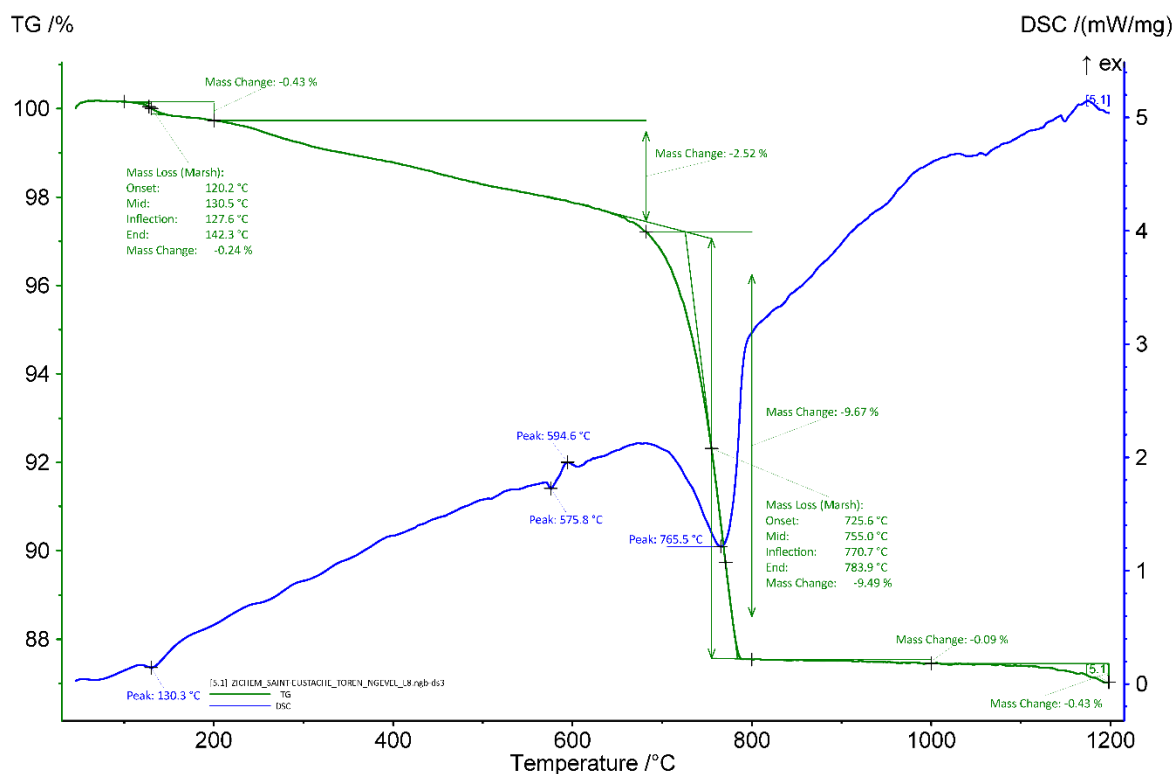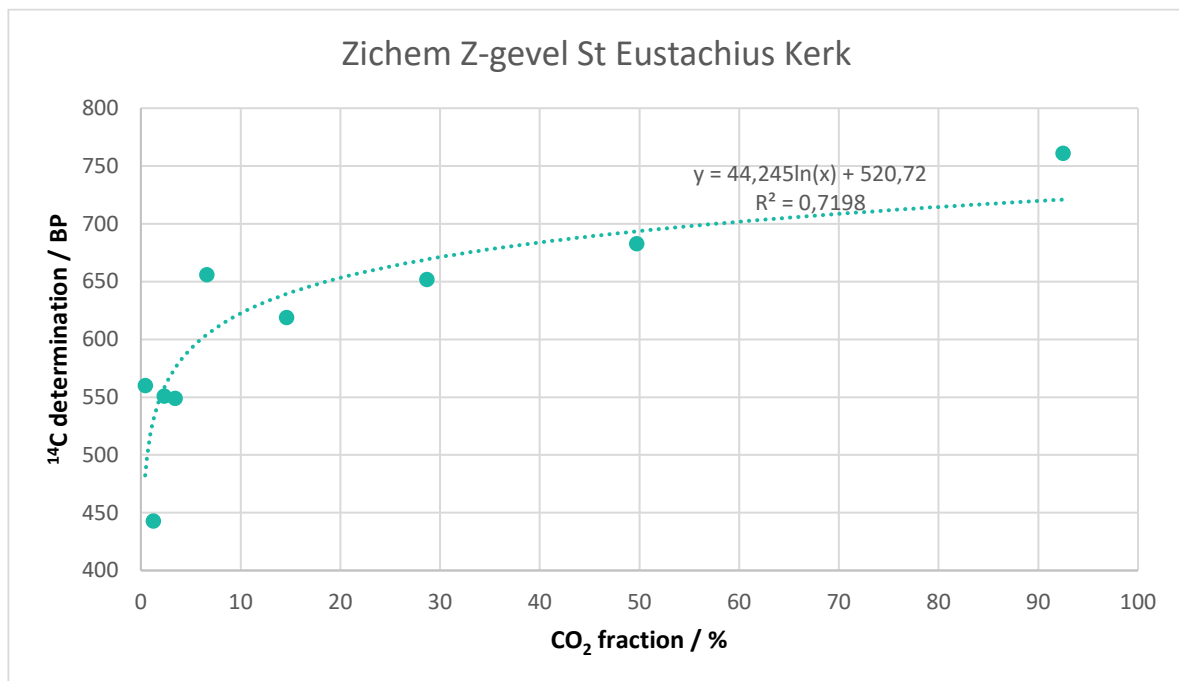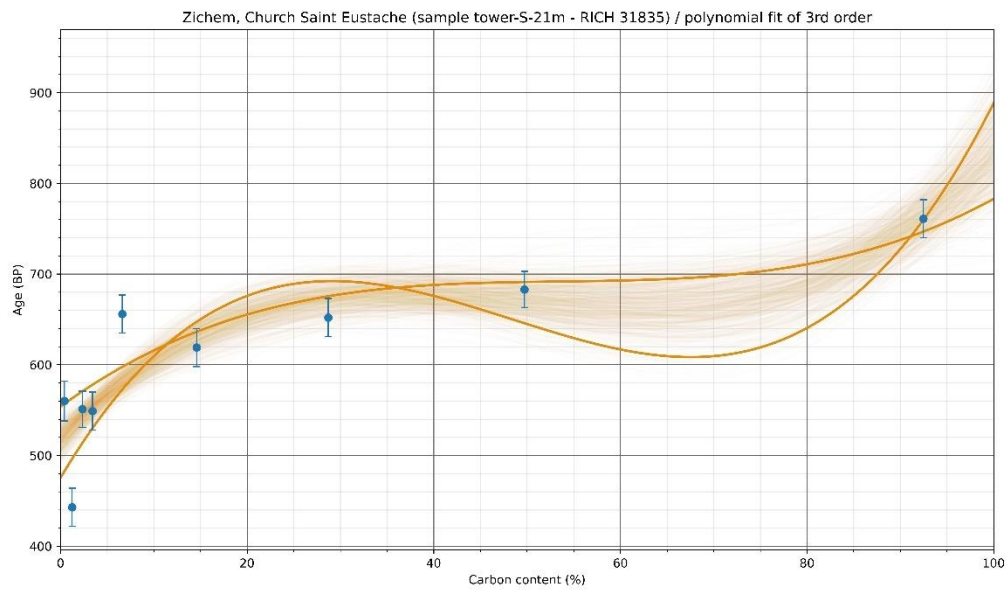

Figure 11: Coupled TG-DSC analysis of the mortar sample from the north façade at 16.60 m upon heating to a temperature of 1200°C at a heating rate of 20°C/min under an inert atmosphere (He flushed at 50 ml/min). The weight loss determined by thermogravimetric analysis (TG, wt%, green curve) and the result of the differential scanning calorimetric analysis (DSC, mW/mg, blue curve) are both presented.

Grinding/particle separation

For the mortar sample from the south façade at 20.90 m around 80 g were gently ground and some grey fragments were removed while grinding.

For the mortar sample from the north façade at 11.25 m brown/soil pieces were removed while gently grinding around 90 g of sample.

Soil particles & grey fragments were removed while grinding around 110 g of the mortar from the north façade at 16.60 m. Some pieces were harder to grind than others. A piece of straw/wood was found and extracted during the process.

FTIR on powders with particle size <75 μm

Both samples analysed show a composition predominantly made of calcite with silicates including quartz, aragonite and organic matter (Figure 12).
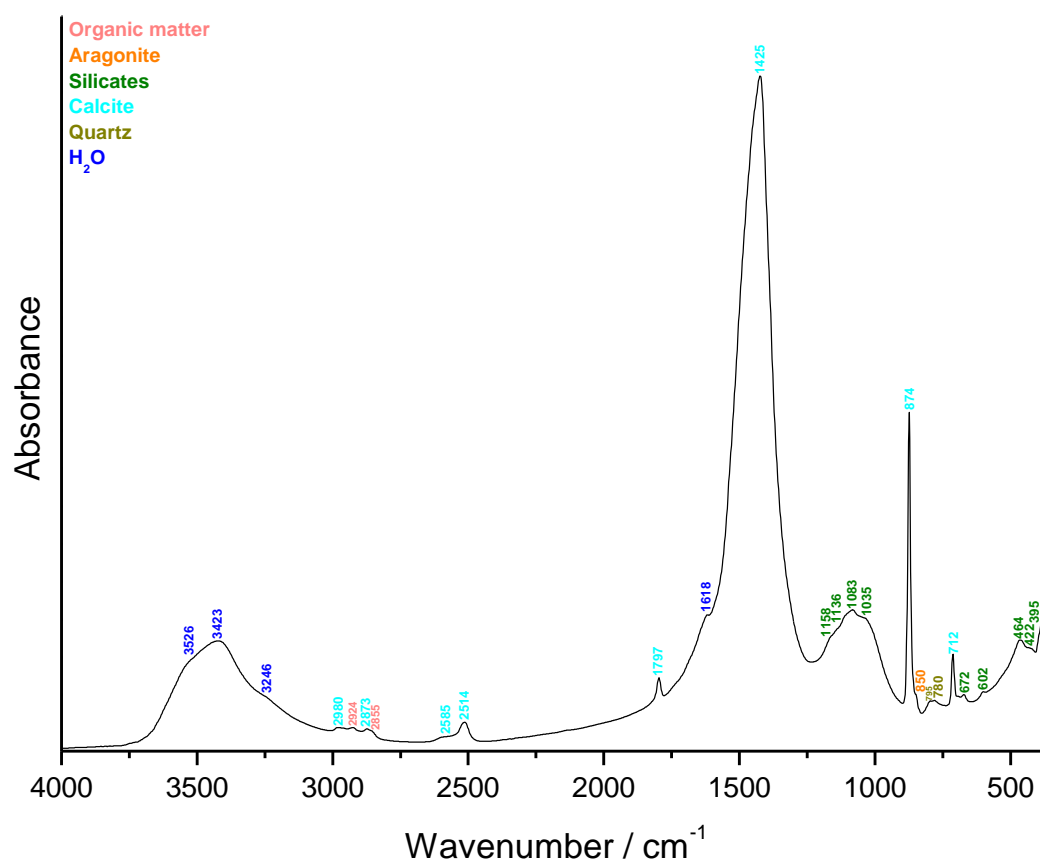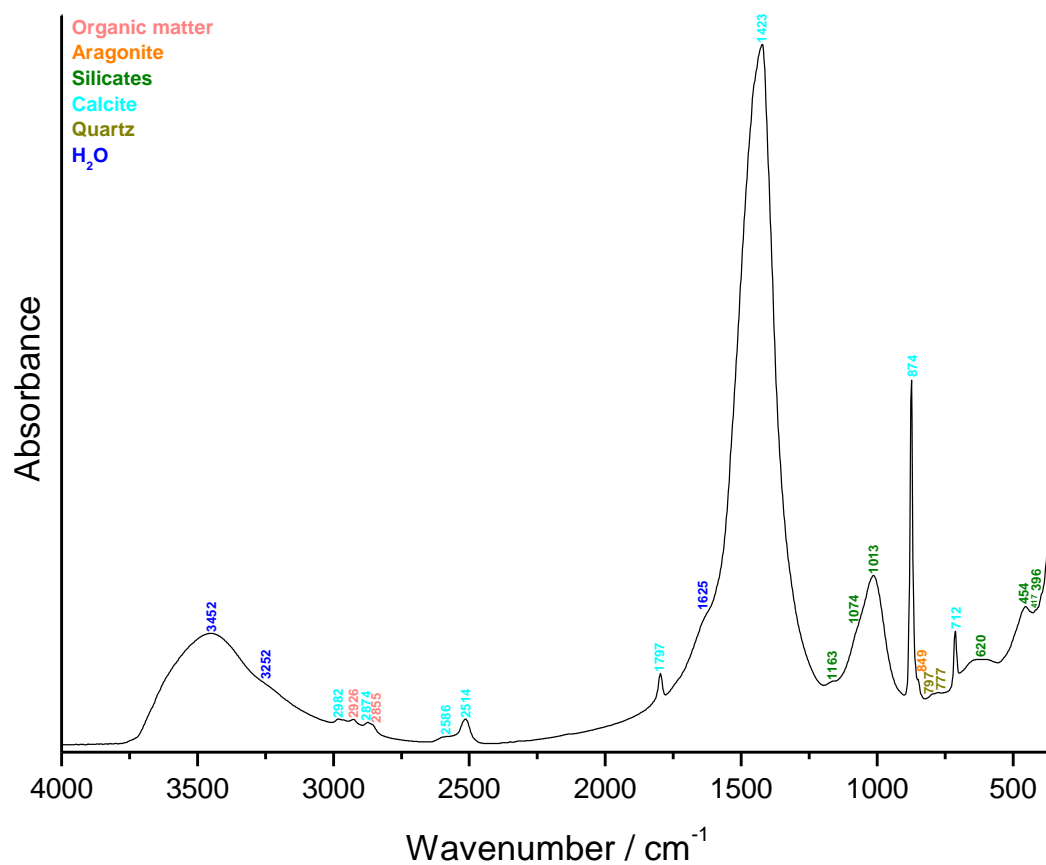
Figure 12: FTIR spectra obtained on the powders with a particle size < 75 μm of the mortar sample from the south façade at 20.90 m (top), and from the north façade at 16.60 m (bottom).

TGA on powders with particle size <75 μm

For the mortar sample from the north façade at 11.25 m, the aHI is the same for the powder with particle size <75 μm and the whole mortar sample (35 %). The two other samples show a difference between the two values: for the whole sample from the north façade at 16.60 m, the aHI is 20 % in opposition to 27 % for the powdered sample with particle size <75 μm, and for the mortar sample from the south façade at 20.90 m , it is 42% for the whole sample and 37 % for the powder with particle size lower than 75 μm. These differences could be explained by the presence of ferruginous sandstone that end up in more or less important quantities in the powdered sieved samples. The quantity of carbonates is higher in the powder compared to the whole samples since a large part of the sand is removed (33.29 wt% for the mortar at 11.25 m, 47.83 wt% for the sample at 16.60 m and 47.19 wt% for the one at 20.90 m). Indeed, no quartz was detected in the powders. As for the whole mortar sample at 16.60 m, gypsum was also detected in the powder at 2.4 wt% (peak around 134 °C – Figure Z) (Moropoulou, Bakolas, and Bisbikou 2000). For all samples (Figures 13 to 15), a peak around 400 °C is observed and might be due to the release of water from calcium hydroxide (Moropoulou, Bakolas, and Bisbikou 1995; Klimesch and Ray 1996) indicating that the mortar did not fully carbonated. This was not observed for the whole mortar samples. It was probably present in too low concentration to be noticeable. The end temperatures of calcium carbonate decomposition are 822, 827 and 836 °C for the powdered samples at 11.25 m, 16.60 m and 20.90 m, respectively. It is higher compared to the whole samples. A possible explanation could be that the powder is more pure compared to the whole mortar sample which increases the decomposition temperature.

Figure 13: Coupled TG-DSC analysis of the powdered mortar sample from the south façade at 20.90 m with particle size < 75 μm upon heating to a temperature of 1200 ° C at a heating rate of 20 °C/min under an inert atmosphere (He flushed at 50 ml/min). The weight loss determined by thermogravimetric

analysis (TG, wt%, green curve) and the result of the differential scanning calorimetric analysis (DSC, mW/mg, blue curve) are both presented.

Figure 14: Coupled TG-DSC analysis of the powdered mortar sample from the north façade at 11.25 m with particle size < 75 µm upon heating to a temperature of 1200 °C at a heating rate of 20 °C/min under an inert atmosphere (He flushed at 50 ml/min). The weight loss determined by thermogravimetric analysis (TG, wt%, green curve) and the result of the differential scanning calorimetric analysis (DSC, mW/mg, blue curve) are both presented.

Figure 15: Coupled TG-DSC analysis of the powdered mortar sample from the north façade at 16.60 m with particle size < 75 μm upon heating to a temperature of 1200 ° C at a heating rate of 20 °C/min under an inert atmosphere (He flushed at 50 ml/min). The weight loss determined by thermogravimetric analysis (TG, wt%, green curve) and the result of the differential scanning calorimetric analysis (DSC, mW/mg, blue curve) are both presented.

Radiocarbon results

The test prior to the CO_2 extraction revealed a relatively good amount of carbon for all samples (Table 5) (~5 to 7 %), a relatively low amount of powder < 75 μm was necessary for the carbon extraction (~1 to 2 g). This confirms the good state of preservation of the mortars.

RICH	Sample type	Method	C (%)	σ (%)	m (g)	Age BP	Calibrated date	Age BP extrapolated	Calibrated date	Age BP extrapolated with stat	Calibrated date (oxcal - 95.4%)	Age BP average first 4 dates	Calibrated date (oxcal - 95.4%)	Reliability of dating
31835 (S 20.9 m)	Mortar	HCl (8 fractions)	6.697	0.143	1.44	-	-	520 ± 21	1395-1440 calAD	519.2 ± 12	1406-1432 calAD	(fractions 1, 3 & 4) 553 ± 12	1325-1425 calAD	☒
32109 (N 11.25 m)	Mortar	HCl (7 fractions)	4.78	0.003	1.99	-	-	551 ± 22	1320-1430 calAD	571 ± 12.6	1323-1410 calAD	(6 first fractions) 588 ± 9	1320-1405 calAD	☑
34109 (N 11.25 m)	Lime lump	H₃PO₄	8.927	-	0.072	517 ± 32	1327-1446 calAD	-	-	-	-	-	-	☑
32108 (N 16.60 m)	Mortar	HCl (8 fractions)	5.96	0.064	1.7	-	-	411 ± 22	1430-1620 calAD	411 ± 11.6	1446-1478 calAD	(3 first fractions) 406 ± 13	1440-1490 calAD	☒
31330 (N 16.60 m)	Plant material	HCl cold few hours	47.69	-	0,00021	678 ± 35	1270-1400 calAD	-	-	-	-	-	-	☑

Table 5: Radiocarbon results

Both the extrapolated date and extrapolated date with statistics (Figure 16 and Table 5) obtained for the sample at 20.90 m are younger compared to the presumed historical date (~1300 AD). The average date (Table 5) obtained for the fractions below 75 μm from both mortars from the core work (at 20.90 m height at the south façade and at 11.25 m height at the north façade) in addition to the extrapolated date and extrapolated date with statistics (Figure 16 and Table 5) obtained for the sample at 11.25 m are in accordance with the presumed historical date. Both samples were taken from the core work at ca. 20 to 30 cm depth. The date obtained for the lime lump extracted from the mortar from the core work at the north façade at 11.25 m (Table 5) also falls within the range of the expected date. However, the date obtained for the bedding mortar sample from the north façade at 16.60 m does not match the expectations and is younger than expected (Figure 18 & Table 5). This could, despite the efforts taken when sampling, be due to a more recent repair (already in the 15th century) compared to the original core of the tower. Nevertheless, the piece of plant material extracted from the mortar falls within the presumed historical date. Either, the date is correct or it could give an older age due to the old wood effect.

Figure: Zichem Z-gevel St Eustachius Kerk. Scatter plot of ^{14}C determination / BP versus CO_2 fraction / %, with fit $y = 44,245\ln(x) + 520,72$ and $R^2 = 0,7198$.

Figure 16: Radiocarbon results for the powdered mortar sample from the south façade at 20.90 m from the core work with particles < 75 μm as a function of the CO_2 fraction.
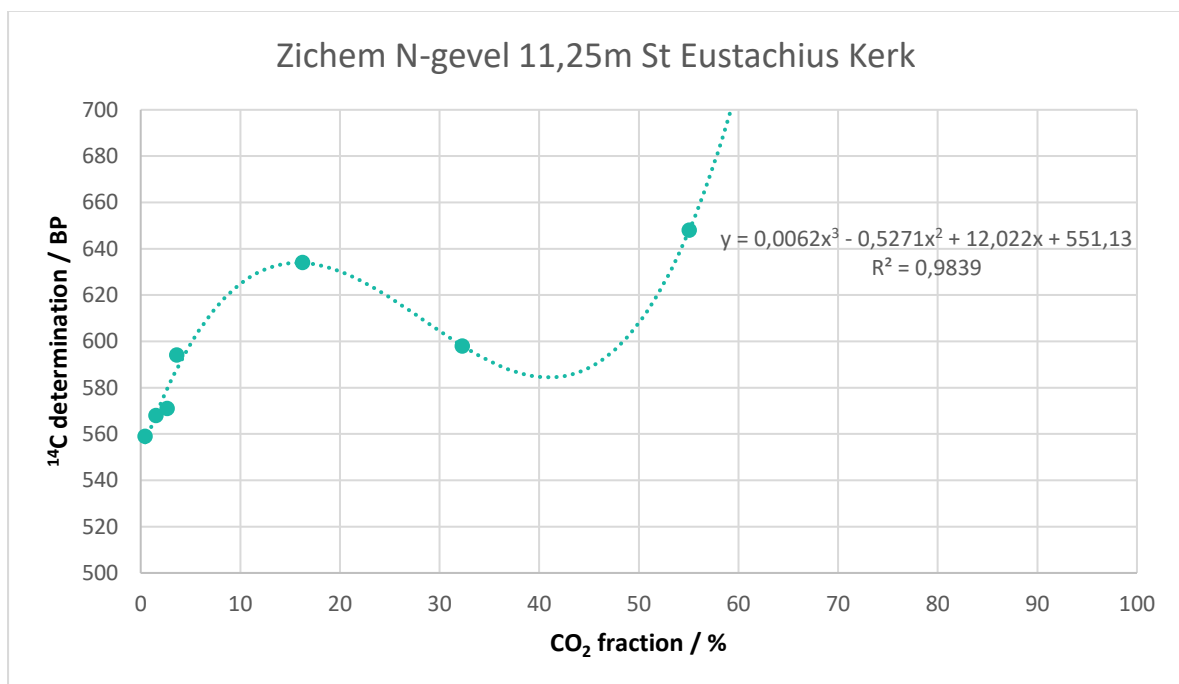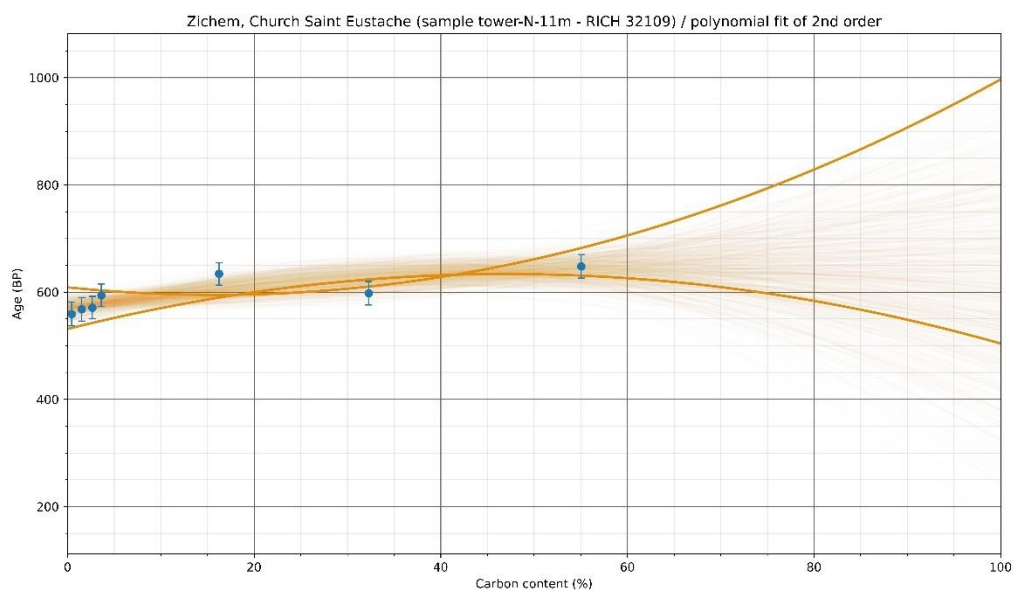
Figure 17: Radiocarbon results for the powdered mortar sample from the north façade at 11.25 m from the core work with particles < 75 µm as a function of the CO_2 fraction.
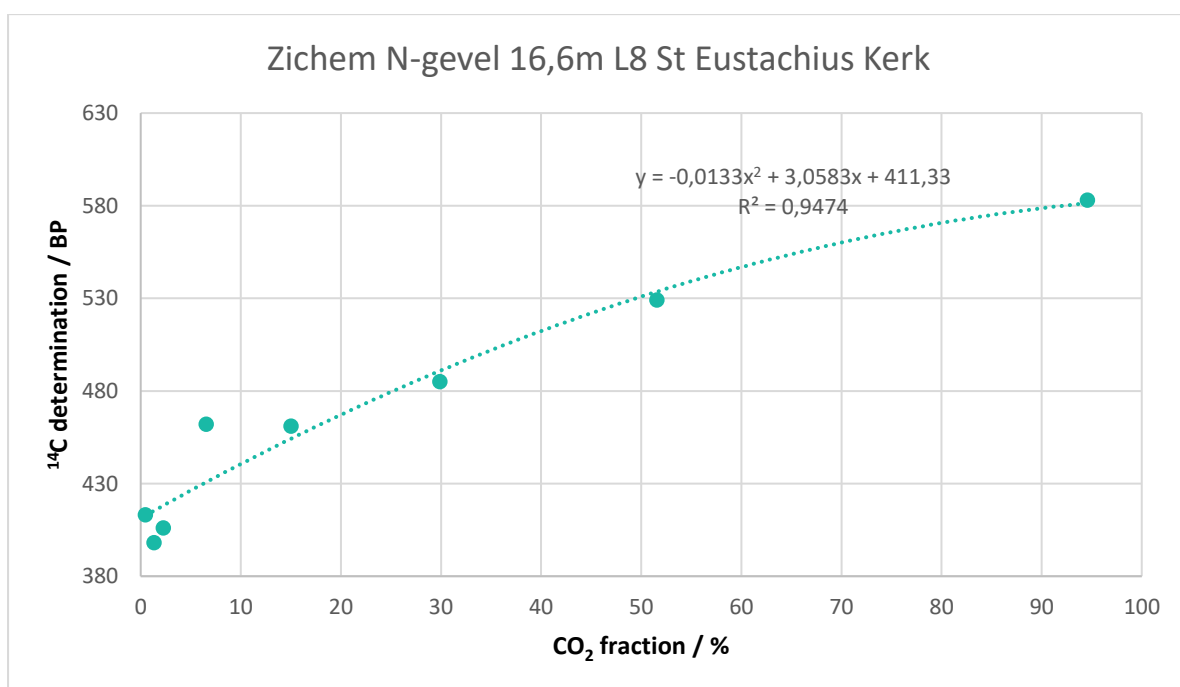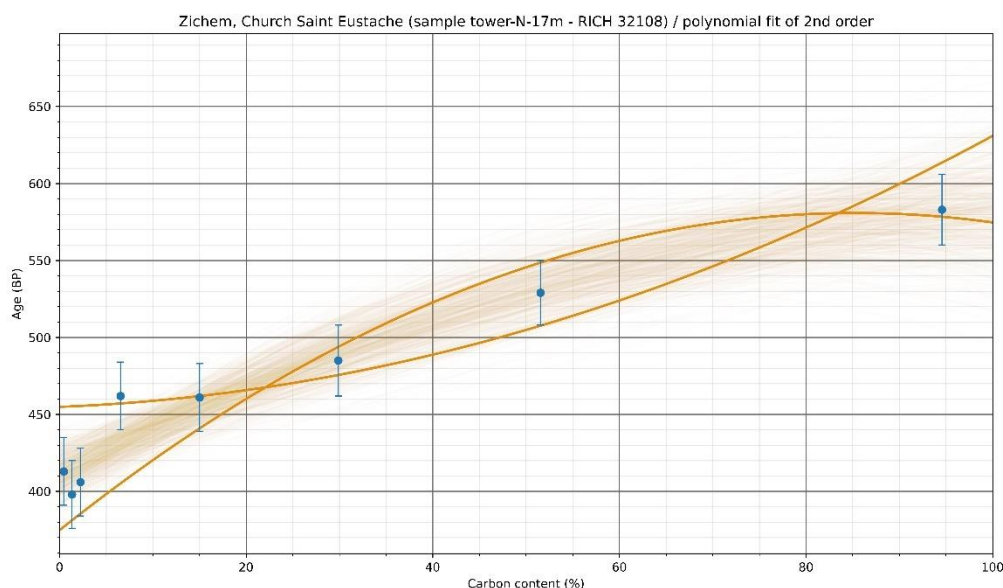
Figure 18: Radiocarbon results for the powdered bedding mortar sample from the north façade at 16.60 m with particles < 75 μm as a function of the CO_2 fraction.

Conclusions

The samples at 20.90 and 11.25 m show a very strong apparent hydraulicity index (aHI) according to the thermal analyses, they were sampled rather deep into the masonry. Since the value of aHI was probably amplified by the presence of ferruginous sandstone and glauconite grains in the mortars, we consider a strong hydraulicity for these samples. They should not considered for radiocarbon dating since they most probably underwent delayed hardening. However, the sample at 11.25 m provides a radiocarbon date matching the presumed historical date. For the mortar sampled at 16.60 m, the aHI is moderate but the radiocarbon date is younger than expected. The same remark as previously can be made and the mortar is most probably only slightly hydraulic. It show a good preservation state and it was sample on the surface. It would be considered for radiocarbon dating but the date obtained is younger than expected. As the mortar has been taken close to the surface, and restorations have been carried out, it cannot be excluded that the mortar stems from a later restoration phase.

Bibliography

Ahmmed, Tanjil, Ana Raquel Silva, José Carlos Quaresma, Patrícia Moita, and Cristina Galacho. 2024. "Analytical Characterization of Historical Mortars from the Roman Villa of Frielas (Loures, Portugal)." *Acta IMEKO* 13 (3): 1–11.

De munten van Reinhard, II van. n.d. "DE MUNTKLAPPER." Accessed April 8, 2024. https://www.egmp-vzw.be/Pdf/online_artikels/Muntkl77A.pdf.

Klimesch, Danielle S., and Abhi Ray. 1996. "The Use of DTA/TGA to Study the Effects of Ground Quartz with Different Surface Areas in Autoclaved Cement: Quartz Pastes. Part 1: A Method for Evaluating DTA/TGA Results." *Thermochimica Acta* 289 (1): 41–54. https://doi.org/10.1016/S0040-6031(96)03033-X.

Moropoulou, Antonia, Asterios Bakolas, and Katerina Bisbikou. 1995. "Characterization of Ancient, Byzantine and Later Historic Mortars by Thermal and X-Ray Diffraction Techniques." *Thermochimica Acta* 269:779–95.

———. 2000. "Investigation of the Technology of Historic Mortars." *Journal of Cultural Heritage* 1 (1): 45–58.

"Parochiekerk Sint-Eustachius." 2021. October 8, 2021. https://inventaris.onroerenderfgoed.be/erfgoedobjecten/42745.

Rickard, William D. A., Arie Van Riessen, and Philip Walls. 2010. "Thermal Character of Geopolymers Synthesized from Class F Fly Ash Containing High Concentrations of Iron and α-Quartz." *International Journal of Applied Ceramic Technology* 7 (1): 81–88. https://doi.org/10.1111/j.1744-7402.2008.02328.x.

Study of mortars from Archaeological crypt of the Sainte-Gertrude collegiate (Nivelles) for the BRAIN 2.0 PalC project

Context of the site

At Nivelles, the abbey consisted of at least three churches from the time of its foundation in the middle of the 7th century. One of them, Saint-Pierre, which became the collegiate church of Saint Gertrude, was dedicated to the dead. This church was originally a converted secular building. The development of the cult of Gertrude overturned the original functions of Saint-Pierre. A new building with three naves was probably planned as early as the end of the 7th century. This church was replaced at a date that is still unclear, perhaps around the second quarter of the tenth century. New observations suggest that it was this church that was burnt down at the beginning of the 11th century, and that it is still largely what we see today (Chantinne and Mignot 2017; 2014).

Figure 1: Engraving of the collegiate church (from the grand théâtre sacré du duché de Brabant ed. 1729 and 1734 The Hague, t. II)

Material

Two samples were taken from the different phases of the building's development:

1.   NIV21STG Z02 (Facts 2, 3, 4, 5, 6, 7): Mortar from the masonry of the first forebuilding dated between 700 and 900 (State IIIb), prior to the mid-10th century reconstruction. A charcoal has already been dated by ^{14}C in this masonry from the 9th to 11th century (RICH-27702- Z02 F04 South pillar, transept phase IV).
2.   NIV21STG Z01 (Fact 4): Mortar from the south cruciform pillar of the transept of the present collegiate church dated to the middle, or even 2nd quarter, of the 10th century.

Results & Discussion

Macroscopic descriptions

Both samples are beige (Figure 2) tending towards pale yellow (2.5Y 8/3) according to the Munsell soil colour charts. The lime lumps exhibit various sizes, some of them are cubic for sample NIV21STG Z01 (Figure 2 bottom) which is rather uncommon. A large brown inclusion (4 cm) is observed for NIV21STG Z02 (Figure 2 top) and is probably a fragment of ferruginous sandstone. Both samples contain red soft and angular inclusions that are probably terracotta. The grey inclusions in NIV21STG Z02 seems to be made of siliceous aggregate and the ones in NIV21STG Z01 are probably made of limestone since they seem to react weakly with HCl. Black and soft inclusions are present in both samples and are probably charcoal. Some plant fragments that are most probably straw were noted for NIV21STG Z01 (Figure 2 bottom).
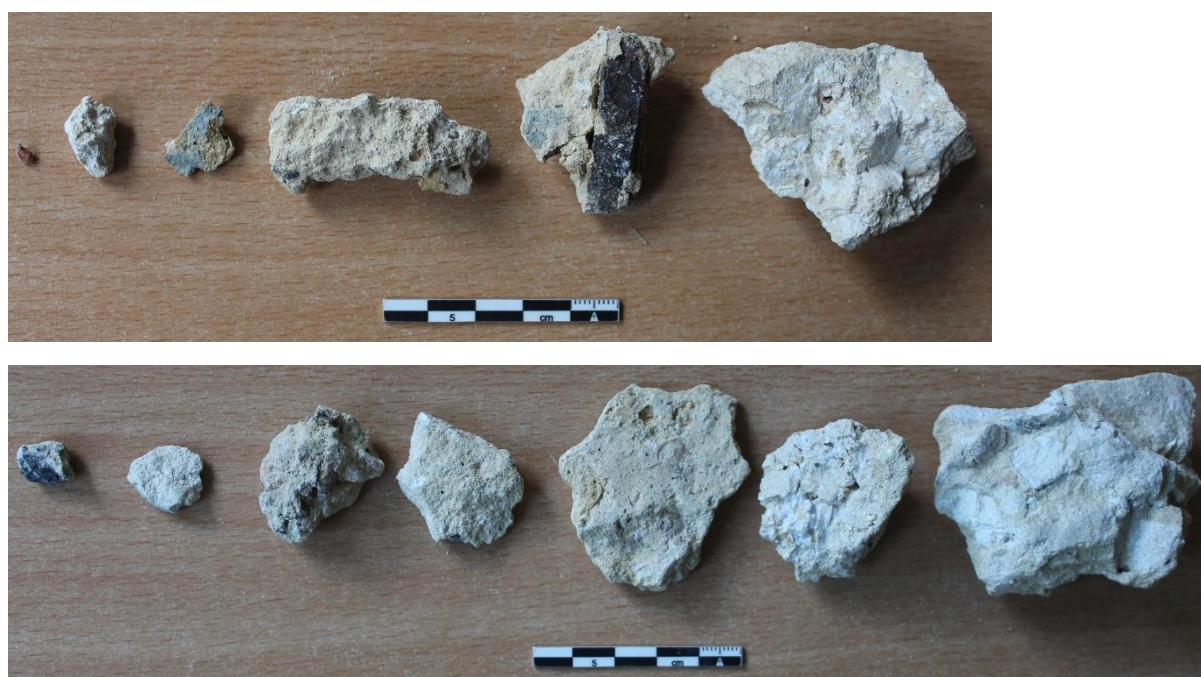
Figure 2: Mortar samples NIV21STG Z02 (top) and NIV21STG Z01 (bottom).

Fourier transform Infrared (FTIR) spectroscopy on inclusions & binder

The binders (beige, Figure 3) mainly contain calcium carbonates, silicates and nitrates. The later are also present in all the inclusions analysed in both mortars showing a certain alteration. The spectra of lime lumps (white or white cube, Figure 3) are similar to the binder ones. The relative concentration of carbonates compared to silicates is rather low for both binders and lumps which might show a certain dissolution. Moreover, no aragonite was detected in the sample NIV21STG Z02. This might confirm a dissolution of the carbonates. The large brown

inclusion in NIV21STG Z02 is made of silicates including quartz and clay. The black inclusions (black, Figure 3) of both samples contain amorphous carbon. The red and grey inclusions (Figure 3) contain silicates including quartz in addition to clay for the grey ones. No limestone fragments were detected for the grey inclusions as initially expected from the macroscopic descriptions. The white crust on the surface of NIV21STG Z01 comprises carbonates, silicates and organic matter.
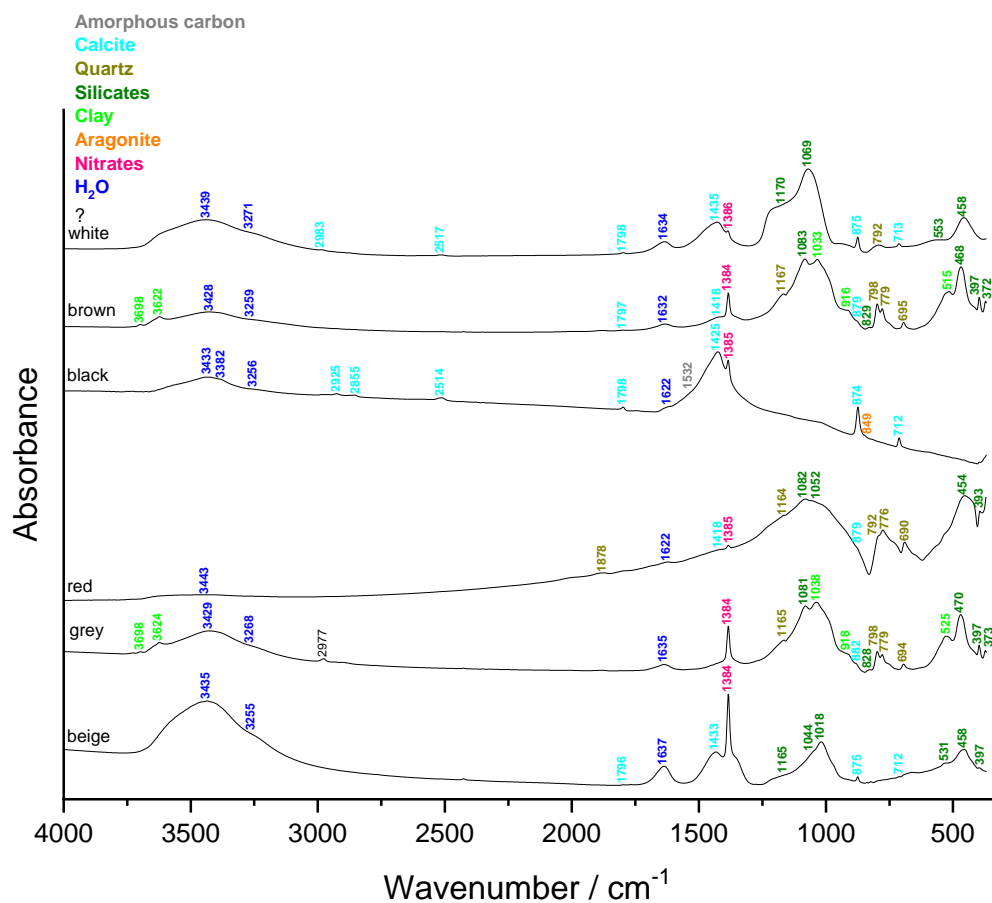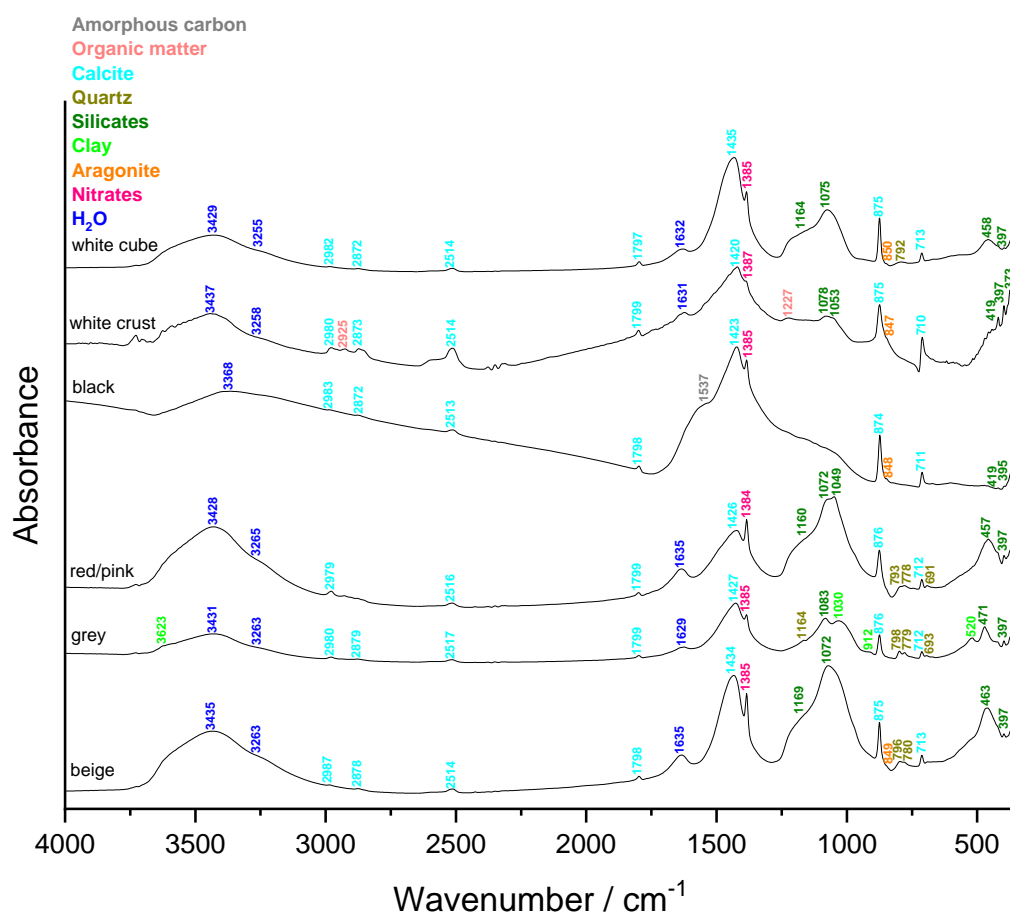
Figure 3: FTIR spectra obtained on the inclusions and binder (beige) of the mortar samples NIV21STG Z02 (top) and NIV21STG Z01 (bottom).

Binder:aggregate ratio

The calculated binder:aggregate ratio using a bulk density of 1.35 kg/dm^3 for the sand and 0.575 kg/dm^3 for the lime is close to 2:1 in volume unit for the sample Z02 and close to 3:2 for the sample Z01.

	Z02	Z01
Sample weight (g)	0.7	2.9
Crucible weight (g)	14.9	15.3
Weight calcined (g)	15.3	17.1
%ins	**57.1**	**62.5**

Table 1: Percentage of insoluble residue

Cathodoluminescence

The cathodoluminescence observation of the thin section from the mortar NIV21STG Z02 (Figure 4a) shows the presence of quartz grain in dark purple, K-feldspars in bright blue and the binder is dull. The thin section of sample NIV21STG Z01 shows similar results in addition to some lime lumps that are partially burned. The later exhibit a bright red colour that is more of less intense depending on the area. The powdered sample NIV21STG Z02 mortar with particle size lower than 75 µmis mainly dull with a few bright blue K-felspar grains and some bright red limestones grains. For the powdered mortar NIV21STG Z01 mortar with particle

size lower than 75 µm, only one bright red limestone grain is observed with a few bright green plagioclases and bright blue K-feldspars.
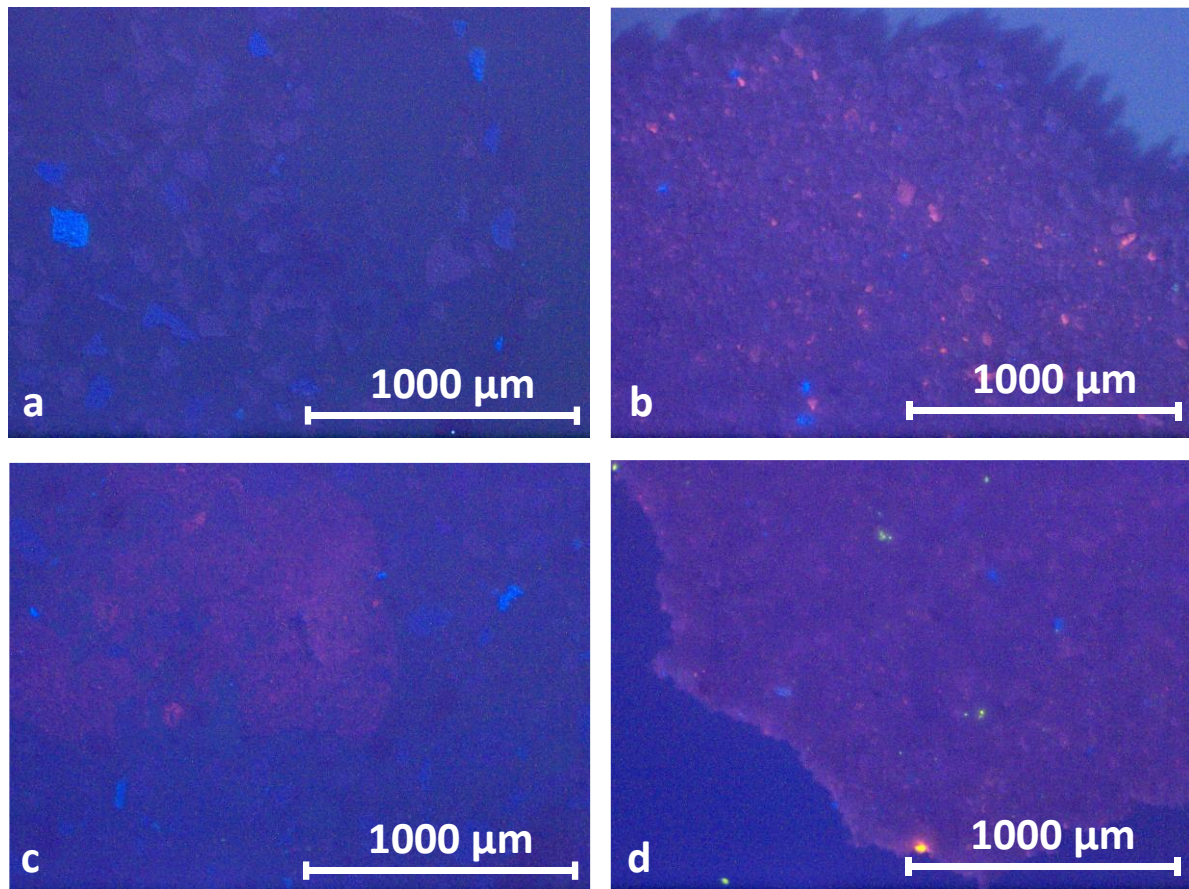
Figure 4: Characteristic cathodoluminescence images of a) the thin section X2297 of NIV21STG Z02 b) the powdered NIV21STG Z02 mortar with particle size lower than 75 µm, c) the thin-section X2298 of NIV21STG Z01 and, d) the powdered NIV21STG Z01 mortar with particle size lower than 75 µm.

Thin-section petrography

The mortar NIV21STG Z02 is extremely deteriorated, it has been dissolved (Figure 5 & Table 2) as expected from the FTIR analyses. The rare lime lumps still present (Figure 5c & d) are completely burned. The aggregate used is made of siliceous sand without calcareous fraction.
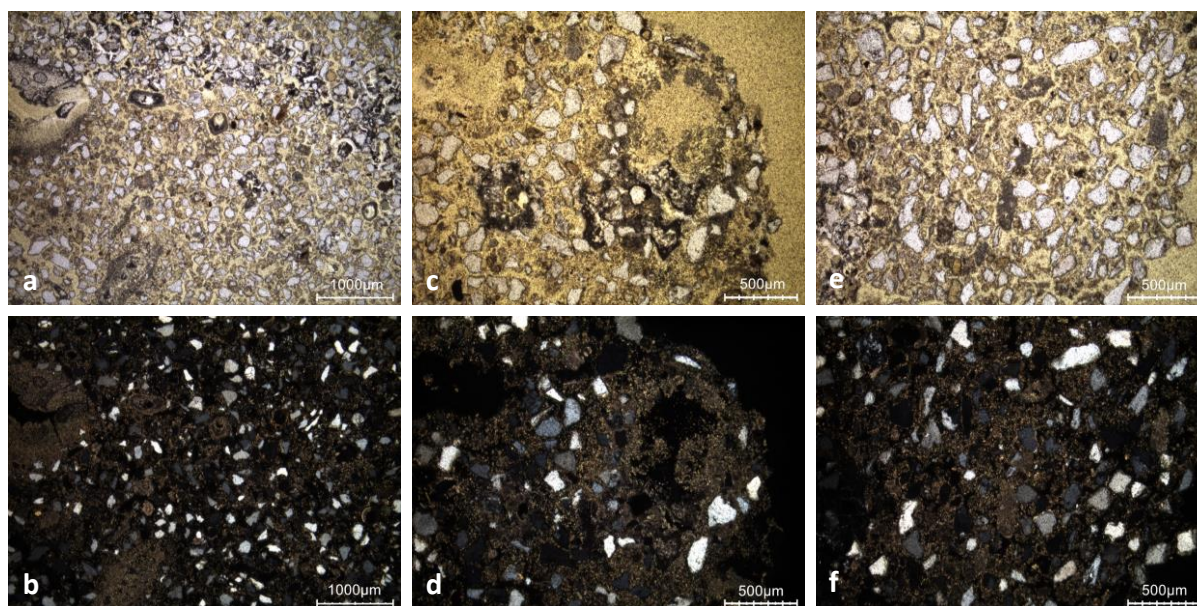
Figure 5: Representative photomicrographs of the thin-section X2297 of NIV21STG Z02: a) overview image in plain polarised light (PPL); b) overview image in cross polarised light (XPL); c) PPL image showing a partially dissolved lime inclusion; d) same image in XPL; e) PPL image with small lime inclusions or binder's remnants not dissolved; f) same image in XPL.

Binder	**Texture**	micritic
	Lump state	completely burned
	Lump size	max 2.5 mm
	Lump frequency	medium
Aggregate	**Grain size**	very fine (<125 μm) to fine (<250 μm)
	Mineralogy	pure siliceous sand (quartz, feldspars, glauconite)
	Shape	subangular / subrounded
Appearance	**Homogeneity**	relatively heterogeneous
	Macroporosity	high due to dissolution
	Pore structure	highly connected due to dissolution
Admixtures	**Type**	charcoal
Alteration	**Type**	dissolution, secondary carbonates?

Table 2: Main characteristics of the sample NIV21STG Z02 retrieved from the observations of the thin-section X2297.

The mortar NIV21STG Z01 is extremely deteriorated, it has been dissolved (Figure 6 & Table 3). The limestone used naturally contains silicates and bioclasts (Brussels stone), since they are

part of the lime inclusions. Most lime lumps are completely burned but some inclusions are partially burned (Figure 6c & d).
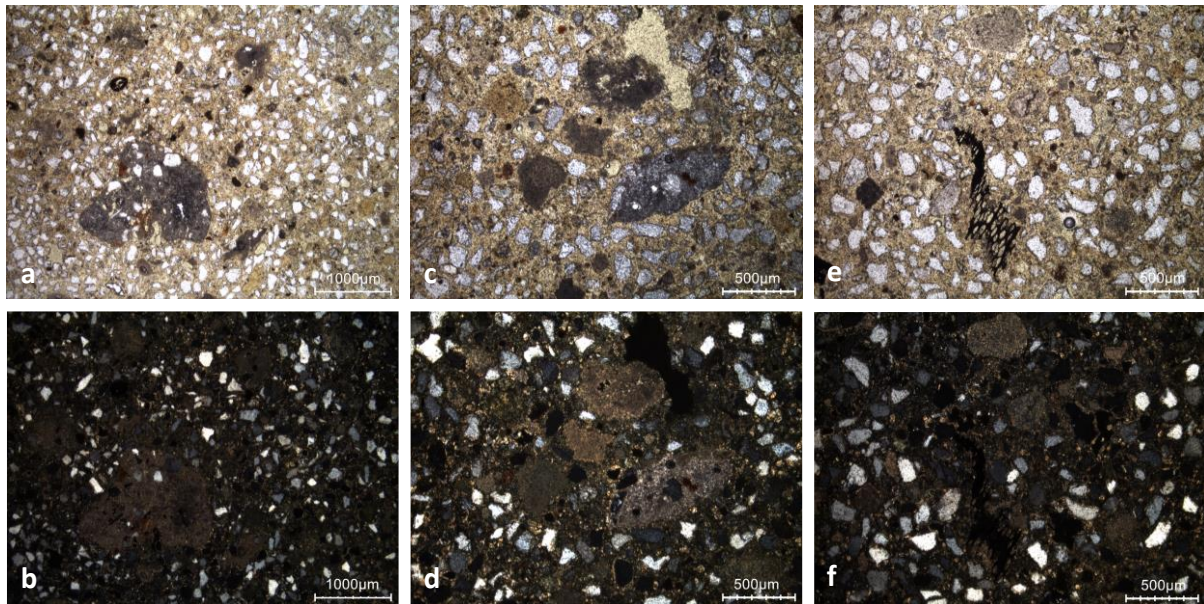
Figure 6: Representative photomicrographs of the thin-section X2298 of NIV21STG Z01: a) overview image in PPL; b) overview image in XPL; c) PPL image showing completely burned and incompletely burned lime inclusions; d) same image in XPL; e) PPL image with a charcoal fragment; f) same image in XPL.

Binder	**Texture**	micritic
	Lump state	completely burned & incompletely burned
	Lump size	max 1.5 mm
	Lump frequency	medium
Aggregate	**Grain size**	very fine (<125 μm) to fine (<250 μm)
	Mineralogy	pure siliceous sand (quartz, feldspars, glauconite)
	Shape	subangular / subrounded
Appearance	**Homogeneity**	relatively heterogeneous
	Macroporosity	high due to dissolution
	Pore structure	highly connected due to dissolution
Admixtures	**Type**	charcoal
Alteration	**Type**	dissolution

Table 3: Main characteristics of the sample NIV21STG Z01 retrieved from the observations of the thin-section X2298.

Thermogravimetric analysis (TGA) on whole samples

The graphs of the thermal analyses are presented in Figures 7 and 8. The apparent hydraulicity indexes (aHI) determined on the basis of the weight loss between 200 and ca. 650°C (usually attributed to water loss from calcium-silicate-hydrates-phases) show that the mortar binders are very strongly hydraulic (51 and 45 % for Z01 and Z02, respectively). The hydraulicity indexes cannot be considered reliable, due to the high degree of dissolution of the binders, which strongly influences the obtained value upwards. The amount of carbonates is ~11 wt% for the mortar Z01 and 14 wt% for Z02. An exothermic peak is found at 385°C for sample Z01, possibly because of the decomposition of organic compounds, the conversion of soluble to insoluble anhydrite, or the rearrangement in anhydrous $CaSO_4$ from hemihydrate to anhydrate structure (Brunello 2020). The temperature of quartz transition phase is observed around 573°C (Rickard, Riessen, and Walls 2010) for both samples. The main weight loss of ancient mortars is expected between 600 and 900 °C and is indicative of the decomposition of calcium carbonate ($CaCO_3$) into calcium oxide (CaO) and carbon dioxide (CO_2) (Ahmmed et al. 2024). The end temperature of calcium carbonate decomposition is 781°C for Z02 (it was not possible to calculate for Z01). No gypsum was detected.
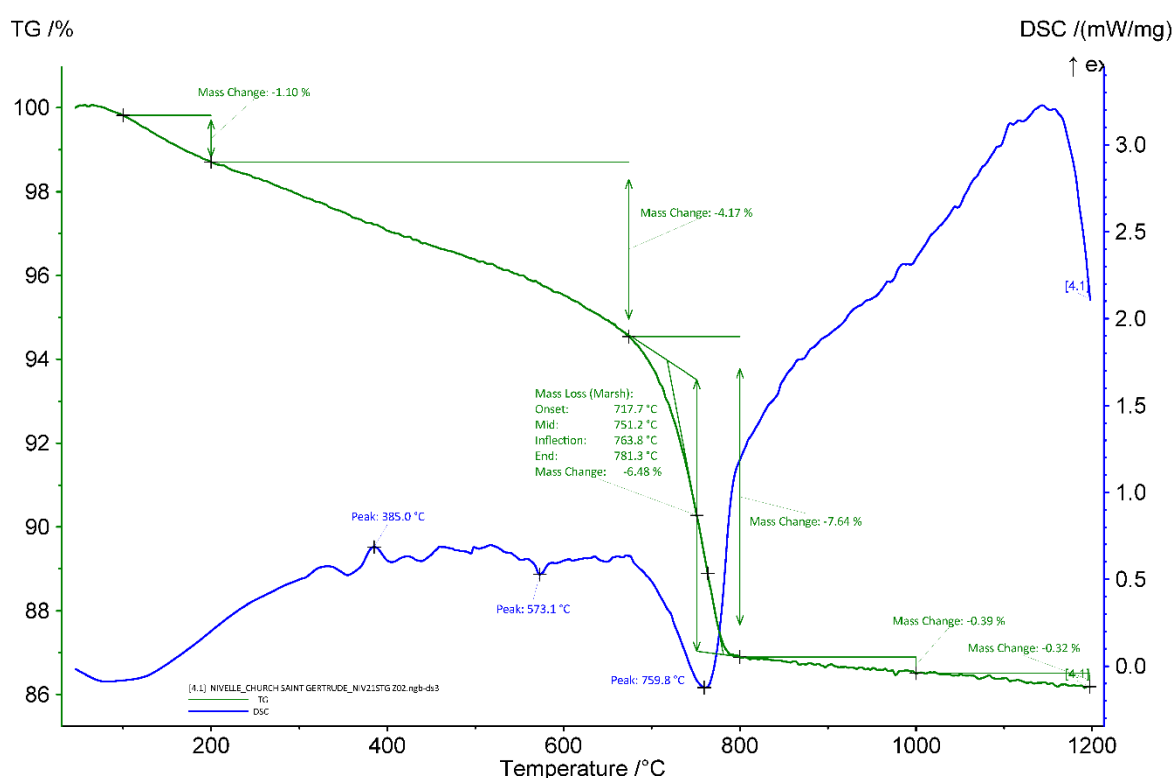
Figure 7: Coupled TG-DSC analysis of the sample NIV21STG Z02 upon heating to a temperature of 1200° C at a heating rate of 20 °C/min under an inert atmosphere (He flushed at 50 ml/min). The weight loss determined by thermogravimetric analysis (TG, wt%, green curve) and the result of the differential scanning calorimetric analysis (DSC, mW/mg, blue curve) are both presented.
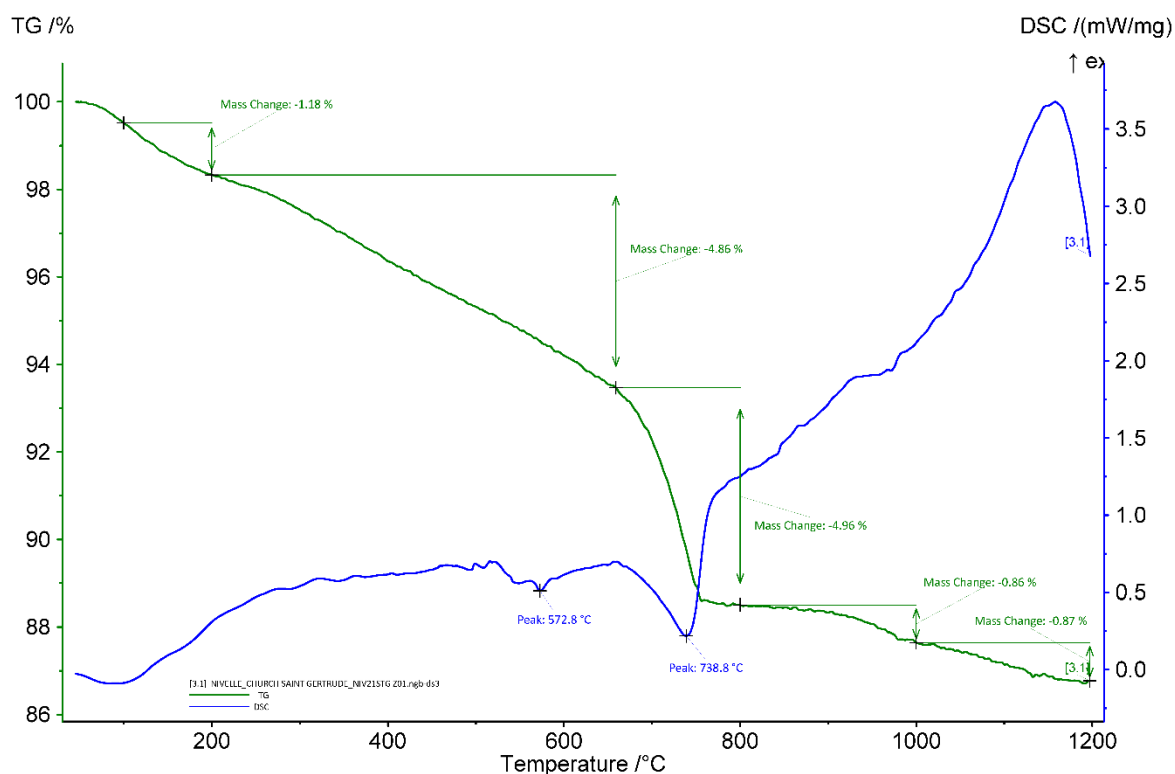
Figure 8: Coupled TG-DSC analysis of the sample NIV21STG Z01 upon heating to a temperature of 1200° C at a heating rate of 20 °C/min under an inert atmosphere (He flushed at 50 ml/min). The weight loss determined by thermogravimetric analysis (TG, wt%, green curve) and the result of the differential scanning calorimetric analysis (DSC, mW/mg, blue curve) are both presented.

XRD

X-ray diffraction analyses show the presence of quartz and calcite (Figure 9).
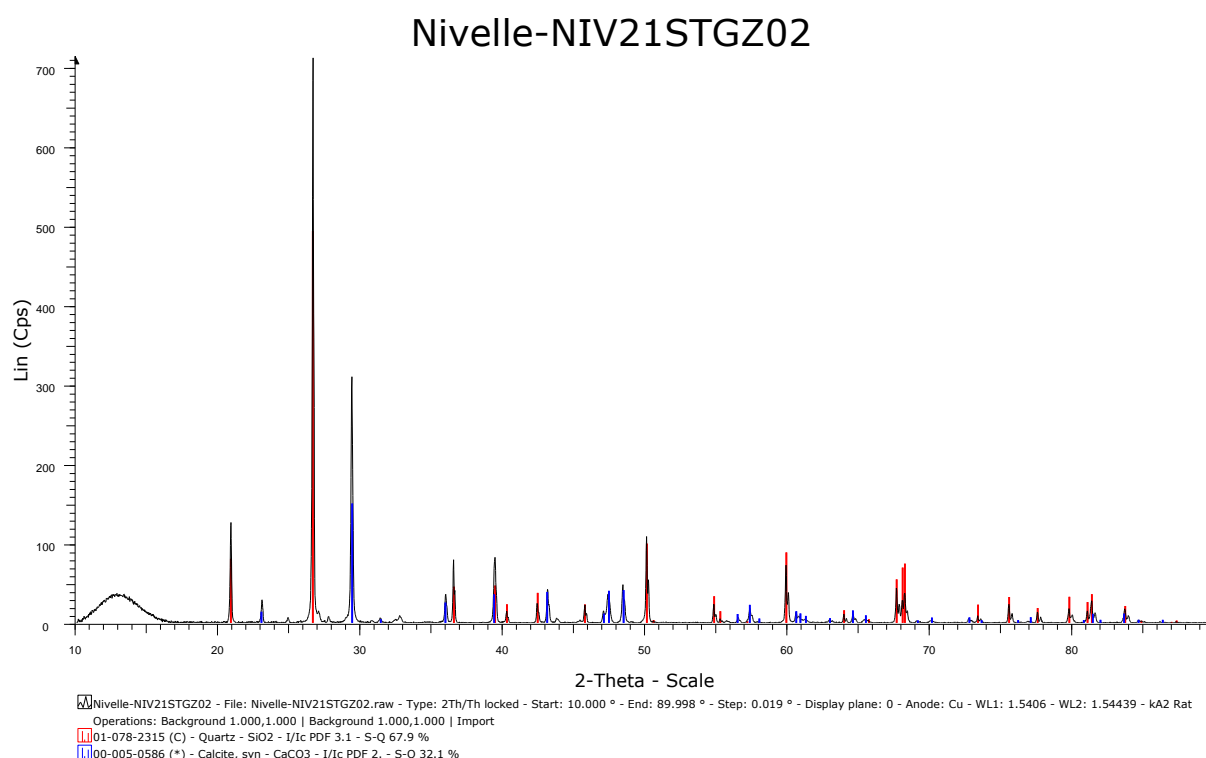
Figure 9: XRD diffractogram of the sample NIV21STG Z02.

TGA on powders with particle size <75 μm

The aHI of the powders with particles < 75 μm, determined on the basis of the weight loss between 200 and ca. 650°C, are 72 % for Z01 and 53 % for Z02 (Figures 10 and 11). The obtained values on powders are thus higher than those on whole samples. These differences could be explained by the presence of clay that end up in more quantities in the powdered sieved samples. The quantity of carbonates is the same for the powder and the whole sample for Z01 (11 w%) and it is higher in the powdered sample Z02 (22 w%) compared to the whole (14 w%) samples since a large part of the sand was removed when sieving. Indeed, no quartz was detected in the powders. For Z01 (Figure 11), a peak at 385°C is observed and is possibly due either to the decomposition of organic compounds, or to the conversion of soluble to insoluble anhydrite, or to the rearrangement in anhydrous $CaSO_4$ from hemihydrate to anhydrate structure (Brunello 2020). Both samples show a peak around 404-5°C (Figure 10 and 11) that might be due to the release of water from calcium hydroxide (Moropoulou, Bakolas, and Bisbikou 1995; Klimesch and Ray 1996) indicating that the mortars did not fully carbonated. This was not observed for the whole mortar samples. It was probably present in too low concentration to be noticeable. The end temperatures of calcium carbonate decomposition are ~772 and 790°C for the powdered samples Z01 and Z02, respectively. For, Z02, it is slightly higher compared to the whole samples. A possible explanation could be that the powder is more pure compared to the whole mortar sample which increases the decomposition temperature.
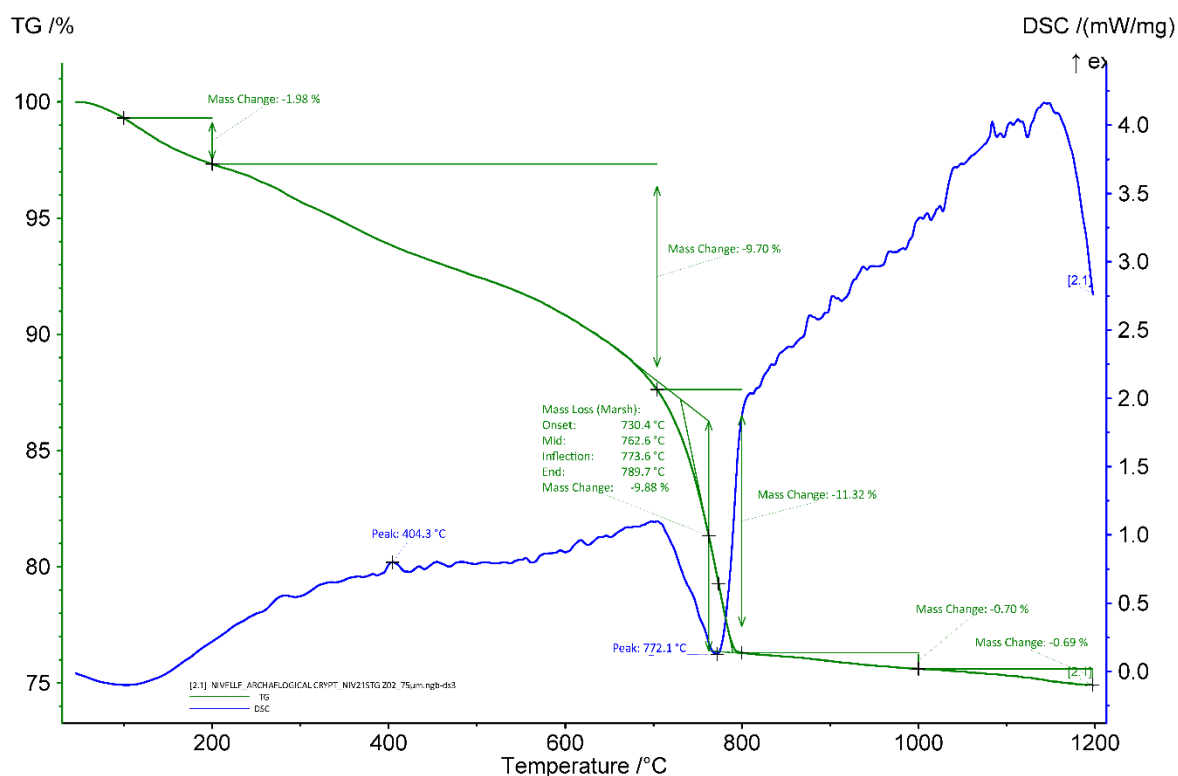
Figure 10: Coupled TG-DSC analysis of the powdered sample NIV21STG Z02 with particle size < 75 µm upon heating to a temperature of 1200°C at a heating rate of 20°C/min under an inert atmosphere (He flushed at 50 ml/min). The weight loss determined by thermogravimetric analysis (TG, wt%, green curve) and the result of the differential scanning calorimetric analysis (DSC, mW/mg, blue curve) are both presented.
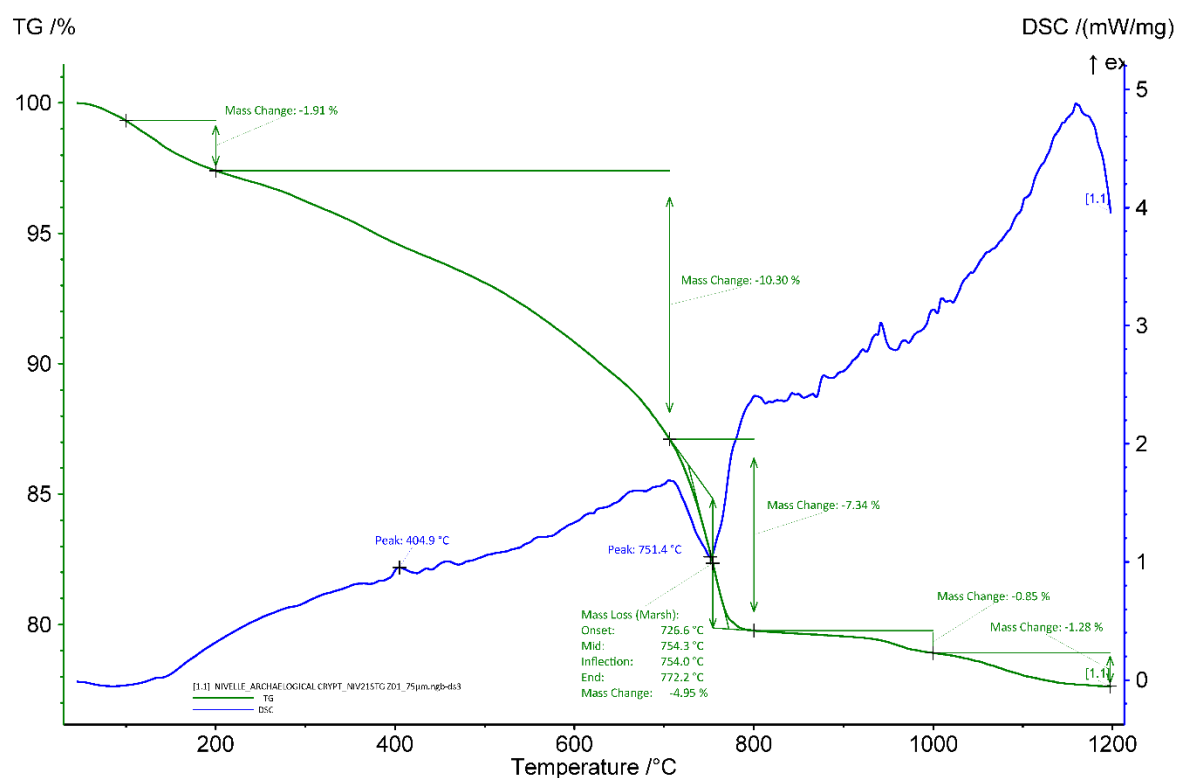
Figure 11: Coupled TG-DSC analysis of the powdered sample NIV21STG Z01 with particle size < 75 µm upon heating to a temperature of 1200°C at a heating rate of 20°C/min under an inert atmosphere (He flushed at 50 ml/min). The weight loss determined by thermogravimetric analysis (TG, wt%, green curve) and the result of the differential scanning calorimetric analysis (DSC, mW/mg, blue curve) are both presented.

Radiocarbon results

As expected from the FTIR and petrographic results, the test prior to the CO_2 extraction revealed a relatively low amount of carbon (Table 4) in the samples (~3 to 4 %). Around 2 to 3 g of powder with particle size <75 µm was necessary for the carbon extraction.

RICH	Sample type	Method	C (%)	σ (%)	m (g)	Age BP	Calibrated date (oxcal - 95.4%)	Age BP extrapolated	Calibrated date (oxcal - 95.4%)	Age BP extrapolated with stat	Calibrated date (oxcal - 95.4%)	Age BP average first 4 dates	Calibrated date (oxcal - 95.4%)	Reliability of dating
31532 (NIV21STG Z02)	Mortar	HCl (8 fractions)	3.79316	0.261	2.53	-	-	158 ± 25	1670-1950 calAD	159.2 ± 12.7	1668-1950 calAD	(first 5 fractions) 184 ± 10	1660-now calAD	☒
27702 (NIV21STG Z02)	Charcoal from mortar	HCl 1h	69.7466	-	0	1117 ± 26	890-1000 calAD	-	-	-	-	-	-	☑
30743 (NIV21STG Z01)	Mortar	HCl (8 fractions)	3.0608	0.023	3.13	-	-	114 ± 25	1683-1936 calAD	94.6 ± 16.3	1694-1917 calAD	(first 4 fractions) 167 ± 23	1663-now calAD	☒
30744 (NIV21STG Z01)	Lime lump	H₃PO₄	5.12	-	0.03	355 ± 23	1459-1634 calAD	-	-	-	-	-	-	☒
30329 (NIV21STG Z01)	Charcoal from mortar	HCl 8 % few hours	-	-	-	908 ± 27	1041-1215 calAD	-	-	-	-	-	-	☑
30330 (NIV21STG Z01)	Straw from mortar	HCl 8 % few hours	-	-	-	928 ± 26	1034-1175 calAD	-	-	-	-	-	-	☑

Table 4: Radiocarbon results

The radiocarbon results obtained for both mortars (Figures 12 & 13, Table 4) and the lime lump extracted from NIV21STG Z01 are too young. This is explained by the poor state of the samples due to dissolution processes making them unsuitable for radiocarbon dating. The organic matter extracted from the samples allowed however to date the mortars. For sample NIV21STG Z02, the date of the charcoal extracted (890-1000 calAD) is in the upper limit of the range expected by the archaeologists (700-900). The charcoal and the straw from the sample NIV21STG Z01 give a similar result ranging from 1034 to 1215 calAD which is slightly younger than the expected date (middle or 2nd quarter of the 10th century).
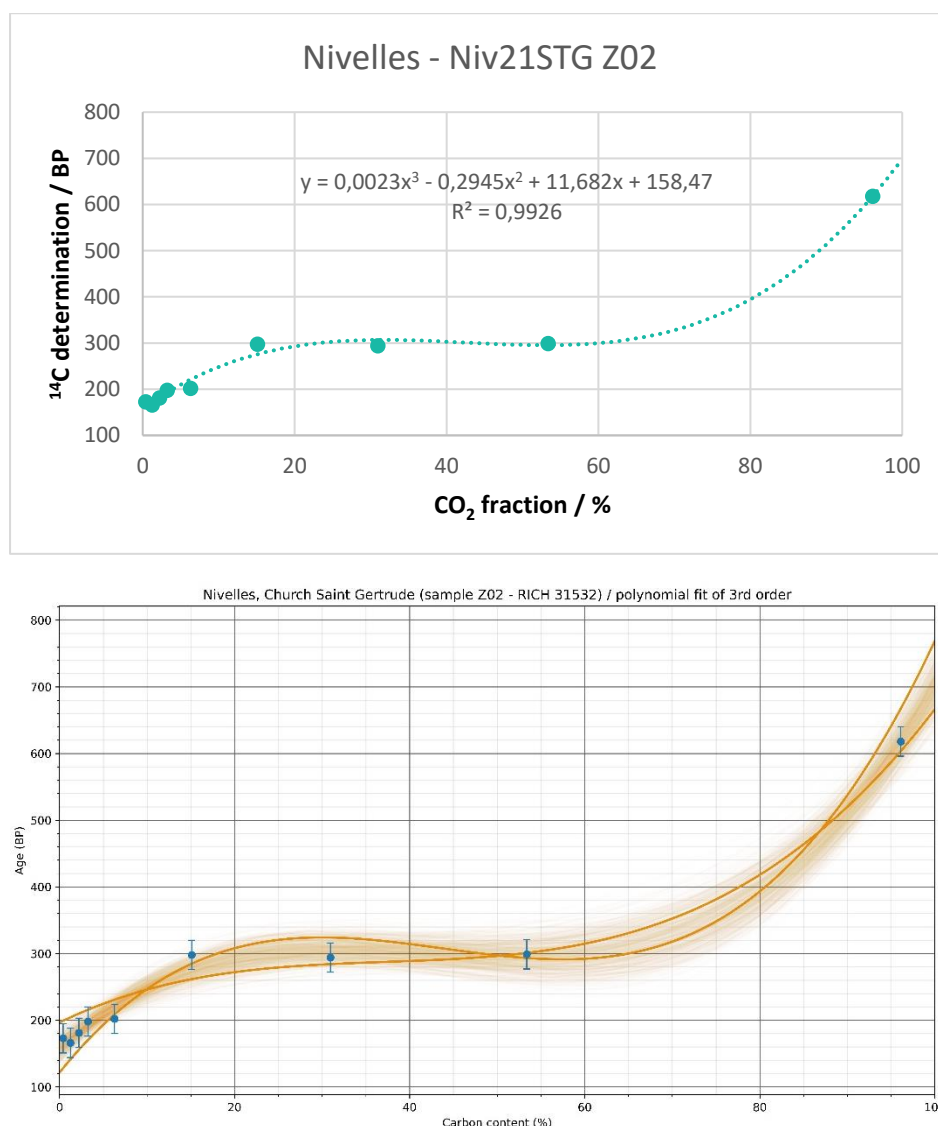
Figure 12: Radiocarbon results for the powdered NIV21STG Z02 sample with particles < 75 μm as a function of the CO_2 fraction (the graph at the bottom shows the statistic on the results).
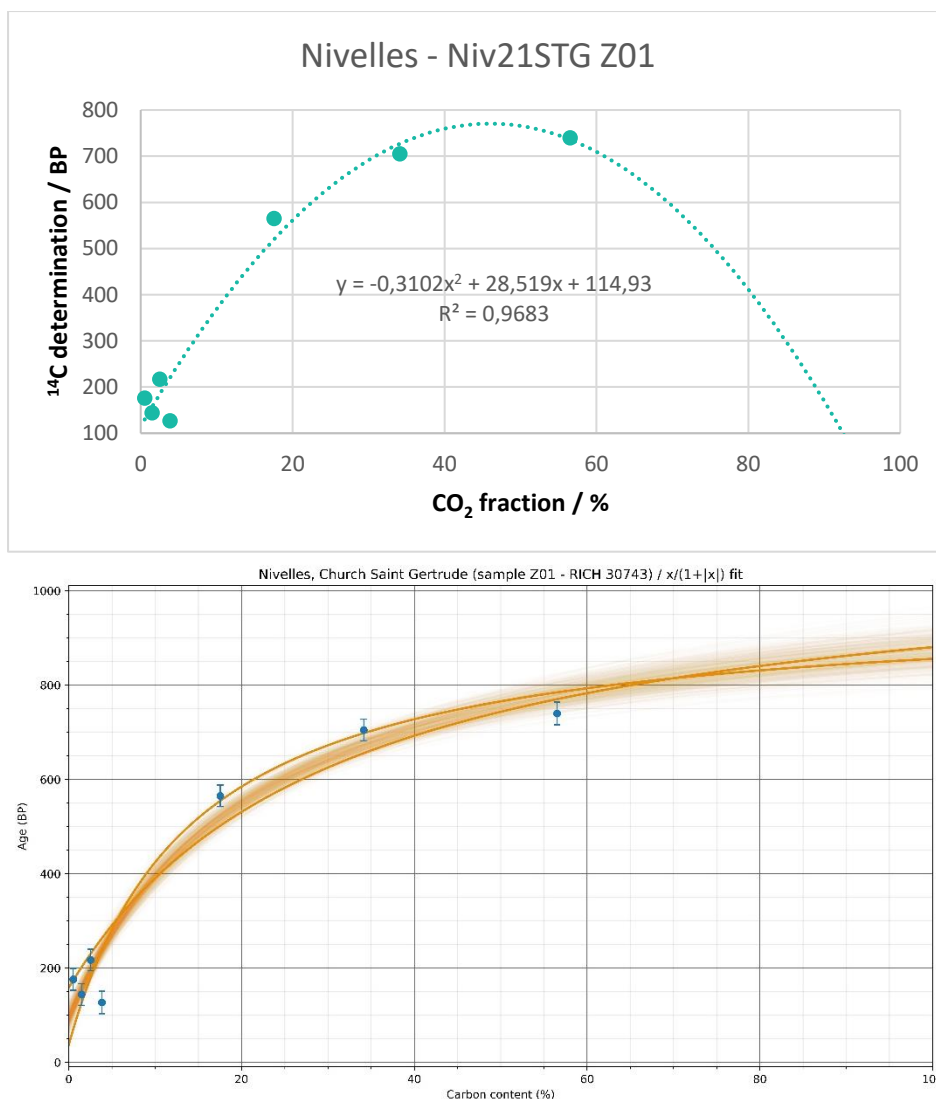
Figure 13: Radiocarbon results for the powdered NIV21STG Z01 sample with particles < 75 μm as a function of the CO_2 fraction (the graph at the bottom shows the statistic on the results).

Conclusions

All the characterization methods used showed that the two mortars sampled in the archaeological crypt of the Sainte-Gertrude collegiate are extremely deteriorated. The carbonates used to date the samples have been largely dissolved. The organic matter present inside the mortar samples is very precious in this case and should be more generally favoured to date lime mortars. The date obtained for the charcoal extracted from the sample NIV21STG Z02 (from the masonry of the first forebuilding) is 890-1000 calAD which can correspond to the expected date (700-900) but could also have been built during the mid-10th century reconstruction. For the sample NIV21STG Z01, both the charcoal and the straw date to the 11th or 12th century and could have been added after the fire (and are not from the 10th century as initially expected).

Bibliography

Ahmmed, Tanjil, Ana Raquel Silva, José Carlos Quaresma, Patrícia Moita, and Cristina Galacho. 2024. "Analytical Characterization of Historical Mortars from the Roman Villa of Frielas (Loures, Portugal)." *Acta IMEKO* 13 (3): 1–11.

Brunello, Vallentina. 2020. "Mortars: A Complex Material in Cultural Heritage. A Multi-Analytical Procedure to Characterize Historical Mortars." Università degli studi dell'insubria. https://core.ac.uk/reader/322778010.

Chantinne, Frédéric, and Philippe Mignot. 2014. "La collégiale Sainte-Gertrude de Nivelles. Réexamen du dossier archéologique." *Hortus Artium Medievalium* 20 (2): 513–19. https://doi.org/10.1484/J.HAM.5.102667.

———. 2017. "De l'atrium à l'aître. À Propos de Quelques Sites Religieux de Belgique." In *GENTSE GESCHIEDENISSEN OF TE, NIEUWE HISTORIËN*.

Klimesch, Danielle S., and Abhi Ray. 1996. "The Use of DTA/TGA to Study the Effects of Ground Quartz with Different Surface Areas in Autoclaved Cement: Quartz Pastes. Part 1: A Method for Evaluating DTA/TGA Results." *Thermochimica Acta* 289 (1): 41–54. https://doi.org/10.1016/S0040-6031(96)03033-X.

Moropoulou, Antonia, Asterios Bakolas, and Katerina Bisbikou. 1995. "Characterization of Ancient, Byzantine and Later Historic Mortars by Thermal and X-Ray Diffraction Techniques." *Thermochimica Acta* 269:779–95.

Rickard, William D. A., Arie Van Riessen, and Philip Walls. 2010. "Thermal Character of Geopolymers Synthesized from Class F Fly Ash Containing High Concentrations of Iron and α-Quartz." *International Journal of Applied Ceramic Technology* 7 (1): 81–88. https://doi.org/10.1111/j.1744-7402.2008.02328.x.

Study of mortars from the Abbatial church Sainte-Marie (Floreffe) for the BRAIN 2.0 PalC project

Context of the site

Little is known about Floreffe before the 12th century, but scattered clues reveal the importance of the place well before the arrival of the Premonstratensian canons, led by Saint Norbert, in 1121. The control of traffic routes, both the Sambre, a navigable tributary of the Meuse, and the roads that crossed it, made it a key crossroads (Figure 1).

Figure 1: Floreffe and its spur between the Sambre and the Wéry (P.-M. Warnier © SPW).

At the head of a sizeable territory straddling the river, Floreffe was, by the end of the 7th century, the residence of a prince, a member of the high aristocracy, and was certainly already a dynamic town. Unfortunately, there is an enormous gap between the meagre first mentions and the attestation that Floreffe was in the hands of the Count family of Namur at the time of their donation to Saint Norbert. On 27 November 1121, the Countess Ermesinde and Count Godefroy ceded part of their property and rights over Floreffe. These included the estate's main church, Sainte-Marie. Entrusted to the Prémontré order, the site undeniably underwent a number of transformations. But the main question is: what was there in 1121? And what work was undertaken during the first decades of the canons' establishment? If the canons wanted people to believe that they were setting up a new church in a deserted area, the arguments put forward make it impossible to believe them. Both the text of the donation and other diplomatic acts attest to the fact that the abbey church existed in 1121. The texts describe

construction from 1165 onwards (*Annales Floreffienses NaSo A068* 1859). The work carried out between 1170 and 1180 is known and has been cross-checked by dendrochronology of the oldest parts of the church's roof structure (Hoffsummer 1995). This roof does not rest on new walls but on the dismantled masonry of a monumental building (Figure 2) of even more remarkable dimensions (where the samples for PALc were taken).
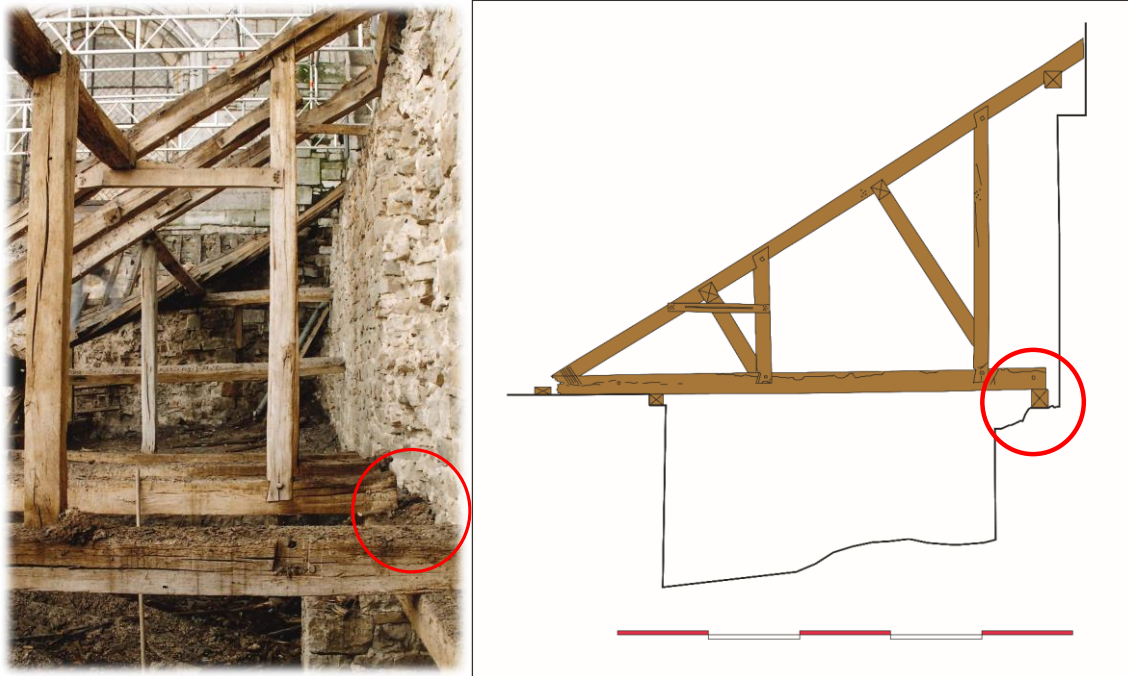
Figure 2: Floreffe framework (left, J.-L. Javaux © SPW) and wall dismantled (right, P. Gautier et Fl. Vander Eecken from Royal Museums for Art and History, Brussels).

Evidence of this can be seen in the remains of a tribune (vaulted or semi-domed apse) on the first floor of the transept. (Figure 3).

Figure 3: Tribune first floor.

If this building, covered in the second half of the 12th century, is older, is it really the one given in 1121? If so, when does it date from? Above all, for whom and why was this building so large? 100 m long, the size of a cathedral! The difficulty today lies in distinguishing the construction phases and analysing the material history of this monument.

Material

In total, four mortar samples and a wood sample from a putlog hole were added to the PALc project in 2021 (Figure 4).

Figure 4: Location of the samples.

Frédéric Chantinne and Olivier Vrielynck, both archaeologists working for the Walloon heritage agency (SPW/AWaP) sampled the three first samples (21A, 21B & 21C) and the sampling of the two other ones (21D & 21E) was performed by members of the PALc team. Table 1 summarises the different samples with their locations and presumed historical dates.

Sample name	Sample description/location	Presumed historical date
21A	Mortar from buttress	10-12th centuries
21B	Mortar masonry angle to the north-east of the transept crossing	
21C	Wood from the putlog hole	
21D	Mortar from wall north-south between stairs & buttress	
21E	Mortar from the side aisle of the north heart (wall West-East)	13th or 17th

Table 1: List of samples from the Abbatial church Sainte-Marie for the PALc project.

Results & Discussion

Macroscopic descriptions

The main colour of all the samples is beige (Figure 5) tending towards very pale brown for 21A (10YR 8/3) and 21B (10YR 8/2) and pale yellow for 21D (2.5Y 8/2) and 21E (2.5Y 8/3)

according to the Munsell soil colour charts. All samples contained lime lumps with an average size of 1 mm and the biggest ranged from 0.5 to 1 cm. Black and soft inclusions probably consisting of charcoal were observed for 21A, 21B and 21E. Grey inclusions not reacting with dilute hydrochloric acid (10% HCl solution) and possibly made of silicates were noticed for 21B, 21D and 21E. For 21A, the grey inclusions reacted with acid which indicates they should be made of limestone. 21A and 21E contained red, soft and round inclusions that might come from the loamy sand aggregate used. A black crust was present on some surfaces of the mortar fragments 21A. 21B exhibited a round and beige inclusion measuring around 7 mm in diameter. For one fragment of mortar 21E, a purple inclusion was observed.
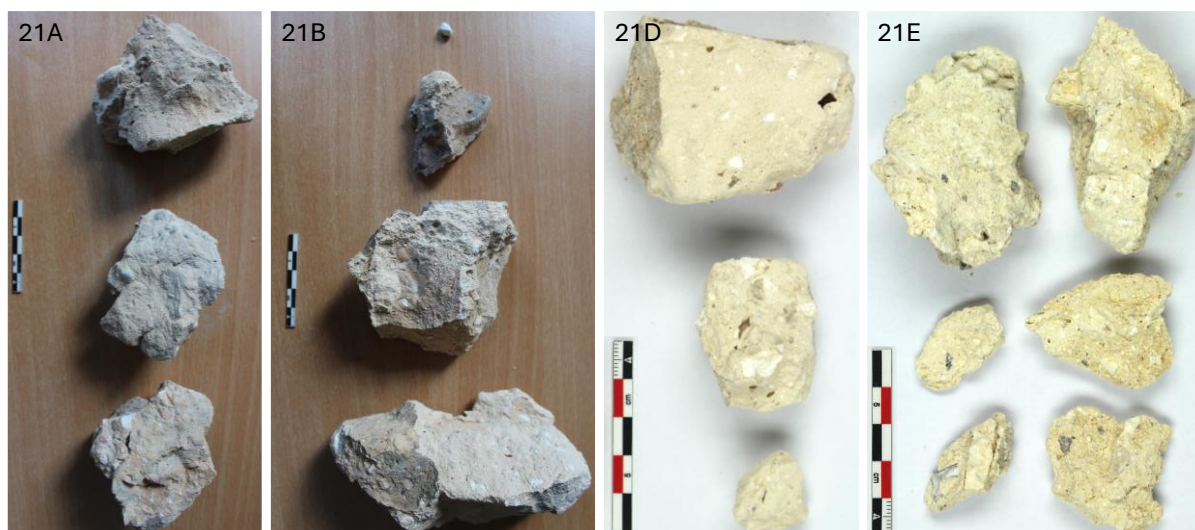
Figure 5: Photographs of the four mortar samples from the Abbatial church Sainte-Marie.

Fourier transform Infrared (FTIR) spectroscopy on inclusions & binder

The binders (beige, Figure 6) mainly contained calcium carbonates (calcite and aragonite) and silicates including clay. The black inclusions (black, Figure 6) are made of amorphous organic matter (which may be charcoal); the red ones (red, Figure 6) contain silicates and quartz. Most of the grey inclusions are limestone (calcite), but some are made of silicates. In addition to calcite, all mortars contain clay and nitrates. While the presence of clay can be linked to impurities in the sand, the detection of nitrates suggests slight contamination by soluble salts. The presence of gypsum detected in the mortar of the buttress (21A) revealed contamination linked to contact with rainwater (direct exposure to rain when the framework was uncovered or water infiltration). Except for the mortar 21D, the lime lumps (white, Figure 6) are only made of calcium carbonates and don't contain any clay. The round and transparent inclusion (Figure 6) observed for the mortar 21B is a quartzite cobble and the purple inclusion (purple, Figure 6) in 21E is made of silicates and organic matter.
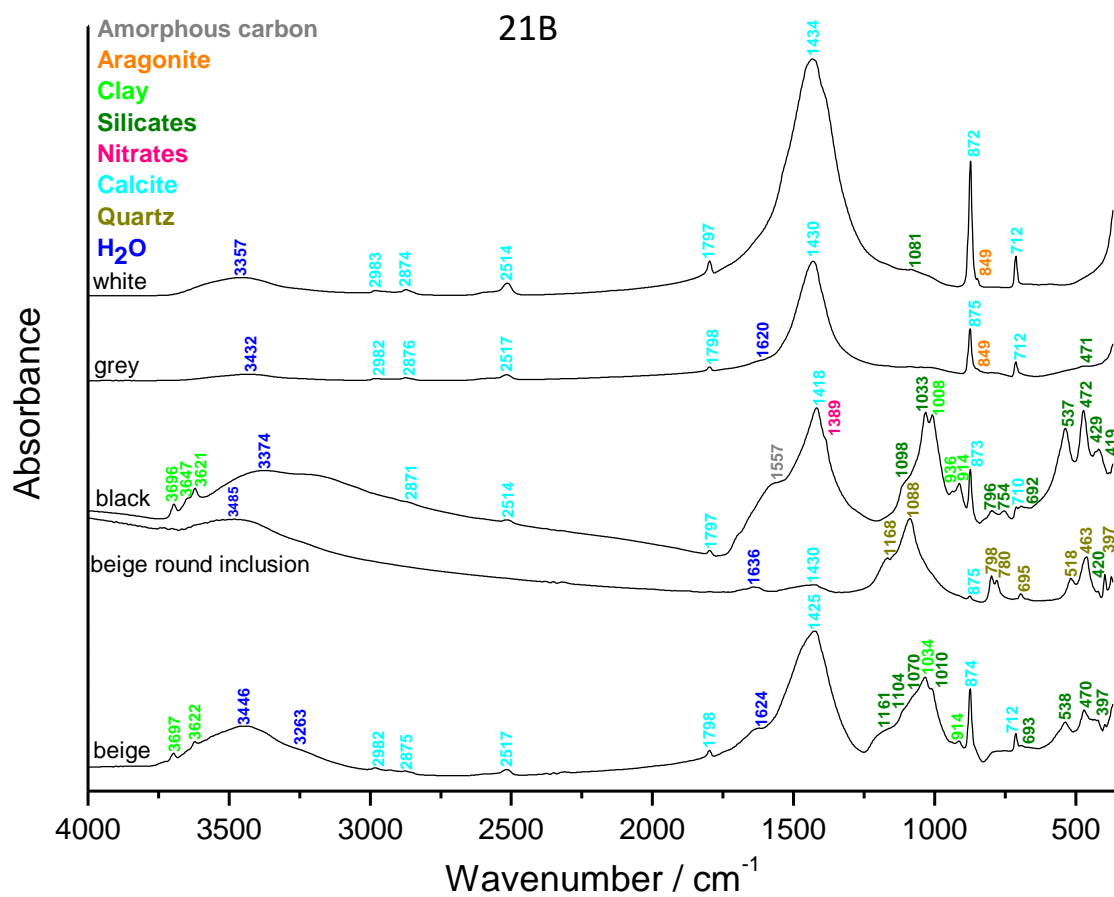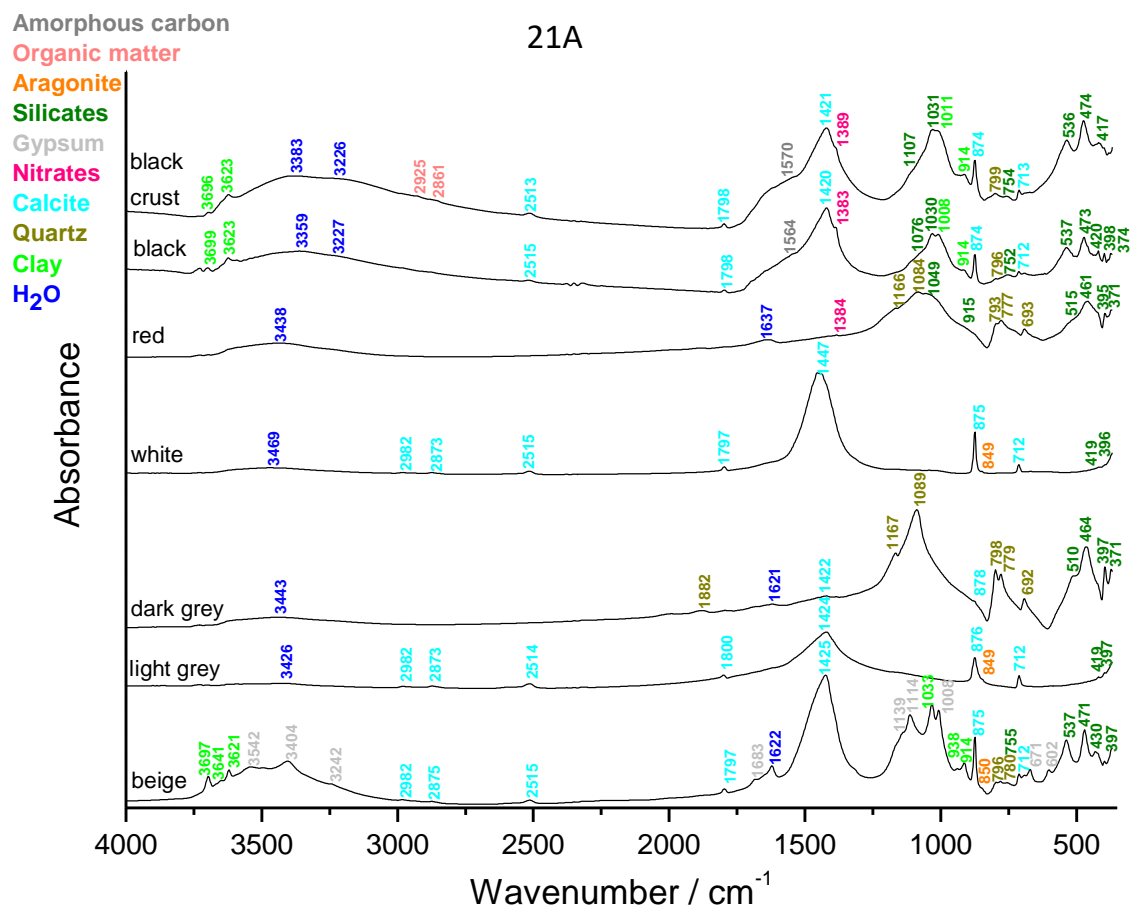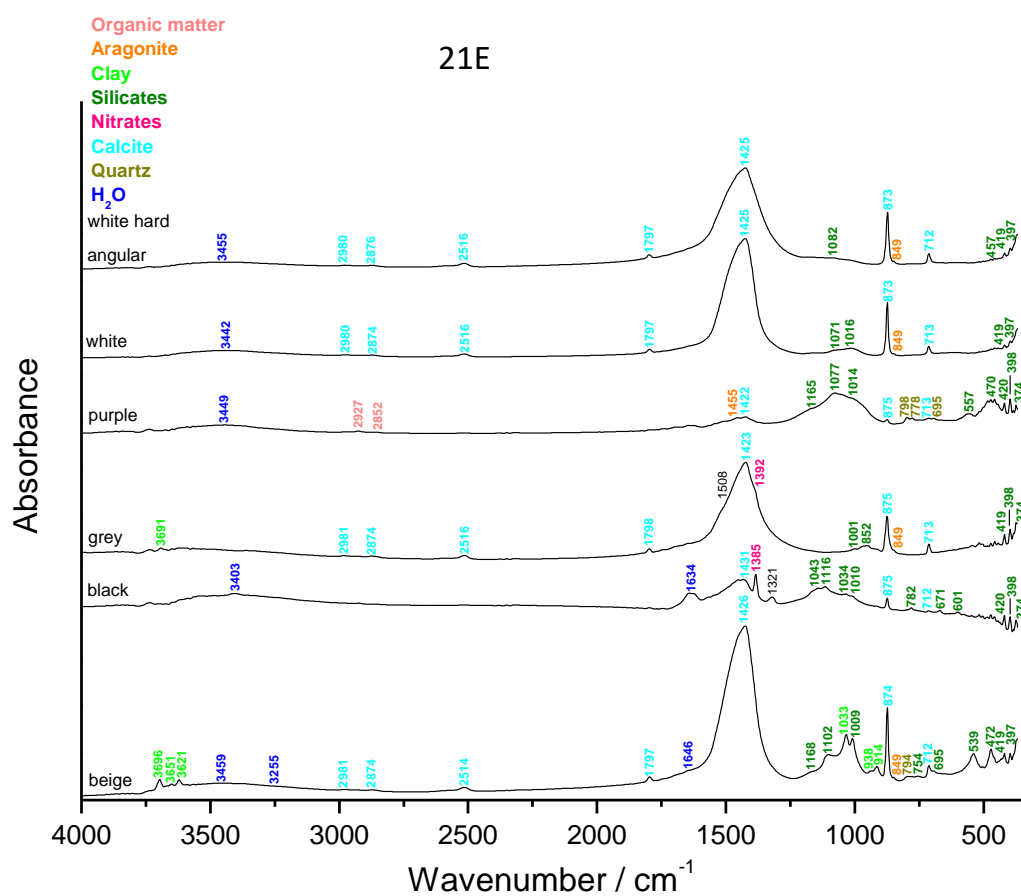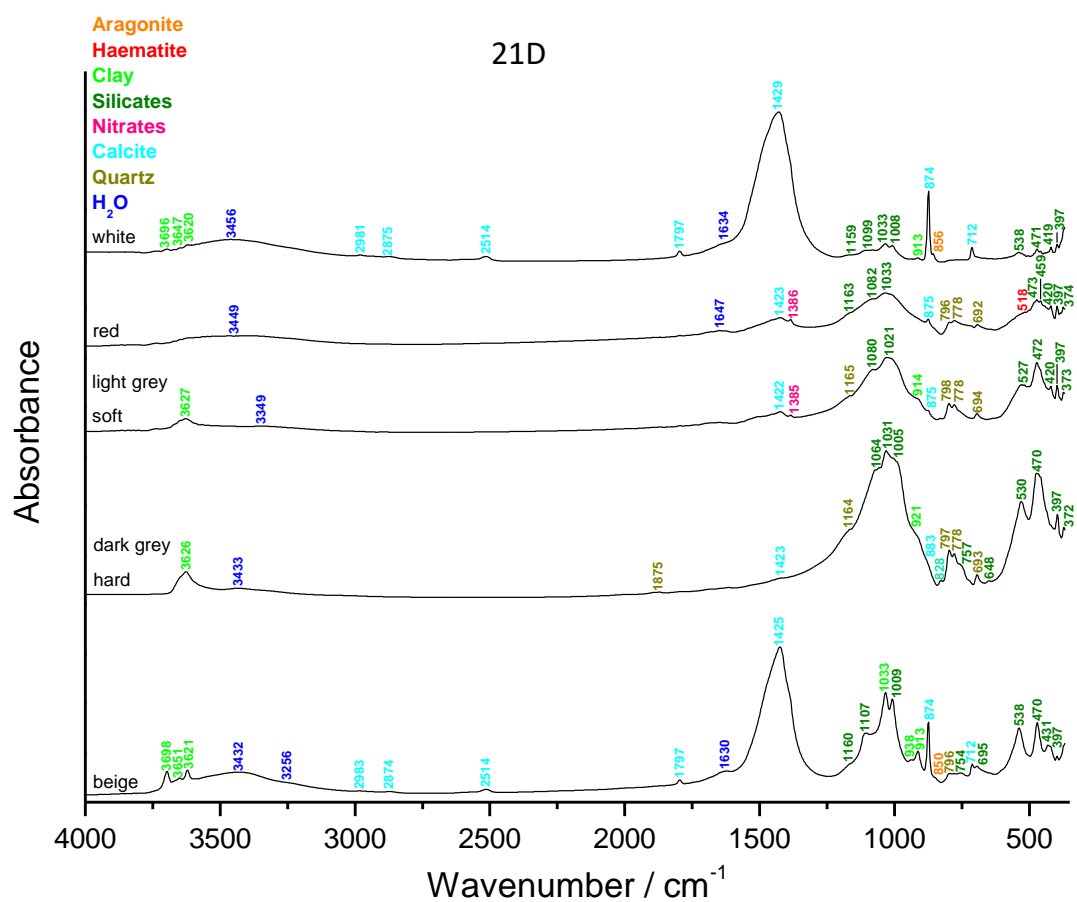
Figure 6: FTIR spectra obtained on the inclusions and binder (beige) of the four mortar samples.

Binder:aggregate ratio

The calculated binder:aggregate ratio using a bulk density of 1.35 kg/dm^3 for the sand and 0.575 kg/dm^3 for the lime, is close to 1:1 in volume unit for 21A, 21B & 21D and close to 5:1 for 21E. The difference for the mortar 21E suggests a different manufacturing method.

	21A	21B	21D	21E
Sample weight (g)	2,99	2,45	2,81	2,73
Crucible weight (g)	16,86	14,70	14,89	15,33
Weight calcined (g)	18,97	16,43	16,86	16,23
%ins	**70,6**	**70,6**	**70,1**	**33,0**

Table 2: Percentage of insoluble residue.

Cathodoluminescence

Cathodoluminescence observations of the thin-sections and powders show similar results (Figure 7). The thin-sections (Figure 7a, c, e, & g) exhibit the presence of quartz grains with two different hues (purple & bluish) indicating two different origins. K-feldspars are noticed in bright blue and the binder and the lime lumps are dull. For the sample 21E (Figure 7g), much less aggregate particles are present in accordance with the determined binder:sand ratio. The powdered samples (Figure 7b, d, f & h) are mainly dull with a few bright red limestone grains and very few blue potassic feldspars.
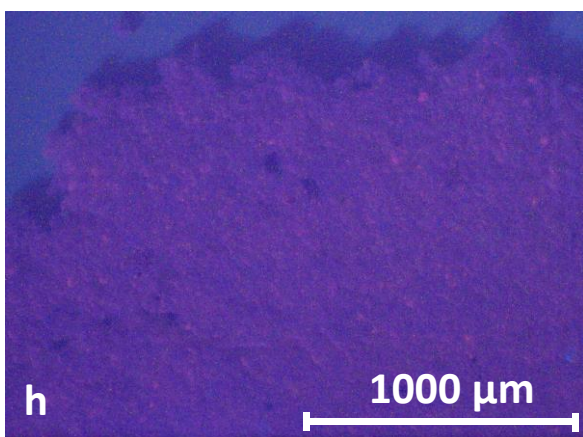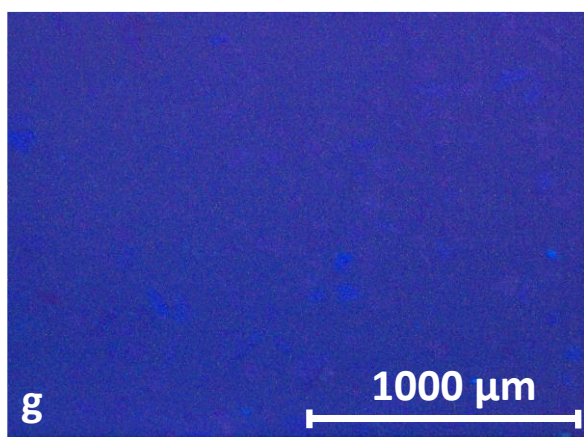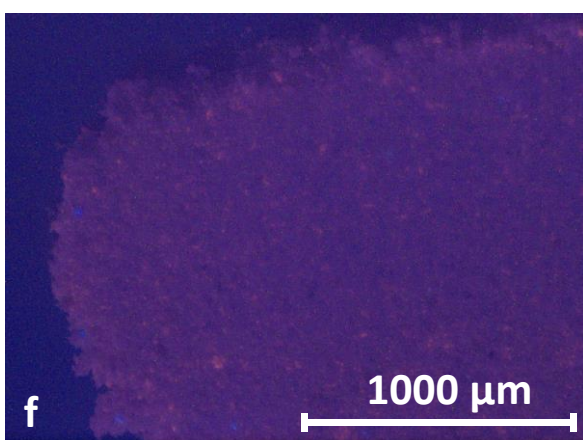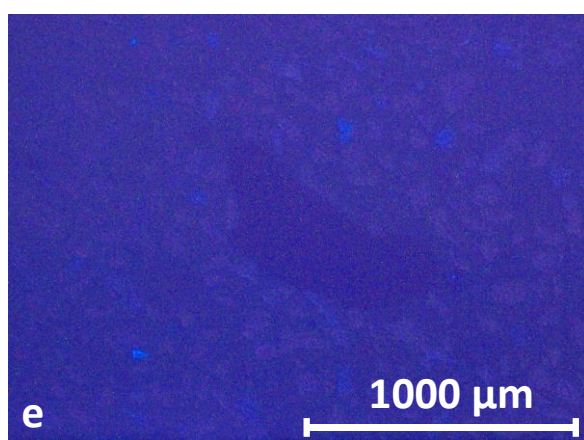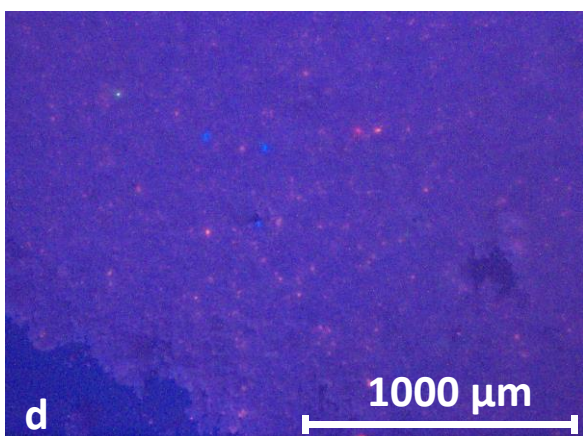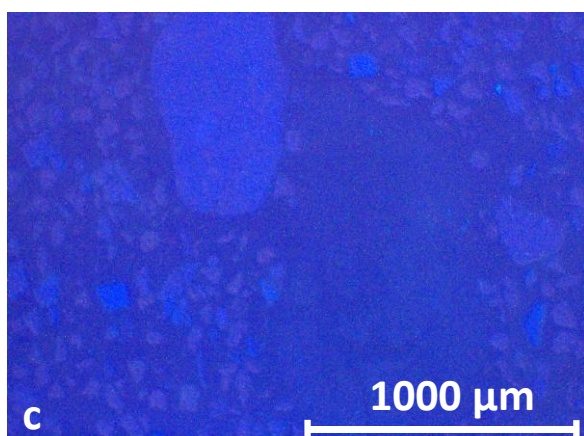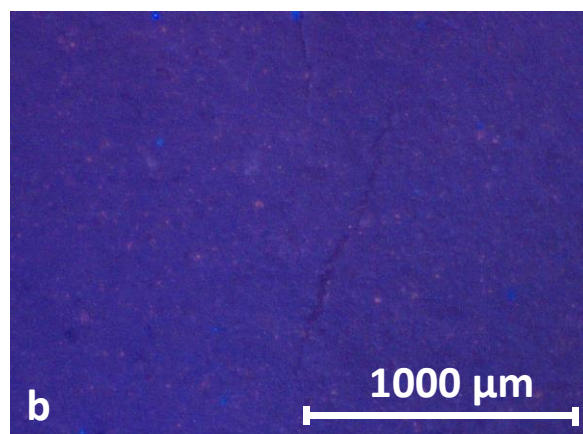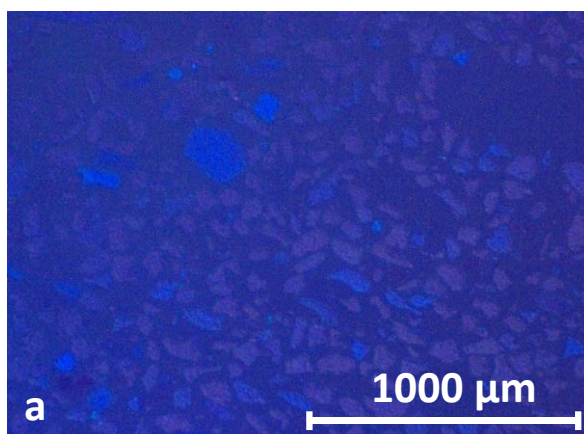
Figure 7: Characteristic cathodoluminescence images of a) the thin-section X2202 of 21A, b) the powdered 21A mortar with particle size lower than 75 μm, c) the thin-section X2203 of 21B, d) the powdered 21B mortar with particle size lower than 75 μm, e) the thin-section X2252 of 21D, f) the powdered 21D mortar with particle size lower than 75 μm g) the thin-section X2253 of 21E, h) the powdered 21E mortar with particle size lower than 75 μm.

The thin section of the lime lump extracted from the mortar 21B was dull, it didn't show any signs of luminescence (Figure 8) which indicates that it should not contain any relicts of underburned limestone.
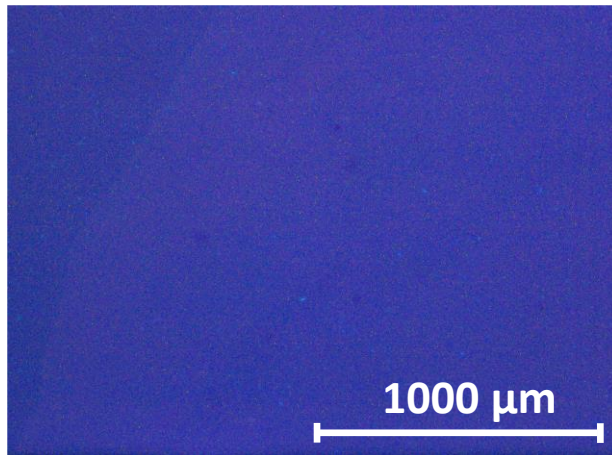
Figure 8: Characteristic cathodoluminescence image of the lime lump extracted from 21B (thin section X2254.

Thin-section petrography

The lime binder of the mortar 21A (Figure 9 & Table 3) is in good state; no secondary carbonate deposits in the macropores or at the edges of the microcracks is observed. Lime lumps are regularly observed, the largest reaching up to 3-4 mm in diameter. Whether small or large, the lime lumps have been completely burned (Figure 9c), except one (Figure 9e & f) that still contains limestone relicts. The aggregate used is a (very) fine siliceous sand with sub-angular grains, slightly clayey (Figure 9d), not containing calcareous fraction.
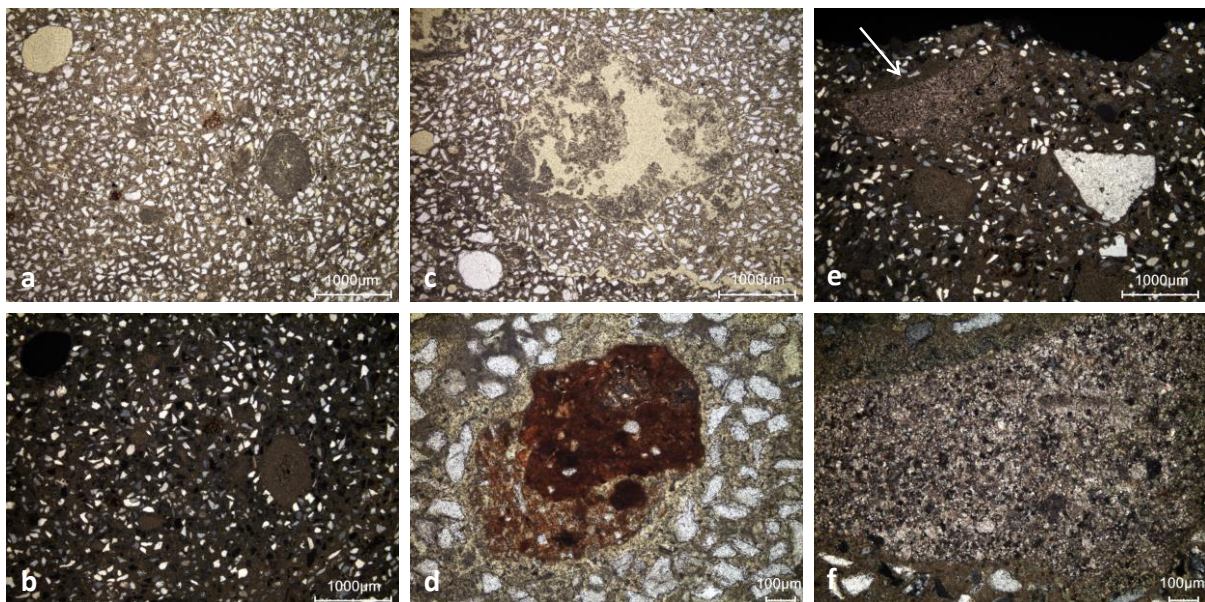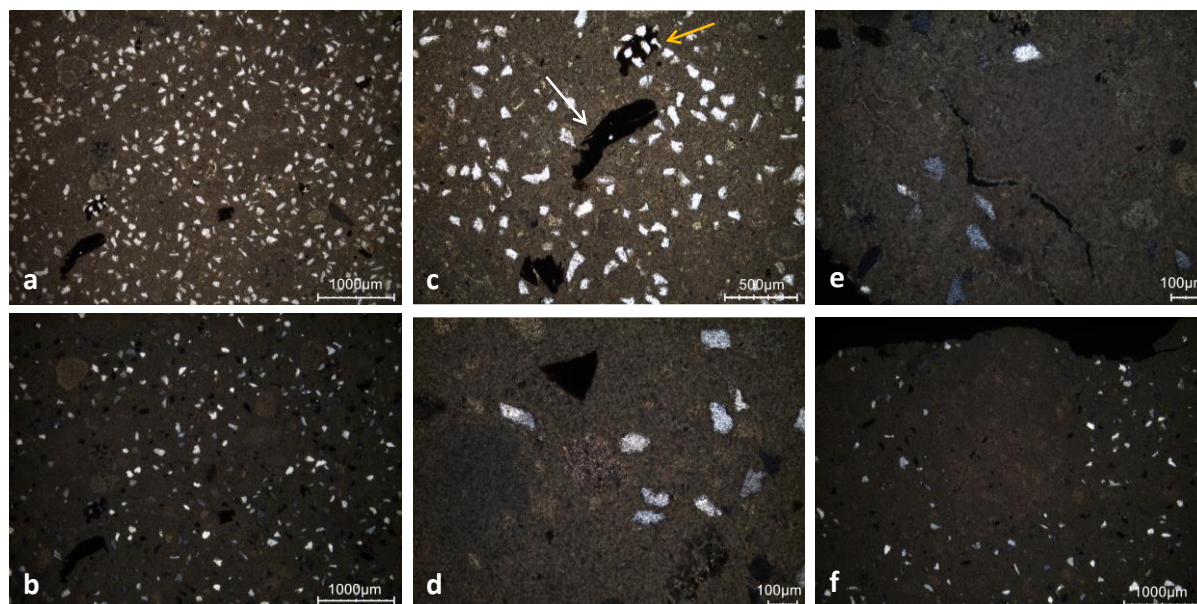
Figure 9: Representative photomicrographs of the thin-section of the sample 21A (code X2202): a) overview image in plain polarised light (PPL); b) overview image in cross polarised light (XPL); c) PPL image showing a lime lump; d) sandy clay agglomerate in PPL; e) XPL image with a large limestone fragment; f) zoom in on the limestone fragment in XPL.

Binder	**Texture**	micritic
	Lump state	completely burned & unburned
	Lump size	max 3-4 mm
	Lump frequency	numerous
Aggregate	**Grain size**	very fine (<125 μm) to fine (<250 μm)
	Mineralogy	siliceous sand (quartz, K-feldspar, sandy clay agglomerate, muscovite)
	Shape	subangular / subrounded
Appearance	**Homogeneity**	relatively homogeneous
	Macroporosity	low / medium
	Pore structure	irregular / not connected
Admixtures	**Type**	-
Alteration	**Type**	-

Table 3: Main characteristics of the beige mortar 21A retrieved from the observations of the thin-section X2202.

The lime binder of the mortar 21B (Figure 10 & Table 4) is in good condition and there are no secondary carbonate deposits in the macropores or at the edges of the microcracks. Lime lumps are regularly observed, the largest reaching 3 to 4 mm in maximum diameter (Figure 10a & b). The lime lumps, whether small or large, have been completely burned. The aggregate used is a (very) fine siliceous sand with sub-angular grains, slightly clayey (Figure 10c), not containing calcareous fraction. The thin section of the lime lump extracted from the mortar 21B shows that it is completely burned, the pores observed are due to the original porosity of the limestone (remnants of microfossils' voids).
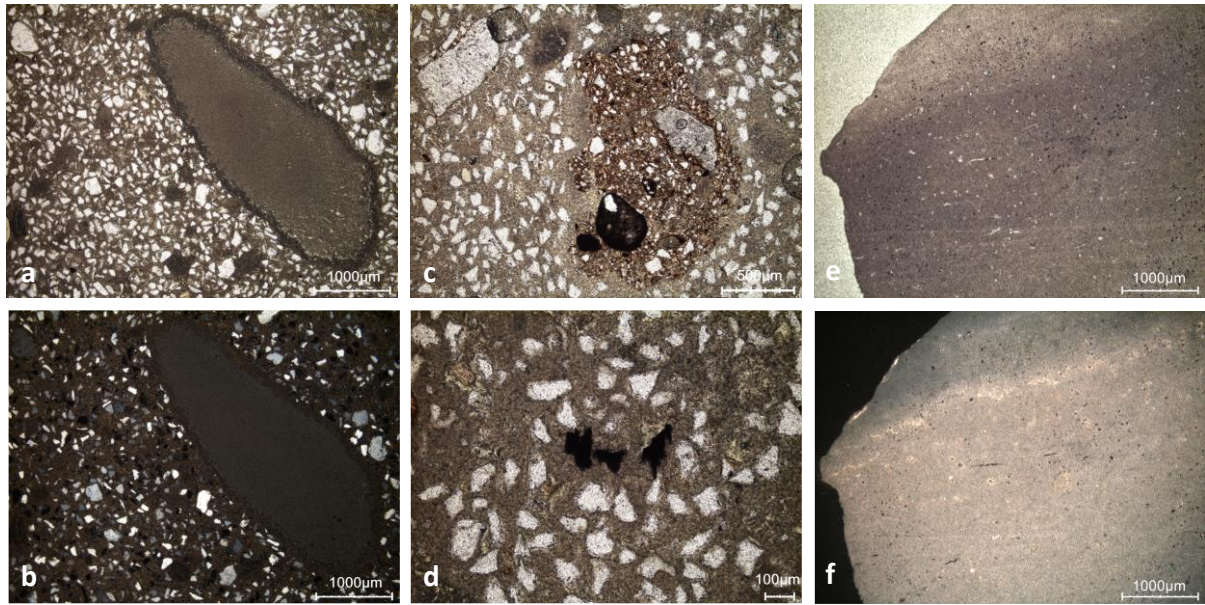
Figure 10: Representative photomicrographs of the thin-section of the sample 21B (code X2203): a) overview image in PPL; b) overview image in XPL; c) PPL image showing a sandy clay agglomerate; d) charcoal pieces in PPL; and of the extracted lime lump (thin-section X2254): e) overview PPL image; f) same image in XPL.

| Binder	Texture	micritic
	Lump state	completely burned
	Lump size	max 3-4 mm
	Lump frequency	numerous
Aggregate	Grain size	very fine (<125 µm) to fine (<250 µm)
	Mineralogy	pure siliceous sand (quartz, feldspar, sandy clay agglomerate, muscovite)
	Shape	subangular / subrounded
Appearance	Homogeneity	relatively homogeneous
	Macroporosity	low / medium
	Pore structure	irregular / not connected
Admixtures	Type	charcoal (very fine fragments, up to a hundred micrometres)
Alteration	Type	-

Table 4: Main characteristics of the beige mortar 21B retrieved from the observations of the thin-section X2203.

The mortar 21D (Figure 11 & Table 5) is well preserved and contain completely burned lime inclusions. The aggregate is made of a (very) fine, slightly clayish, siliceous sand (Figure 11e & f).
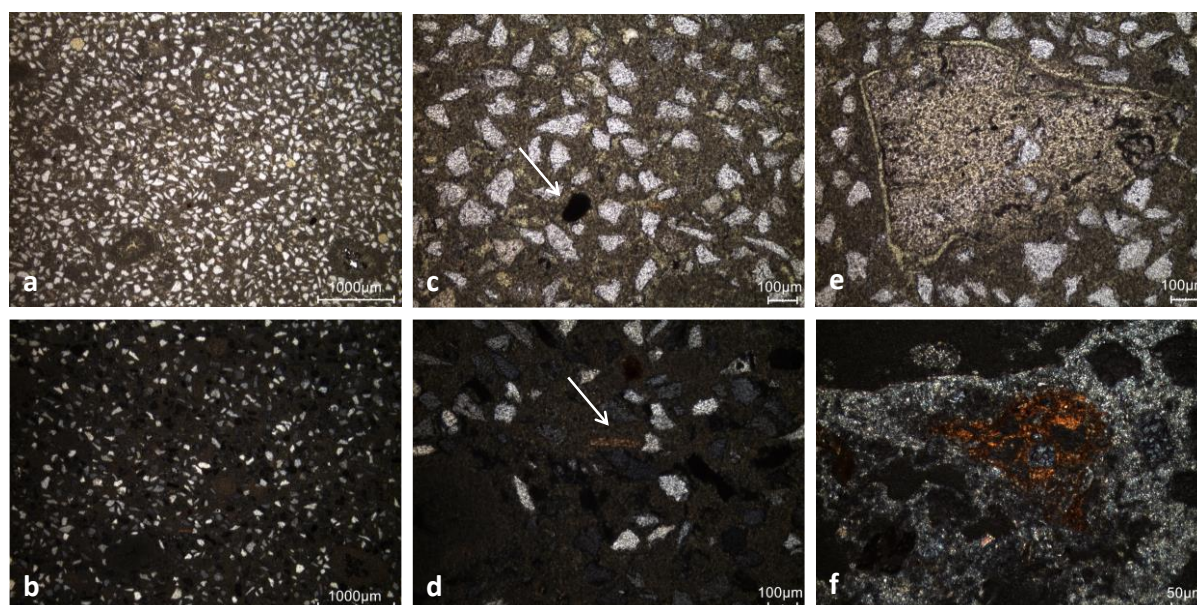
Figure 11: Representative photomicrographs of the thin-section of the sample 21D (code X2252): a) overview image in PPL; b) overview image in XPL; c) PPL image showing a glauconite grain d) muscovite flake in XPL; e) PPL image of a sandy-clay agglomerate with crack around; f) sand-clay agglomerate in XPL.

Binder	**Texture**	micritic
	Lump state	completely burned
	Lump size	max 6.5 mm
	Lump frequency	medium
Aggregate	**Grain size**	very fine (<125 μm) to fine (<250 μm)
	Mineralogy	pure siliceous sand (quartz, feldspar, muscovite, glauconite, sandy-clay agglomerate)
	Shape	subangular / subrounded
Appearance	**Homogeneity**	relatively homogeneous
	Macroporosity	low
	Pore structure	irregular / not connected
Admixtures	**Type**	-
Alteration	**Type**	-

Table 5: Main characteristics of the beige mortar 21D retrieved from the observations of the thin-section X2252.

The mortar 21E (Figure 12 & Table 6) shows a good state of preservation. The lime inclusions are completely burned (Figure 12f). The aggregate is made of a (very) fine siliceous sand and is less present compared to the three other mortars accordingly to the determined binder:sand ratio. Secondary carbonates are only observed in some microcracks (Figure 12d). One inclusion corresponds to an unburned limestone piece (not shown).

Figure 12: Representative photomicrographs of the thin-section of the sample 21E (code X2253): a) overview image in PPL; b) overview image in XPL; c) PPL image showing a sandy clay agglomerate (orange arrow) and bottom ash (white arrow); d) possible limestone fragment in XPL (in the centre of the image); e) XPL image with secondary carbonates lining microcracks; f) large completely burned lime inclusion in XPL.

Binder	**Texture**	micritic
	Lump state	completely burnt and not burnt
	Lump size	max 2.8 mm
	Lump frequency	medium
Aggregate	**Grain size**	very fine to fine
	Mineralogy	pure siliceous sand (quartz, feldspar, sandy clay agglomerate, muscovite)
	Shape	subangular / subrounded
Appearance	**Homogeneity**	relatively homogenous
	Macroporosity	low
	Pore structure	cracks often around lumps/irregular/not connected

Admixtures	**Type**	bottom ash
Alteration	**Type**	secondary carbonates in microcracks

Table 6: Main characteristics of the beige mortar 21E retrieved from the observations of the thin-section X2253.

Thermogravimetric analysis (TGA) on whole samples

The results of the thermal analyses are presented in Figures 13 to 16.. The apparent hydraulicity indexes (aHI) determined on the basis of the weight loss between 200 and ca. 650°C (usually attributed to water loss from calcium-silicate-hydrates-phases) show at first sight that the mortar 21E is moderately hydraulic (22.0 %), the mortars 21A and 21D are strongly hydraulic (29.3 and 28.0, respectively) and that the mortar 21B is very strongly hydraulic (43.5%). The hydraulic indexes of the lime lumps are lower (6.0 % for 21A, 14.0 % for 21B & 8.7 % for 21D), except for the lime lump extracted from 21E which is moderately hydraulic (21.8 %). However, the relatively high values of the calculated hydraulicity indexes could be influenced here by the use of a slightly clayey sand, since loss from structurally bound water of some clays takes place at a similar temperature to structurally bound water in hydraulic components (Middendorf et al. 2005). For the lime lump extracted from sample 21B (Figure 14, bottom), the presence of gypsum was estimated at 1.2 wt% (peak around 123°C) (Moropoulou, Bakolas, and Bisbikou 2000). This lime lump also shows a peak around 405°C that might be due to the release of water from calcium hydroxide (Moropoulou, Bakolas, and Bisbikou 1995; Klimesch and Ray 1996) indicating that it did not fully carbonated. The temperature of quartz transition phase is observed only for the whole mortar samples around 571-5°C (Rickard, Riessen, and Walls 2010). The amount of carbonates is ~15 wt% for the mortar 21A, 93 w% for the 21A lime lump, 17 w% for the mortar 21B, 80 w% for the 21B lime lump, 21 % for the mortar 21D, 88 w% for 21D lime lump, and 47 wt% for the mortar 21E. The main weight loss of ancient mortars is expected between 600 and 900 °C and is indicative of the decomposition of calcium carbonate ($CaCO_3$) into calcium oxide (CaO) and carbon dioxide (CO_2) (Ahmmed et al. 2024). The end temperature of calcium carbonate decomposition is ~783°C for the mortar 21A, 841°C for the 21A lime lump, 802°c for the mortar 21B, 831°C 21B lime lump, 794°C for the mortar 21D, 848°C for the 21D lime lump, and 823°C for the mortar 21E. The end temperature of calcium carbonate decomposition is higher for the lime lumps compared to the whole samples. A possible explanation could be that the powder is more pure compared to the whole mortar sample which increases the decomposition temperature.
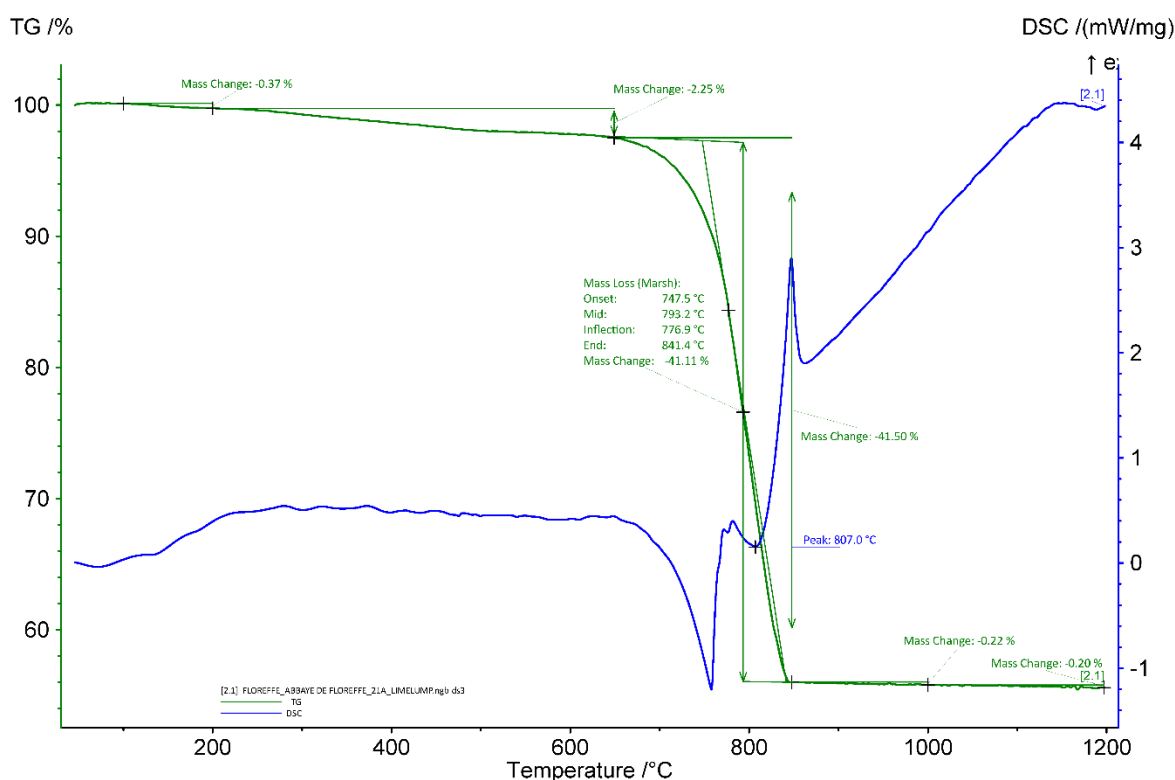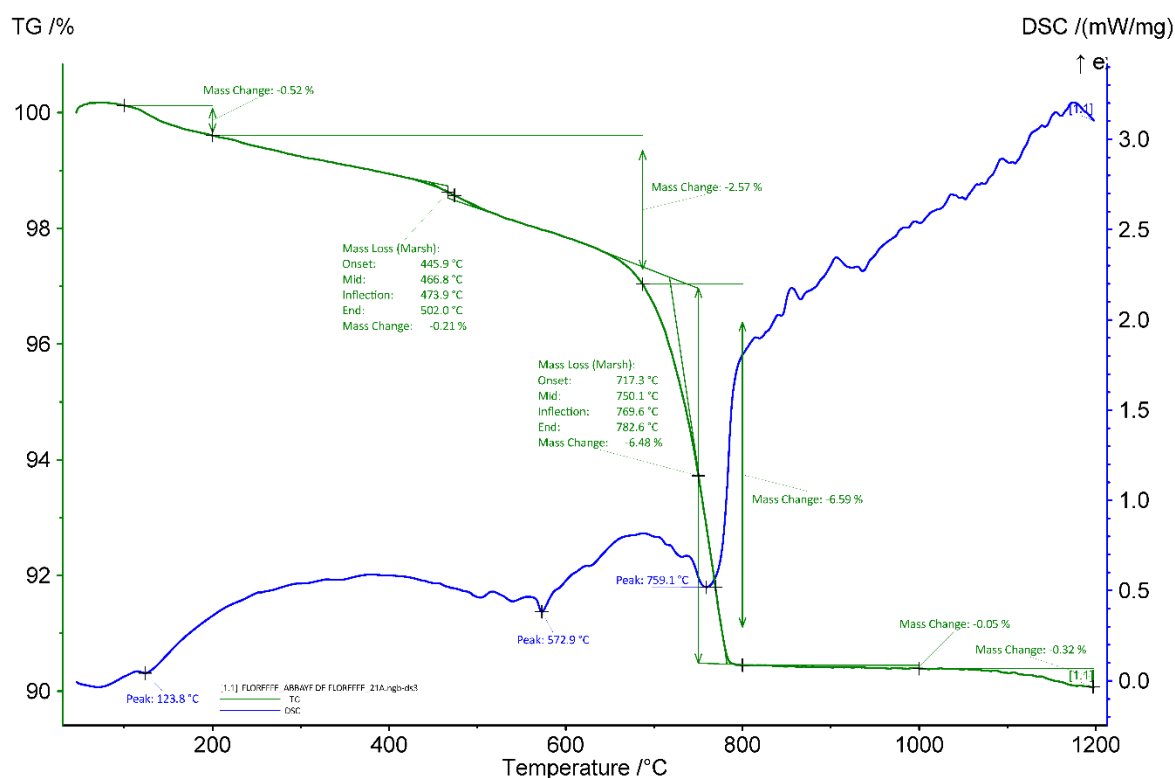
Figure 13: Coupled TG-DSC analysis of the mortar 21A (top) and the lime lump extracted from 21A (bottom) upon heating to a temperature of 1200°C at a heating rate of 20°C/min under an inert atmosphere (He flushed at 50 ml/min). The weight loss determined by thermogravimetric analysis (TG, wt%, green curve) and the result of the differential scanning calorimetric analysis (DSC, mW/mg, blue curve) are both presented.
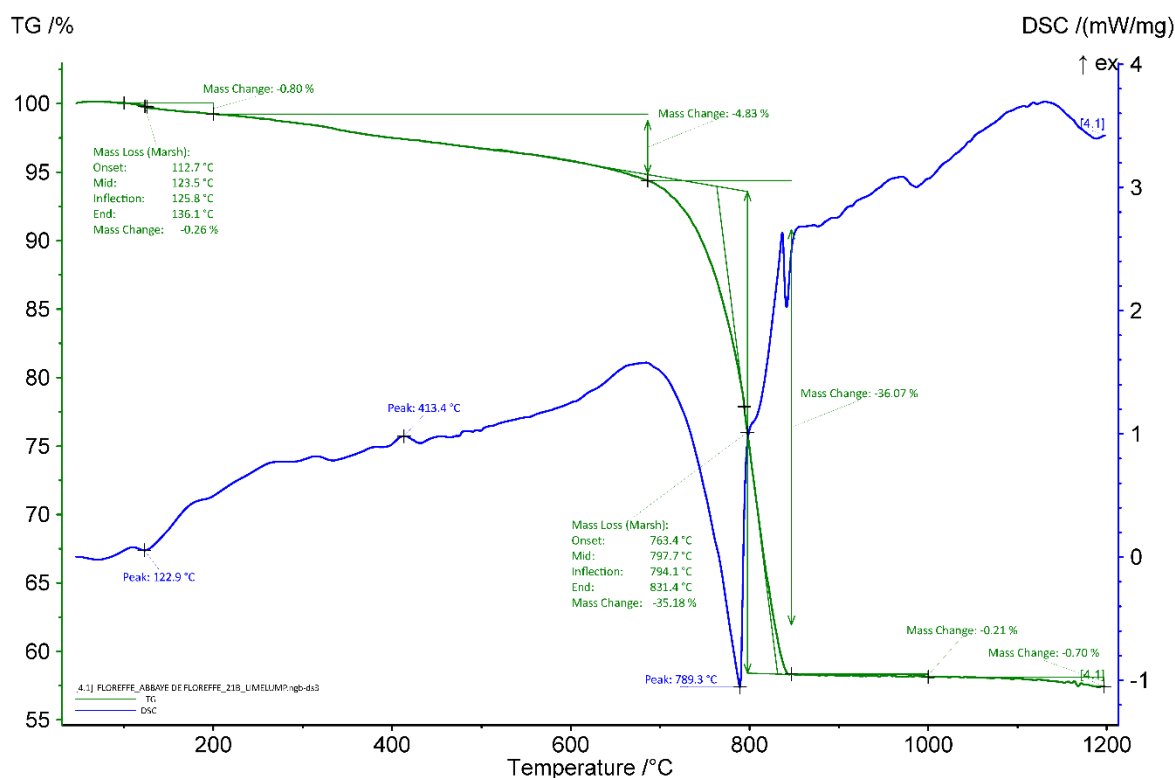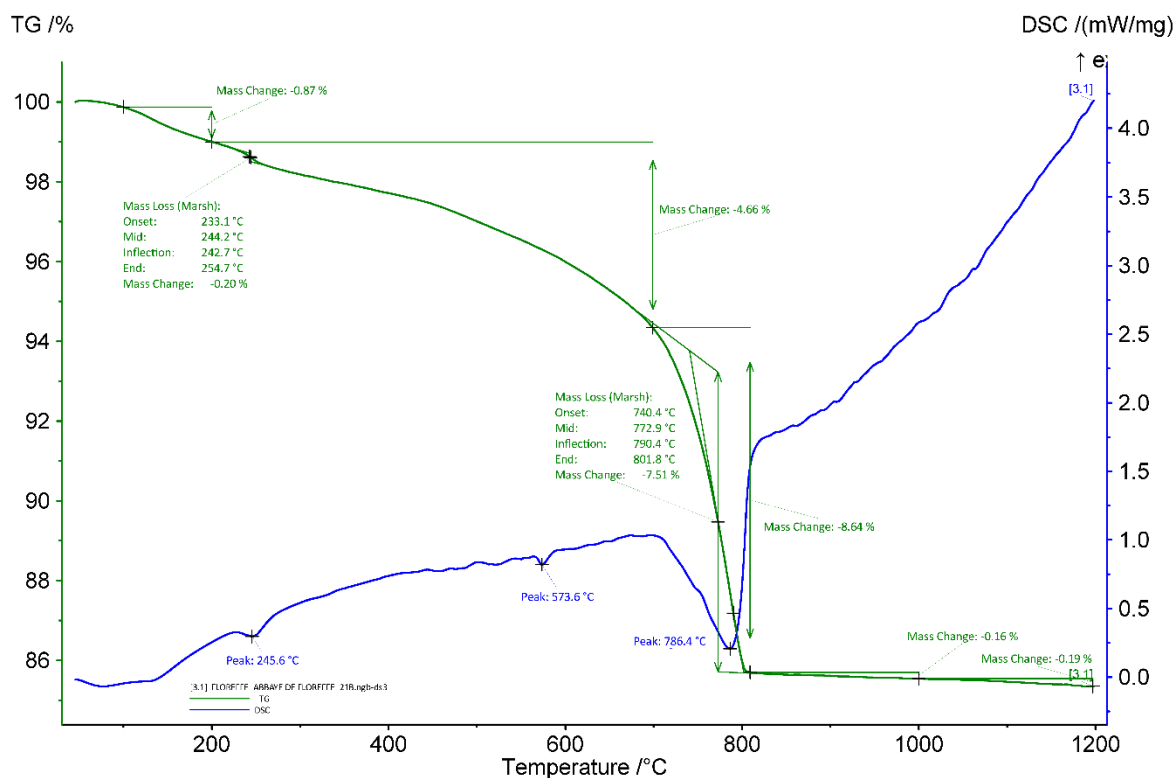
Figure 14: Coupled TG-DSC analysis of the mortar 21B (top) and the lime lump extracted from 21B (bottom) upon heating to a temperature of 1200°C at a heating rate of 20°C/min under an inert atmosphere (He flushed at 50 ml/min). The weight loss determined by thermogravimetric analysis (TG, wt%, green curve) and the result of the differential scanning calorimetric analysis (DSC, mW/mg, blue curve) are both presented.
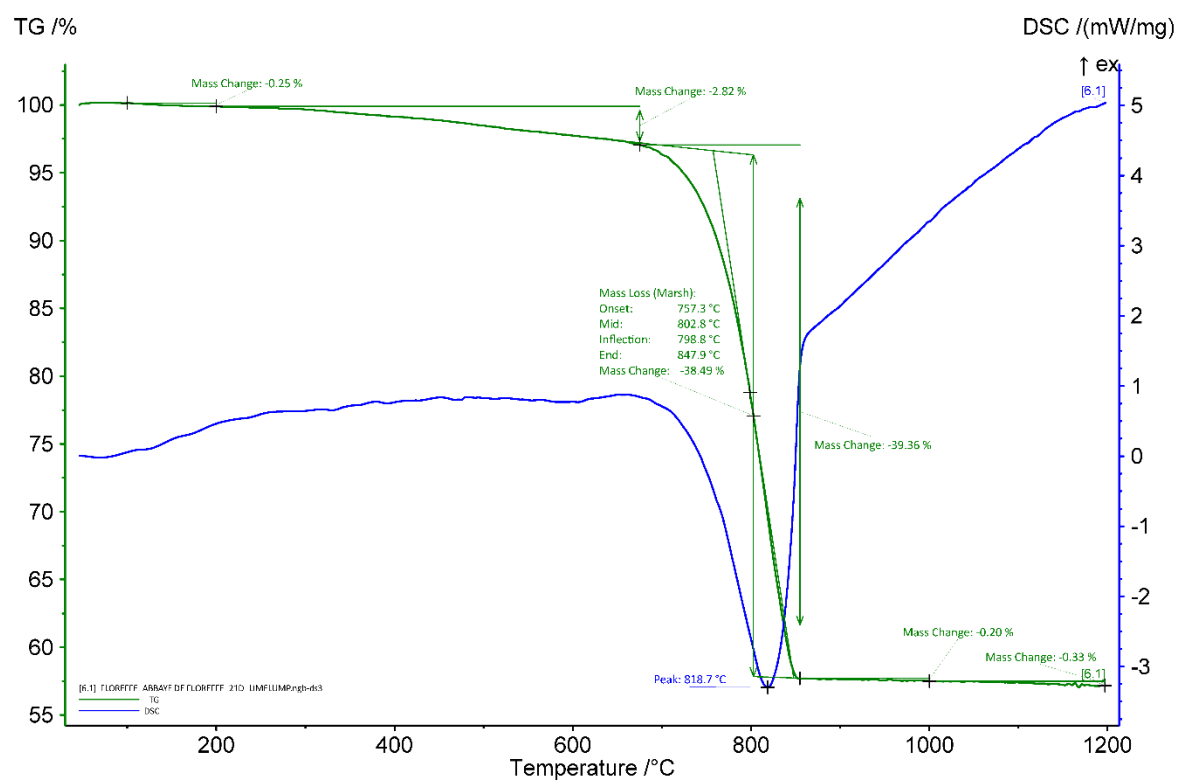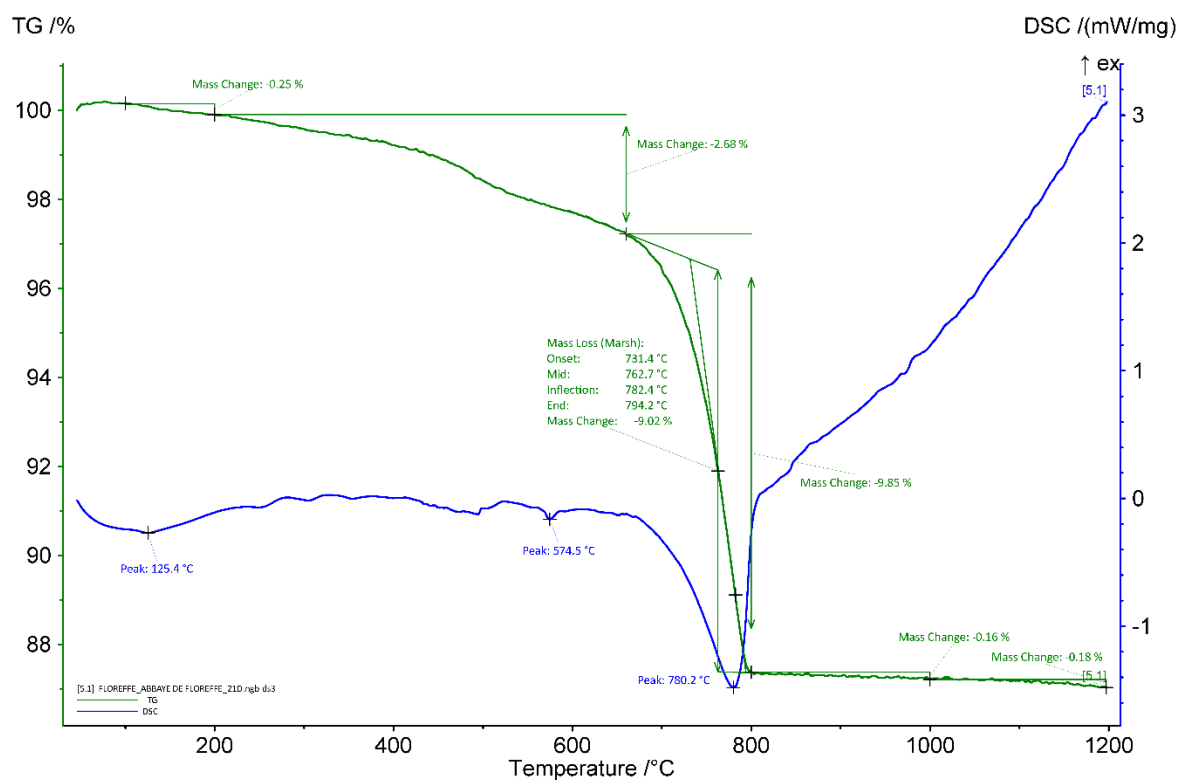
Figure 15: Coupled TG-DSC analysis of the mortar 21D (top) and the lime lump extracted from 21D (bottom) upon heating to a temperature of 1200°C at a heating rate of 20 °C/min under an inert atmosphere (He flushed at 50 ml/min). The weight loss determined by thermogravimetric analysis (TG, wt%, green curve) and the result of the differential scanning calorimetric analysis (DSC, mW/mg, blue curve) are both presented.
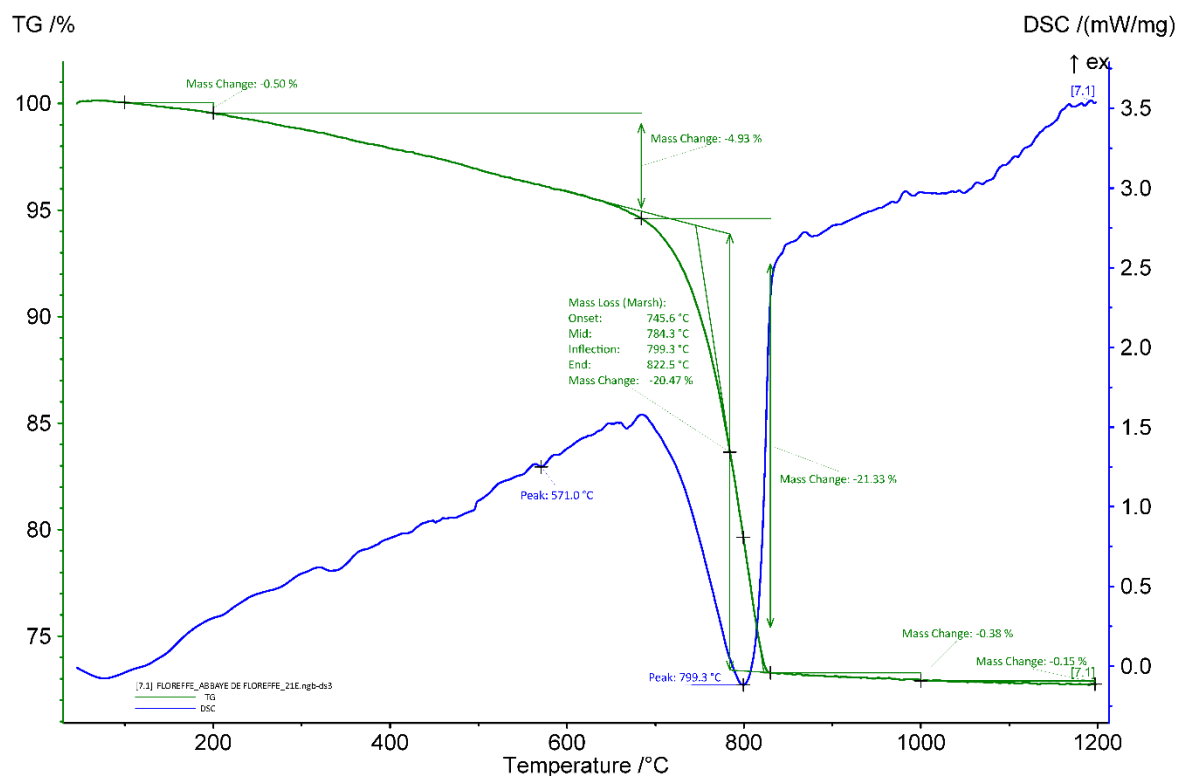
Figure 16: Coupled TG-DSC analysis of the mortar 21E upon heating to a temperature of 1200°C at a heating rate of 20 °C/min under an inert atmosphere (He flushed at 50 ml/min). The weight loss determined by thermogravimetric analysis (TG, wt%, green curve) and the result of the differential scanning calorimetric analysis (DSC, mW/mg, blue curve) are both presented.

XRD

X-ray diffraction analyses were performed for the mortar 21B (Figure 17). The diffractogram exhibit the characteristic features of quartz and calcite.
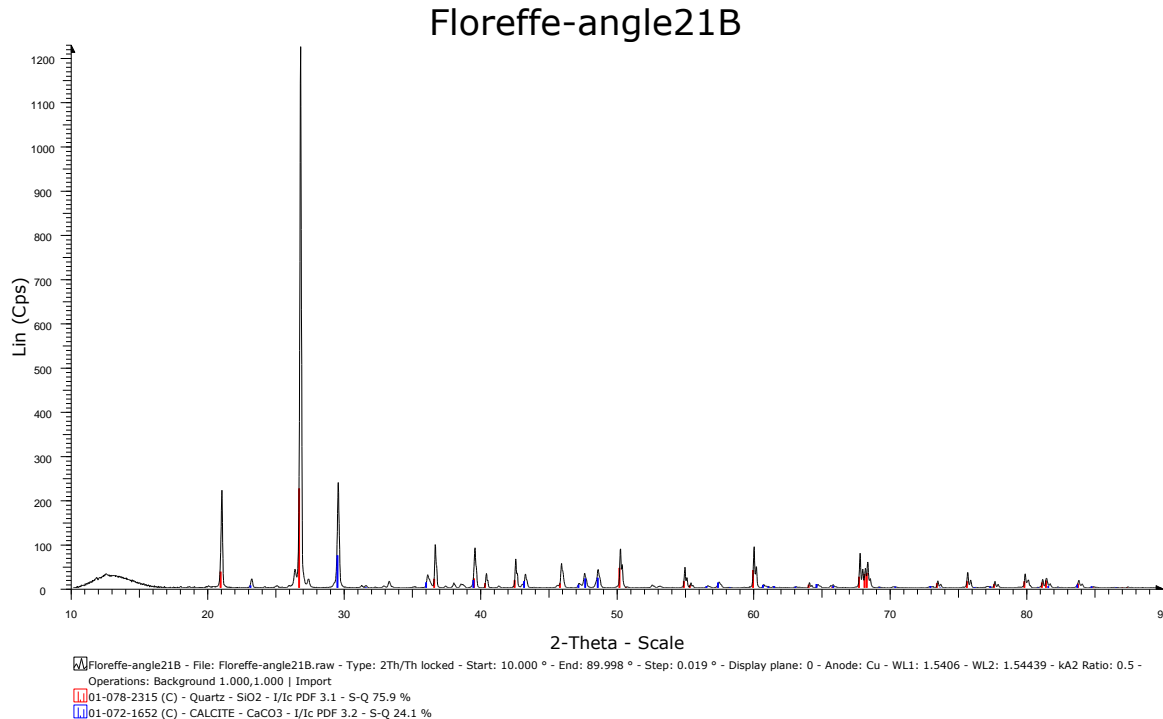
Figure 17: XRD diffractogram of the mortar 21B.

Scanning electron microscopy and Energy-dispersive X-ray spectroscopy (SEM-EDX)

SEM-EDX (Figure 18, left) revealed the presence of silicon and aluminum, showing the presence of a significant quantity of clay in the binder. Against all expectations, analyses of the lime lumps (Figure 18, right) also show the presence of aluminium and silicon, but in smaller proportions. This suggests that the limestone used was not pure, but already contains some clay impurities that may have led to the formation of a slightly hydraulic lime binder, provided that a sufficiently high burning temperature was reached. The hydraulic properties of the binder might have been amplified by the use of a slightly clayey sand. To verify this hypothesis, complementary analyses with SEM-EDX were performed around sandy clay agglomerates (data not shown) to see if more silicates had been formed around them but no significant difference was observed. The amount of silicates was lower both for the binder and the lime lumps of the cross section made from the mortar sample 21E (data not shown).
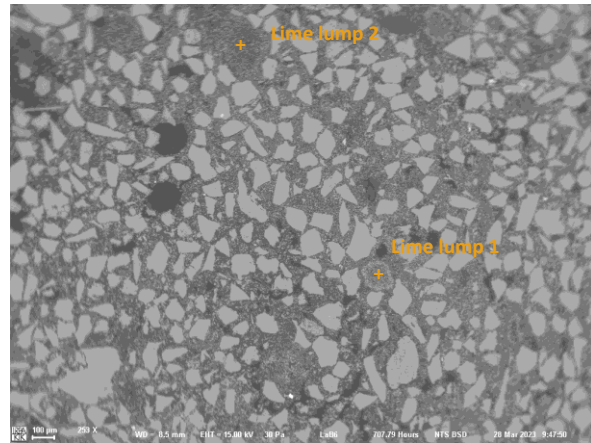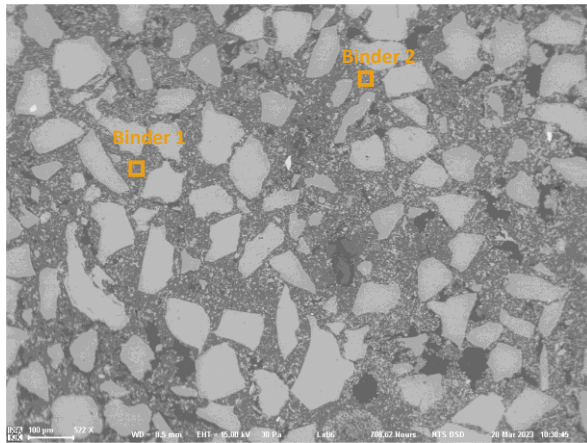
		Binder 1		Binder 2	
Element	Oxide	Atomic %	Oxide %	Atomic %	Oxide %
O		63,72		63,13	
Mg	MgO	0,46	0,87	0,44	0,82
Al	Al_2O_3	4,45	10,72	4,77	11,34
Si	SiO_2	25,08	71,31	23,65	66,33
Ca	CaO	5,44	14,44	7,25	18,97
Fe	$Fe2O_3$	0,47	1,76	0,50	1,88

		Lime lump 1		Lime lump 2	
Element	Oxide	Atomic %	Oxide %	Atomic %	Oxide %
O		58,68		62,35	
Mg	MgO	0,57	0,97	0,54	1,00
Al	Al_2O_3	2,38	5,14	4,28	10,06
Si	SiO_2	16,17	41,15	22,65	62,70
Ca	CaO	22,21	52,74	10,01	25,88

Figure 18: Representative SEM-EDX results obtained on cross section made from sample 21A: on left analyses were performed on the binder and on right on the lime lumps.

Grinding/particle separation

Since a large amount of mortar was provided for sample 21A, the more representative and homogeneous pieces were selected. A harder grey layer was scratched away with a scalpel and the sample was cleaned with a metallic brush. The same procedure was applied for all the samples. For sample 21B, the particles > 500 µm were crushed a bit more and sieved again to obtain more powder with a particle size < 75 µm.

FTIR on powders with particle size < 75 µm

The FTIR analyses performed on the powder with particle size < 75 µm of sample 21A (Figure 19) show the presence of calcite, clay and other silicates including quartz, gypsum, aragonite and organic matter.
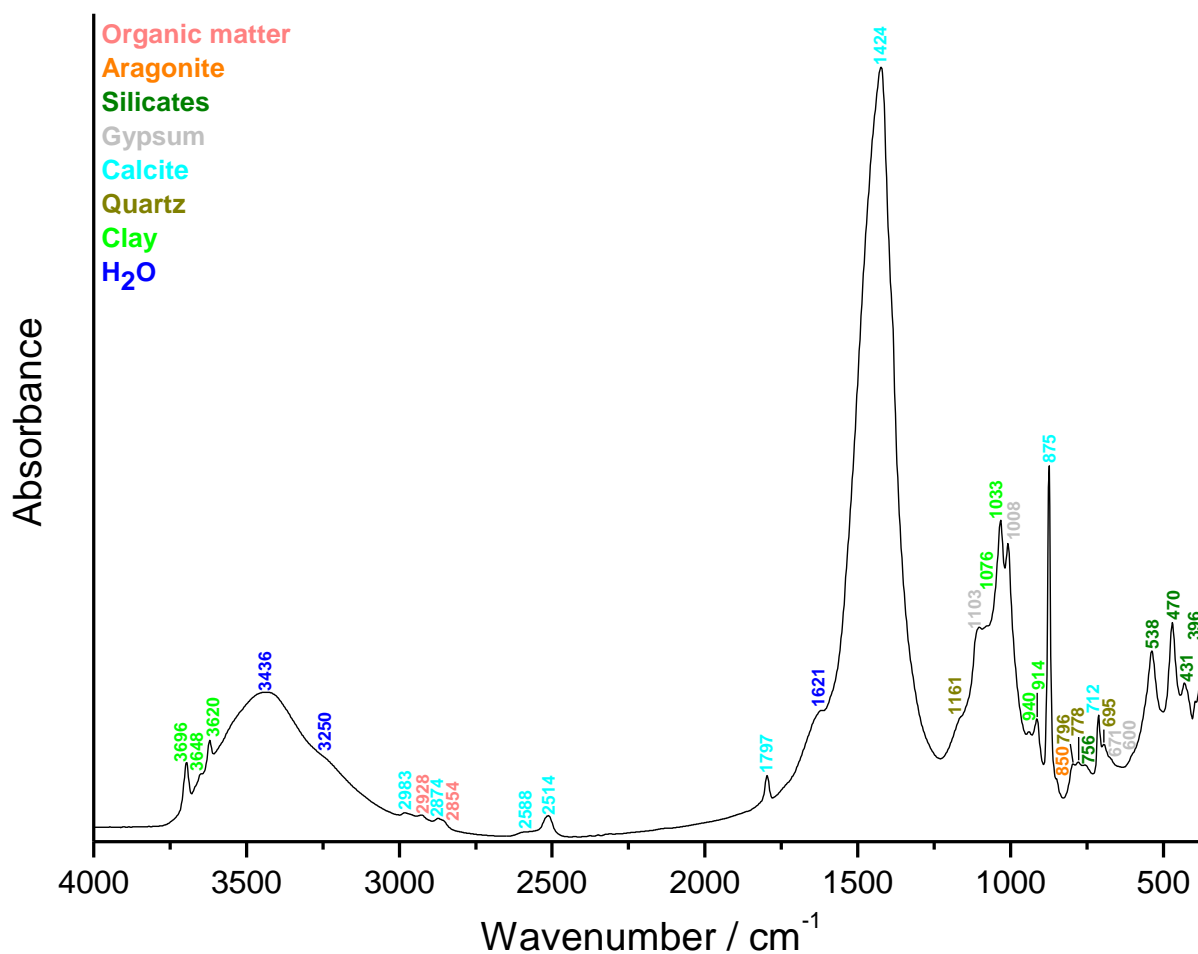
Figure 19: FTIR spectrum of the powder < 75 μm extracted from the mortar 21A.

TGA on powders with particle size < 75 μm

The coupled TG-DSC analysis of the powdered mortars with particles lower than 75 μm are presented Figures 20 to 23. The aHI of the powders with particles < 75 μm, determined on the basis of the weight loss between 200 and ca. 650°C, are relatively the same than the ones obtained for the whole mortar samples. As already mentioned, the relatively high values of the calculated hydraulicity indexes could be influenced here by the use of a slightly clayey sand and the use of a limestone containing clay, since loss from structurally bound water of some clays takes place at a similar temperature to structurally bound water in hydraulic components (Middendorf et al. 2005). The quantity of carbonates is higher in the powders compared to the whole samples since a large part of the sand is removed when sieving (~42 wt% for the sample 21A, 35 w% for the sample 21B, 44 w% for the sample 21D, and 62 wt% for for the sample 21E). Indeed, no quartz was detected in the powders. For all the powders (Figure 20-3), a peak around ~403-7°C is observed and might again be due to the release of water from calcium hydroxide (Moropoulou, Bakolas, and Bisbikou 1995; Klimesch and Ray 1996) and might indicate that the mortars did not fully carbonated. The exothermic peak at 457°C observed for the sample 21E (Figure 23) could be related either to some organic impurities in the material, or to the conversion of soluble to insoluble anhydrite, or to the rearrangement in $CaSO_4$ from hemihydrate to anhydrate structure (Brunello 2020). These were not observed for the whole mortar samples. It was probably present in too low concentration to be noticeable. The end temperatures of calcium carbonate decomposition are 827, 834, 820, and 830°C for the

powdered samples 21A, 21B, 21D, and 21E, respectively. It is higher compared to the whole samples. As for the lime lumps, a possible explanation could be that the powder is more pure compared to the whole mortar sample which increases the decomposition temperature.

Figure 20: Coupled TG-DSC analysis of the powdered mortar 21A with particle size < 75 µm upon heating to a temperature of 1200°C at a heating rate of 20°C/min under an inert atmosphere (He flushed at 50 ml/min). The weight loss determined by thermogravimetric analysis (TG, wt%, green curve) and the result of the differential scanning calorimetric analysis (DSC, mW/mg, blue curve) are both presented.

Figure 21: Coupled TG-DSC analysis of the powdered mortar 21B with particle size < 75 µm upon heating to a temperature of 1200°C at a heating rate of 20°C/min under an inert atmosphere (He flushed at 50 ml/min). The weight loss determined by thermogravimetric analysis (TG, wt%, green curve) and the result of the differential scanning calorimetric analysis (DSC, mW/mg, blue curve) are both presented.

Figure 22: Coupled TG-DSC analysis of the powdered mortar 21D with particle size < 75 μm upon heating to a temperature of 1200°C at a heating rate of 20°C/min under an inert atmosphere (He flushed at 50 ml/min). The weight loss determined by thermogravimetric analysis (TG, wt%, green curve) and the result of the differential scanning calorimetric analysis (DSC, mW/mg, blue curve) are both presented.

Figure 23: Coupled TG-DSC analysis of the powdered mortar 21E with particle size < 75 μm upon heating to a temperature of 1200°C at a heating rate of 20°C/min under an inert atmosphere (He flushed at 50 ml/min). The weight loss determined by thermogravimetric analysis (TG, wt%, green curve) and the result of the differential scanning calorimetric analysis (DSC, mW/mg, blue curve) are both presented.

Radiocarbon results

The test prior to the CO_2 extraction revealed a fair amount of carbon (Table 7) in the samples (~4 to 7 % for the mortars and 8 % for the lime lumps). A relatively low amount of powder <75 μm was necessary for the carbon extraction (Table 7). The percentage of carbon for the charcoal extracted from the mortar 21B is low (11 %), it should be around 50 % as for the putlog.

RICH	Sample type	Method	C (%)	σ (%)	m (g)	Age BP	Calibrated date (oxcal - 95.4%)	Age BP extrapolated	Calibrated date (oxcal - 95.4%)	Age BP extrapolated with stat	Calibrated date (oxcal - 95.4%)	Age BP average	Calibrated date (oxcal - 95.4%)	Reliability of dating
30262 (21A)	Mortar from buttress	HCl (8 fractions)	5.43	0.02	1.75	-	-	660 ± 25	1281-1392 calAD	659.4 ± 12.9	1286-1389 calAD	(first 4 fractions) 678 ± 11	1281-1381 calAD	☒
30183 (21A)	Lime lump extracted from mortar	H₃PO₄	7.88	-	0.017	850 ± 22	1162-1260 calAD	-	-	-	-	-	-	☑
30813 (21A)		HCl (9 fractions)	8.34	-	0.23	-	-	803 ± 25	1215-1276 calAD	804.1 ± 26.5	1183-1277 calAD	(all 9 fractions) 850 ± 8	1175-1225 calAD	☑
30422 (21B)	Mortar masonry angle to the north-east of the transept crossing	HCl (8 fractions)	5.51	0.14	1.86	-		654 ± 25	1282-1394 calAD	655.8 ± 22.6	1285-1391 calAD	(first 4 fractions) 602 ± 11	1308-1399 calAD	☒
30422.2 (21B)		HCl (8 fractions)	4.20	0.52	2.05	-	-	606 ± 25	1301-1405 calAD	606.6 ± 12.6	1305-1399 calAD	(first 7 fraction) 607 ± 8	1306-1399 calAD	☒
30184 (21B)	Lime lump extracted from mortar	H₃PO₄	8.46	-	0.017	824 ± 23	1176-1270 calAD	-	-	-	-	-	-	☑
30686 (21B)	Charcoal extracted from mortar	HCl	11.00	-	0.0002	1194 ± 26	710-945 calAD	-	-	-	-	-	-	☑
30166 (21C)	Wood from the putlog hole	AAA	53.13	-	0.0028	961 ± 21	1027-1157 calAD	-	-	-	-	-	-	☑

30860 (21D)	Mortar from wall between stairs & buttress	HCl (8 fractions)	4.13	1.61	3.19	-	-	801 ± 25	1216-1276 calAD	737.5 ± 28.1	1226-1299 calAD	(first 4 fractions) 791 ± 12	1225-1270 calAD	☒
30745 (21D)	Lime lump extracted from mortar	H$_3$PO$_4$	8.19	-	0.041	852 ± 24	1160-1261 calAD	-	-	-	-	-	-	☑
31022 (21E)	Mortar from the side aisle of the north heart	HCl (8 fractions)	7.41	0.12	1.34	-	-	325 ± 25	1490-1641 calAD	325.8 ± 11.8	1500-1639 calAD	(first 5 fractions) 352 ± 25	1476-1631 calAD	☑
30770 (21E)	Wood found inside mortar	HCl	59.90	-	0.00151	977 ± 27	998-1158 calAD	-	-	-	-	-	-	☑

Table 7: Radiocarbon results

The radiocarbon results obtained for the mortar 21A is younger than expected (Table 7 & Figure 24). The calibrated results are around the 13th or 14th century when the estimated historical date is around the 10th to 12th century (the framework was dated by dendrochronology to 1170-80d). In addition, the lime lump extracted from the mortar gives an older result (Table 7 & Figure 25). The later was dated twice. The first time, it was dated as a single fraction (RICH-30183) which resulted in a plausible calibrated date (1162-1260 calAD). It was then dated with a method similar to the mortar with 9 CO_2 fractions (Table 7 & Figure 25). The result of the resulting extrapolated date is slightly older compared to the single fraction (13th century) but if we look at the result from the average of the 9 fractions (Table 7), the same result as the single fraction was obtained (1175-1225 calAD).
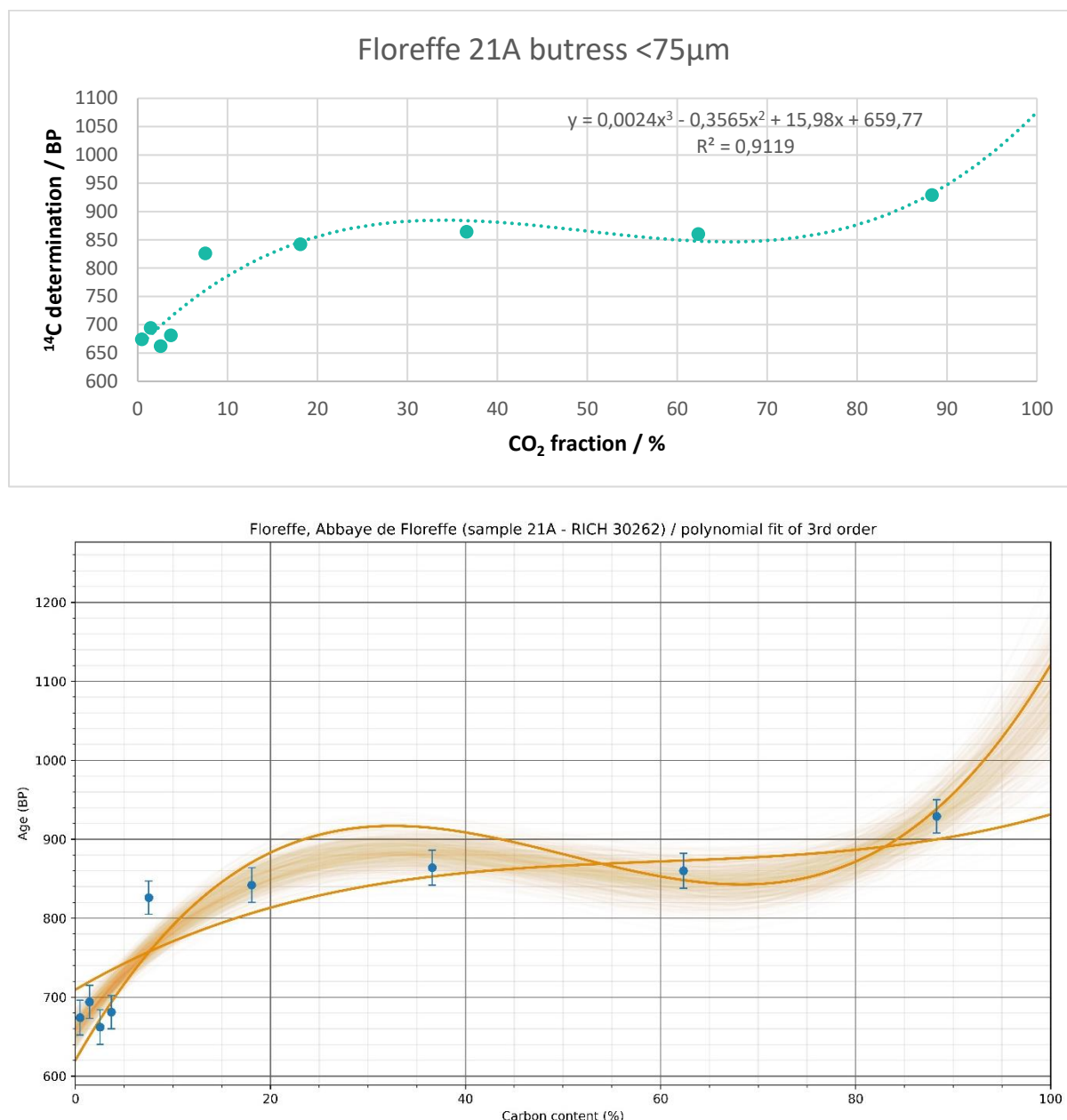
Figure 24: Radiocarbon results for the powdered mortar 21A with particles < 75 μm as a function of the CO_2 fraction (the graph at the bottom shows the statistic on the results).

Floreffe 21 A lime lump

$$y = 0,0004x^3 - 0,0929x^2 + 5,0217x + 802,89$$
$$R^2 = 0,8472$$

Floreffe, Abbaye de Floreffe (sample 21A-LL - RICH 30813) / polynomial fit of 3rd order
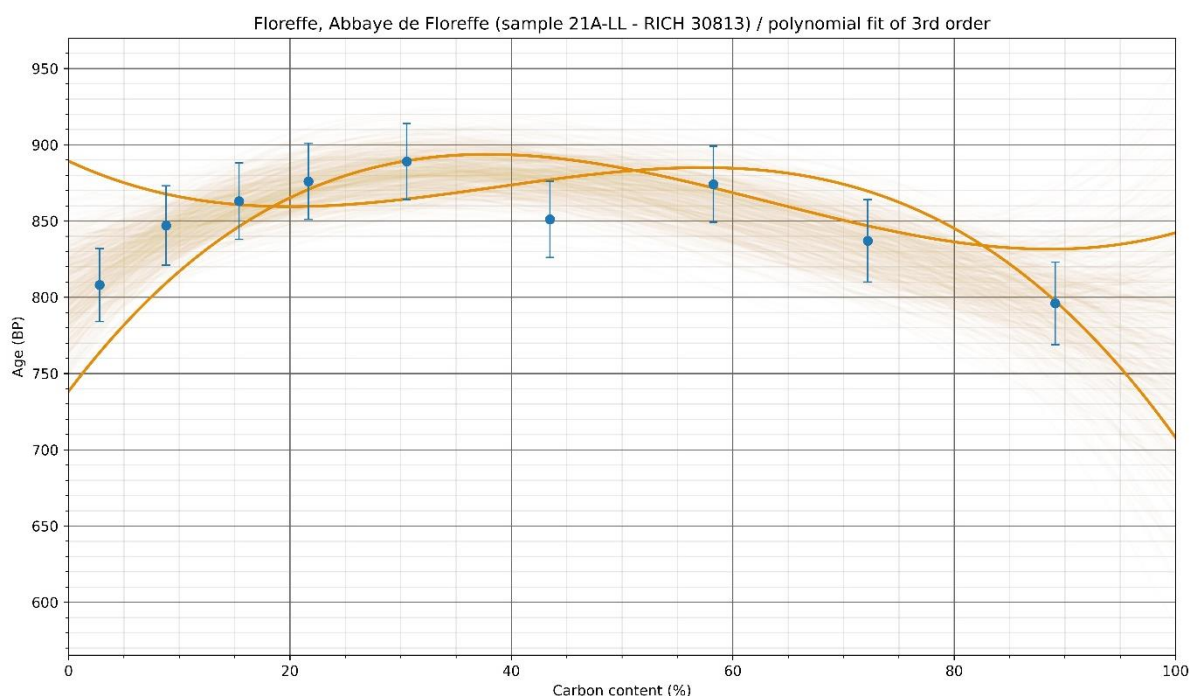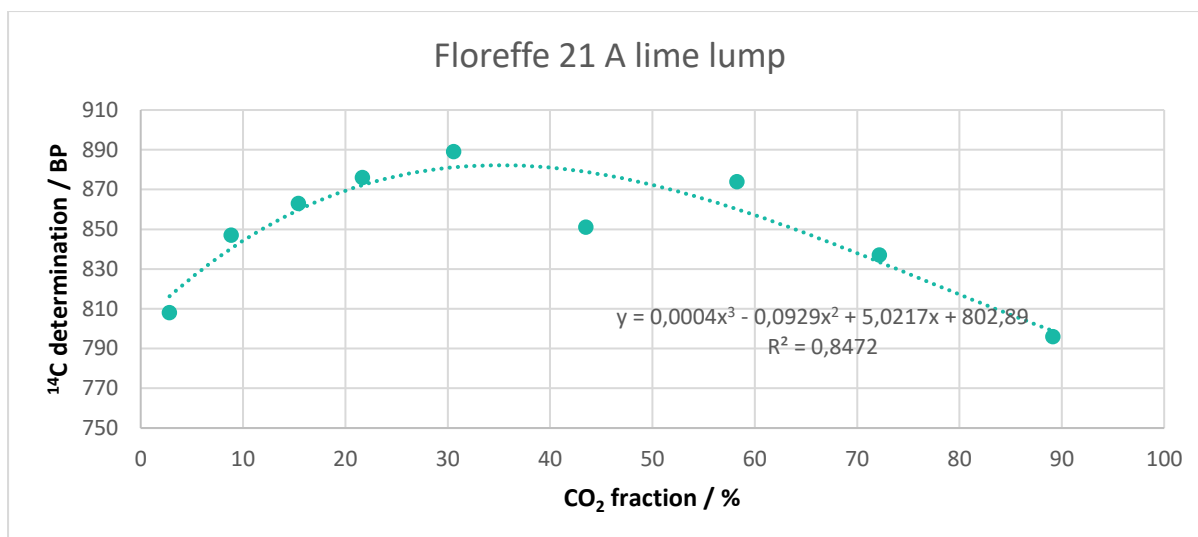
Figure 25: Radiocarbon results for the lime lump extracted from the mortar 21A as a function of the CO_2 fraction (the graph at the bottom shows the statistic on the results).

Because of technical issues, only the four first fractions (Figure 26) could be dated for the mortar sample 21B (RICH-30422). They are the more important to determine the age of the sample but another full CO_2 extraction was performed in order to confirm the results (Figure 27, RICH-30422.2). The results obtained for both dates are within the same range and younger (13th-14th century) than the estimated historical date (10th-12th century). As for the mortar sample 21A, the lime lump is older and corresponds better to the estimated date. The charcoal extracted from the mortar 21B (Table 7) gives a calendar age of 710-945 calAD, the old wood effect need to be considered but at least it gives a terminus post quem. The date of the wood from the putlog (sample 21C) is slightly younger (1027-1157 calAD) but within the range of the expected date.
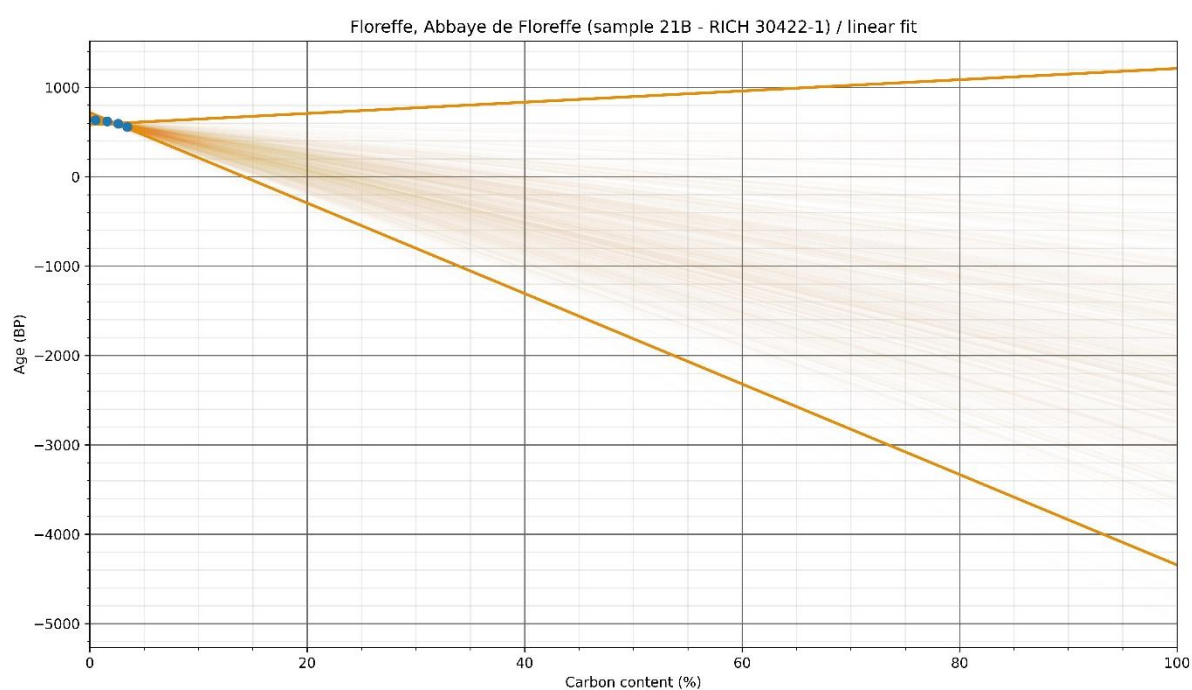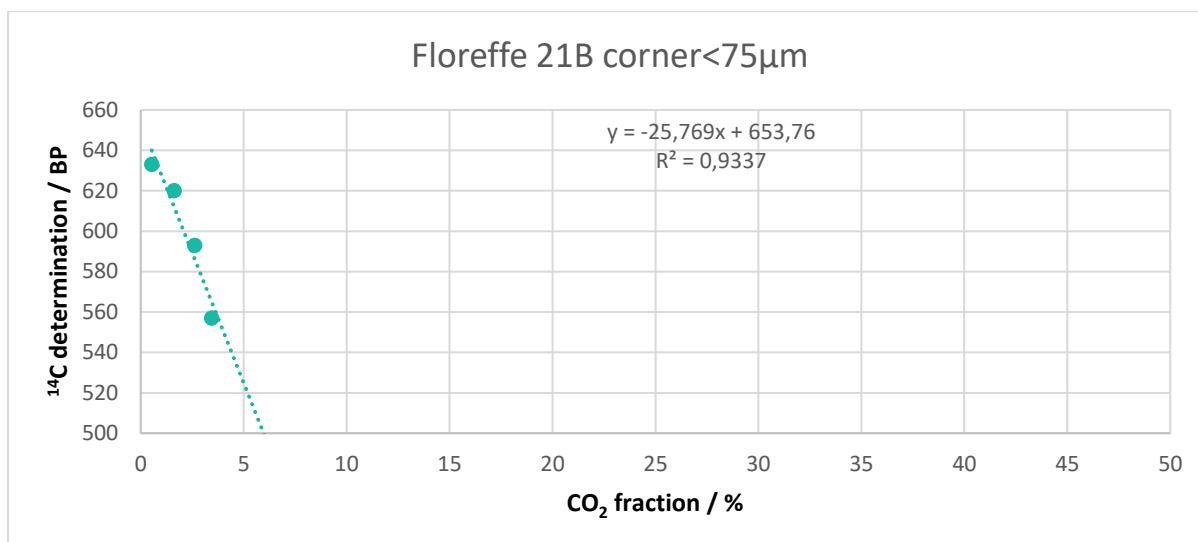
Figure 26: Radiocarbon results for the powdered mortar 21B with particles < 75 µm (RICH-30422) as a function of the CO_2 fraction (the graph at the bottom shows the statistic on the results).
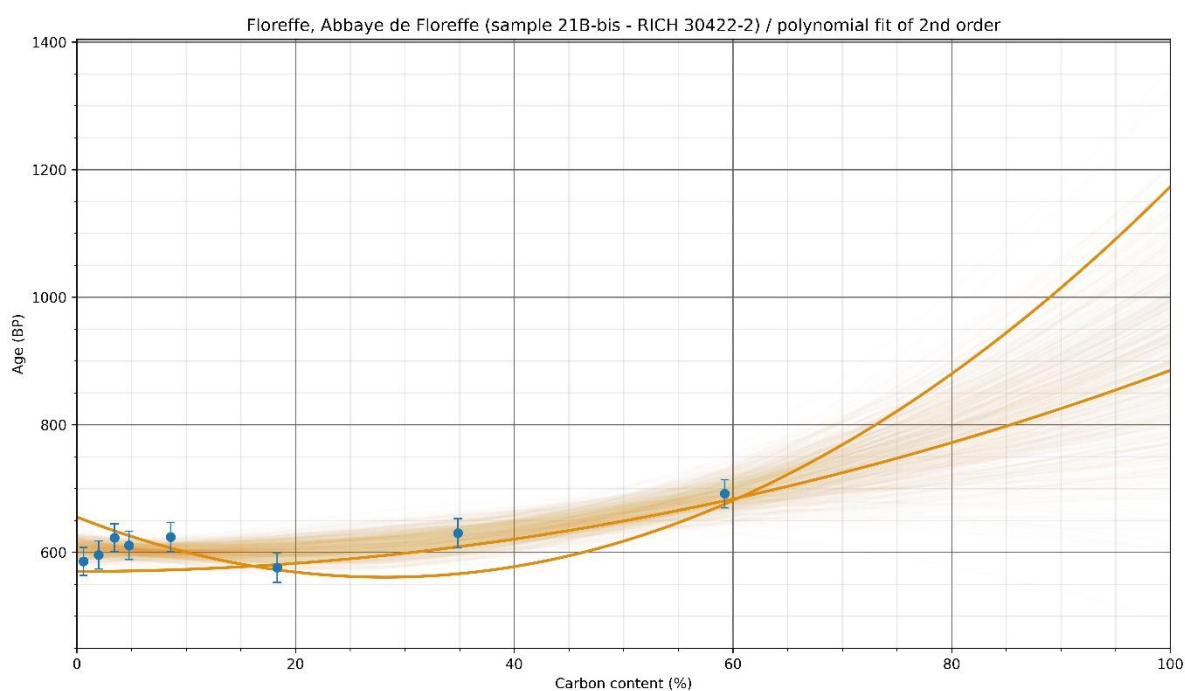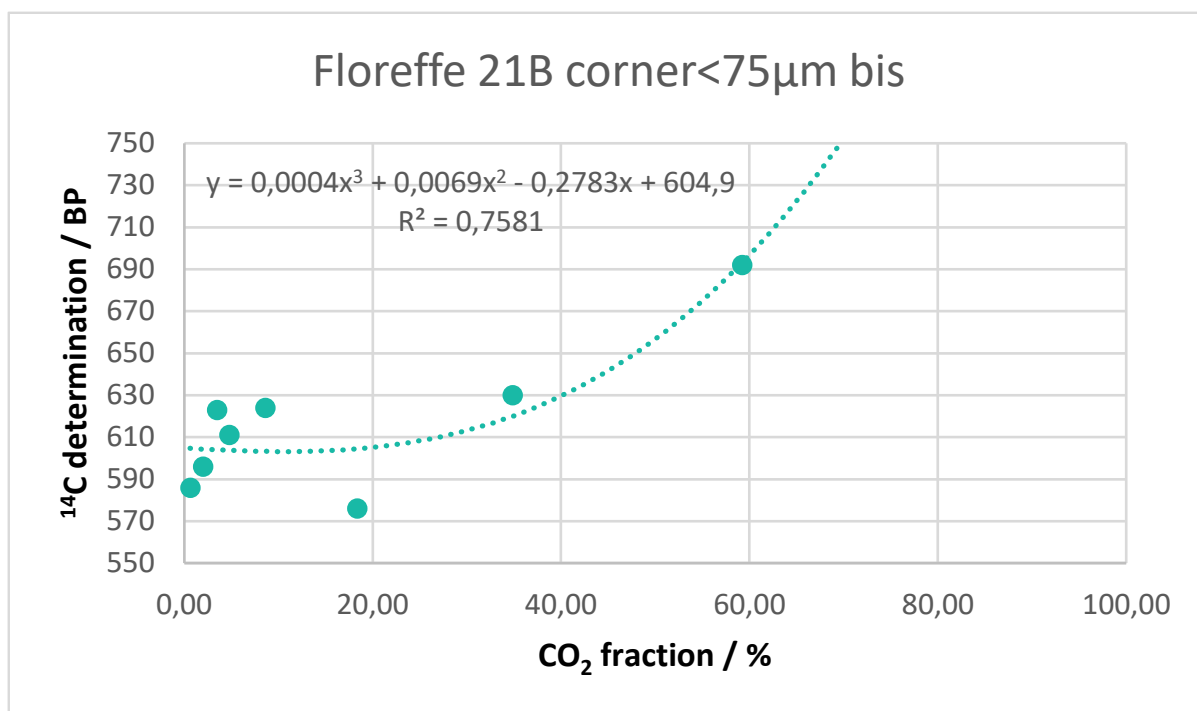
Figure 27: Radiocarbon results for the powdered mortar 21B with particles < 75 μm bis (RICH-30422.2) as a function of the CO_2 fraction (the graph at the bottom shows the statistic on the results).

For the mortar sample 21D (Table 7 & Figure 28), similar results compared to the samples 21A and 21B. The mortar date is younger than expected and the lime lump date is within the range of the historical date.

Figure title: Floreffe 21 D

$$y = 29{,}804\ln(x) + 800{,}91$$
$$R^2 = 0{,}9291$$

X-axis: CO_2 fraction / %
Y-axis: ${}^{14}C$ determination / BP

Chart title: Floreffe, Abbaye de Floreffe (sample 21D - RICH 30860) / x/(1+|x|) fit

X-axis: Carbon content (%)
Y-axis: Age (BP)
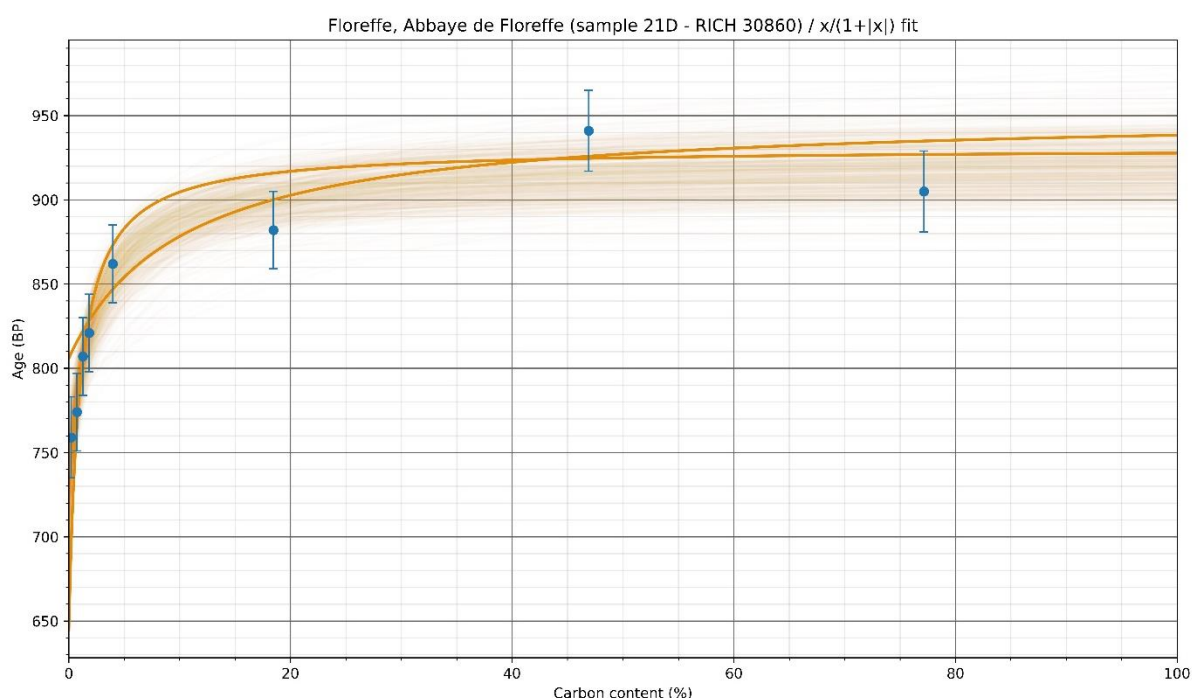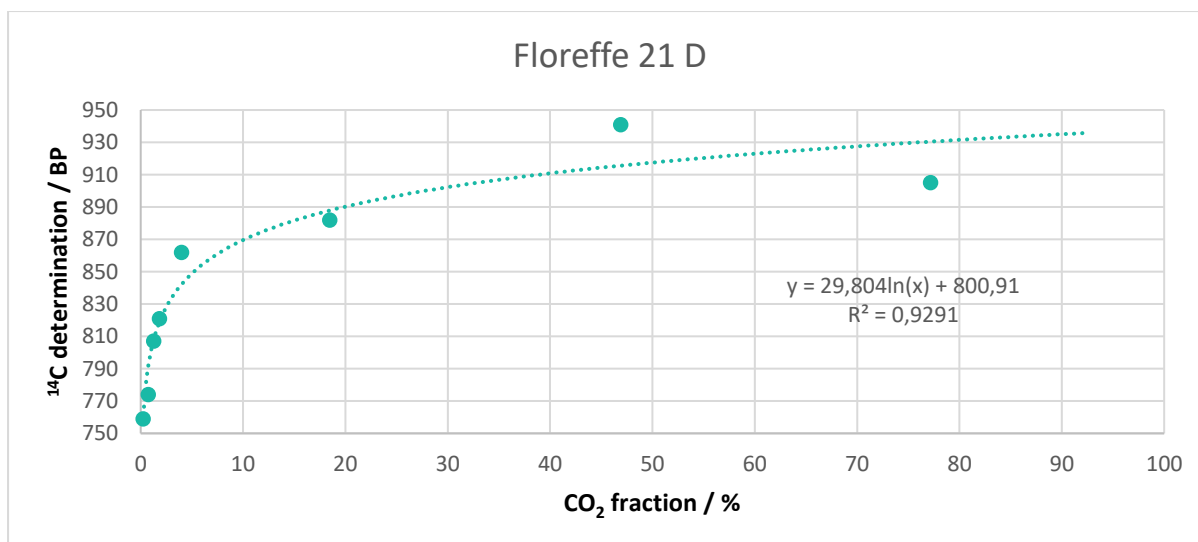
Figure 28: Radiocarbon results for the powdered mortar 21D with particles < 75 µm bis (RICH-30820) as a function of the CO_2 fraction (the graph at the bottom shows the statistic on the results).

The mortar 21E was estimated to have been made in the 13th or the 17th century. The calendar results for the mortar (Table 7 and Figure 29) are between the 15th and the 17th century. The piece of wood found inside the mortar is estimated to the 11th or 12th century. As for the charcoal earlier, it gives a terminus post quem.
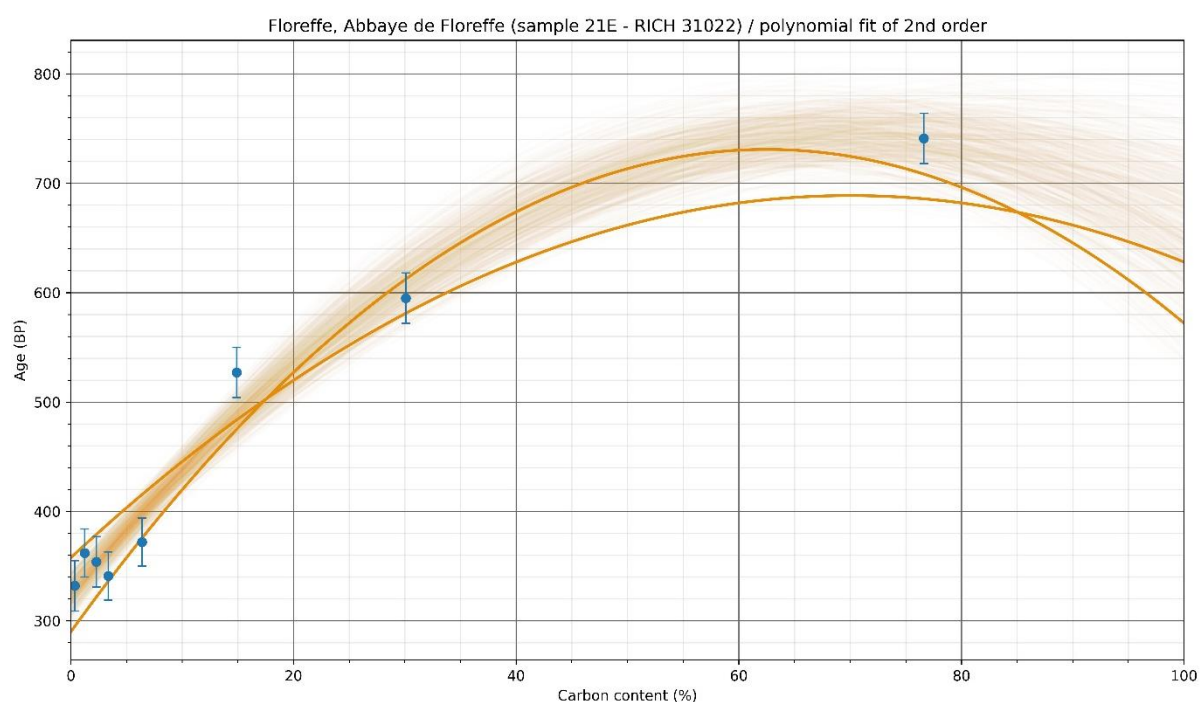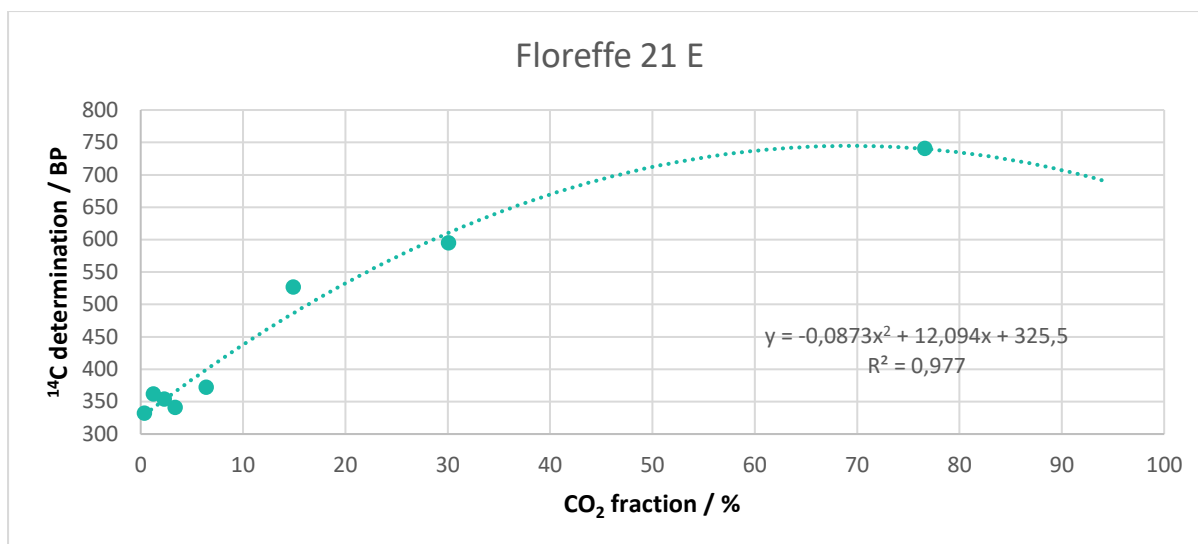
Figure 29: Radiocarbon results for the powdered mortar 21E with particles < 75 μm bis (RICH-31022) as a function of the CO_2 fraction (the graph at the bottom shows the statistic on the results).

Conclusions

The mortars 21A, 21B and 21D estimated to have been made during the 10 to 12th centuries have a similar composition. The radiocarbon dating of these mortars is not reliable, it results in too young ages. Surprisingly, the radiocarbon dating of the lime lumps extracted from these mortars give a plausible date (1160-1270 calAD). Both carbonated in the same time and should provide the same result. An hypothesis can be that the fine clay particles present in the sand have pozzolanic properties, i.e. they can form hydraulic phases with the lime binder. These hydraulic compounds improve the speed at which the mortar sets, but delay hardening

by carbonation, which could explain why the dates on the binder are systematically more recent than those on the lumps. The result obtained for the charcoal found inside the mortar 21B gives a terminus post quem of 710-945 calAD.

The mortar 21E appears to have been a later addition, either from the 13th or the 17th century according to the archaeologists. The composition is clearly different compared to the three other mortars, especially the ratio between the sand and the binder. It results in a less hydraulic mortar that could provide more reliable results compared to the other samples. The size of the lime lumps was not large enough to date them. However, a piece of wood was found while grinding the mortar and was dated to 11th or 12th century which confirms the presumed historical date. The date obtained for the mortar ranges between the 15th and the 17th centuries. The hydraulicity is lower compared to the other samples but it is still moderate and could also have provoked a delay in the carbonation.

Bibliography

Ahmmed, Tanjil, Ana Raquel Silva, José Carlos Quaresma, Patrícia Moita, and Cristina Galacho. 2024. "Analytical Characterization of Historical Mortars from the Roman Villa of Frielas (Loures, Portugal)." *Acta IMEKO* 13 (3): 1–11.

Annales Floreffienses NaSo A068. 1859. Bethmann L. C. Vol. MGH, SS, t. XVI, pp. 624–625.

Brunello, Vallentina. 2020. "Mortars: A Complex Material in Cultural Heritage. A Multi-Analytical Procedure to Characterize Historical Mortars." Università degli studi dell'insubria. https://core.ac.uk/reader/322778010.

Hoffsummer, Patrick. 1995. *Les charpentes de toitures en Wallonie. Typologie et dendrochronologie (XIe-XIXe siècle)*. Études et documents, Monuments et sites. Namur: Ministère de la Région wallonne, Division du Patrimoine.

Klimesch, Danielle S., and Abhi Ray. 1996. "The Use of DTA/TGA to Study the Effects of Ground Quartz with Different Surface Areas in Autoclaved Cement: Quartz Pastes. Part 1: A Method for Evaluating DTA/TGA Results." *Thermochimica Acta* 289 (1): 41–54. https://doi.org/10.1016/S0040-6031(96)03033-X.

Middendorf, B., J. J. Hughes, K. Callebaut, G. Baronio, and I. Papayianni. 2005. "Investigative Methods for the Characterisation of Historic Mortars—Part 1: Mineralogical Characterisation." *Materials and Structures* 38 (8): 761–69. https://doi.org/10.1007/BF02479289.

Moropoulou, Antonia, Asterios Bakolas, and Katerina Bisbikou. 1995. "Characterization of Ancient, Byzantine and Later Historic Mortars by Thermal and X-Ray Diffraction Techniques." *Thermochimica Acta* 269:779–95.

———. 2000. "Investigation of the Technology of Historic Mortars." *Journal of Cultural Heritage* 1 (1): 45–58.

Rickard, William D. A., Arie Van Riessen, and Philip Walls. 2010. "Thermal Character of Geopolymers Synthesized from Class F Fly Ash Containing High Concentrations of Iron and

α-Quartz." *International Journal of Applied Ceramic Technology* 7 (1): 81–88. https://doi.org/10.1111/j.1744-7402.2008.02328.x.

Study of mortars from Sagalossos (Turkey) for the BRAIN 2.0 PalC project

Context of the site

Sagalassos is an archaeological site located in the Taurus mountains, north of Ağlasun and ca. 109 km north of Antalya in southwest Turkey. Its origin goes back to late Bronze Age, and it was occupied by different cultures (Pisidians, Achaemenids, Antigonids, Seleucids, Attalids) before being part of the Roman republic (Waelkens 2012; "The History of Sagalassos," n.d.). Numerous construction of buildings were developed during the Roman Imperial period ("The History of Sagalassos," n.d.). The Catholic University of Leuven is involved in the excavations since 1990 (Waelkens 2012) and was able to borrow some samples for the PALc project.

Figure 1: View of the Taurus mountains with a part of Sagalassos Roman buildings (from "The History of Sagalassos," n.d.).

Material

Figure 2: Sampling of the mortars SA02TH03 (left), SA02TH04 (middle) and SA02TH12 (right) – pictures from (Hofkens 2003).

Three samples were selected for the PALc project: SA02TH03 (Figure 2, left) is a bedding mortar sampled between bricks in room XXII (see Figure 3) on a low wall; SA02TH04 (Figure 2, middle) is a bedding mortar sampled in the same room also in the lower part of the wall; and SA02TH12 (Figure 2, right) was sampled 1.5 m above floor level in room IX, it is also a bedding mortar. The presumed historical date of samples SA02TH03 and SA02TH04 is late 4th to early 5th centuries AD and sample SA02TH12 seems to be a later intervention estimated to the 6th century AD.
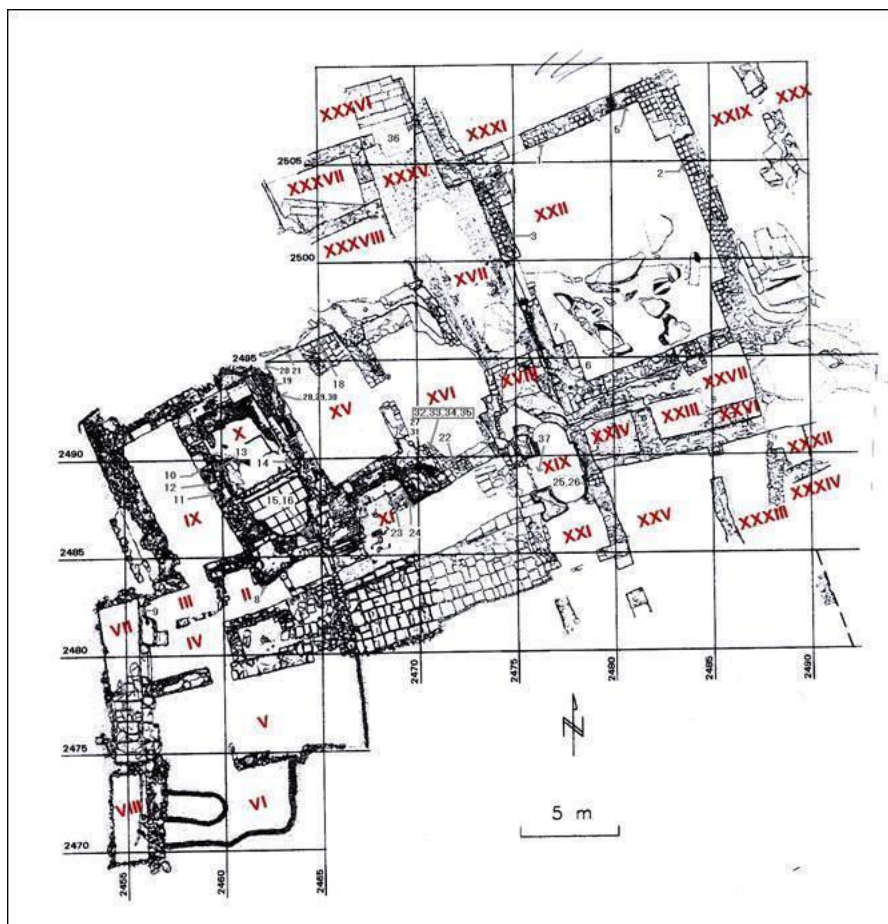
Figure 2: Map of the site (Hofkens 2003).

Results & Discussion

Macroscopic descriptions

The main colour of the three samples is beige (Figure 4) tending towards pale yellow (2.5Y 8/2) for SA02TH03 and SA02TH04, and to very pale brown (10YR 8/3) for SA02TH12. SA02TH03 and SA02TH12 are slightly specular, probably due to the presence of coarse grains of quartz, mica or well crystallised calcite. They all contains soft black inclusions most probably due to the presence of charcoal, grey inclusions not reacting with acid that are possibly siliceous aggregates, and soft and round red inclusions probably made of terracotta. The white inclusions are lime lumps measuring between 0.3 to 0.7 cm. Soil can be noticed at the surface of SA02TH03 and SA02TH12. SA02TH03 possibly shows some salts on its surface (white smear). A large milky inclusion was observed on SA02TH04 and was suspected to be quartzite.
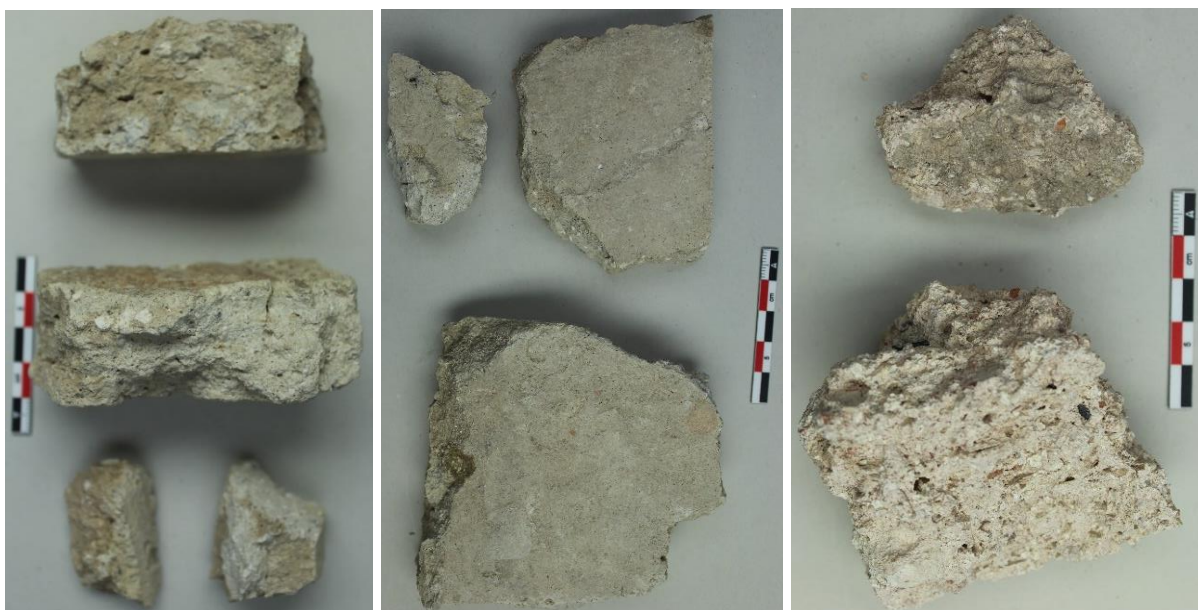
Figure 4: Samples SA02TH03 (left), SA02TH04 (middle), and sample SA02TH12 (right).

Fourier transform Infrared (FTIR) spectroscopy on inclusions & binder

The binders (beige, Figure 5) contain calcium carbonates and silicates. The relative quantities of calcium carbonates compared to silicates is rather low for SA02TH03 and SA02TH04 (beige, Figure 5 top and middle). The binder of SA02TH04 also contains gypsum and clay. For SA02TH12, the relative ratio silicates versus carbonates is common for a mortar. Aragonite and organic matter were also detected for SA02TH12. The lime lumps (white Figure 5) are made of calcium carbonates (calcite and aragonite) with some silicates for SA02TH12. The FTIR spectra of the black inclusions show only silicates with a low amount of calcite for SA02TH03, amorphous carbon/degraded organic matter with calcite for SA02TH04 and SA02TH12. The soil sampled on the surface of SA02TH03 is made of silicates including clay. The grey inclusions from SA02TH03 and SA02TH12 are siliceous aggregate as expected. The smeared white on SA02TH03 believed to be a salt give a FTIR spectrum showing silicates including quartz with calcite and aragonite. The large milky inclusion observed on SA02TH04 is not made of quartzite as initially suspected but of calcite and aragonite. It might rather be a limestone inclusion. Silicates including quartz were detected for the red inclusions of samples SA02TH04 and SA02TH12.
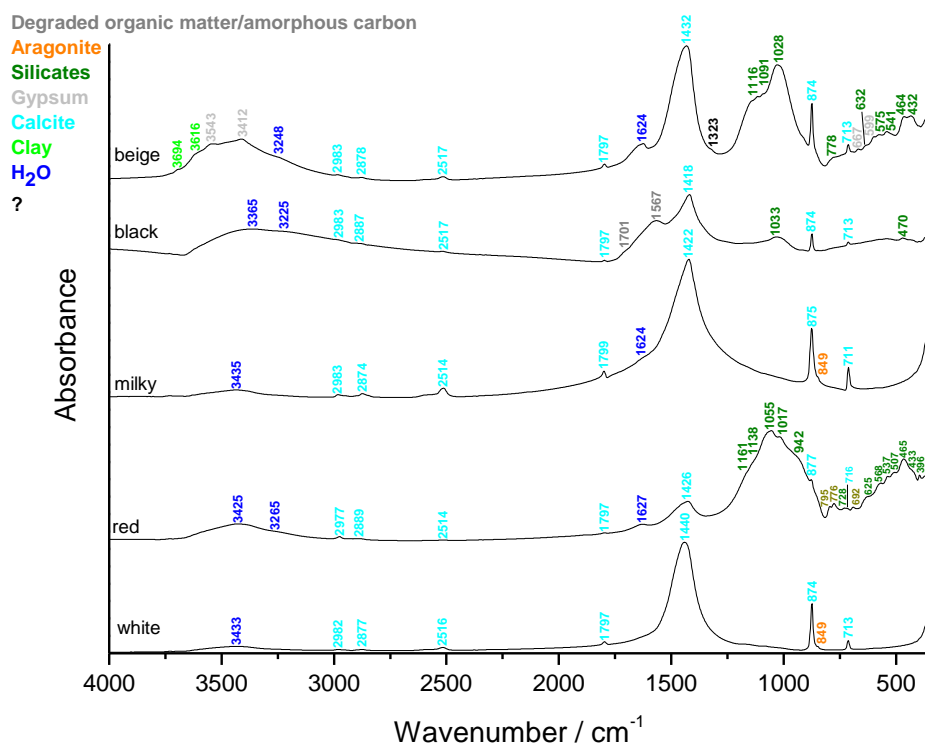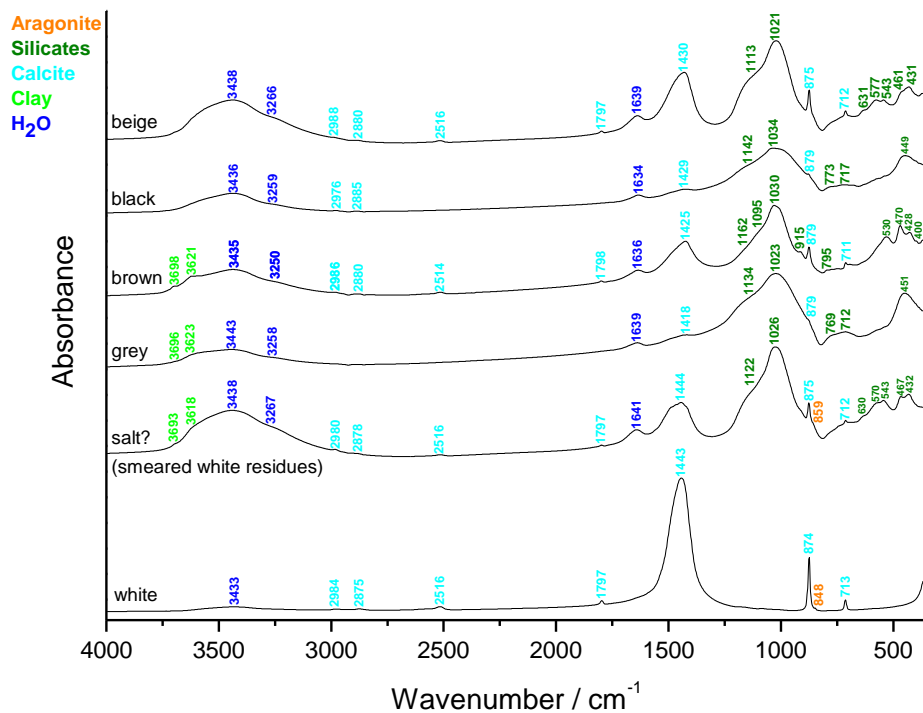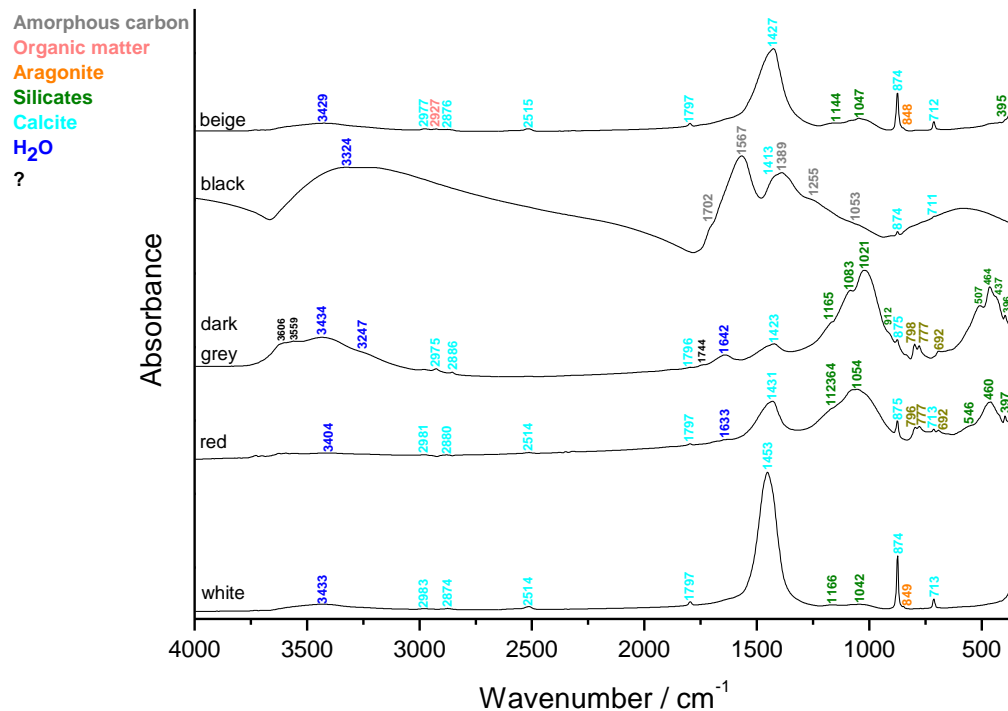
Figure 5: FTIR spectra obtained on the inclusions and binder (beige) of SA02TH03 (top), SA02TH04 (middle) and SA02TH12 (bottom).

Binder:sand ratio

The calculated binder:sand ratio (in volume unit) using a bulk density of 1.35 kg/dm^3 for the sand and 0.575 kg/dm^3 for the lime are different for the three samples: close to 2:1 for SA02TH03, exactly 5:2 for SA02TH04, and close to 5:1 for SA02TH12

	SA02TH03	SA02TH04	SA02TH12
Sample weight (g)	2.6	2.4	2.7
Crucible weight (g)	17.2	17.8	18.4
Weight calcined (g)	18.7	19.0	19.3
%ins	**56.8**	**48.4**	**34.0**

Table 1: Percentage of insoluble residue.

Cathodoluminescence

Cathodoluminescence observations of thin-sections and powders of SA02TH03 and SA02TH04 show similar results (Figure 6a-d). The binder is dull and two types of quartz are observed with different shades of purple/blue/red. For SA02TH12 (Figure 6e-f), the binder is also dull, purple quartz inclusions are noticed as well as blue K-feldspar. The bright red grain on top right of Figure 6e is not a limestone fragment but a terracotta piece because it also appears as red in plain polarised light. The powder of SA02TH12 appears as tile and bright red but as for the thin section, it might also be due to the presence of terracotta rather than limestone.
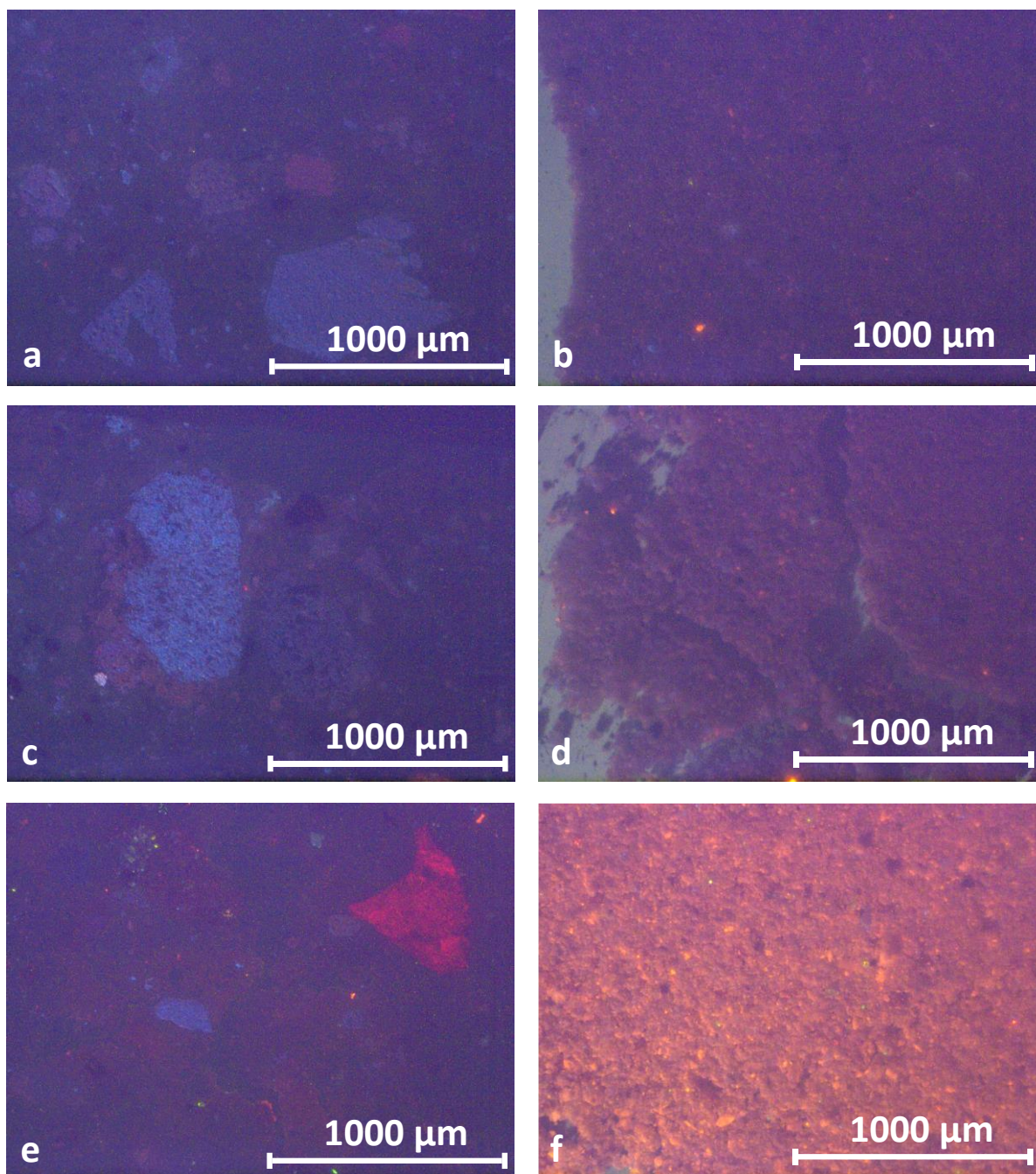
Figure 6: Characteristic cathodoluminescence images of a) the thin section X2393 of SA02TH03, b) the powdered SA02TH03 mortar with particle size lower than 75 μm, c) the thin section X2394 of SA02TH04, d) the powdered SA02TH04 mortar with particle size lower than 75 μm, e) the thin section X2395 of SA02TH12, and f) the powdered SA02TH12 mortar with particle size lower than 75 μm.

Thin-section petrography

The mortar SA02TH03 shows a good state of preservation (Figure 7 and Table 2). The lime inclusions are completely burned. The aggregate is made of siliceous volcanic sand with few limestone grains. Secondary carbonates are observed around microcracks and pores.
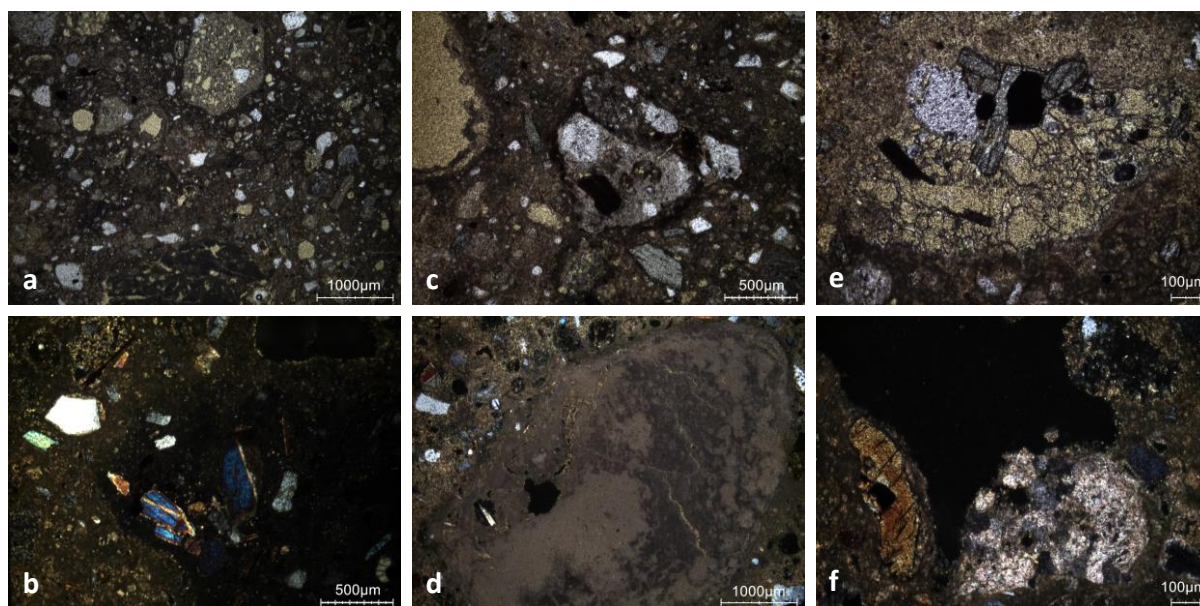
Figure 7: Representative photomicrographs of the SA02TH03 thin-section X2393: a) overview image in plain polarised light (PPL); b) amphibole in cross polarised light (XPL); c) PPL image showing a volcanic fragment slightly weathered; d) large lime lump with secondary carbonates in cracks in XPL; e) PPL image with pumice; f) limestone fragment in XPL.

Binder	**Texture**	micritic
	Lump state	completely burned
	Lump size	2.1 mm ; 5.3 mm ; 3.7 mm
	Lump frequency	few
Aggregate	**Grain size**	very fine to coarse
	Mineralogy	siliceous volcanic sand (feldspar, quartz, mica, pyroxene, amphibole, pumice, opaque minerals) slightly calcareous and possible ceramic fragments
	Shape	subangular / subrounded
Appearance	**Homogeneity**	relatively heterogeneous
	Macroporosity	medium / high
	Pore structure	cracks / rounded / sometimes connected
Admixtures	**Type**	-
Alteration	**Type**	secondary carbonates in cracks & pores

Table 2: Main characteristics of the mortar SA02TH03 retrieved from the observations of the thin-section X2393.

The mortar SA02TH04 shows a good state of preservation (Figure 8 & Table 3). The lime inclusions are completely burned (Figure 8d) but some are partially dissolved (Figure 8f). The aggregate is made of siliceous volcanic sand with possible fragments of terracotta (Figure 8e). Secondary carbonates are observed in microcracks and pores (Figure 8d & f).
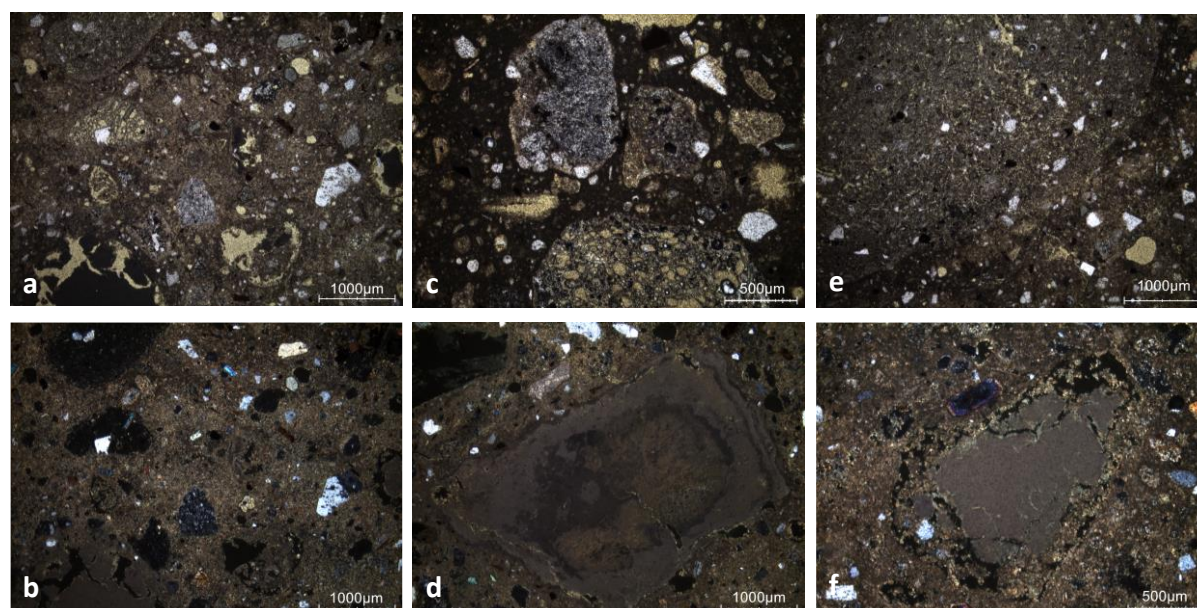
Figure 8: Representative photomicrographs of the SA02TH04 thin-section X2394: a) overview image in plain polarised light; b) overview image in cross polarised light; c) PPL image showing pumice; d) large lime lump with secondary carbonates in cracks in XPL; e) PPL image with possible large ceramic fragment; f) partially dissolved lime lump with secondary carbonates in cracks in XPL.

Binder	**Texture**	micritic
	Lump state	completely burned
	Lump size	756 µm ; 2.5 mm ; 4.7 mm ; 385 µm
	Lump frequency	medium
Aggregate	**Grain size**	very fine to very coarse
	Mineralogy	siliceous volcanic sand (feldspar, quartz, pumice, pyroxene, black mica, opaque minerals) and possible terracotta fragments
	Shape	subangular / subrounded
Appearance	**Homogeneity**	relatively homogenous
	Macroporosity	medium
	Pore structure	cracks / rounded / irregular
Admixtures	**Type**	-

Alteration	**Type**	secondary carbonates in cracks & pores some lumps dissolved

Table 3: Main characteristics of the mortar SA02TH04 retrieved from the observations of the thin-section X2394.

The mortar SA02TH12 shows a good state of preservation (Figure 9 & Table 4). The lime inclusions are completely burned. The aggregate is made of siliceous sand with few limestone grains/bioclasts (Figure 9d). Secondary carbonates are observed in some microcracks (Figure 9b & f).
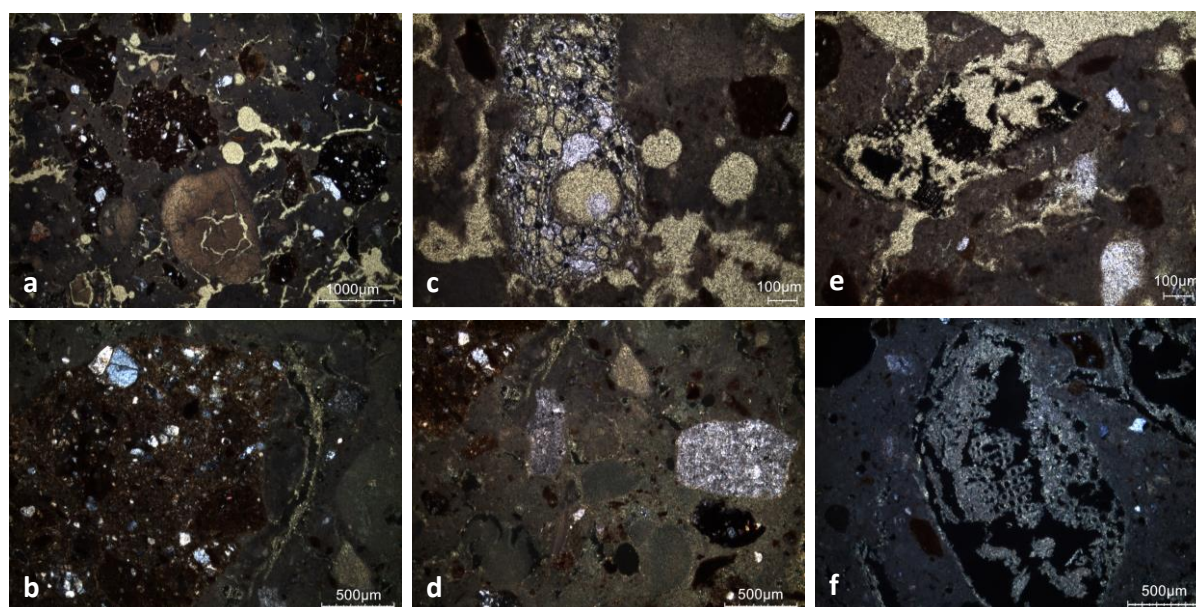
Figure 9: Representative photomicrographs of the SA02TH12 thin-section X2395: a) overview image in PPL; b) crushed ceramic and secondary carbonates in crack in XPL; c) PPL image showing pumice fragment; d) limestone grains in XPL; e) PPL image with charcoal fragment; f) secondary carbonates taking on the morphology of a pre-existent plant fragment in XPL.

Binder	**Texture**	micritic
	Lump state	completely burnt
	Lump size	1.7 mm ; 400 µm ; 390 µm ; 1.7 mm
	Lump frequency	medium
Aggregate	**Grain size**	very fine to coarse
	Mineralogy	siliceous sand with few limestone fragments (quartz, K-feldspar, crushed ceramic, pumice)
	Shape	subangular / subrounded
Appearance	**Homogeneity**	relatively homogenous
	Macroporosity	medium
	Pore structure	cracks / rounded / irregular / sometimes connected

Admixtures	**Type**	-	
Alteration	**Type**	secondary carbonates in cracks	

Table 4: Main characteristics of the mortar SA02TH12 retrieved from the observations of the thin-section X2395.

Thermogravimetric analysis (TGA) on whole samples

The curves of the thermal analyses carried out on the whole samples (Figure 10) clearly show a large endothermic peak between around 650 and 850°C linked to the decarbonation of the lime binder and other possible carbonates. The apparent hydraulicity index (aHI) determined on the basis of the weight loss between 200 and ca. 650°C (usually attributed to water loss from calcium-silicate-hydrates-phases) was calculated from Figure 10, and is around 68 % for SA03, 55% for SA04, and 14 % for SA12, indicating that the mortars SA03 and SA04 are very strongly hydraulic and SA12 slightly hydraulic. However, the values obtained from the thermal analyses might not entirely reflect the reality since the mortars possibly contain ceramic fragments. The amount of carbonates present in the mortars is around 8, 15 and 64 wt% for SA03, SA04 and SA12, respectively. The main weight loss of ancient mortars is expected between 600 and 900 °C and is indicative of the decomposition of calcium carbonate ($CaCO_3$) into calcium oxide (CaO) and carbon dioxide (CO_2) (Ahmmed et al. 2024). The end temperature of the calcium carbonate decomposition for the mortar sample is around 783, 801 and 850°C for SA03, SA04 and SA12, respectively. No gypsum nor quartz were detected. An additional peak is present around 958, 975 and 976°C for SA03, SA04 and SA12, respectively. The later could be attributed to the presence of pumice in the samples, which is thermally stable until 900°C and completely melts at about 1200°C (Alraddadi and Assaedi 2021). Indeed, melted residues were left in the crucible for the determination of the binder:aggregate ratio.
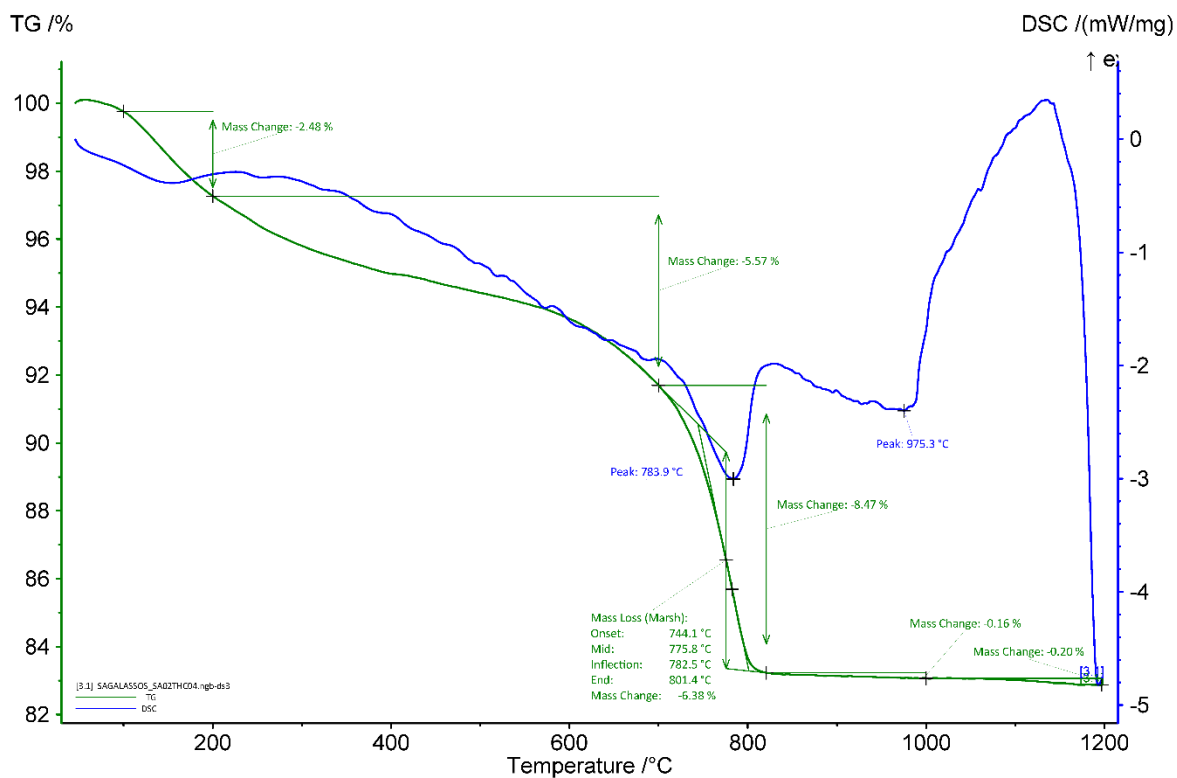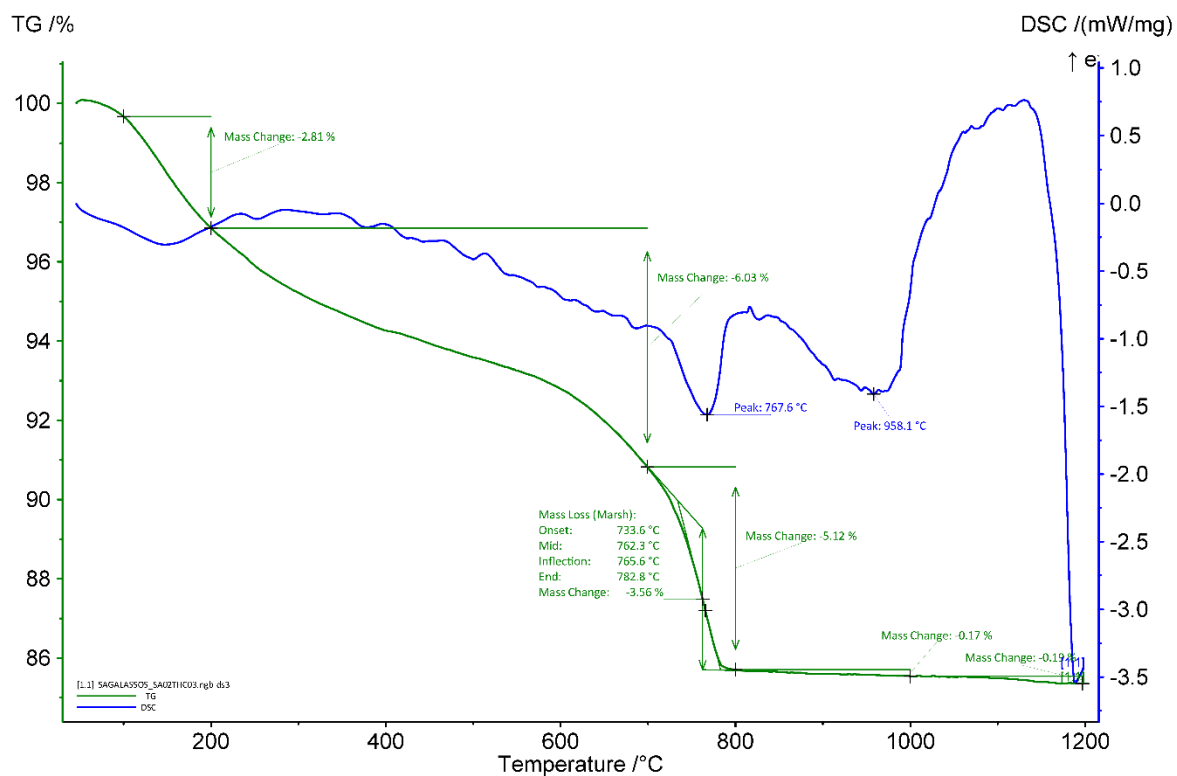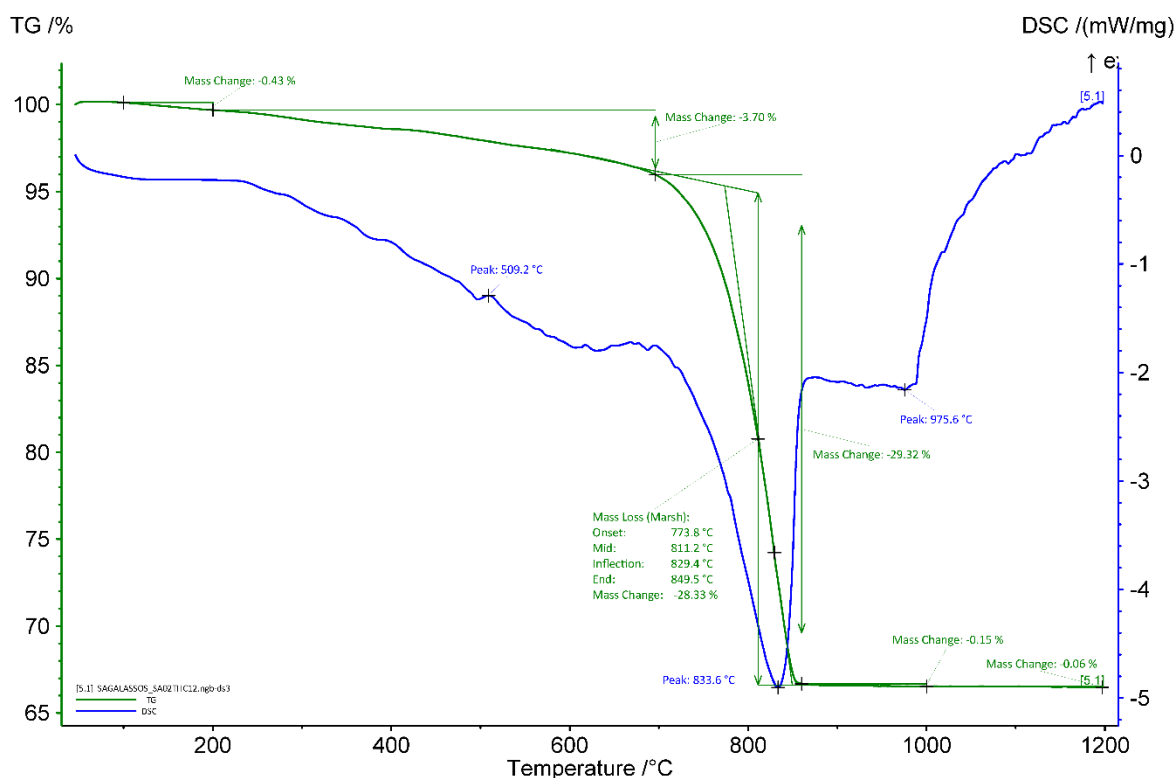
Figure 10: Coupled TG-DSC analysis of the mortars SA02TH03 (top), SA02TH04 (middle) and SA02TH12 (bottom) upon heating to a temperature of 1200°C at a heating rate of 20°C/min under an inert atmosphere (He flushed at 50 ml/min). The weight loss determined by thermogravimetric analysis (TG, wt%, green curve) and the result of the differential scanning calorimetric analysis (DSC, mW/mg, blue curve) are both presented.
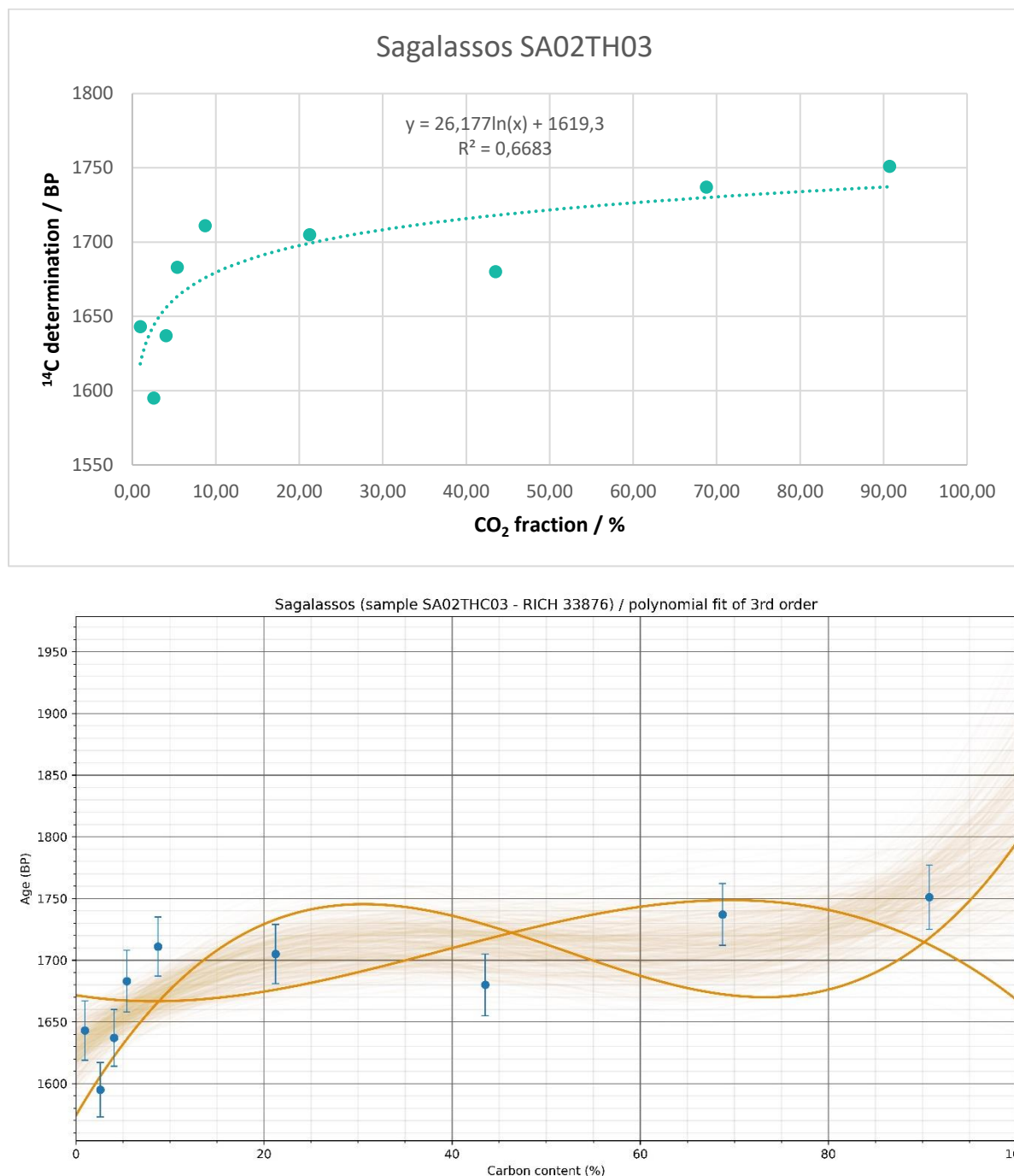
Grinding/particle separation

SA02TH03 was scratched with a metallic brush to remove the cross in felt tip pen in addition to soil and precipitated calcite; grey and hard white fragments were removed while crushing. For SA02TH04, hard white and grey inclusions were also removed while grinding. The red and grey inclusions were removed while grinding SA02TH12.

TGA on powders with particle size <75 μm

The curves of the thermal analyses carried out on the powder used for dating (Figure 11) also clearly show a large endothermic peak between around 650 and 800°C linked to the decarbonation of the lime binder. The aHI of the powders with particles < 75 μm, determined on the basis of the weight loss between 200 and ca. 650°C, are 62 % for SA03 and SA04, and 20 % for SA12. The quantity of carbonates is higher or similar in the powders compared to the whole samples (13, 14 and 64 wt% for SA03, SA04 and SA12, respectively). For all samples (Figure 11), a peak around 403-6°C is observed and might be due to the release of water from calcium hydroxide (Moropoulou, Bakolas, and Bisbikou 1995; Klimesch and Ray 1996) indicating that the mortar did not fully carbonated. This was not observed for the whole mortar samples. It was probably present in too low concentration to be noticeable. The end temperatures of calcium carbonate decomposition are 798, 800 and 849°C for the powdered SA03, SA04 and SA12, respectively. It is higher compared to the whole sample for SA03. A possible explanation could be that the powders are more pure compared to the whole mortar

samples which increases the decomposition temperature. The separation of peak for the carbonate decomposition for SA12 (Figure 11, bottom), might be due a measurement artefact.
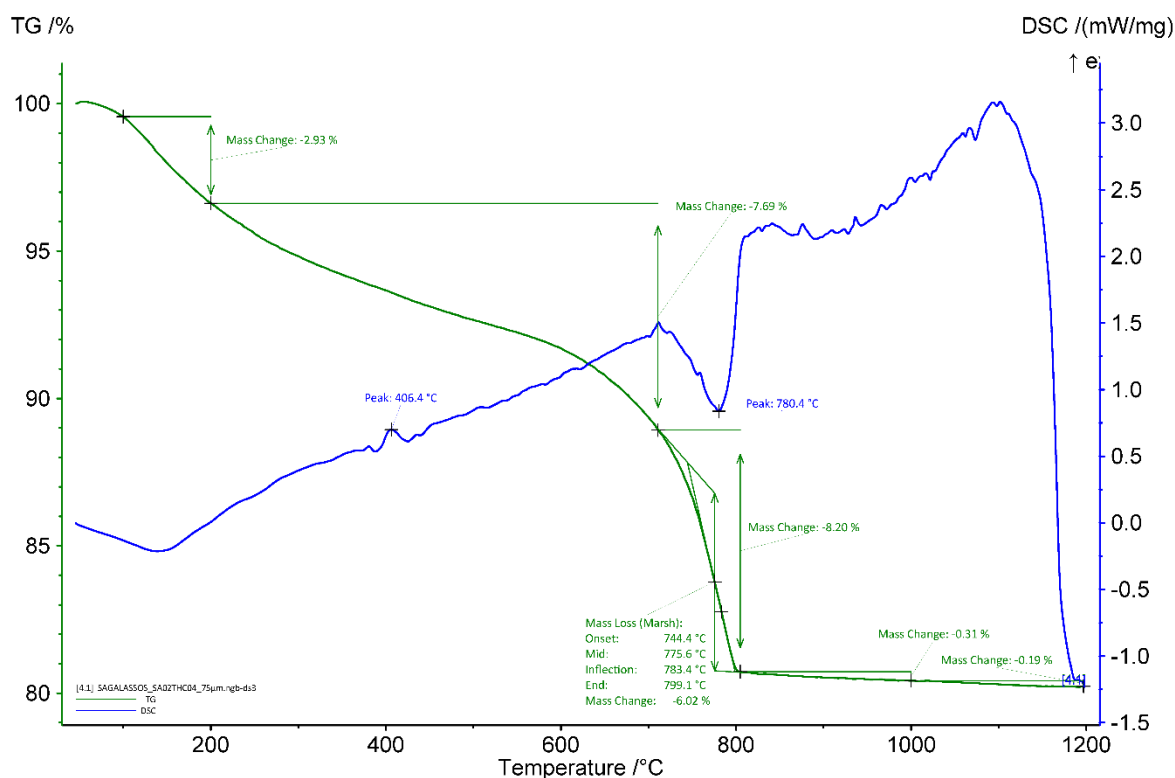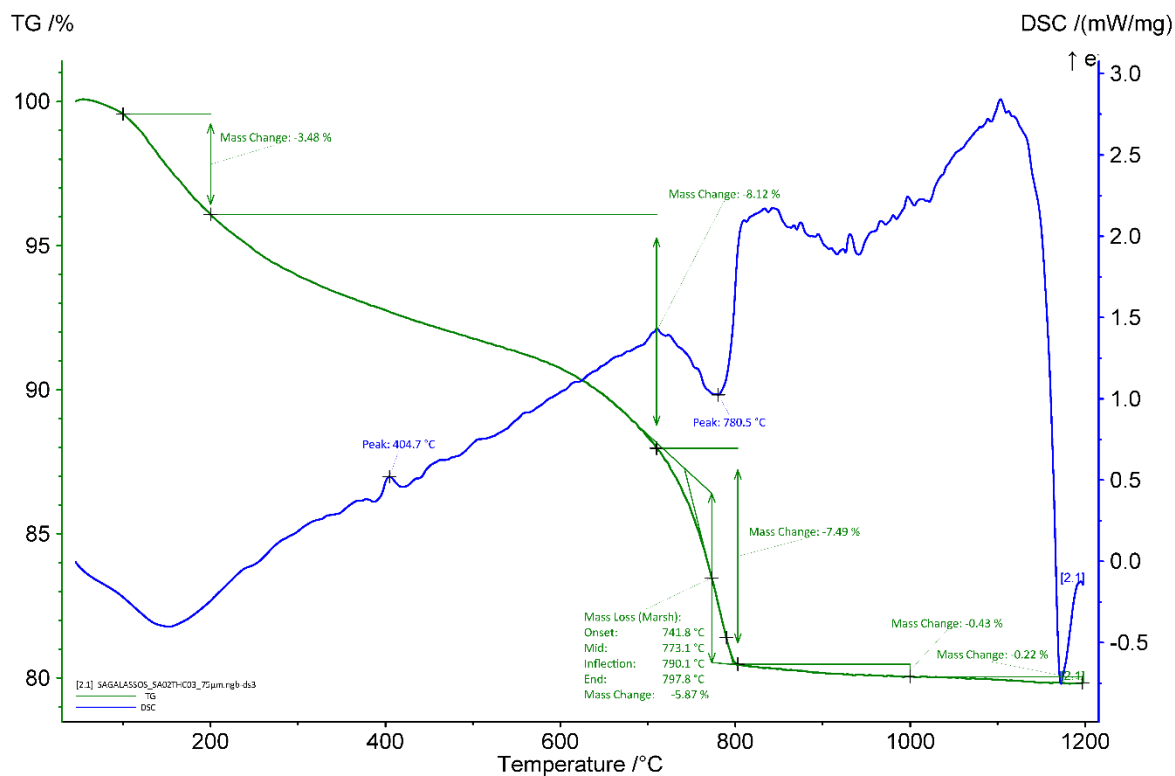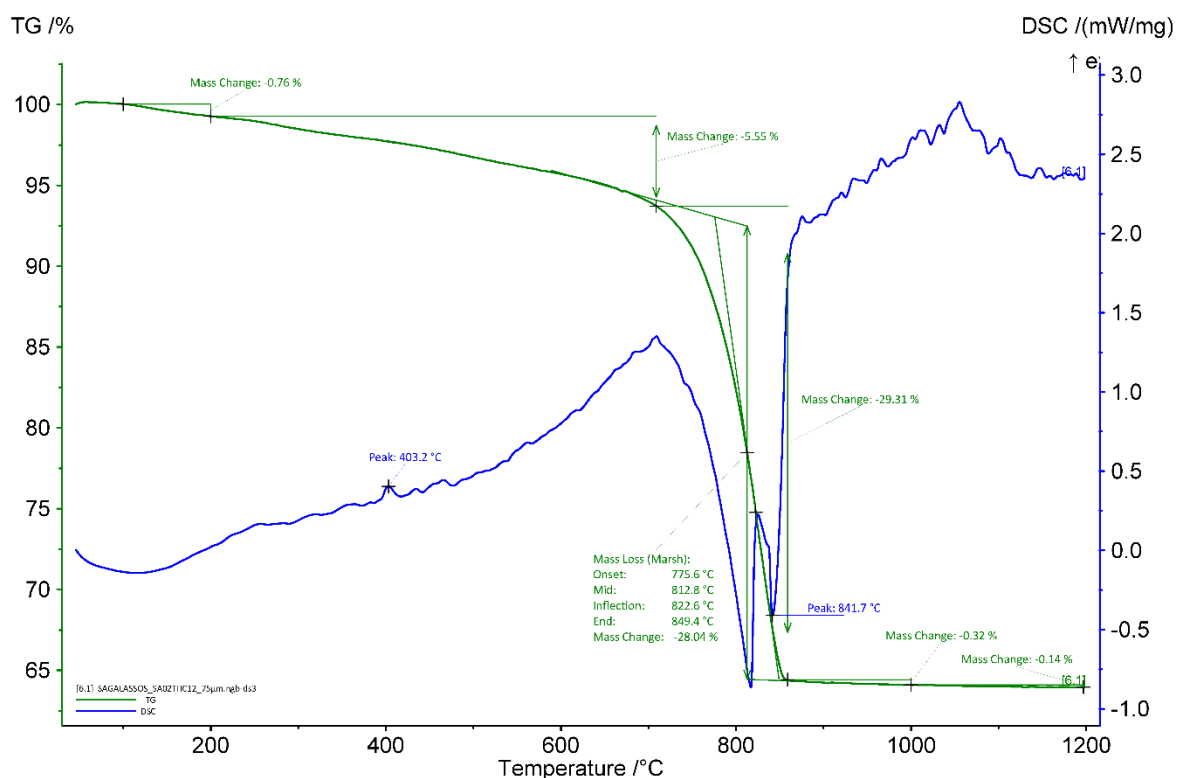
Figure 11: Coupled TG-DSC analysis of the powdered mortars with particle size < 75 µm SA02TH03 (top), SA02TH04 (middle) and SA02TH12 (bottom) upon heating to a temperature of 1200°C at a heating rate of 20°C/min under an inert atmosphere (He flushed at 50 ml/min). The weight loss determined by thermogravimetric analysis (TG, wt%, green curve) and the result of the differential scanning calorimetric analysis (DSC, mW/mg, blue curve) are both presented.

Radiocarbon results

The test prior to the CO_2 extraction revealed a low amount of carbon (Table 5) for the samples SA02THC03 and SA02THC04 (~0.8 and 2.5 % respectively). This explains the FTIR spectra of the binders showing a relatively low amount of calcium carbonates in these samples. For SA02THC12, the amount of carbon is rather good (~7 %) and a lower amount of powder with particles < 75 µm was necessary to perform the CO_2 extraction.

RICH	Sample type	Method	C (%)	σ (%)	m (g)	Age BP	Calibrated date (oxcal - 95.4%)	Age BP extrapolated	Calibrated date (oxcal - 95.4%)	Age BP extrapolated with stat	Calibrated date (oxcal - 95.4%)	Age BP average extrapolated	Calibrated date (oxcal - 95.4%)	Reliability of dating
33876 (SA02TH03)	mortar <75 µm room XXII	HCl (9 fractions)	0.84	0.04	10.48	-	-	1619 ± 24 BP	410-540 calAD	1629.5 ± 15.4 BP	407-535 calAD	1637 ± 12 BP	410-540 calAD	☑
34104 (SA02TH04)	mortar <75 µm room XXII	HCl (8 fractions)	2,54	0,14	4,02	-	-	1630 ± 32 BP	376-544 calAD	1628.8 ± 18.4 BP	407-536 calAD	1642 ± 15 BP	401-534 calAD	☑
33400 (SA02TH04)	charcoal extracted from mortar	HCl 8%	45,84	-	2,87	1786 ± 23 BP	219-338 calAD	-	-	-	-	-	-	☑
34105 (SA02TH12)	mortar <75 µm room IX	HCl (10 fractions)	6,88	0,22	2,5	-	-	1781 ± 31 BP	212-362 calAD	1780.6 ± 14.2 BP	236-330 calAD	1811 ± 14 BP	211-319 calAD	☑
33399 (SA02TH12)	charcoal extracted from mortar	HCl 8%	47,38	-	0,00263	1843 ± 23 BP	127-244 calAD	-	-	-	-	-	-	☑
34106 (SA02TH12)	lime lump extracted from mortar	H_3PO_4	9,67	-	0,0516	1826 ± 33 BP	125-325 calAD	-	-	-	-	-	-	☑

Table 5: Radiocarbon results

The radiocarbon dating results (407-540 calAD) obtained for sample SA02TH03 (Table 5 & Figure 12) with the three calculation methods correspond to the presumed historical date (late 4th to early 5th centuries AD).

Sagalassos SA02TH03

$$y = 26{,}177\ln(x) + 1619{,}3$$
$$R^2 = 0{,}6683$$

Sagalassos (sample SA02THC03 - RICH 33876) / polynomial fit of 3rd order

Figure 12: Radiocarbon results for the powdered SA02TH03 mortar with particles < 75 μm as a function of the CO_2 fraction (the graph at the bottom shows the statistic on the results).

The results (376-544 calAD) for the binder SA02TH04 (Table 5 & Figure 13) are very similar to SA02TH03 which is encouraging since they were sampled in the same room and had the same presumed historical date. For the charcoal fragment extracted from the mortar SA02TH04, the results are slightly older (219-338 calAD) than the expected date (late 4th to early 5th centuries AD) but this could be due to the old wood effect.
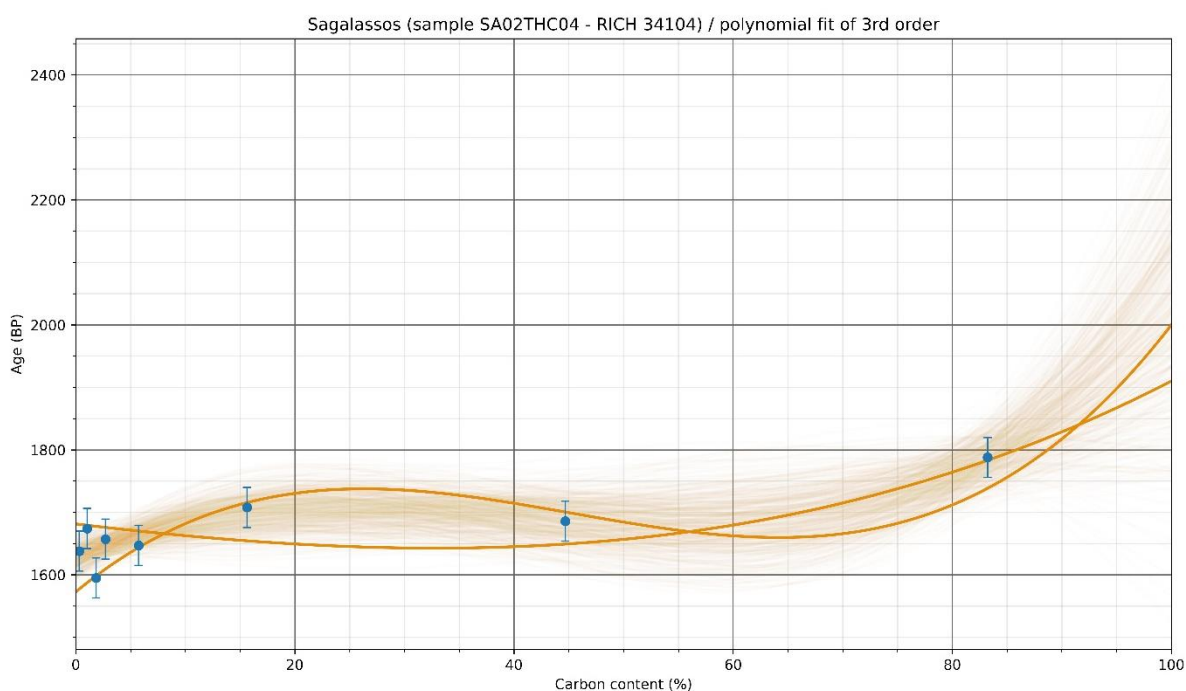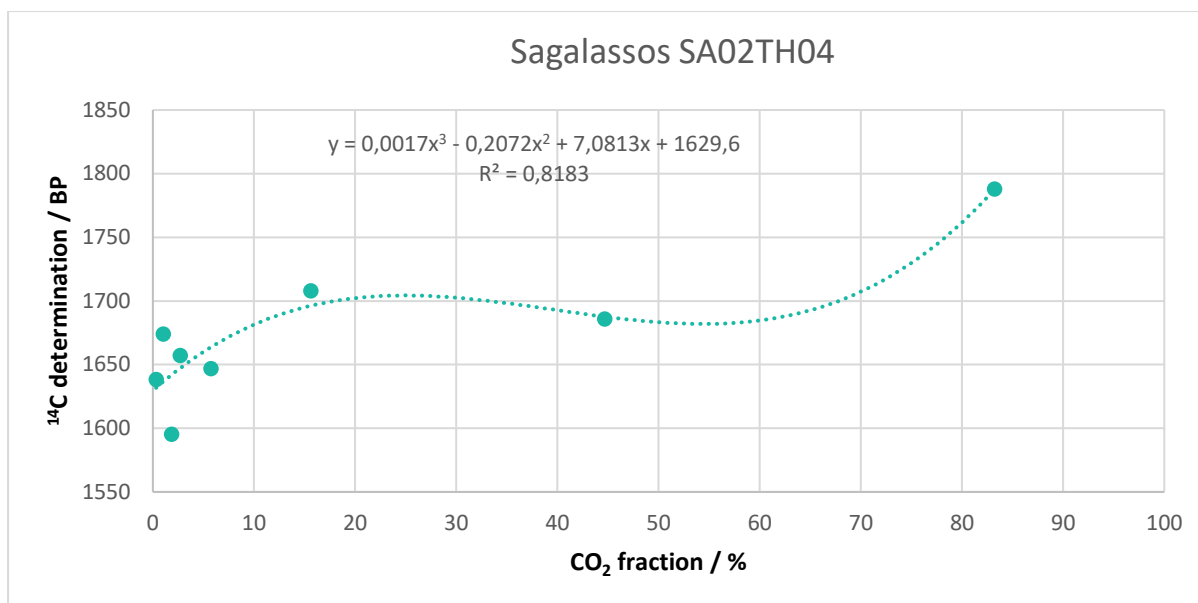
Figure 13: Radiocarbon results for the powdered SA02TH04 mortar with particles < 75 µm as a function of the CO_2 fraction (the graph at the bottom shows the statistic on the results).

The lime binder of sample SA02TH12, presumed to be a later intervention estimated to the 6th century AD, was actually dated to be older (212-362 calAD) compared to the sample SA02TH03 and SA02TH04 (Table 5 & Figure 13). The result seems reliable because the dates obtained for the lime lump (125-325 calAD) and the charcoal fragment (127-244 calAD) extracted from the sample show a similar range.
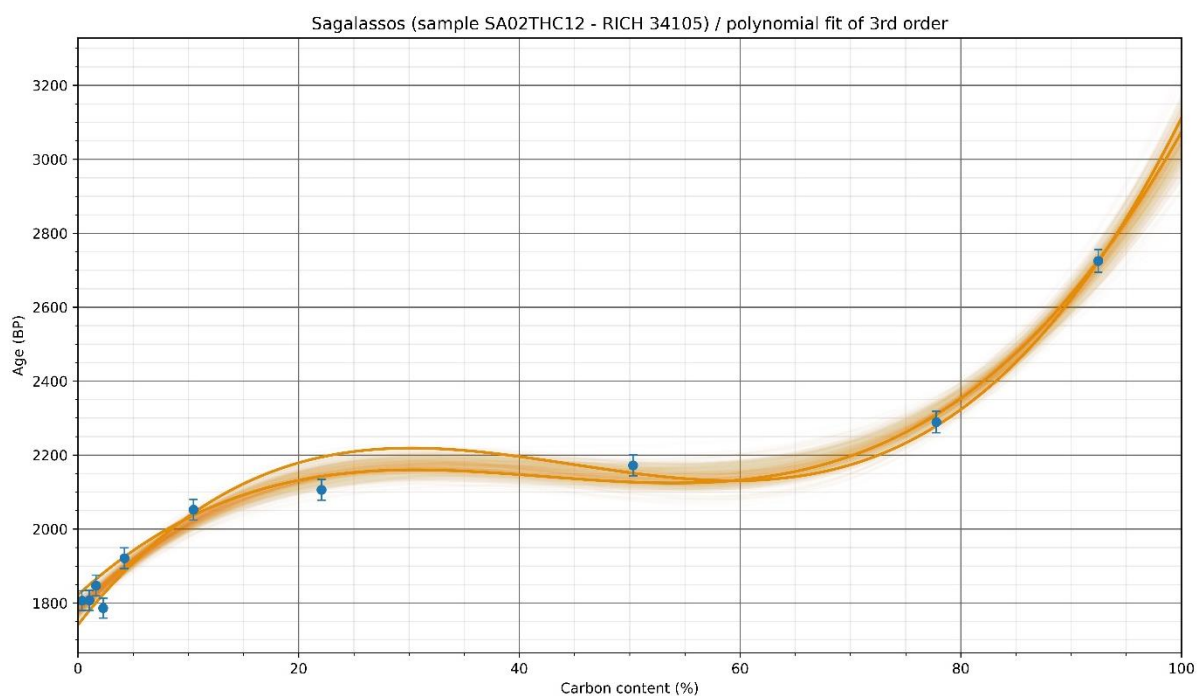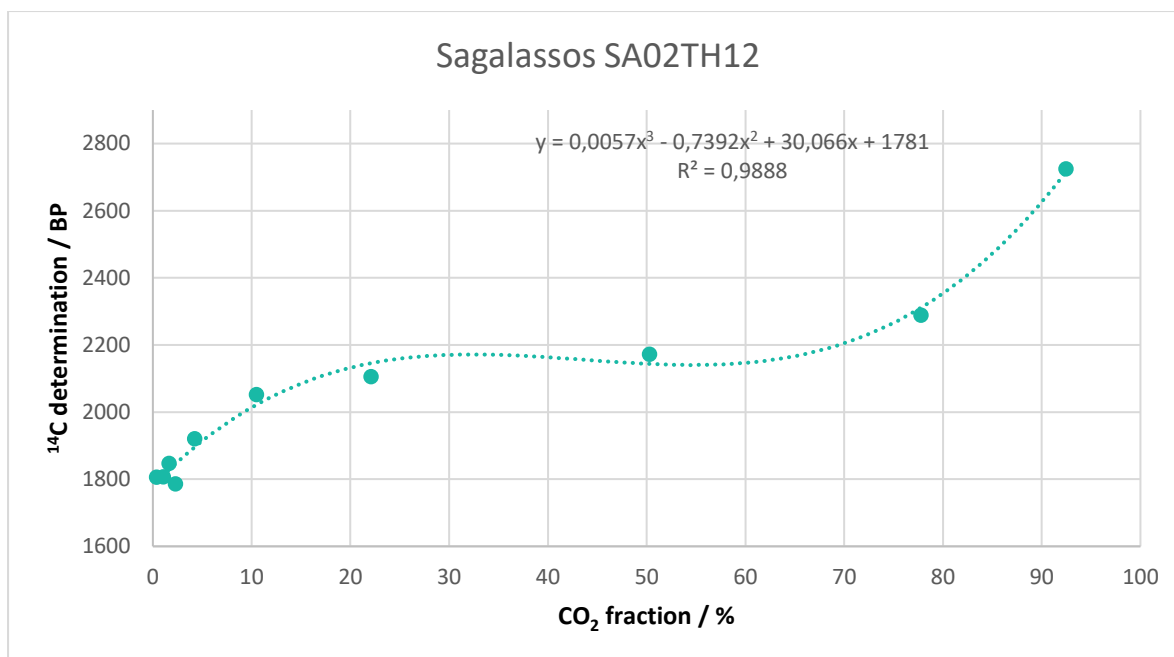
Figure 14: Radiocarbon results for the powdered SA02TH12 mortar with particles < 75 µm as a function of the CO_2 fraction (the graph at the bottom shows the statistic on the results).

Conclusions

Despite being highly hydraulic according to the TGA measurements, the radiocarbon results obtained for the mortars SA02TH03 and SA02TH04 correspond to the presumed historical date (late 4th to early 5th centuries AD). The charcoal piece extracted from SA02TH04 is dated from the 3rd to the 4th centuries AD which could be due to an old wood effect. Without knowing the presumed historical date, we would have presumed that a delayed hardening happened because of the hydraulicity of the mortars and, we would have considered the mortars as unreliable. However, in this context, we can consider them as reliable and the higher hydraulicity index should be due to the low content of binder combined to the presence of ceramic fragments that did not induce hydraulic properties. For the

sample SA02TH12, the presumed historical date was uncertain because of renovation and was estimated to the 4th to 6th centuries AD. The radiocarbon results obtained for the mortar are slightly older (3rd to 4th centuries AD) and are in accordance with the charcoal (2nd to 3rd centuries AD) and the lime lump (2nd to 4th centuries AD) extracted from the mortar. In this case, the sample is non hydraulic with a good state of preservation so the mortar is considered as reliable for radiocarbon dating.

Bibliography

Ahmmed, Tanjil, Ana Raquel Silva, José Carlos Quaresma, Patrícia Moita, and Cristina Galacho. 2024. "Analytical Characterization of Historical Mortars from the Roman Villa of Frielas (Loures, Portugal)." *Acta IMEKO* 13 (3): 1–11.

Alraddadi, Shoroog, and Hasan Assaedi. 2021. "Physical Properties of Mesoporous Scoria and Pumice Volcanic Rocks." *Journal of Physics Communications* 5 (11): 115018.

Hofkens, Tine. 2003. "Chemisch-Mineralogische Karakterisering van de Mortels van de Domestic Area Te Sagalassos (Turkije)." Master (unpublished), KULeuven.

Klimesch, Danielle S., and Abhi Ray. 1996. "The Use of DTA/TGA to Study the Effects of Ground Quartz with Different Surface Areas in Autoclaved Cement: Quartz Pastes. Part 1: A Method for Evaluating DTA/TGA Results." *Thermochimica Acta* 289 (1): 41–54. https://doi.org/10.1016/S0040-6031(96)03033-X.

Moropoulou, Antonia, Asterios Bakolas, and Katerina Bisbikou. 1995. "Characterization of Ancient, Byzantine and Later Historic Mortars by Thermal and X-Ray Diffraction Techniques." *Thermochimica Acta* 269:779–95.

"The History of Sagalassos." n.d. Accessed May 13, 2024. https://www.arts.kuleuven.be/sagalassos/history/history.

Waelkens, Marc. 2012. "Sagalassos." In *The Encyclopedia of Ancient History*. John Wiley & Sons, Ltd. https://doi.org/10.1002/9781444338386.wbeah14266.

Study of mortars from Aleria (Corsica, France) for the BRAIN 2.0 PalC project

Context of the site

The ancient town of Aleria lies in the centre of Corsica's eastern plain, on the coast (Coutelas and Allegrini-Simonetti 2017). It is believed that around 565 BCE, the Phoceans created the settlement of *Alalia* (Bats 1994) possibly at the ancient city centre (Cesari 2010). They left in 540 BCE, opening the city for Greeks, Etruscans, Romans and Punics (Jehasse 1993). It became Roman in 259 BCE and lasted throughout the High Empire and Late Antiquity, remaining the political centre of Corsica for a long time (Coutelas and Allegrini-Simonetti 2017; Gailledrat and Fontaine 2023).

Figure 1: Aerial view of the south of the Roman city of Aleria with the river Tavigano and the Étang de Diane (picture from Coutelas and Allegrini-Simonetti 2017).

Material

Three samples were collected in 2021 (Figure 2) as a part of the joint archaeological research programme (PCR) 2018-2021 'Aléria and its territories: cross approaches' (under the direction of V. Jolivet, Director of Research at the CNRS and coordinated by Franck Allegrini-Simonetti, DRAC). The analysis focuses on the mortar of the Roman enclosure, dated to 50-25 BC, using both ceramics embedded in the mortar and ceramics from two stratigraphic sections of the walls, carried out in 1980 and 1981 (cf. Lenoir and Rebuffat 1984). ECH10 is a mortar from the wall core (50 cm deep), eastern section (no. 3) of the Roman wall. ECH13 is a mortar from the core of the foundation wall, western section (no. 1) of the Roman wall, external face.

ECH14 is a mortar of the wall core (elevation), western section (no. 1) of the Roman wall, external face.

Figure 2: View from the sampling area of ECH10 (left), ECH13 (middle) and ECH14 (right) in 2021.

Results & Discussion

Macroscopic descriptions

The main colour of ECH10 is beige (Figure 3) tending towards very pale brown (10YR 8/2) and ECH13 and ECH14 are beige tending to pale yellow (2.5Y 8/3) according to the Munsell soil colour charts. ECH10 and ECH14 are very slightly specular, probably due to the presence of coarse grains of quartz, mica or well crystallised carbonates. The three samples contain very few white inclusions measuring less than 1 mm. ECH10 comprises many inclusions with various colours (different tons of grey, black, green, violet, red) and a large quartzite inclusion (1.5-2 cm). Some of the fragments exhibit polished/cut surfaces due to the preparation of the thin sections. ECH13 and ECH14 display many inclusions with grey and black tones and are dusty/crumbly.
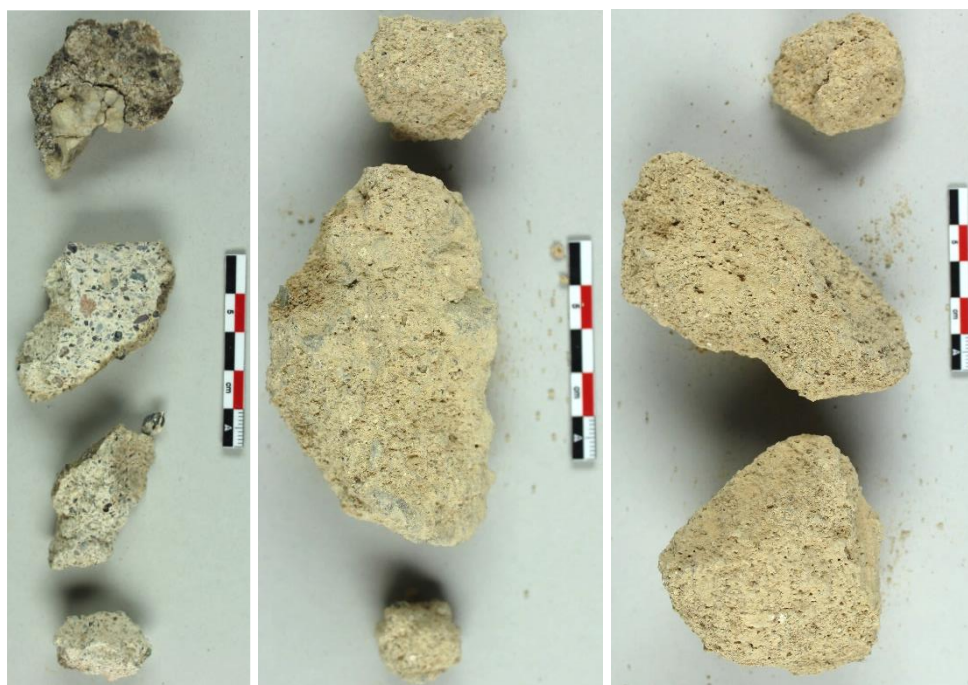
Figure 3: Mortar samples ECH10 (left), ECH13 (middle) and ECH14 (left).

Fourier transform Infrared (FTIR) spectroscopy on inclusions & binder

The binders (beige Figure 4) mainly contain calcium carbonates (calcite and aragonite) and silicates. The binders of ECH13 and ECH14 also contain organic matter and clay, as well as nitrates but only for ECH14. The white inclusions of ECH10 were too tiny to be analysed but the lime lumps of ECH13 and ECH14 could be analysed. As expected, they are both made of calcite, aragonite and silicates. All the other inclusions exhibit vibrational features of silicates sometimes including quartz, clay, organic matter and gypsum.
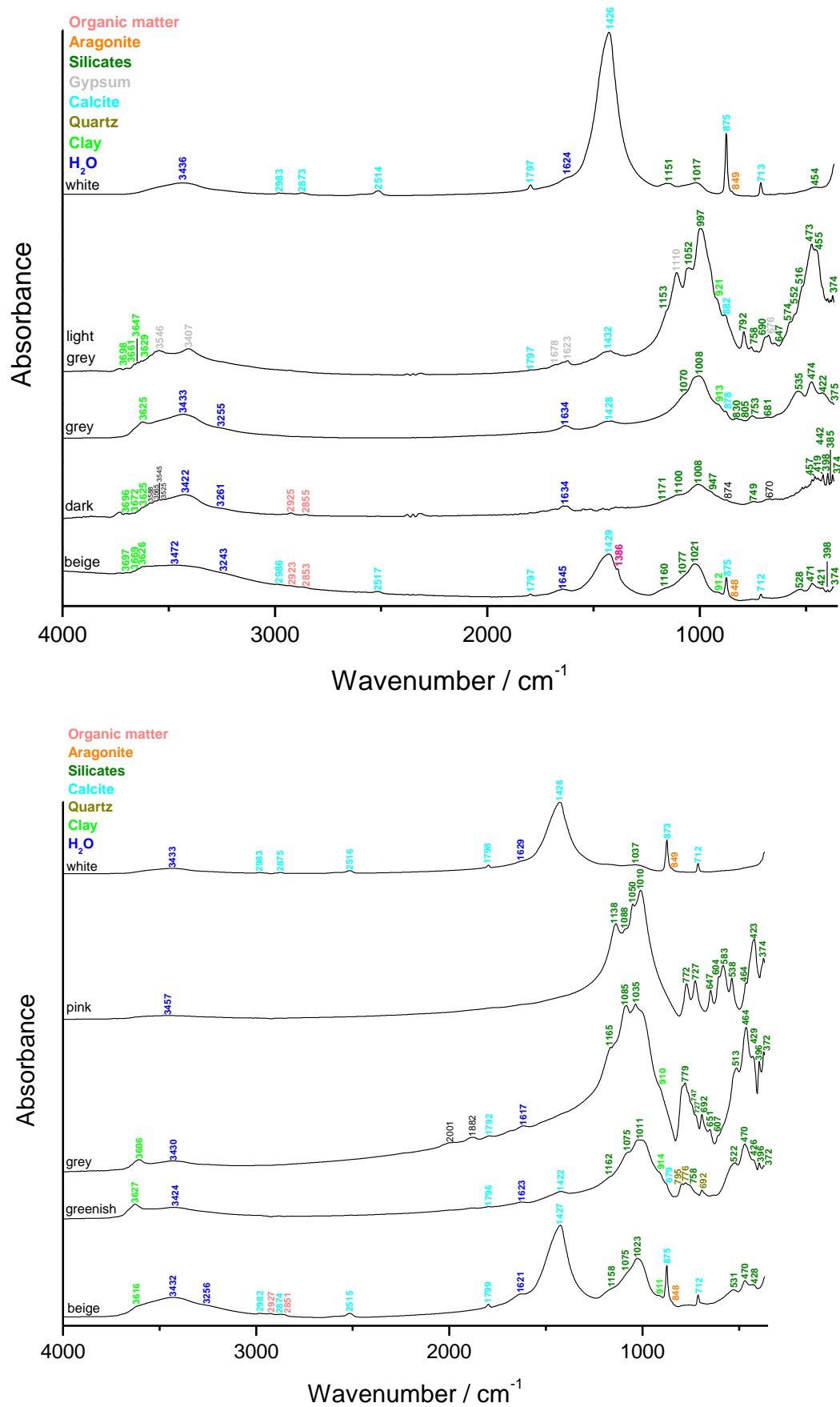
Figure 4: FTIR spectra obtained on the inclusions and binder (beige) of the mortar samples ECH10 (top), ECH13 (middle) and ECH14 (bottom).

Binder:sand ratio

The calculated binder:sand ratio (in volume unit) using a bulk density of 1.35 kg/dm^3 for the sand and 0.575 kg/dm^3 for the lime is around 3:2 for the sample ECH10, close to 3:4 for the sample ECH13, and close to 5:6 for the sample ECH14.

	E10	E13	E14
Sample weight (g)	2.7	2.5	2.7
Crucible weight (g)	18.1	18.2	20.2
Weight calcined (g)	19.7	20.1	22.2
%ins	**59.6**	**76.1**	**73.8**

Table 1: Percentage of insoluble residue

Cathodoluminescence

Cathodoluminescence observations of the three thin-sections and powders show slightly different results (Figure 5). The thin section of ECH10 (Figure 5a) exhibits bright red areas containing some dull sections most probably made of siliciclastic-carbonate rocks. It also contains bright blue potassic feldspars and green plagioclases. ECH13 and ECH14 (Figure 5c & e) barely show the presence of bright red, many bright blue K-feldspars, a few green plagioclases and dark purple quartz grains are also present. For all the powders (Figure 5b, d & f), a few bright red limestone grains are present with a few bright blue K-feldspars and very few green plagioclases.
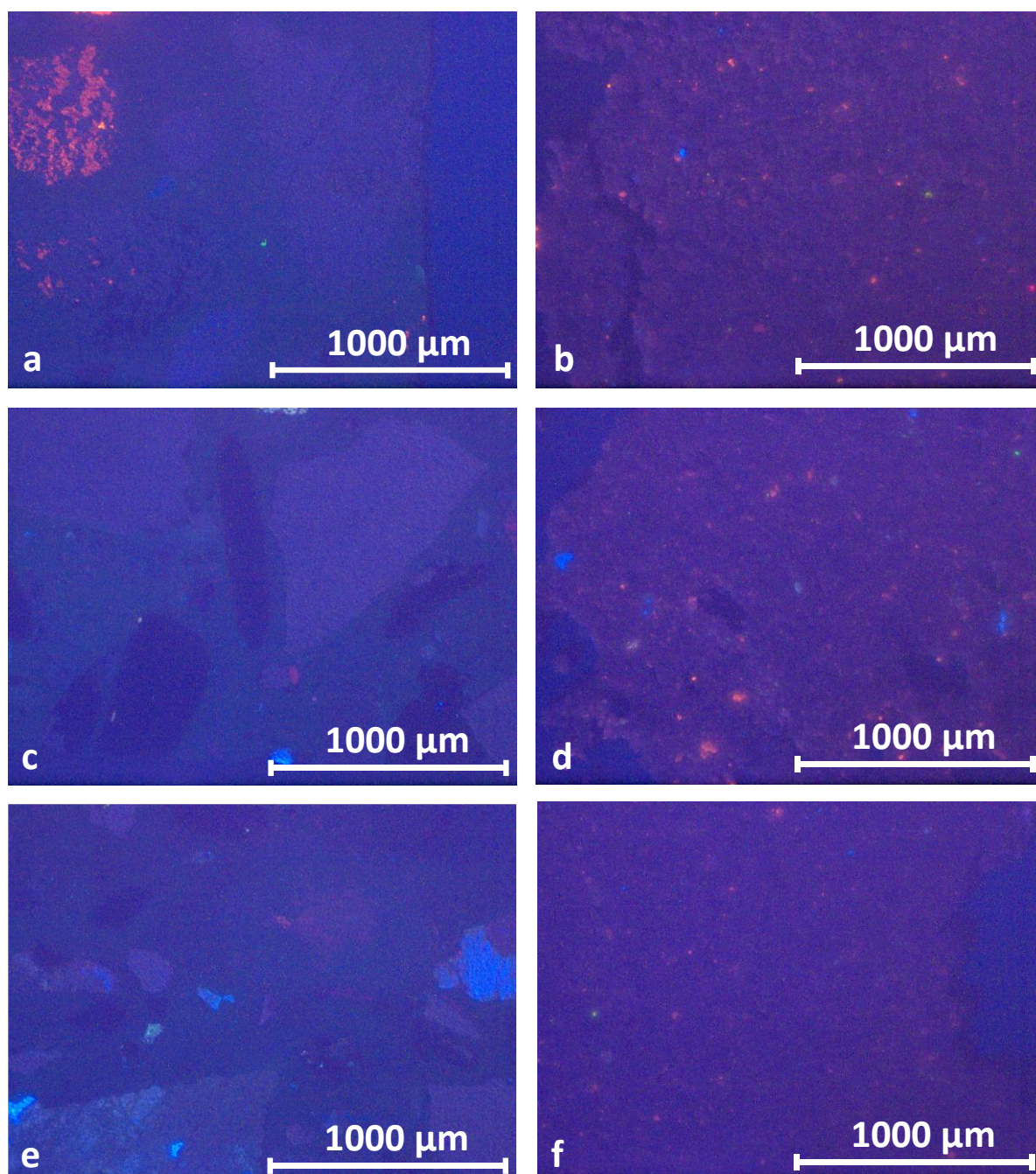
Figure 5: Characteristic cathodoluminescence images of a) the thin section X2261b of ECH10, b) the powdered ECH10 with particle size lower than 75 μm, c) the thin section X2264b of ECH13, d) the powdered ECH13 with particle size lower than 75 μm, e) the thin section X2265b of ECH14, f) the powdered ECH14 with particle size lower than 75 μm.

Thin-section petrography

The mortar ECH10 (Figure 6 & Table 2) is composed a polymictic aggregate containing magmatic, metamorphic and sedimentary rocks. The sedimentary ones present mixed siliciclastic-carbonate rocks (Figure 6f) and limestone (Figure 6c) that could affect the dating of the mortar. The binder is in good condition, the lime inclusions are completely burned but secondary calcite can be observed in the cracks of some of them (Figure 6d).
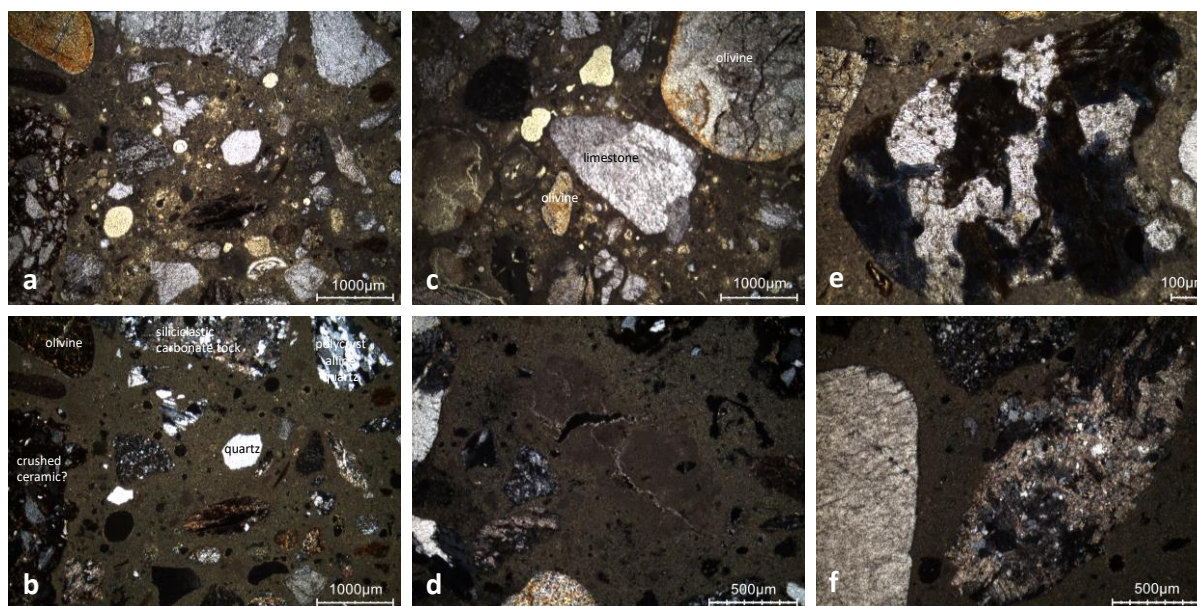
Figure 6: Representative photomicrographs of the thin-section X2261b made from ECH10: a) overview image in plain polarised light (PPL); b) overview image in cross polarised light (XPL); c) PPL image showing a limestone fragment and olivine; d) lime lump with secondary calcite in cracks in XPL; e) PPL image with glaucophane; f) mixed siliciclastic-carbonate rock in XPL.

Binder	**Texture**	micritic
	Lump state	completely burned
	Lump size	from 230 to 1100 µm
	Lump frequency	medium
Aggregate	**Grain size**	very fine to coarse
	Mineralogy	mixed siliceous & calcareous sand: polycrystalline quartz, mixed siliciclastic-carbonate rocks, magmatic / metamorphic rocks (olivine, glaucophane), *etc*.
	Shape	various
Appearance	**Homogeneity**	relatively heterogeneous
	Macroporosity	low
	Pore structure	rounded
Admixtures	**Type**	-
Alteration	**Type**	secondary carbonates in lime inclusions

Table 2: Main characteristics of the mortar ECH10 retrieved from the observations of the thin-section X2261b.

The binder of ECH13 (Figure 7 & Table 3) is light in colour because of a partial dissolution. Sparitic secondary carbonates are observed in some of the pores (Figure 7d). The individual aggregate grains are surrounded by clay cutans (Figure 7c). A few siliciclastic-carbonate rock fragments (Figure 7e) & olivine grains are observed (Figure 7c - much less compared to ECH10).
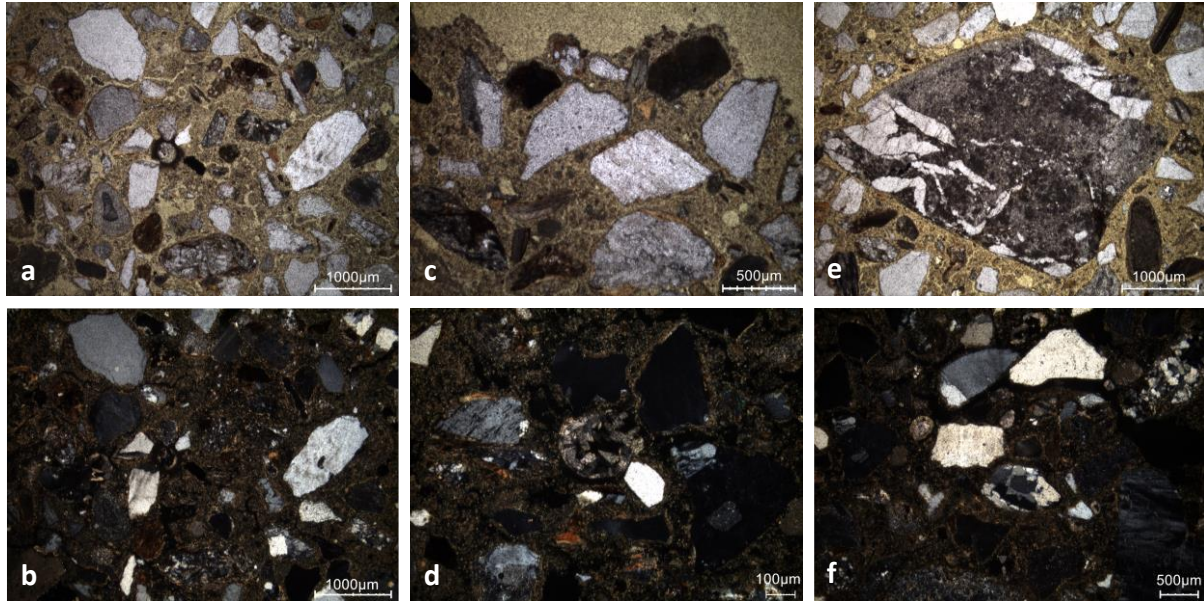
Figure 7: Representative photomicrographs of the thin-section X2264b made from ECH13: a) overview image in PPL; b) overview image in XPL; c) PPL image showing the aggregate including olivine and clay cutans (illuvial clay coating around quartz grains); d) lime lump with secondary calcite in cracks in XPL; e) PPL image with possible glaucophane; f) mixed siliciclastic-carbonate rock in XPL.

Binder	Texture	micritic
	Lump state	completely burned
	Lump size	max 2 mm
	Lump frequency	few
Aggregate	Grain size	very fine to coarse
	Mineralogy	mixed siliceous & calcareous sand with clay cutans: polycrystalline & monocrystalline quartz, feldspar, siliciclastic-carbonate rock, olivine, one ceramic fragment
	Shape	subangular / subrounded
Appearance	Homogeneity	rather heterogenous
	Macroporosity	low
	Pore structure	round & irregular
Admixtures	Type	-

Alteration	Type	dissolution, secondary carbonates

Table 3: Main characteristics of the mortar ECH13 retrieved from the observations of the thin-section X2264b.

The mortar ECH14 (Figure 8 & Table 4) is slightly dissolved and few (micro)sparitic secondary carbonates are observed on pore rims and in microcracks (Figure 8d & f). The individual aggregate grain are surrounded by clay cutans (Figure 8c) that can possibly create reaction rims containing calcium silicate hydrates (CSH).
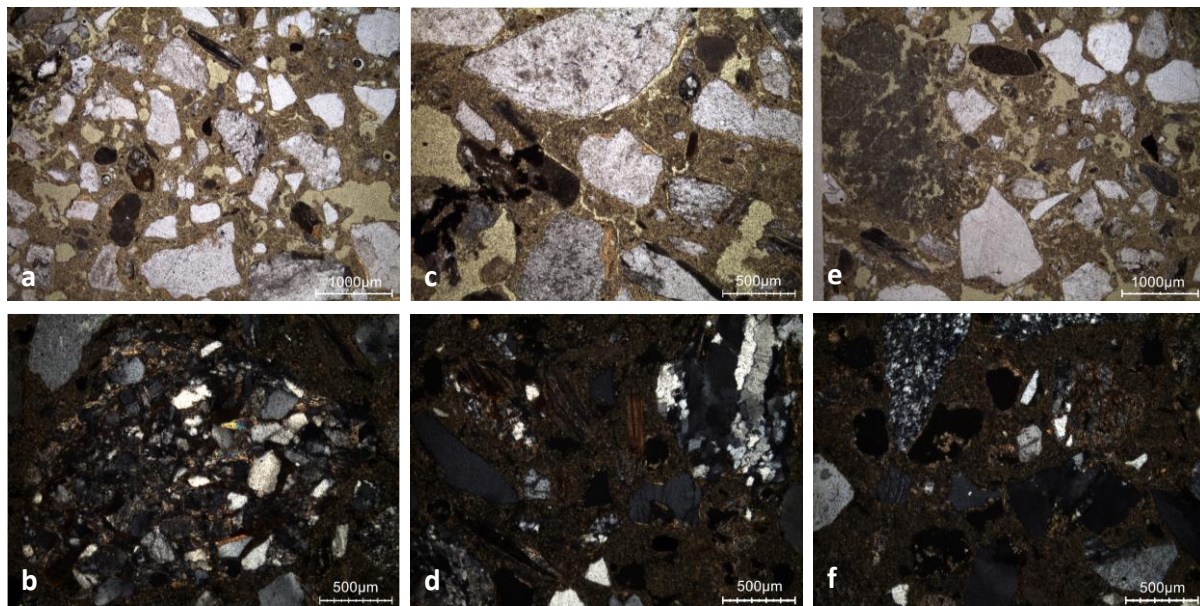
Figure 8: Representative photomicrographs of the thin-section X2265b made from ECH14: a) overview image in PPL; b) siliciclastic-carbonate rock in XPL; c) PPL image showing cutans around aggregates; d) secondary carbonates in a crack inside a mica flake and on macropore rim in XPL; e) PPL image of a large lime lump; f) sparitic secondary carbonates in XPL.

Binder	**Texture**	micritic
	Lump state	completely burned
	Lump size	max 2.7 mm
	Lump frequency	few
Aggregate	**Grain size**	very fine to very coarse
	Mineralogy	mixed siliceous & calcareous sand with clay cutans: polycrystalline & monocrystalline quartz, feldspar, siliciclastic-carbonate rock, mica flakes
	Shape	subangular / subrounded
Appearance	**Homogeneity**	relatively heterogeneous
	Macroporosity	medium
	Pore structure	irregular / sometimes connected

Admixtures	Type	-
Alteration	Type	secondary carbonates, slight dissolution

Table 4: Main characteristics of the mortar ECH14 retrieved from the observations of the thin-section X2265b.

Thermogravimetric analysis (TGA) on whole samples

The apparent hydraulicity index (aHI) determined on the basis of the weight loss between 200 and ca. 650°C (usually attributed to water loss from calcium-silicate-hydrates-phases) was calculated from Figure 9, and is around 47 % for ECH10 and ECH13, and 36 % for ECH14, indicating that the mortars are very strongly hydraulic. However, the values obtained from the thermal analyses might not entirely reflect the reality since the mortars 13 and 14 were partly dissolved and contain clay cutans. Loss from structurally bound water of some clays takes place at a similar temperature to structurally bound water in hydraulic components (Middendorf et al. 2005). The amount of carbonates present in the mortars is around 20, 9 and 12 wt% for ECH10, 13 and 14, respectively. The quartz transition phase can be observed around 573-4°C (Rickard, Riessen, and Walls 2010) for all the samples. The main weight loss of ancient mortars is expected between 600 and 900 °C and is indicative of the decomposition of calcium carbonate ($CaCO_3$) into calcium oxide (CaO) and carbon dioxide (CO_2) (Ahmmed et al. 2024). The end temperature of the calcium carbonate decomposition for the mortar sample is around 780, 742 and 779°C for ECH10, 13 and 14, respectively. Two peaks at 610 and 639°C are observed for ECH10 (Figure 9, top), and could be due to the presence of a different form of carbonate possibly coming from the hydraulic phases. For ECH13, two additional peaks are also observed at 473°C which is possibly attributed to the decomposition of portlandite (Brunello 2020) and at 742°C that could be due to the presence of a different form of carbonate possibly coming from the hydraulic phases as well. No gypsum was detected.
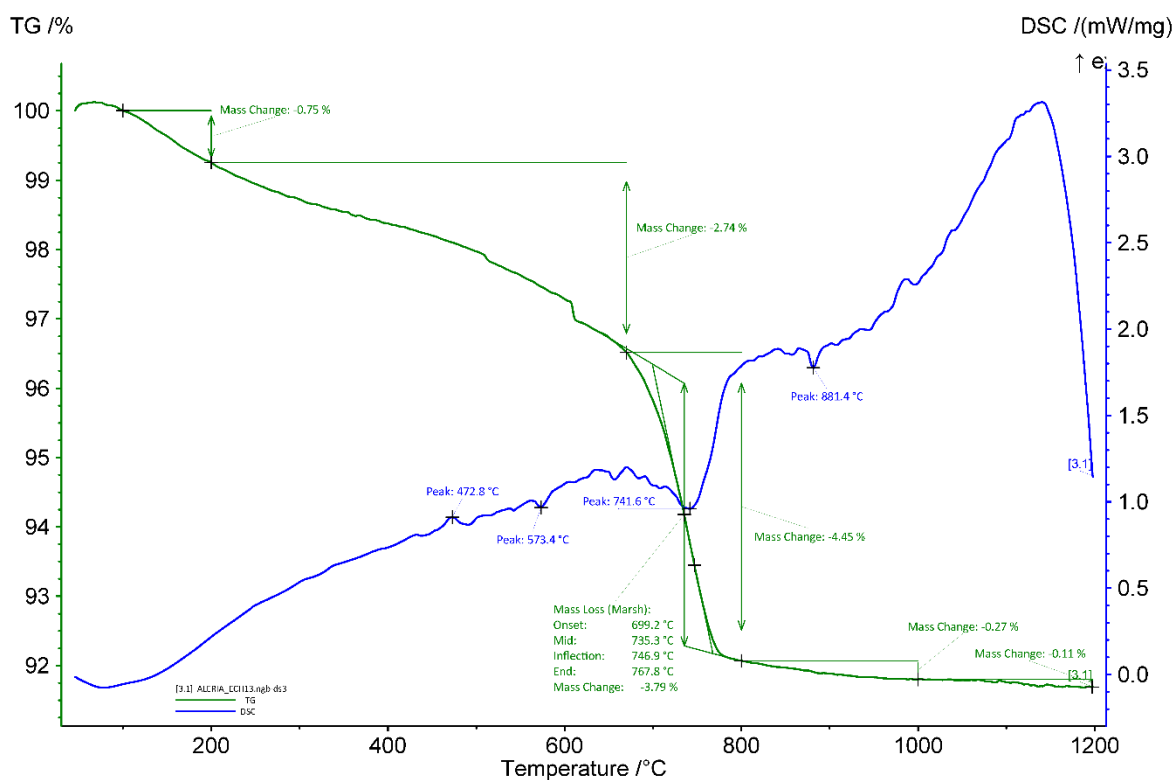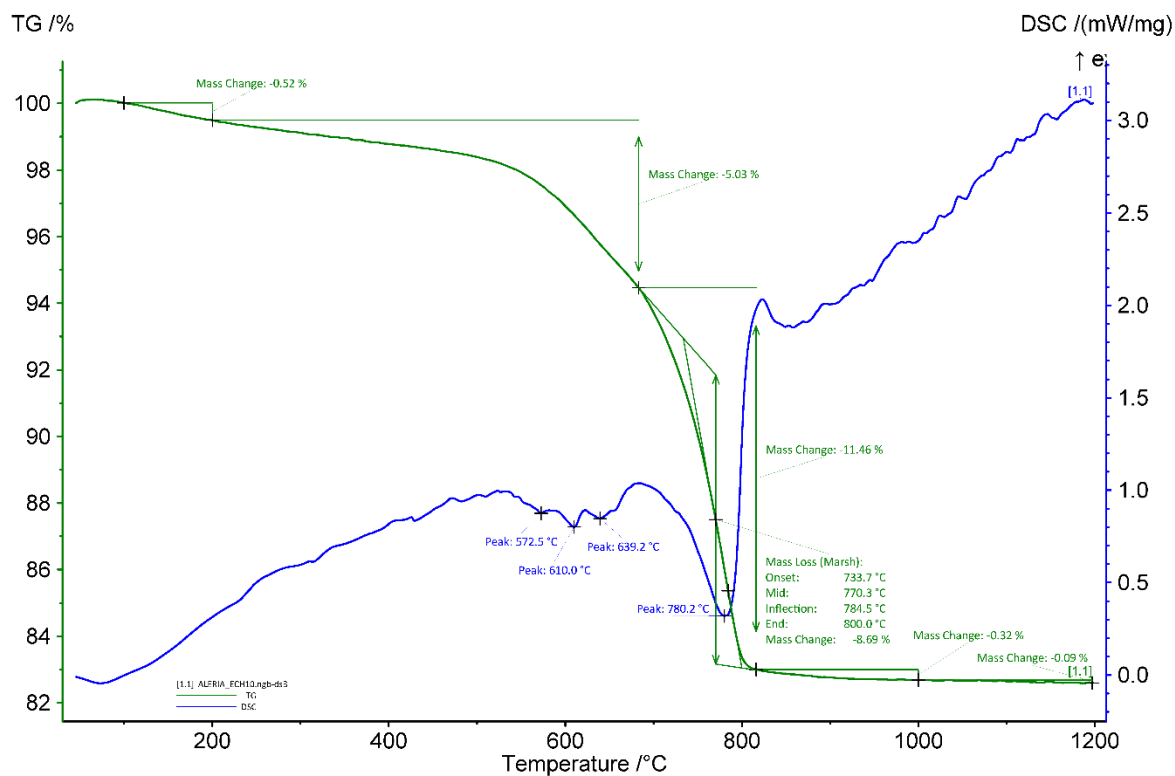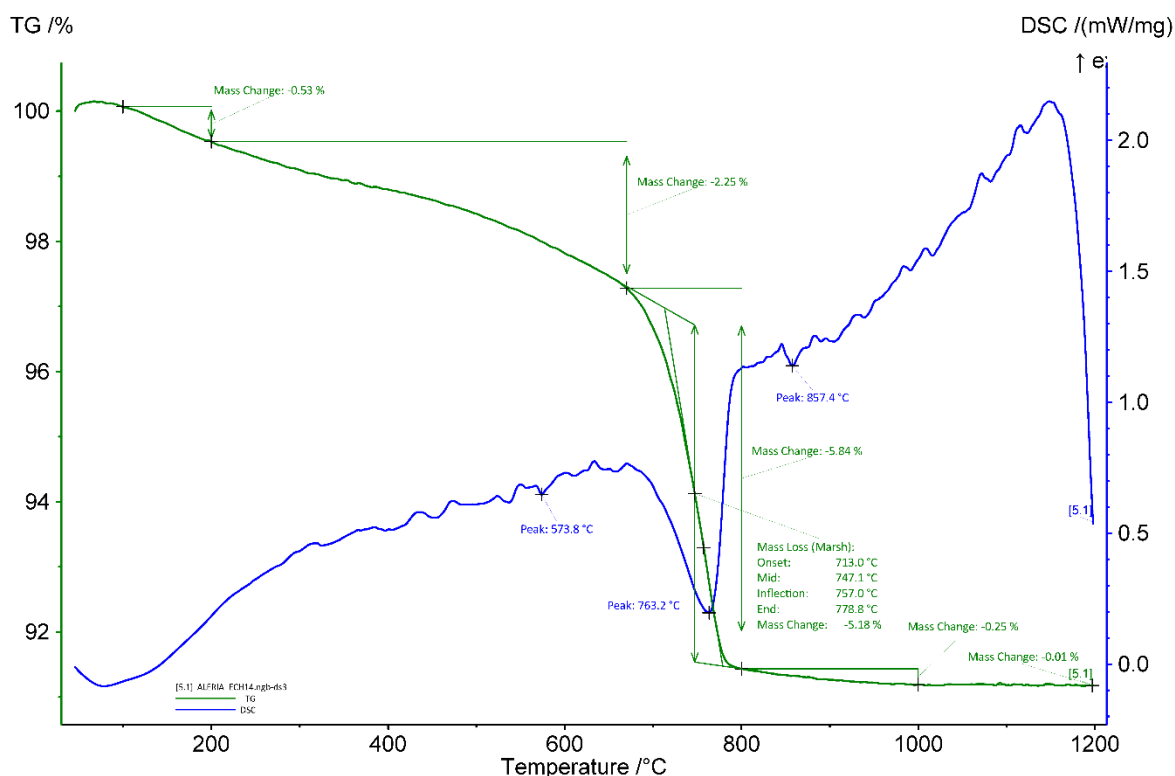
Figure 9: Coupled TG-DSC analysis of ECH10 (top), ECH13 (middle) and ECH14 (bottom) upon heating to a temperature of 1200°C at a heating rate of 20 °C/min under an inert atmosphere (He flushed at 50 ml/min). The weight loss determined by thermogravimetric analysis (TG, wt%, green curve) and the result of the differential scanning calorimetric analysis (DSC, mW/mg, blue curve) are both presented.

Grinding/particle separation

ECH10 was very hard, the pieces selected were cleaned with a metallic brush before being ground. ECH13 was much softer compared to ECH10, hard pieces (including a very large one) were removed while grinding. ECH14 was very brittle and easy to grind.

TGA on powders with particle size <75 μm

The coupled TG-DSC analysis of the powdered mortars with particles lower than 75 μm are presented Figure 10. The aHI of the powders with particles < 75 μm, determined on the basis of the weight loss between 200 and ca. 650°C, are around 38, 34 and 33 % for ECH10, 13 and 14, respectively. They are lower compared to the whole samples which could be explained by the fact that some of the clay present in the whole sample was extracted when sieving. The quantity of carbonates is higher in the powders compared to the whole samples since a large part of the sand is removed when sieving (~37, 35 and 34 wt% for ECH10, 13 and 14, respectively). Indeed, no quartz was detected in the powders. For the powdered samples ECH10 and 13 (Figure 10), a peak around ~405-13°C is observed and might again be due to the release of water from calcium hydroxide (Moropoulou, Bakolas, and Bisbikou 1995; Klimesch and Ray 1996) which might indicate that the mortars did not fully carbonated. The exothermic peak at 603°C observed for ECH.14 (Figure 10) could be related to the presence of a different form of carbonate possibly coming from the hydraulic phases. The end temperatures of calcium carbonate decomposition are 826, 801 and 820°C for the powdered ECH10, 13 and

14, respectively. It is higher compared to the whole samples. As possible explanation could be that the powders are more pure compared to the whole mortar samples which increases the decomposition temperature.
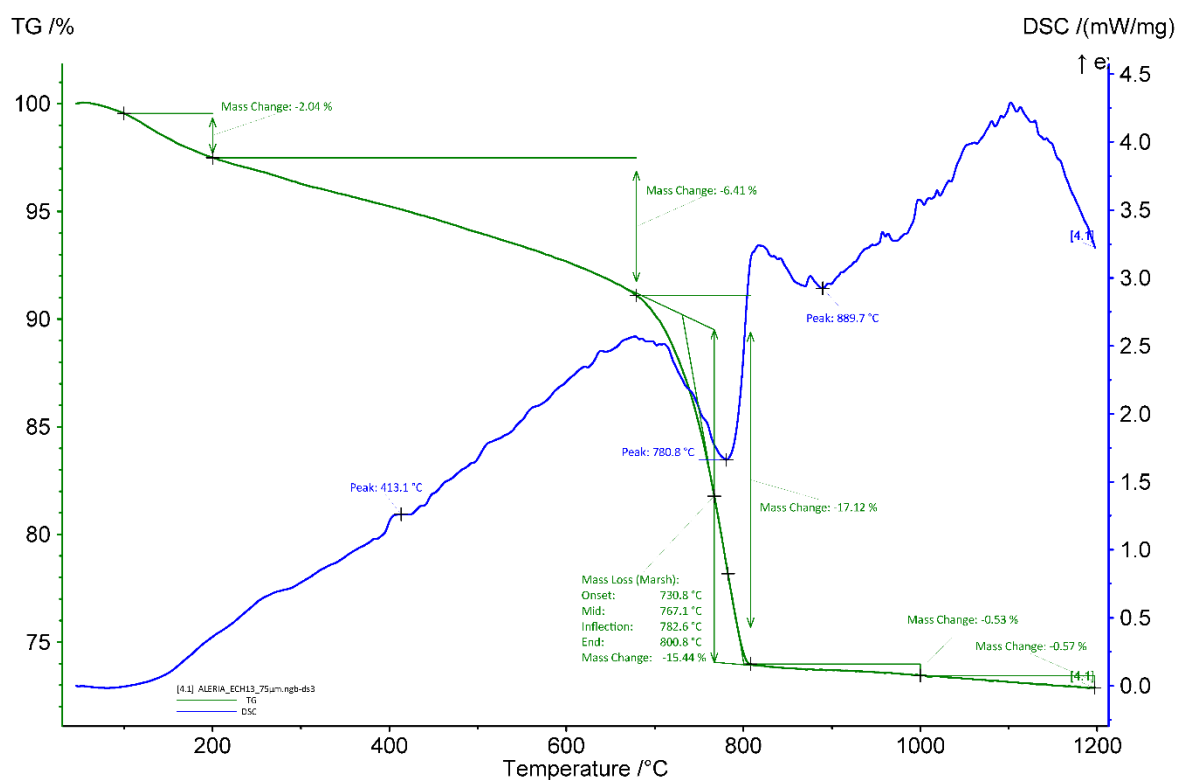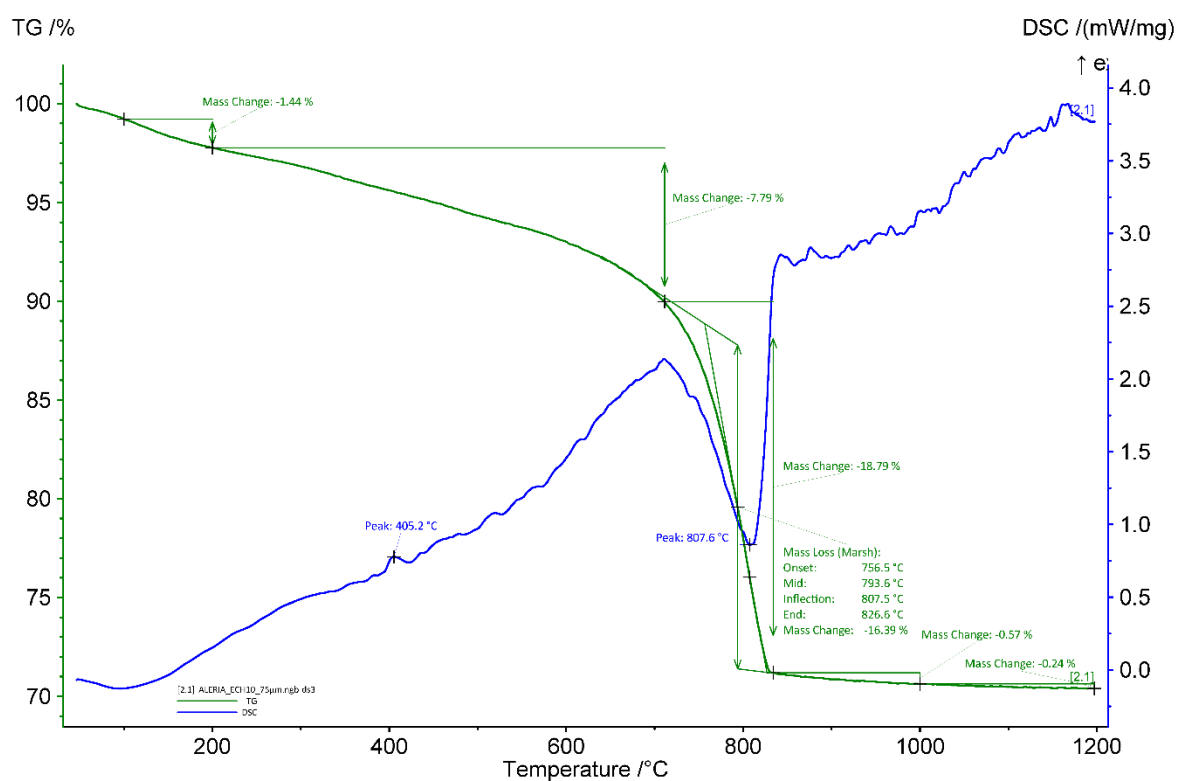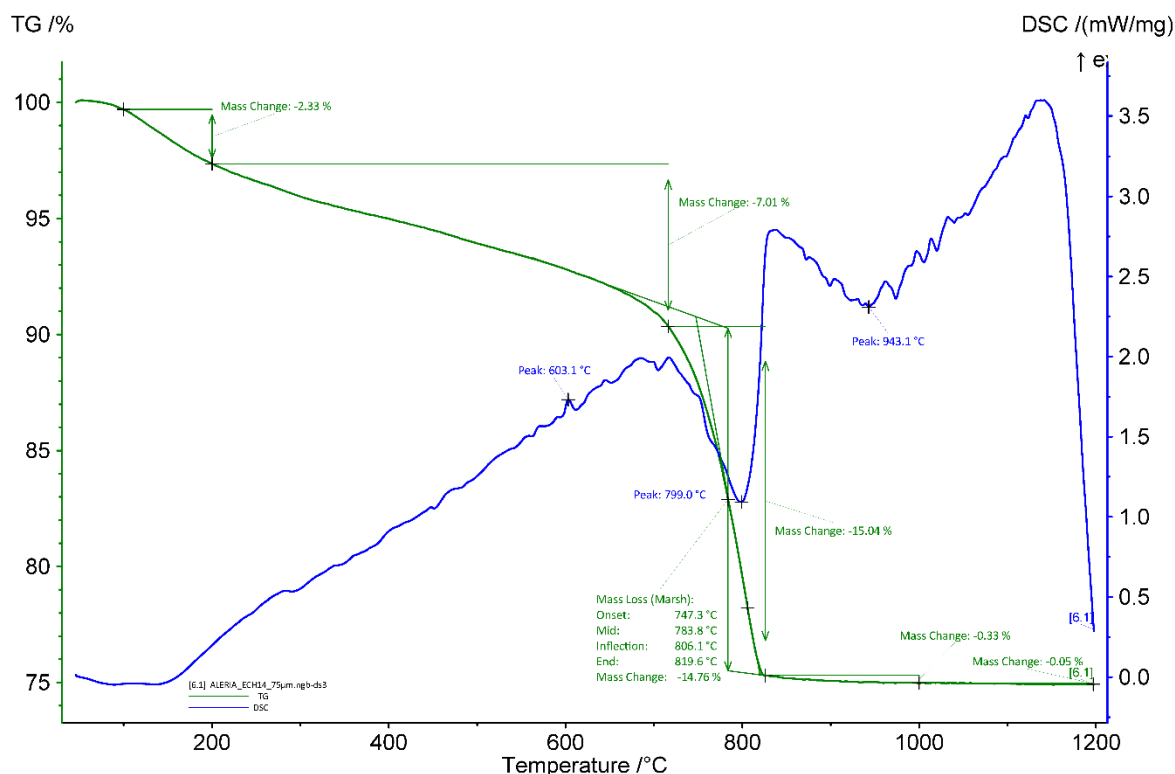
Figure 10: Coupled TG-DSC analysis of the powdered ECH10 (top), ECH13 (middle) and ECH14 (bottom) with particle size < 75 μm upon heating to a temperature of 1200°C at a heating rate of 20 °C/min under an inert atmosphere (He flushed at 50 ml/min). The weight loss determined by thermogravimetric analysis (TG, wt%, green curve) and the result of the differential scanning calorimetric analysis (DSC, mW/mg, blue curve) are both presented.

Radiocarbon results

The test prior to the CO_2 extraction revealed a correct amount of carbon (Table 5) in the samples (~3.5 to 5 %).

RICH	Sample type	Method	C (%)	σ (%)	m (g)	Age BP extrapolated	Calibrated date (oxcal - 95.4%)	Age BP extrapolated with stat	Calibrated date (oxcal - 95.4%)	Age BP average	Calibrated date (oxcal - 95.4%)	Reliability of dating
34100 (ECH10)	mortar from the wall core (50 cm deep)	HCl (10 fractions)	5,048	0,339	1,82	1035 ± 29	897-1119 calAD	911.7 ± 16.3	1044-1207 calAD	not possible	-	☒
34101 (ECH13)	mortar for the core of the foundation wall external face	HCl (9 fractions)	3,978	0,156	2,5	1997 ± 29	48 calBC - 113 calAD	1965.7 ± 16.9	26 calBC - 120 calAD	(f1 & f4) 1956 ± 19	13-124 calAD	☑
34099 (ECH14)	mortar of the wall core external face	HCl (10 fractions)	3,589	0,095	2,62	1566 ± 23	423-571 calAD	1178.6 ± 45.7	166-406 calAD	not possible	-	☒

Table 5: Radiocarbon results.

The extrapolated date obtained for ECH10 (Table 5 & Figure 11) is too young compared to the presumed historical date (Ancient Rome - 50-25 BC).The first fractions are also spread and no combination was possible. The non reliable result is most probably due to the presence of secondary carbonates in addition to delay hardening since the sample come from 50 cm depth in the core of the wall.
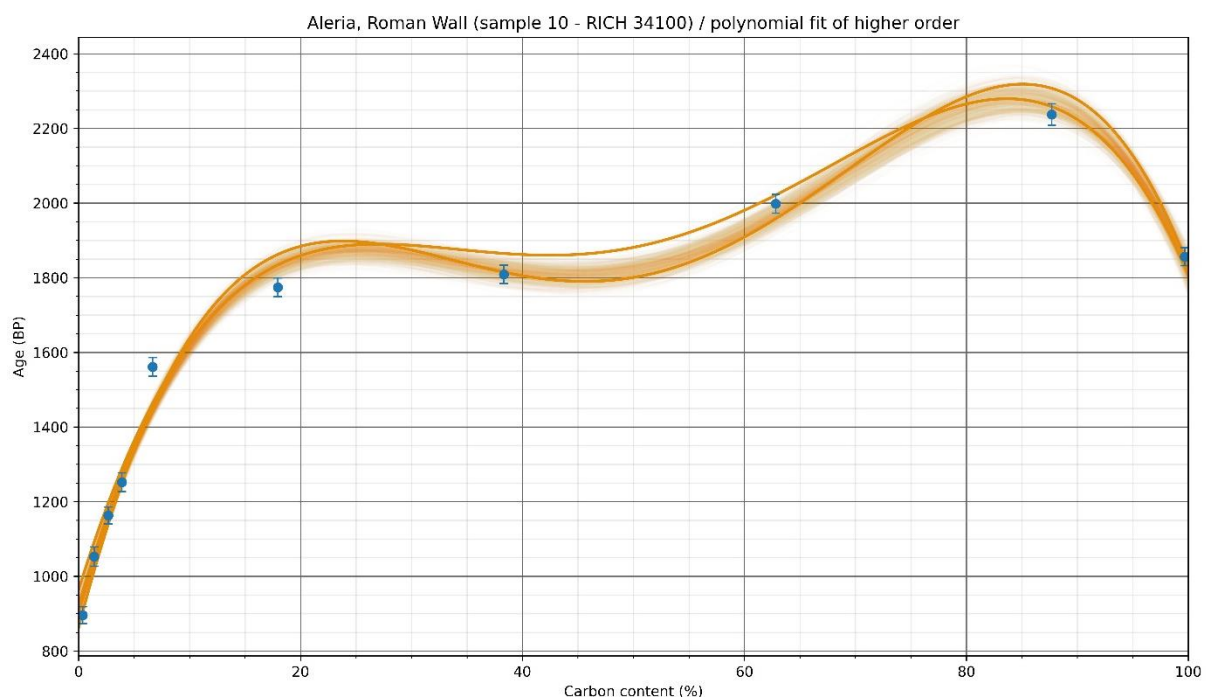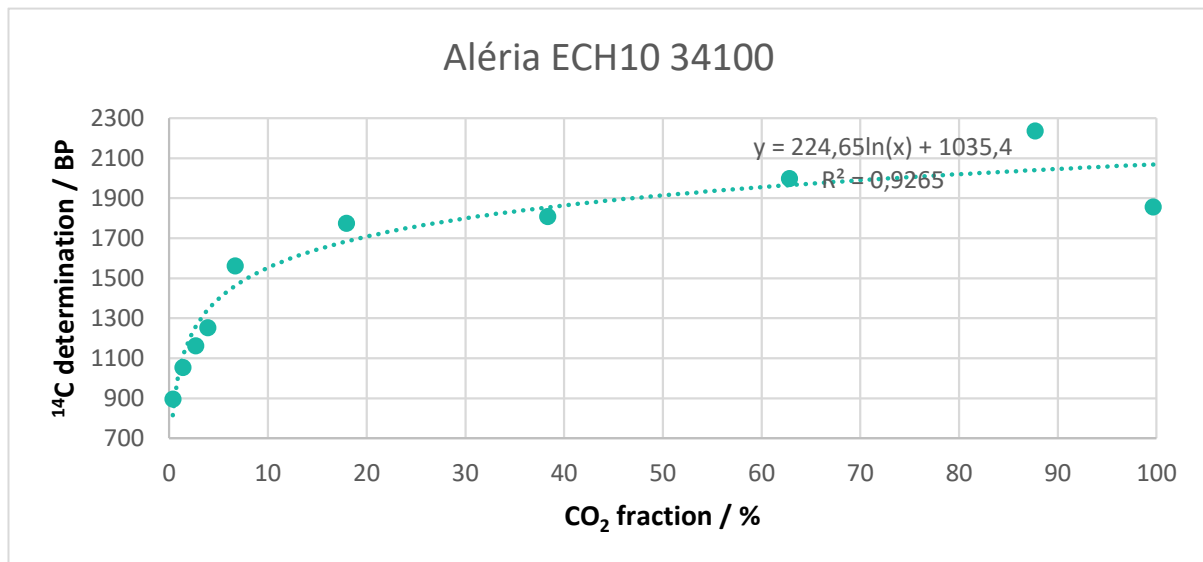
Figure 11: Radiocarbon results for the powdered mortar ECH10 with particles < 75 µm as a function of the CO_2 fraction (the graph at the bottom shows the statistic on the results).

For ECH13, the extrapolated date and the extrapolated date with statistic correspond to the expected date (Table 5 & Figure 12). The combination of date was only possible between fraction 1 and fraction 4. Fraction 2 was lost during the graphitisation process and fraction 3 is

slightly older to 1 and 4. The result of this combination is slightly younger to the presumed date.
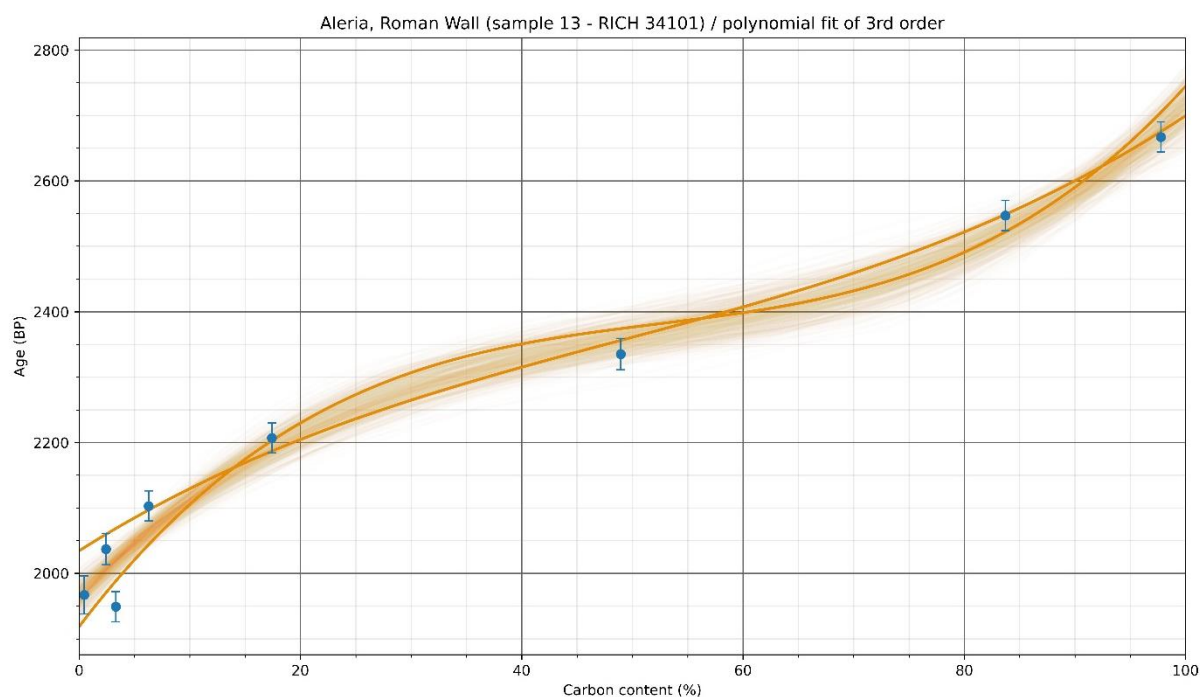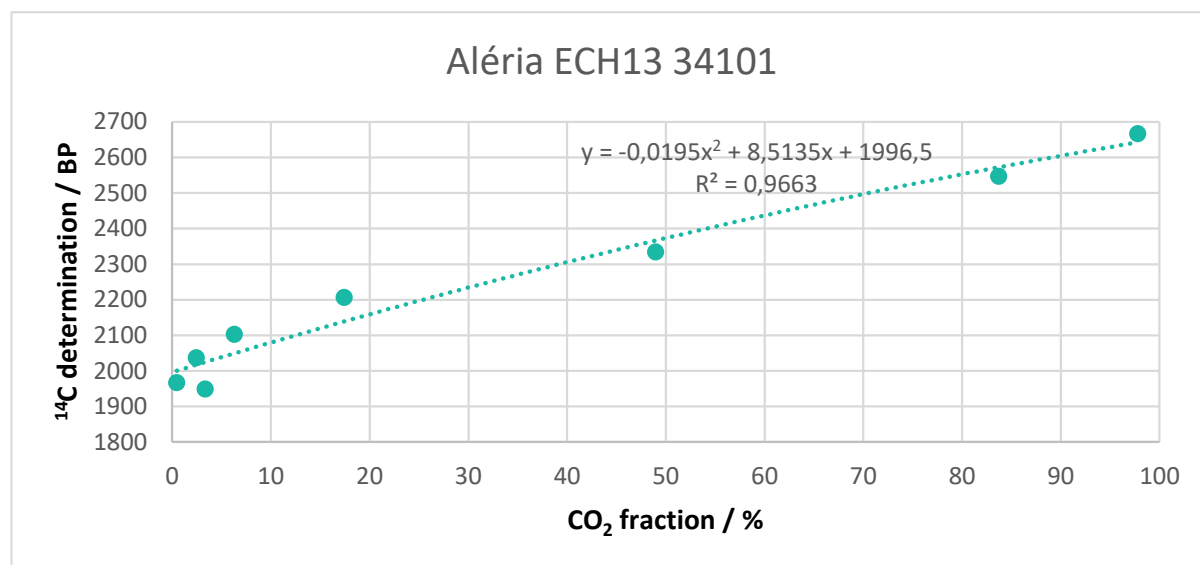
Figure 12: Radiocarbon results for the powdered mortar ECH13 with particles < 75 µm as a function of the CO_2 fraction (the graph at the bottom shows the statistic on the results).

The extrapolated date and the extrapolated date with statistic obtained for ECH14 fall out of the range of the historical date, they are several hundred years younger. The combination of the first fractions was not possible since they are sparse. The numerous occurrences of secondary carbonates in the thin sections, and the presence of clay cutans that may have induced some pozzolanic reactivity, contributed to the obtention of an unreliable date.
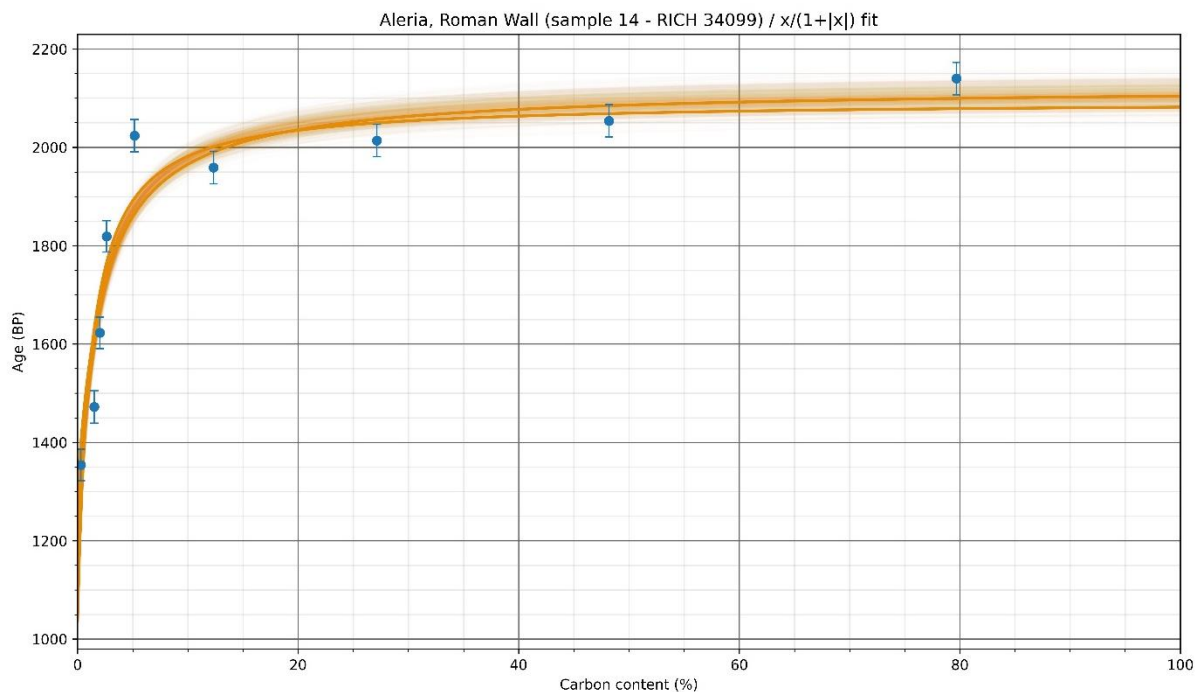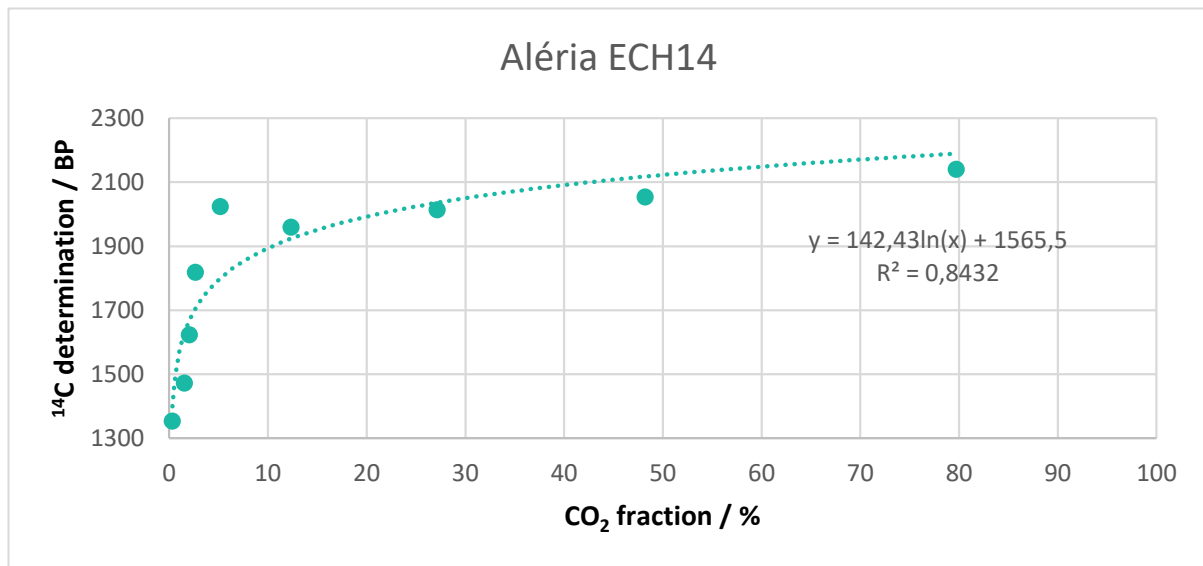
Figure 13: Radiocarbon results for the powdered mortar ECH14 with particles < 75 µm as a function of the CO_2 fraction (the graph at the bottom shows the statistic on the results).

Conclusions

From the analyses, the samples show an altered preservation state with the presence of leaching and secondary carbonates. They are also very strongly hydraulic which leads in most cases to the obtention of youngers dates because of delayed hardening. These samples are not suitable for the radiocarbon dating of their binders. However, the sample ECH13 give plausible dates which could be due to a compensation between the delayed hardening and the degradation phenomena or to a false hydraulicity.

Bibliography

Ahmmed, Tanjil, Ana Raquel Silva, José Carlos Quaresma, Patrícia Moita, and Cristina Galacho. 2024. "Analytical Characterization of Historical Mortars from the Roman Villa of Frielas (Loures, Portugal)." *Acta IMEKO* 13 (3): 1–11.

Bats, Michel. 1994. "Les Silences d'Hérodote Ou Marseille, Alalia et Les Phocéens En Occident Jusqu'à La Fondation de Vélia." *Annali Di Archeologia e Storia Antica*, no. 1, 133–48.

Brunello, Vallentina. 2020. "Mortars: A Complex Material in Cultural Heritage. A Multi-Analytical Procedure to Characterize Historical Mortars." Università degli studi dell'insubria. https://core.ac.uk/reader/322778010.

Cesari, Joseph. 2010. *Corse Antique*. Éditions du Patrimoine, Centre des monuments nationaux.

Coutelas, Arnaud, and Franck Allegrini-Simonetti. 2017. "Une Capitale Méconnue: La Ville Romaine d'Aléria (Corse) et Sa Parure Urbaine." *Mélanges de l'École Française de Rome-Antiquité*, no. 129–2. https://journals.openedition.org/mefra/4527.

Gailledrat, Éric, and Paul Fontaine. 2023. "Aléria (Corse). Nouvelles Recherches Sur Les Fortifications Antiques (2018-2021)." *Res Antiquae* 20:163–72.

Jehasse, Jean. 1993. *La Corse Antique*. FeniXX. https://books.google.be/books?hl=fr&lr=&id=15gAEQAAQBAJ&oi=fnd&pg=PA2&dq=jehasse+laurence+1993&ots=PQ6y0P1IZ-&sig=kAmRs4iGJEu2FnKfieiC__xYO6U.

Lenoir, R, and R Rebuffat. 1984. "Le Rempart Romain d'Aleria. Étude Archéologique." *Archeologia Corsa* 8–9:73–95.

Middendorf, B., J. J. Hughes, K. Callebaut, G. Baronio, and I. Papayianni. 2005. "Investigative Methods for the Characterisation of Historic Mortars—Part 1: Mineralogical Characterisation." *Materials and Structures* 38 (8): 761–69. https://doi.org/10.1007/BF02479289.

Rickard, William D. A., Arie Van Riessen, and Philip Walls. 2010. "Thermal Character of Geopolymers Synthesized from Class F Fly Ash Containing High Concentrations of Iron and α-Quartz." *International Journal of Applied Ceramic Technology* 7 (1): 81–88. https://doi.org/10.1111/j.1744-7402.2008.02328.x.

Study of mortars from burchtmuur (Antwerp) for the BRAIN 2.0 PalC project

Context of the site

The burchtmuur in Antwerp is the wall from the old city (bailey) connected to Het Steen, which was one of the doors of the city. The burchtmuur under Het Steen is also part of the project. It was dated before the start of the project and showed problematic results (see report Het Steen, Antwerp). The part of the burchmuur sampled here is located along the river Schelde, on the docks (Figure 1). After the end of the excavations, the wall will be displayed for people coming out of cruise ships.
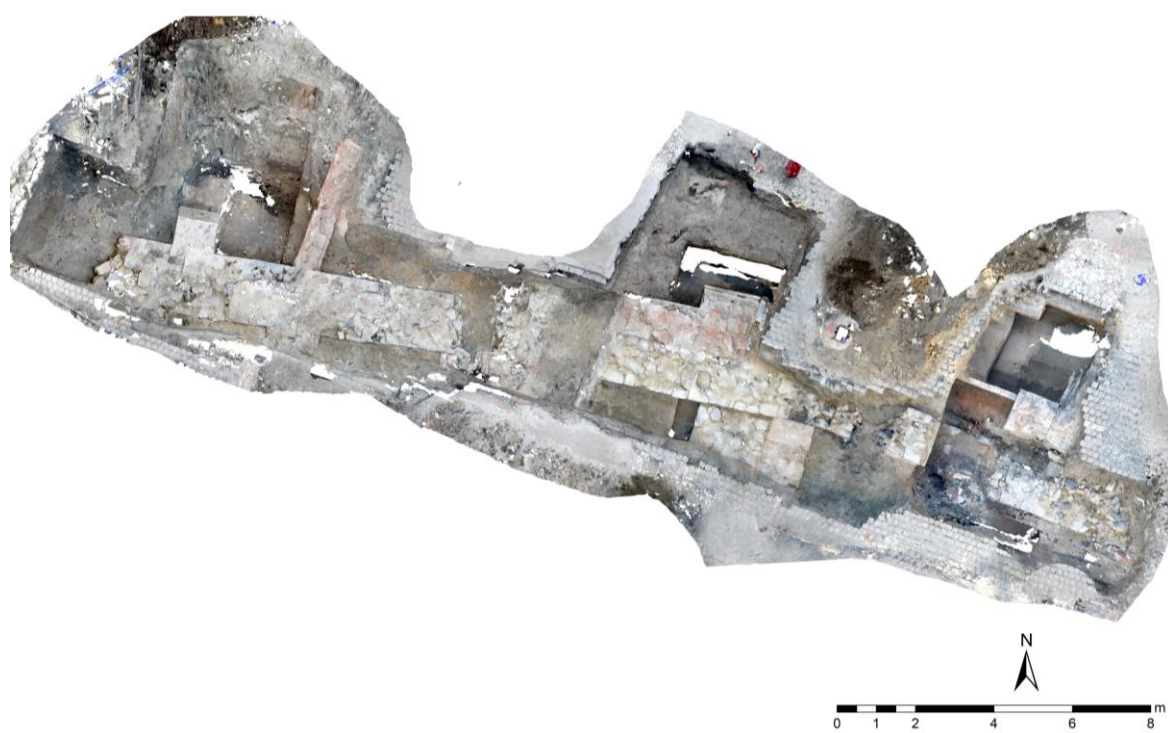
Figure 1: Burchtmuur excavation view (©archaeological department city of Antwerp).

Material

The sampling was performed in 2021 in two different locations (Figure 2). For one of the locations (A539 - SL2 (A) – 23), we sampled both at the surface (KIK2) and 50 cm deeper for comparison (KIK1). For the other location (A539 - SL4 (A) - S88), only one mortar was sampled (KIK3) in the core of the masonry (infill mortar). The presumed historical date is estimated between 1000 and 1200 CE.

Figure 2: Locations of the three mortar samples KIK1 (left), KIK2 (middle) and KIK3 (right) (©archaeological department city of Antwerp).

Results & Discussion

Macroscopic descriptions

The main colour of the three sample is beige (Figure 3) tending towards pale yellow (2.5Y 8/2 for KIK & KIK2 and 2.5Y 8/3 for KIK3) according to the Munsell soil colour charts. The lime lumps appear as white inclusions with a main size < 1 mm and the biggest ones measure ~2 to 8 mm. All samples contain soft black inclusions that are probably charcoal fragments and KIK3 also contain hard black inclusions possibly made of bottom ashes. KIK1 & KIK2 include grey inclusions reaction with HCl which shall be some limestone fragments. A very large one (5 cm – Figure 3 left) was observed for KIK1. KIK2 comprised a fragment of shell (Figure 3 middle) and was covered by a lot of soil particles. KIK3 was very moist when sampled and show a white crust on one of the fragments.
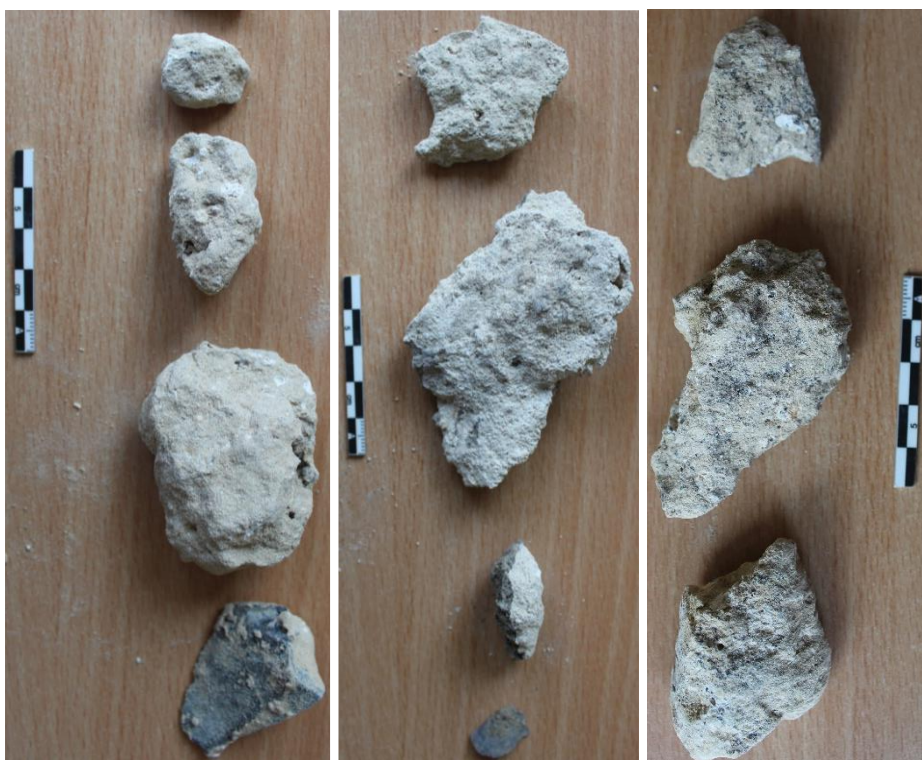
Figure 3: Mortar samples KIK1 (left), KIK2 (middle) and KIK3 (right).

Fourier transform Infrared (FTIR) spectroscopy on inclusions & binder

The FTIR spectra of the three binders (beige, Figure 4) show a relatively low amount of carbonates compared to the silicate content, especially for KIK1 and KK3 for which the intensity of the main silicates vibrational band (~1000 cm^{-1}) is higher than the intensity of the main carbonate band (~1400 cm^{-1}). As expected, the lime lumps (white, Figure 4) mainly contain calcite with a bit of aragonite and silicates except for KIK2 for which the silicates exhibit a higher relative concentration. As for all the binders, the calcium carbonates present in lime lumps of KIK2 have probably been dissolved. The grey inclusions are mainly made of calcium carbonates with silicates including quartz as well as clay for KIK2 and nitrates for KIK3. The later are most probably limestone fragments. The shell fragment found in KIK2 is as expected also made of calcium carbonates (mainly calcite). The soil particles present on KIK2 mainly contain silicates including quartz and clay. The spectrum of white crust found on KIK3 shows the features of calcite, nitrates, silicates and aragonite.
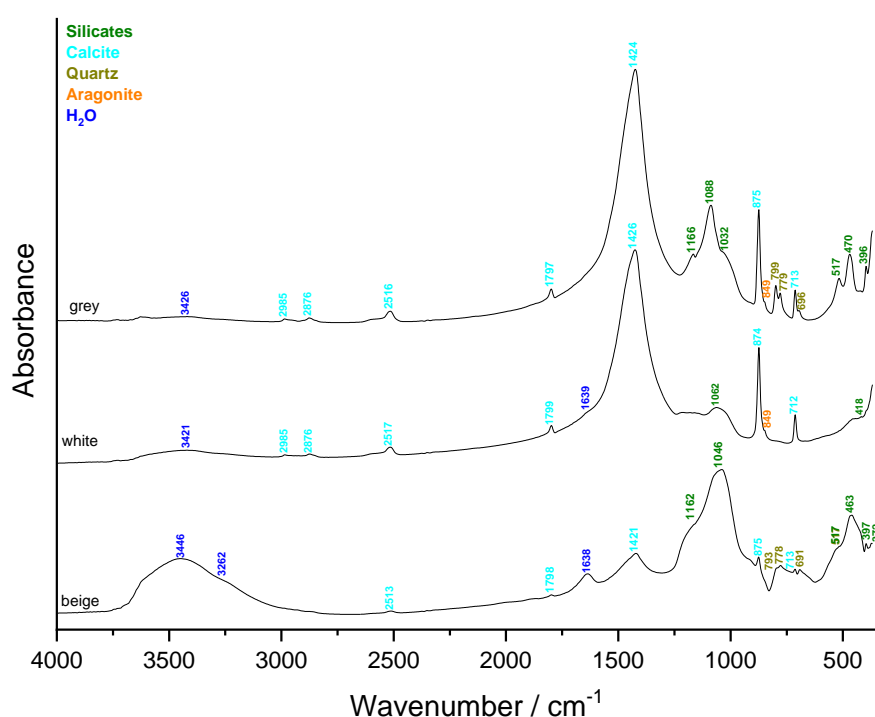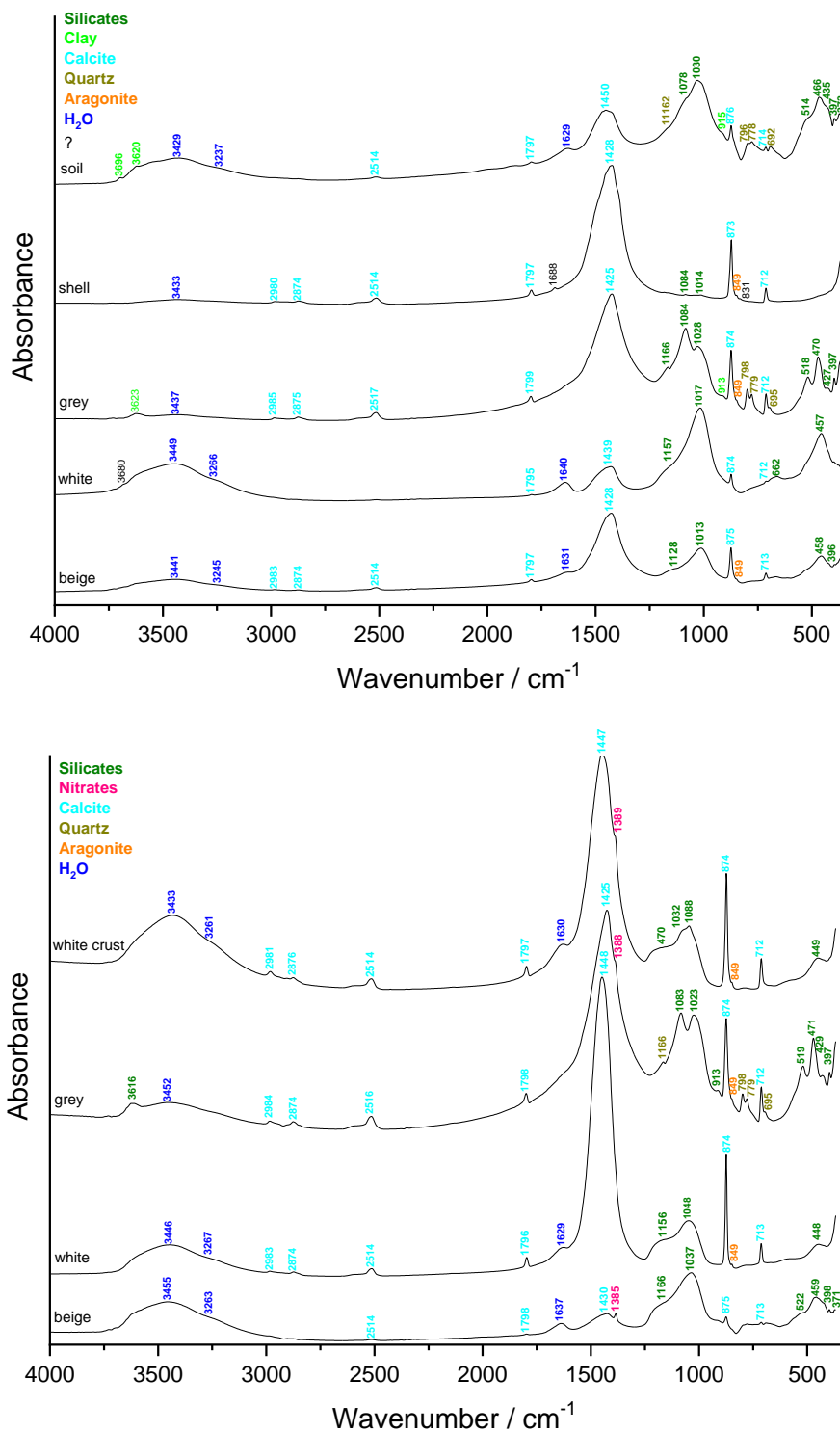
Figure 4: FTIR spectra obtained on the inclusions and binder (beige) of the mortar sample KIK1 (top), KIK2 (middle) and KIK3 (bottom).

Binder:sand ratio

The calculated binder:sand ratio (in volume unit) using a bulk density of 1.35 kg/dm^3 for the sand and 0.575 kg/dm^3 for the lime is close to 1:2 for KIK1, 5:3 in volume unit for KIK2 and 3:4 for KIK3. This values might be overestimated because of the possible dissolution of the binder.

	KIK1	KIK2	KIK3
Sample weight (g)	2.9	1.6	2.6
Crucible weight (g)	16.9	19.3	19.2
Weight calcined (g)	19.3	20.3	21.2
%ins	**83.2**	**57.8**	**76.0**

Table 1: Percentage of insoluble residue

Cathodoluminescence

Cathodoluminescence observations of the three thin-sections and powders show similar results (Figure 5). The thin-sections (Figures 5a, c and e) exhibit the presence of two types of quartz, one with a reddish-brown colour and another one dark purple. K-feldspars can also be observed in bright blue and the binder is dull. Limestone fragments are also present exhibiting a bright red colour. The powdered samples are mainly dull (binder) with a few bright blue K-feldspars, a plagioclase green grain for KIK2 (Figure 5d) and a few bright red limestone grains.
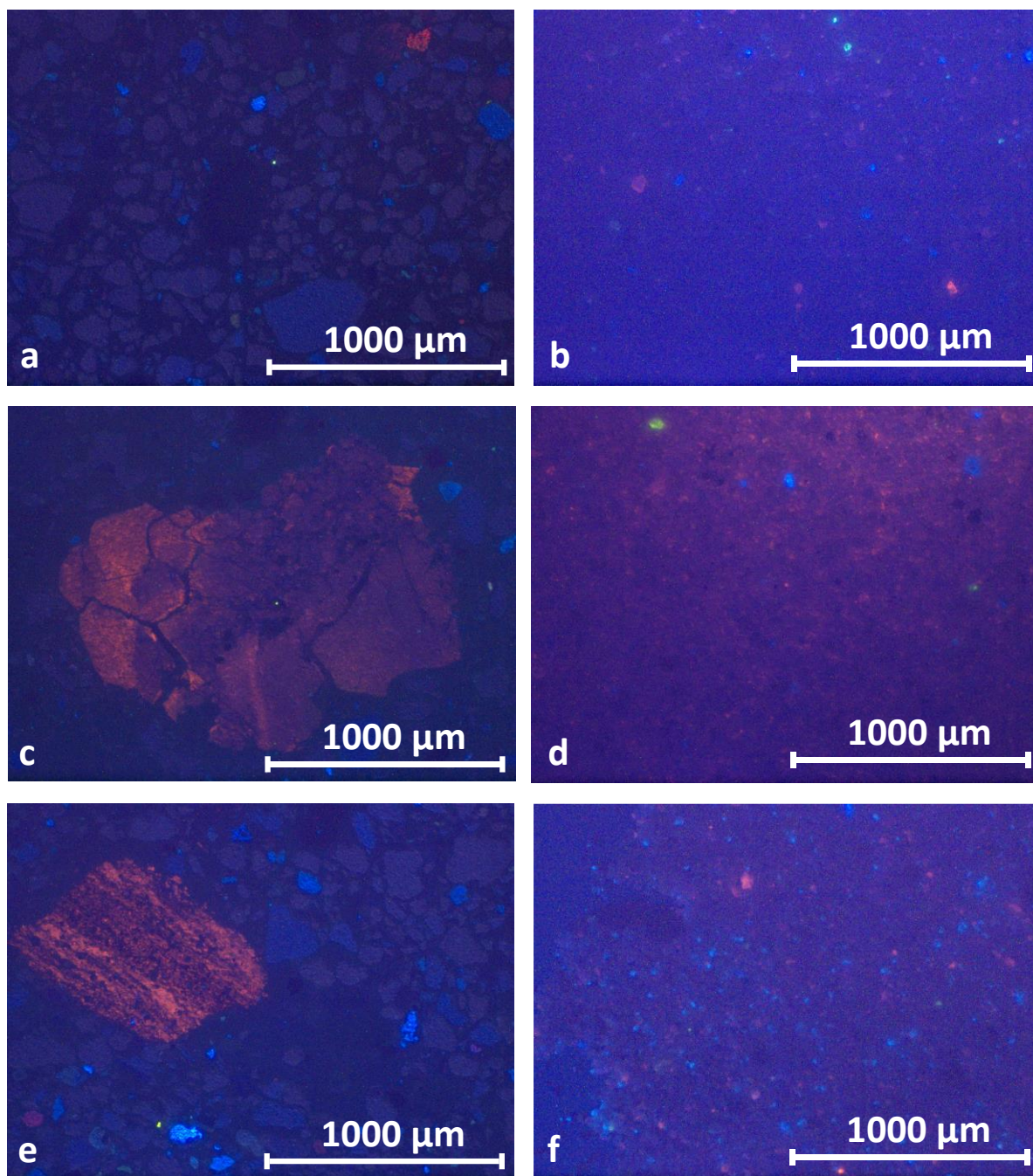
Figure 5: Characteristic cathodoluminescence images of a) the thin section X2155 of KIK1, b) the powdered KIK1 mortar with particle size lower than 75 μm, c) the thin section X2156 of KIK2, d) the powdered KIK2 mortar with particle size lower than 75 μm, e) the thin section X2157 of KIK3, and f) the powdered KIK3 mortar with particle size lower than 75 μm.

Thin-section petrography

The mortar KIK1 (Figure 6 and Table 2) is extremely deteriorated, it has been dissolved and some secondary carbonates can also be observed (Figure 6b, c and e). Some lime lumps are underburned (Figure 6b), other completely burned (Figure 6d) and most of them are partially dissolved (Figure 6a, b and d), and sometimes, even totally dissolved (Figure 6a). Secondary carbonates are observed at the border of the dissolved lumps (Figure 6a) and inside cracks within lumps (Figure 6b).
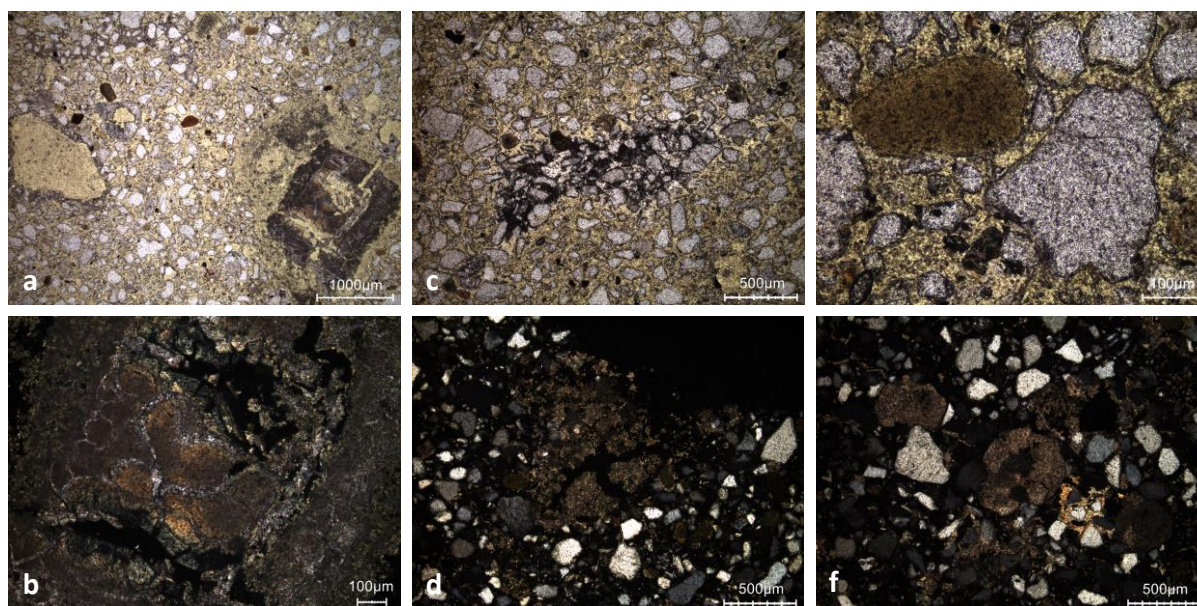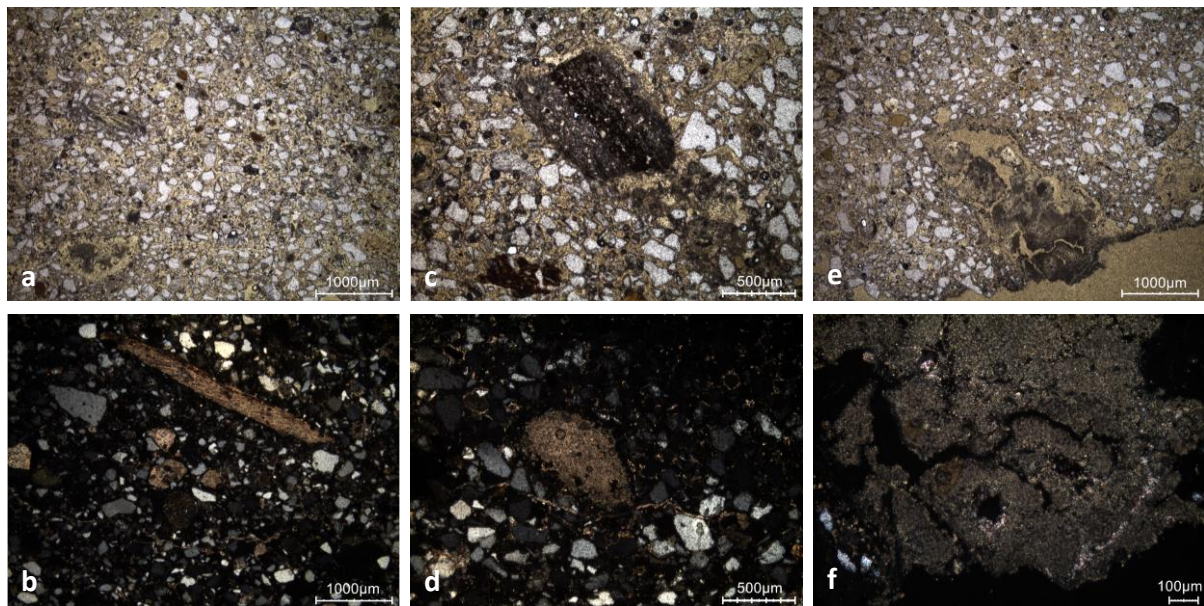
Figure 6: Representative photomicrographs of the KIK1 thin-section X2155: a) overview image in plain polarised light (PPL); b) underburned lime lump partially dissolved with secondary carbonates in cracks in cross polarised light (XPL); c) PPL image showing secondary carbonates deposits; d) completely burnt lime lump partially dissolved in XPL; e) PPL image of glauconite and quartz; f) secondary carbonates (large crystals) in XPL.

Binder	**Texture**	micritic & secondary carbonates micritic / microsparitic
	Lump state	underburned & completely burned
	Lump size	from 300 µm to 3 mm
	Lump frequency	few (because of dissolution?)
Aggregate	**Grain size**	fine (125-250 µm)
	Mineralogy	pure siliceous sand (quartz, feldspar, mica glauconite) with few carbonates grains
	Shape	subangular / subrounded
Appearance	**Homogeneity**	relatively heterogeneous
	Macroporosity	high (due to dissolution)
	Pore structure	connected due to dissolution
Admixtures	**Type**	shell, charcoal & coal
Alteration	**Type**	dissolution & secondary carbonates (dissolution / precipitation)

Table 2: Main characteristics of the mortar KIK1 retrieved from the observations of the thin-section X2155.

329

The mortar KIK2 (Figure 7 and Table 3) is also extremely deteriorated, it has been dissolved and some secondary carbonates can also be observed (Figure 7b). Some lumps are underburned (Figure 7e & f), other completely burned (Figure 7b) and most of them are partially dissolved and even totally dissolved (Figure 7a and b). Secondary carbonates are observed at the border of the dissolved lumps (Figure 7b).
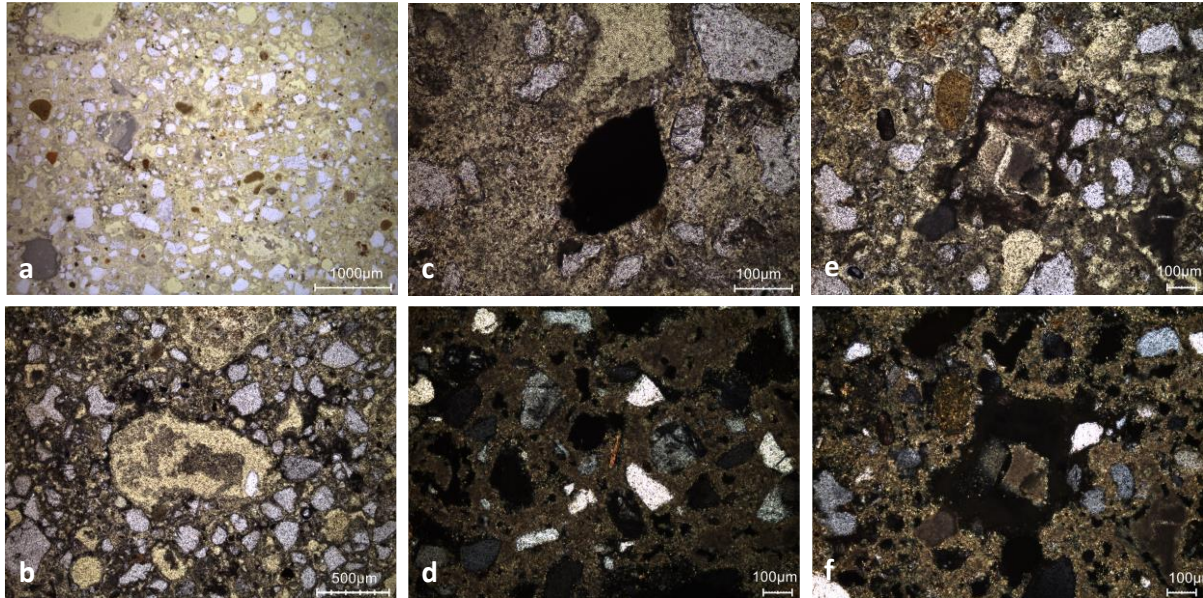
Figure 7: Representative photomicrographs of the KIK2 thin-section X2156: a) overview image in PPL; b) partially dissolved lump with secondary carbonates around the border in PPL; c) PPL image showing a charcoal fragment; d) mica flake in XPL; e) PPL image of an underburned lime lump; f) same image in XPL.

Binder	**Texture**	micritic
	Lump state	underburned & completely burned
	Lump size	from 100 µm to 2 mm
	Lump frequency	few (because of dissolution?)
Aggregate	**Grain size**	very fine to medium (50-500 µm)
	Mineralogy	pure siliceous sand (quartz, mica, glauconite)
	Shape	subangular / subrounded
Appearance	**Homogeneity**	relatively heterogeneous
	Macroporosity	high (due to dissolution)
	Pore structure	connected due to dissolution
Admixtures	**Type**	coal

Alteration	Type	dissolution & secondary carbonates (dissolution / precipitation)

Table 3: Main characteristics of the mortar KIK2 retrieved from the observations of the thin-section X2156.

The mortar KIK3 (Figure 8 and Table 4) is also extremely deteriorated, it has been dissolved and some secondary carbonates can also be observed (Figure 8d and f). Some lime inclusions are unburned (not shown), other completely burned and most of them are partially dissolved (Figure 8e). Secondary carbonates are observed in cracks (Figure 8d) and in the dissolved lime inclusions (Figure 8f).

Figure 8: Representative photomicrographs of the KIK3 thin-section X2157: a) overview image in PPL; b) shell fragment from aggregate; c) PPL image showing a limestone fragment; d) secondary carbonates in cracks in XPL; e) PPL image of a lime inclusion partially dissolved; f) secondary carbonates in partially dissolved lime inclusion in XPL.

Binder	**Texture**	micritic
	Lump state	completely burned & partially dissolved / unburned
	Lump size	max 1.4 mm
	Lump frequency	a few (because of dissolution)
Aggregate	**Grain size**	very fine to medium
	Mineralogy	pure siliceous sand (quartz, feldspar, glauconite)
	Shape	subangular / subrounded
Appearance	**Homogeneity**	relatively heterogeneous
	Macroporosity	high (due to dissolution)
	Pore structure	connected due to dissolution

Admixtures	**Type**	-
Alteration	**Type**	dissolution & secondary carbonates

Table 4: Main characteristics of the mortar KIK3 retrieved from the observations of the thin-section X2157.

Thermogravimetric analysis (TGA) on whole samples

The apparent hydraulicity index (aHI) determined on the basis of the weight loss between 200 and ca. 650°C (usually attributed to water loss from calcium-silicate-hydrates-phases) was calculated from Figures 9-11, and is around 29-30% for KIK1 and KIK2, and 48 % for KIK3, indicating that the mortars KIK1 and KIK2 are strongly hydraulic, and KIK3 is very strongly hydraulic. However, the values obtained from the thermal analyses might not entirely reflect the reality since the mortars were intensively dissolved. The amount of carbonates present in the mortars is around 7.5, 21 and 7 wt% for KIK1, KIK2 and KIK3, respectively. The quartz transition phase can be observed around 571-3°C (Rickard, Riessen, and Walls 2010) for all the samples. The main weight loss of ancient mortars is expected between 600 and 900 °C and is indicative of the decomposition of calcium carbonate ($CaCO_3$) into calcium oxide (CaO) and carbon dioxide (CO_2) (Ahmmed et al. 2024). The end temperature of the calcium carbonate decomposition for the mortar samples is around 770, 798 and 718°C for KIK1, KIK2 and KIK3, respectively. A peak at 622°C is observed for KIK1 and KIK3 (Figure 9 and 11), and could be due to the presence of a different form of carbonate possibly coming from the hydraulic phases. No gypsum was detected.
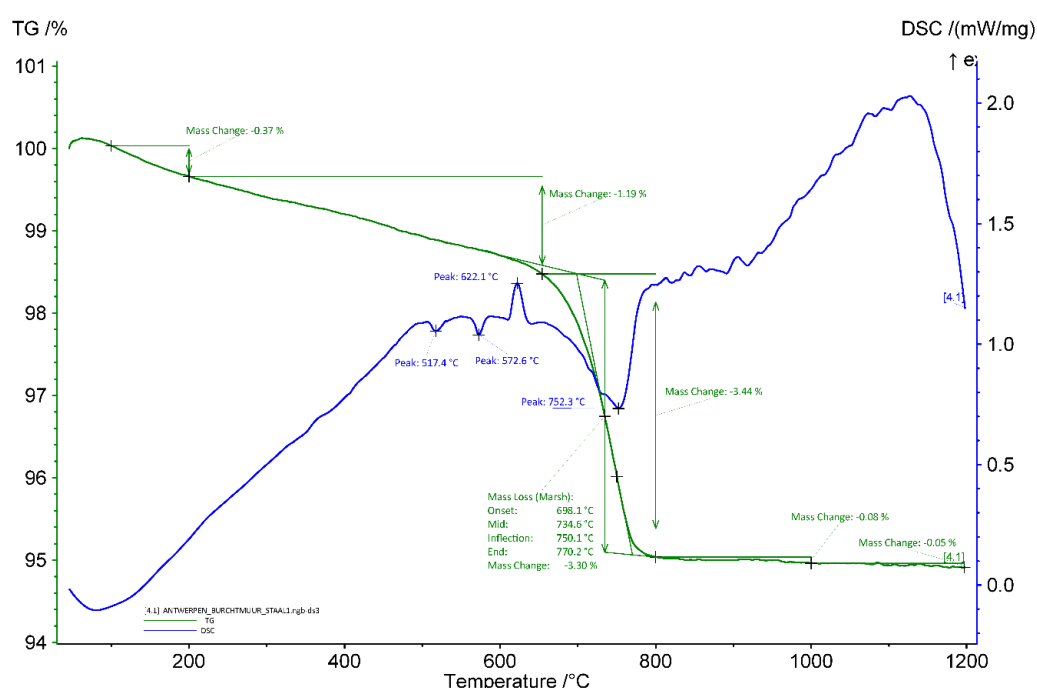
Figure 9: Coupled TG-DSC analysis of the sample KIK1 upon heating to a temperature of 1200°C at a heating rate of 20°C/min under an inert atmosphere (He flushed at 50 ml/min). The weight loss determined by thermogravimetric analysis (TG, wt%, green curve) and the result of the differential scanning calorimetric analysis (DSC, mW/mg, blue curve) are both presented.
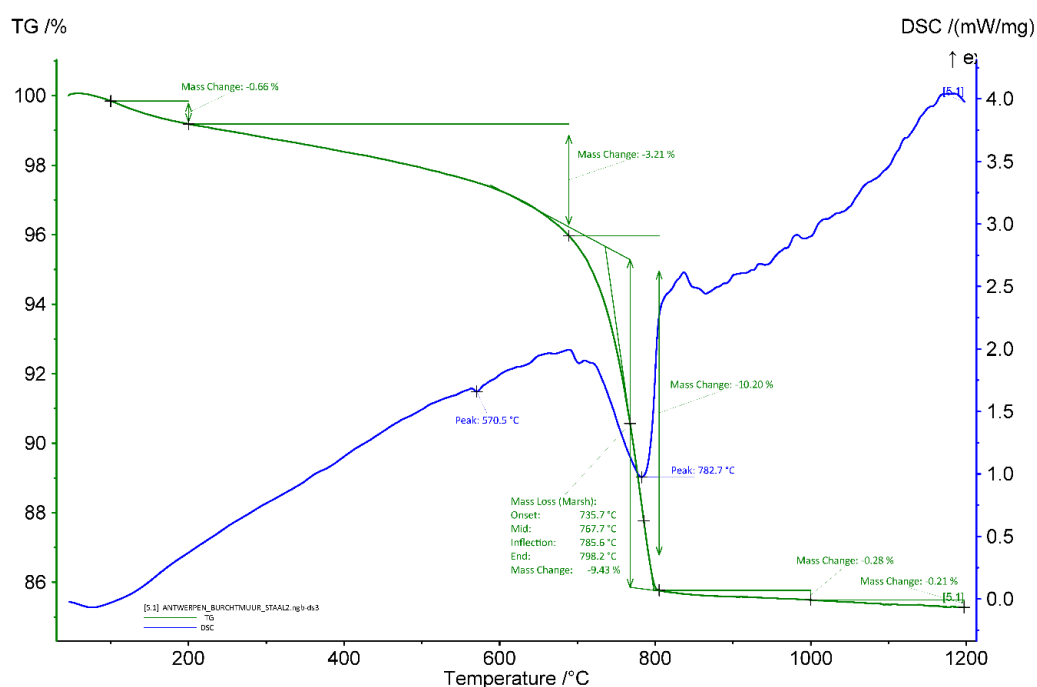

Figure 10: Coupled TG-DSC analysis of the sample KIK2 upon heating to a temperature of 1200°C at a heating rate of 20°C/min under an inert atmosphere (He flushed at 50 ml/min). The weight loss determined by thermogravimetric analysis (TG, wt%, green curve) and the result of the differential scanning calorimetric analysis (DSC, mW/mg, blue curve) are both presented.
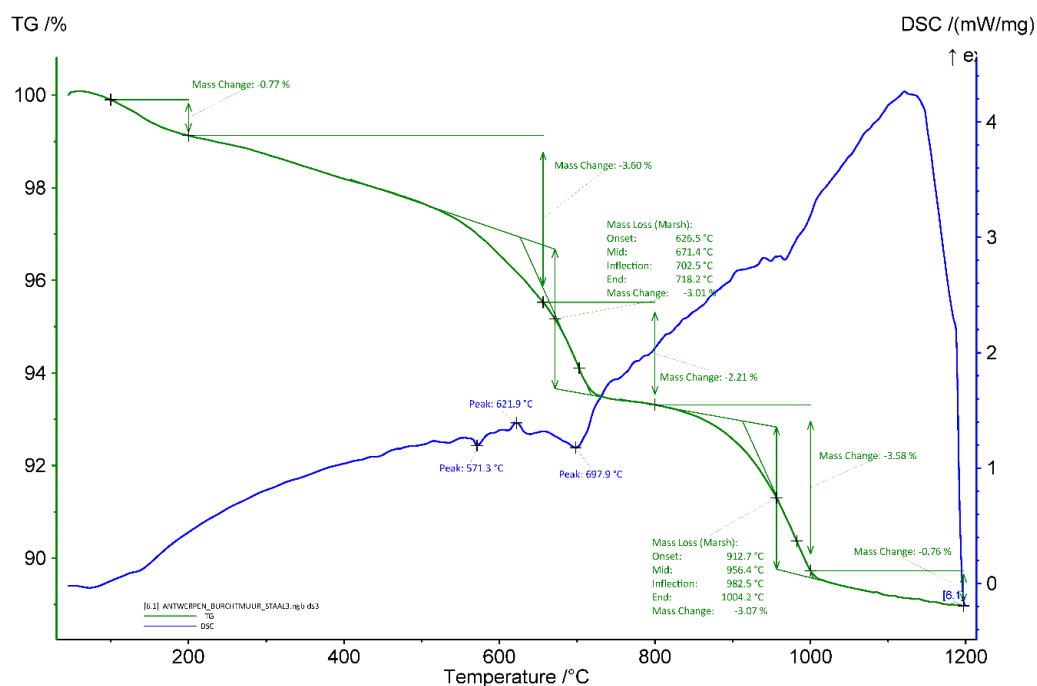
Figure 11: Coupled TG-DSC analysis of the sample KIK3 upon heating to a temperature of 1200°C at a heating rate of 20°C/min under an inert atmosphere (He flushed at 50 ml/min). The weight loss determined by thermogravimetric analysis (TG, wt%, green curve) and the result of the differential scanning calorimetric analysis (DSC, mW/mg, blue curve) are both presented.

XRD

KIK1 and KIK3 were analysed with powdered XRD (Figure 12). The diffractograms show the presence of quartz, calcite and feldspars.
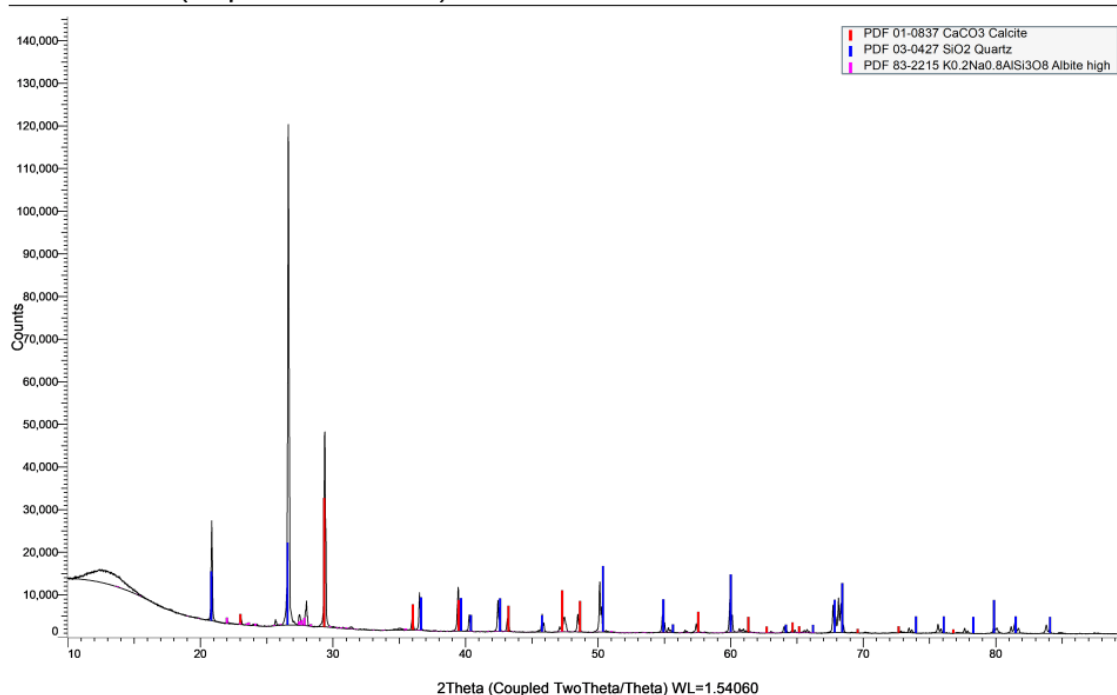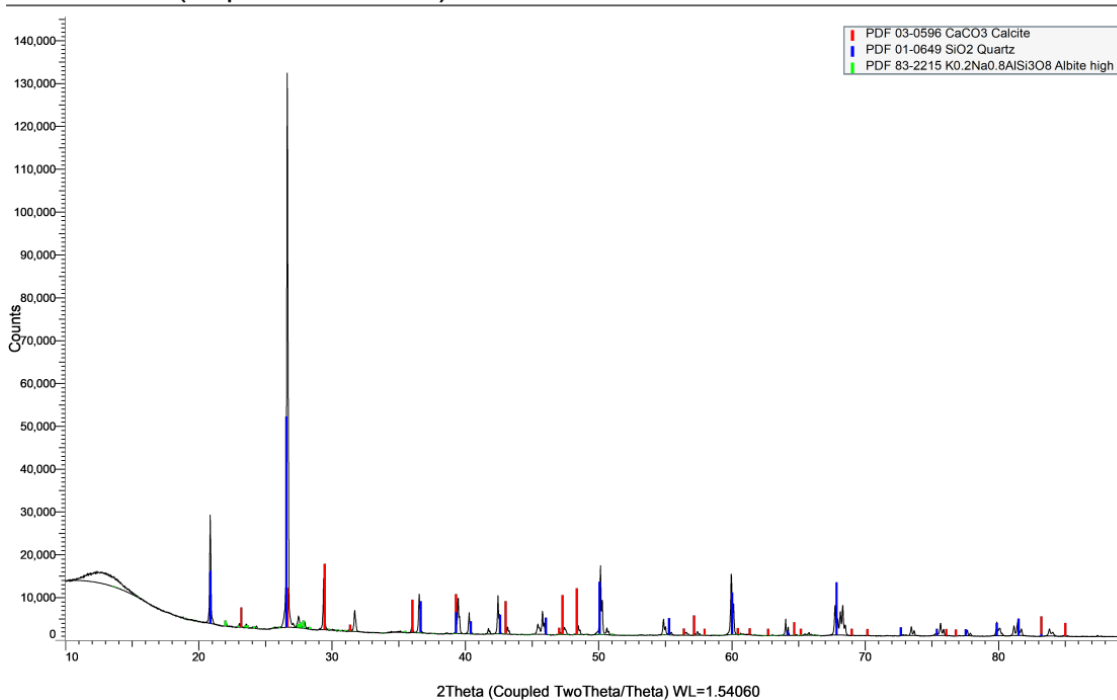
Figure 12: Diffractograms of KIK1 (top) and KIK3 (bottom).

Grinding/particle separation

KIK1 was ground and sieved twice because a lot of powder with particles < 75 μm was needed for dating since the carbon content is very low (~1%). KIK2 was very hard and it was difficult to separate the mortar from the soil (charcoal fragment might have been present in the soil). KIK3 was soft and easy to grind.

TGA on powders with particle size <75 μm

The coupled TG-DSC analysis of the powdered mortars with particles lower than 75 μm are presented Figures 13-15. The aHI of the powders with particles < 75 μm, determined on the basis of the weight loss between 200 and ca. 650°C, are around 38, 21 and 52 % for KIK1, KIK2 and KIK3, respectively. The quantity of carbonates is higher in the powders compared to the whole samples since a part of the sand is removed when sieving (~9, 38 and 8 wt% for KIK1, KIK2 and KIK3, respectively). Indeed, no quartz was detected in the powders. The end temperatures of calcium carbonate decomposition are 781, 818 and 729°C for the powdered samples KIK1, KIK2 and KIK3, respectively. It is higher compared to the whole samples. As possible explanation could be that the powders are more pure compared to the whole mortar samples which increases the decomposition temperature.
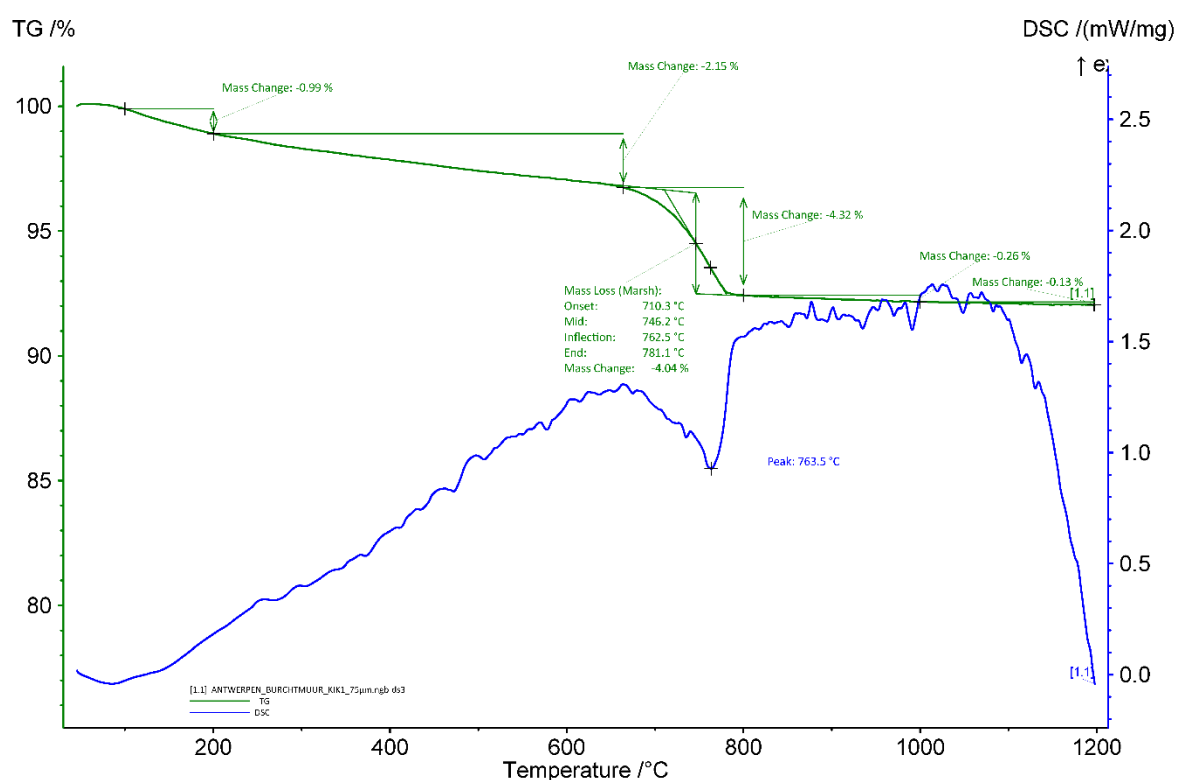
Figure 13: Coupled TG-DSC analysis of the powdered sample KIK1 with particle size <w75 μm upon heating to a temperature of 1200°C at a heating rate of 20°C/min under an inert atmosphere (He flushed at 50 ml/min). The weight loss determined by thermogravimetric analysis (TG, wt%, green curve) and the result of the differential scanning calorimetric analysis (DSC, mW/mg, blue curve) are both presented.
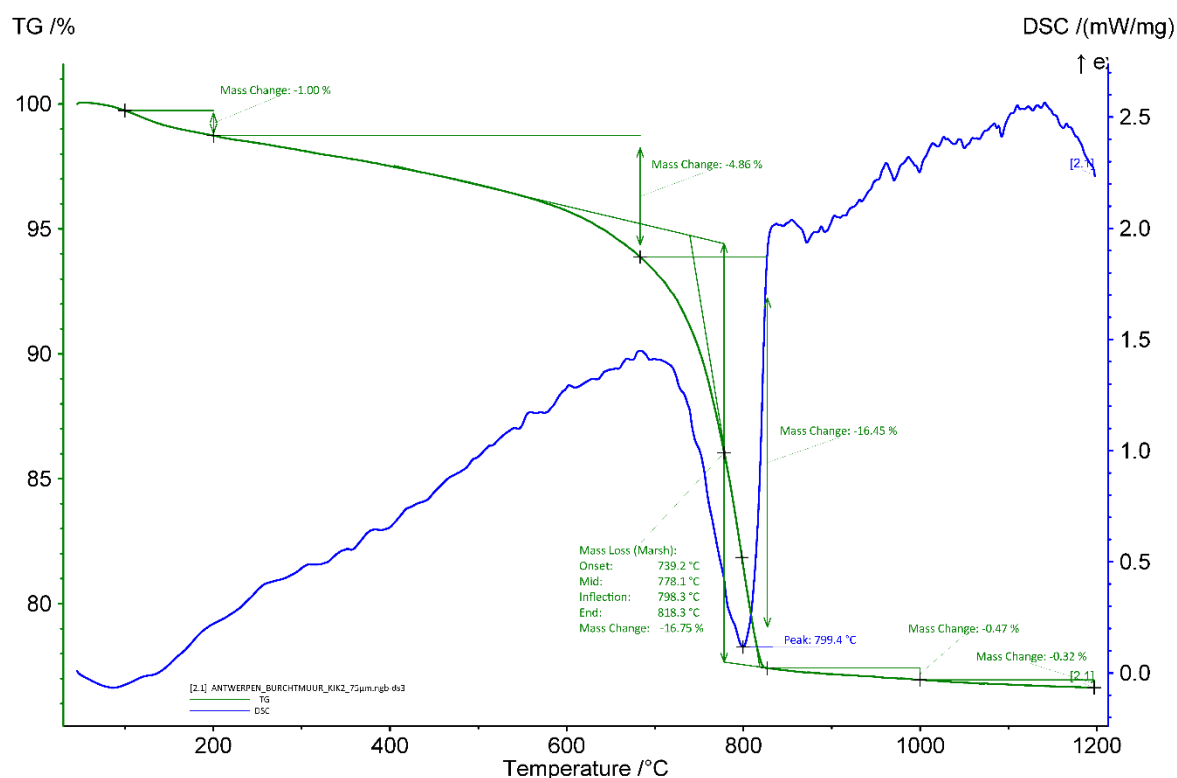
Figure 14: Coupled TG-DSC analysis of the powdered sample KIK2 with particle size <w75 µm upon heating to a temperature of 1200°C at a heating rate of 20°C/min under an inert atmosphere (He flushed at 50 ml/min). The weight loss determined by thermogravimetric analysis (TG, wt%, green curve) and the result of the differential scanning calorimetric analysis (DSC, mW/mg, blue curve) are both presented.
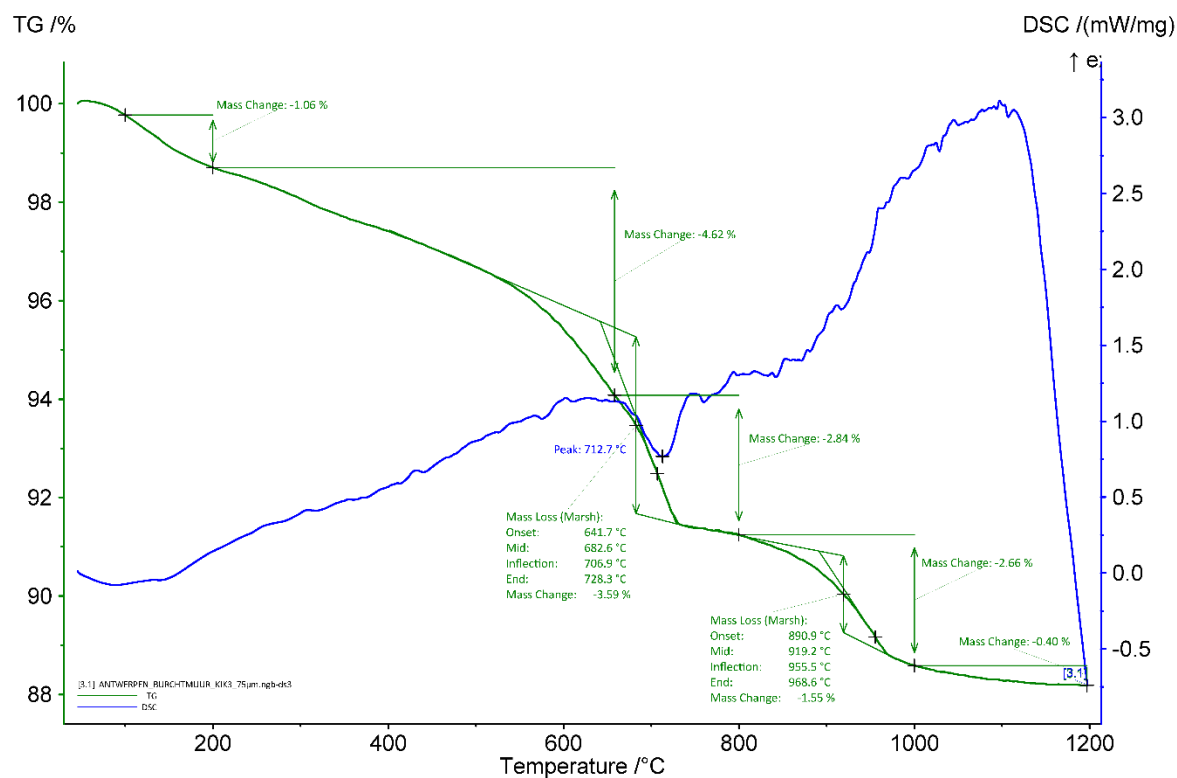
Figure 15: Coupled TG-DSC analysis of the powdered sample KIK3 with particle size <w75 µm upon heating to a temperature of 1200°C at a heating rate of 20°C/min under an inert atmosphere (He flushed at 50 ml/min). The weight loss determined by thermogravimetric analysis (TG, wt%, green curve) and the result of the differential scanning calorimetric analysis (DSC, mW/mg, blue curve) are both presented.

Radiocarbon results

The test prior to the CO_2 extraction revealed a low amount of carbon (Table 4) in the samples (1 to 4 %) showing again the dissolution of the binder. Large quantities of powders with particles size < 75 µm were necessary for the CO_2 extraction (Table 4).

RICH	Sample type	Method	C (%)	σ (%)	m (g)	Age BP extrapolated	Calibrated date (oxcal - 95.4%)	Age BP extrapolated with stat	Calibrated date (oxcal - 95.4%)	Age BP R_combine	Calibrated date (oxcal - 95.4%)	Reliability of dating
30766 (KIK1)	mortar core of the masonry (~50 cm from the wall surface)	HCl (8 fractions)	1.79	1.11	8.47	1120 ± 26	881-994 calAD	1129.8 ± 15.5	885-980 calAD	(last fivre fractions) 970 ± 11	1028-1151 calAD	☒
31536 (KIK2)	mortar outer surface of the masonry	HCl (8 fractions)	3.95	0.14	2.42	1326 ± 20	650-780 calAD	1326 ± 12.8	656-774 calAD	not possible	-	☒
31741 (KIK3)	mortar core of the masonry	HCl (8 fractions)	1.07	0.19	7.60	1192 ± 20	770-890 calAD	1183 ± 11	772-890 calAD	(last 3 fractions) 1064 ± 12	904-1023 calAD	☒

Table 4: Radiocarbon results

For KIK1 (Figure 16), the first fractions are older than last ones which is rather unusual. The extrapolated date (Table 4) is older than the expected date (1000-1200 CE) probably due to the presence of limestone fragments, the dissolution of the binder and the presence of secondary carbonates. The first fractions are spread which is a sign of an unreliable radiocarbon dating. The combination of the last five fractions fall into the expected date but the result cannot be considered as reliable because of the poor state of preservation of the sample.
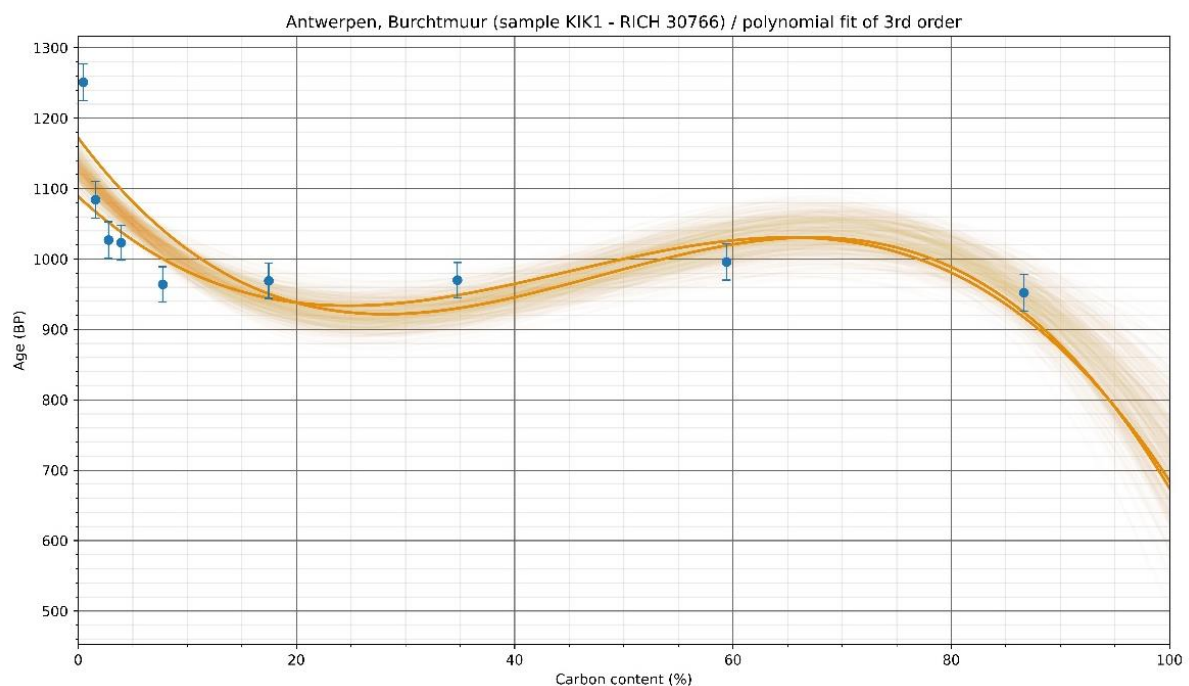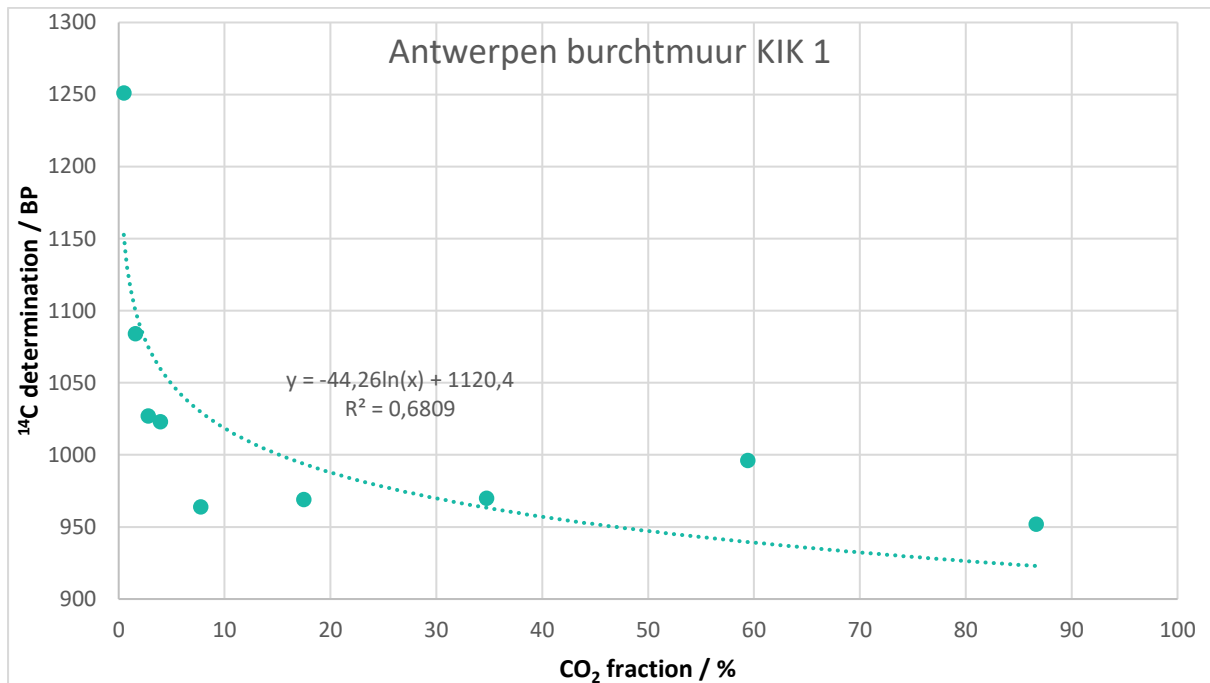
Figure 16: Radiocarbon results for the powdered mortar KIK1 with particles < 75 μm as a function of the CO_2 fraction (the graph at the bottom shows the statistic on the results).

There is a large difference between the first fraction and the next three for KIK2 (Figure 17). This is also uncommon and could be indicative of an unreliable radiocarbon result. The combination of these first fractions was impossible. Again, the extrapolated date is older compared to the presumed historical date probably because of the presence of limestone and secondary carbonates.
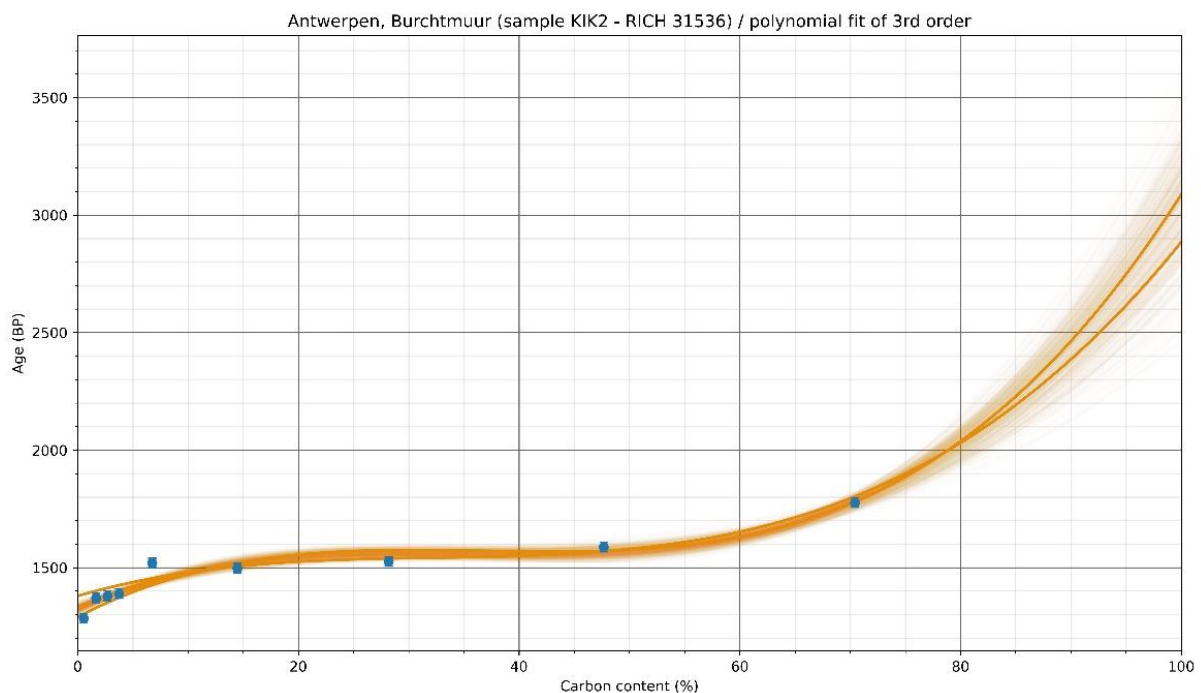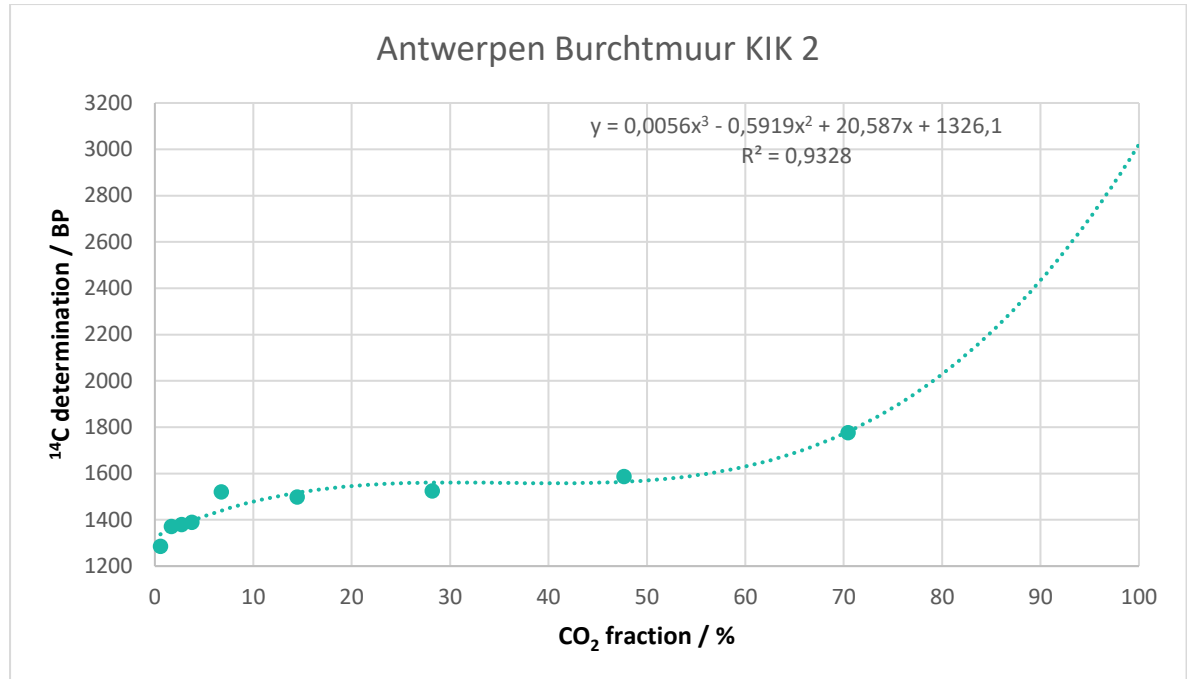
Figure 17: Radiocarbon results for the powdered mortar KIK2 with particles < 75 μm as a function of the CO_2 fraction (the graph at the bottom shows the statistic on the results).

As for KIK1, the radiocarbon dates obtained for the first fractions of KIK3 (Figure 18) are older compared to the last fractions. The first fractions are spread and the last three fractions could be combined to a date close to the expected date of construction of the burchtmuur.

However, as mentioned for KIK1, this result cannot be considered because of the poor state of the sample.
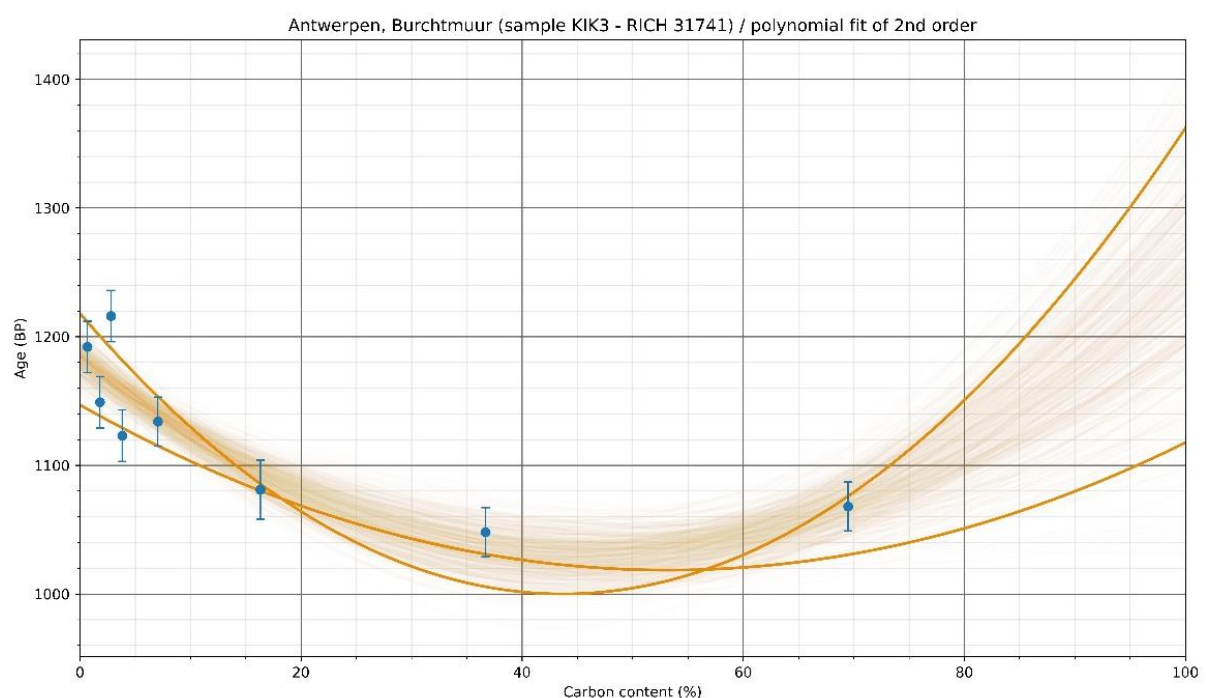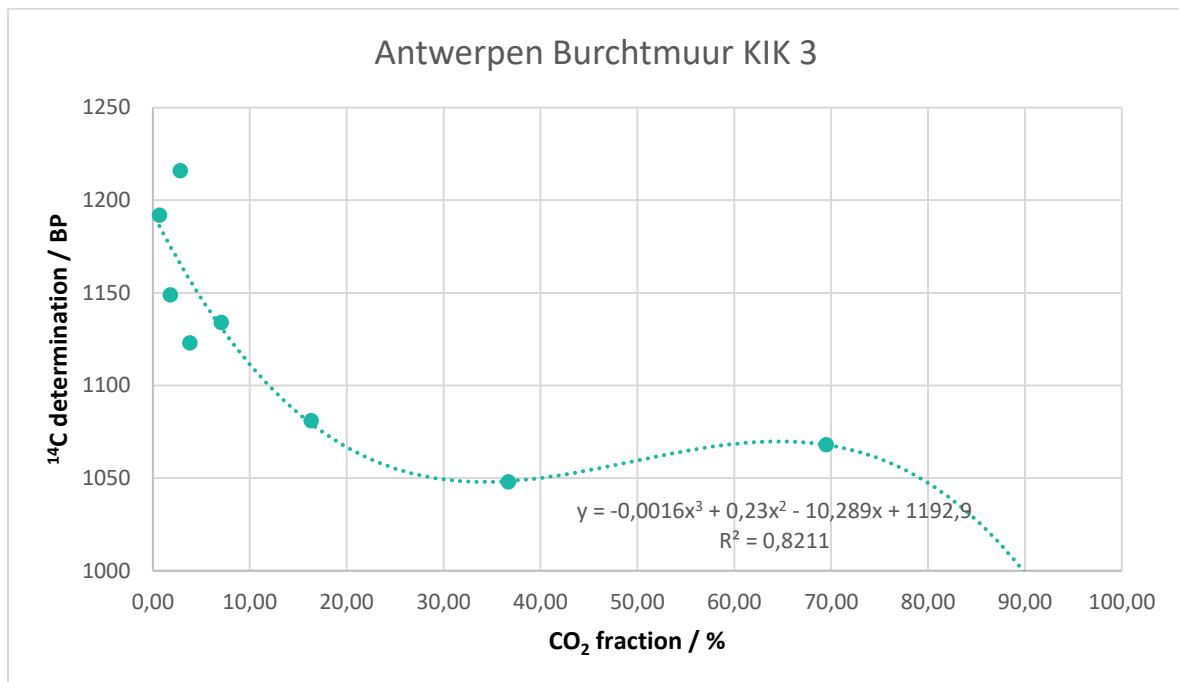
Figure 18: Radiocarbon results for the powdered mortar KIK3 with particles < 75 μm as a function of the CO_2 fraction (the graph at the bottom shows the statistic on the results).

Conclusions

Both of the samples taken deeper in the wall (KIK1 & KIK3) give rather unusual plots for the CO_2 fraction as a function of the ^{14}C determination with the first fractions older than the last ones. The later give an age in accordance with the presume historical date. The sample coming from the surface of the wall (KIK2) give a more common curve but the results are older than

expected. The three samples are in poor condition. They have been dissolved and secondary carbonates are observed in different locations within the matrix. Additionally, they contain limestone and shell fragments. Being located along the river created a moist and inconvenient environment for the preservation of the mortars leading to samples inappropriate for radiocarbon dating.

Study of mortars from Ostia (Italy) for the BRAIN 2.0 PalC project

Context of the site

Ostia is an archaeological site located 30 km far from Rome. The site has a relatively long history of occupation starting as a small Roman colony that later became a major port for the city Rome (Murgatroyd 2016). The state of preservation of the site is remarkable (Bracci et al. 2022) making it suitable for mortar studies (Murgatroyd 2016; Morricone et al. 2013; Baragona, Anghelone, and Weber 2019).
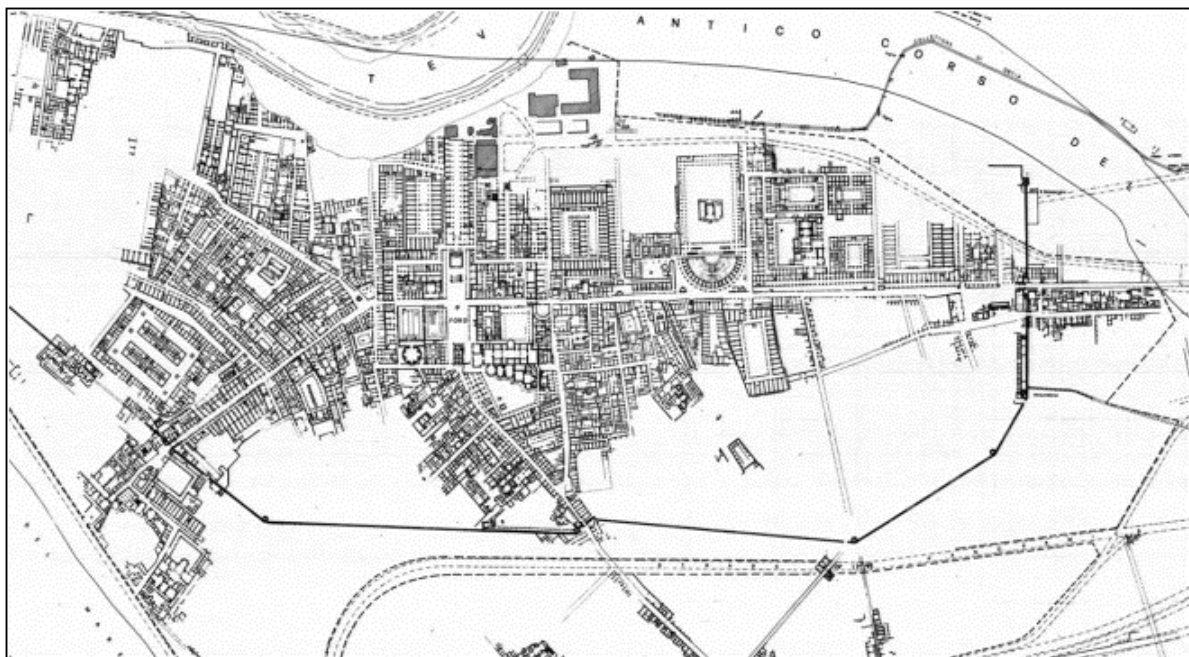
Figure 1: Map of Ostia antica (from Murgatroyd 2016).

Material

Three samples were provided in 2021 by Paolo Tomassini from the Catholic University of Louvain who collaborates with Prof. Nicolas Laubry and Dr. Evelyne Bukowiecki from the École française de Rome: 1) a purple fragment (OS-1) corresponding to the Second Style wall decoration from the excavations of the Caseggiato delle Taberne Finestrate (IV, V, 18) in Ostia and dating from 1st century BC, 2) a yellow fragment (OS-2) with a Fourth Style wall decoration also from the excavations of the Caseggiato delle Taberne Finestrate (IV, V, 18) in Ostia and dating from the second half of the 1st century AD and, 3) a mortar fragment coming from a preparation layer of a wall decoration from the Insula delle Ierodule (III, IX, 6) in Ostia dating from the first half of the 2nd century AD. Only the purple (OS-1) and yellow (OS-2) fragments were provided in quantity large enough (50-80 g) to perform all the required analyses.

Results & Discussion

## *Macroscopic descriptions*

The main colour of the two samples is beige (Figure 2) tending towards very pale brown (210YR 8/2) according to the Munsell soil colour charts. Both are specular probably due to the presence of coarse grains of quartz, mica or well crystallised calcite. They both contain hard black inclusions. The lime lumps appear as white inclusions with a main size of ~ or < 1 mm and the biggest ones measure ~2 or 4 mm. For the purple fragment OS-1, transparent, brown and beige inclusions not reacting with HCl are present and might correspond to silica-based particles (volcanic ash). Only brown and beige inclusions are observed for the yellow fragment OS-2. They shall also be silica-based particles since they don't react from HCl.
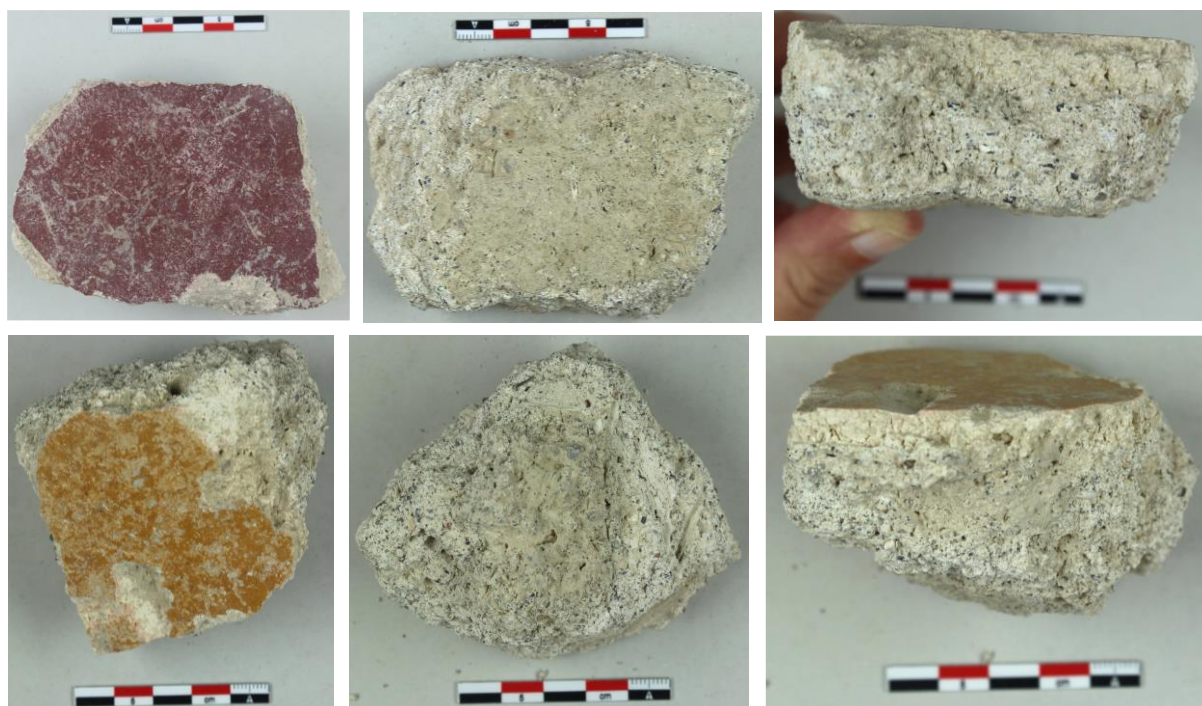
Figure 2: Purple fragment OS-1 (top pictures) and yellow fragment OS-2 (bottom pictures).

Fourier transform Infrared (FTIR) spectroscopy on inclusions and binder

The binders (beige Figure 3) mainly contain calcium carbonates (calcite and aragonite) and silicates. The relative proportion of silicates seems higher in the yellow fragment OS-2 with the presence of clay. The brown inclusions of the two samples both give the signal of calcium carbonates (calcite and aragonite) with a few silicates. The same signal attributed to silicates (volcanic ash) was also obtained for the black inclusions of both samples. The white inclusions are as excepted mainly made of calcite and aragonite. The spectra of the pigments exhibit the vibrational features of calcite, aragonite with silicates including quartz and for the yellow pigment, clay is also present.
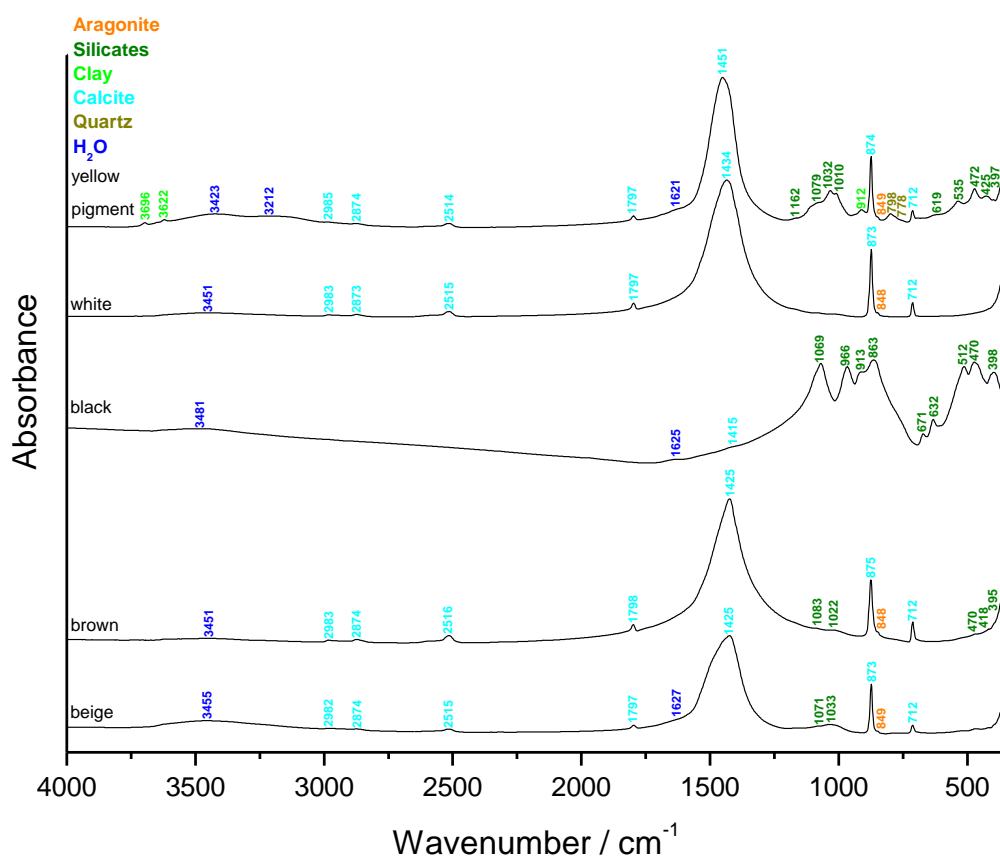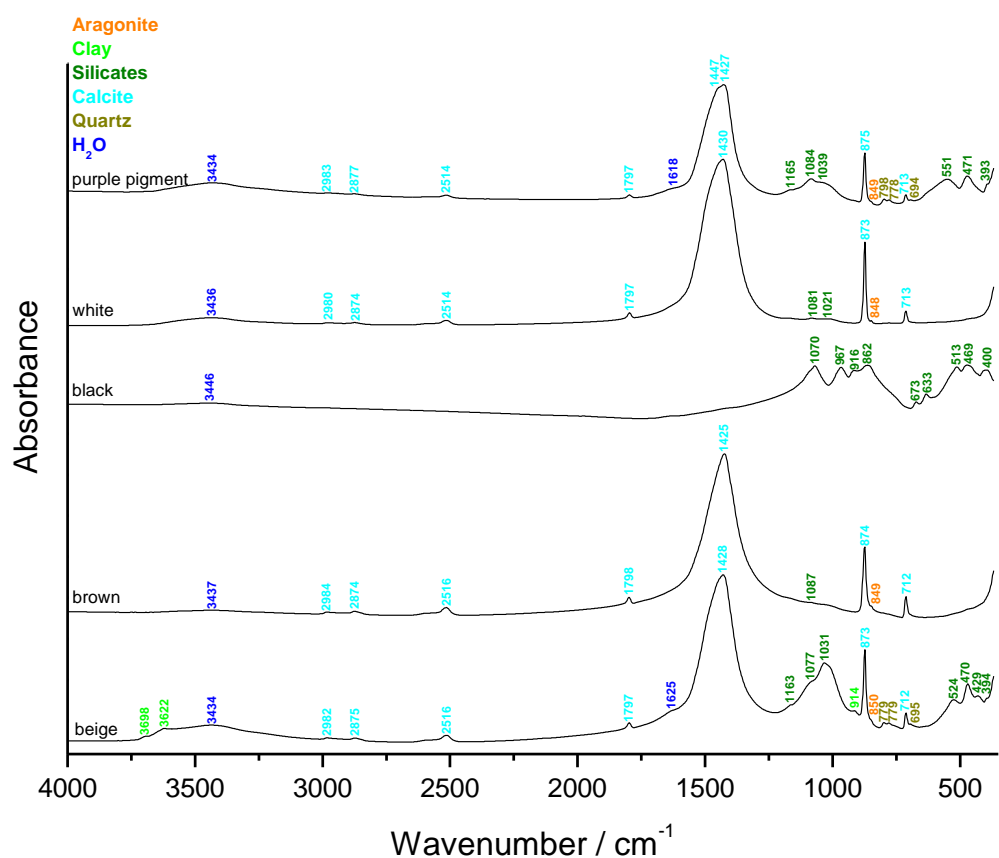
Figure 3: FTIR spectra obtained on the inclusions and binders (beige) of the mortar sample from the purple fragment OS-1 (top) and the yellow fragment OS-2 (bottom).

Binder:aggregate ratio

The calculated binder:aggregate ratio using a bulk density of 1.35 kg/dm^3 for the sand and 0.575 kg/dm^3 for the lime is close to 3:2 in volume unit for the mortar OS-1 and around 2:1 for the sample OS-2.

	OS-1	OS-2
Sample weight (g)	2.2	2.2
Crucible weight (g)	18.3	18.7
Weight calcined (g)	19.6	20.0
%ins	**60.9**	**57.8**

Table 1: Percentage of insoluble residue.

Cathodoluminescence

Cathodoluminescence observations of the thin section made from the purple fragment OS-1 shows the presence of limestone in bright red and K-feldspar in bright blue in the *arricio*, *intonaco* and *rinzaffo* (Figure 4a & b). Some limestone grains ended up in the fraction of powder with particle size < 75 μm as well as some K-felspar grains (Figure 4c). The same observations can be made for the yellow fragment (Figure 4d-f). The observation of the powder with particle size < 75 μm shows a very bright red result that might indicate a high concentration of limestone (Figure 4f).
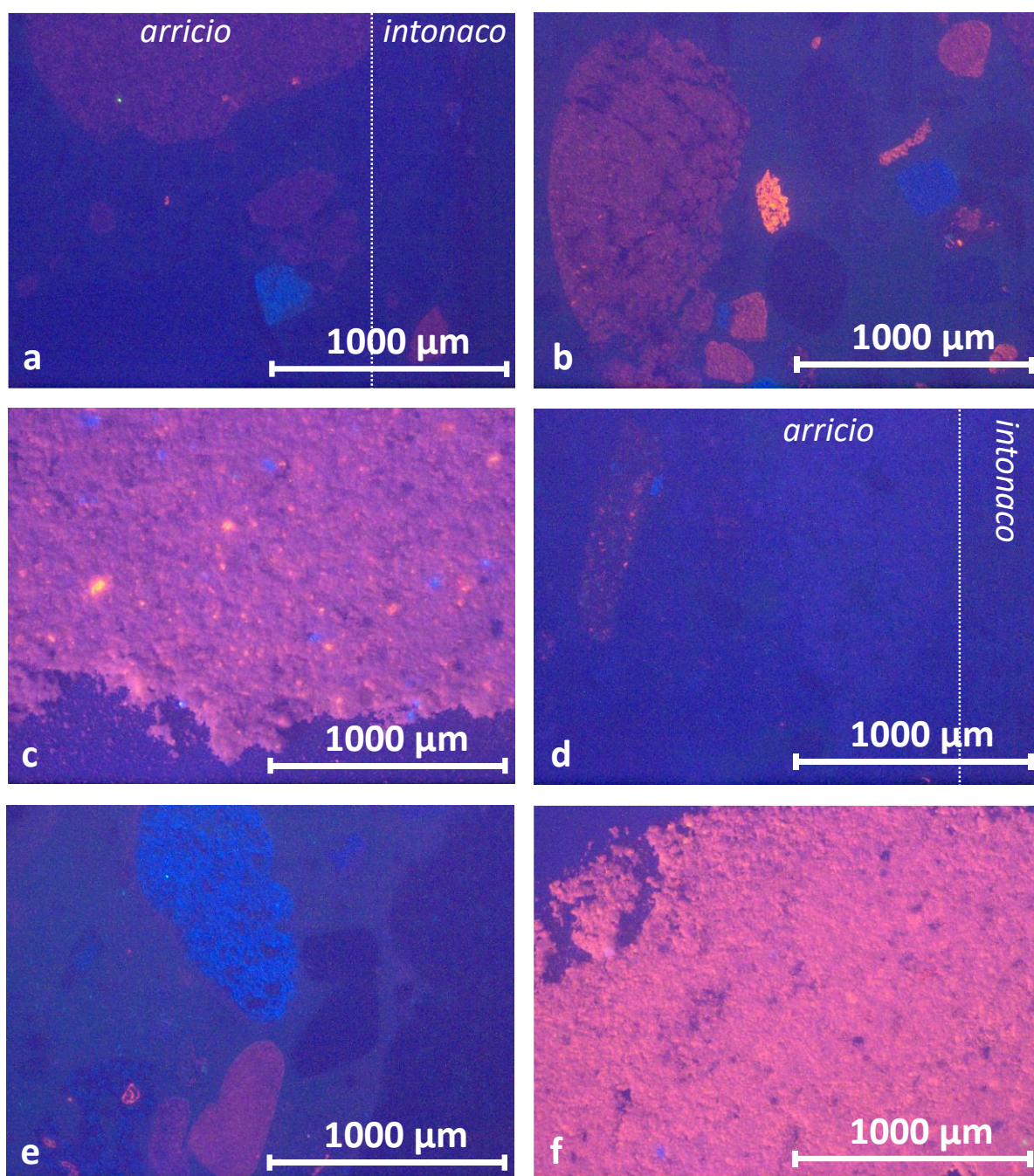
Figure 4: Characteristic cathodoluminescence images of a) the thin section X2272 of the purple fragment OS-1 showing the arricio and intonaco, b) the thin section X2272 of the purple fragment OS-1 showing the *rinzaffo*, c) the powdered *rinzaffo* of the purple fragment OS-1 with particle size lower than 75 μm, d) the thin section X2273 of the yellow fragment OS-2 showing the arricio and intonaco, e) the thin section X2273 of the yellow fragment OS-2 showing the *rinzaffo*, f) the powdered *rinzaffo* of the yellow fragment OS-2 with particle size lower than 75 μm.

Thin-section petrography

The mortar of the purple fragment OS-1 is well preserved and contains completely burnt lime lumps (Figure 5 and Table 2). Two types of grains are found in the aggregate of the *rinzaffo*: different kinds of limestone grains (micritic, micro-sparitic, partially to totally silicified) and siliceous (volcanic) sand grains. The fact that these two types of grains are found together might

347

suggests the use of beach sand for the aggregate, with a possible deliberate addition of crushed volcanic scoria. The arricio only contains crushed recrystallised sedimentary limestone (not shown, because not dated).
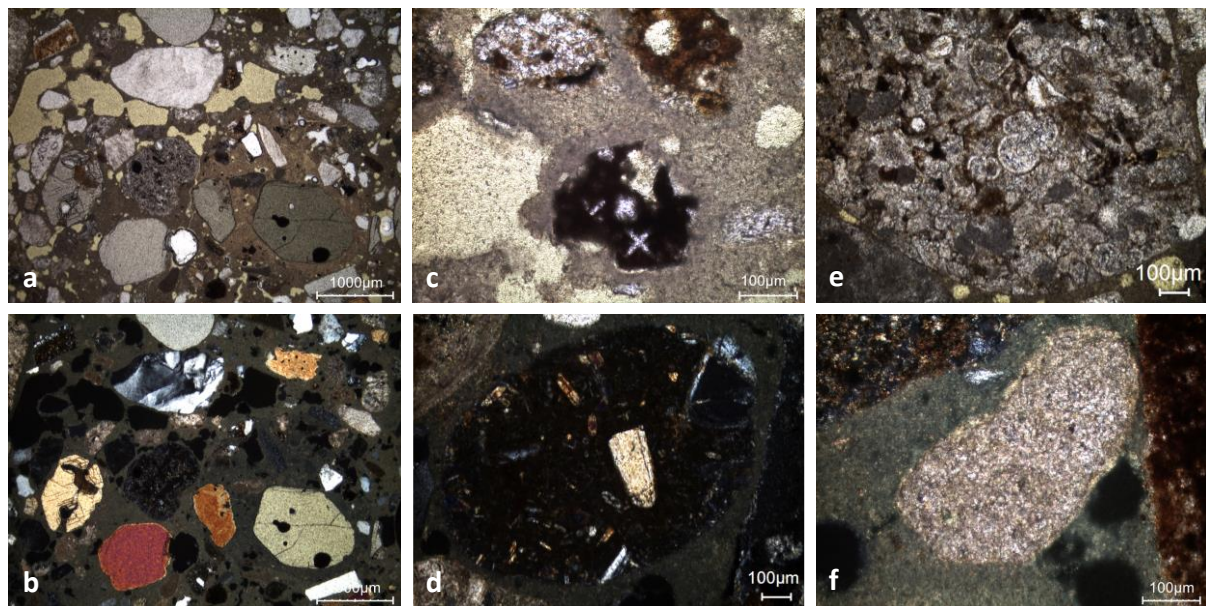
Figure 5: Representative photomicrographs of the OS-1 thin-section X2272 showing different features of the *rinzaffo*: a) overview image in plain polarised light (PPL) with quartz, pyroxene and olivine; b) same overview image in cross polarised light (XPL); c) PPL image showing *pozzolane rosse* scoria; d) XPL image of a lava clast; e) PPL image of partially silicified limestone fragment and f) XPL image showing a microsparitic limestone inclusion.

Binder	**Texture**	micritic
	Lump state	completely burned
	Lump size	from 55 to 1040 μm
	Lump frequency	few
Aggregate	**Grain size**	very fine to very coarse
	Mineralogy	mixed aggregate containing siliceous (volcanic) sand (feldspars, pyroxene, olivine, *pozzolane rosse* scoria, lava clast) with limestone grains / bioclasts
	Shape	various
Appearance	**Homogeneity**	relatively heterogeneous
	Macroporosity	low in *arricio* & intonaco / medium in *rinzaffo*
	Pore structure	irregular / sometimes connected
Admixtures	**Type**	-

Alteration	**Type**	-

Table 2: Main characteristics of the rinzaffo layer from the purple fragment OS-1 retrieved from the observations of the thin-section X2272.

Figure 6 and Table 3 present the main characteristics extracted from the petrographic observations of the yellow fragment OS-2. The *rinzaffo* (dated part) is in good state. It contains various types of siliceous (volcanic) grains, some having pozzolanic properties (seen thanks to the presence of reaction rims) in addition to limestone grains. The fact that these two types of grains are found together might suggests the use of beach sand for the aggregate, with a possible deliberate addition of crushed volcanic scoria.
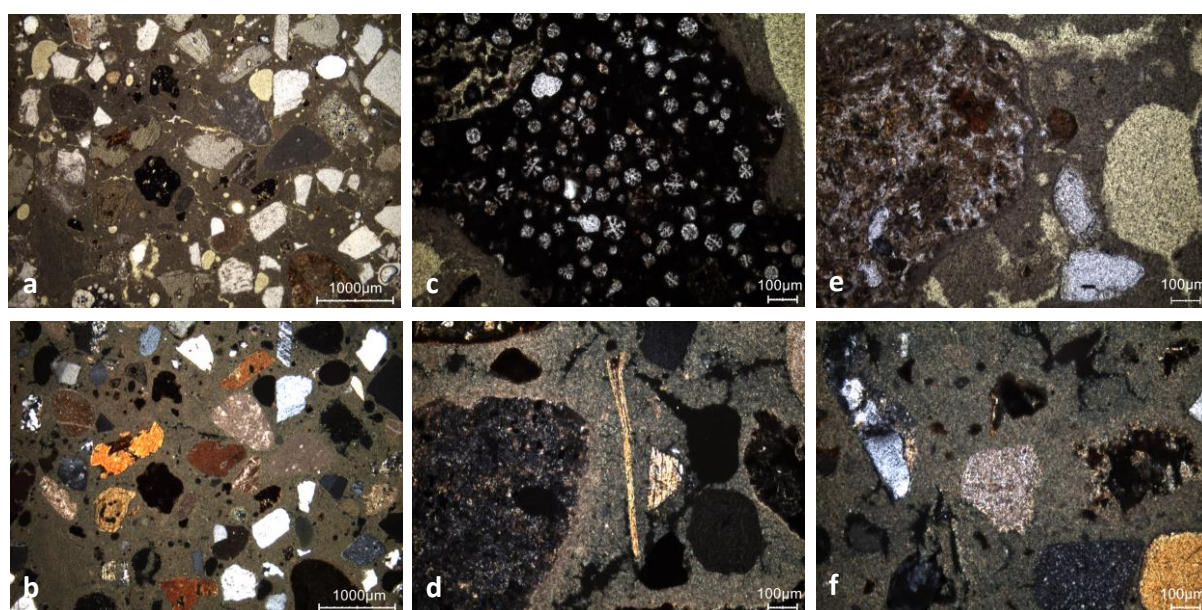
Figure 6: Representative photomicrographs of the OS-2 thin-section X2273 showing different features of the *rinzaffo*: a) overview image in plain polarised light (PPL); b) same overview image in cross polarised light (XPL); c) PPL image showing italite clasts (leucite + clinopyroxene); d) XPL image of lava clast on left, mica in the middle and pyroxenes on right; e) PPL image showing a pozzolanic reaction rim around a volcanic fragment and f) XPL image showing a limestone inclusion.

Binder	**Texture**	micritic
	Lump state	completely burned in *rinzaffo*
	Lump size	around 300 µm
	Lump frequency	few
Aggregate	**Grain size**	very fine to very coarse
	Mineralogy	siliceous (volcanic) sand with limestone grains
	Shape	various
Ap pe	**Homogeneity**	relatively heterogeneous

	Macroporosity	medium
	Pore structure	irregular (often rounded) & cracks
Admixtures	Type	-
Alteration	Type	-

Table 3: Main characteristics of the rinzaffo layer from the yellow fragment OS-2 retrieved from the observations of the thin-section X2273.

Thermogravimetric analysis (TGA) on whole samples

The graphs of the thermal analyses are presented in Figures 7. The apparent hydraulicity indexes (aHI) determined on the basis of the weight loss between 200 and ca. 650°C (usually attributed to water loss from calcium-silicate-hydrates-phases) show that the mortar binder is slightly hydraulic for sample OS-1 (16 %) and moderately hydraulic for sample OS-2 (19 %). The amount of carbonates is ~41 wt% for the mortar OS-1 and 36 wt% for OS-2. The main weight loss of ancient mortars is expected between 600 and 900 °C and is indicative of the decomposition of calcium carbonate ($CaCO_3$) into calcium oxide (CaO) and carbon dioxide (CO_2) (Ahmmed et al. 2024). The end temperature of calcium carbonate decomposition is ~820°C for OS-1 and 815°C for OS-2. No gypsum nor quartz were detected.
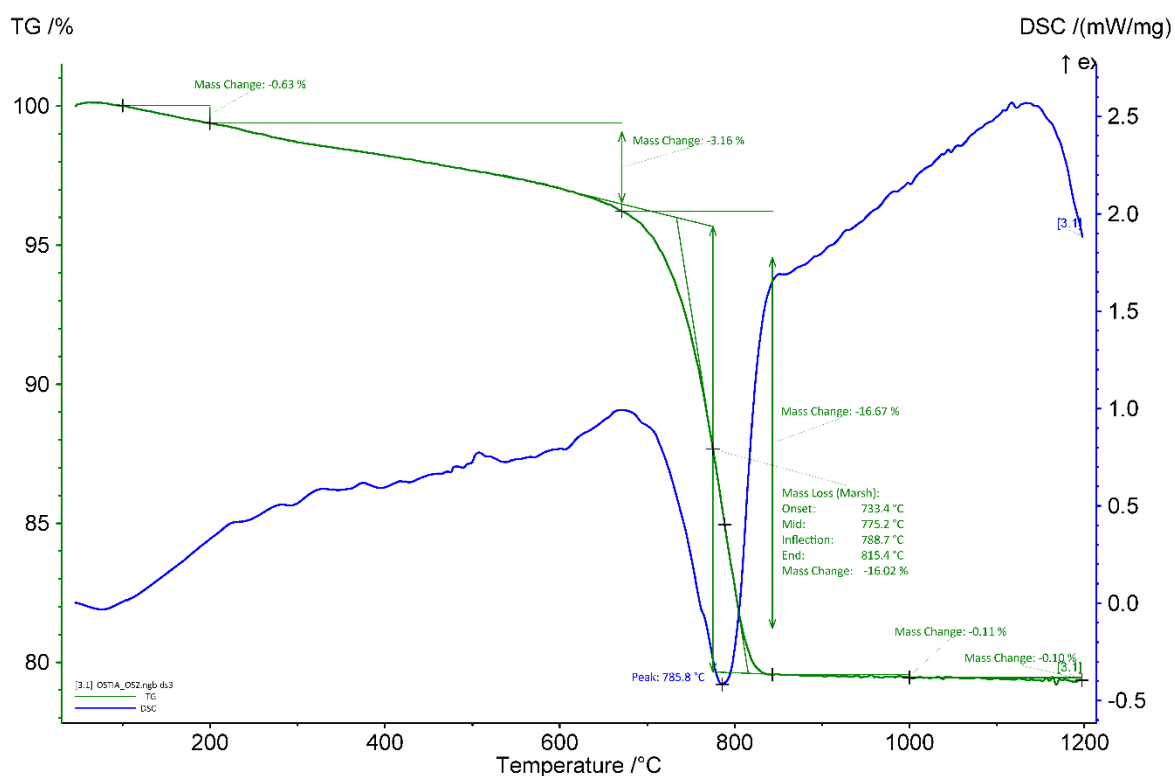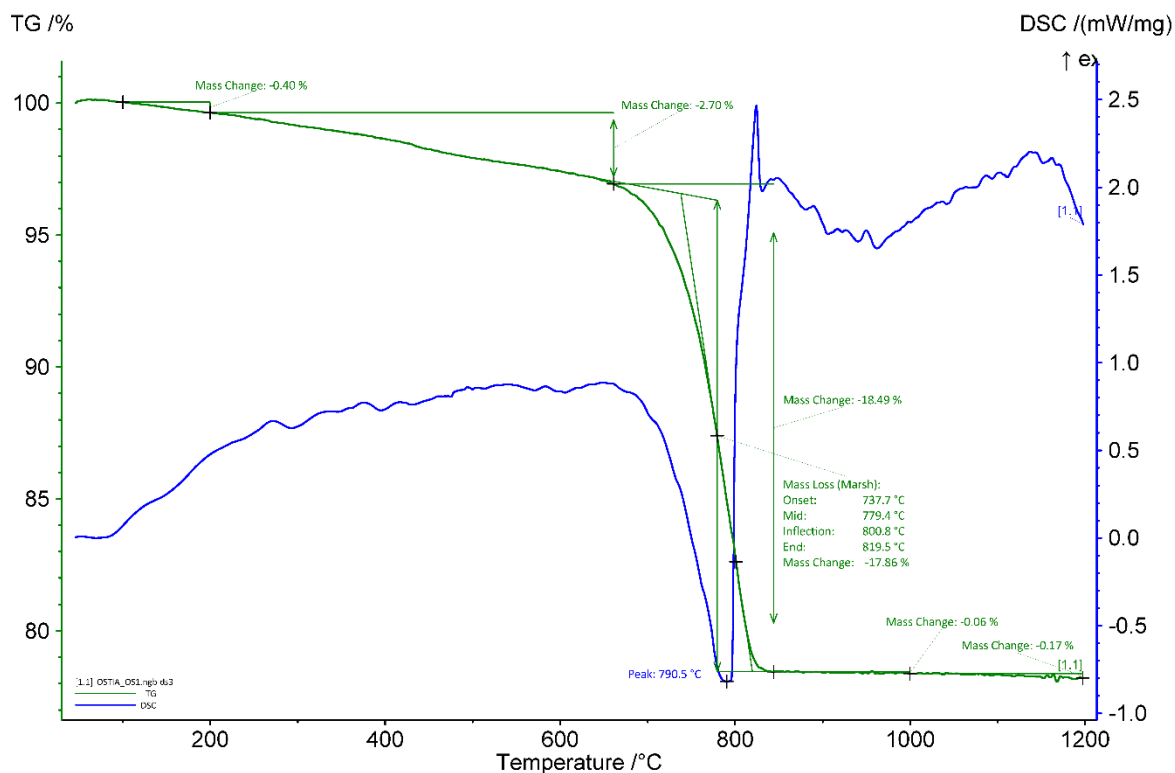
Figure 7: Coupled TG-DSC analysis of the mortars OS-1 (top) and OS-2 (bottom) upon heating to a temperature of 1200°C at a heating rate of 20°C/min under an inert atmosphere (He flushed at 50 ml/min). The weight loss determined by thermogravimetric analysis (TG, wt%, green curve) and the result of the differential scanning calorimetric analysis (DSC, mW/mg, blue curve) are both presented.

Grinding/particle separation

Before grinding, the darker layer present on the internal surface (see Figure 2 middle) was scratched away. The sides were also cleaned by scratching. The *rinzaffo* was separated from the *arricio* with hammer and chisel. For OS-1, a low amount (~0.5 g) of particles < 75 μm was obtained after grinding.

FTIR on powders with particle size <75 μm

The FTIR spectra (Figure 8) of both samples used for radiocarbon dating exhibit similar features: the ones of calcite, silicates including quartz, aragonite, and organic matter. In addition, the spectrum of OS-1 shows the presence of clay (Figure 8 top).
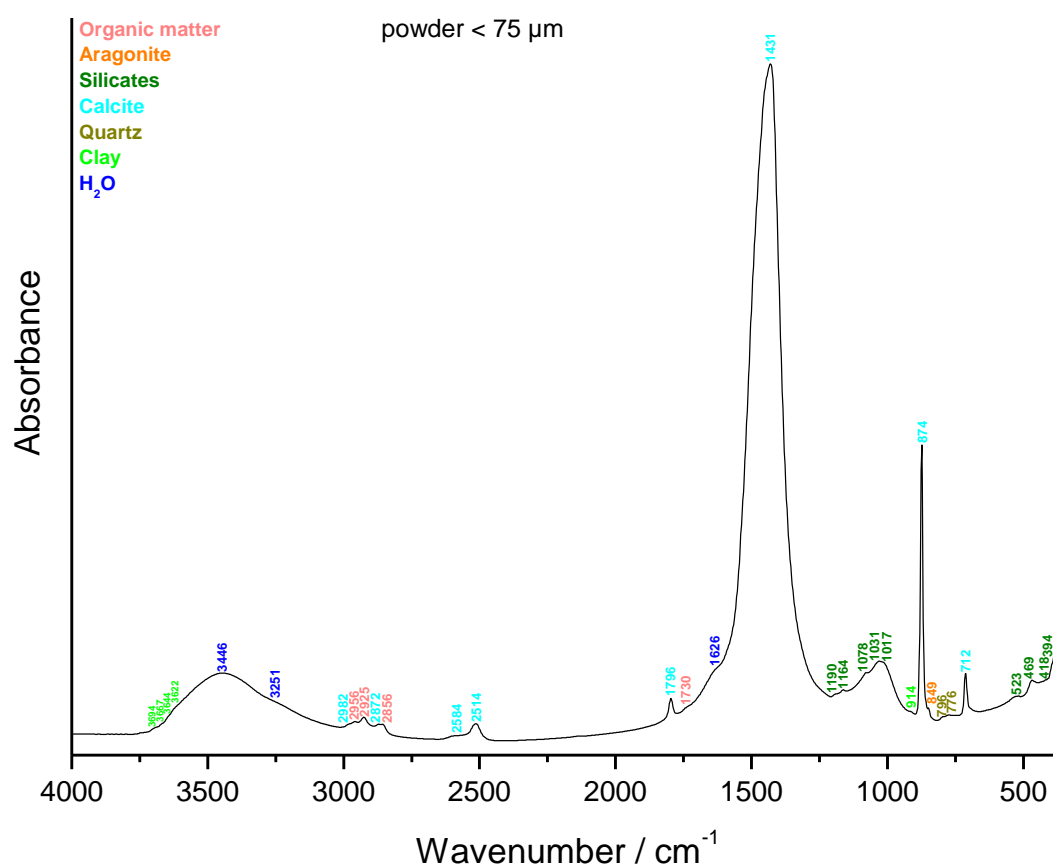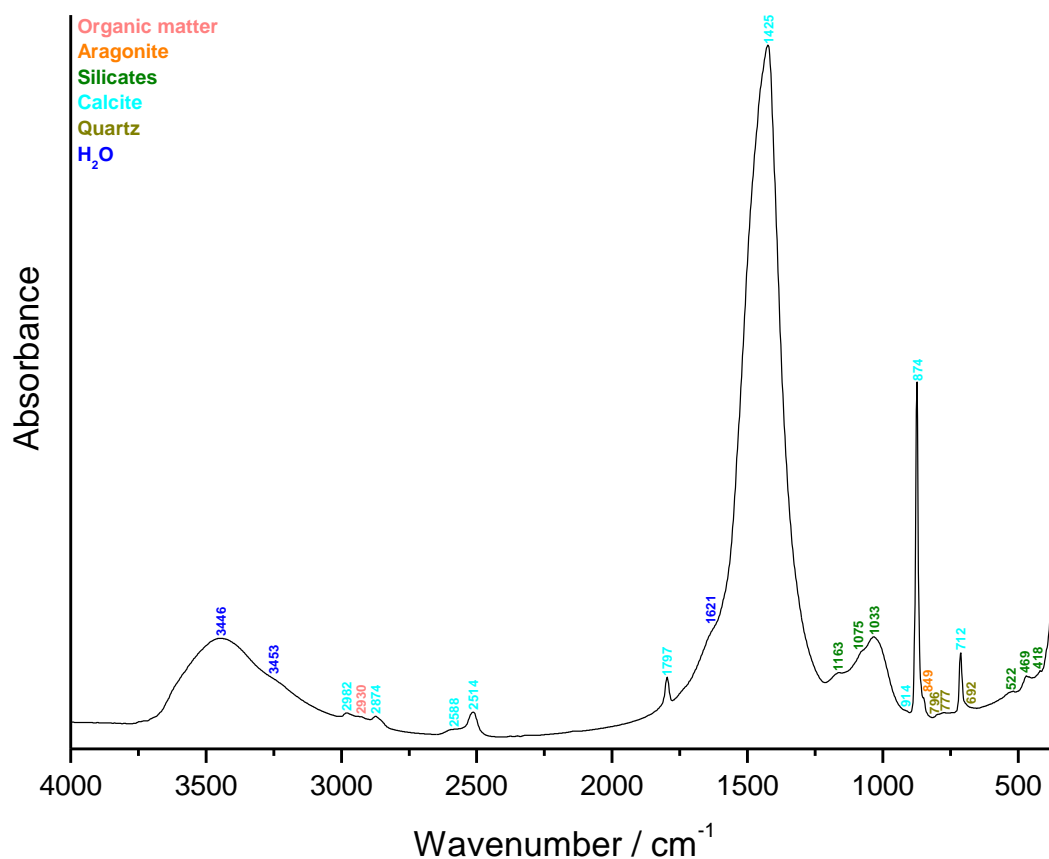
Figure 8: FTIR spectra obtained on the powders with particle size < 75 µm of the mortar sample from the purple fragment OS-1 (top) and from the yellow fragment OS-2 (bottom).

TGA on powders with particle size <75 µm

The aHI of the powders with particles < 75 µm, determined on the basis of the weight loss between 200 and ca. 650°C, are 17 % for OS-1 and 21 % for OS-2 (Figures 9 and 10). The obtained values on powders are thus similar those of whole samples. The quantity of carbonates is higher in the powders compared to the whole samples since a large part of the aggregate is removed (67 and 68 wt% for OS-1 and OS-2, respectively). The end temperatures of calcium carbonate decomposition are ~834 and 841°C for the powdered samples OS-1 and OS-2, respectively. It is higher compared to the whole samples. A possible explanation could be that the powder is more pure compared to the whole mortar sample which increases the decomposition temperature. The splitting of the peak attributable to the outgassing of CO_2 from the calcite might due to measurement artefact.
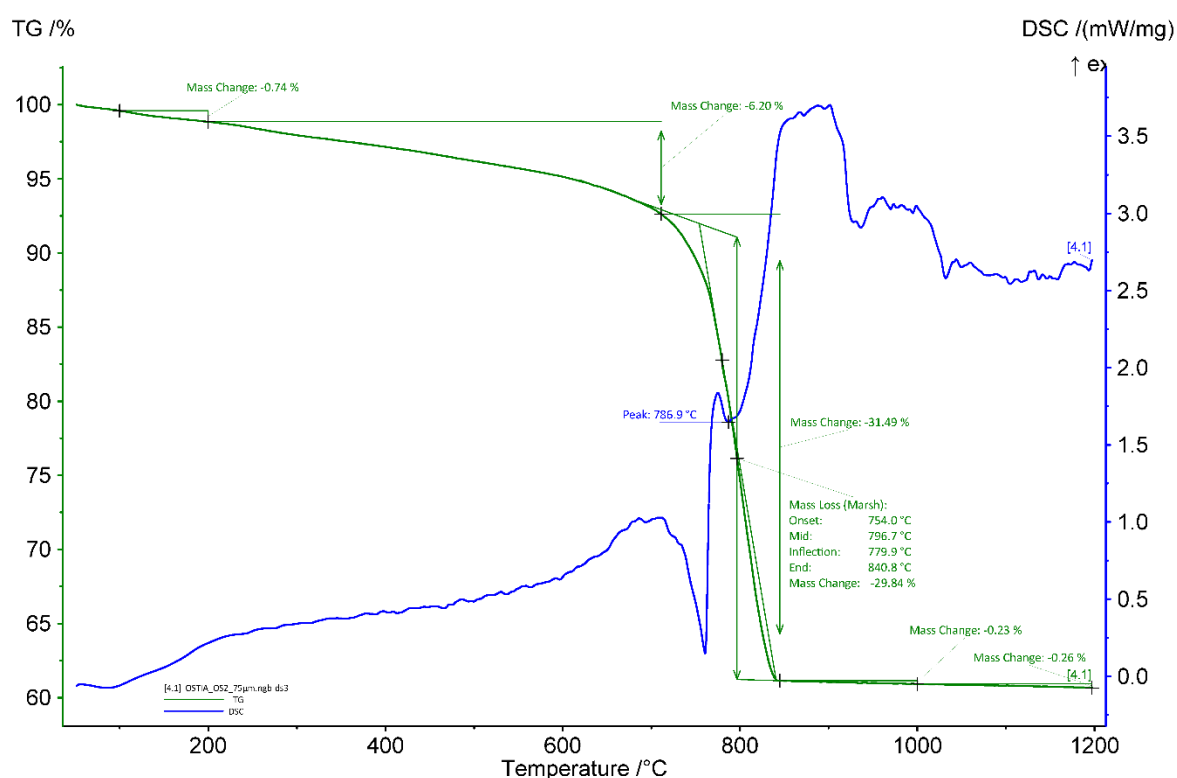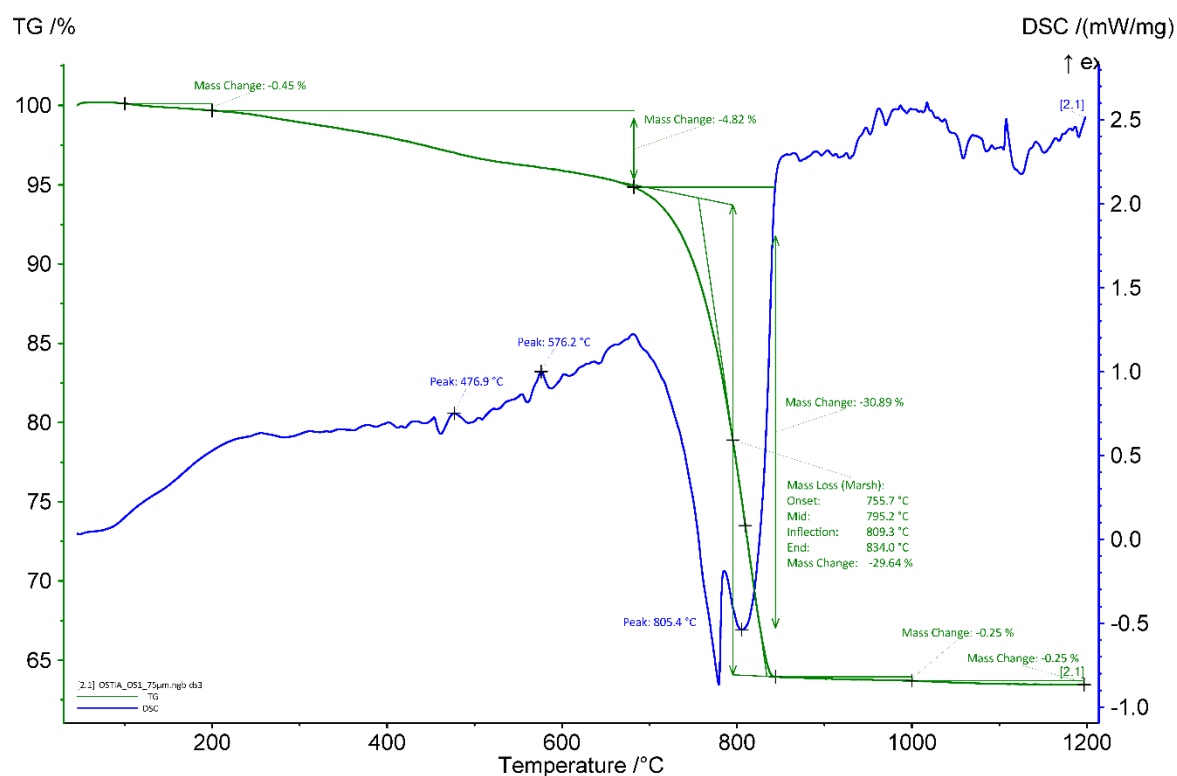
Figure 9: Coupled TG-DSC analysis of the powdered mortars OS-1 (top) and OS-2 (bottom) with particle size < 75 μm upon heating to a temperature of 1200°C at a heating rate of 20°C/min under an inert atmosphere (He flushed at 50 ml/min). The weight loss determined by thermogravimetric analysis (TG, wt%, green curve) and the result of the differential scanning calorimetric analysis (DSC, mW/mg, blue curve) are both presented.
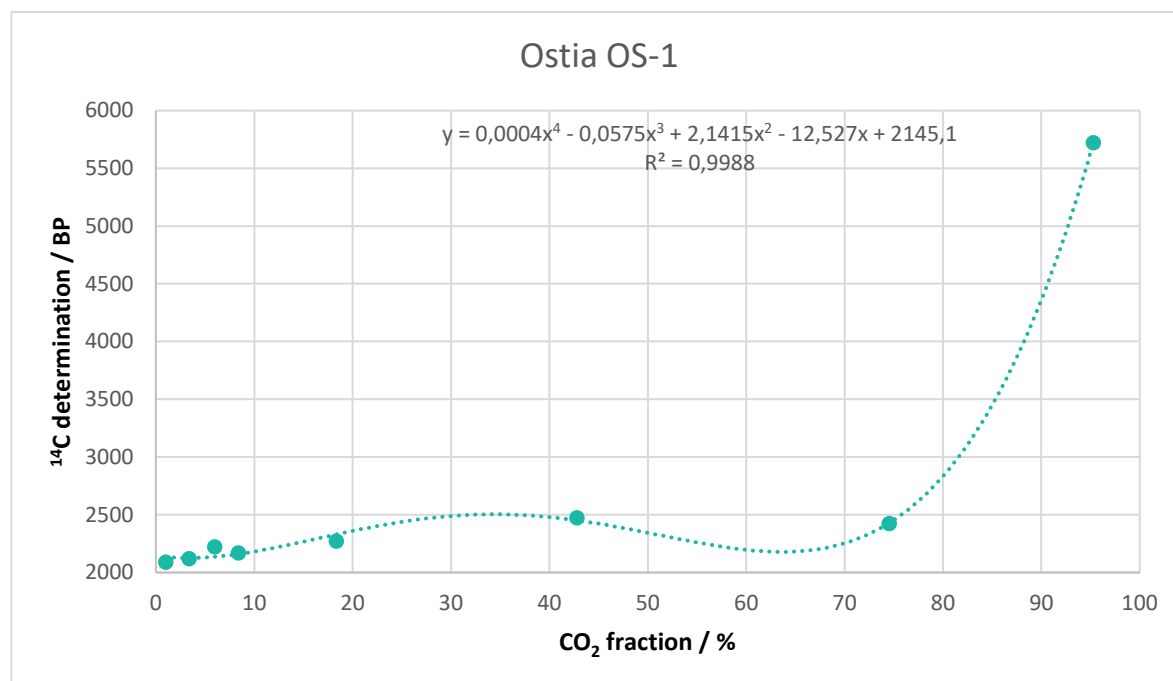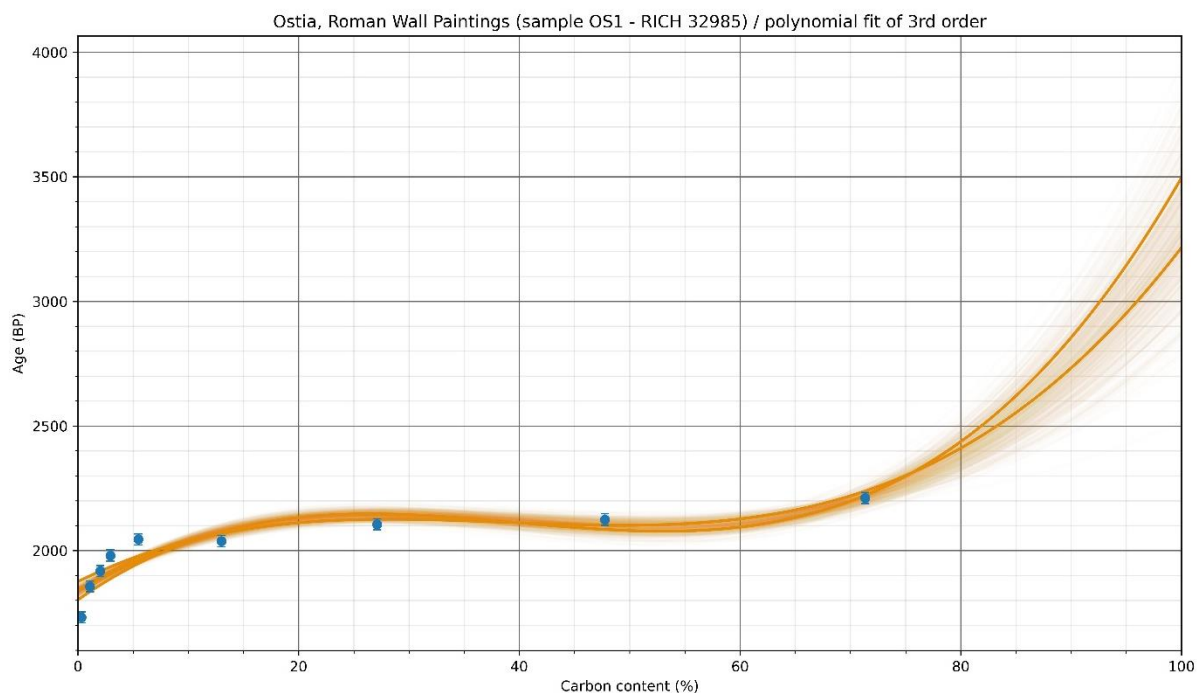
Radiocarbon results

The test prior to the CO_2 extraction revealed a fair amount of carbon (Table 4) in the samples (~6 or 7 %).

| RICH	Sample type	Method	C (%)	σ (%)	m (g)	Age BP extrapolated	Calibrated date (oxcal - 95.4%)	Age BP extrapolated with stat	Calibrated date (oxcal - 95.4%)	Age BP average (R_combine)	Calibrated date (oxcal - 95.4%)	Reliability of dating
32985 (OS-1)	*rinzaffo*	HCl (8 fractions)	7.13	-	0.49	2145 ± 27BP	350-50 calBC	1837.9 ± 13.3BP	132-244 calAD	(2 first fractions) 2105 ± 19BP	180-40 calBC	☑
33172 (OS-2)	*rinzaffo*	HCl (8 fractions)	7.58	0.31	1.38	1856 ± 22BP	120-240 calAD	1665.6 ± 39.6BP	256-537 calAD	-	-	☒

Table 4: Radiocarbon results

For OS-1, the procedure gathering the first four individual percents of CO_2 (1, 2, 3 and 4 %) was not possible because of the low amount of powder < 75 μm available (~0.5 g). The measurements were performed at ~2, 5, 7, 10, 30, 60, 90 and 100 % (Figure 10). Despite the measurement being more spread compared to the recommended procedure, the result obtained by combining the two first fractions and the extrapolated date are in accordance with the historical date (first half of 1st century BC, Table 4). However, the statistic on the results give an age that is too young.
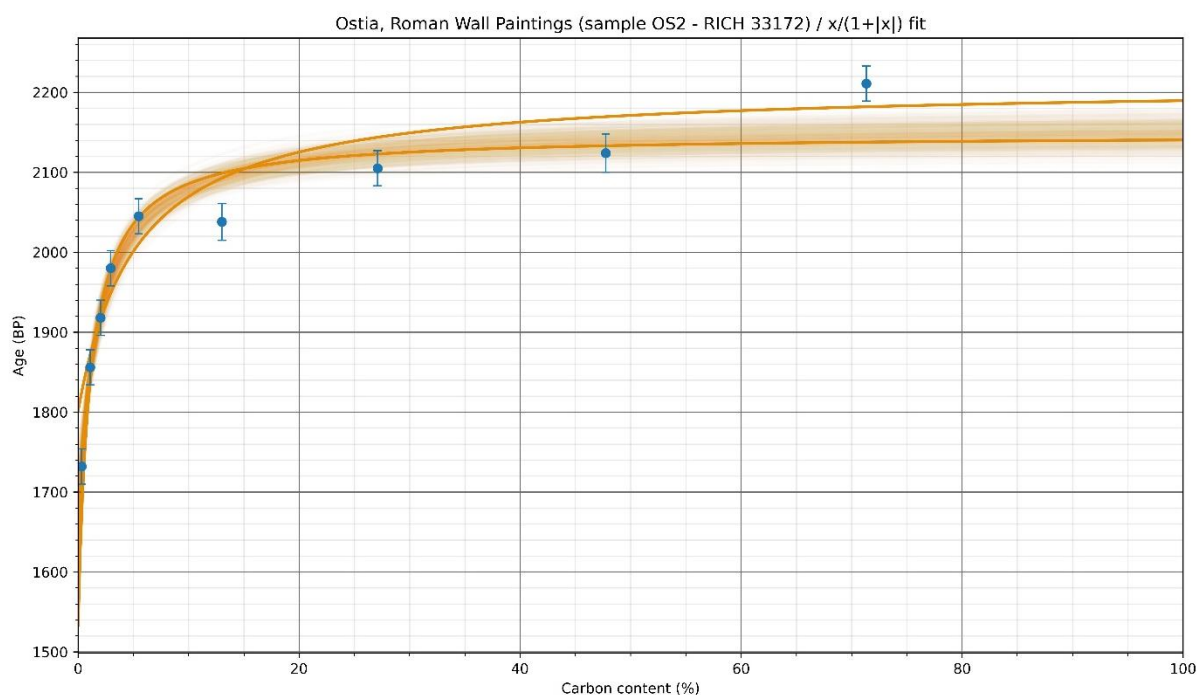
Figure 10: Radiocarbon results for the powdered *rinzaffo* OS-1 with particles < 75 µm as a function of the CO_2 fraction (the graph at the bottom shows the statistic on the results).

Even though the fractions 1, 2, 3 and 4 percent of CO_2 could be gather for OS-2 since enough powder was available, the results of the ^{14}C determination are widely spread (Figure 11). For this reason, the radiocarbon date of the first fractions could not be combined. The extrapolated date (120-240 calAD) is older compared to the expected date (second half of the 4th century AD). This shall be attributed to the presence of limestone grains (dead carbon) in the aggregate. This effect has certainly been partly counterbalanced by the slower carbonation speed indicated by the presence of pozzolanic reaction rims (Figure 6e) that would result in a younger date. However, in this case, the statistic on the results helped obtaining a plausible date (256-537 calAD).
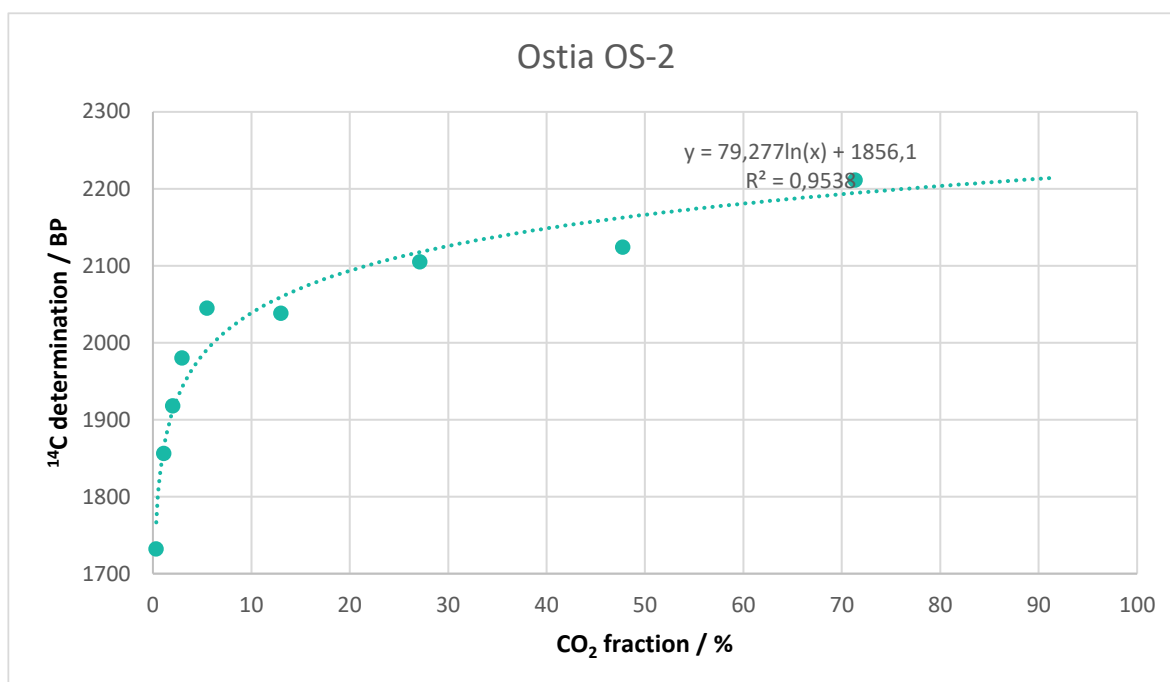
Figure 11: Radiocarbon results for the powdered *rinzaffo* OS-2 with particles < 75 μm as a function of the CO_2 fraction (the graph at the bottom shows the statistic on the results).

Conclusions

OS-1 is well preserved, it is only slightly hydraulic and shows two radiocarbon calculation results within the expected historical date. It is then considered reliable for radiocarbon dating. OS-2 contains more limestone that ended up in large quantity in the powdered binder fraction used for radiocarbon dating according to the cathodoluminescence observations. It is also more hydraulic and the radiocarbon dating are spread. It is a not reliable sample for radiocarbon dating.

Bibliography

Ahmmed, Tanjil, Ana Raquel Silva, José Carlos Quaresma, Patrícia Moita, and Cristina Galacho. 2024. "Analytical Characterization of Historical Mortars from the Roman Villa of Frielas (Loures, Portugal)." *Acta IMEKO* 13 (3): 1–11.

Baragona, Anthony J., Marta Anghelone, and Johannes Weber. 2019. "A Map Is Worth a Thousand Pictures: Using FTIR-Imaging to Analyze Petrographic Thin Sections of Historical and Experimental Mortar." In *5th Historic Mortars Conference RILEM Proceedings Pro 130*, 482–94. RILEM Publications.

Bracci, Susanna, Emma Cantisani, Claudia Conti, Donata Magrini, Silvia Vettori, Paolo Tomassini, and Martina Marano. 2022. "Enriching the Knowledge of Ostia Antica Painted Fragments: A Multi-Methodological Approach." *Spectrochimica Acta Part A: Molecular and Biomolecular Spectroscopy* 265:120260.

Morricone, Andrea, Andrea Macchia, Luigi Campanella, Massimiliano David, Stefano de Togni, Marcello Turci, Adriana Maras, Costantino Meucci, and Sara Ronca. 2013. "Archeometrical Analysis for the Characterization of Mortars from Ostia Antica." *Procedia Chemistry* 8:231–38.

Murgatroyd, Jennifer. 2016. "Ancient Mortar Production in Ostia, Italy: Builders and Their Choices." PhD Thesis, University of Oxford.

Study of mortars from Castle of Horst (Holsbeek) for the BRAIN 2.0 PalC project

Context of the site

Horst Castle (Figure 1) is located in Sint-Pieters-Rode (borough of Holsbeek in Flanders). The history of the site seems to start around 1151 when the Lords of Horst Ruger van Linden and his son Iwein, came to settle (Herremans, 2021). Amelric Boot(e) is historically seen as the commissioner of the castle. He bought a 'hof' that followed the structure that would nowadays be classified as an early medieval castle in 1369. When he passed away in 1405, his daughter sold the castle to her cousin Almeric Pynnock, who transformed the fortified farm into a moated castle. It officially appears in writings in 1434, when it is described as a moated castle used as a base for hunting parties. The castle was set on fire by the Leuveners during the unrest under Maximilian I in 1489. Only the donjon tower (where the samples we analysed come from), a part of the entrance gate and defensive wall remained standing after this catastrophe (Herremans, 2021). The castle was then owed by a succession of families until it was sold in 2007 by the countess de Hemricourt de Grunne to the Flemish region.

Figure 1: Castle of Horst courtyard (left) and donjon (right).

Materials

Three mortars/plasters were sampled in June 2021 on the demand of Marjolein Deceuninck (study bureau Fenikx): KVH1, KVH2 and KVH3 in the donjon tower (Figure 2).
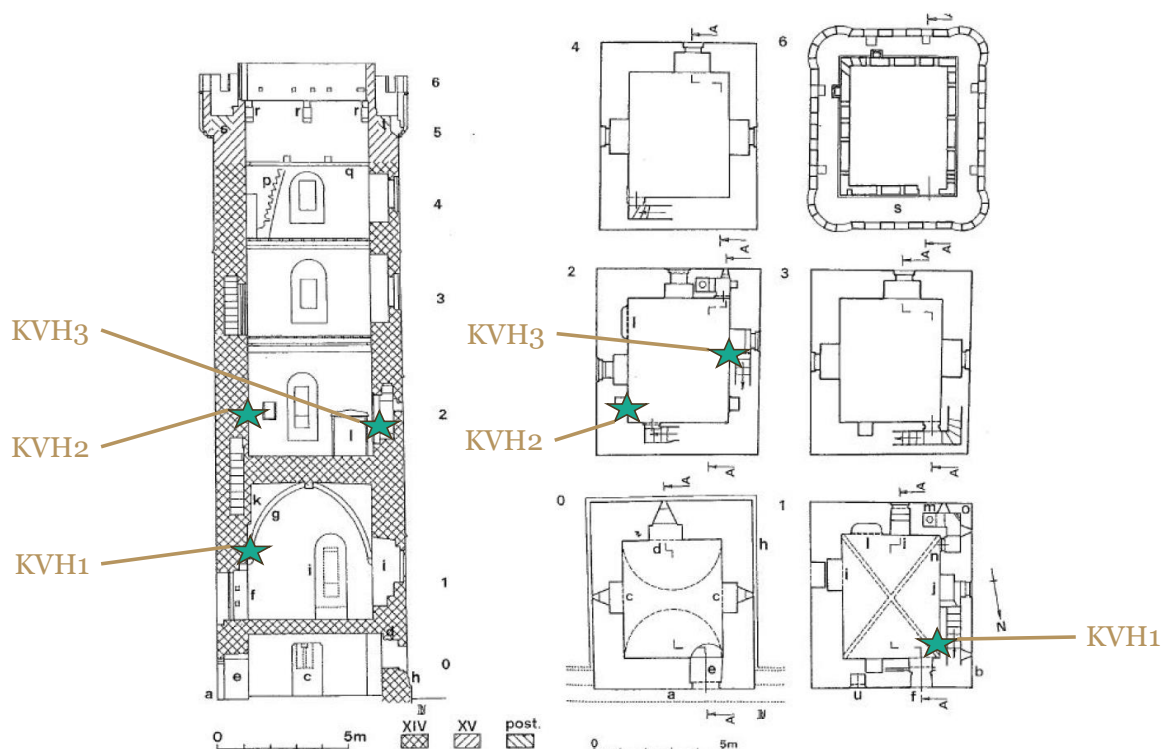
Figure 2: Location of the samples in the donjon tower (plans modified from Doperé & Ubregts 1991).

KVH1 was sampled in the first level of the donjon. It is a thin layer of beige plaster (0.5 to 2 mm). A wooden door in the same room was dated with dendrochronology to 1420-30 (Figure 3, right). It shows a relief engraving of a stag bowing down and the same painting is present on the wall (Figure 3, left). This wall painting is thought to date from the construction of the castle between 1375 and 1400.

Figure 3: Wooden door in the first level of the donjon dated with dendrochronology to 1420-30 (right) and wall painting (left) discovered in 1985. The wall painting covers the entire walls and vault and consists of a regular repetition of the same motif on a red background: a kneeling stag on a blue background surrounded by a trilobed decorative motif.

We sampled in a corner (Figure 4, left) and we were extra careful to avoid the obvious repair of the crack (white in Figure 4, left). The repair was also sampled to be analysed with Fourier transformed infrared spectroscopy (FTIR). The two other samples were taken from the second level of the donjon on opposite walls. One was a pink plaster (KVH2 – Figure 4, middle) sampled in the middle of the wall and the other a bedding mortar (KVH3 – Figure 4, left) at

the right corner facing the window in between bricks. KVH3bis was sampled two bricks on top.

Figure 4: Sampling KVH1, KVH2, KVH3, and KVH3bis.

Results & Discussion

Macroscopic descriptions

The main colour of the KV1 and KVH3 is beige (Figure 5) tending towards pale yellow (2.5Y 8/3) for KVH1 and white (10YR 8/1) for KVH3; KVH2 is pink (5YR 8/3) according to the Munsell soil colour charts. KVH1 and KVH2 are slightly specular, probably due to the presence of coarse grains of quartz, mica or well crystallised calcite. The lime lumps appear as white inclusions with a main size of ~ or < 1 mm and the biggest ones measure ~4 or 5 mm. KVH1 presents a brown inclusion probably made of ferruginous sandstone, there is a fine pink layer on its surface and some red coming from the bricks is spread on the back of some pieces. KVH2 also shows some brick residues and grey inclusions probably made of siliceous aggregates.

Some red inclusions are observed in KVH3 that are probably sandstone and brown ones that probably come from soil.


Figure 5: Beige plaster first level KVH1 (left), pink plaster second level KVH2 (middle) and bedding mortar second level KVH3 (right).

Fourier transform Infrared (FTIR) spectroscopy on inclusions & binder

The binders (beige or pink, Figure 6) mainly contain calcium carbonates (calcite and aragonite) and silicates. The later include quartz and clay in the case of KVH2. The binders of KVH2 and KVH3 also contain nitrates due to weathering. The lime lumps (white, Figure 6) are also mainly made of calcium carbonates (calcite and aragonite) in addition to silicates and nitrates for KVH2 and KVH3. The brown inclusion in KVH1 is made of silicates including quartz and clay and also contains calcite and nitrates. The pink paint layer on top of the plaster comprises calcium carbonates (calcite and aragonite), silicates (including quartz and clay) and nitrates. The spectrum of red spread on the back of the plaster shows features of calcite, nitrates and silicates including quartz. The grey inclusions observed for KVH2 are not composed of siliceous aggregates as described in the macroscopic description but are limestone grains (calcite, aragonite and nitrates). The brick residues (red, Figure 6 KVH2) contain silicates including quartz, haematite and nitrates. All the features present in the spectrum of the brown inclusion of KVH3 couldn't be attributed. It contains a hight content of nitrates with calcite, silicates and other features possibly from the presence of organic matter. The red/purple inclusion in KVH3 is made of silicates including quartz, nitrates and organic matter.
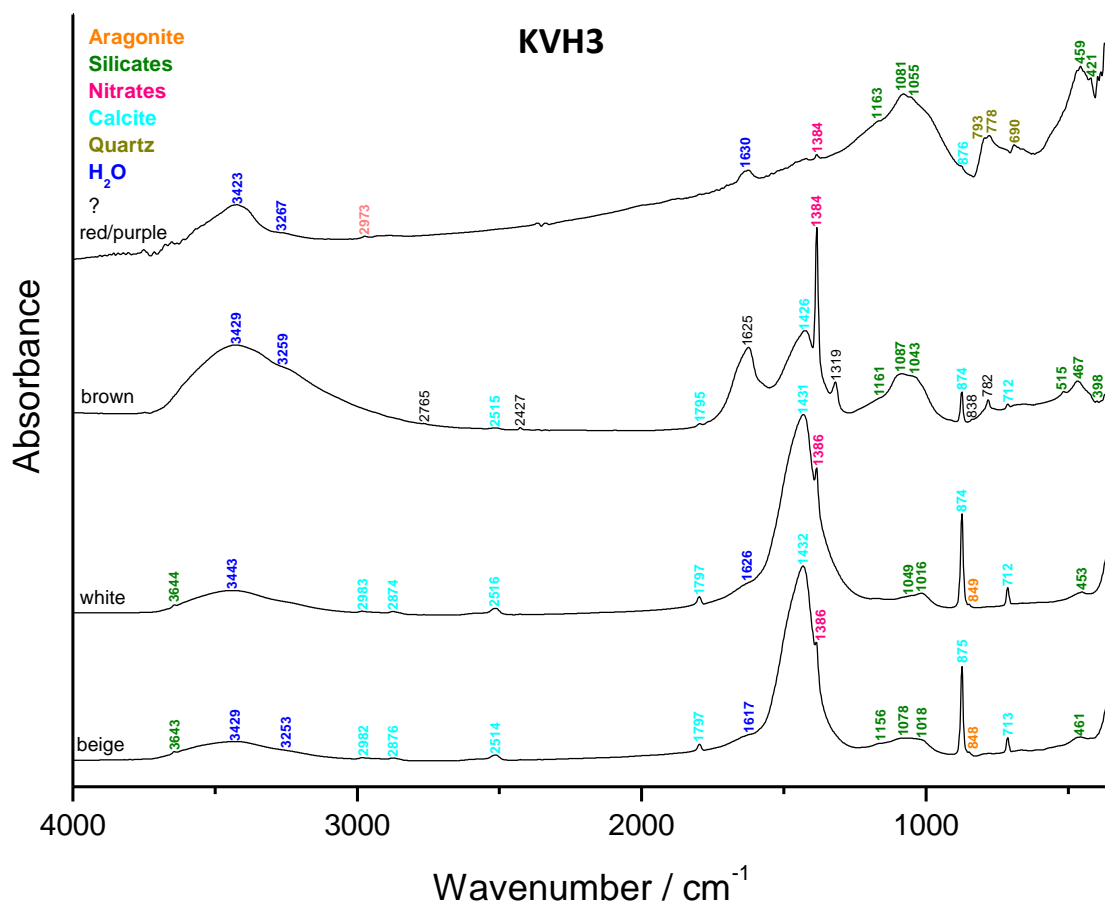
Figure 6: FTIR spectra obtained on the inclusions and binder (beige or pink) of KVH1 (top), KVH2 (middle) and KVH3 (bottom).

For KVH1, two other samples were analysed by FTIR (Figure 7). The first one is the repair grout below KVH1. The spectrum shows the presence of calcite, aragonite, silicates and apatite. The second sample analysed is a piece of plant material found when crushing KVH1. The FTIR analyses confirms that it is composed of cellulose and lignin with calcite and silicates.
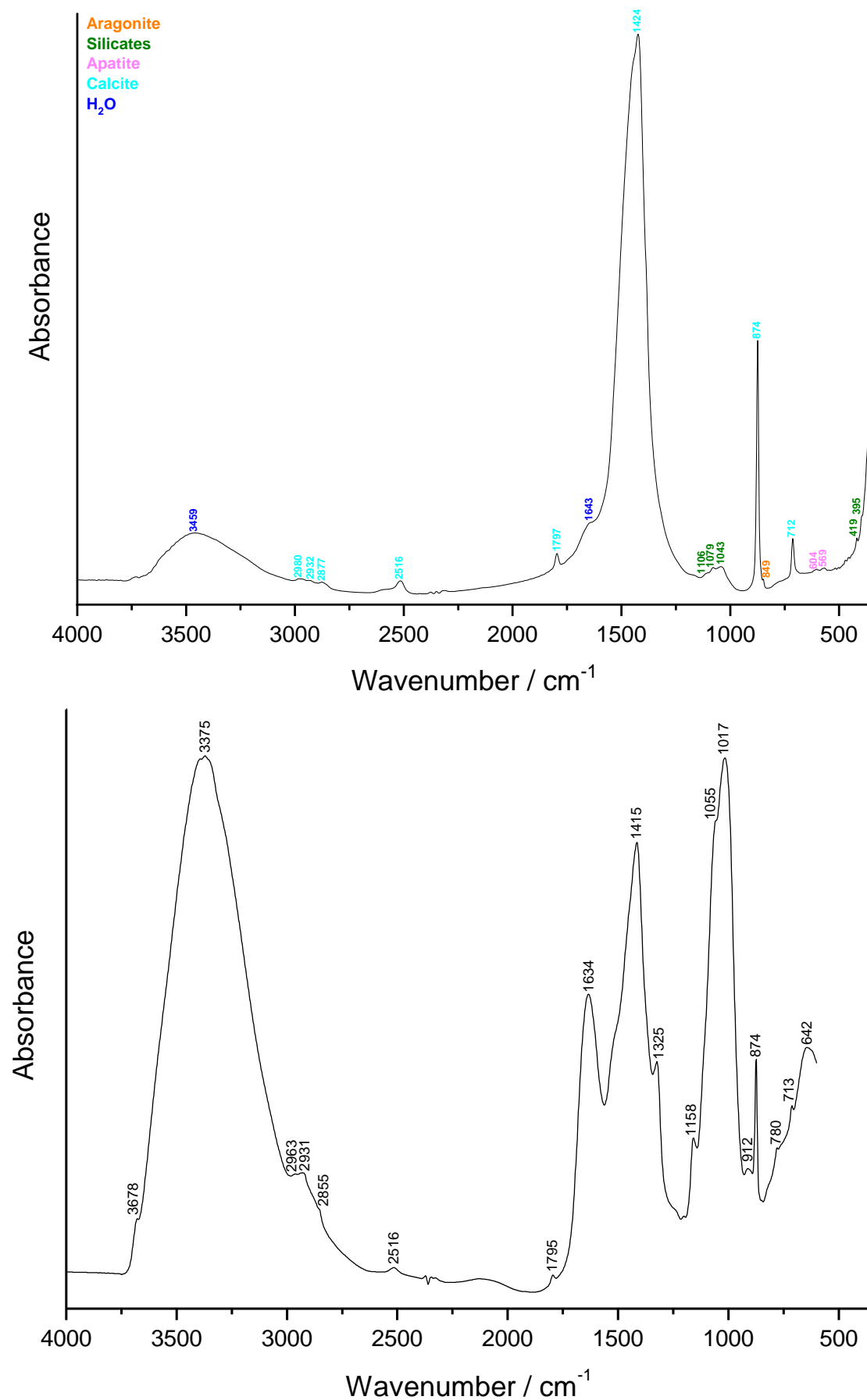
Figure 7: FTIR spectra of the repair grout of the crack near KVH1 (top) and of the piece of plant material found inside the KVH1 (bottom).

Binder:sand ratio

The calculated binder:sand ratio using a bulk density of 1.35 kg/dm^3 for the sand and 0.575 kg/dm^3 for the lime is around 1:1 in volume unit for the three samples.

	KVH1	KVH2	KVH3
Sample weight (g)	1.6	1.8	1.9
Crucible weight (g)	17	19.3	19.3
Weight calcined (g)	18.0	20.6	20.5
%ins	**68.3**	**70.3**	**63.9**

Table 1: Percentage of insoluble residue.

Cathodoluminescence

Cathodoluminescence observations of the three thin-sections and powders show similar results (Figure 8). The thin-sections exhibit the presence of quartz grains with a dark purple hue, K-feldspars in bright blue and the binder is dull. For KVH1 (Figure 8a), the paint layer on top of the plaster appears as bright red and probably contains limestone powder (it was removed before grinding the sample for dating). The powdered samples display mainly a red tile colour (binder) with a few bright blue K-feldspars, also some plagioclases green grains for KVH1 (Figure 8b) and a few bright red limestone grains for KVH1 and KVH3 (Figures 8b and 8f).
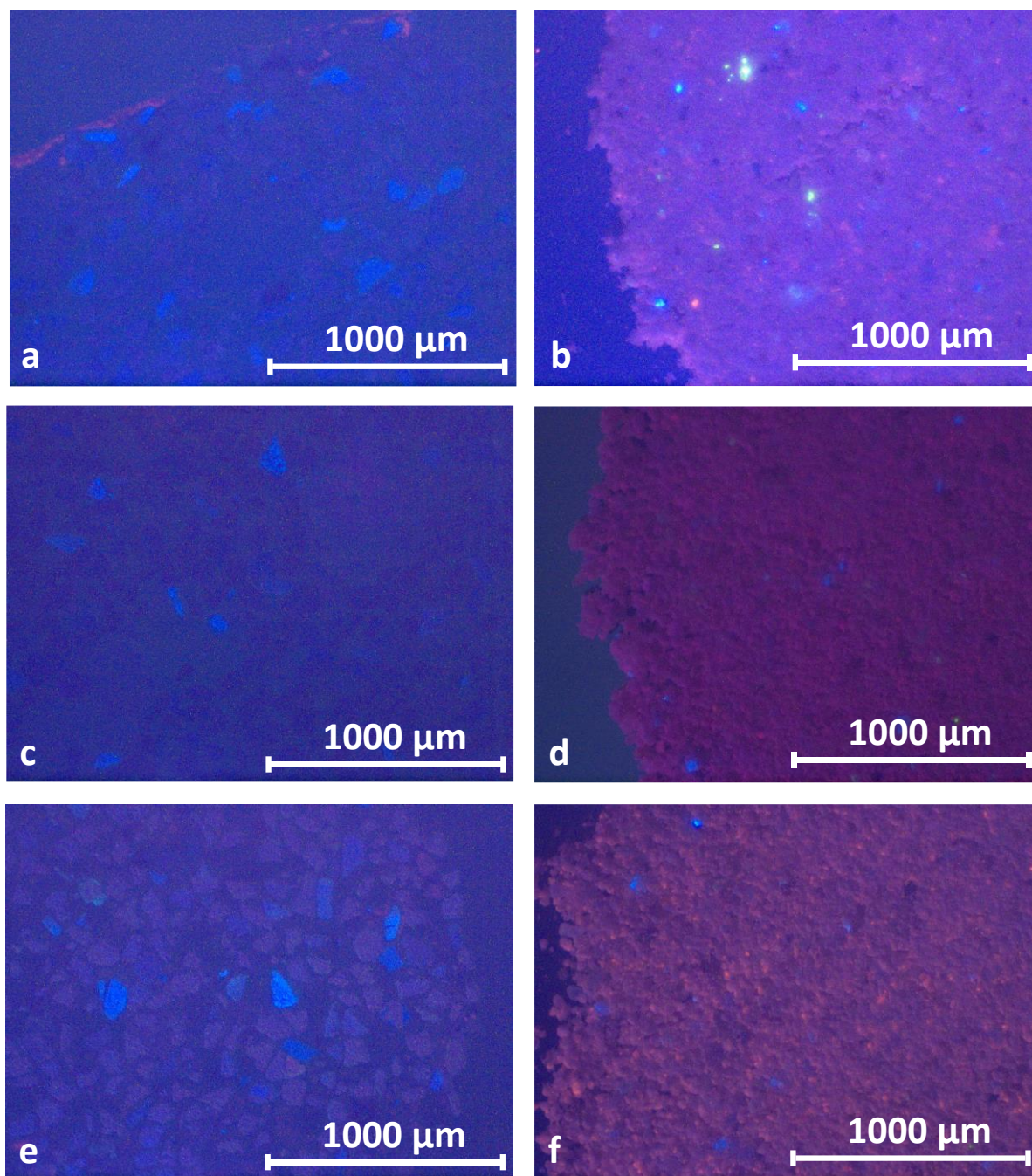
Figure 8: Characteristic cathodoluminescence images of a) the thin-section X2248 of KVH1, b) the powdered KVH1 plaster with particle size lower than 75 µm, c) the thin-section X2249 of KVH2, d) the powdered KVH2 pink plaster with particle size lower than 75 µm, e) the thin-section X2250 of KVH3, and f) the powdered KVH3 mortar with particle size lower than 75 µm.

Thin-section petrography

The beige plaster KVH1 (Figure 9 and Table 2) is very porous but in good state (no alteration observed). The lime inclusions are completely burned, and the aggregate doesn't contain any limestone grains. It might contain plant fibres (Figure 9e and 9f).
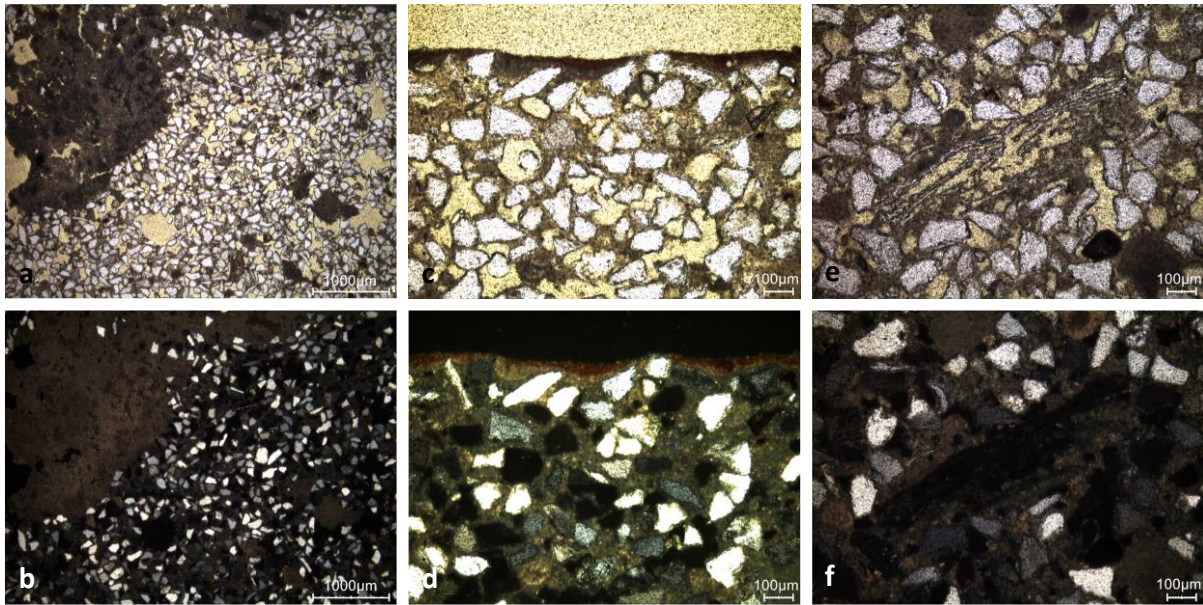
Figure 9: Representative photographs of the KVH1 thin-section X2248: a) overview image in plain polarised light (PPL); b) overview image in cross polarised light (XPL); c) PPL image showing the preparation layer and the red pigment layer; d) same image in XPL; e) PPL image with a possible plant fibre; f) same image in XPL.

Binder	Texture	micritic
	Lump state	completely burned
	Lump size	max 5 mm
	Lump frequency	numerous
Aggregate	Grain size	very fine to fine
	Mineralogy	pure siliceous sand (quartz, feldspar, mica, glauconite)
	Shape	subangular / subrounded
Appearance	Homogeneity	relatively heterogenous
	Macroporosity	high / medium
	Pore structure	irregular / often connected
Admixtures	Type	plant fibres?
Alteration	Type	-

Table 2: Main characteristics of the beige plaster KVH1 retrieved from the observations of the thin-section X2248.

The pink plaster KVH2 (Figure 10 and Table 3) is in good condition. It displays completely burned lime inclusions (Figure 10c and 10d) and a siliceous sand aggregate. It is less porous

compared to KVH1. Clay cutans are observed around quartz grains (Figure 10e) that are responsible for the pink colouration of the binder.
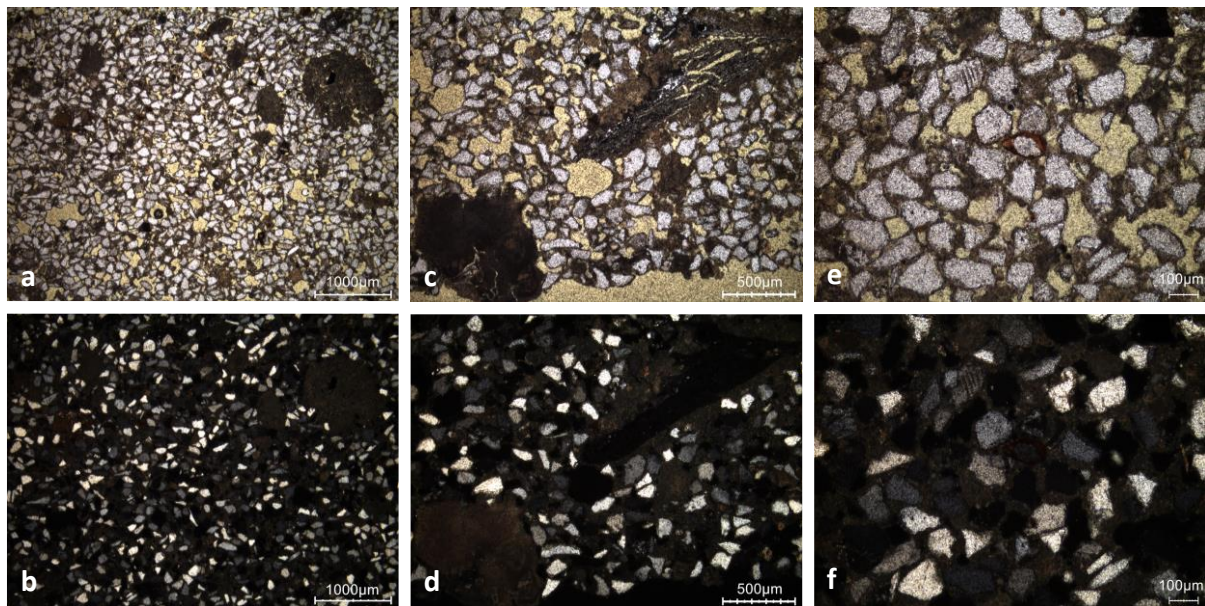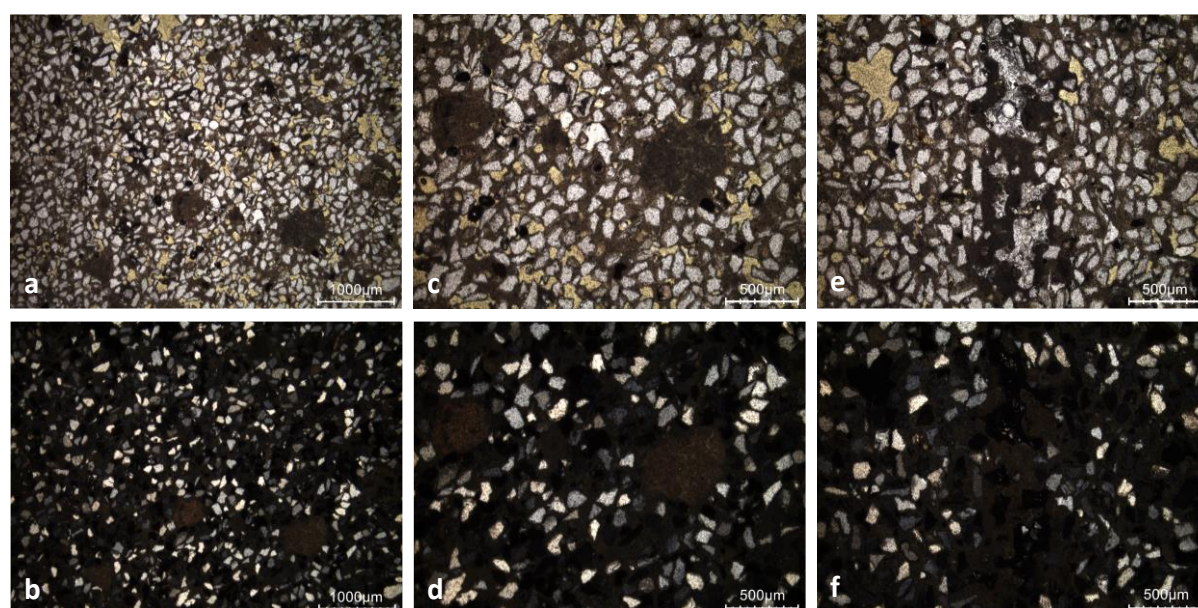

Figure 10: Representative photographs of the KVH2 thin-section X2248: a) overview image in PPL; b) overview image in XPL; c) PPL image showing completely burned lime inclusions; d) same image in XPL; e) PPL image with clay cutans around quartz grains; f) same image in XPL.

Binder	**Texture**	micritic
	Lump state	completely burned
	Lump size	max 1.8 mm
	Lump frequency	numerous
Aggregate	**Grain size**	very fine to fine
	Mineralogy	pure siliceous sand (quartz, feldspar, mica, glauconite)
	Shape	subangular / subrounded
Appearance	**Homogeneity**	relatively homogenous
	Macroporosity	medium
	Pore structure	irregular / sometimes connected
Admixtures	**Type**	-
Alteration	**Type**	-

Table 3: Main characteristics of the beige plaster KVH2 retrieved from the observations of the thin-section X2249.

The lime binder of KVH3 (Figure 11 and Table 4) is in good condition and there are no secondary calcite deposits in the macropores. Lime inclusions are regularly observed and have been completely burned. The aggregate used is a siliceous sand with sub-angular grains and do not contain calcareous fraction.

Figure 11: Representative photographs of the KVH3 thin-section X2250: a) overview image in PPL; b) overview image in XPL; c) PPL image showing completely burned lime lumps; d) same image in XPL; e) PPL image of an unidentified inclusion; f) same image in XPL.

| Binder	Texture	micritic
	Lump state	completely burned
	Lump size	max 882 μm
	Lump frequency	numerous
Aggregate	Grain size	very fine to medium
	Mineralogy	pure siliceous sand (quartz, feldspar, glauconite, mica)
	Shape	subangular / subrounded
Appearance	Homogeneity	relatively homogenous
	Macroporosity	medium
	Pore structure	irregular / sometimes connected
Admixtures	Type	-
Alteration	Type	-

Table 4: Main characteristics of the beige mortar KVH3 retrieved from the observations of the thin-section X2250.

### *Thermal analysis on whole samples*

The curves of the thermal analyses carried out on the whole samples (Figures 12-14) clearly show a large endothermic peak between around 650 and 780°C linked to the decarbonation of the lime binder. In the case of the two plaster, the endothermic peaks around 450 to 500°C could be explained by the dehydroxylation of clay fraction in the sand used. In the case of the mortar sample KVH3, the virtual absence of dehydroxylation peak at around 450-500°C confirms that the sand used is much less clayey than the one used for plaster. The quartz transition phase can be observed around 573-4°C (Rickard, Riessen, and Walls 2010) for all the samples. The apparent hydraulicity index (aHI) determined on the basis of the weight loss between 200 and ca. 650°C (usually attributed to water loss from calcium-silicate-hydrates-phases) was calculated from Figures 12-14, and is around 42 % for KVH1, 48% for KVH2, and 27 % for KVH3, indicating that the mortars KVH1 and KVH2 are very strongly hydraulic and KVH3 strongly hydraulic. However, the values obtained from the thermal analyses might not entirely reflect the reality since the mortars contain clay. Loss from structurally bound water of some clays takes place at a similar temperature to structurally bound water in hydraulic components (Middendorf et al. 2005). The amount of carbonates present in the mortars is around 17, 13 and 17 wt% for KVH1, KVH2 and KVH3, respectively.
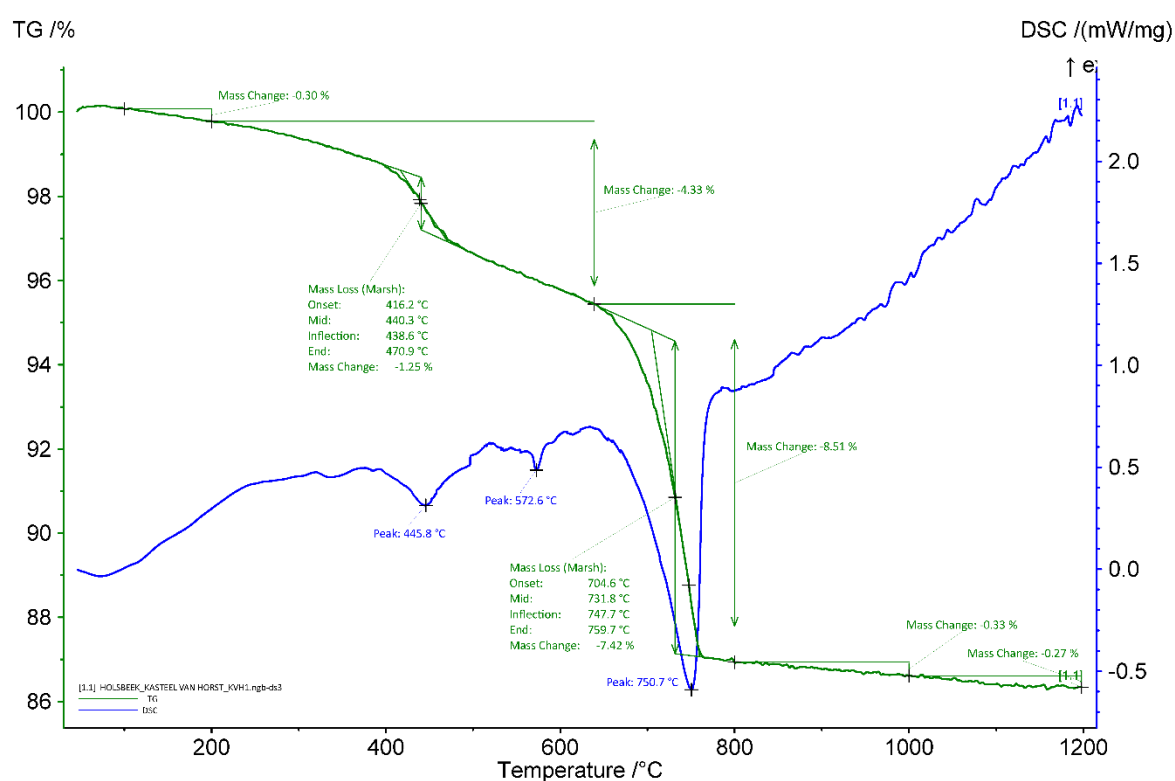
Figure 12: Coupled TG-DSC analysis of the plaster KVH1 upon heating to a temperature of 1200°C at a heating rate of 20°C/min under an inert atmosphere (He flushed at 50 ml/min). The weight loss determined by thermogravimetric analysis (TG, wt%, green curve) and the result of the differential scanning calorimetric analysis (DSC, mW/mg, blue curve) are both presented.
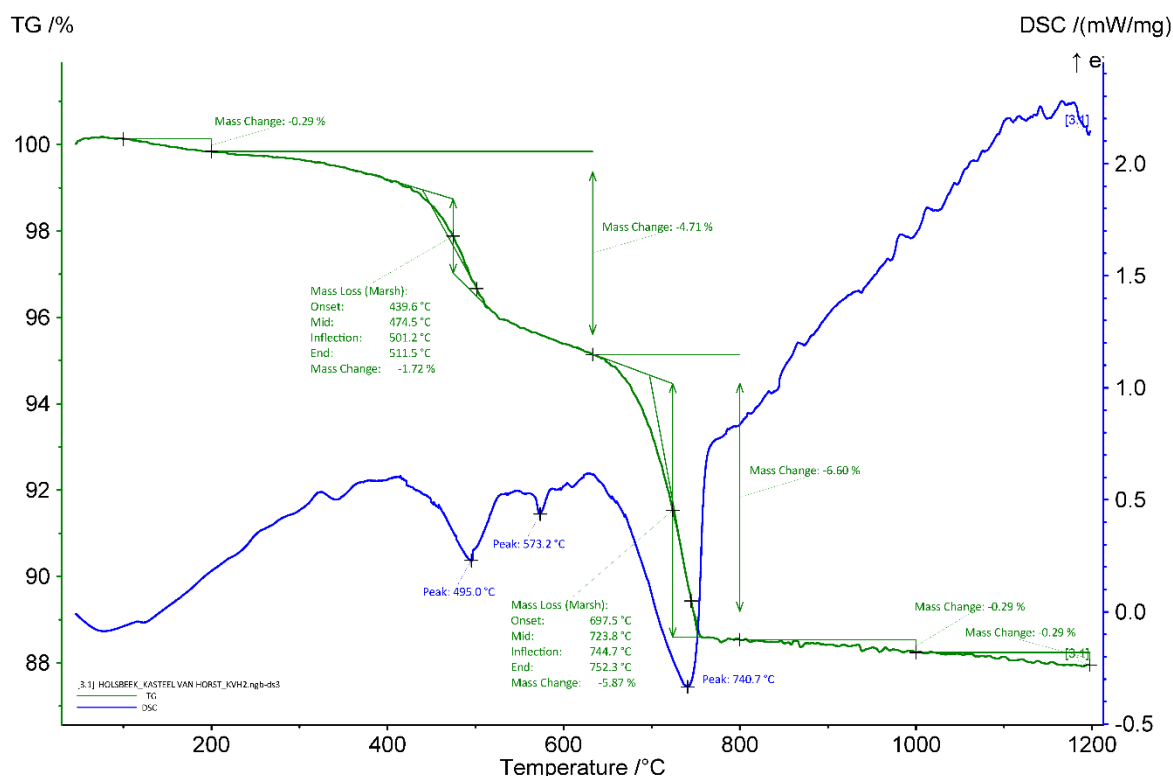
Figure 13: Coupled TG-DSC analysis of the plaster KVH2 upon heating to a temperature of 1200°C at a heating rate of 20°C/min under an inert atmosphere (He flushed at 50 ml/min). The weight loss determined by thermogravimetric analysis (TG, wt%, green curve) and the result of the differential scanning calorimetric analysis (DSC, mW/mg, blue curve) are both presented.
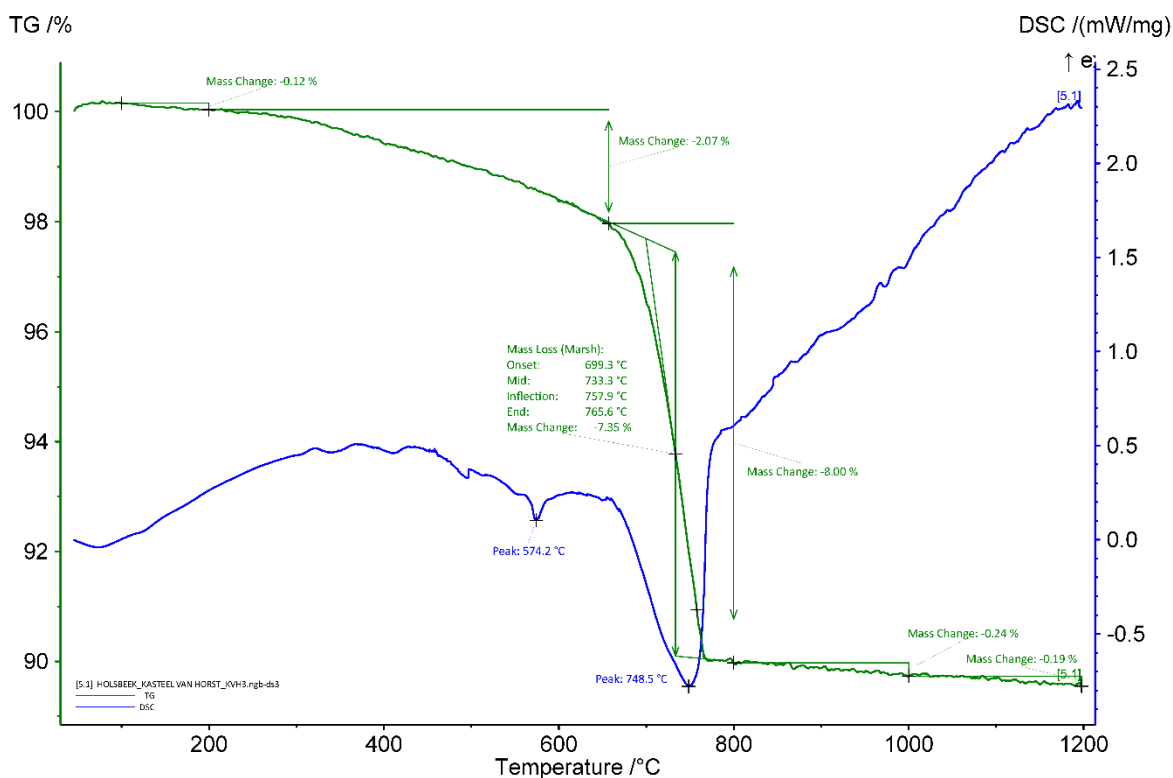
Figure 14: Coupled TG-DSC analysis of the bedding mortar KVH3 upon heating to a temperature of 1200°C at a heating rate of 20°C/min under an inert atmosphere (He flushed at 50 ml/min). The weight loss determined by thermogravimetric analysis (TG, wt%, green curve) and the result of the differential scanning calorimetric analysis (DSC, mW/mg, blue curve) are both presented.

X-ray diffraction (XRD)

X-ray diffraction analyses show the presence of quartz, calcite and K-feldspars (Figure 15).
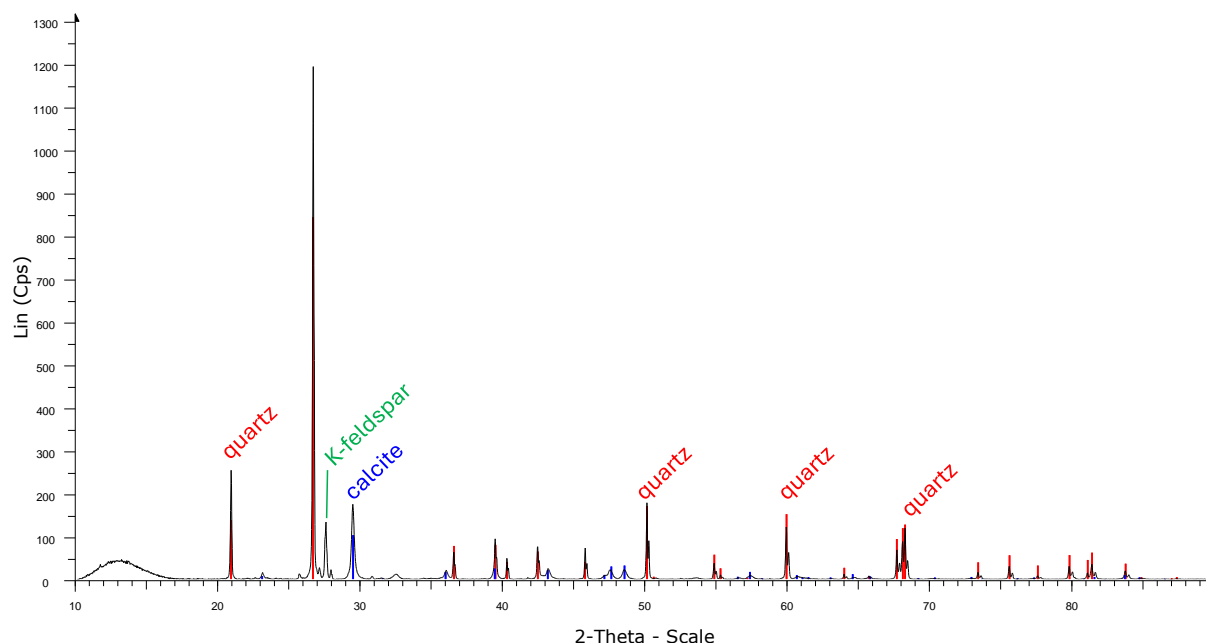
Figure 15: XRD diffractogram of KVH2 pink plaster.

Grinding/particle separation

For KVH1, the pink paint layer on top of the plaster and the red residues from bricks on the other side were scratched away before grinding. Some grey fragments were removed while grinding and woody/straw fragments were found within the ground particles. The particles with a size < 75 µm were sparse but sufficient to perform radiocarbon dating.

For KVH2, red bricks residues on surface were scratched away before grinding and grey and white angular fragments of possible limestone inclusions were removed while grinding. The presence of black shinny fragment was observed.

The red residues from bricks present on the surface of KVH3 were also scratched away.

Thermal analysis on powders with particle size <75 µm

The curves of the thermal analyses carried out on the powder used for dating (Figures 16-18) also clearly show a large endothermic peak between around 650 and 780°C linked to the decarbonation of the lime binder. The exothermic peaks at around 800°C are most probably due to crystalline phase transition of clay, which are only visible in the binder-concentrated powder. The aHI of the powders with particles < 75 µm, determined on the basis of the weight loss between 200 and ca. 650°C, are 42 % for KVH1, 50 % for KVH2, and 27 % for KVH3. The obtained values on powders are thus the same than those on whole samples. The quantity of carbonates is higher in the powders compared to the whole samples since a large part of the sand is removed (43, 40 and 46 wt% for KVH1, KVH2 and KVH3, respectively). Indeed, no

quartz was detected in the powders. For KVH1 (Figure 16), a peak around 466°C is observed and might be due to the release of water from calcium hydroxide (Moropoulou, Bakolas, and Bisbikou 1995; Klimesch and Ray 1996) indicating that the mortar did not fully carbonated. This was not observed for the whole mortar samples. It was probably present in too low concentration to be noticeable. Another peak is also observed for KVH1 at 645°C and could be related to the presence of a different form of carbonate possibly coming from the hydraulic phases. For KVH2 (Figure 17), a large peak is observed around 511°C and was not identified, it is possibly due to the presence of clay. The large peak around 800°C is a measurement artefact.
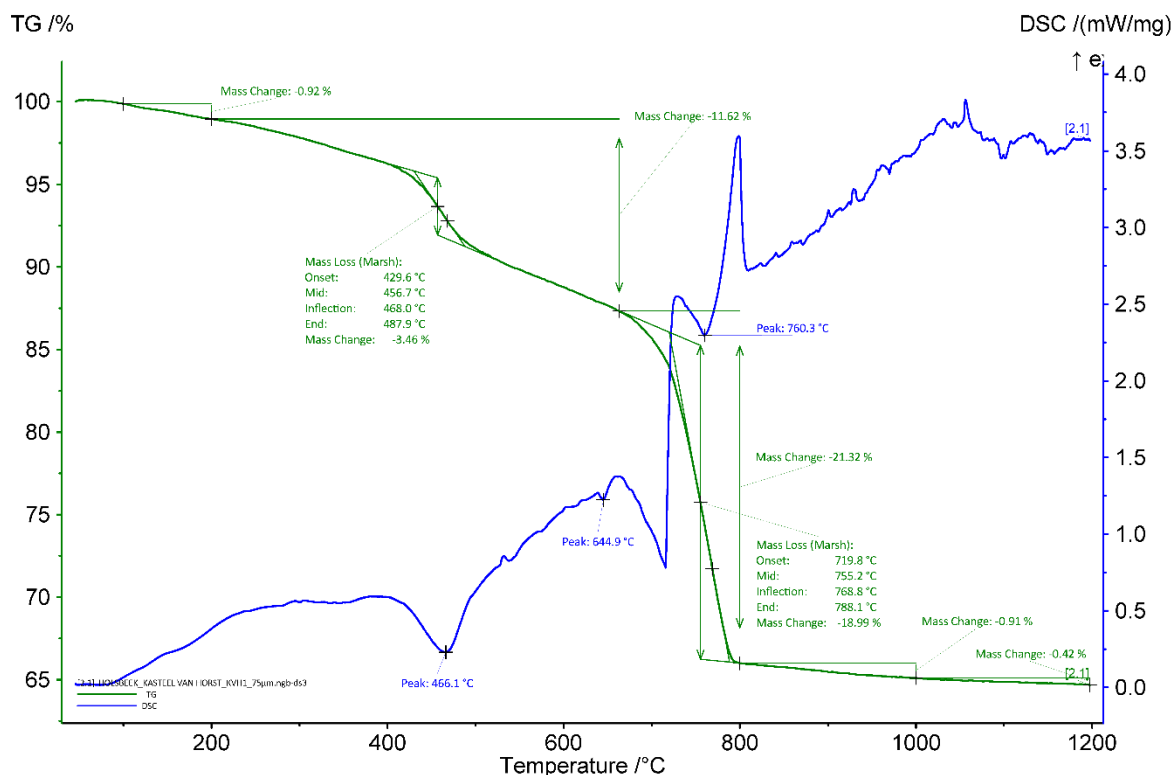
Figure 16: Coupled TG-DSC analysis of the powdered primer KVH1 with particle size < 75 μm upon heating to a temperature of 1200°C at a heating rate of 20°C/min under an inert atmosphere (He flushed at 50 ml/min). The weight loss determined by thermogravimetric analysis (TG, wt%, green curve) and the result of the differential scanning calorimetric analysis (DSC, mW/mg, blue curve) are both presented.
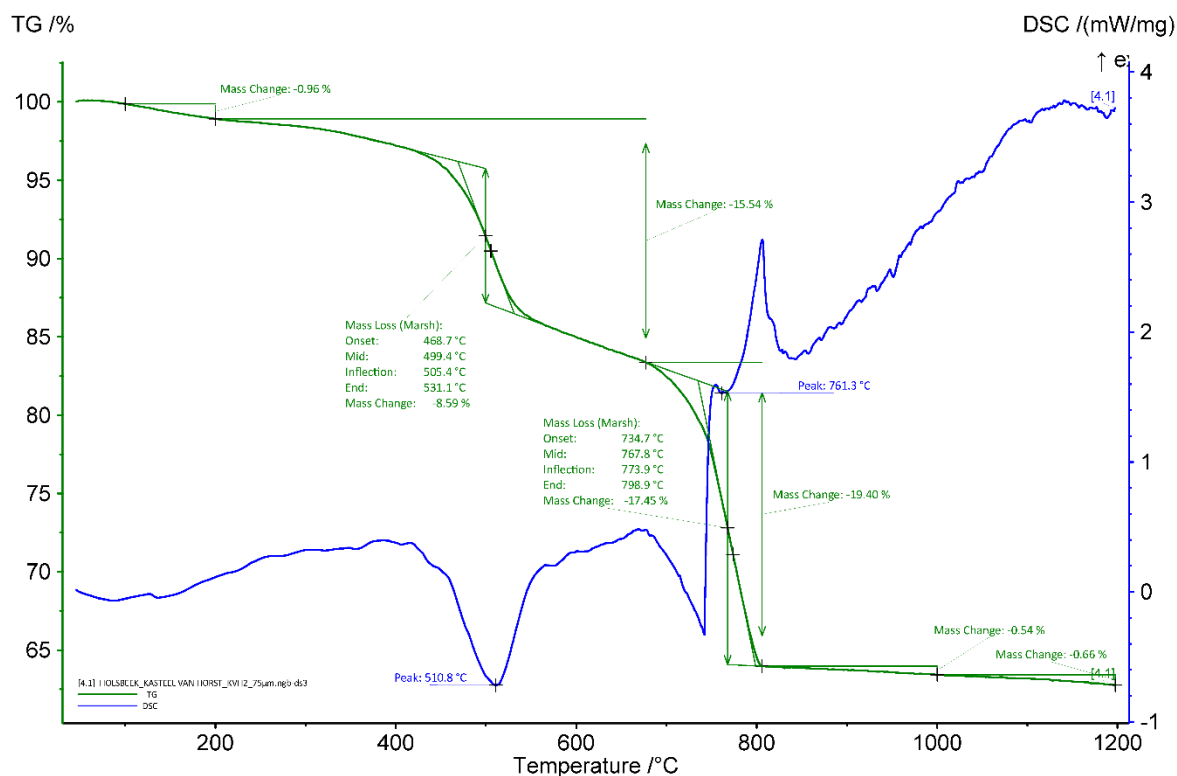
Figure 17: Coupled TG-DSC analysis of the powdered primer KVH2 with particle size < 75 µm upon heating to a temperature of 1200°C at a heating rate of 20°C/min under an inert atmosphere (He flushed at 50 ml/min). The weight loss determined by thermogravimetric analysis (TG, wt%, green curve) and the result of the differential scanning calorimetric analysis (DSC, mW/mg, blue curve) are both presented.
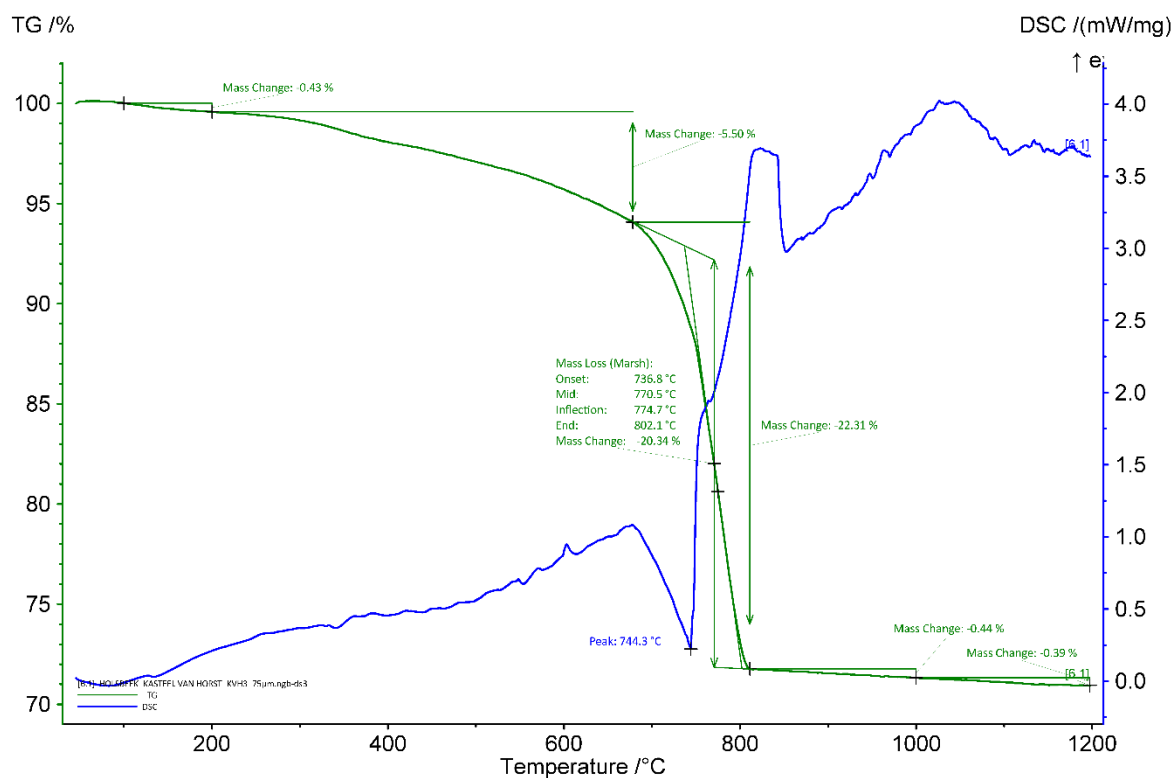
Figure 18: Coupled TG-DSC analysis of the powdered mortar KVH3 with particle size < 75 μm upon heating to a temperature of 1200°C at a heating rate of 20°C/min under an inert atmosphere (He flushed at 50 ml/min). The weight loss determined by thermogravimetric analysis (TG, wt%, green curve) and the result of the differential scanning calorimetric analysis (DSC, mW/mg, blue curve) are both presented.
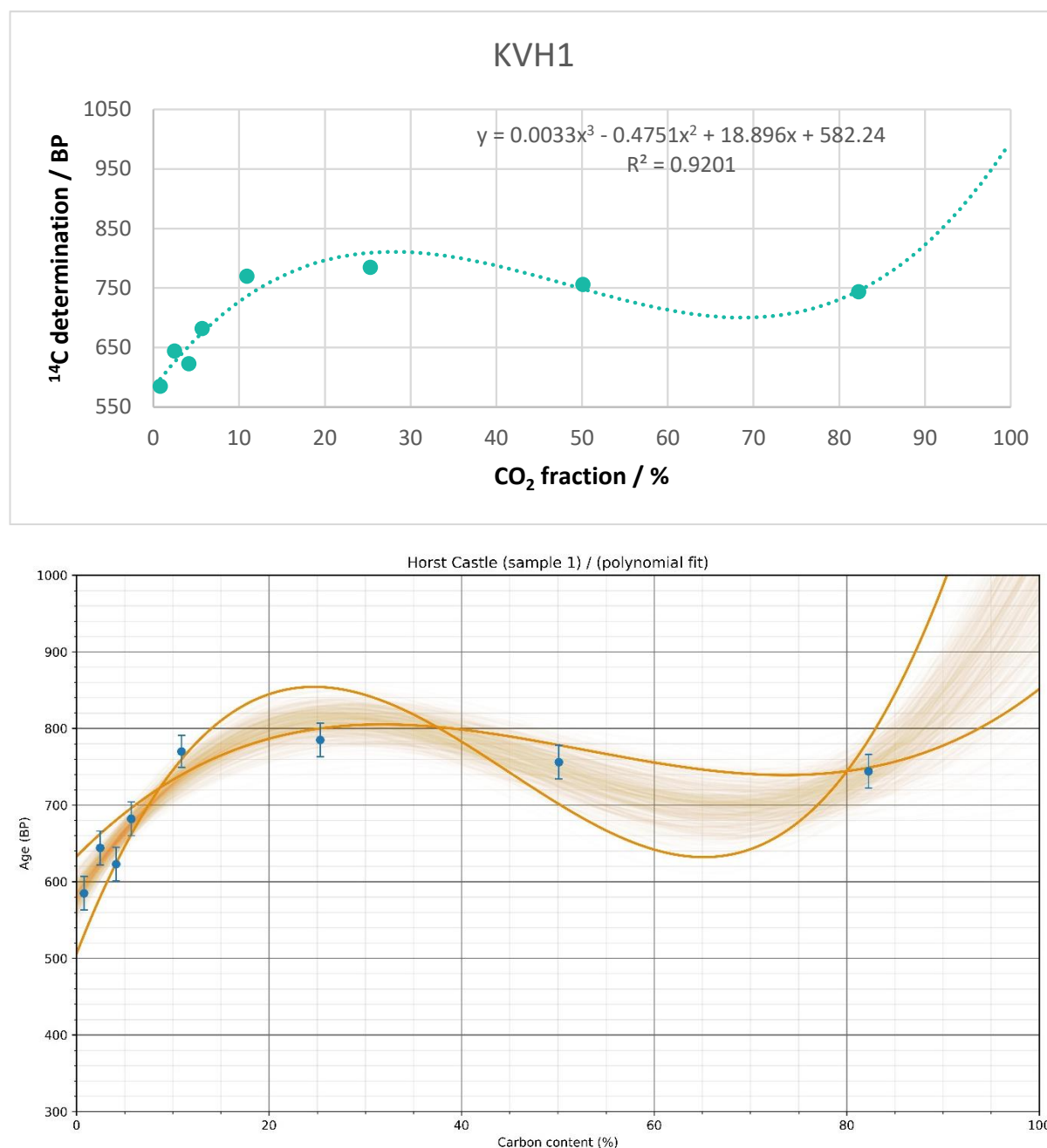
Radiocarbon results

The test prior to the CO_2 extraction revealed a good amount of carbon (Table 5) in the samples (~6 or 7 %). A relatively low amount of powder <75 μm was necessary for the carbon extraction (~1 g).
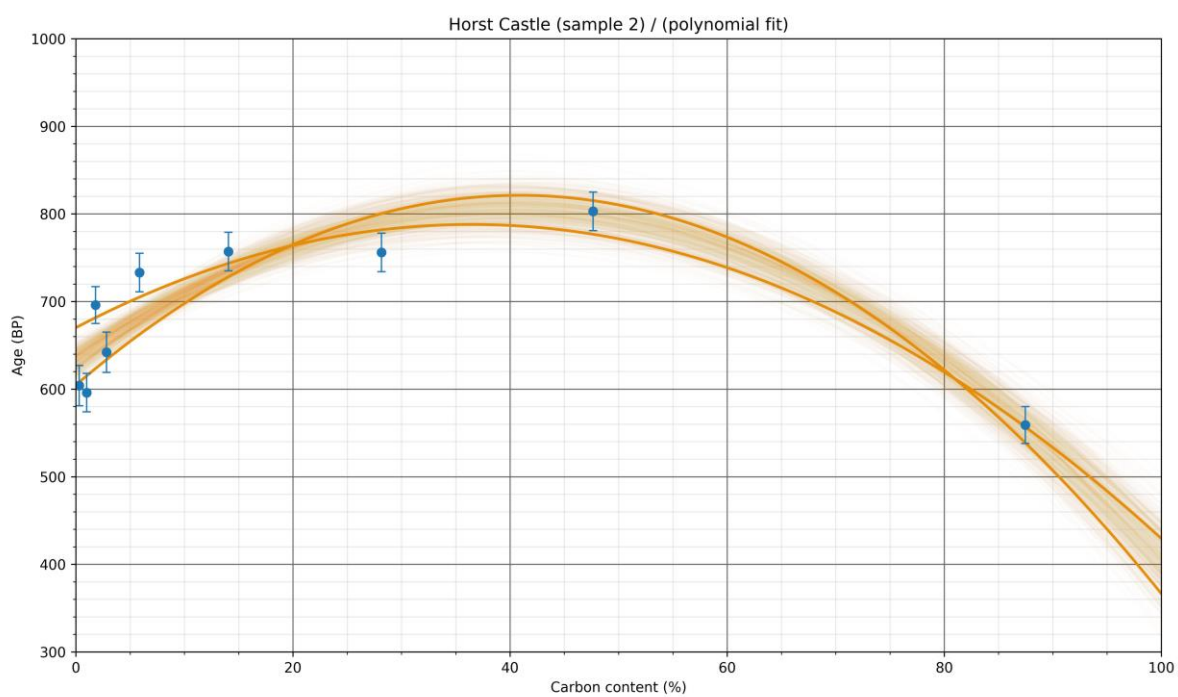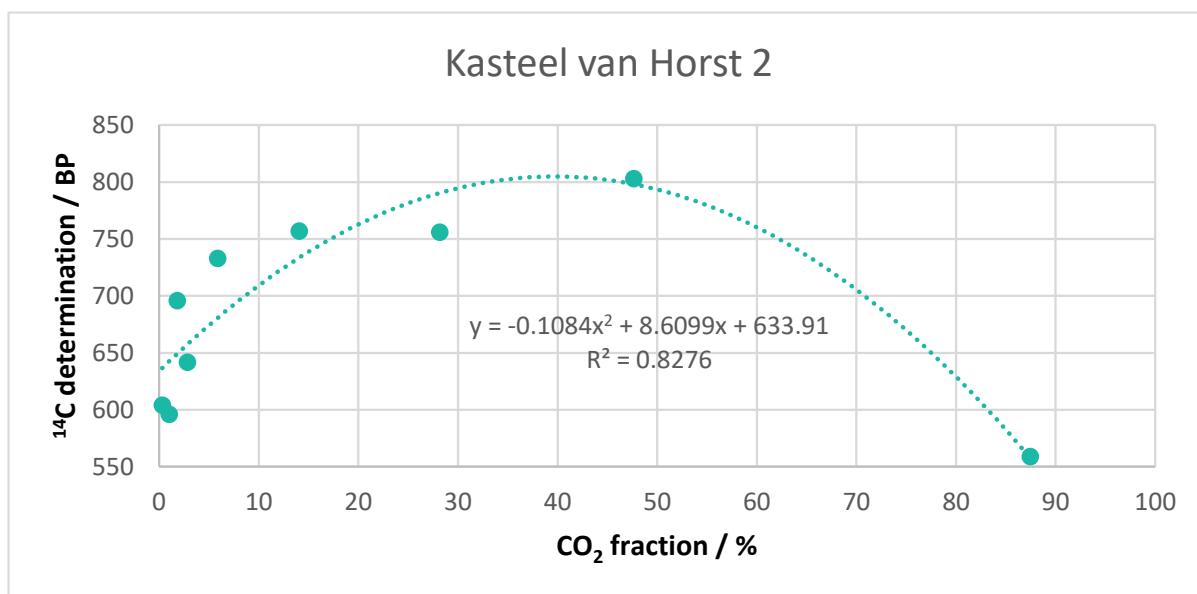
| RICH	Sample type	Method	C (%)	σ (%)	m (g)	Age BP extrapolated	Calibrated date (oxcal - 95.4%)	Age BP extrapolated	Calibrated date (oxcal - 95.4%)	Age BP extrapolated with stat	Calibrated date (oxcal - 95.4%)	Age BP average extrapolated	Calibrated date (oxcal - 95.4%)	Reliability of dating
31022 (KVH1)	Donjon, level +1 - beige plaster	HCl (8 fractions)	5.84	1.592	0.95	-	-	582 ± 22	1320-1410 calAD	582.2 ± 15.9	1319-1408 calAD	582 ± 22	1320-1410 calAD	☑
30768 (KVH1)	Plant material found inside plaster	HCl	28.9	-	0.00135	727 ± 27	1231-1379 calAD	-	-	-	-	-	-	☑
31442 (KVH2)	Donjon, level +2 - pink plaster	HCl (8 fractions)	6.78	0.957	1.52	-	-	634 ± 22	1300-1400 calAD	633.7 ± 10.7	1299-1393 calAD	634 ± 22	1300-1400 calAD	☑
31490 (KVH3)	Donjon, level +2 - bedding mortar	HCl (8 fractions)	6.28	0.605	0.95	-	-	447 ± 23	1430-1470 calAD	431.6 ± 15.4	1436-1471 calAD	447 ± 23	1430-1470 calAD	☒

Table 5: Radiocarbon result

The radiocarbon results for plasters KVH1 and KVH2 are fairly consistent with the results for the plant material found inside KVH1 and with the presumed date (Table 5 & Figure 19 & 20). The result for the KVH3 bedding mortar (Table 5 & Figure 21) is younger than the KVH2 plaster, which was taken from the same room. At first sight, this is counter-intuitive, but it may be explained by the fact that the masonry was directly covered by the plaster, which delayed the carbonation process of the mortar.

Figure 19: Radiocarbon results for the powdered KVH1 pink plaster with particles < 75 μm as a function of the CO_2 fraction (the graph at the bottom shows the statistic on the results).

Kasteel van Horst 2

$y = -0.1084x^2 + 8.6099x + 633.91$
$R^2 = 0.8276$

Horst Castle (sample 2) / (polynomial fit)

Figure 20: Radiocarbon results for the powdered KVH2 beige plaster with particles < 75 μm as a function of the CO_2 fraction (the graph at the bottom shows the statistic on the results).
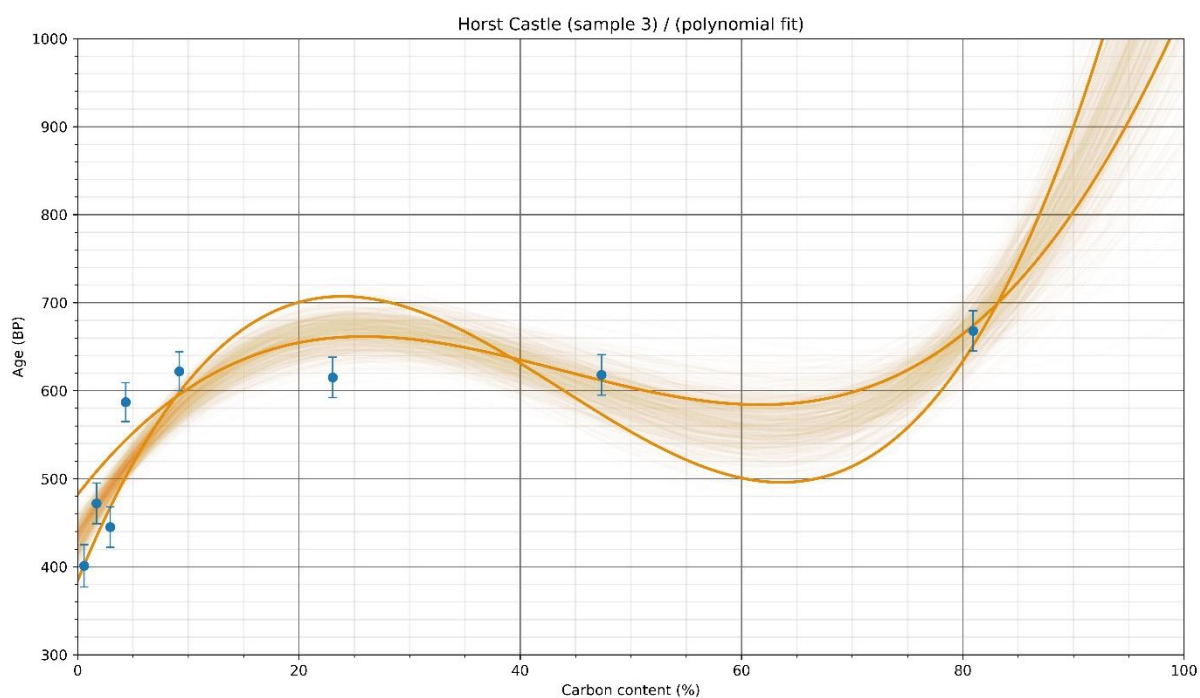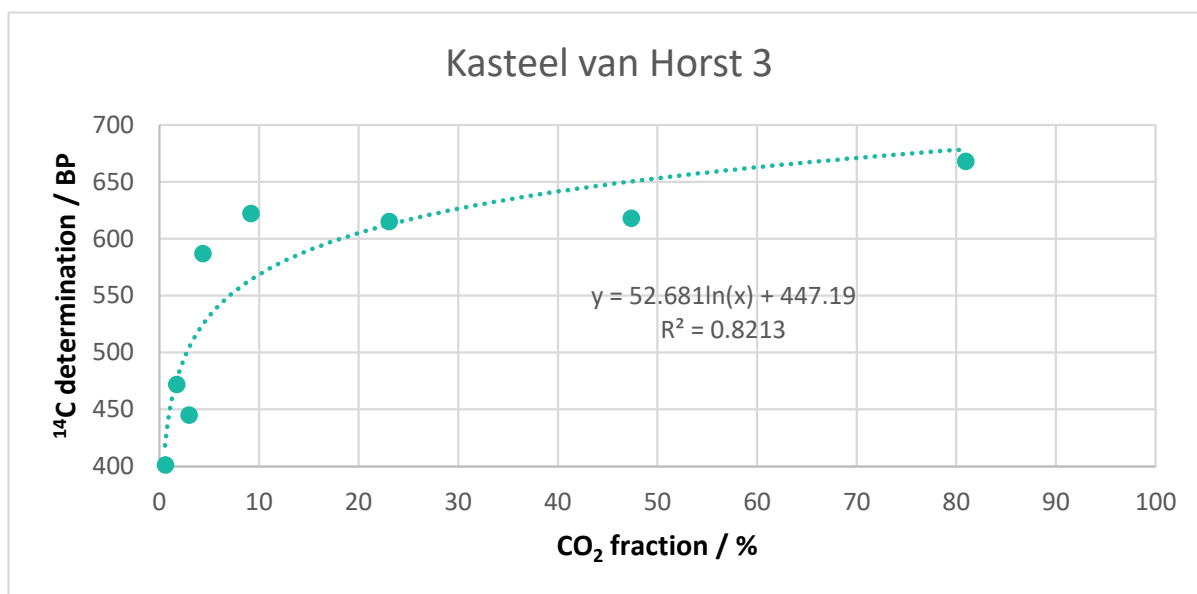
Figure 21: Radiocarbon results for the powdered KVH3 bedding mortar with particles < 75 μm as a function of the CO_2 fraction (the graph at the bottom shows the statistic on the results).

Conclusions

In the case of Horst Castle, radiocarbon dating of the lime binder in the plasters used to support the wall paintings has confirmed that these primers were applied during the last quarter of the 14th century. Assuming that the wall paintings were painted at the same time, they would therefore constitute the original decoration of the donjon tower, as the archaeologists thought. This case study also shows that in order to date the construction of a wall covered with a plaster assumed to be original, it may be worth dating the plaster in addition to the mortar used to lay the masonry, as the latter may have been delayed in hardening by several decades.

Bibliography

Doperé, F., Ubregts, W. (1991). *De donjon in Vlaanderen*. Leuven University

Press.Herremans, E. (2021). *Horst castle: A translation into the 21st century*.

https://documentserver.uhasselt.be//handle/1942/35344

Study of mortars from Park abbey (Leuven) for the BRAIN 2.0 PalC project

Context of the site

Park Abbey (Abdij van Park) is a Premonstratensian abbey in Belgium, at Heverlee just south of Leuven, in Flemish Brabant. It was founded in 1129 by Duke Godfrey "the Bearded", who possessed an immense park near Leuven and had invited the Premonstratensians to take possession of a small church he had built there.

Material

In the context of the building archaeological investigations conducted in the east wing of Park Abbey in Heverlee, Joke Lagaert from Patrimonium Research Consulting bv sent a sample of white mortar from the south facade of the former south transept. The presumed historical date is the 13th-century (ca. 1225-1228).

Results & Discussion

Macroscopic descriptions

The main colour of the sample is light beige/white (Figure 1) tending towards white (10YR 8/1) according to the Munsell soil colour charts. White inclusions cannot be distinguished from the binder. It is very fragmented, most of the pieces measure less than 2 mm. Red fragments might come from bricks and flat grey fragments (white other side) were observed.


Figure 1: Mortar sample from the south facade of the former south transept of Park Abbey in Heverlee

Fourier transform Infrared (FTIR) spectroscopy on inclusions & binder

The binder (white, Figure 2) mainly contains calcium carbonates (calcite and aragonite) with very few silicates. The red fragments suspected to come from bricks are made of silicates including quartz and clay in addition to nitrates and gypsum. The spectrum of the flat grey fragments exhibits the vibrational features of carbonates (calcite & aragonite) with silicates including clay, nitrates, gypsum and organic matter.
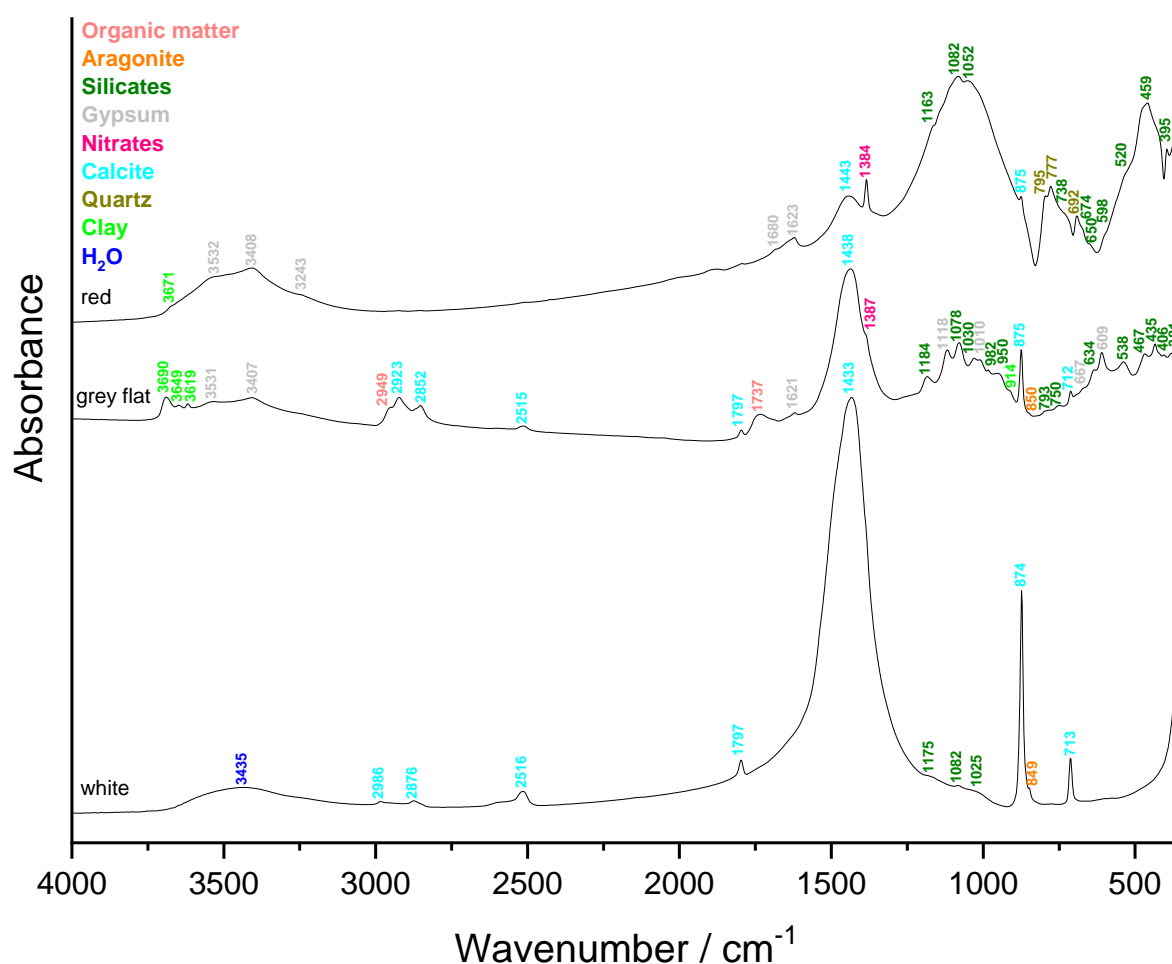
Figure 2: FTIR spectra obtained on the inclusions and binder (white) of the mortar sample.

Binder:sand ratio

The calculated binder:sand ratio using a bulk density of 1.35 kg/dm^3 for the sand and 0.575 kg/dm^3 for the lime is 1:0.05 (or 20:1) in volume unit, which suggests that the mortar virtually contains no aggregate.

	OO.0.8 Trapzall
Sample weight (g)	1.9
Crucible weight (g)	18.3
Weight calcined (g)	18.5
%ins	**10.7**

Table 1: Percentage of insoluble residue

Cathodoluminescence

The thin section of the sample was covered by a glass slide preventing to perform cathodoluminescence observations. Only the powdered sample with particle size lower than 75 μm was observed (Figure 3). Mainly the red tile binder is observed with a few bright green plagioclase grains and a bright red few limestone fragments.
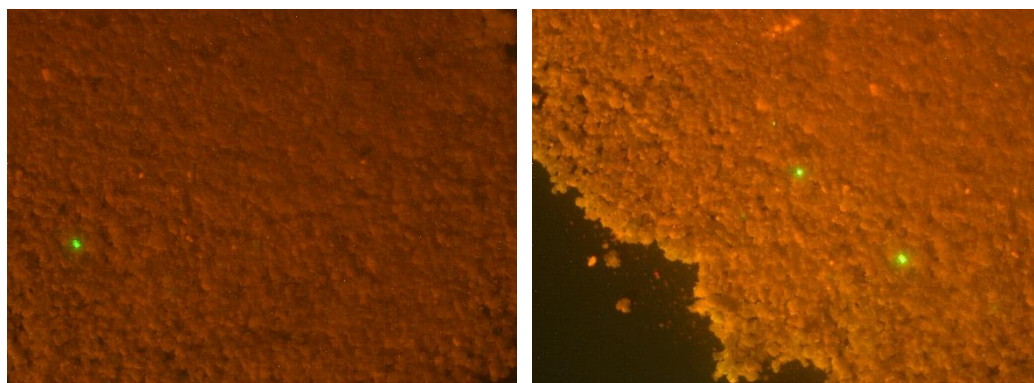

Figure 3: Characteristic cathodoluminescence images of the powdered sample with particle size lower than 75 μm.

Thin-section petrography

The mortar consists almost exclusively of binder (Figure 3) as previously observed with the FTIR analyses and the binder:sand ratio. Two fragments of plant fibres can be recognised in the thin-section (Figure 3, 4a & b). A single limestone fragment, measuring 300 μm long, can be found in the thin-section. The mortar shows several microcracks, but they do not appear to be covered by secondary carbonate deposits (Figure 3). Lime lumps, with dimensions of up to 4 mm in diameter, occur frequently in the mortar (Figure 3). Unburned, or not completely burned limestone grains can be recognised here and there in the mortar (Figure 4c & d). Most probably these are limestone fragments originating from the limestone used to produce the mortar. The fact that the calcite crystals (sparite) are much larger than those of the binder (micrite) means that there is little chance that these limestone pieces could affect the ^{14}C content of the first CO_2 fractions measured during progressive acid hydrolysis. No aggregate was recovered in the mortar. Rare quartz grains can still be recognised in the binder, but these most probably correspond to impurities in the limestone used for lime production or to dust from the worksite or dirt on the tools used.
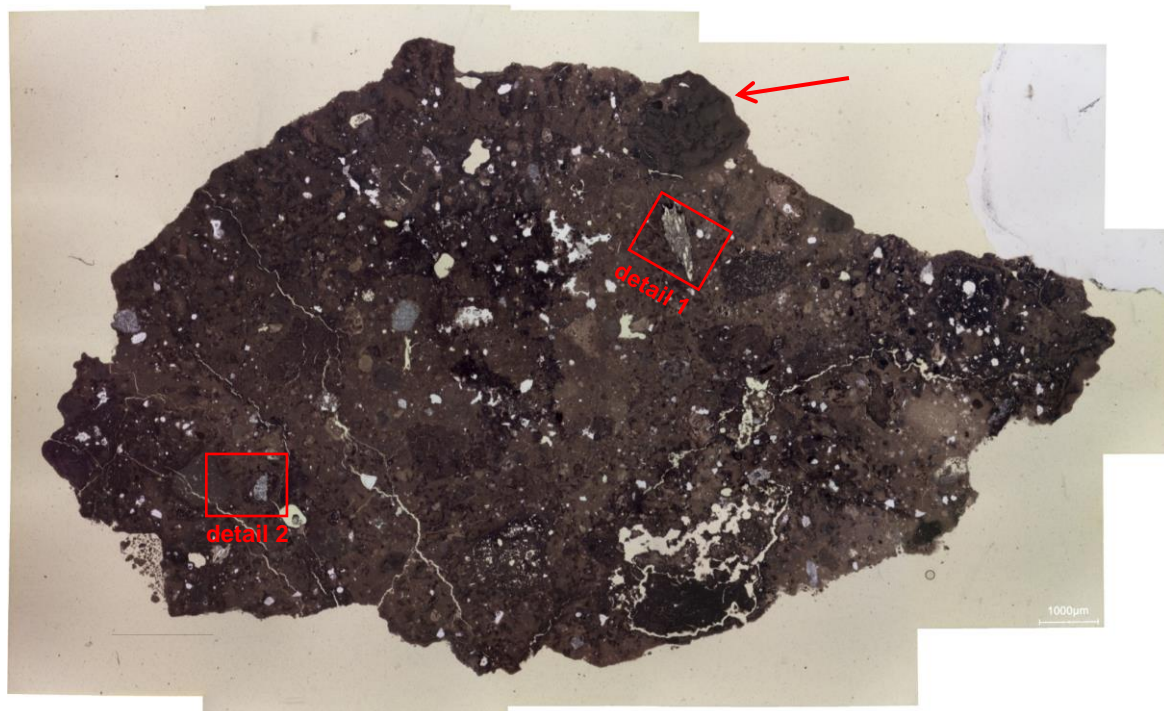
Figure 3: Photomicrograph of the thin-section X2421.
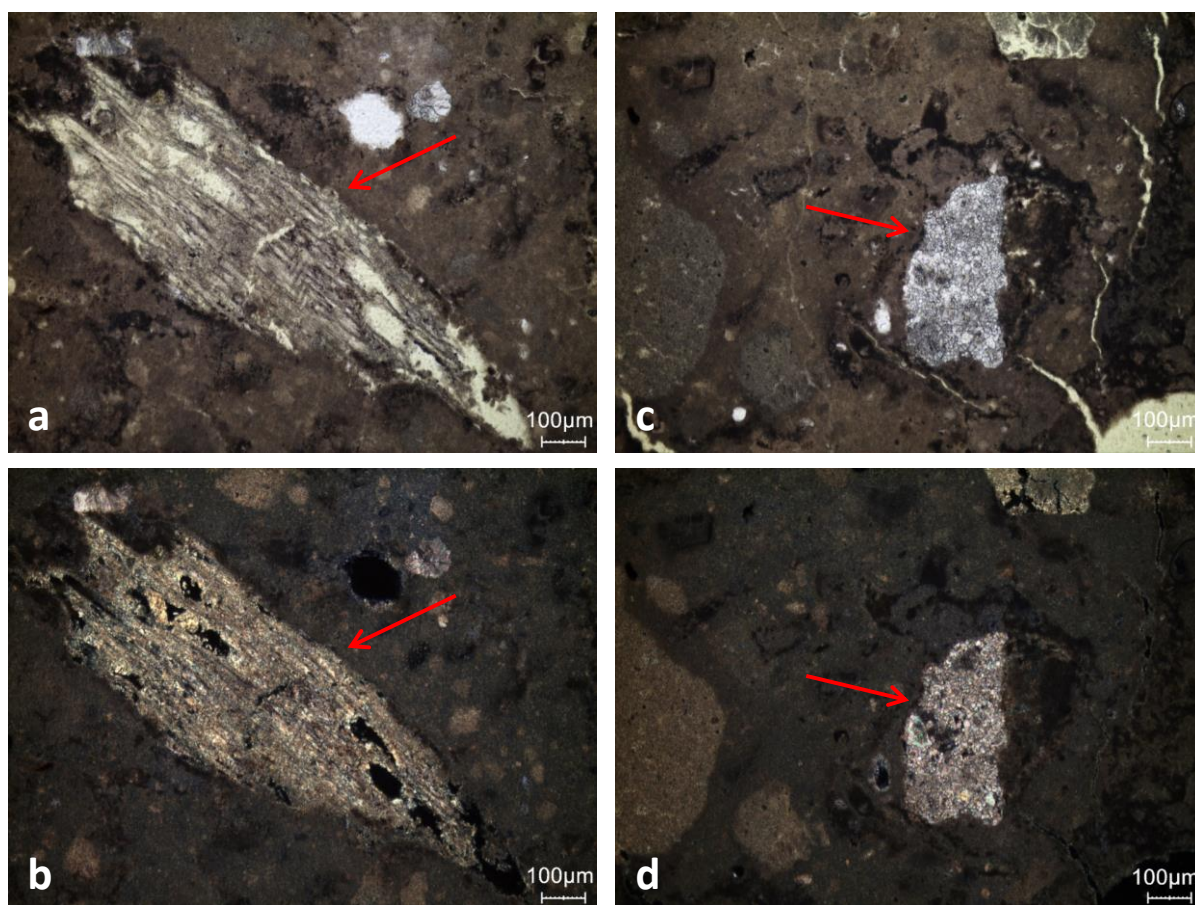
Figure 4: Representative photographs of the thin-section X2421: a) detail 1 on Figure 3 showing a plant fibre in plain polarised light (PPL); b) same image in cross polarised light (XPL); c) PPL image showing detail 2 on Figure 3 with a unburned limestone fragment; and d) same image in XPL.

Thermogravimetric analysis (TGA) on whole samples

The results of the thermal analysis (Figure 5) indicate the use of an air hardening lime mortar (= non-hydraulic lime mortar). Indeed, the apparent hydraulicity index is around 8 %. The amount of carbonates present in the mortar is around 89 wt%. No gypsum nor quartz were detected.
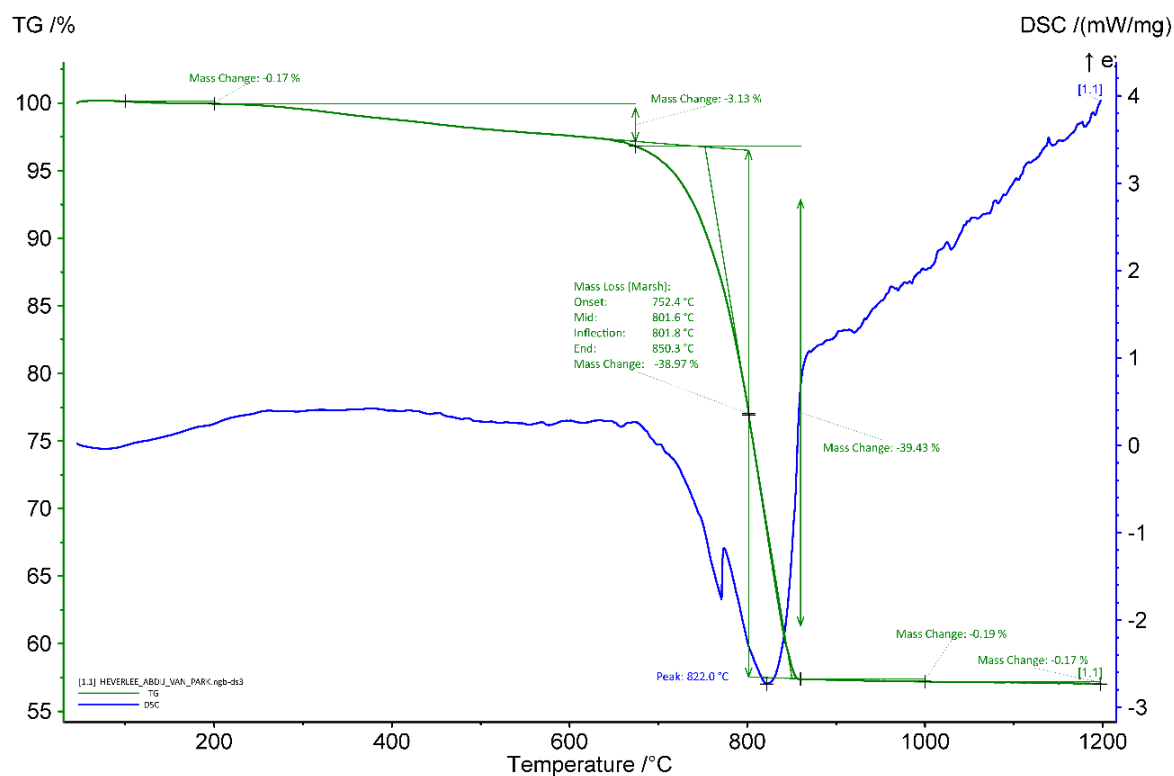
Figure 5: Coupled TG-DSC analysis of the sample upon heating to a temperature of 1200°C at a heating rate of 20°C/min under an inert atmosphere (He flushed at 50 ml/min). The weight loss determined by thermogravimetric analysis (TG, wt%, green curve) and the result of the differential scanning calorimetric analysis (DSC, mW/mg, blue curve) are both presented.

Grinding/particle separation

Red, grey and flat fragments where removed before grinding.

Radiocarbon results

The test prior to the CO_2 extraction revealed a high amount of carbon (Table 2) as expected from the previous analyses. A black fragment that was possibly identified as a charcoal fragment was present in the bag and it was pre-treated for dating (Table 2).

RICH	Sample type	Method	C (%)	σ (%)	m (g)	Age BP	Calibrated date (oxcal - 95.4%)	Age BP extrapolated	Calibrated date (oxcal - 95.4%)	Age BP extrapolated with stat	Calibrated date (oxcal - 95.4%)	Age BP average	Calibrated date (oxcal - 95.4%)	Reliability of dating
34667	possible charcoal	HCl 1%	26,89	-	0,00299	25871 ± 108	28368-28019 calBC	-	-	-	-	-	-	☒
34369	mortar < 75 µm	9 fractions	8,28	0,02	1,176	-	-	833 ± 21	1174-1265 calAD	832.8 ± 13.1	1179-1263 calBC	(first 3 fractions) 848 ± 13	1166-1253 calAD	☑

Table 4: Radiocarbon results

The black fragment is not a piece of charcoal because the date obtained is way too old (~28 000 calBC) and might rather be a piece of coal. The extrapolated date, the extrapolated date with statistic and the average date obtained for the mortar sample (1166 to 1265 calAD) all fall within the expected historical date (13th century).
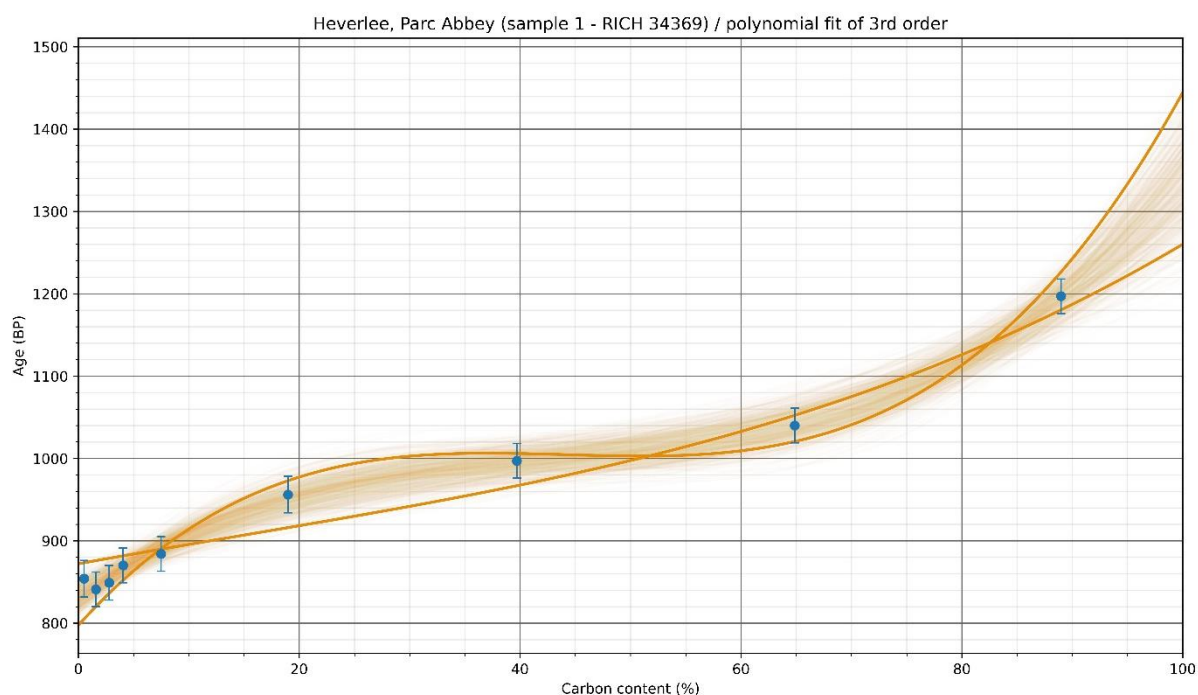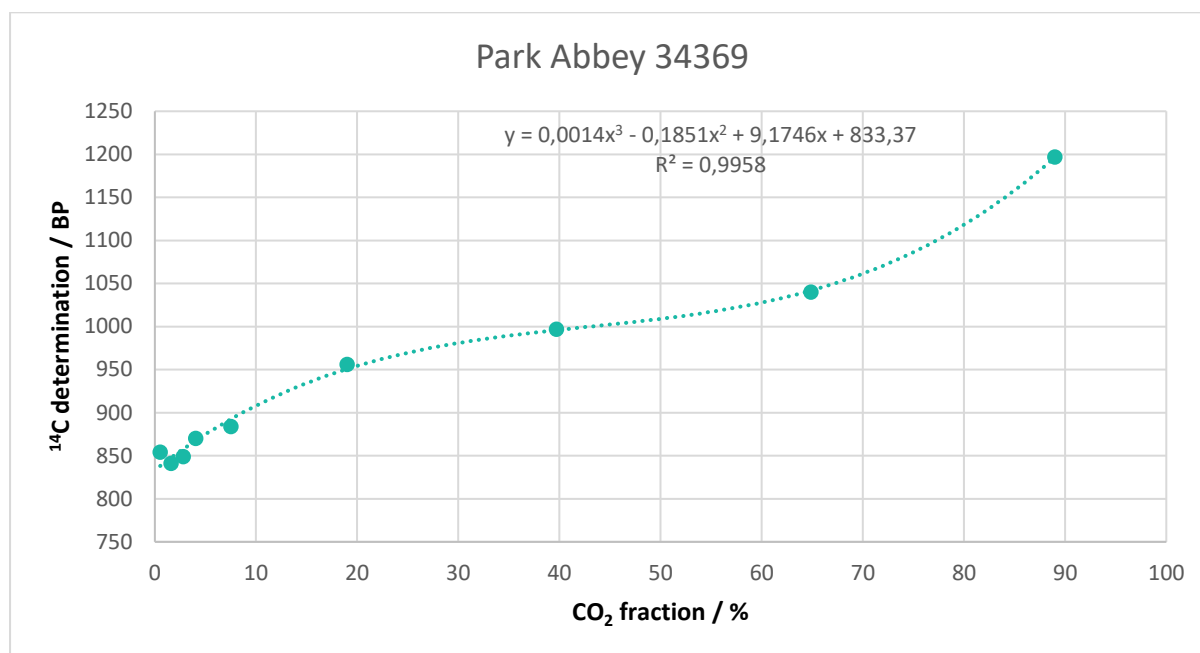
Figure 6: Radiocarbon results for the powdered mortar with particles < 75 μm as a function of the CO_2 fraction (the graph at the bottom shows the statistic on the results).

Conclusions

The analysis of the mortar (sample OO.0.8, stair hall) from the south facade of the former south transept of Park Abbey in Heverlee showed that the lime binder, on which radiocarbon dating was carried out, is in good condition. The mortar shows several microcracks, but they do not

seem to be covered by secondary carbonate deposits. Unburned, or not fully burnt limestone grains can be recognised here and there in the mortar. The fact that the calcite crystals of these limestone grains are much larger than those of the binder means that there is little chance that these limestone fragments could influence the ^{14}C content of the first CO_2 fractions measured during progressive acid hydrolysis. Based on the analyses, it can be inferred that the preserved mortar sample provides a reliable radiocarbon dating corresponding to the presumed historical date (13th century).